

Numerical and Physical Modelling of Aerated Skimming Flows over Stepped Spillways



UNIVERSITY OF LEEDS

Jacob Christian van Alwon

University of Leeds

School of Civil Engineering

Submitted in accordance with the requirements for the degree of

Doctor of Philosophy

December, 2019

Intellectual Property Statement

The candidate confirms that the work submitted is his own, except where work which has formed part of jointly authored publications has been included. The contribution of the candidate and the other authors to this work has been explicitly indicated below. The candidate confirms that appropriate credit has been given within the thesis where reference has been made to the work of others.

The work presented in Chapters 3 and 6 of this thesis has appeared in publication as follows:

van Alwon, J., Borman, D., Sleigh, A. and Kapur, N. 2017. Experimental and numerical modelling of aerated flows over stepped spillways. In: *Proceedings of the 37th IAHR World Congress, Kuala Lumpur, Malaysia*. 13-18th August.

I was responsible for the design of the experimental stepped spillway, and carried out all experimental and numerical modelling, as well as data processing and preparation of the manuscript. D. Borman, A. Sleigh and N. Kapur provided advice on experimental and numerical approaches and D. Borman contributed to editing the manuscript.

The work presented in Chapter 5 of this thesis has been accepted for publication and is due to appear in publication as follows:

van Alwon, J., Borman, D., Matos, J., Sleigh, A. and Kapur, N. 2019. Prediction of air entrainment in skimming flow over stepped spillways using numerical methods. In: *Proceedings of the 38th IAHR World Congress, Panama City, Panama*. 1-6th September.

I was responsible for all numerical modelling, numerical data processing and preparation of the manuscript. Matos, J provided the experimental data, D. Borman, A. Sleigh and N. Kapur provided advice on numerical approaches and D. Borman and Matos, J contributed to editing the manuscript.

This copy has been supplied on the understanding that it is copyright material and that no quotation from the thesis may be published without proper acknowledgement.

The right of Jacob Christian van Alwon to be identified as Author of this work has been asserted by him in accordance with the Copyright, Designs and Patents Act 1988.

© 2019 The University of Leeds and Jacob Christian van Alwon.

ACKNOWLEDGEMENTS

Firstly, I would like to thank my supervisors, especially Duncan Borman, for their help and advice throughout this project. I have thoroughly enjoyed working with them during my research project. I would also like to extend my gratitude to Claire Savy, and all others involved in the Leeds CDT in Fluid Dynamics, for their support throughout my research. Thanks also to my fellow CDT students for making the office such a happy place to work.

I wish to say a huge thank you to Jorge Matos, for providing me with invaluable experimental data and hosting me in Lisbon. It was a pleasure to work with Jorge and I hope to collaborate with him again in the future. My gratitude is also due to Hydrotec Consultants Ltd for constructing my experimental spillway and for being extremely fun to work with.

Thank you to my friends and family, who have been brilliant over the last five years. I am hugely grateful to my parents, who have been so helpful throughout this project. My most important thank you goes to my big brother, John, who has always been my biggest fan and has provided me with the perfect environment in which to write this thesis. A special thanks also goes to Virgil, for keeping me calm during stressful times.

Finally, I'd like to thank EPSRC for providing the funding which made this research project possible.

ABSTRACT

Stepped spillways are commonly used to control overflows from reservoirs, as they dissipate significantly more energy than smooth spillways. At high discharges, skimming flow occurs over stepped spillways, in which significant air entrainment occurs. Numerical modelling has the potential to provide a useful tool to predict the important features of skimming flows over stepped spillways. However, numerical models must be validated against physical data sets, in order to determine whether they are able to accurately predict the required flow characteristics.

This project investigates the ability of the Volume of Fluid (VOF), mixture and Eulerian multiphase models, in combination with a range of turbulence models, to predict a range of variables in skimming flows over stepped spillways, with particular focus on the ability of the models to predict air entrainment. A complex pattern of 3D vortices which occur in the step cavities is also investigated, both experimentally and numerically. The pressures acting on the step faces and spillway side walls are also studied.

A narrow experimental stepped spillway was studied and pressures, flow depths and the locations of the inception point of air entrainment were measured. The spillway was numerically modelled in 3D, using a range of multiphase and turbulence models, and the results were compared to the experimental data. Experimental data from a second, significantly wider, stepped spillway was provided for this project. This spillway was numerically modelled in 2D and the numerical results were compared to the experimental data.

A complex pattern of 3D vortices occurs in the step cavities of the narrow experimental stepped spillway. The direction of circulation of these vortices reverses at each consecutive step. The direction of circulation of the vortices is affected by

the flow rate and was observed to vary unpredictably over time.

The Eulerian and mixture models were both shown to predict air entrainment, whereas the VOF model did not. All numerical models predicted the 3D vortex structures observed in the narrow experimental stepped spillway, and their associated effect on pressure. The time dependant behaviour of the vortices, however, was not predicted by the numerical models. 2D modelling using the Eulerian model, with the SST $k - \omega$ turbulence model, was found to be able to accurately predict velocities, AVFs, flow depths and the location of the inception point of air entrainment. The pressures and flow depth were also predicted reasonably accurately in 3D, using the Eulerian model with the SST $k - \omega$ model. The VOF model made accurate predictions of certain flow characteristics, however, the model's performance is limited by its inability to predict air entrainment. The mixture model was found to be significantly less accurate than the Eulerian model.

Numerical modelling of spillways of various widths showed that, as the width of the channel increases, the 3D vortex structures in the step cavities repeat across the channel. This behaviour was confirmed experimentally, by modifying the narrow experimental spillway, in order to change the ratio of step height to channel width. An expression is presented, based on the channel width and step height, which is able to accurately predict the number of repetitions of the 3D vortices for all spillway geometries investigated in this project. The 3D vortex structures were shown to have a small effect on the velocities above the steps, however, these effects were highly localised and did not effect the width averaged velocities. The 3D vortex structures were also observed in channels of varying slope.

The pressures acting on the step faces and side walls of the narrow stepped spillway were shown, both experimentally and numerically, to be significantly affected by the 3D vortex structures. This resulted in large pressure variations over short distances, which can pose a risk to masonry stepped spillways. Air entrainment was shown to reduce the high pressures acting on the step faces. The low pressures, however, were not significantly affected by the presence of air in the flow. Low pressures have the potential to cause damage to both concrete and masonry stepped spillways. The results of this project suggest that potentially damaging low pressures may occur in both the non-aerated and aerated regions

of skimming flow over stepped spillways.

This study demonstrates that a complex pattern of 3D vortices may occur in the step cavities of stepped spillways with varying geometries. This may have important implications for stepped spillways which are currently in service. The Eulerian multiphase model, in combination with the SST $k-\omega$ turbulence model, is able to accurately predict a range of important flow features over the two spillways investigated in this project. This shows that, this combination of multiphase model and turbulence model has the potential to provide a valuable tool for the design and inspection of stepped spillways. This study also shows that low pressures, which can potentially cause damage to both concrete and masonry spillways, may occur in both the non-aerated and aerated regions of skimming flows over stepped spillways.

CONTENTS

| | |
|---|---------------|
| Acknowledgements | iii |
| Abstract | iv |
| Table of Contents | vii |
| List of Figures | xv |
| List of Tables | xxxvii |
| Nomenclature | xxxix |
| 1 Introduction | 1 |
| 1.1 The Role of Spillways | 2 |
| 1.2 Flow Characteristics over Stepped Spillways | 3 |
| 1.3 Modelling of Hydraulic Structures | 4 |
| 1.4 Aims and Objectives | 5 |
| 1.5 Thesis Structure | 7 |
| 2 Current Understanding of Stepped Spillways and Associated Modelling Techniques | 11 |
| 2.1 Introduction | 12 |
| 2.2 Characteristics of Skimming Flows over Stepped Spillways | 12 |
| 2.2.1 Non-Aerated Region | 13 |
| 2.2.2 Inception Point of Air Entrainment | 14 |
| 2.2.3 Aerated Region | 15 |
| 2.2.4 Pressure | 16 |

CONTENTS

| | | |
|----------|--|-----------|
| 2.3 | Cavitation and Plucking Damage in Stepped Spillways | 17 |
| 2.3.1 | Cavitation Damage | 18 |
| 2.3.2 | Plucking Damage | 20 |
| 2.4 | Modelling of Hydraulic Structures | 22 |
| 2.4.1 | Scale Effects in Aerated Flows | 25 |
| 2.4.2 | Overview of Numerical Modelling Techniques for Air-Water Free-Surface Flows | 27 |
| 2.4.2.1 | The Volume of Fluid (VOF) Model | 28 |
| 2.4.2.2 | The Mixture Model | 29 |
| 2.4.2.3 | The Eulerian Multiphase Model | 30 |
| 2.5 | Summary | 31 |
| 3 | Design and Study of a Narrow Experimental Stepped Spillway | 33 |
| 3.1 | Introduction | 34 |
| 3.2 | Design of Experimental Spillway | 34 |
| 3.2.1 | Design Constraints | 34 |
| 3.2.2 | Spillway Geometry Design | 35 |
| 3.2.3 | Crest Design | 35 |
| 3.2.4 | Final Spillway Design | 37 |
| 3.3 | Flow measurement Techniques | 38 |
| 3.3.1 | Pressure Measurement | 38 |
| 3.3.2 | Free-Surface Measurement | 40 |
| 3.3.3 | Limitations | 43 |
| 3.4 | Initial Observations | 43 |
| 3.4.1 | Cross-stream Vorticity | 44 |
| 3.5 | Experimental Results | 48 |
| 3.5.1 | Free-Surface Position | 48 |
| 3.5.2 | Inception Point | 50 |
| 3.5.3 | Pressures Acting on the Step Faces and Spillway Side Walls | 53 |
| 3.5.3.1 | Horizontal Step Faces | 53 |
| 3.5.3.2 | Vertical Step Faces | 60 |
| 3.5.3.3 | Spillway Side Wall | 66 |
| 3.5.3.4 | Cross-stream Vorticity Direction and Vortex Switching | 70 |

| | | |
|----------|--|------------|
| 3.6 | Conclusions | 74 |
| 4 | Numerical Modelling Theory | 77 |
| 4.1 | Introduction | 78 |
| 4.2 | Governing Equations | 78 |
| 4.3 | Multiphase Numerical Models | 79 |
| 4.3.1 | VOF Model | 79 |
| 4.3.2 | Eulerian Multiphase Model | 81 |
| 4.3.3 | Mixture Model | 83 |
| 4.3.4 | Summary | 85 |
| 4.4 | Turbulence Modelling | 86 |
| 4.4.1 | RANS Models | 87 |
| 4.4.1.1 | Eddy Viscosity Models | 88 |
| 4.4.1.2 | Reynolds Stress Models | 94 |
| 4.4.2 | Near Wall Treatment for Turbulent Flows | 95 |
| 4.5 | The Finite Volume Method | 99 |
| 4.6 | Numerical Modelling Error | 100 |
| 4.7 | Assumptions and Limitations | 102 |
| 4.8 | Solver Settings | 104 |
| 5 | Two-Dimensional Numerical Model Study of a Large Experimental Stepped Spillway | 105 |
| 5.1 | Experimental Set-Up | 106 |
| 5.1.1 | Instrumentation | 107 |
| 5.2 | Modelling Procedure | 109 |
| 5.2.1 | Domain | 110 |
| 5.2.2 | Numerical Error | 111 |
| 5.2.2.1 | Grid Convergence | 111 |
| 5.2.2.2 | Time Step Independence | 116 |
| 5.2.3 | Transient Behaviour | 119 |
| 5.3 | Results and Discussion of a 2D Numerical Modelling Study of Skimming Flow over the LNEC Stepped Spillway | 122 |
| 5.3.1 | Experimental Inception Point Locations | 122 |

CONTENTS

| | | |
|----------|--|------------|
| 5.3.2 | Velocity Profiles | 124 |
| 5.3.2.1 | VOF Model | 124 |
| 5.3.2.2 | Mixture Model | 129 |
| 5.3.2.3 | Eulerian Model | 130 |
| 5.3.2.4 | Percentage Error | 134 |
| 5.3.2.5 | Summary | 139 |
| 5.3.3 | Air Volume Fraction Profiles | 140 |
| 5.3.3.1 | Experimental Data | 142 |
| 5.3.3.2 | VOF Model | 143 |
| 5.3.3.3 | Mixture Model | 144 |
| 5.3.3.4 | Eulerian Model | 145 |
| 5.3.3.5 | Quantification of Errors between the Numerical and Experimental AVF Data | 150 |
| 5.3.3.6 | Summary | 153 |
| 5.3.4 | Flow Depths | 153 |
| 5.3.5 | Further Turbulence Models | 158 |
| 5.3.5.1 | Standard $k - \omega$ Model | 158 |
| 5.3.5.2 | Standard $k - \epsilon$ Model | 160 |
| 5.3.5.3 | Reynolds Stress Model | 162 |
| 5.3.5.4 | Comparison of $k - \epsilon$ and $k - \omega$ Turbulence Models | 165 |
| 5.3.6 | Inception Point | 167 |
| 5.3.6.1 | Intersection of the Turbulent Boundary Layer and the Free-Surface | 167 |
| 5.3.6.2 | Visual Inspection | 172 |
| 5.3.6.3 | Depth Averaged Air Volume Fraction | 174 |
| 5.3.6.4 | Air Volume Fraction at the Pseudo-Bottom | 176 |
| 5.3.7 | Prototype Scale Numerical Modelling | 177 |
| 5.4 | Conclusions | 181 |
| 6 | Three-dimensional Numerical Model Study of a Narrow Stepped Spillway at the University of Leeds | 183 |
| 6.1 | Introduction | 184 |
| 6.2 | Modelling Procedure | 184 |

| | | |
|----------|--|------------|
| 6.2.1 | Domain | 185 |
| 6.2.2 | Numerical Error | 186 |
| 6.2.2.1 | Grid Convergence | 187 |
| 6.2.2.2 | Time Step Independence | 192 |
| 6.3 | Results and Discussion of a 3D Numerical Modelling Study of Skimming Flow over the University of Leeds Stepped Spillway | 194 |
| 6.3.1 | 3D Free-Surface Profiles | 194 |
| 6.3.2 | Air Entrainment | 196 |
| 6.3.3 | Cross-Stream Vortices | 197 |
| 6.3.4 | The Effect of Air Entrainment on Pressure | 201 |
| 6.3.5 | Unsteady Behaviour | 204 |
| 6.3.6 | Pressures Acting on the Step Faces and Spillway Side Walls | 208 |
| 6.3.6.1 | Horizontal Step Face | 209 |
| 6.3.6.2 | Vertical Step Face | 215 |
| 6.3.6.3 | Wall | 222 |
| 6.3.6.4 | Summary | 228 |
| 6.3.7 | Flow Depths | 230 |
| 6.3.7.1 | Flow Depth at the Centreline | 230 |
| 6.3.7.2 | Flow Depth at the Wall | 235 |
| 6.3.7.3 | Comparison of Numerically Predicted Flow Depths at the Wall and the Centreline | 241 |
| 6.3.7.4 | Summary | 244 |
| 6.3.8 | Inception Point | 245 |
| 6.3.8.1 | Intersection of the Turbulent Boundary Layer and the free-surface | 245 |
| 6.3.8.2 | Visual Inspection | 251 |
| 6.3.8.3 | Depth Averaged Air Volume Fraction and Air Volume Fraction at the Pseudo-Bottom | 253 |
| 6.4 | Conclusions | 254 |
| 7 | Study into the Occurrence of Cross-Stream Vortices in Stepped Spillways of Varying Geometry | 257 |
| 7.1 | Introduction | 258 |
| 7.2 | Cross-Stream Vorticity in Channels of Varying Width | 258 |

CONTENTS

| | | |
|----------|---|------------|
| 7.3 | Experimental and Numerical Investigation into Cross-Stream Vorticity in a Spillway of Modified Step Size | 265 |
| 7.4 | Cross-Stream Vorticity in Stepped Spillways of Varying Slope | 268 |
| 7.5 | Investigation into 3D behaviour in the LNEC Stepped Spillway | 270 |
| 7.5.1 | Modelling Procedure | 270 |
| 7.5.2 | 3D Flow Structures in the Step Cavities | 271 |
| 7.5.3 | Velocities | 273 |
| 7.5.4 | Free-Surface Profiles | 279 |
| 7.5.5 | Numerical Velocities and Air Volume Fractions Above the Steps of a 3D Stepped Spillway | 283 |
| 7.6 | Prediction of Cross-Stream Vortices | 287 |
| 7.7 | Conclusions | 292 |
| 8 | Conclusions and Further Work | 295 |
| 8.1 | Overview of Research Conducted for this Project | 296 |
| 8.2 | Key Findings | 296 |
| 8.3 | Conclusions | 298 |
| 8.3.1 | Project Aim 2: Investigate Complex Flow Structures Within the Step Cavities using Experimental and Numerical Methods | 298 |
| 8.3.2 | Project Aim 1: Investigate the Ability of Three Mesh Based Multiphase Models to Predict Air Entrainment, and other Important Flow Characteristics, in Skimming Flows over Stepped Spillways | 301 |
| 8.3.3 | Project Aim 3: Conduct an Experimental and Numerical Investigation into the Pressures Acting on the Side Walls and Step Faces of Stepped Spillways | 305 |
| 8.4 | Recommendations for Further Research | 306 |
| | References | 308 |
| | Appendix A Additional Information for Chapter 5 | A-1 |
| A.1 | Grid Convergence | A-2 |
| A.1.1 | Eulerian Model | A-2 |
| A.1.1.1 | AVFs | A-2 |
| A.1.2 | VOF Model | A-7 |

CONTENTS

| | | |
|--|---|------------|
| A.1.2.1 | Velocities | A-8 |
| A.1.3 | Mixture Model | A-10 |
| A.1.3.1 | Velocities | A-10 |
| A.1.3.2 | AVFs | A-12 |
| A.2 | Time Step Independence | A-14 |
| A.2.1 | VOF Model | A-15 |
| A.2.2 | Mixture Model | A-17 |
| A.3 | VOF Air Volume Fraction Profiles | A-18 |
| Appendix B Additional Information for Chapter 6 | | B-1 |
| B.1 | Grid Convergence | B-2 |
| B.1.1 | Pressure | B-2 |
| B.1.2 | Flow depths | B-4 |
| B.2 | Time Step Independence | B-6 |
| B.3 | 3D Free-Surface Profiles | B-9 |
| Appendix C Additional Information for Chapter 7 | | C-1 |
| C.1 | 3D Velocity Profiles Above the Steps of the LNEC Stepped Spillway | C-2 |

CONTENTS

LIST OF FIGURES

| | | |
|-----|---|----|
| 1.1 | (a) Concrete stepped spillway at the Pedrógão Dam in Portugal. (b) Masonry stepped spillway at Bottoms Reservoir in the UK | 3 |
| 2.1 | Characteristics of skimming flow over a stepped spillway. Above the steps the flow is divided into two regions: the non-aerated region followed by the aerated region. Recirculating vortices form in the step cavities | 13 |
| 2.2 | Typical pressure distributions acting on the step faces during skimming flow . . . | 17 |
| 3.1 | Various crest designs modelled using FLOW-3D. In all cases jet deflection is observed at one or more steps | 36 |
| 3.2 | Experimental crest profile and the equation used to approximate the curve . . . | 37 |
| 3.3 | Diagram of the final design of experimental stepped spillway. The width of the spillway is 150 mm | 38 |
| 3.4 | Pressure measurement locations on the step faces and spillway sidewalls. The dimensions h , l , and w and the distances h_s , l_s and W are indicated in the diagram. | 40 |
| 3.5 | One frame of a video used for image analysis to measure the location of the free-surface. Though the use of lighting, background and the ISO of the camera, a sharp contrast between the water and the background is observed at the free-surface | 41 |
| 3.6 | Procedure used to measure the free-surface position for a single video frame: (a) the original image converted into grey scale; (b) the grey scale image converted into either black or white; (c) the final free-surface plot calculated using the black and white image | 42 |

LIST OF FIGURES

3.7 Experimental spillway under a discharge of 20.2 l/s. The non-aerated region, inception point and aerated region can be clearly seen. The pressure measurement locations are indicated 44

3.8 Cross-stream vortices viewed from behind the vertical step face, at $Q = 15$ l/s, at steps 9 and 10, with associated diagrams detailing the direction of circulation of the cross-stream vortices 45

3.9 Schematic showing the structure of the stream-wise vortices as viewed from the side of the spillway, with the direction of circulation of the stream-wise vortices indicated by arrows 46

3.10 Experimentally measured mean free-surface positions \pm the standard deviation. Data is averaged over 180 s of data (10800 frames) and is shown for all four flow rates investigated 49

3.11 Experimentally measured mean free-surface profiles for the four discharges investigated 50

3.12 CFD contours of air volume fraction and streamlines using the VOF multiphase model with the SST $k - \omega$ turbulence model. The approximate distance from the downstream end of the recirculation zone and the top of the first step is approximately 825 mm 52

3.13 Inception point locations for different flow rates as predicted by empirical relationships and with adjusted experimental data. The precision error for each experimentally measured inception point location is indicated in the figure 53

3.14 Mean pressure acting on the horizontal step faces \pm standard deviation. w is the distance across the channel width from the spillway sidewall and l is the distance along the horizontal step face from the inside step corner. These dimensions are detailed in figure 3.4a 56

3.15 10 second moving averages of the pressure acting at the centreline and close to the wall, at the downstream end of the horizontal step faces. Data is shown at steps 2, 5 and 12 for varying flow rates 58

3.16 Mean pressure acting on the vertical step faces \pm standard deviation. w is the distance across the channel width from the spillway sidewall and h is the distance up the vertical step face from the inside step corner. These dimensions are detailed in figure 3.4a 62

| | |
|--|-----|
| 3.17 10 second moving averages of the pressure acting at the centreline and close to the wall, at the top of the vertical step faces. Data is shown at steps 2, 5 and 12 for varying flow rates | 64 |
| 3.18 Experimentally observed pressure patterns on the step faces according to the direction of circulation of the cross-stream vortices | 66 |
| 3.19 Numbered pressure measurement positions at the wall | 67 |
| 3.20 Mean pressure acting on the wall \pm standard deviation. h is the distance up the vertical step face from the inside step corner and l is the distance along the horizontal step face from the inside step corner. These dimensions are detailed in figure 3.4b | 68 |
| 3.21 10 second moving averages of the pressure acting at the centreline and close to the wall, at the downstream end of the horizontal step face of step 12. Each flow rate is shown in a separate sub-plot | 72 |
| 3.22 Mean pressures acting at the centreline and close to the wall, at the downstream end of the horizontal step face of step 12, for varying flow rates. The flow rates displayed are the same as those displayed in figure 3.21 | 74 |
| 4.1 Schematic of the various layers of near wall turbulent flows | 97 |
| 4.2 Schematic of the FVM with reference to node P. Nodes W and E are connected to node P by faces w and e respectively | 99 |
| 5.1 Skimming flow over the stepped spillway at the LNEC: (a) view from the side of the spillway (image taken from Matos and Meireles (2014)); (b) view from in front of the spillway with the conductivity probe and back flushing Pitot tube indicated (image taken from Bombardelli et al. (2011)) | 109 |
| 5.2 Numerical domain detailing the inlet, crest, steps and outlet. s is defined as the distance from the maximum height of the spillway crest, along the WES curve and the pseudo-bottom. The corner of step 11 is located at $s = 440$ mm | 111 |
| 5.3 Grid convergence index percentage error of velocity at numerous locations above the pseudo-bottom. The solutions were calculated for three meshes, using the Eulerian model with the Realisable $k - \epsilon$ model, at $Q = 180$ l/s | 114 |

LIST OF FIGURES

| | | |
|------|--|-----|
| 5.4 | Asymptotic verification of velocity at numerous locations above the pseudo-bottom. The solutions were calculated for three meshes, using the Eulerian model with the Realisable $k - \epsilon$ model, at $Q = 180$ l/s | 115 |
| 5.5 | Diagram of 2D mesh used for numerical modelling of the stepped spillway at the LNEC. The mesh is refined at the steps, the WES curve and at the inlet. The rest of the domain is relatively coarse in order to reduce the computational cost of simulations. The total number of cells in the domain is 934068 | 116 |
| 5.6 | Velocity profiles at different time steps for the Eulerian model with the SST $k - \omega$ turbulence model. $Q = 180$ l/s | 118 |
| 5.7 | AVF profiles at different time steps for the Eulerian model with the SST $k - \omega$ turbulence model. $Q = 180$ l/s | 119 |
| 5.8 | Velocity profiles at $Q = 180$ l/s for the VOF and SST $k - \omega$ models at various time steps | 120 |
| 5.9 | Air volume fraction profiles at $Q = 180$ l/s for the VOF and SST $k - \omega$ models at various time steps | 121 |
| 5.10 | View of the visually observed inception point (IP2) from the side of the experimental spillway. The darker regions indicate the presence of air bubbles | 123 |
| 5.11 | Comparison of experimental and numerical velocity profiles for $Q = 100$ l/s. Numerical data is shown for the VOF model with various turbulence models. The experimental inception point locations, IP1 and IP2, are indicated by the colour of the title of the subplots | 126 |
| 5.12 | Comparison of experimental and numerical velocity profiles for $Q = 140$ l/s. Numerical data is shown for the VOF model with various turbulence models. The experimental inception point locations, IP1 and IP2, are indicated by the colour of the title of the subplots | 127 |
| 5.13 | Comparison of experimental and numerical velocity profiles for $Q = 180$ l/s. Numerical data is shown for the VOF model with various turbulence models. The experimental inception point locations, IP1 and IP2, are indicated by the colour of the title of the subplots | 128 |

5.14 Comparison of experimental and numerical velocity profiles for $Q = 200$ l/s. Numerical data is shown for the VOF model with various turbulence models. The experimental inception point locations, IP1 and IP2, are indicated by the colour of the title of the subplots 129

5.15 Comparison of experimental and numerical velocity profiles for $Q = 180$ l/s. Numerical data is shown for the mixture model with various turbulence models. The experimental inception point locations, IP1 and IP2, are indicated by the colour of the title of the subplots 130

5.16 Comparison of experimental and numerical velocity profiles for $Q = 100$ l/s. Numerical data is shown for the Eulerian model with various turbulence models. The experimental inception point locations, IP1 and IP2, are indicated by the colour of the title of the subplots 131

5.17 Comparison of experimental and numerical velocity profiles for $Q = 100$ l/s. Numerical data is shown for the Eulerian model with various turbulence models. The experimental inception point locations, IP1 and IP2, are indicated by the colour of the title of the subplots 132

5.18 Comparison of experimental and numerical velocity profiles for $Q = 100$ l/s. Numerical data is shown for the Eulerian model with various turbulence models. The experimental inception point locations, IP1 and IP2, are indicated by the colour of the title of the subplots 133

5.19 Comparison of experimental and numerical velocity profiles for $Q = 100$ l/s. Numerical data is shown for the Eulerian model with various turbulence models. The experimental inception point locations, IP1 and IP2, are indicated by the colour of the title of the subplots 134

5.20 Velocity percentage error between the experimental data and the VOF model with the SST $k - \omega$ model, at all flow rates. The colour of each cell represents the range of values that the PE falls within. These ranges are defined in the key of the figure 136

5.21 Velocity percentage error between the experimental data and the Eulerian model with the SST $k - \omega$ model, at all flow rates. The colour of each cell represents the range of values that the PE falls within. These ranges are defined in the key of the figure 138

LIST OF FIGURES

| | | |
|------|--|-----|
| 5.22 | Velocity vectors close to a step corner for the Eulerian model with the SST $k-\omega$ model at $Q = 180$ l/s. The location of the velocity measurement closest to the pseudo-bottom, at $z = 3.175$ mm, is indicated in the diagram | 139 |
| 5.23 | Air volume fraction contours of the stepped spillway at the LNEC from the VOF, mixture and Eulerian models, at $Q = 180$ l/s. Streamlines are shown at step 34. The SST $k-\omega$ turbulence model was used in each case | 141 |
| 5.24 | Comparison of experimental and numerical air volume fraction profiles for $Q = 180$ l/s. Numerical data is shown for the VOF model with various turbulence models. The experimental inception point locations, IP1 and IP2, are indicated by the colour of the title of the subplots. Note that at $AVF = 0$ and $AVF = 1$, the numerical AVF values are exactly 0 and 1 so overlap one another | 144 |
| 5.25 | Comparison of experimental and numerical air volume fraction profiles for $Q = 180$ l/s. Numerical data is shown for the mixture model with various turbulence models. The experimental inception point locations, IP1 and IP2, are indicated by the colour of the title of the subplots | 145 |
| 5.26 | Comparison of experimental and numerical air volume fraction profiles for $Q = 100$ l/s. Numerical data is shown for the Eulerian model with various turbulence models. The experimental inception point locations, IP1 and IP2, are indicated by the colour of the title of the subplots | 147 |
| 5.27 | Comparison of experimental and numerical air volume fraction profiles for $Q = 140$ l/s. Numerical data is shown for the Eulerian model with various turbulence models. The experimental inception point locations, IP1 and IP2, are indicated by the colour of the title of the subplots | 148 |
| 5.28 | Comparison of experimental and numerical air volume fraction profiles for $Q = 180$ l/s. Numerical data is shown for the Eulerian model with various turbulence models. The experimental inception point locations, IP1 and IP2, are indicated by the colour of the title of the subplots | 149 |
| 5.29 | Comparison of experimental and numerical air volume fraction profiles for $Q = 200$ l/s. Numerical data is shown for the Eulerian model with various turbulence models. The experimental inception point locations, IP1 and IP2, are indicated by the colour of the title of the subplots | 150 |

5.30 Air volume fraction absolute error error between the experimental data and the Eulerian model with the SST $k - \omega$ model, at all flow rates. The corresponding experimental AVFs are also shown so that the total AVF at each location can be observed 152

5.31 Schematic of y_{90} and d in the non-aerated region, in relation to the experimental free-surface where waves are observed 154

5.32 Experimental and numerical y_{90} and equivalent clear water depth profiles for the VOF model, with various turbulence models, at all flow rates investigated . . 155

5.33 Experimental and numerical y_{90} and equivalent clear water depth profiles for the Eulerian, with various turbulence models, model at all flow rates investigated 157

5.34 Experimental and numerical y_{90} and equivalent clear water depth profiles for the mixture model, with various turbulence models, at 180 l/s, the only flow rate investigated with this multiphase model 158

5.35 Comparison of experimental and numerical velocity profiles for $Q = 180$ l/s. Numerical data is shown for the Eulerian model with various turbulence models, including the standard $k - \omega$ model. The experimental inception point locations, IP1 and IP2, are indicated by the colour of the title of the subplots 159

5.36 Comparison of experimental and numerical air volume fraction profiles for $Q = 180$ l/s. Numerical data is shown for the Eulerian model with various turbulence models, including the standard $k - \omega$ model. The experimental inception point locations, IP1 and IP2, are indicated by the colour of the title of the subplots . . 160

5.37 Comparison of experimental and numerical velocity profiles for $Q = 180$ l/s. Numerical data is shown for the Eulerian model with various turbulence models, including the standard $k - \epsilon$ model. The experimental inception point locations, IP1 and IP2, are indicated by the colour of the title of the subplots 161

5.38 Comparison of experimental and numerical air volume fraction profiles for $Q = 180$ l/s. Numerical data is shown for the Eulerian model with various turbulence models, including the standard $k - \epsilon$ model. The experimental inception point locations, IP1 and IP2, are indicated by the colour of the title of the subplots . . 162

LIST OF FIGURES

5.39 Comparison of experimental and numerical velocity profiles for $Q = 180$ l/s. Numerical data is shown for the Eulerian model with various turbulence models, including the Reynolds stress model. The experimental inception point locations, IP1 and IP2, are indicated by the colour of the title of the subplots 163

5.40 Comparison of experimental and numerical air volume fraction profiles for $Q = 180$ l/s. Numerical data is shown for the Eulerian model with various turbulence models, including the Reynolds stress model. The experimental inception point locations, IP1 and IP2, are indicated by the colour of the title of the subplots . . . 164

5.41 Comparison of experimental and numerical y_{90} profiles for $Q = 180$ l/s. Numerical data is shown for the Eulerian model with various turbulence models, including the Reynolds stress model 165

5.42 Contours of turbulent kinetic energy (k), with streamlines also displayed, at step 33 for the the Eulerian model with a range of turbulence model for $Q = 180$ l/s, highlighting the similarity between the $k - \epsilon$ and $k - \omega$ models respectively . . . 167

5.43 Equivalent clear water depth and turbulent boundary layer for the VOF model, with various turbulence models, at all flow rates considered. The locations of IP1 and IP2 are also indicated 169

5.44 Equivalent clear water depth and turbulent boundary layer for the Eulerian model, with various turbulence models, at all flow rates considered. The locations of IP1 and IP2 are also indicated 171

5.45 Equivalent clear water depth and turbulent boundary layer for the mixture model, with various turbulence models, at $Q = 180$ l/s. The locations of IP1 and IP2 are also indicated 172

5.46 Contours of air entrainment at the inception point for the Eulerian model with the SST $k - \omega$ model. The locations of IP1 and IP2, at each flow rate, are indicated in the figure 173

5.47 Numerical and experimental depth averaged AVFs for all flow rates. The numerical data is shown for the Eulerian multiphase model with the SST $k - \omega$ turbulence model 175

5.48 Numerical and experimental velocities at prototype scale with $\lambda = 15$. The experimental scale physical and numerical data is scaled using Froude similarity. The Eulerian model with the SST $k - \omega$ model was used for numerical modelling 179

| | |
|--|-----|
| 5.49 Numerical and experimental AVFs at prototype scale with $\lambda = 15$. The Eulerian model with the SST $k - \omega$ model was used for numerical modelling | 180 |
| 6.1 Diagram of the 3D domain and mesh used for numerical modelling of the experimental stepped spillway at the University of Leeds. The mesh is refined at the steps, inlet and approach channel in order to reduce the computational cost of simulations. The total number of cells within the domain is 4243488 | 186 |
| 6.2 Grid convergence pressure data for three meshes at several locations within the spillway, calculated using the Eulerian multiphase model with the Realisable $k - \epsilon$ turbulence model. The pressure data, grid convergence index error and asymptotic verification values are displayed | 189 |
| 6.3 Grid convergence flow depth data for three meshes, calculated using the Eulerian multiphase model with the Realisable $k - \epsilon$ turbulence model. The pressure data, grid convergence index error and asymptotic verification values are displayed. Flow depths are displayed at the centreline of the spillway | 191 |
| 6.4 Pressure data at several locations within the spillway, calculated using two different time steps. The Eulerian multiphase model with the Realisable $k - \epsilon$ turbulence model was used for numerical modelling | 193 |
| 6.5 Flow depth data calculated using two different time steps. The Eulerian multiphase model with the Realisable $k - \epsilon$ turbulence model was used for numerical modelling. Flow depths are displayed at the centreline of the spillway | 193 |
| 6.6 Isosurfaces at air volume fractions of 0.9 for the VOF, mixture and Eulerian multiphase models, with the SST $k - \omega$ turbulence model, at $Q = 15$ l/s. The images are mirrored at the centreline of the spillway due to the symmetry boundary condition used centreline | 195 |
| 6.7 Images showing splashing occurring at the centreline of the experimental stepped spillway. Splashing can be observed from in front of the spillway as well as from the side of the spillway | 196 |
| 6.8 Contours of air volume fraction for the the VOF, mixture and Eulerian models at $Q = 15$ l/s. The contours are displayed at the spillway centreline and data for the Realisable $k - \epsilon$ turbulence model has been displayed in each case | 197 |

LIST OF FIGURES

6.9 Numerical streamlines at steps 7 and 8 from four different view points: (a) 3D view of the steps; (b) view from the side of the steps; (c) view from behind the steps; (d) view from beneath the steps. The step geometry is displayed in black and the streamlines are displayed in red. The streamlines are shown for the Eulerian model with the SST $k - \omega$ model 199

6.10 Numerical pressure profiles and streamlines at steps 7 and 8 for various numerical models at $Q = 12$ l/s 200

6.11 Numerical pressures acting on all of the step faces for the VOF, mixture and Eulerian models at $Q = 15$ l/s. Data for the SST $k - \omega$ turbulence model is displayed in each case 203

6.12 Numerical pressures acting on the spillway side wall for the VOF, mixture and Eulerian models at $Q = 15$ l/s. Data for the Realisable $k - \epsilon$ turbulence model is displayed in each case 204

6.13 Contours of air volume fraction, at the centreline of the spillway and at the wall, for different values of t , for the VOF model with the SST $k - \omega$ model, at $Q = 15$ l/s 206

6.14 Isosurfaces of an air volume fraction of 0.9 for different values of t , for the VOF model with the SST $k - \omega$ model, at $Q = 15$ l/s 207

6.15 Mean flow depth \pm the standard deviation for the VOF model with the SST $k - \omega$ model. The mean and standard deviation are calculated using data at 0.01 s over a 5.00 s period 208

6.16 Experimental and numerical pressures acting on the horizontal step faces of steps 2, 5 and 12, at $Q = 12$ l/s. All combinations of multiphase and turbulence models are displayed. w is the distance across the channel width from the spillway side wall and l is the distance along the horizontal step face from the inside step corner. These dimensions are detailed in figure 3.4a 210

6.17 Experimental and numerical pressures acting on the horizontal step faces of steps 2, 5 and 12, at $Q = 15$ l/s. All combinations of multiphase and turbulence models are displayed. w is the distance across the channel width from the spillway side wall and l is the distance along the horizontal step face from the inside step corner. These dimensions are detailed in figure 3.4a 211

6.18 Experimental and numerical pressures acting on the horizontal step faces of steps 2, 5 and 12, at $Q = 18$ l/s. All combinations of multiphase and turbulence models are displayed. w is the distance across the channel width from the spillway side wall and l is the distance along the horizontal step face from the inside step corner. These dimensions are detailed in figure 3.4a 212

6.19 Experimental and numerical pressures acting on the horizontal step faces of steps 2, 5 and 12, at $Q = 21$ l/s. All combinations of multiphase and turbulence models are displayed. w is the distance across the channel width from the spillway side wall and l is the distance along the horizontal step face from the inside step corner. These dimensions are detailed in figure 3.4a 214

6.20 Experimental and numerical pressures acting on the horizontal step face of step 12, at $Q = 21$ l/s. The experimental mean pressure and standard deviation are calculated using only the data measured between 152.0245 s and 162.0245 s, when the moving averages, shown in figure 3.15, indicate that vortex switching has occurred and the direction of circulation of the cross-stream vortices is the same as that predicted by the CFD models. Experimental data is also only shown at $l = 55$ mm, the downstream end of the step. All combinations of multiphase and turbulence models are displayed. w is the distance across the channel width from the spillway side wall and l is the distance along the horizontal step face from the inside step corner. These dimensions are detailed in figure 3.4a 215

6.21 Experimental and numerical pressures acting on the vertical step faces of steps 2, 5 and 12, at $Q = 12$ l/s. All combinations of multiphase and turbulence models are displayed. w is the distance across the channel width from the spillway side wall and h is the distance up the vertical step face from the inside step corner. These dimensions are detailed in figure 3.4a 217

6.22 Experimental and numerical pressures acting on the vertical step faces of steps 2, 5 and 12, at $Q = 15$ l/s. All combinations of multiphase and turbulence models are displayed. w is the distance across the channel width from the spillway side wall and h is the distance up the vertical step face from the inside step corner. These dimensions are detailed in figure 3.4a 218

LIST OF FIGURES

| | | |
|------|--|-----|
| 6.23 | Experimental and numerical pressures acting on the vertical step faces of steps 2, 5 and 12, at $Q = 18$ l/s. All combinations of multiphase and turbulence models are displayed. w is the distance across the channel width from the spillway side wall and h is the distance up the vertical step face from the inside step corner. These dimensions are detailed in figure 3.4a | 219 |
| 6.24 | Experimental and numerical pressures acting on the vertical step faces of steps 2, 5 and 12, at $Q = 21$ l/s. All combinations of multiphase and turbulence models are displayed. w is the distance across the channel width from the spillway side wall and h is the distance up the vertical step face from the inside step corner. These dimensions are detailed in figure 3.4a | 221 |
| 6.25 | Experimental and numerical pressures acting on the vertical step face of step 12, at $Q = 21$ l/s. The experimental mean pressure and standard deviation are calculated using only the data measured between 234.1488 s and 244.1488 s, when the moving averages, shown in figure 3.17, indicate that vortex switching has occurred and the direction of circulation of the cross-stream vortices is the same as that predicted by the CFD models. Experimental data is also only shown at $h = 55$ mm, the top of the step. All combinations of multiphase and turbulence models are displayed. w is the distance across the channel width from the spillway side wall and l is the distance along the horizontal step face from the inside step corner. These dimensions are detailed in figure 3.4a | 222 |
| 6.26 | Experimental and numerical pressures acting on the wall at steps 2, 5 and 12, at $Q = 12$ l/s. All combinations of multiphase and turbulence models are displayed. h is the distance up the vertical step face from the inside step corner and l is the distance along the horizontal step face from the inside step corner. These dimensions are detailed in figure 3.4a | 224 |
| 6.27 | Experimental and numerical pressures acting on the wall at steps 2, 5 and 12, at $Q = 15$ l/s. All combinations of multiphase and turbulence models are displayed. h is the distance up the vertical step face from the inside step corner and l is the distance along the horizontal step face from the inside step corner. These dimensions are detailed in figure 3.4a | 225 |

| | |
|--|-----|
| 6.28 Experimental and numerical pressures acting on the wall at steps 2, 5 and 12, at $Q = 18$ l/s. All combinations of multiphase and turbulence models are displayed. h is the distance up the vertical step face from the inside step corner and l is the distance along the horizontal step face from the inside step corner. These dimensions are detailed in figure 3.4a | 226 |
| 6.29 Experimental and numerical pressures acting on the wall at steps 2, 5 and 12, at $Q = 21$ l/s. All combinations of multiphase and turbulence models are displayed. h is the distance up the vertical step face from the inside step corner and l is the distance along the horizontal step face from the inside step corner. These dimensions are detailed in figure 3.4a | 228 |
| 6.30 Comparison of experimental and and numerical flow depths for $Q = 12$ l/s. The experimental mean flow depth \pm the standard deviation is displayed. The numerical flow depths are calculated at the centreline of the spillway, for all combinations of multiphase and turbulence model | 232 |
| 6.31 Comparison of experimental and and numerical flow depths for $Q = 15$ l/s. The experimental mean flow depth \pm the standard deviation is displayed. The numerical flow depths are calculated at the centreline of the spillway, for all combinations of multiphase and turbulence model | 233 |
| 6.32 Comparison of experimental and and numerical flow depths for $Q = 18$ l/s. The experimental mean flow depth \pm the standard deviation is displayed. The numerical flow depths are calculated at the centreline of the spillway, for all combinations of multiphase and turbulence model | 234 |
| 6.33 Comparison of experimental and and numerical flow depths for $Q = 21$ l/s. The experimental mean flow depth \pm the standard deviation is displayed. The numerical flow depths are calculated at the centreline of the spillway, for all combinations of multiphase and turbulence model | 235 |
| 6.34 Comparison of experimental and and numerical flow depths for $Q = 12$ l/s. The experimental mean flow depth \pm the standard deviation is displayed. The numerical flow depths are calculated at the wall of the spillway, for all combinations of multiphase and turbulence model | 238 |

LIST OF FIGURES

| | |
|--|-----|
| 6.35 Comparison of experimental and numerical flow depths for $Q = 15$ l/s. The experimental mean flow depth \pm the standard deviation is displayed. The numerical flow depths are calculated at the wall of the spillway, for all combinations of multiphase and turbulence model | 239 |
| 6.36 Comparison of experimental and numerical flow depths for $Q = 18$ l/s. The experimental mean flow depth \pm the standard deviation is displayed. The numerical flow depths are calculated at the wall of the spillway, for all combinations of multiphase and turbulence model | 240 |
| 6.37 Comparison of experimental and numerical flow depths for $Q = 21$ l/s. The experimental mean flow depth \pm the standard deviation is displayed. The numerical flow depths are calculated at the wall of the spillway, for all combinations of multiphase and turbulence model | 241 |
| 6.38 Comparison of experimental and numerical flow depths for the Eulerian model with the SST $k - \omega$ model, at all flow rates investigated. The experimental mean flow depth is displayed and the numerical flow depths at both the centreline and at the wall of the spillway are displayed | 243 |
| 6.39 Equivalent clear water depth and turbulent boundary layer for the VOF model, with various turbulence models, at all flow rates considered. The experimental locations of L_i and the precision error are also indicated | 247 |
| 6.40 Equivalent clear water depth and turbulent boundary layer for the mixture model, with various turbulence models, at all flow rates considered. The experimental locations of L_i and the precision error are also indicated | 248 |
| 6.41 Equivalent clear water depth and turbulent boundary layer for the Eulerian model, with various turbulence models, at all flow rates considered. The experimental locations of L_i and the precision error are also indicated | 249 |
| 6.42 Velocity contours at planes parallel to the pseudo-bottom at different values of z for the Eulerian multiphase model with the SST $k - \omega$ turbulence model, at $Q = 18$ l/s | 251 |

| | | |
|------|---|-----|
| 6.43 | Contours of air volume fraction for the Eulerian multiphase model, with the SST $k - \omega$ turbulence model, at each flow rate investigated. The contours of air volume fraction are shown at $w = 0$ mm (wall), $w = 37.5$ mm and $w = 75$ mm (centreline). The locations of the experimentally defined inception points (IP) are also indicated | 252 |
| 6.44 | The depth averaged air volume fraction (c_{mean}) across the channel width for the Eulerian multiphase model, with the SST $k - \omega$ turbulence model, at $Q = 18$ l/s. c_{mean} is calculated at $x = 452$ mm (step 5), the experimentally observed inception point at $Q = 18$ l/s | 253 |
| 6.45 | The air volume fraction at the pseudo-bottom, across the channel width for the Eulerian multiphase model, with the SST $k - \omega$ turbulence model, at $Q = 18$ l/s. The AVF is recorded at $x = 452$ mm (step 5), the experimentally observed inception point at $Q = 18$ l/s | 254 |
| 7.1 | Pressure contours and streamlines of a 300 mm wide spillway for the Eulerian model with a range of turbulence models. Each image shows steps 2 and 3 of the spillway | 259 |
| 7.2 | Pressure contours and streamlines of a 300 mm wide spillway for the VOF model with two different turbulence models. Each image shows steps 2 and 3 of the spillway | 260 |
| 7.3 | Pressure contours and streamlines of a 300 mm wide spillway for various multiphase and turbulence models with symmetry boundary conditions at the spillway walls. Each image shows steps 2 and 3 of the spillway | 261 |
| 7.4 | Pressure contours and streamlines of a 300 mm wide spillway for the VOF model with two different turbulence models with periodic boundary conditions at the spillway walls. Each image shows steps 2 and 3 of the spillway | 262 |
| 7.5 | Pressure contours and streamlines of spillways of varying widths for the VOF model. Symmetry boundary conditions have been used at the spillway walls for all cases | 263 |
| 7.6 | Pressure contours and streamlines of a 1000 mm wide spillway for the VOF model with the Realisable $k - \epsilon$ turbulence model. Symmetry boundary conditions are used at either side of the spillway | 264 |

LIST OF FIGURES

| | | |
|------|--|-----|
| 7.7 | Pressure contours and streamlines of the 40 mm step height spillway, at steps 2 and 3, for the Eulerian multiphase model with the SST $k - \omega$ turbulence model | 266 |
| 7.8 | Numerical and experimental representation of cross-stream vortices. The numerical data is shown at step 2 and the experimental data is shown at step 12, at a time when the cross-stream vortex pattern matched that of the numerical data displayed in the figure | 267 |
| 7.9 | Numerical and experimental representation of cross-stream vortices. The numerical data is shown at step 3 and the experimental data is shown at step 12, at a time when the cross-stream vortex pattern matched that of the numerical data displayed in the figure | 268 |
| 7.10 | Pressure contours and streamlines of spillways of varying slope angles for the Eulerian model with the SST $k - \omega$ model turbulence. Each spillway is 150 mm wide and each image shows steps 2 and 3 of the spillway | 269 |
| 7.11 | Flow with attached wool fibres at the LNEC stepped spillway, viewed from below the chute. Image taken from Matos and Meireles (2014) | 271 |
| 7.12 | Pressure contours and stream lines of a three dimensional model of the first 17 steps of the LNEC stepped spillway. The VOF model with the SST $k - \omega$ model is used in each case and $Q = 180$ l/s | 273 |
| 7.13 | Velocity contours above steps 11 to 17, parallel to the pseudo-bottom, at different values of z for the simulations of the upstream section of the LNEC spillway. Data is displayed for the VOF model with the SST $k - \omega$ model at $Q = 180$ l/s . | 274 |
| 7.14 | Numerical velocity profiles at different channel widths of the 3D simulation of the upstream region of the LNEC spillway using symmetry boundary conditions at the spillway walls. The width averaged, 2D and experimental velocity profiles are also shown | 275 |
| 7.15 | Numerical velocity profiles at different channel widths of the 3D simulation of the upstream region of the LNEC spillway using wall boundary conditions at the spillway walls. The width averaged, 2D and experimental velocity profiles are also shown | 276 |

7.16 Velocity profiles across the channel width of step 14, at different values of z , for the 3D simulation of the upstream section of the LNEC spillway using symmetry boundary conditions. The mean velocity and standard deviation are also shown and the locations of $w= 500$ mm and $w= 571$ are indicated 277

7.17 Pressure contours and streamlines on steps 14-17 from $w = 500$ mm to $w = 784$ mm, for the 3D simulation of the upstream section of the LNEC spillway using symmetry boundary conditions. 279

7.18 Free-surface deformation upstream of the inception point at the LNEC stepped spillway in two instances in time. The images are viewed from upstream of the probe tip. In each image a probe tip, used to measure the flow depth, can be observed. In image (a) the probe tip practically submerged and in image (b) the probe tip is above the free-surface. Images taken from Matos and Meireles (2014) 280

7.19 Free-surface profiles across the channel width of for the 3D simulation of the upstream section of the LNEC spillway using wall boundary conditions, at different steps. The 2D free-surface depth is also shown at $w = 500$ mm 282

7.20 Free-surface profiles across the channel width of for the 3D simulation of the upstream section of the LNEC spillway using symmetry boundary conditions, at different steps. The 2D free-surface depth is also shown at $w = 500$ mm . . . 282

7.21 Velocity contours above the steps, parallel to the pseudo-bottom, at different values of z for the simulations of the 300 mm wide University of Leeds spillway geometry. Data is displayed for the Eulerian model with the SST $k - \omega$ model, at $Q = 180$ l/s 284

7.22 Numerical velocity profiles at different channel widths of the simulation of the 300 mm wide University of Leeds spillway geometry. The width averaged velocity profiles are also shown 285

7.23 Air volume fraction contours above the steps, parallel to the pseudo-bottom, at different values of z for the simulations of the 300 mm wide University of Leeds spillway geometry. Data is displayed for the Eulerian model with the SST $k - \omega$ model, at $Q = 180$ l/s 286

LIST OF FIGURES

7.24 Numerical air volume fraction profiles at different channel widths of the simulation of the 300 mm wide University of Leeds spillway geometry. The width averaged air volume fraction profiles are also shown 287

7.25 N against W for the three step geometries investigated in this project. A line representing $W/\sqrt{\pi}h_s$ is also displayed 289

7.26 N against W/h_s for the three step geometries investigated in this project. A line representing $W/\sqrt{\pi}h_s$ is also displayed 289

7.27 λ_w/h_s against W/h_s for the wavelengths calculated by equation (7.3), as well as the wavelengths observed in the numerical and experimental models. A line representing $\sqrt{\pi}$ is also displayed 291

A.1 Grid convergence index percentage error of air volume fraction at numerous locations above the pseudo-bottom. The solutions were calculated for three meshes, using the Eulerian model with the Realisable $k - \epsilon$ model, at $Q = 180$ l/s A-3

A.2 Asymptotic verification of air volume fraction at numerous locations above the pseudo-bottom. The solutions were calculated for three meshes, using the Eulerian model with the Realisable $k - \epsilon$ model A-5

A.3 Air volume fraction data for three meshes at numerous locations above the pseudo-bottom. The solutions were calculated using the Eulerian model with the Realisable $k - \epsilon$ model, at $Q = 180$ l/s A-6

A.4 Absolute error between numerically predicted and experimentally measure AVFs, for meshes 2 and 3. Numerical results predicted by the Eulerian model with the SST $k - \omega$ turbulence model, at $Q = 180$ l/s. The colour of each cell represents which range of values the error falls within at the corresponding location. These ranges are defined in the key of the figure A-7

A.5 Grid convergence index percentage error of velocity at numerous locations above the pseudo-bottom. The solutions were calculated for three meshes, using the VOF model with the Realisable $k - \epsilon$ model, at $Q = 180$ l/s A-8

A.6 Asymptotic verification of velocity at numerous locations above the pseudo-bottom. The solutions were calculated for three meshes, using the VOF model with the Realisable $k - \epsilon$ model, at $Q = 180$ l/s A-9

A.7 Velocity data for three meshes at numerous locations above the pseudo-bottom. The solutions were calculated using the VOF model with the Realisable $k - \epsilon$ model, at $Q = 180$ l/s A-10

A.8 Grid convergence index error of velocity at numerous locations above the pseudo-bottom. The solutions were calculated for three meshes, using the mixture model with the Realisable $k - \epsilon$ model, at $Q = 180$ l/s A-11

A.9 Asymptotic verification of velocity at numerous locations above the pseudo-bottom. The solutions were calculated for three meshes, using the mixture model with the Realisable $k - \epsilon$ model, at $Q = 180$ l/s A-12

A.10 Grid convergence index error of air volume fraction at numerous locations above the pseudo-bottom. The solutions were calculated for three meshes, using the mixture model with the Realisable $k - \epsilon$ model, at $Q = 180$ l/s A-13

A.11 Asymptotic verification of air volume fraction at numerous locations above the pseudo-bottom. The solutions were calculated for three meshes, using the mixture model with the Realisable $k - \epsilon$ model, at $Q = 180$ l/s A-14

A.12 Velocity profiles calculated using different time steps for the VOF model with the SST $k - \omega$ turbulence model. $Q = 180$ l/s A-15

A.13 Air volume fraction profiles calculated using different time steps for the VOF model with the SST $k - \omega$ turbulence model. $Q = 180$ l/s A-16

A.14 Velocity profiles calculated using different time steps for the Mixture model with the SST $k - \omega$ turbulence model. $Q = 180$ l/s A-17

A.15 Air volume fraction profiles calculated using different time steps for the mixture model with the SST $k - \omega$ turbulence model. $Q = 180$ l/s A-18

A.16 Comparison of experimental and numerical air volume fraction profiles for $Q = 100$ l/s. Numerical data is shown for the VOF model with various turbulence models. The experimental inception point locations, IP1 and IP2, are indicated by the colour of the title of the subplots. Note that at $AVF = 0$ and $AVF = 1$, the numerical AVF values are exactly 0 and 1 so overlap one another A-19

LIST OF FIGURES

- A.17 Comparison of experimental and numerical air volume fraction profiles for $Q = 140$ l/s. Numerical data is shown for the VOF model with various turbulence models. The experimental inception point locations, IP1 and IP2, are indicated by the colour of the title of the subplots. Note that at $AVF = 0$ and $AVF = 1$, the numerical AVF values are exactly 0 and 1 so overlap one another A-20
- A.18 Comparison of experimental and numerical air volume fraction profiles for $Q = 200$ l/s. Numerical data is shown for the VOF model with various turbulence models. The experimental inception point locations, IP1 and IP2, are indicated by the colour of the title of the subplots. Note that at $AVF = 0$ and $AVF = 1$, the numerical AVF values are exactly 0 and 1 so overlap one another A-21
- B.1 Grid convergence pressure data for three meshes at several locations within the spillway, calculated using the VOF multiphase model with the Realisable $k - \epsilon$ turbulence model. The pressure data, grid convergence index error and asymptotic verification values are displayed B-3
- B.2 Grid convergence pressure data for three meshes at several locations within the spillway, calculated using the mixture multiphase model with the Realisable $k - \epsilon$ turbulence model. The pressure data, grid convergence index error and asymptotic verification values are displayed B-4
- B.3 Grid convergence flow depth data for three meshes, calculated using the VOF multiphase model with the Realisable $k - \epsilon$ turbulence model. The pressure data, grid convergence index error and asymptotic verification values are displayed. Flow depths are displayed at the centreline of the spillway B-5
- B.4 Grid convergence flow depth data for three meshes, calculated using the mixture multiphase model with the Realisable $k - \epsilon$ turbulence model. The pressure data, grid convergence index error and asymptotic verification values are displayed. Flow depths are displayed at the centreline of the spillway B-6
- B.5 Pressure data at several locations within the spillway, calculated using two different time steps. The VOF multiphase model with the Realisable $k - \epsilon$ turbulence model was used for numerical modelling B-7
- B.6 Pressure data at several locations within the spillway, calculated using two different time steps. The mixture multiphase model with the Realisable $k - \epsilon$ turbulence model was used for numerical modelling B-8

B.7 Flow depth data calculated using two different time steps. The VOF multiphase model with the Realisable $k - \epsilon$ turbulence model was used for numerical modelling. Flow depths are displayed at the centreline of the spillway B-8

B.8 Flow depth data calculated using two different time steps. The mixture multiphase model with the Realisable $k - \epsilon$ turbulence model was used for numerical modelling. Flow depths are displayed at the centreline of the spillway B-8

B.9 Isosurfaces at air volume fractions of 0.9 for the VOF, mixture and Eulerian multiphase models, with the Realisable $k - \epsilon$ and RNG $k - \epsilon$ turbulence model, at $Q = 15$ l/s. The images are mirrored at the centreline of the spillway due to the symmetry boundary condition used centreline B-10

C.1 Velocity profiles across the channel width of step 15, at different values of z , for the 3D simulation of the upstream section of the LNEC spillway using symmetry boundary conditions. The mean velocity and standard deviation are also shown and the locations of $w = 500$ mm and $w = 571$ are indicated C-3

C.2 Velocity profiles across the channel width of step 14, at different values of z , for the 3D simulation of the upstream section of the LNEC spillway using wall boundary conditions. The mean velocity and standard deviation are also shown and the locations of $w = 500$ mm and $w = 571$ are indicated C-4

C.3 Velocity profiles across the channel width of step 15, at different values of z , for the 3D simulation of the upstream section of the LNEC spillway using wall boundary conditions. The mean velocity and standard deviation are also shown and the locations of $w = 500$ mm and $w = 571$ are indicated C-5

LIST OF FIGURES

LIST OF TABLES

| | | |
|-----|--|-----|
| 2.1 | Advantages and limitations of physical and numerical modelling | 24 |
| 3.1 | Inception point locations | 51 |
| 3.2 | The predominant direction of circulation of the cross-stream vortices for different steps and flow rates | 54 |
| 4.1 | Summary of key solver settings used for numerical modelling conducted in this project | 104 |
| 5.1 | Numbers of cells and cell sizes for meshes used in the grid convergence study . | 112 |
| 5.2 | Locations of experimental inception points | 123 |
| 5.3 | Details of figures showing velocity profiles | 124 |
| 5.4 | Details of figures showing air volume fraction profiles | 142 |
| 5.5 | Depth averaged air volume fractions at IP1 and IP2 for different discharges . . . | 176 |
| 5.6 | Pseudo-bottom air volume fractions at IP1 and IP2 for different discharges . . . | 177 |
| 6.1 | Numbers of cells and cell sizes for meshes used in the grid convergence study . | 187 |
| 7.1 | Data on the number of repetition's of the cross-stream vortices, and their associated wavelengths, which were observed in the three step geometries investigated in this project | 288 |
| 7.2 | Data on the number of repetition's of the cross-stream vortices, which were observed in the three step geometries investigated in this project, and the values of N predicted by equation (7.25) | 290 |

LIST OF TABLES

NOMENCLATURE

Symbols

| | |
|------------|--|
| C | Air concentration |
| C_D | Drag coefficient |
| C_{mean} | Depth averaged air concentration |
| d | Equivalent clear water depth |
| d_d | Dispersed phase particle diameter |
| d_i | Perpendicular distance from the pseudo-bottom to the inception point |
| e | Error between computational grids |
| F | Body forces acting on a fluid |
| Fr | Froude number |
| F_s | Factor of safety |
| F_s | Surface tension |
| f_{drag} | Drag function |
| g | Acceleration due to gravity |
| h | Vertical distance from the inside step corner |
| hg | Measure of computational grid refinement |
| h_s | Step height |
| k | Turbulent kinetic energy |
| L | Known length scale |
| L_i | Streamwise distance to the inception point |
| l | Horizontal distance from the inside step corner |

| | |
|--------------------------|---|
| l_s | Step length |
| l_t | Turbulent length scale |
| M | Interaction between phases in the Eulerian multiphase model |
| M_D | Drag force |
| M_L | Lift force |
| M_m | Mixture momentum source |
| M_{TD} | Turbulent dispersion force |
| M_{VM} | Virtual mass force |
| M_{WL} | Wall lubrication force |
| N | Number of repetitions of the cross-stream vortices across the width of a channel |
| p | Pressure |
| ρg | Observed grid convergence rate |
| Q | Flow rate |
| q_w | Flow rate per unit width |
| Re | Reynolds number |
| Re_r | Relative Reynolds number between phases |
| r | Grid refinement ratio |
| S | Area of surface between computational cells |
| S_{ij} | Mean rate of strain tensor |
| s | Streamwise distance along the pseudo-bottom from the maximum height of the spillway crest |
| \mathbf{U} | Instantaneous component of fluid velocity vector |
| $\mathbf{u} = (u, v, w)$ | Fluid velocity vector |
| \mathbf{u}' | Fluctuating component of fluid velocity vector |
| u_τ | Shear velocity |
| u^+ | Dimensionless wall velocity |
| V | Volume of computational cell |
| W | Channel width |
| We | Weber number |
| w | Distance across the channel width from the wall |
| x | Streamwise distance along the pseudo-bottom from the first outside step corner |

| | |
|-------------|---|
| y | Perpendicular distance from the wall |
| y_{90} | Perpendicular distance from the pseudo-bottom to and air concentration of 90% |
| y_c | Critical flow depth |
| y^+ | Dimensionless wall distance |
| z | Perpendicular distance above the pseudo-bottom |
| α | Volume fraction in a computational cell |
| Γ | Scalar diffusion coefficient |
| Δt | Time step |
| ϵ | Turbulent energy dissipation |
| θ | Spillway slope angle |
| κ | Empirically derived von Karman's constant |
| λ | Geometric scale factor |
| λ_T | Tapping coefficient |
| λ_w | Wavelength of the cross-stream vortices |
| ρ | Fluid density |
| μ | Dynamic viscosity |
| μ_t | Eddy viscosity |
| τ | Viscous stress tensor |
| τ_{ij} | Reynolds stress tensor |
| τ^T | Turbulent stress tensor |
| τ_w | Wall shear stress |
| ω | Specific dissipation rate |

Subscripts

| | |
|------|------------------|
| c | Continuous phase |
| d | Dispersed phase |
| k | Phase k |
| m | Fluid mixture |
| p | Prototype scale |
| sm | Model scale |

Abbreviations

| | |
|-----|---------------------------------|
| AV | Asymptotic verification |
| AVF | Air volume fraction |
| CFD | Computational fluid dynamics |
| DNS | Direct numerical simulation |
| EWT | Enhanced wall treatment |
| GCI | Grid convergence index |
| LES | Large eddy simulation |
| NS | Navier-Stokes |
| PE | Percentage error |
| SD | Standard deviation |
| SPH | Smoothed particle hydrodynamics |
| TBL | Turbulent boundary layer |
| WES | Waterways Experimental Station |

CHAPTER 1

Introduction

1. INTRODUCTION

1.1 The Role of Spillways

Dams are high risk structures as they impound large volumes of water. The failure of a dam can result in significant loss of life and destruction of property. Dams are also often constructed in cascade so the failure of an upstream dam can lead to the failure of downstream dams. Heavy rainfall can cause the volume of water in a reservoir to exceed the maximum capacity of the dam. This excess water must be released from the reservoir in a controlled manner. Spillways are used to control the overflow from reservoirs and prevent overtopping of the dam, which can cause the dam to fail. The energy of overflows through spillways can be extremely high. Spillways must dissipate large amounts of this energy to prevent scour at the toe of the dam, which can undermine the foundation and lead to failure. It is important for air entrainment to occur over spillways as this can help to protect the spillway surface from damage (discussed further in chapter 2). Aeration of the flow also helps to re-oxygenate the water, which may have a low dissolved oxygen content due to long residence times in the reservoir, in order to support downstream ecosystems.

There are many different spillway designs which can be used to control overflows from reservoirs. Some spillways, such as morning glory spillways, consist of a tunnel which passes through the dam. Other spillway designs consist of open channels which either pass over the dam or along the side of the dam. In some cases, more than one spillway is used at a dam. This often happens when the reservoir storage is increased, or older dams are refurbished to meet new design guidelines.

Stepped spillways have been shown to dissipate significantly more energy than smooth chutes (Rice and Kadavy (1996), Rajaratnam (1990) & Christodoulou (1993)), reducing the required size of the stilling basin and negating the need for additional dissipators.

The development of roller compacted concrete (RCC) in the 1980s resulted in more wide spread use of stepped spillways. This led to increased research into the flow characteristics of stepped spillways. Masonry stepped spillways have been a common overflow design for embankment dams since the 18th century. In the UK there are around 2000 embankment dams which fall under the 1975 reservoirs act (Environment Agency, 2017), with a large number of these reservoirs using masonry stepped spillways as overflow structures. The average age of UK dams exceeds 110 years (Mason and Hinks, 2008) so the primary concern of UK reservoir engineers is inspection and maintenance to ensure the spillway is able to safely operate under

1.2 Flow Characteristics over Stepped Spillways

the required design discharges. An example of a concrete stepped spillway and a masonry stepped spillway are shown in figure 1.1.

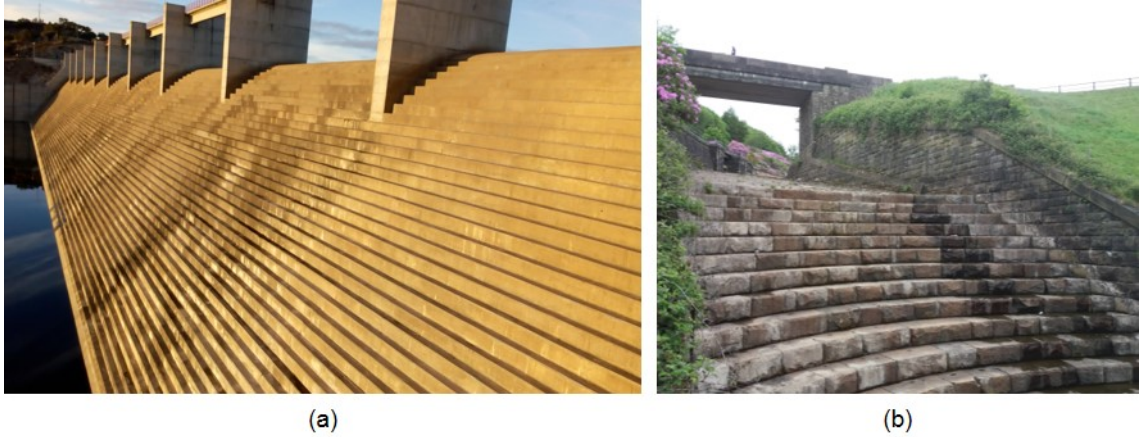


Figure 1.1: (a) Concrete stepped spillway at the Pedrógão Dam in Portugal. (b) Masonry stepped spillway at Bottoms Reservoir in the UK

1.2 Flow Characteristics over Stepped Spillways

There are three distinct flow regimes which occur over stepped spillways. For a given spillway geometry, nappe flow occurs at low discharges, transition flow occurs at moderate discharges and skimming flow at higher discharges (Chanson, 2002).

The nappe flow regime is described by a number of authors, including Chamani and Rajaratnam (1994) and Chanson (2002). In the nappe flow regime, water cascades down each step in a series of free-falling jets. At each step the water falls from the upstream step edge and impacts on the downstream step. At the upstream end of the step there is an air cavity beneath the free-falling jet and a hydraulic jump may occur on the step, depending on the flow rate and the length of the horizontal step face. Energy is dissipated during nappe flow by jet breakup and jet mixing on the down stream step and through friction between the spillway surface and the fluid. Energy is also dissipated in the hydraulic jump. Air entrainment occurs as the falling jet intersects the water on the downstream step and air is drawn into the flow from the air cavity and from the atmosphere. Nappe flow is more likely to occur on spillways with shallow slopes and large step heights.

The transition flow regime is described by several authors, including Chanson (2002) and Chanson and Toombes (2004). During transition flows, a recirculation pool of water occurs at

1. INTRODUCTION

the upstream end of the horizontal step face and there may also be an air cavity at the top of the vertical step face. Immediately downstream of the recirculating flow there is a stagnation point, followed by significant splashing. The flow varies significantly along the length of each step, as well as from one step to another. At a certain location down the spillway, free-surface aeration begins and air is drawn into the flow from the atmosphere.

In the skimming flow regime, the majority of the flow "skims" over the steps and recirculating vortices form in the step cavities. In the upstream region of the spillway no air entrainment occurs. Further downstream, free-surface aeration begins and high levels of air entrainment are observed. For most spillways, the design discharge will produce skimming flow, so it is this flow regime which is of most importance for the design and operation of stepped spillways. For this reason, only the skimming flow regime is investigated in this project. The hydraulics of the skimming flow regime are described in detail in chapter 2.

1.3 Modelling of Hydraulic Structures

Modelling is an important tool in both the design and inspection of hydraulic structures, including stepped spillways. Mason and Hinks (2008) state that "There are many dams in the UK which feature masonry chutes and reviewing the safe passage of water down such chutes is therefore an integral part of safety inspections and maintenance." This requires models of overflow structures to provide accurate information on the critical aspects of the flow.

Modelling of hydraulic structures is typically done using either physical modelling, numerical modelling or a combination of the two approaches. Both physical and numerical modelling of skimming flows over stepped spillways are conducted as part of this project. Physical and numerical modelling techniques are discussed further in chapter 2. There are benefits and limitations to both modelling approaches, which are summarised in table 2.1. One of the main limitations of physical modelling is scale effects. Overflow structures at reservoirs often include many large hydraulic features, including tumble bays, stilling basins and bridge piers. All of these features must be modelled in order to give a full understanding of the performance of a spillway. The inclusion of these features often requires a large scale factor between the physical model and full scale (prototype) spillway. This scale factor can have an important impact in the physics of the flow.

Numerical modelling does not require scaling. However, numerical models are relatively

new and less well understood. Before a numerical model can be used with confidence it must be proven to accurately predict the important features of the flows being considered. There are a wide range of numerical models available for predicting fluid flows. Each of these models use different assumptions and techniques, so will perform differently for different flow conditions. Research into numerical modelling techniques, therefore, must be conducted in order to validate numerical models against physical data sets. This will allow the most appropriate models for a particular type of flow to be identified.

Numerical modelling of air entrainment is challenging due to the complex interaction between the air and water phases and the fact that entrained air bubbles are usually at scales smaller than the computational mesh. A number of multiphase models are available which have the potential to model air entrainment. However, the accuracy of these models in predicting open channel free-surface air entrainment is yet to be proven. These multiphase models are discussed further in chapters 2 and 4.

1.4 Aims and Objectives

The purpose of this research project is to investigate a number of aspects of skimming flows over stepped spillways using both experimental and numerical modelling. The ability of a number of multiphase models to predict important flow features of skimming flows over stepped spillways is investigated, with particular focus is given to the prediction of air entrainment. Experimental and numerical investigation is also conducted into complex 3D behaviour in the spillway and into the pressures acting on the spillway surface. The Aims of this project are listed as follows:

1. Investigate the ability of three mesh based multiphase models to predict air entrainment, and other important flow characteristics, in skimming flows over stepped spillways. In order to achieve this aim the following objectives must be completed:
 - i. Create the geometries and computational meshes of two experimental stepped spillways which are to be numerically modelled.
 - ii. Quantify and minimise numerical errors for both of these stepped spillway geometries.

1. INTRODUCTION

- iii. Numerically model an experimental stepped spillway, for which the experimental data has been provided for this project, in two dimensions (2D), using a range of multiphase and turbulence models. Analyse the ability of the various numerical models to predict flow velocities, air volume fractions (AVFs) above the steps, as well as the flow depths and inception point locations.
 - iv. Design an experimental stepped spillway which can be used for experimental investigation of the flow characteristics of skimming flows, as well as to provide data for validation of numerical models.
 - v. Numerically model the experimental stepped spillway which is to be designed for this project, in three dimensions (3D), using a range of multiphase and turbulence models. Analyse the ability of the various numerical models to predict the pressures in the step cavities as well as the flow depths and inception point locations.
2. Investigate complex flow structures within the step cavities using experimental and numerical methods. In order to achieve this aim the following objectives must be completed:
- i. Identify the flow structures within the step cavities, of an experimental stepped spillway which is to be designed for this project, by visual observation and analysis of pressure measurements.
 - ii. Analyse flow structures in the numerical models and compare these flow structures to the experimental data.
 - iii. Conduct numerical modelling of stepped spillways of varying geometry in order to identify the flow structures within the step cavities.
 - iv. Use numerical and experimental modelling to identify the effect that the flow structures in the step cavities have on the main flow above the steps.
3. Conduct an experimental and numerical investigation into the pressures acting on the side walls and step faces of stepped spillways. This will include analysis of how the pressures acting on the step faces vary across the width of the channel. The effect of air entrainment on the pressure acting on the both the side walls of the spillway and the step faces will also be investigated. In order to achieve this aim the following objectives must be completed:

- i. Measure the pressures acting on the surfaces of the experimental stepped spillway which is to be designed for this project. Pressures will be measured at different locations within the step cavities and at a number of steps throughout the aerated and non-aerated regions.
- ii. Conduct numerical modelling of the experimental stepped spillway using a range of multiphase and turbulence models.
- iii. Analyse the experimental and numerical pressures acting on the spillway surfaces in order to identify the pressure profiles in the step cavities and the effect of air entrainment on pressure. Regions of the spillway which may be at risk of damage due to adverse pressure conditions will be also be identified.

1.5 Thesis Structure

Chapter 2: Current Understanding of Stepped Spillways and Associated Modelling Techniques

In this chapter, the characteristics of skimming flows over stepped spillways are described in detail, as are two potential causes of damage to stepped spillways under skimming flows. Physical and numerical modelling techniques are described and the limitations and benefits of these approaches are outlined. The last part of the chapter discusses previous research into numerical modelling of stepped spillways, and other free-surface flows, using the multiphase models which are investigated in this project.

Chapter 3: Design and Study of a Narrow Experimental Stepped Spillway

Chapter 3 presents the design of an experimental stepped spillway, as well as an experimental investigation into the flow within the experimental spillway. The design process of the spillway and measurement techniques used to collect data are reported. Flow structures within the step cavities are described and pressures and flow depth data are presented and analysed.

Chapter 4: Numerical Modelling Theory

This chapter describes the the numerical modelling approaches which are employed in this research project. The general concepts of numerical modelling of fluid flows are discussed.

1. INTRODUCTION

Then the multiphase models and turbulence models which are used in this projects are described in detail. The forms of numerical error are outlined and the last part of the chapter lists the assumptions made for numerical modelling in this project and the limitations of these numerical modelling approaches.

Chapter 5: Two-Dimensional Numerical Model Study of a Large Experimental Stepped Spillway

In this chapter, a large scale experimental stepped spillway is numerically modelled in 2D for several flow rates using a range of multiphase and turbulence models. The numerical errors in the simulations are quantified to ensure that they fall within acceptable limits. Numerically predicted velocities, air volume fractions (AVFs), flow depths and other flow variables are compared to experimental data. Further investigation is conducted in order to determine the causes of disparities observed between numerical results.

Chapter 6: Three-dimensional Numerical Model Study of a Narrow Stepped Spillway at the University of Leeds

In this chapter, a 3D numerical model study, of the experimental stepped spillway designed in chapter 3, is presented. The numerical error of the numerical modelling is quantified to ensure that the model solutions are reasonably independent of grid resolution and time step size. The 3D flow features and aeration predicted by the numerical models are analysed. The numerically predicted pressures, flow depths and inception point locations are then compared to experimental data.

Chapter 7: Study into the Occurrence of Cross-Stream Vortices in Stepped Spillways of Varying Geometry

This chapter presents a numerical model study into 3D flow structures within the step cavities of stepped spillways of varying geometries. Spillways of different widths and slopes are investigated. 3D modelling is also conducted of a small section of the experimental spillway modelled in chapter 5, in order to investigate how 3D structures in the step cavities affect the flow above the steps.

Chapter 8: Conclusions and Further Work

Chapter 8 discusses the key findings of this research project and gives further details on the conclusions which have been drawn. Suggestions for further research are then made.

1. INTRODUCTION

CHAPTER 2

Current Understanding of Stepped Spillways and
Associated Modelling Techniques

2. CURRENT UNDERSTANDING OF STEPPED SPILLWAYS AND ASSOCIATED MODELLING TECHNIQUES

2.1 Introduction

This chapter discusses previous research into skimming flows over stepped spillways and some of the surrounding issues as they relate to this research project. The features of skimming flows are described and factors affecting the safe operation of stepped spillways under the skimming flow regime are discussed. The final part of the chapter reviews modelling techniques for air-water flows at hydraulic structures with specific focus on skimming flows over stepped spillways.

2.2 Characteristics of Skimming Flows over Stepped Spillways

The hydraulics of skimming flows have been described by many authors, including Sorensen (1985), Rajaratnam (1990), Chanson (1994) and Chamani and Rajaratnam (1999). In the skimming flow regime most of the flow skims over the steps with recirculating vortices occurring in the spaces between the steps (Figure 2.1). The bulk flow and recirculating vortices are separated by the pseudo-bottom, an imaginary line joining the outer step edges. The form of the recirculating vortices varies depending on the slope of the spillway. This is discussed further in chapter 3.

At the upstream extent of the spillway, turbulence is created due to the interaction of the water and the spillway surface and a turbulent boundary layer (TBL) forms. This boundary layer increases in depth until it meets the free-surface. This point is known as the inception point of air entrainment and is where free-surface aeration begins, due to turbulence at the free-surface drawing air into the flow. The depth of this aerated region increases over a short distance, until the entire flow is aerated and air bubbles are transported into the recirculating vortices. The location of the point of inception moves downstream as the flow rate increases (Chanson, 2002, Zhang et al., 2012)

Downstream of the step corners, a shear layer develops (Gonzalez and Chanson, 2004). In the shear layer small scale vortices form which are separate from the recirculating vortices in the step cavities. These small scale vortices are transported downstream and impact on the next step edge (Felder and Chanson, 2011). Unsteady momentum exchanges occur between the cavities and main flow. At irregular times, the recirculating flow is ejected into the main flow and is replaced. This is a sequential process in that, when fluid is ejected from a step cavity, it causes the same process to occur at the next step cavity (Chanson, 2002, Chanson

2.2 Characteristics of Skimming Flows over Stepped Spillways

et al., 2002).

Skimming flow is an efficient means of energy dissipation. The primary energy dissipation mechanism is the transfer of shear stress from the main flow to maintain the recirculating vortices (Chanson et al., 2002, Gonzalez and Chanson, 2004). Some energy is also dissipated through turbulence in the aerated region (Carosi and Chanson, 2008). Energy dissipation is related to flow resistance. In stepped spillways with a shallow slope, flow resistance is caused by the interaction between the shear layer and the horizontal step face, as well as skin friction at the step faces. On steeper spillways, there is no skin friction between the main flow and the step faces. Flow resistance is caused by the recirculating vortices, and energy dissipation is dominated by the unsteady transfer of momentum from the main flow to the step cavities Chanson et al. (2002).

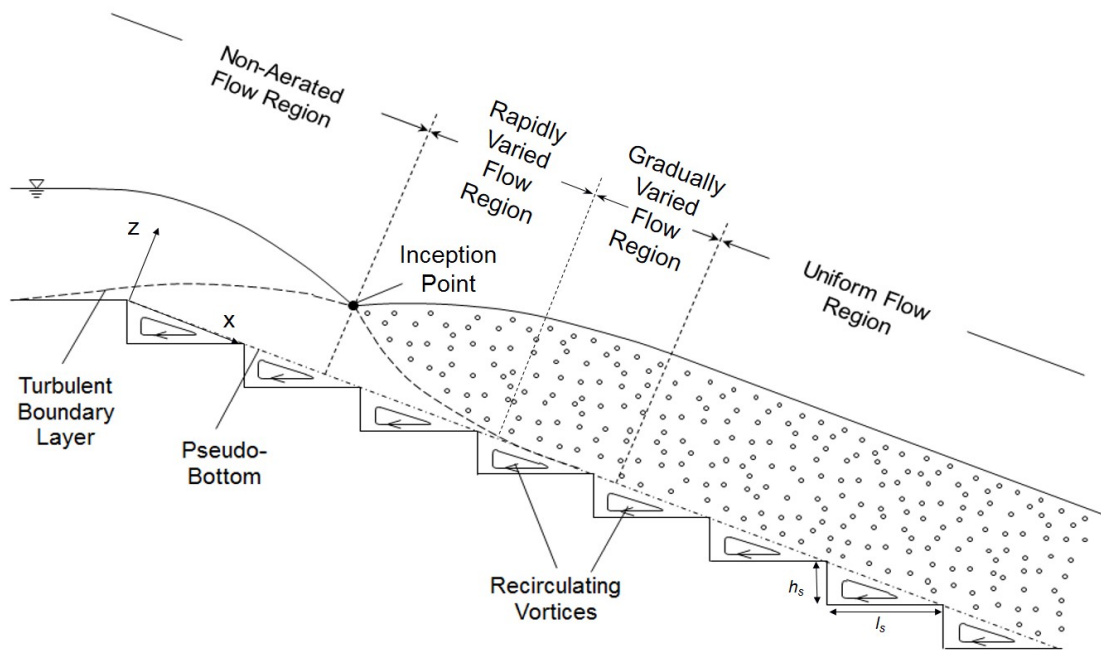


Figure 2.1: Characteristics of skimming flow over a stepped spillway. Above the steps the flow is divided into two regions: the non-aerated region followed by the aerated region. Recirculating vortices form in the step cavities

2.2.1 Non-Aerated Region

In the upstream region of the spillway, there is no air entrainment, however, close to the free-surface, some entrapped air is observed (Meireles et al., 2012). Further upstream, the free-surface is smooth and free-surface waves can be observed. The free-surface becomes more turbulent approaching the inception point (Meireles and Matos, 2009). The flow accelerates in

2. CURRENT UNDERSTANDING OF STEPPED SPILLWAYS AND ASSOCIATED MODELLING TECHNIQUES

the downstream direction, causing the flow depth to decrease. The flow can be separated into the TBL adjacent to the pseudo-bottom and the frictionless fluid flow region above (Amador et al., 2006). In the boundary layer, the velocity increases with z and follows a power law distribution. There are large turbulent velocity fluctuations in the boundary layer due to high turbulence caused by the interaction between the flow and the step corners (Chanson, 2002, Matos, 2000). Above the boundary layer, the mean velocity is constant and can be described by the ideal-fluid flow velocity. Immediately upstream of the inception point, unsteady surface scars may be observed (Chanson, 2013b).

2.2.2 Inception Point of Air Entrainment

The inception point of air entrainment is the location where self-aeration of the flow begins. Self-aeration of the flow occurs as the turbulent boundary layer approaches the free-surface. Turbulent shear stress in the flow is large enough to overcome buoyancy and surface tension forces, which causes free-surface aeration to begin (Zhang and Chanson, 2017).

The location of the inception point moves downstream with increasing discharge (Chanson, 2002). Meireles et al. (2012) show that the boundary layer thickness is not practically affected by discharge, based on experimental measurement of velocity profiles. This, therefore, suggests that, as the flow depth increases with discharge, the depth of the TBL reaches the free-surface further downstream, causing the inception point to appear further downstream. Boes and Hager (2003a) show that the step height has a relatively small effect on the location of the inception point, when compared with the flow rate.

The instantaneous position of the inception point varies around a time averaged position (Pfister and Hager, 2011) due to turbulence causing unsteadiness in the free-surface and the depth of the boundary layer (Meireles et al., 2012). Due to the temporal variability of the position of the inception point, a number of methods can be used to define its location. L_i is the streamwise distance to the inception point and d_i is the perpendicular distance from the pseudo-bottom to the inception point. Different authors define the point from which L_i is measured differently. This is discussed further in chapter 3.

The location of the inception point may be defined by a number of methods, each of which may identify slightly different locations. Many authors, including Yasuda and Chanson (2003) and Hunt and Kadavy (2010), determine the location of the inception point using visual observation of the location where air entrainment begins. This method is commonly used as it

2.2 Characteristics of Skimming Flows over Stepped Spillways

requires no additional equipment and can be used to make comparisons with other methods of defining the inception point location.

Meireles et al. (2012) and Bombardelli et al. (2011), amongst others, define the inception point as the location where the TBL meets the free-surface. The depth of the TBL is calculated using velocity measurements and the equivalent clear water depth is used to define the location of the free-surface.

Boes and Hager (2003a) found the location of the inception point by visual observation of the surface flow conditions to correspond with the location where the air concentration at the pseudo-bottom is equal to 0.01. This method was used to define the location of the inception point by Pfister and Hager (2011).

Matos (2000) and Boes and Hager (2003a) found that the depth averaged air concentration, C_{mean} , at the inception point is approximately 0.2. This method was used to define the inception point by Bung (2011). These methods which are used to define the location of the inception point are discussed further in chapters 5 and 6.

2.2.3 Aerated Region

Immediately downstream of the inception point there is a rapidly varied flow region (Chanson, 2002) where air is quickly entrained into the flow from the free-surface. In the rapidly varied flow region the depth averaged air concentration, C_{mean} , increases significantly to a local maximum (Matos, 2000). Air is transported throughout the entire depth of flow and into the step cavities. The addition of air to the flow mixture increases its volume and, therefore, the flow depth, in a process known as flow bulking (Boes and Hager, 2003b). This is important for the design of the spillway side walls (Coombs, 2016), especially at embankment dams, as these spillways often run down the mitre of the dam and the dam is at risk of erosion due to the granular construction materials used in its construction. Downstream of the local maximum, there is a small decrease in C_{mean} .

Downstream of this region, the flow is gradually varied and C_{mean} increases, but at a slower rate than in the rapidly varied flow region (Chanson, 2002, Matos, 2000). The increase in the air concentration through the gradually varied flow region results in a gradual increase in the flow depth. Downstream of the inception point the air water mixture is fully turbulent. The velocity profiles are similar to those in the non-aerated region, in that they follow a power law and the velocity increases with z . At a certain depth the velocity no longer follows a power law

2. CURRENT UNDERSTANDING OF STEPPED SPILLWAYS AND ASSOCIATED MODELLING TECHNIQUES

and reaches its maximum value (Boes and Hager, 2003a). The flow continues to accelerate through the gradually varied flow region. If the spillway is sufficiently long, downstream of the gradually varied flow region, the flow may become fully developed and a quasi-uniform flow region occurs where the flow depth, air concentrations and velocities remain constant along the length of the spillway (Chanson, 2002). A uniform flow region may not always be achieved, however, as Felder and Chanson (2009a,b) and others observed a "seesaw" pattern to certain air-water flow variables in this region. This is discussed further in chapter 3.

2.2.4 Pressure

High pressures occur at the downstream end of the horizontal step edge and at the bottom of the vertical step edges, where the recirculating vortex impinges on the step. The top of the vertical step edge and the upstream end of the horizontal step edge are subject to low pressures, due to flow separation in the recirculating vortices. A number of authors, including Amador et al. (2009), Sánchez-Juny et al. (2007), Sánchez-Juny et al. (2000) and Zhang et al. (2012) have conducted experimental studies into the pressures acting on step edges. The same general pressure profiles are found in each case and are shown in figure 2.2. These pressure profiles have also been found in several numerical studies, including Chen et al. (2002), Husain et al. (2014), Chakib (2013) and Qian et al. (2009). Although the expected pressure profiles were shown, only Chen et al. (2002) provided any physical data for validation, and reasonable agreement was found.

As far as the author is aware, Winter et al. (2010) conducted the only study into the pressures acting on the spillway side walls. The study found that high pressures occur towards the downstream end of the step and extend out beyond the end of the step. Low pressures occur at the upstream end of the step.

Sánchez-Juny et al. (2000) show that upstream of the inception point there are large variations in the maximum, mean and minimum pressures acting at the centreline of the horizontal steps. Downstream of the inception point, there is significantly less variation in the pressures. Both the maximum and minimum recorded pressures occur upstream of the inception point, as does the highest value of mean pressure. This suggests that the entrainment of air into the flow reduces pressure fluctuations. However, as the pressures are recorded at different steps there may be other factors affecting the pressure acting on the horizontal step faces. The study also shows that sub atmospheric pressures occur at the top of the vertical step

2.3 Cavitation and Plucking Damage in Stepped Spillways

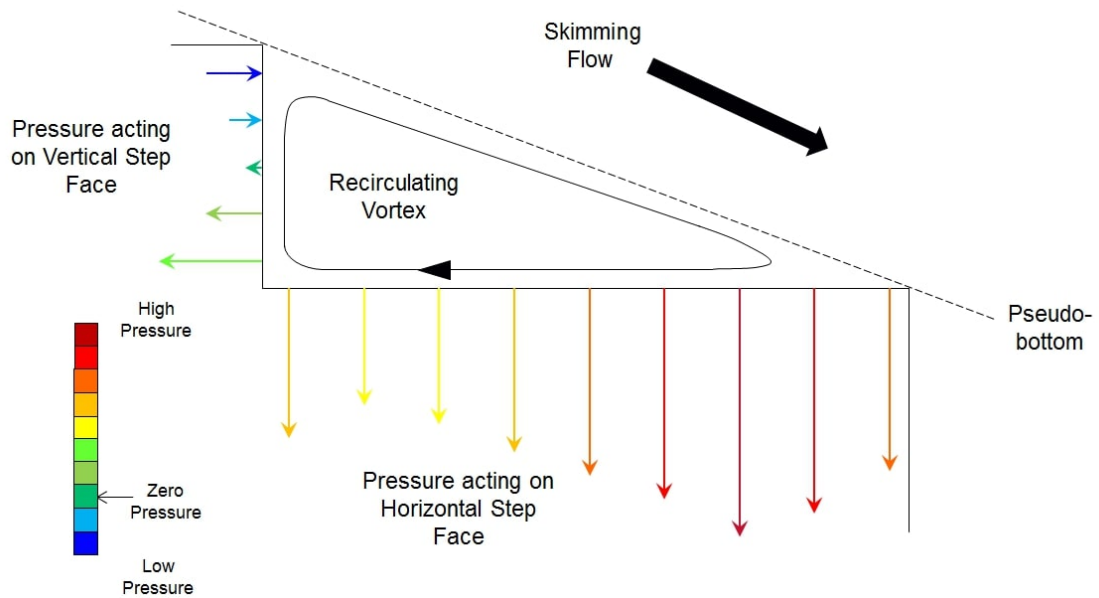


Figure 2.2: Typical pressure distributions acting on the step faces during skimming flow

face in the aerated flow region. These results agree with the findings of Sánchez-Juny and Dolz (2005) who used the 5th and 95th percentiles as a measure of the variation in pressure rather than maximum and minimum pressures.

The development of the pressures acting on the vertical step face along the length of the spillway have been studied to a lesser extent than the pressures acting on the horizontal step face. Amador et al. (2009) show that the root mean square pressure coefficient acting close to the top of the vertical step face increases up to the inception point and then decreases downstream of the inception point. As far as the author is aware, previous studies into the pressures acting on the step faces have measured pressures acting at the centreline of the spillway only.

2.3 Cavitation and Plucking Damage in Stepped Spillways

The primary purpose of reservoir spillways is to safely direct excess water into the downstream watercourse. The spillway must dissipate the energy of the flow to prevent downstream scour which can undermine the dam. In open channel spillways, the side walls of the spillway must be of sufficient height to prevent overtopping of flow which can cause damage to the dam,

2. CURRENT UNDERSTANDING OF STEPPED SPILLWAYS AND ASSOCIATED MODELLING TECHNIQUES

especially in embankment dams constructed of granular materials. It is also important that the flows over a spillway do not cause damage to the spillway itself as the failure of a spillway can quickly lead to failure of the dam. This section discusses two forms of damage which may occur during skimming flows over a stepped spillway: cavitation damage and plucking damage.

2.3.1 Cavitation Damage

If the local pressure of a flowing liquid falls below the vapour pressure of the liquid (2.3 kPa for water at 20°C), vapour bubbles are formed. This is known as cavitation (Batchelor, 2000). When the pressure surrounding the vapour bubble increases, usually as the bubble is transported to higher pressure regions of the flow, the bubble collapses, producing extremely high localised pressures. If this collapse occurs at, or close to, a solid boundary, then pitting damage can occur (Kells and Smith, 1991).

The low pressures which cause cavitation are often found where flow separation occurs. In smooth spillways, any small discontinuities or protrusions in the spillway's surface can cause flow separation at high velocities (Kells and Smith, 1991). In stepped spillways, the top of the vertical steps are thought to be at most risk of cavitation damage where flow separation occurs due to the recirculating vortices (Amador et al., 2009).

It is widely accepted that the entrainment of air into the flow will significantly reduce cavitation damage. Two reasons have been suggested for why this is the case. Vischer et al. (1982), Wood (1984) and several other authors state that the increased compressibility of the fluid mixture, due to the entrained air, acts to reduce pressure of the collapsing vapour bubble so that cavitation damage does not occur. Experiments by Dong et al. (2010) and McGee (1988) show that aeration of the flow acts to increase the minimum pressures and prevent vapour bubbles from forming.

Smooth spillways are particularly susceptible to cavitation damage due to the surface irregularities inherent in construction and high flow velocities causing flow separation at the spillway surface. Although free-surface aeration does occur on smooth spillways, it often occurs much further downstream than on stepped spillways (Pfister and Hager, 2011).

Stepped spillways are widely accepted to be less prone to cavitation damage than smooth spillways. Free-surface aeration occurs much further upstream in stepped spillways than in smooth spillways so much of the spillway is protected from cavitation. Upstream of the incep-

2.3 Cavitation and Plucking Damage in Stepped Spillways

tion point, however, no aeration occurs so steps in this region may be susceptible to cavitation damage. Amador et al. (2009) show that sub vapour pressures can occur towards the top of the vertical step, where flow separation occurs.

The exact conditions under which cavitation damage may occur on stepped spillways remain unknown, so there is uncertainty as to how to address cavitation (Frizell et al., 2013). Boes and Hager (2003a) suggest a maximum flow velocity of 20 m/s to prevent cavitation, whereas Pfister et al. (2006) suggest that flow velocities should be limited to 30 m/s, considerably lower than the maximum velocity of 100 m/s advised for smooth spillways with appropriate aeration devices. This has resulted in conservative design practices being employed for concrete stepped spillways (Frizell et al., 2013).

There are no recorded cases of cavitation damage being observed on stepped spillways in service. Frizell et al. (2013) claim that this is due to conservative designs preventing the conditions which could produce cavitation from occurring. At higher discharges, the inception point is pushed further downstream, so less of the spillway is protected from cavitation by entrained air. Conservative design would reduce the likelihood of these conditions occurring. Experiments conducted by Frizell et al. (2013) show that cavitation can occur on stepped spillway geometries. Chanson (2002) claims, however, that the the risk of cavitation damage to stepped spillways is basically zero due to slower flow velocities and greater water depths producing a cavitation index, a ratio of pressure and velocity used to evaluate cavitation risk, 10 to 100 times greater than on smooth spillways with identical discharges.

It is clear that the risk of cavitation damage to stepped spillways is not fully understood and there is uncertainty around the conditions which may cause cavitation. Until a better understanding of cavitation in stepped spillways is reached, it is likely that designs will remain conservative due to the high risk nature of dam design. Accurate numerical modelling techniques would provide a useful tool in increasing this understanding and help to identify areas at risk of cavitation for future stepped spillway design.

There have been a number of studies into numerical modelling of cavitation damage. One study by Dular and Coutier-Delgosha (2009) used single fluid CFD model, coupled with an erosion model, to simulate cavitation damage on a hydrofoil. The model showed good agreement with the experimental results on the intensity and downstream extent of the erosion. The upstream extent of the erosion was predicted less accurately. The study also found that the accuracy of the solution depends strongly on the prediction of pressure in the CFD model.

2. CURRENT UNDERSTANDING OF STEPPED SPILLWAYS AND ASSOCIATED MODELLING TECHNIQUES

Peters et al. (2015) also modelled cavitation over a hydrofoil, using the Eulerian multiphase model with the Schnerr-Sauer cavitation model. The model accurately predicted the areas at risk of cavitation erosion and the intensity of erosion in those areas.

With regard to spillways, research into numerical modelling has concentrated on the conditions which cause cavitation rather than modelling the cavitation damage explicitly. For example, Chen et al. (2002) and Cheng et al. (2006) used the VOF and mixture models respectively to predict pressures acting on the spillway steps. Further details of these studies are found in section 2.4.2. This project also investigates whether numerical models can be used to predict the conditions which may cause cavitation damage, rather than attempting to model cavitation directly.

2.3.2 Plucking Damage

In masonry spillways, low pressures can cause "plucking" damage as low pressures can act to pull masonry blocks from the spillway into the flow. The removal of blocks can lead to erosion of backing material and catastrophic failure of the spillway (Mason and Hinks, 2008).

In 2007 the side wall of one of two masonry stepped spillways at the Ulley Reservoir in Rotherham collapsed under 1:200 year flood conditions (Winter et al., 2010), much less than the design discharge of the spillway. This created a large scour hole at the base of the downstream face of the embankment and emergency procedures were conducted resulting in the evacuation of approximately 1000 people and the closure of a section of the M1 motorway. Investigation concluded that the likely cause of the collapse was erosion of backing material through gaps in the sidewall caused by plucking of masonry blocks. The Environment Agency predicts that the emergency procedures and subsequent repair works cost in the region of £5,000,000 (Environment Agency, 2007). A similar incident also occurred at the Boltby reservoir in 2005, again believed to be as a result of masonry plucking (Winter et al., 2010).

Although cavitation and plucking damage are fundamentally different processes, they are both caused by low pressures acting on the spillway surface and side walls. Increasing the pressure in these regions through air entrainment can, therefore, help to prevent both cavitation and plucking damage.

Plucking in masonry stepped spillways has not been investigated to the same extent as cavitation. Following the spillway failures at Boltby and Ulley reservoirs due to plucking damage, the UK environment agency commissioned a comprehensive research project to clarify

2.3 Cavitation and Plucking Damage in Stepped Spillways

the safety of stepped spillways. This project and its findings are presented by Winter et al. (2010) and several factors which contribute to the plucking of masonry blocks from stepped spillways are identified:

- A large pressure difference between the front and back of a masonry block can cause the block to shift position or be removed from the spillway surface. In addition to the low pressure region on the vertical step face, low pressure regions also occur on the spillway side walls. Missing blocks were observed on the side wall of the Boltby spillway following the failure. This shows that both the step pressures and side wall pressures must be considered by reservoir engineers. It is also common for water to ingress behind masonry blocks into the backing material. This increases the pressure behind the blocks which can increase the risk of plucking damage.
- High and low pressure regions can occur over short spatial distances. If a masonry block has high pressures acting at one end and low pressures acting at the other, then it can cause the block to rotate out of position.
- The pressures acting on the spillway can fluctuate considerably causing vibrations. The magnitude and frequency of these vibrations can cause blocks to loosen, or remove blocks which are already loose.
- If a block has shifted in position through any of the above mechanisms, then it can cause protrusions and recesses in the spillway surface. Protrusion and recesses in the spillway side wall can cause significant pressure fluctuations, increase maximum pressures and decrease minimum pressures.

Down and Wearing (2012) describe physical testing works carried out on a masonry stepped spillway following recommendations by the inspecting engineer. A 1:30 scaled model was used to determine the spillway capacity and tapping points were used to measure pressures. The resultant pressure data were scaled to prototype scale and compared to theoretical calculations made in accordance with Environment Agency guidelines. The measured pressures were almost three times smaller than the theoretical calculations, which was attributed to scale effects. The study also acknowledges that high and low pressure regions can be highly localised. A large number of pressure measurement locations would be required to

2. CURRENT UNDERSTANDING OF STEPPED SPILLWAYS AND ASSOCIATED MODELLING TECHNIQUES

identify these local pressure variations, which was not possible in this case due to the small size of the physical model.

Physical testing of the loads required to move the masonry blocks in the spillway invert was also conducted by Down and Wearing (2012). It was found that some blocks did not move at the maximum test load, while others moved at loads significantly smaller than the maximum. This shows that there is variability as to how susceptible different blocks are to plucking damage. Down and Wearing (2012) also identifies the need for further research into pressures acting on stepped spillways during skimming flow.

A common method to prevent plucking damage is to leave mortar joints open, or to install pressure relief drains (Mason and Hinks, 2008). Winter et al. (2010) show that by leaving joints open the pressure fluctuations on the spillway side wall are significantly reduced, the maximum pressures are reduced and the minimum pressures are increased.

Accurate numerical modelling would provide an invaluable tool to identify localised areas of high or low pressures. This would allow critical areas of the spillway to be identified where the stability of blocks must be ensured and pressure relief measures may be required.

2.4 Modelling of Hydraulic Structures

For the design and maintenance of stepped spillways (and other hydraulic structures), it is important to be able to predict the important flow features of the structure in question. One method to do this is through the use of empirical expressions, based on experimental research, which can be used to predict the important flow characteristics of skimming flows over stepped spillways. For example, Boes and Hager (2003b) produced expressions to predict the onset of skimming flow, the equivalent clear water depth, the uniform mixture depth, the residual energy head and the required depth of the spillway side wall. Meireles et al. (2012) developed expressions to predict the location of the inception point, the equivalent clear water depth, the thickness of the boundary layer, the mean air concentration at the inception point and the specific energy. Ohtsu et al. (2004) use empirical relations to produce a hydraulic design chart for stepped spillways based on the channel width, the channel slope, the spillway height and the discharge. These examples are by no means exhaustive and many other authors have produced empirical relations to predict a wide range of flow characteristics for skimming flows over stepped spillways.

2.4 Modelling of Hydraulic Structures

These empirical relations are a useful method for predicting flow features of stepped spillways. However, for complex and high risk hydraulic structures, such as reservoir spillways, it is often necessary to conduct a hydraulic investigation into the specific structure being considered. This is most commonly achieved using two techniques: physical and numerical modelling. Both modelling techniques have limitations, however, so it is common to use a combination of physical and numerical modelling to investigate flows at hydraulic structures. Table 2.1 summarises the important advantages and limitations of physical and numerical modelling.

2. CURRENT UNDERSTANDING OF STEPPED SPILLWAYS AND ASSOCIATED MODELLING TECHNIQUES

Table 2.1: Advantages and limitations of physical and numerical modelling

| Physical Modelling | Numerical Modelling |
|--|---|
| Physical models will be limited by scale effects. Although criteria can be recommended to minimise these effects, as described for stepped spillways in section 2.4.1, some scale effects will always occur. It is also not always possible to meet these recommendations. | Modelling can be conducted at prototype scale. |
| Measurements may only be made at specific positions in a physical model, which must be considered during the design of the model. Accurate flow measurements may also be difficult to achieve. | Measurements of any flow variable can be made at any point in the domain. |
| Some measurement techniques are intrusive and affect the flow conditions. | All measurements are non-intrusive. |
| Small changes to the model, such as varying the flow rate or making small alterations to the geometry, are easy to implement. | For each change of flow rate or geometry the solution must be recalculated. For complex 3D models this can require a significant computational cost. |
| Large changes to the geometry of the model are often difficult or impossible to implement. | Many different geometries can be created and modelled. |
| The true physical behaviour of the fluids is always shown. | The accuracy of the model is dependent on its implementation. Large 3D free-surface models are highly complex so unphysical fluid behaviour may be predicted if the model is implemented incorrectly. Even with correct implementation, a numerical model may predict inaccurate flow conditions due to the limitations of the model. |
| Physical models have been in use for a long time and the advantages and limitations are relatively well understood. | Numerical models are relatively new and less well understood. Assumptions are made in each numerical model so evidence is required to support a model's suitability for a particular application. |
| Physical models are usually large and impracticable to store so are often decommissioned after their original use. | Model data can be saved relatively easily for future use. This can be useful for the inspection and maintenance of hydraulic structures. |

2.4.1 Scale Effects in Aerated Flows

Physical modelling of hydraulic structures is most often conducted at geometric scales smaller than the prototype structure, as full scale modelling of large hydraulic structures is expensive and often unfeasible. This introduces scale effects which can cause the flow behaviour in the scaled model to differ from that which would be found in the prototype structure. These scale effects are one of the most important limitations in physical modelling and, therefore, it is important to understand how scaling of a hydraulic structure will affect the flow characteristics, so that scale effects can be minimised.

Chanson (2013a) conducts a detailed review of the current understanding of scale effects on aeration. Physical model testing usually applies Froude scaling, however, in turbulent shear flows, viscous effects are dominant and bubble break up and coalescence is controlled by surface tension. Therefore, to achieve true dynamic similarity in aerated flows, Froude, Reynolds and Morton similarity is required, which is only possible at prototype scale. When the same fluids are used (air and water) both Froude and Morton similitude is easily achieved, however, this results in a much lower Reynolds number (Re), creating viscous scale effects.

The review also raises the question that, if most CFD analysis of aerated flows is validated against physical scale models, can these CFD models be trusted to accurately predict prototype scale aerated flows? Aydin and Ozturk (2009) compared both CFD and scaled model air entrainment rates against prototype data. The study found that air entrainment rates were accurately predicted in the CFD model but vastly underestimated in the physical model.

Chanson and Gonzalez (2005) showed that significant scale effects occur in bubble count rates and turbulence intensity in flows over stepped spillways, and that stepped spillways are more sensitive to scale effects than smooth chutes.

Boes and Hager (2003a) conducted experiments using stepped spillways of geometric scale factors, λ , ranging from 6.5 to 26.0 with reference to a standard prototype step height of 600 mm. From measurements of air concentrations and flow velocities, the following suggestions for physical modelling of aerated flows overstepped spillways were made:

- $Re \geq 10^5$.
- $We \geq 100$, where We is the Weber number.
- $\lambda < 15$.

2. CURRENT UNDERSTANDING OF STEPPED SPILLWAYS AND ASSOCIATED MODELLING TECHNIQUES

These values were based on scaling the velocity and air concentration measurements for each spillway scale to prototype dimensions of step height 600 mm. The results were compared and any deviations attributed to scale effects. While this is useful in understanding how different sized models behave when scaled up, without prototype data for comparison the reliability of these results cannot be guaranteed.

Boes and Hager (2003a) also review several previous studies into scale effects on stepped spillways. In these studies, minimum Reynolds numbers of 1.0×10^4 to 7.5×10^4 , maximum scale factors of 15 to 20 and a minimum Weber number of 110 are suggested to minimise scale effects in stepped spillway models. These studies could not be accessed, however, and the criteria on which these suggestions have been made is unclear.

Coombs (2016) compared the flow depth over the steps of a 1:30 scale model of the Grassholme reservoir spillway with photographs taken during a flood event in 1991. The exact discharge over the spillway is unknown, but is estimated using data recorded from downstream measurement points during the event. Only qualitative analysis of the free-surface position can be made, however, it is clear that the physical model underestimates the depth of flow over the steps. This is attributed to flow bulking due to aeration not being sufficiently predicted in the scale model.

Down and Wearing (2012) state that a scale factor of less than 10 should be used to minimise inaccuracies in pressure measurements due to scale effects. The study shows scale effects in pressure readings for a 1:30 scale model but does not indicate how the limit of $\lambda = 10$ was determined.

It is clear that air entrainment, and other important flow variables, are subject to scale effects in physical models. This has important consequences for predicting flow characteristics over stepped spillways. Guidance is available on how to avoid scale effects, however, this should be used with caution. Each spillway is unique, so the exact air entrainment rates, velocities and other flow parameters will vary in each case.

Although scale effects place limitations on physical modelling of hydraulic structures, it can be difficult to investigate flows in prototype hydraulic structures which are in service. Inflow conditions can be difficult to control and measure and it is often impossible or unsafe to take detailed flow measurements. It can also be extremely expensive or unfeasible to construct prototype scale physical models in a laboratory. Scaled physical models can be designed to investigate specific problems and allow inflow conditions to be controlled and detailed meas-

urements to be made. Therefore, experimental modelling remains the most common and viable method to investigate hydraulic structures and provide data for validation of numerical models.

2.4.2 Overview of Numerical Modelling Techniques for Air-Water Free-Surface Flows

As outlined in table 2.1, each numerical model contains assumptions. In order for a numerical model to be used with confidence, it must be proven to be reliable. This is achieved by validating numerical models against physical data sets, at either experimental or prototype scales. Validation of numerical models must be conducted for each specific situation. A model which has been shown to accurately predict velocities over smooth spillways cannot be assumed to perform to the same accuracy for skimming flows over stepped spillways, as the hydraulics of the two flows are different. Validation of a numerical model may show that the model has limitations but is still able to predict certain flow features accurately. As long as these limitations are understood, the model can still provide a useful tool for hydraulic engineers.

Skimming flows over stepped spillways are air-water flows in which both phases play an important role. Therefore, numerical models which can model more than one fluid, known as multiphase models, are required to predict skimming flows over stepped spillways. In this project, three mesh based multiphase models have been investigated: the Volume of Fluid (VOF) model, the mixture model and the Eulerian multiphase model. Relevant studies into the performance of these multiphase models in predicting skimming flows over stepped spillways, and other free-surface air-water flows, are reviewed below.

Other multiphase numerical modelling techniques are also available. For example, smoothed particle hydrodynamics (SPH) is a Lagrangian technique in which no computational mesh is required and the fluid is modelled as a discrete set of particles. The model was first developed by Gingold and Monaghan (1977) to model astrophysical problems, but has now been developed for use in a variety of fields, including free-surface flows. SPH simulations tend to require a significantly larger computational cost than mesh based methods and the implementation of inflow boundary conditions can be problematic. In most cases, the SPH method only models the water phase and treats the air phase as a void, preventing air entrainment from being predicted. Some SPH formulations now allow the air phase to be modelled, how-

2. CURRENT UNDERSTANDING OF STEPPED SPILLWAYS AND ASSOCIATED MODELLING TECHNIQUES

ever, this further increases the already significant computational cost. For these reasons SPH was not investigated as part of this project.

2.4.2.1 The Volume of Fluid (VOF) Model

The VOF model is specifically a free-surface modelling technique. The model solves a single momentum equation for the fluid mixture and tracks the position of the free-surface. As such, there is no relative velocity between phases within a computational cell and any cell which contains more than one phase is assumed to contain a free-surface, which is defined using an interface capturing scheme. Therefore, the VOF model can only predict air entrainment if the computational mesh is significantly smaller than the size of the air bubbles, so that each air bubble can be modelled. For flows with a large number of air bubbles, such as aerated flows over stepped spillways, this would require a computational cost which is unfeasible with current computational resources. The VOF model, therefore, is unable to predict air entrainment in its standard form. Despite this, several studies have been shown to be able to accurately predict certain flow characteristics over stepped spillways.

Bombardelli et al. (2011) and Bayon et al. (2018) modelled skimming flows over an experimental stepped spillway at the LNEC in Lisbon (which is also numerically modelled in this project) using the VOF model. These studies focused on the non-aerated region only. Bombardelli et al. (2011) used the TruVOF approach, implemented in the CFD package Flow-3D, in which only the water phase is modelled and the air phase is assumed to be a void. Bayon et al. (2018) used interFoam, the VOF formulation in OpenFOAM. In both studies, and with both VOF formulations, velocities, flow depths and the location of the inception point were all predicted accurately. Bayon et al. (2018) also showed that the standard, Realisable and RNG $k - \epsilon$ turbulence models produced almost identical results. The SST $k - \omega$ results differed slightly from those of the $k - \epsilon$ models, however, were still similarly accurate.

Although not able to predict air entrainment, several studies have used the VOF model to investigate flows downstream of the inception point in the aerated region. Chen et al. (2002) showed that the VOF model could predict pressures on the step faces reasonably well at several steps throughout the length of the spillway. The location of the inception point was not reported, however, so it is unclear whether the presented data was in the aerated or non-aerated region. Chakib (2013) used the VOF model, with the $k - \epsilon$ turbulence model, to accurately predict flow velocities in both the aerated and non-aerated region. The results of

this study show air entrainment of the flow. As air entrainment is not predicted by the VOF model, it is unclear how this result was achieved. The study claims good agreement with the experimental data on the location of the inception point, however, the method used to define the location of the inception point in the numerical model is not defined. Kositgittiwong et al. (2013) modelled a large scale experimental stepped spillway using the VOF model. A range of RANS turbulence models were investigated and all were found to produce similarly accurate velocity profiles, both upstream and downstream of the inception point. Lopes et al. (2017) also predicted velocities accurately throughout the spillway using the VOF model and the flow depth was predicted accurately in non-aerated region. In the aerated region the flow depth were predicted reasonably accurately as the experimental depths fell within the numerical free-surface thickness. However, in the aerated region the numerical flow depths were noticeably lower, when compared with the experimental flow depths, than in the non-aerated region. This is likely due to the fact that the standard VOF model does not predict air entrainment and, therefore, flow bulking.

In its standard form, the VOF model is unable to predict air entrainment, however, modifications to the model have been developed which allow aeration to be predicted. Valero and Bung (2015) modelled skimming flow over a stepped spillway using the TruVOF approach with an additional air entrainment model. Air entrainment was observed in the simulations, however, the air entrainment, and therefore the flow depth downstream of the inception point, were overestimated. In the model used by Valero and Bung (2015), a calibration parameter is required to model air entrainment. In the study, the value of the calibration parameter used had been shown to be valid for smooth spillways, however, it was shown that this value is not suitable for stepped spillways. Lopes (2016) used the interface tracking VOF model, with a sub-grid air-entrainment model developed to predict self-aeration using the interFoam solver in OpenFOAM. The model was able to accurately predict air concentrations and the flow depth in the aerated region in skimming flow over a stepped spillway of slope 1:2.

2.4.2.2 The Mixture Model

The mixture model (also known as the algebraic slip model) is similar to the VOF model in that a single momentum equation is solved for the fluid mixture. However, the model uses an algebraic formulation to allow the phases to move relative to one another within a computational cell so that the phases can interpenetrate and air entrainment can be predicted at scales

2. CURRENT UNDERSTANDING OF STEPPED SPILLWAYS AND ASSOCIATED MODELLING TECHNIQUES

smaller than the computation grid size. The mixture model does not require a free-surface to be captured at cells containing more than one phase.

Cheng et al. (2006) modelled flow over a stepped spillway using the mixture model. Both velocity distributions and pressure profiles showed good agreement with physical data at a number of step locations. Nikseresht et al. (2013) showed accurate predictions of energy loss down a stepped chute using the mixture model combined with a range of turbulence models. Qian et al. (2009) modelled a stepped spillway using a range of turbulence models in combination with the mixture model and made comparisons with experimental data on velocities, span-wise vorticity and boundary layer thickness in the non-aerated region. The realizable $k - \epsilon$ turbulence model was found to be generally more accurate, although the SST $k - \omega$ and LES models were also reasonably accurate. Aydin and Ozturk (2009) used the mixture model to simulate flow through a spillway aerator. The air entrainment rates showed good agreement with the prototype data, however, did not agree with the physical model data due to scale effects. This shows that the mixture model can be used to accurately predict air entrainment and also highlights the limitations of physical scale models in predicting flow aeration.

2.4.2.3 The Eulerian Multiphase Model

The Eulerian multiphase model (also known as the Eulerian-Eulerian model and referred to as the Eulerian model from here forward) differs from the VOF and mixture models in that it solves a momentum equation for each phase. This allows the phases within a computational cell to move relative to one another and, like the mixture model, there is no requirement for a free-surface to be captured in cells which contain more than one phase. This allows air entrainment to be predicted by the Eulerian model and additional models are used to describe the interaction between phases. Research into the modelling of self aeration in air-water free-surface flows using the Eulerian multiphase models is relatively scarce.

Cheng and Chen (2011) modelled a hydraulic jump using the Eulerian approach with a modified drag function. Different bubble diameters and drag coefficients were tested and the free-surface surface position, air volume fraction and velocities showed good agreement with experimental data.

Teng et al. (2016) investigated a chute aerator using the Eulerian model in combination with the Realisable $k - \epsilon$ turbulence model. The numerical model predicted the cavity length

well. Reasonable predictions of the air volume fractions (AVFs) are made in some locations, however, in other locations the AVFs are significantly overestimated. A range of bubble sizes in the numerical model were investigated and the larger bubble sizes were generally found to produce more accurate results. Yang et al. (2019) also investigated a chute aerator using the Eulerian model, but with the RNG $k - \epsilon$ turbulence model, and a modified drag function was used. Again, the cavity length was predicted accurately and the AVFs were predicted well in some locations but not others. However, Yang et al. (2019) found that more accurate predictions were made with smaller bubble sizes, which is the opposite trend to that found by Teng et al. (2016). This may be due to the different turbulence and drag models used in the two studies.

Zhan et al. (2016) conducted numerical modelling of an experimental stepped spillway using the VOF, mixture and Eulerian models. In the study, both the VOF and mixture model show free-surface aeration, whereas the Eulerian model does not. This is unexpected as, for the reasons described above, the standard VOF model (as implemented in the study by Zhan et al. (2016)) is unable to predict air entrainment, whereas the Eulerian model is. Therefore, it is difficult to draw conclusions on the performance of the VOF or Eulerian models from this study. The accuracy of the mixture model in predicting AVFs was inconsistent.

2.5 Summary

Skimming flow over stepped spillways has been investigated extensively using experimental modelling and the general flow conditions are well established for a range of step geometries. Previous investigation into the pressures acting on the step faces, however, is limited to the centreline of the spillway only. Winter et al. (2010) is the only study into the pressures acting on the side wall of a stepped spillway, however, in the study no indication is given to whether the flow was aerated in the locations where pressures were measured. There have been a number of investigations into cavitation damage on stepped spillways, however, it is clear that the risk of cavitation damage to stepped spillways is not fully understood. There have also been only a small number of investigations which have considered plucking damage to masonry stepped spillways. A relatively large number of studies have investigated the performance of the VOF model in predicting skimming flow over stepped spillways, including a small number of cases which have included modifications which allow the model to predict air entrainment. There are

2. CURRENT UNDERSTANDING OF STEPPED SPILLWAYS AND ASSOCIATED MODELLING TECHNIQUES

significantly fewer studies, however, which have modelled skimming flow, or other free-surface aerated flows, using either the mixture model or Eulerian model.

CHAPTER 3

Design and Study of a Narrow Experimental
Stepped Spillway

3. DESIGN AND STUDY OF A NARROW EXPERIMENTAL STEPPED SPILLWAY

3.1 Introduction

Experimental modelling is conducted in order to investigate pressures, flow depths, inception point locations and 3D flow characteristics in a stepped spillway and also to provide validation data for CFD modelling. This chapter describes the design of an experimental stepped spillway and the investigations conducted using the spillway. Flow depths, inception point locations and the pressures acting on the step faces and side wall, for a number of flow rates, are measured and analysed.

3.2 Design of Experimental Spillway

An experimental stepped spillway has been designed for this project so that the experimental modelling could be conducted. The details of this design are described below.

3.2.1 Design Constraints

The design of the experimental stepped spillway was subject to the following constraints.

- The geometry of the spillway must allow skimming flow to occur over a range of available flow rates.
- There must be enough steps in the spillway so that the inception point, rapidly varied flow region, gradually varied flow region and uniform flow region occur over the steps, for a range of flow rates.
- The maximum height of the spillway rig, including side walls and circulation equipment, must not exceed 2700 mm, due to the space available in the laboratory.
- The steps must be large enough so that pressure measurements can be taken at multiple locations.
- The size of the steps should be as large as possible, within the above constraints, in order to reduce scale effects.
- The maximum discharge of the available pump is 23 l/s.

3.2.2 Spillway Geometry Design

Empirical relationships were used to determine the most appropriate step size and channel width. Chanson (2002) used data from a large number of experimental stepped spillways, with different step sizes and chute angles, to produce the following empirical relationship to predict the flow rate at which the onset of skimming flow occurs for a given spillway geometry:

$$\frac{y_c}{h_s} = 1.2 - 0.325 \frac{h_s}{l_s} \quad (3.1)$$

where h_s is the step height, l_s is the step length, $y_c = \sqrt[3]{q_w^2/g}$ is the critical flow depth (for a rectangular channel) and q_w is the discharge per unit width.

Using equation (3.1) it was decided that the spillway would be constructed with a channel width, W , of 150 mm, and 15 steps of height, 80 mm and length, 80 mm. This geometry, according to equation (3.1), will produce skimming flow at 8.7 l/s. The total height of the steps is 1.2 m, allowing sufficient space for side walls, pump, pipework and other equipment required to recirculate the flow.

The 80 mm step height gives a scale factor between the experimental spillway and the reference standard prototype step height (600 mm) of 7.5. This is less than the maximum scale factors suggested by Boes and Hager (2003a) and Down and Wearing (2012). For this geometry the minimum Reynolds number of 10^5 suggested by Boes and Hager (2003a) is achieved at 15 l/s, where $Re = q_w/\nu$. This spillway design, therefore, will allow skimming flow to be investigated over a reasonably large range of flow rates with scale effects minimised.

3.2.3 Crest Design

Spillway crests must be designed to prevent jet deflection, whereby the flow jets over the first several steps, rendering these steps redundant and reducing the efficiency of the spillway (Chanson, 2002). Common crest designs used to prevent jet deflection include broad crested weirs, circular crests and ogee crests. The CFD package FLOW-3D was used in the design of the spillway crest, as it uses the Fractional Area/Volume Obstacle Representation (FAVOR) method to incorporate the geometry of a simulation into the mesh. The purpose of this numerical study was, along with empirical relations, to aid in the design of the experimental spillway, rather than for detailed numerical analysis. In the FAVOR method, a mesh is generated to represent the flow domain and the solid geometry is then embedded within the mesh (Flow

3. DESIGN AND STUDY OF A NARROW EXPERIMENTAL STEPPED SPILLWAY

Science Inc., 2002), allowing a large number of geometries to be modelled without the need for a new mesh to be produced for each case. Using FLOW-3D a range of spillway crests were modelled in order to find the most appropriate design. FLOW-3D utilises the TruVOF method, a variation on the VOF model whereby only the liquid phase is modelled (Bombardelli et al., 2011).

Figure 3.1 shows four examples of potential crest designs that were modelled using FLOW-3D. Note that, in all cases, only a small number of steps were included in the model to reduce computational costs. It can be seen that, in each case, jet deflection occurs at one or more of the steps, as was the case for all crest profiles which were investigated. As there is no validation data available for these models, it is impossible to determine whether the observed jet deflection is due to the spillway and crest design, or possible inaccuracies in the FLOW-3D model. For this reason, it was decided that the spillway would be constructed with a removable crest. This allowed different crest profiles to be trialled so that a crest which prevents jet deflection could be found and installed into the experimental model.

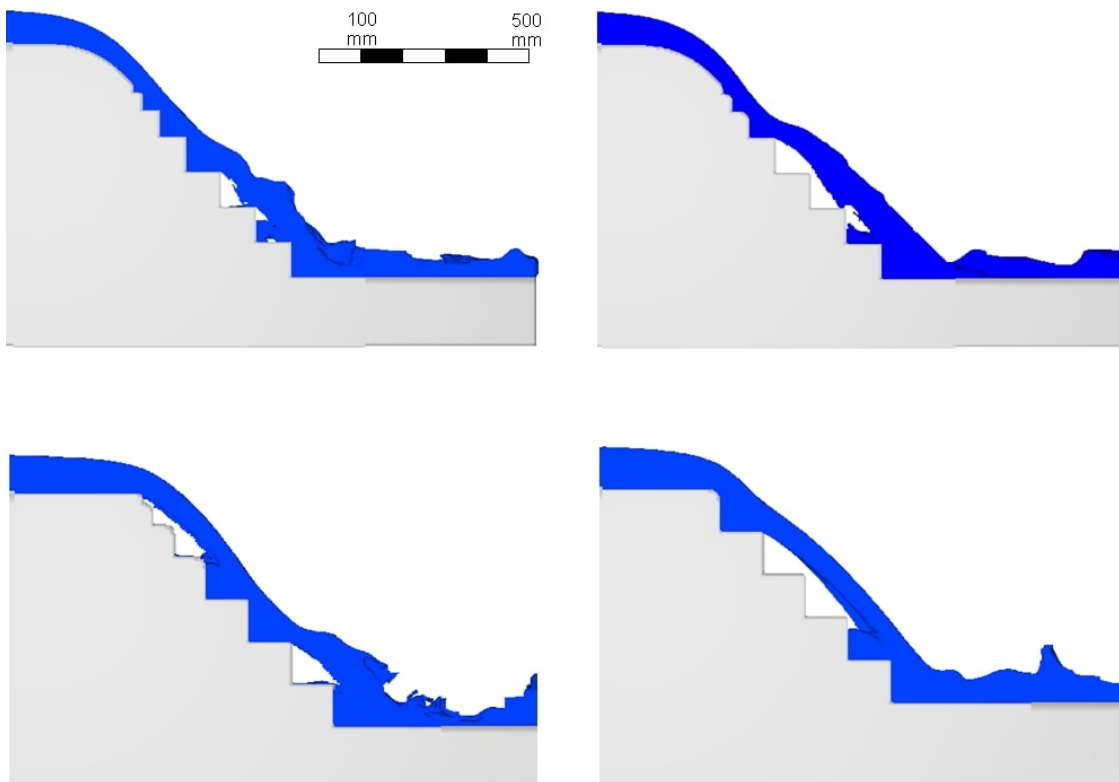


Figure 3.1: Various crest designs modelled using FLOW-3D. In all cases jet deflection is observed at one or more steps

3.2 Design of Experimental Spillway

Figure 3.2 shows the profile of the experimental crest which has been used throughout this study. The coordinates (0,0) represent the top corner of the first step and the coordinates (480,152) represent the end of the approach channel and the start of the curved crest. The curve has been approximated by the equation $z = -7.2 \times 10^{-4}x^2 + 0.659x + 1.8858$. It can be seen that the equation approximates the curve extremely accurately. Note that, in figure 3.2, x and z have been used to represent the horizontal and vertical axes in relation to ground level. Generally, throughout this chapter, x refers to the distance parallel to the pseudo-bottom from the first step corner and z refers to the distance perpendicular to the pseudo-bottom. This is detailed in figure 2.1.

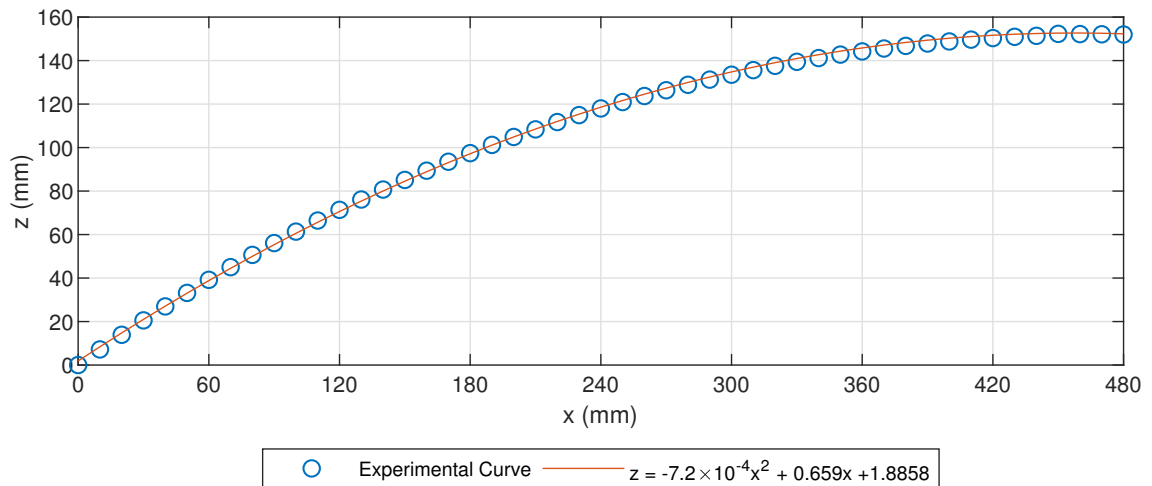


Figure 3.2: Experimental crest profile and the equation used to approximate the curve

3.2.4 Final Spillway Design

The final design of the experimental stepped spillway is shown in figure 3.3. The crest profile, which prevents jet deflection from occurring, is shown in the diagram. The spillway is constructed from 20 mm thick clear acrylic plastic so that the flow can be easily observed. The inflow and outflow consist of 300 mm and 590 mm diameter, cylindrical end boxes respectively. The water is pumped around the system using a Lowara single-impeller centrifugal pump with a flow rate range of 5 l/s to 25 l/s (although the company involved in the construction of the spillway advised that the flow rate should not exceed 23 l/s). Two flow control valves are used to control the flow rate and the discharge is measured using a calibrated 150 orifice plate flow meter.

3. DESIGN AND STUDY OF A NARROW EXPERIMENTAL STEPPED SPILLWAY

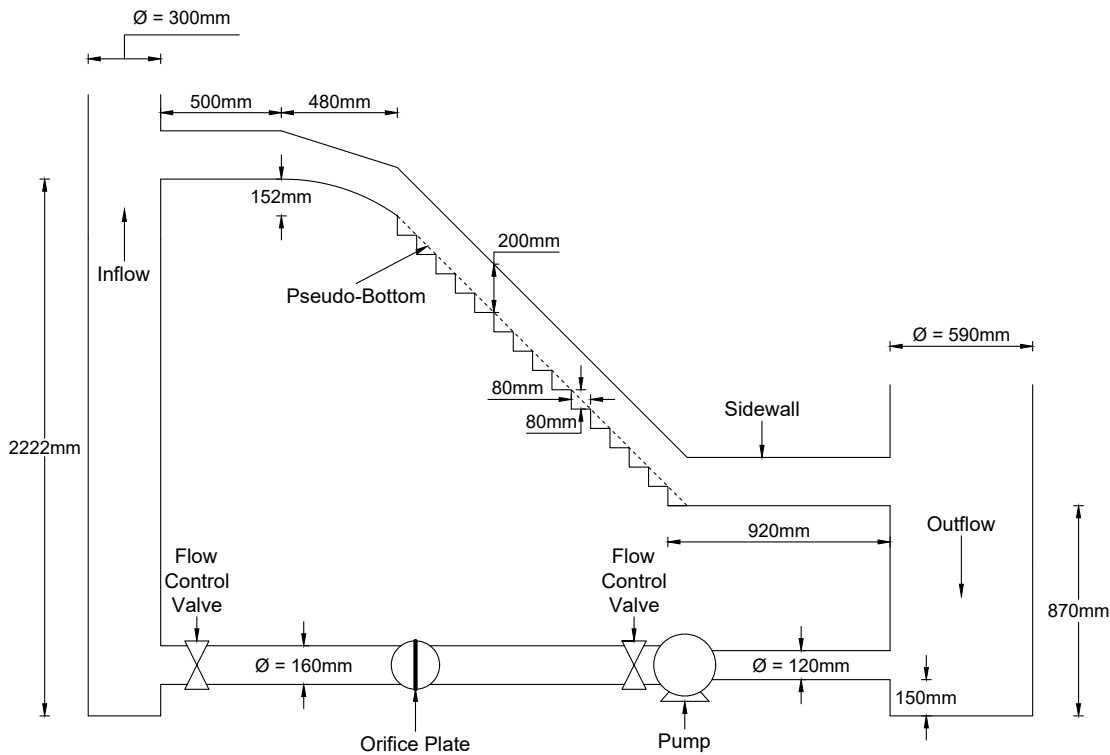


Figure 3.3: Diagram of the final design of experimental stepped spillway. The width of the spillway is 150 mm

3.3 Flow measurement Techniques

3.3.1 Pressure Measurement

Pressure measurements are taken at steps 2, 5 and 12. These steps are chosen for a number of reasons. Step 12 is always located in the fully aerated uniform flow region. For the majority of flow rates step 2 is located in the non-aerated region and step 5 is in the region where the location of the inception point varies over time. At the lower range of flow rates which produce skimming flow, step 2 is located in the upstream end of the region of the spillway where the inception point varies over time. The location of the three steps, in distinctly different regions of the spillway, will allow the effect of air entrainment on pressure to be investigated, and also provide validation data for CFD simulations in both the aerated and non-aerated regions.

A further reason that these steps were chosen for pressure measurements is that steps 2 and 12 are even numbered whereas step 5 is odd numbered. 3D vortex structures are

observed in the step cavities and have different forms at odd and even steps. These 3D structures are described further in section 3.4.

At each step, pressures are measured in the same locations. Figure 3.4a shows the pressure measurement locations on the step faces. In order to investigate the 3D effects, observed within the step cavities, pressure measurements are taken at the centreline of the spillway and also 20 mm from one of the spillway walls. These 3D effects are also discussed further in section 3.4. Figure 3.4a also shows the origin from where the distance across the channel width, w , the distance along the horizontal step face, l , and the distance up the vertical step face, h , are measured.

Figure 3.4b shows the pressure measurement locations at the spillway side wall. These locations are relatively spread out so that the general pattern of pressure on the side wall can be determined. Three of the sensors are located within the step cavity, where the recirculating vortices occur, and the other is located above the pseudo-bottom, allowing the difference in pressure between these locations to be investigated.

At each pressure measurement location, holes were drilled and tapped so that the pressure transducers could be securely screwed into position. When not in use, rubber bungs were inserted into the holes to form a water tight seal and sit flush with the spillway surface. Pressures were measured using two Omega PX409 pressure transducers with a measurement range of atmospheric pressure ± 6894.8 Pa. Note that, in accordance with the scale of the pressure sensor, all pressures in this study are presented relative to atmospheric pressure, which is defined as 0 Pa. A National Instruments cDAQ-9178 CompactDAQ chassis and National Instruments NI-9215 Input Module, in combination with the systems engineering software LabVIEW, were used to record the data measured by the pressure transducer. All pressures were recorded at a frequency of 1 kHz. On the step faces, at each horizontal or vertical position, pressures are measured at the centreline and at $w = 20$ mm simultaneously. On the side wall pressures are measured simultaneously at $h = 20$ mm and at $h = 60$ mm.

3. DESIGN AND STUDY OF A NARROW EXPERIMENTAL STEPPED SPILLWAY

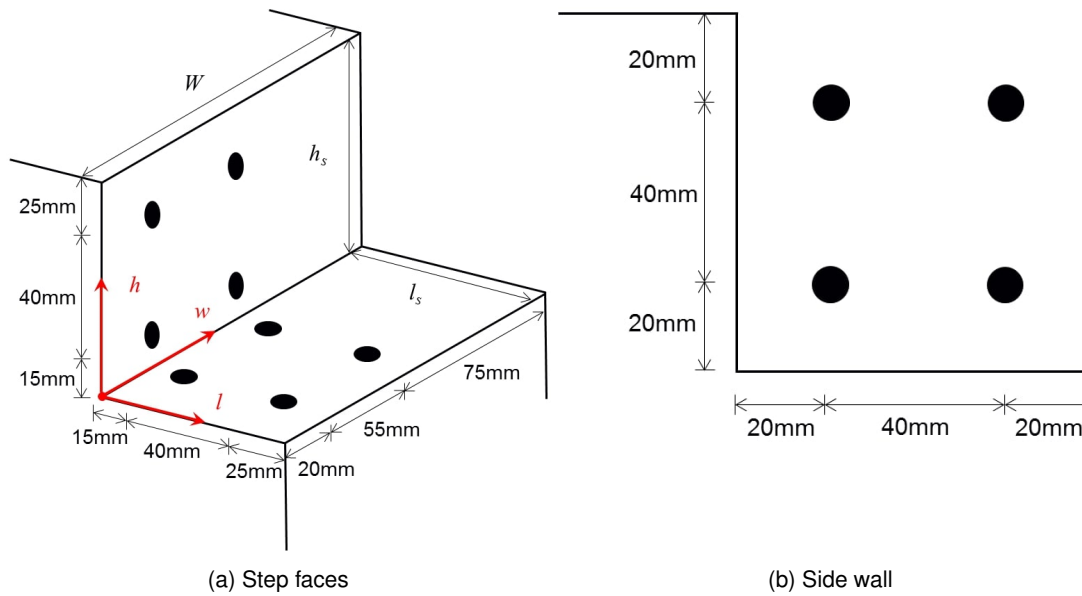


Figure 3.4: Pressure measurement locations on the step faces and spillway sidewalls. The dimensions h , l , and w and the distances h_s , l_s and W are indicated in the diagram.

3.3.2 Free-Surface Measurement

Image analysis was used to measure the position of the free-surface. One of the main advantages of this method of free-surface measurement is that it can measure the free-surface depth at all points along the spillway simultaneously, rather than at specific measurement locations. Images of the flow depth were collected by recording videos of the flow from the side of the spillway and ensuring there was large contrast between the colour of the water and the colour of the background. This allows the position of the free-surface to be calculated as the boundary between two colours. The contrast was achieved by lighting the spillway from below and installing a black background behind the spillway. The spillway was lit with three Yongnuo YN-600 Pro LED photography lights, each with 600 LEDs, to maximise the uniformity of the light on the spillway. Videos were recorded using a Nikon D3300 digital camera with a Nikon Nikkor 18mm - 55mm zoom lens. All videos were recorded at 60 frames per second with a resolution of 1920 by 1080 pixels. The ISO of the camera was set to 400 to increase the contrast between the fluid and the background. Figure 3.5 shows one frame of a video of the spillway. It can be seen that, along the entire length of the spillway there is a sharp contrast, at the free-surface, between the brightly lit fluid and the dark background. It should be noted that in the downstream end of the spillway the entire depth of flow is lit due to the presence of air bubble in the aerated region. Upstream, in the non-aerated region, there are no air bubbles

and the flow is brightly lit only adjacent to the free-surface.



Figure 3.5: One frame of a video used for image analysis to measure the location of the free-surface. Though the use of lighting, background and the ISO of the camera, a sharp contrast between the water and the background is observed at the free-surface

To determine the location of the free-surface, the video recordings were analysed using the computation and visualisation software MATLAB. Each frame of the video recording was processed individually and stored in a matrix. The following procedure was used to process each frame:

1. The image is rotated anticlockwise by 45° .
2. The image is cropped in the vertical direction from the pseudo-bottom to a depth above the maximum free-surface height. In the horizontal direction the image is cropped from $x = 0$ mm, at the corner of the first step, to $x = 1697$ mm, at the downstream end of the last step.
3. The image is converted from colour to greyscale (figure 3.6 (a)).
4. The greyscale image is then converted to a purely black and white image. Pixels with a colour value below a certain threshold are converted to black and pixels above the threshold are converted to white. The value of the threshold is chosen manually so that the bulk flow is converted to white while the background is converted to black. The use of lighting and a black backdrop results in a distinct change in the image colour at

3. DESIGN AND STUDY OF A NARROW EXPERIMENTAL STEPPED SPILLWAY

the free-surface. This results in the free-surface position being relatively insensitive to the threshold value used. A range of threshold values were trialed and each produced extremely similar free-surface profiles.

5. The dark areas caused by pressure sensor holes and the lower part of the non-aerated region are manually converted to white (figure (3.6 (b))).
6. The free-surface is determined as the boundary between black and white (figure 3.6 (c)).

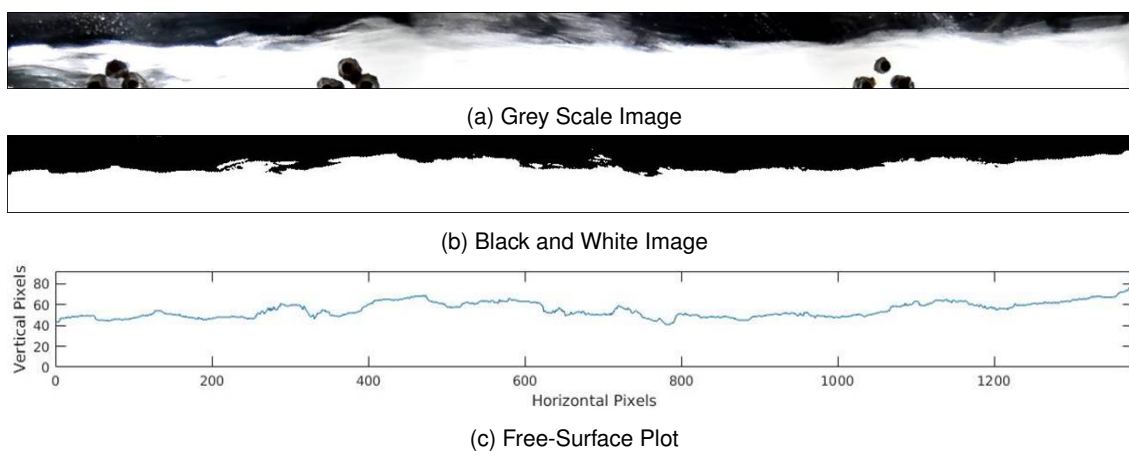


Figure 3.6: Procedure used to measure the free-surface position for a single video frame: (a) the original image converted into grey scale; (b) the grey scale image converted into either black or white; (c) the final free-surface plot calculated using the black and white image

After the image has been rotated and cropped in steps 1 and 2, the total depth of the image is approximately 100 pixels. The threshold value used in step 4 has also been chosen so that splashing near the free-surface is converted to black and only the bulk flow becomes white. However, the colour of the water in the splashes varies significantly and a single threshold value cannot completely remove all splashes from the image. Figure 3.6 (b) shows that at some horizontal positions there are several boundaries between the black and white parts of the image, caused by splashing at the free-surface. The free-surface is chosen as the lowest point at any horizontal position where there is a boundary between black and white pixels. This will help to remove any effects of splashing from the computed free-surface. At each flow rate, the spillway was recorded for 3 minutes, providing 10800 frames of data.

The axes of figure 3.6 (c) have units of pixels which must be converted into units of length. To do this, the number of pixels is measured from a known distance in the image, allowing conversion from the number of pixels to a length in mm using the following equation:

$$z = \text{depth in pixels} \times \frac{\text{known distance}}{\text{pixels covered by known distance}}. \quad (3.2)$$

3.3.3 Limitations

The main limitations in the experimental procedure used in this study are listed below.

- Pressures are only measured at two locations at one time. This allows pressures to be compared over the same measurement period at only two positions, e.g. at the wall and at the centreline. A larger number of pressure transducers and data acquisition modules would allow pressure data from more locations to be compared over the same measurement period.
- The range of the pressure sensors are atmospheric pressure ± 6894.8 Pa. The pressure transducers are able to measure pressures outside of this range, however, pressures outside of this range may not be measured accurately. All of the pressures measured in this study, however, fall within the measurement range of the pressure transducers.
- The pressure transducers used in this study are accurate to 5.5 Pa, which is negligible relative to the range of the pressures being measured.
- The method of free-surface measurement records the data from the side of the spillway so cannot measure any variation in the flow depth across the width of the channel. Some wall effects can be observed in the free-surface profile, however, only the maximum flow depth across the width of the channel is recorded using this measurement technique.
- The images taken to measure the free-surface may be subject to small amounts of barrel and/or pincushion distortion whereby straight lines, particularly close to the edge of the image, appear curved due to the curvature of the camera lens.

3.4 Initial Observations

Figure 3.7 shows an image of skimming flow over the experimental spillway. The non-aerated region, inception point and aerated region can be clearly seen, and recirculating vortices can be observed in the step cavities. The location of the inception point varies around a mean position over time, as described by Meireles et al. (2012).

3. DESIGN AND STUDY OF A NARROW EXPERIMENTAL STEPPED SPILLWAY

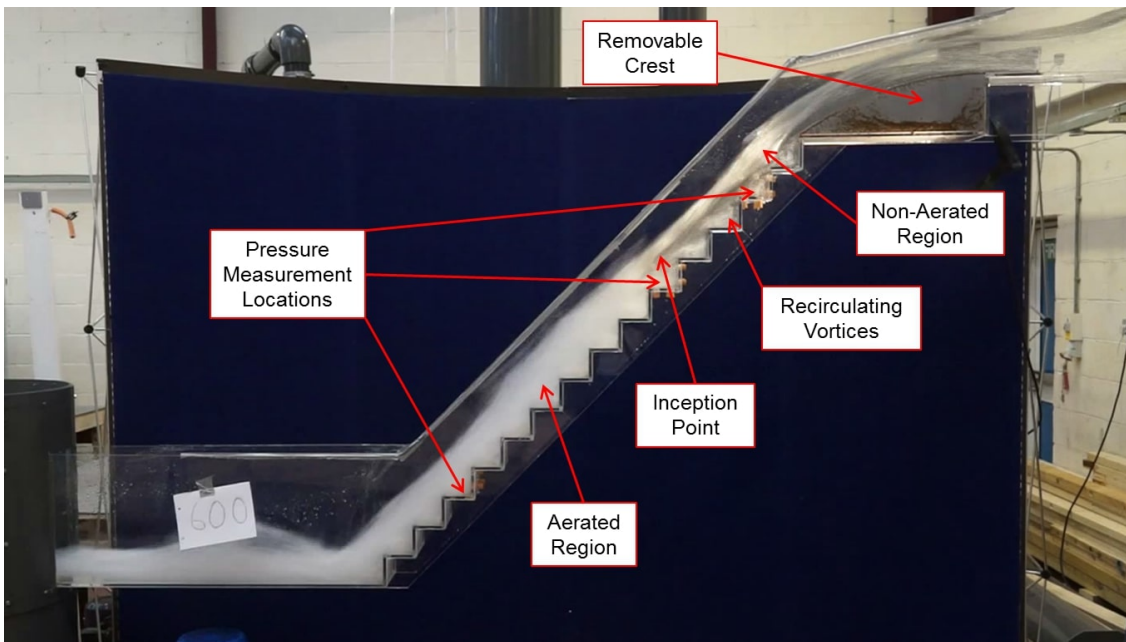


Figure 3.7: Experimental spillway under a discharge of 20.2 l/s. The non-aerated region, inception point and aerated region can be clearly seen. The pressure measurement locations are indicated

3.4.1 Cross-stream Vorticity

The recirculating vortices which occur during skimming flow (figure 2.1) can be observed through the spillway side walls. When viewed from the back of the steps, however, vortices which circulate perpendicular to the main flow direction are also observed in the step cavities. These vortices will be referred to as stream-wise, and cross-stream, vortices respectively. The cross-stream vortices have been observed at all steps, through dye injection into the step cavities in the non aerated region and by observing the movement of air bubbles in the aerated region. The stream-wise vortices are expected to occur and have been described by many authors. The cross-stream vortices, however, were not expected. Studies describing similar behaviour in stepped spillways are detailed below, however, to the best of the author's knowledge, the exact behaviour of cross-vortices observed in this study has not been reported elsewhere.

In each step cavity, there are two cross-stream vortices, circulating in opposite directions and interacting at the centreline of the spillway. It is observed that the vortices circulate in one of two directions depending on which step is considered. At some steps, the vortices flow upwards at the wall and impinge on the horizontal step face at the centreline of the spillway. This will be referred to as inward circulation. At the other steps, the vortices impinge on the

horizontal step face at the wall and flow upwards at the centreline. This will be referred to as outward circulation. The pressure measurement locations were chosen to be at the centreline and close to the wall so that the effect of the cross-stream vortices on the pressures acting on the step faces could be investigated. The direction of circulation of the cross-stream vortices is also observed to change from inward to outward circulation at each consecutive step.

Figure 3.8 shows photographs of the step cavities from behind the steps, and associated diagrams detailing the direction of circulation of the cross-stream vortices, of steps 9 and 10 at $Q = 15$ l/s. It can be seen, from the air bubbles in the photographs, that in each step cavity there are two structures, one on either side of the spillway centreline. These structures are the cross-stream vortices. At step 9 inward circulation is observed, which then changes to outward circulation at step 10. This alternating pattern repeats at every step. Pressures were measured at both odd and even numbered steps (2, 5 and 12) so that the effect of both inward and outward circulation on the step pressures could be investigated.

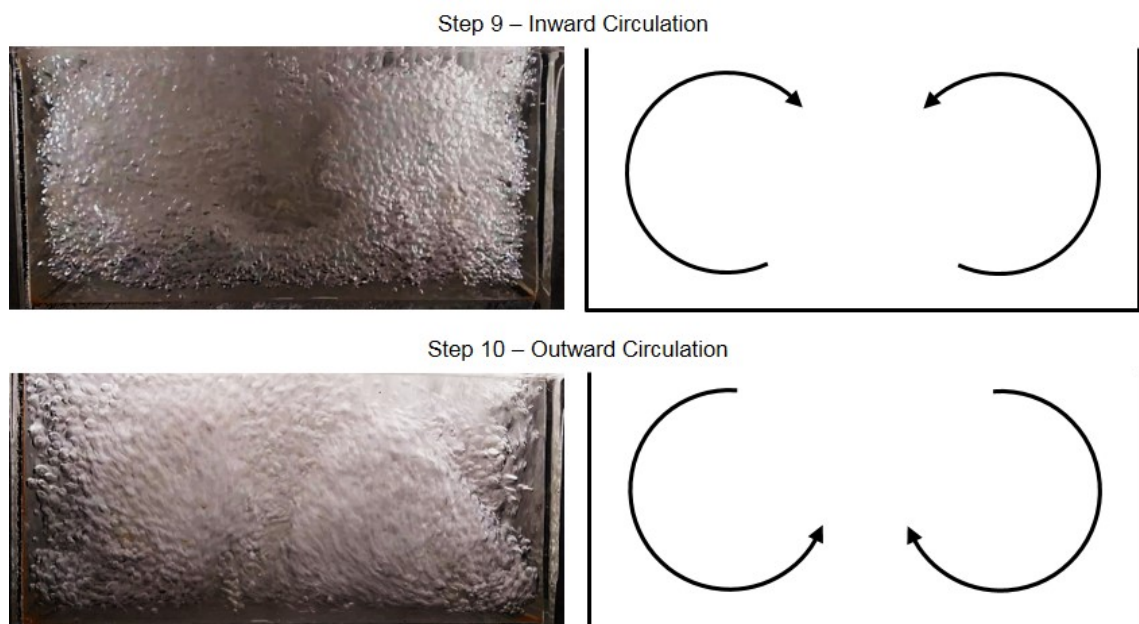


Figure 3.8: Cross-stream vortices viewed from behind the vertical step face, at $Q = 15$ l/s, at steps 9 and 10, with associated diagrams detailing the direction of circulation of the cross-stream vortices

Figure 3.9 shows a schematic of the structure of the stream-wise vortices at two steps, for comparison with the stream-wise vortices. The arrows indicate the direction of circulation of the stream-wise vortices. As viewed from the side of the spillway, the stream-wise vortices appear to have the same structure at each step, unlike the cross-stream vortices. The cross-stream vortices cause the flow within the step cavities to vary across the width of the channel,

3. DESIGN AND STUDY OF A NARROW EXPERIMENTAL STEPPED SPILLWAY

however, this behaviour is not apparent through observation of the stream-wise vortices from the side of the spillway.

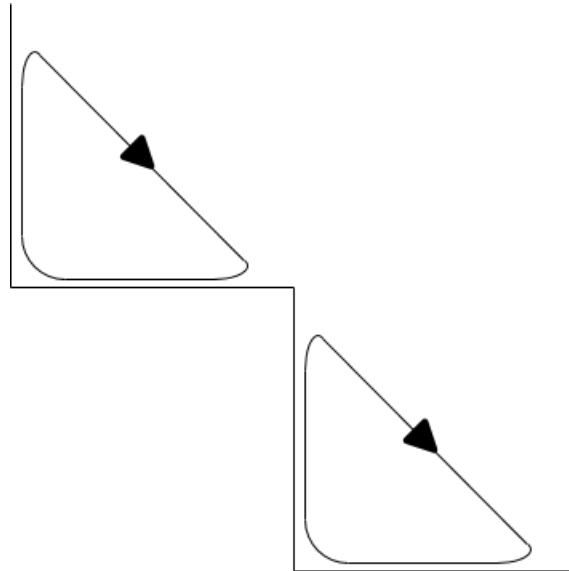


Figure 3.9: Schematic showing the structure of the stream-wise vortices as viewed from the side of the spillway, with the direction of circulation of the stream-wise vortices indicated by arrows

At the lower range of flow rates, for the skimming flow regime, the odd numbered steps show inward circulation and the even numbered steps show outward circulation. As the flow rate is increased, there is a range of flow rates at which the direction of circulation of the cross-stream vortices, at a particular step, can be visually observed to fluctuate between outward and inward circulation. As the flow rate is increased further a value is reached at which the direction of circulation at each step appears to be consistently opposite to that at the lower flow rates. At these higher flow rates, the direction of circulation of the cross-stream vortices can be visually observed to be generally the opposite of that at the lowest flow rates. The direction of circulation, however, is not as stable as at the lower flow rates and some fluctuations can still be observed. This will be discussed in more detail in section 3.5.3.4.

Studies documenting this pattern of alternating cross-stream vortices, or similar phenomena, are rare. This may be partly due to the construction materials of experimental stepped spillways making it impossible to visualise the variation in the flow across the width of the channel.

Chanson (2002) describes different sub-regimes of skimming flow which, depend on the chute angle, θ . Below $\theta \leq 12^\circ - 15^\circ$ the SK1 sub-regime occurs in which there is unstable recirculation and the mixing layer does not reach the end of the step. From $12^\circ - 15^\circ \leq \theta \leq$

$15^\circ - 25^\circ$ the sub-regime SK2 occurs in which there is unstable recirculation and the mixing layer extends to the end of the step. For $\theta \geq 25^\circ - 30^\circ$ sub-regime SK3 occurs whereby stable recirculation occurs with most of the vorticity occurring at the downstream end of the step.

Lopes et al. (2017) found that for a 500 mm wide spillway of $h_s = 60$ mm, $l_s = 120$ mm and $\theta = 26.6^\circ$ the sub-regimes SK1 and SK2 were observed to occur at alternating steps. However, the same step geometry, with a narrower channel width of 300 mm, did not show this pattern. CFD simulations of the 500 mm wide spillway show that the SK1 and SK2 sub-regimes alternate across the width of the channel as well as at each step, which is the same trend that is shown in the current study. Note that, in the current study, θ falls within the range suggested by Chanson (2002) to produce the sub-regime SK3 and SK3 is observed at every step. The alternating pattern of cross-stream vorticity is not perceptible from the side wall of the spillway and can only be observed from behind or beneath the step cavities.

Morovati et al. (2016) conducted experimental and CFD modelling of a number of configurations of pooled steps for a 520 mm wide spillway with $h_s = 100$ mm and $l_s = 200$ mm. CFD streamlines show that secondary flows, which appear similar to the cross-stream vortices observed in this study, occur for a number of step pool configurations. Streamlines were only presented at one step, however, so it is unclear whether the alternating pattern of circulation direction occurred.

Matos et al. (1999) describes 3D behaviour of the recirculating vortices across the width of a 1000 mm stepped spillway channel. It is unclear, however, whether the 3D behaviour is a regular pattern of vortices, as observed here, or whether there is any alternating pattern at each subsequent step. Pressures were measured at the centre of the horizontal step face and a wavy pattern of pressure was observed down the spillway chute. The wavelength of this pattern, however, does not suggest a pattern that alternates at each step. Sánchez-Juny et al. (2000) and Sánchez-Juny and Dolz (2005) also reported a wavy pattern to the pressures acting at the centre of the horizontal step face at different locations along the spillway. The wavelength of the wavy pattern of pressures reported in these studies is approximately two steps, which would correspond to an alternating pattern at each step.

Although not directly related to vorticity in the step cavities, alternating behaviour from step to step of other flow variables have been reported. Felder and Chanson (2009b) and Yasuda and Chanson (2003) conducted experimental modelling of a 1000 mm wide stepped spillway with $\theta = 21.8^\circ$. Both studies tested steps of $h_s = 50$ mm and Felder and Chanson (2009b)

3. DESIGN AND STUDY OF A NARROW EXPERIMENTAL STEPPED SPILLWAY

also tests steps of $h_s = 100$ mm. In all cases, a "seesaw" pattern was observed in a number of flow variables, including the depth-averaged void fraction, characteristic depth, characteristic air-water velocity and turbulence intensity. The seesaw pattern had a wavelength of two steps, equating to an alternating pattern at each step.

3.5 Experimental Results

Experimental data was recorded at discharges of 12 l/s, 15 l/s, 18 l/s and 21 l/s. At $Q = 12$ l/s $Re = 80,000$ which is close the minimum value of 10^5 suggested by Boes and Hager (2003a). This flow rate was chosen, however, to provide data on as large a range of flow rates as possible for both experimental investigation and also validation of CFD models.

3.5.1 Free-Surface Position

Figure 3.10 shows the mean free-surface position, \pm the standard deviation, for the four flow rates investigated. In all cases the minimum flow depth is at the upstream part of the spillway in the non-aerated region. There is then an increase in the depth of the free-surface which represents the inception point. At this point air is entrained into the flow which increases the volume of the air-water mixture, increasing the flow depth. The location of the inception point is discussed further in section 3.5.2. Downstream of the inception point, the flow depth increases due to flow bulking and reaches its maximum value. Further downstream the flow depth decreases in the uniform flow region. These findings agree with well documented theory of skimming flow over stepped spillways. Note that at the far downstream end of the spillway the flow depth increases steeply. This is due to the flow meeting the outflow channel of the spillway which is at 45° to the pseudo-bottom.

The standard deviation is relatively small in the non-aerated region and then increases significantly downstream of the inception point. This greater variation in the free-surface depth is attributed to the intense splashing observed in this area, and the effect of the temporal variation of the location of the inception point. Further downstream, in the uniform flow region, the standard deviation decreases, but still remains generally larger than the non-aerated region. It is also noticeable that at the higher flow rates, there is a greater variation in the flow depth in the non aerated region.

3.5 Experimental Results

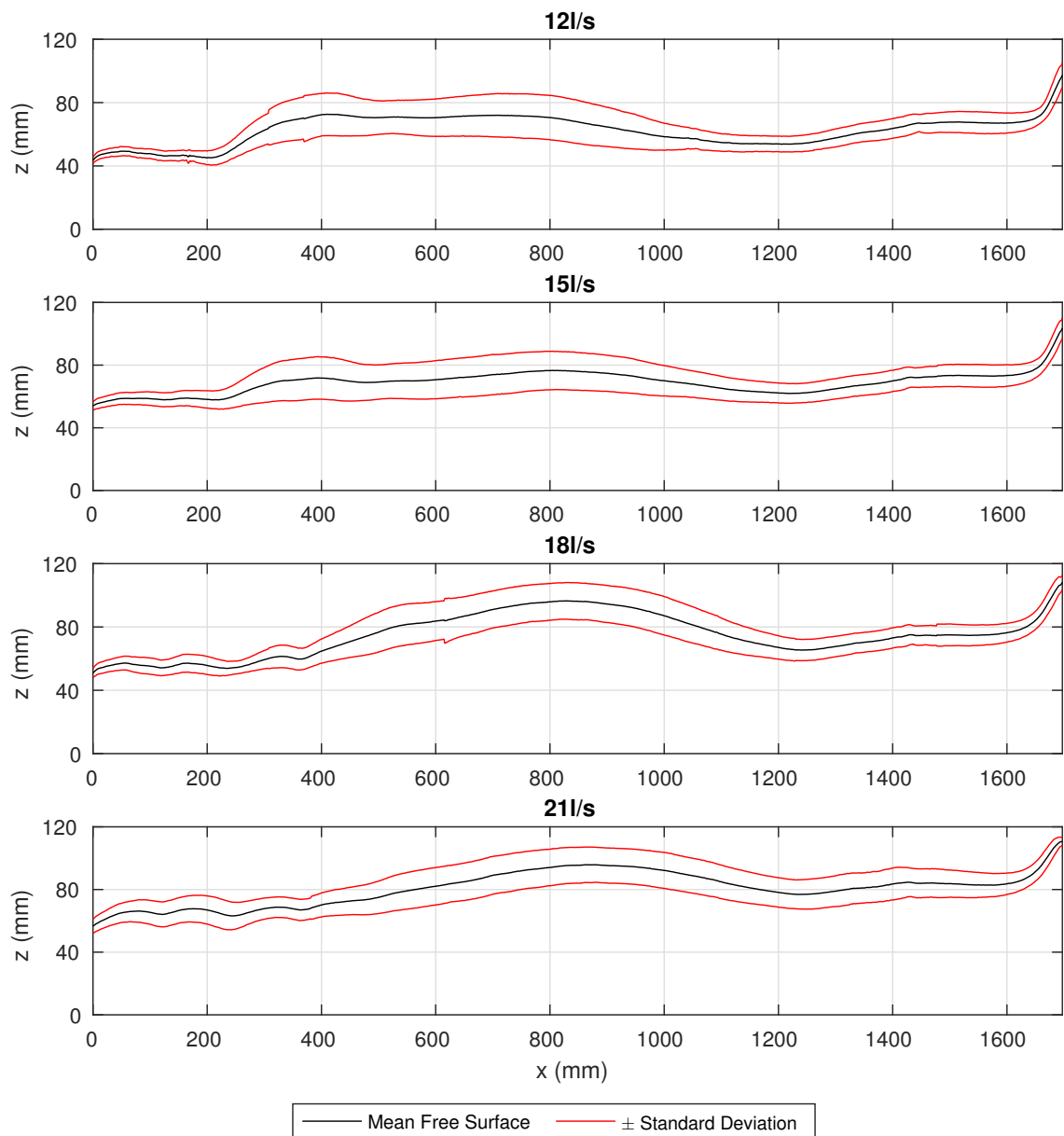


Figure 3.10: Experimentally measured mean free-surface positions \pm the standard deviation. Data is averaged over 180 s of data (10800 frames) and is shown for all four flow rates investigated

Figure 3.11 shows a direct comparison of the mean free-surface positions for the four flow rates. In general the flow depth increases with discharge. At 15 l/s and 18 l/s there is little difference in the flow depth in the non-aerated region and the uniform flow region. Directly downstream of the inception point the flow depths are similar for 12 l/s and 15 l/s and also for 18 l/s and 21 l/s.

3. DESIGN AND STUDY OF A NARROW EXPERIMENTAL STEPPED SPILLWAY

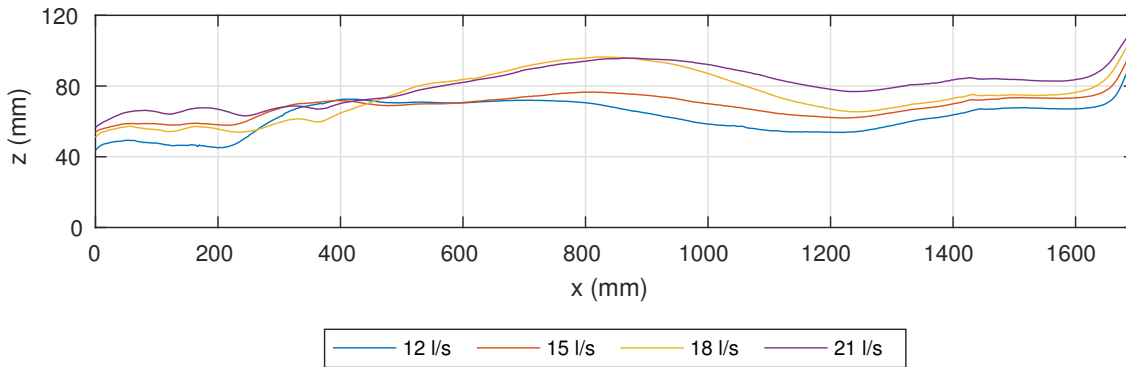


Figure 3.11: Experimentally measured mean free-surface profiles for the four discharges investigated

3.5.2 Inception Point

As described by Meireles et al. (2012), the location of the inception point varies around a mean temporal position. By visual observation it is noticeable that, as the flow rate increases, the location of the inception point varies over a larger distance. This is likely, at least in part, due to the increase in the variation of the free-surface depth in the non-aerated region with increasing discharge (figure 3.10). As the inception point occurs when the free-surface and turbulent boundary layer intersect, a greater variation in the free-surface position will cause a greater variation in the location of the inception point.

The location of the inception point was measured by visual inspection and was recorded as the outside step corner immediately upstream of the of the step cavity that has a continuous presence of air bubbles when viewed from the side walls. L_i is the distance, parallel to the pseudo-bottom, from the corner of step 1 to the inception point. Although the step cavity has a continuous presence of air bubbles, the volume of air bubbles in the cavity is observed to vary as the location of the inception point varies. Table 3.1 shows the inception point locations for various flow rates. The inception point is the same at 15 l/s as it is at 12 l/s. It would be expected that the inception point would appear further downstream at the higher flow rate. Due to the method of recording the location of the inception point, the recorded data is only precise to \pm half the distance between the outside step corners ($113.13/2 = 56.57$ mm). A more precise method of measuring the inception point, such as measuring the depth of the turbulent boundary layer, may produce slightly different values for 12 l/s and 15 l/s.

Table 3.1: Inception point locations

| Q (l/s) | Step | L_i (mm) |
|-----------|------|------------|
| 12 | 3 | 226 |
| 15 | 3 | 226 |
| 18 | 5 | 452 |
| 21 | 6 | 565 |

In order to determine whether the recorded inception point locations show similar behaviour to other experimental studies, the data is compared to empirical relationships developed by Chanson (2002) and Boes and Hager (2003a). However, L_i is defined differently by both Chanson (2002) and Boes and Hager (2003a), and also in this study. In table 3.1, L_i is the distance from the top corner of step 1 to the inception point. Chanson (2002) defines L_i as the distance from the start of the growth of the boundary layer to the inception point. The location of the start of the growth of the boundary layer was not able to be measured in this study, however, it would be expected that it would be located significantly further upstream than the first step corner. Boes and Hager (2003a) define L_i as the distance along the curved crest and pseudo-bottom profile from the maximum height of the spillway crest to the inception point. The spillway configuration is different to that of this study, however, as this study has a relatively long approach channel upstream of the curved section, which is not the case in the study by Boes and Hager (2003a).

CFD data has been used in order to determine where L_i should be measured from, in this study, in order to make comparisons with the empirical relationships proposed by Chanson (2002) and Boes and Hager (2003a). Figure 3.12 shows contours of air volume fraction, for the inlet and approach channel, at the centreline of the spillway, with streamlines superimposed over the contours. The VOF multiphase model, with the SST $k - \omega$ turbulence model, was used for this simulation (described in detail in chapter 4) and the flow rate was 15 l/s. It can be clearly seen that at the upstream end of the horizontal section of the approach channel there is an area of recirculation. It, therefore, follows that the turbulent boundary layer, due to the interaction of the water and the spillway surface, would develop at some point downstream of this area of recirculation.

3. DESIGN AND STUDY OF A NARROW EXPERIMENTAL STEPPED SPILLWAY

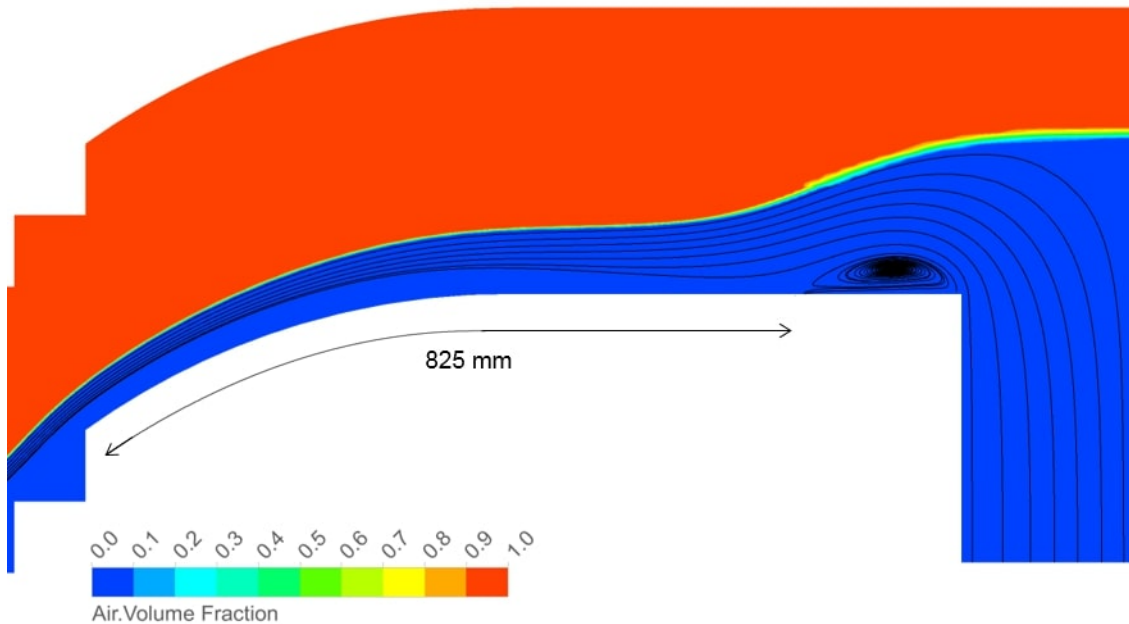


Figure 3.12: CFD contours of air volume fraction and streamlines using the VOF multiphase model with the SST $k - \omega$ turbulence model. The approximate distance from the downstream end of the recirculation zone and the top of the first step is approximately 825 mm

The distance along the curved and horizontal section of the approach channel, from the recirculating region to the first step, is approximately 825 mm. A value of 825 mm has, therefore, been added to the recorded values of L_i in this study so that they can be directly compared to the empirical relationships proposed by Chanson (2002) and Boes and Hager (2003a). Note that the value of 825 mm is only an approximation, as the length of this recirculation region in the CFD model has not been validated against experimental data, and also the value of 825 mm would likely vary with flow rate. However, the addition of 825 mm to L_i will allow more meaningful comparisons of the experimental data and the empirical relationships to be made.

Figure 3.13 shows the experimentally recorded values of $L_i + 825$ mm as well as the predictions of L_i using the empirical relationships. Note that the error bars represent the precision error of half the distance between step corners. The two empirical relationships appear to have almost identical gradients. Although the experimental inception points at $Q = 12$ l/s and $Q = 15$ l/s are recorded at the same step, when the precision error is accounted for, the rate of increase in L_i with Q matches the predictions made using the work of Chanson (2002) and Boes and Hager (2003a) reasonably well.

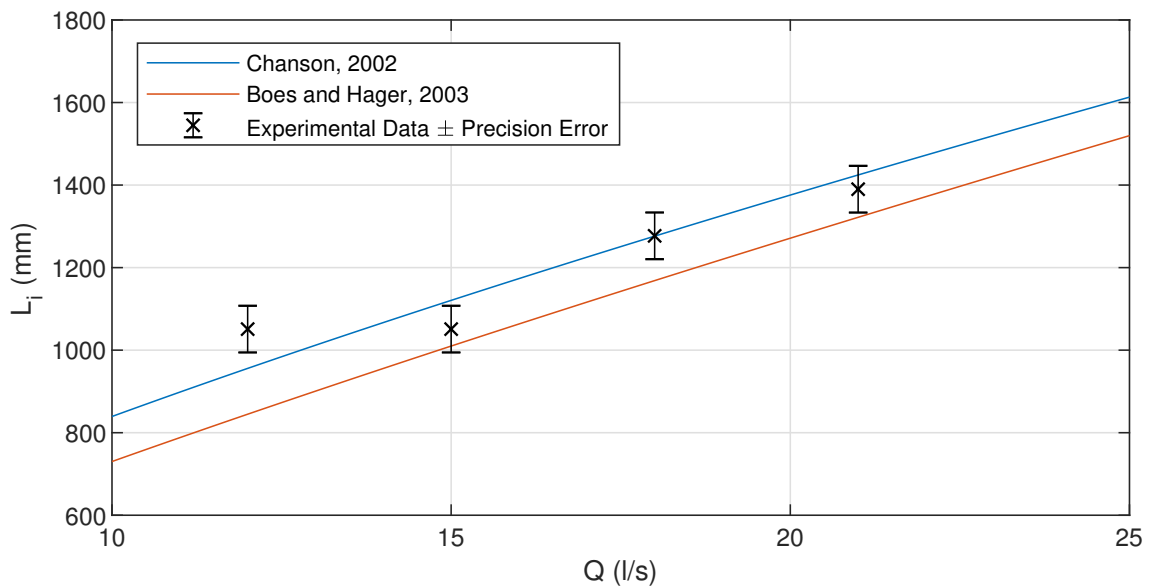


Figure 3.13: Inception point locations for different flow rates as predicted by empirical relationships and with adjusted experimental data. The precision error for each experimentally measured inception point location is indicated in the figure













3.5.3 Pressures Acting on the Step Faces and Spillway Side Walls

3.5.3.1 Horizontal Step Faces

Table 3.2 shows the predominant direction of circulation of the cross-stream vortices. Note that, although this indicates the predominant circulation direction that is observed at these flow rates, fluctuations in the direction of circulation, as described in section 3.4.1, are observed in some cases. The directions of circulation are also indicated in figures 3.14, 3.15, 3.16, 3.17 and 3.20.

3. DESIGN AND STUDY OF A NARROW EXPERIMENTAL STEPPED SPILLWAY

Table 3.2: The predominant direction of circulation of the cross-stream vortices for different steps and flow rates

| Step Number | Q (l/s) | Circulation Direction |
|-------------|---------|--|
| Step 2 | 12 | Outward  |
| | 15 | Outward  |
| | 18 | Outward  |
| | 21 | Inward  |
| Step 5 | 12 | Inward  |
| | 15 | Inward  |
| | 18 | Inward  |
| | 21 | Outward  |
| Step 12 | 12 | Outward  |
| | 15 | Outward  |
| | 18 | Outward  |
| | 21 | Inward  |

The findings of Amador et al. (2009), Chen et al. (2002) and others show that that the pressures on the horizontal step face follow the profile shown in figure 2.2. The maximum pressure act at the downstream end of the step, where the recirculating vortex impinges on the step face. This will be referred to as the the typical pressure profile, for comparison with certain cases in this investigation, where the pressure profiles do not match the findings of the above mentioned authors.

Figure 3.14 contains bar charts showing the mean pressures at different locations in the spillway, with error bars denoting the mean \pm the standard deviation. Firstly consider only the data for the flow rates 12l/s, 15l/s and 18l/s. At step 2, the typical pressure pattern can be seen close to the wall at $w = 20\text{mm}$, where the pressure at $l = 55\text{ mm}$ is much higher than at $l = 15\text{ mm}$. At the centreline of the spillway, however, this pressure pattern is not seen. At the

centreline there is very little difference in pressure across the length of the step. At step 2 the cross-stream vortices show outward circulation so that the cross-stream vortices impinge on the horizontal step face close to the wall but flow away from the step at the centreline.

At step 5, the opposite trend can be observed. The typical pressure profile, with the higher pressure at the downstream end of the step, occurs at the centreline of the spillway, however, at the wall there is very little difference in the pressure across the length of the step. At these flow rates inward circulation occurs at step 5, so the cross-stream vortex impinges at the centreline. It should be noted that although the pattern is the reverse of the pattern at step 2, there is not as much of a variation in pressure across the width of the channel.

At step 12, the direction of circulation of the cross-stream vortices is the same as at step 2 and the pressure profile is also the same. The typical pressure profile occurs at the wall but not the centreline. This is shown in figure 3.18.

3. DESIGN AND STUDY OF A NARROW EXPERIMENTAL STEPPED SPILLWAY

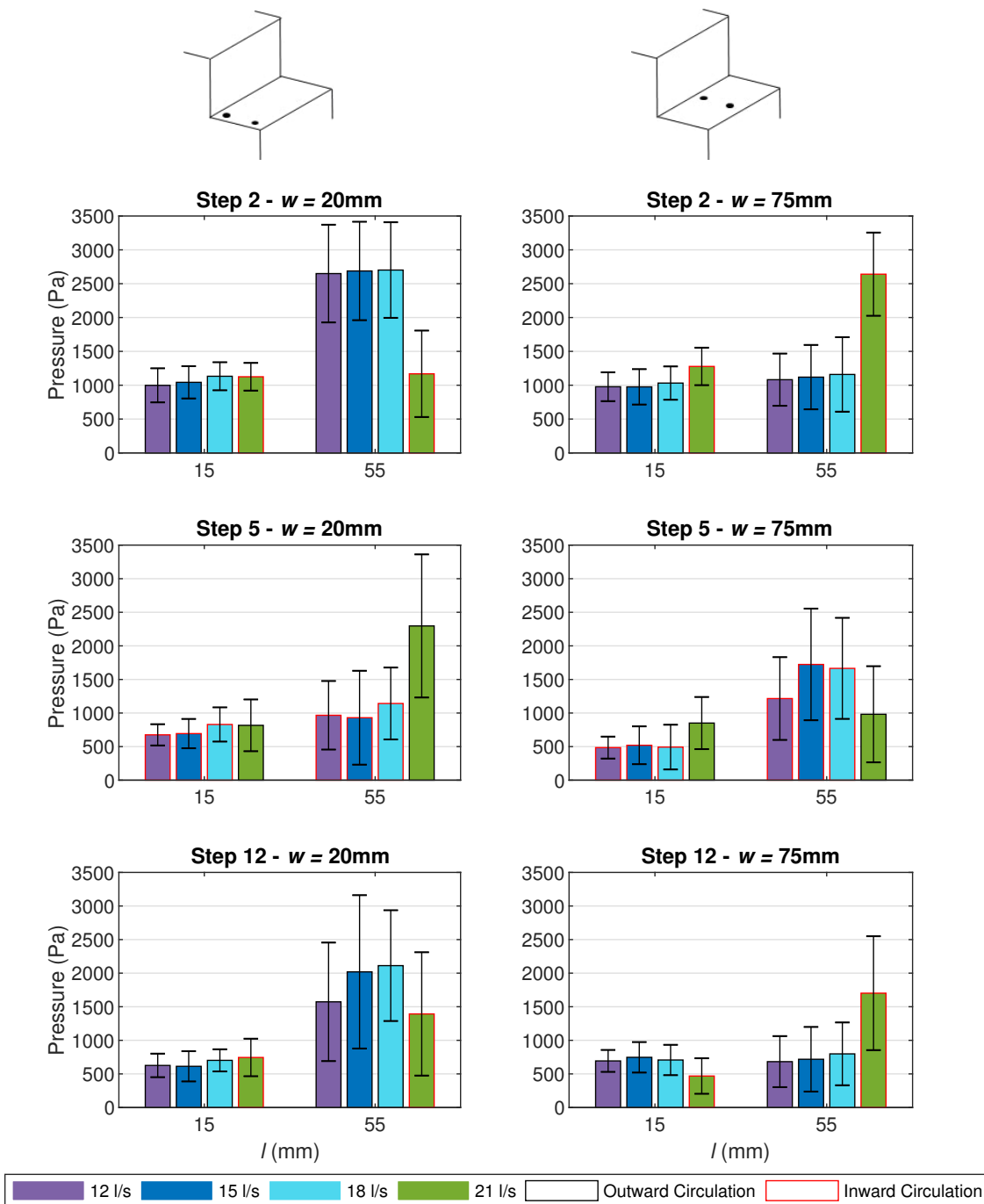


Figure 3.14: Mean pressure acting on the horizontal step faces \pm standard deviation. w is the distance across the channel width from the spillway sidewall and l is the distance along the horizontal step face from the inside step corner. These dimensions are detailed in figure 3.4a

Now consider the data for $Q = 21$ l/s. In this case, it was observed that the direction of circulation of the cross-stream vortices had swapped in the manner previously discussed. At this flow rate we see the opposite trend in the location of the maximum pressures. At steps 2

and 12 the typical pressure pattern is observed at the centreline and at step 5 it is observed at the wall.

Apart from one case, at all locations and for all flow rates the typical pattern of pressure (figure 2.2) is observed at the position where the cross-stream vortices impinge on the horizontal step face. Where the cross-stream vortices flow away from the horizontal step face the typical pressure profile does not occur and there is little variation in the pressure across the length of the step. This very clearly shows that the direction of circulation of the cross-stream vortices affects the pressure across the width of the channel.

The exception to this trend is step 12 at 21 l/s. Here the pressure at $l = 55$ mm is slightly higher at the centreline, where the cross-stream vortices impinge, than at the wall. However, at both the wall and the centreline the pressure is noticeably higher at $l = 55$ mm than at $l = 15$ mm. Therefore it would appear that, although there is variation in the magnitude of the pressure, the typical pressure profile occurs at both the wall and the centreline.

In order to understand how the flow is behaving at step 12 for $Q = 21$ l/s, it is helpful to consider the full pressure signal over the five minute measurement period, rather than just the mean values. Figure 3.15 shows 10 s moving averages of the pressures at the downstream end ($l = 55$ mm) of the horizontal step faces. Each step and flow rate combination is shown in a separate sub-plot and each sub-plot shows the moving average at the wall and the centreline, as well as the the mean of the two moving averages. The predominant direction of circulation of the cross-stream vortices have been shown but, as in figure 3.14, fluctuations in the circulation direction may still occur.

3. DESIGN AND STUDY OF A NARROW EXPERIMENTAL STEPPED SPILLWAY

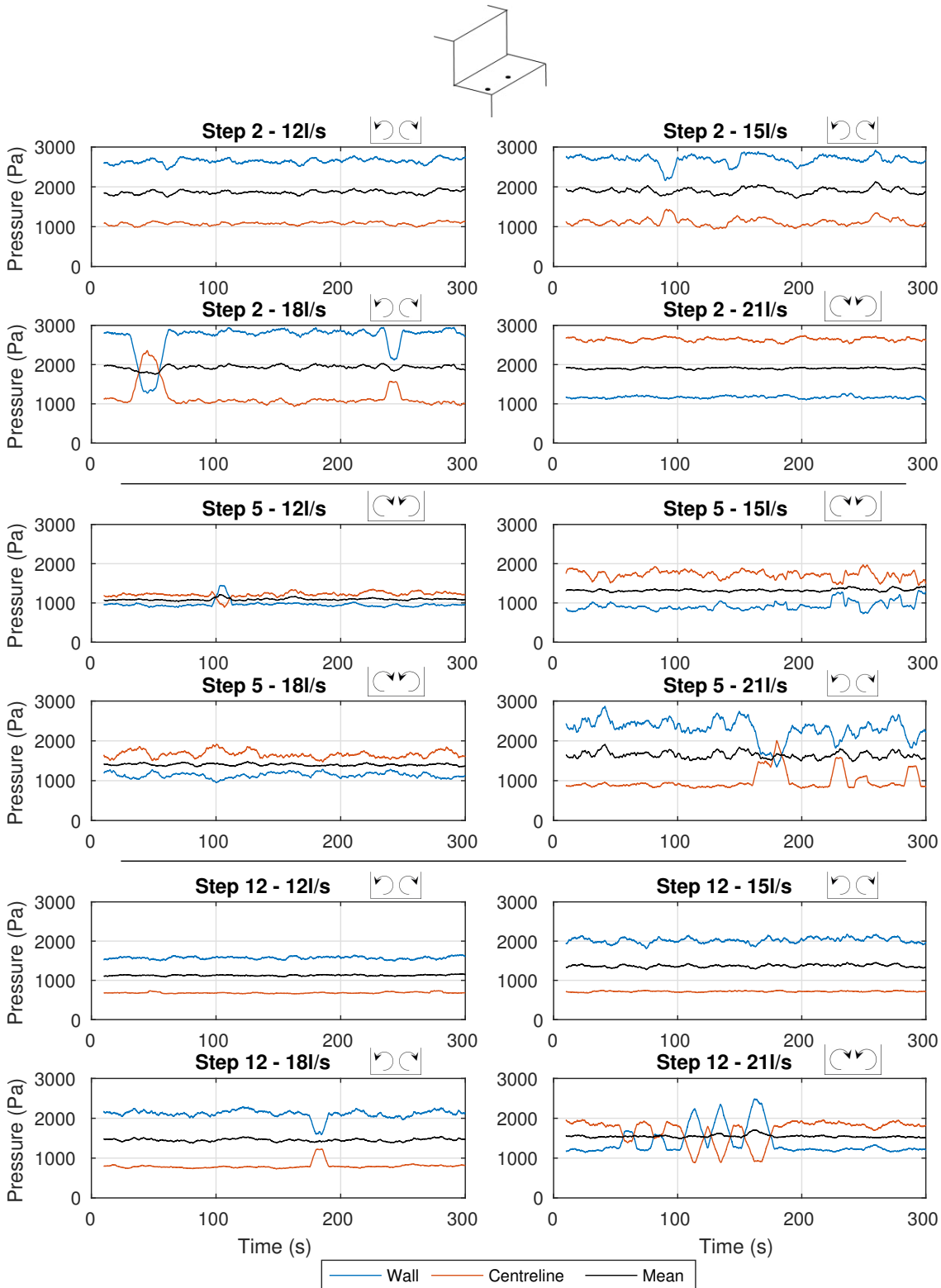


Figure 3.15: 10 second moving averages of the pressure acting at the centreline and close to the wall, at the downstream end of the horizontal step faces. Data is shown at steps 2, 5 and 12 for varying flow rates

The pressure signals generally follow the pattern observed in figure 3.14, with the high

and low pressure locations corresponding to the direction of circulation of the cross-stream vortices. In some cases, however, the two data lines cross one another, showing that the location of highest pressure moves from the wall to the centreline, or vice versa. The direction of circulation of the cross-stream vortices has been visually observed to fluctuate at a particular step, as described in section 3.4, and the highest pressures are generally found where the cross-stream vortices impinge on the horizontal step face. As a decrease in the pressure in one location corresponds to an increase in the pressure at the other location, it is a reasonable assumption that when the two data lines in figure 3.15 cross one another, the direction of circulation of the cross-stream vortices has reversed. This phenomenon will be referred to as vortex switching.

In each case the pressure signals at the wall and the centreline display strong symmetry around the mean and the mean remains relatively constant. The pressures at the end of the step is caused by circulation of the vortices in the step cavity, which in turn are driven by the main flow above the pseudo-bottom. Regardless of which direction the cross-stream vortices circulate in, the total amount of energy driving the vortices remains the same. Therefore it follows that the mean pressure at the downstream end of the horizontal step face will remain relatively constant across the width of the channel, even when vortex switching occurs.

At step 2, for $Q = 18$ l/s it can be seen that the cross-stream vortices switch at approximately 50 s. At approximately 250 s, there is a small dip in the wall pressure and a small increase in the pressure at the centreline, although the pressure data lines do not cross one another. When a 1 s moving average of the same data is plotted, however, the two lines do cross one another. This indicates that when there is a simultaneous decrease and increase in the two pressure signals but the lines do not cross one another, the direction of circulation of the cross-stream vortices has swapped for only a short time period.

Consider the moving averages of pressure at the times when vortex switching does not occur. At 15 l/s, 18 l/s and 21 l/s the data signals at step 5 appear to contain more variation than the signals at steps 2 and 12. This may be because, at these flow rates, step 5 falls within the region affected by the variation in the location of the inception point.

The greatest amount vortex switching occurs at $Q = 21$ l/s, especially at step 12. This explains why there is only a small difference in the mean pressures at the wall and the centreline at step 12 for 21 l/s (figure 3.14). Vortex switching will be discussed in more detail in section 3.5.3.4.

3. DESIGN AND STUDY OF A NARROW EXPERIMENTAL STEPPED SPILLWAY

It is difficult to compare the pressures at step 5 directly to the pressures at the other steps, as the directions of circulation of the vortices are different. At step 12, in the fully aerated region, all of the mean pressures, with one exception, are lower than at step 2, in the non-aerated region. The exception to this is at the wall for $Q = 21$ l/s. Here the mean pressure is slightly higher at step 12 which is due to the significant vortex switching which occurred in this case. The reduction in mean pressure in the aerated region agrees with the findings of Amador et al. (2009), Sánchez-Juny and Dolz (2005) and Sánchez-Juny et al. (2000) and shows that the presence of air in the flow acts to reduce pressure.

In order to analyse how the flow rate affects the mean pressure, consider only the data for $Q = 12 - 18$ l/s, as at $Q = 21$ l/s the cross-stream vortices predominantly circulate in the opposite direction. Generally there is a small increase in the mean pressure with discharge. In some cases, however, there is a larger increase or a small decrease in the mean pressure. These variations in the trend are unsurprising due to the complex pattern of pressures caused by the cross-stream vortices and vortex switching.

The standard deviation (SD) is taken over a relatively long measurement period (300 s giving 300,000 data points) and, therefore, can be used as an indication of the fluctuations in the pressures. In all cases, SD is larger at the downstream end of the step, regardless of which direction the cross-stream vortices are circulating in. This agrees with the findings of Amador et al. (2009). At $l = 55$ mm the fluctuations in pressure, in most cases, are larger at the position in the channel width where the vortices impact the step.

Amador et al. (2009) and Sánchez-Juny and Dolz (2005) both show that on the horizontal step face the fluctuations in the pressure decrease downstream of the inception point, however, this is not the case for this data. Amador et al. (2009) also shows that on the horizontal step faces the fluctuations in pressure increase with discharge in the downstream region. In the current study, however, the pressure fluctuations do not appear to be sensitive to flow rate in any part of the spillway. Again, these differences may be due to the complexity of the vortex structures observed in this study.

3.5.3.2 Vertical Step Faces

Figure 3.16 shows the mean pressures, \pm the standard deviations, of the pressures acting on the vertical step faces. In all cases, the pressure is lowest at the top of the step, in agreement with the findings of Zhang et al. (2012), Sánchez-Juny et al. (2007) and others, and is a result

of flow separation caused by the recirculating vortices within the step cavities.

Figure 3.17 shows the 10 s moving averages of pressure acting on the vertical step faces. The direction of circulation of the cross-stream vortices does affect the pressures acting on the vertical step faces, however, there is far less variation in the pressure across the channel width as there is on the horizontal step faces.

Firstly consider steps 2 and 12. For $Q = 12 - 18$ l/s, outward circulation is generally observed and the lowest pressure is found at the walls whereas for $Q = 21$ l/s inward circulation is generally observed and the lowest pressure is found at the centreline of the spillway.

Now consider step 5. For $Q = 18$ and 21 l/s the same pattern is seen where outward circulation produces the lowest pressure at the wall and inward circulation produces the lowest pressure at the centreline. At $Q = 12$ l/s the pressures at the centreline and at the wall are almost identical so it does not appear that the direction of circulation of the cross-stream vortices has a large effect on the pressure across the width of the channel in this case.

3. DESIGN AND STUDY OF A NARROW EXPERIMENTAL STEPPED SPILLWAY

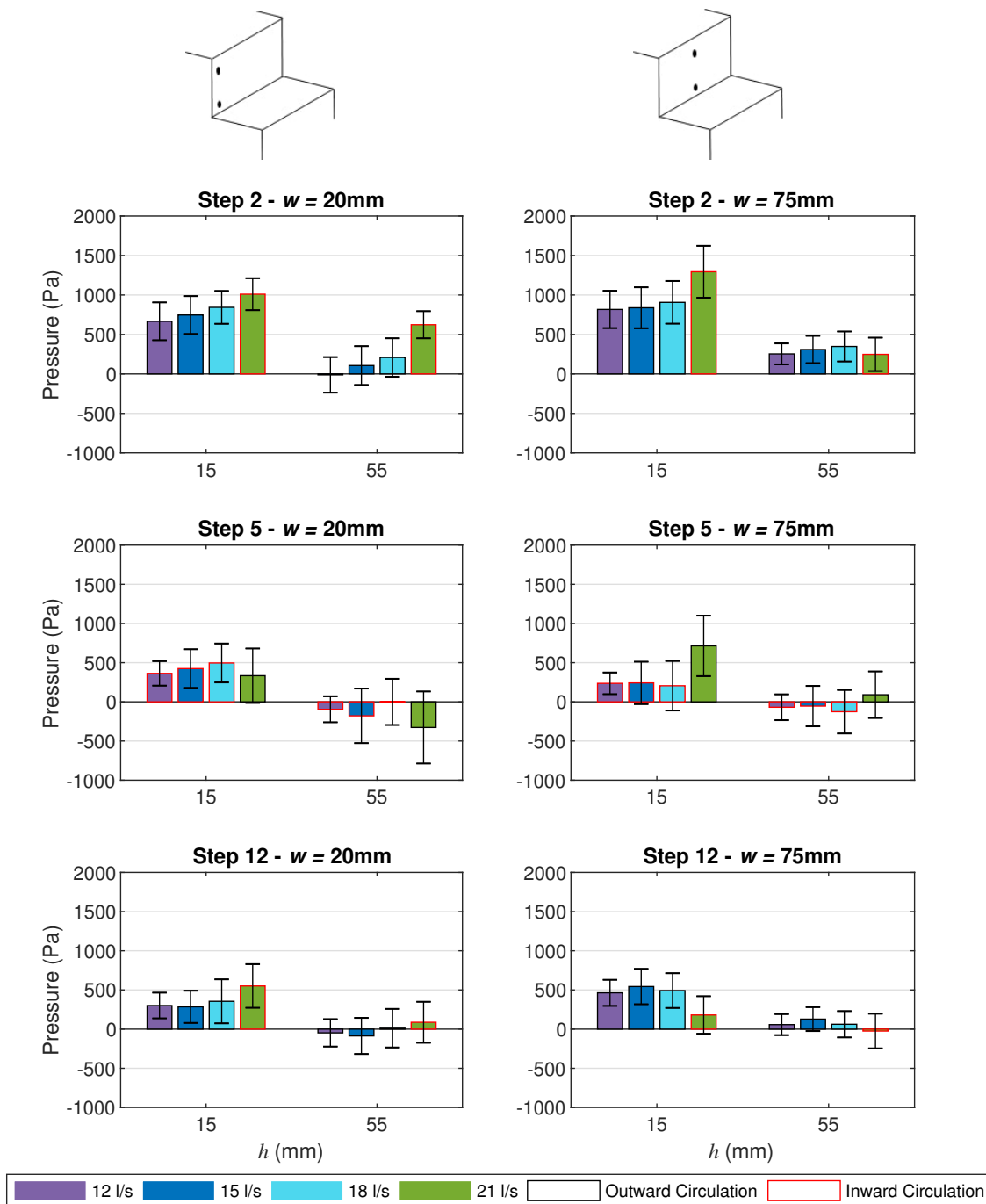


Figure 3.16: Mean pressure acting on the vertical step faces \pm standard deviation. w is the distance across the channel width from the spillway sidewall and h is the distance up the vertical step face from the inside step corner. These dimensions are detailed in figure 3.4a

For $Q = 15$ l/s, at step 5, the mean pressure at $h = 55$ mm is lowest at the wall which, is the opposite pattern to that observed at $Q = 12$ l/s and 18 l/s. The moving averages (figure 3.17) shows that a considerable amount of vortex switching occurs in this case and that outward

and inward circulation can each be observed for approximately half of the measurement time. Therefore, although the mean pressure shows the opposite pattern than at $Q = 12$ l/s and 18 l/s, the vortex switching in this case indicates that the direction of circulation of the vortices affected the pressure across the width of the channel.

On the vertical step faces, the pressures are affected by the direction of circulation of the cross-stream vortices (other than the above discussed case) but to a lesser degree than on the horizontal step faces. It should also be noted that the location of the high and low pressures on the vertical step faces are opposite to the horizontal step faces. Inward circulation causes the highest pressures at the centreline on the horizontal step face, but at the wall on the vertical step face, and vice versa. This is a result of the structure of the vortices and will be discussed further in chapter 6.

As with the horizontal step faces, it is difficult to directly compare pressures with other studies due to the effect on the pressure of the cross-stream vortices. Sánchez-Juny et al. (2007) shows that with increased discharge, the maximum and minimum mean pressures on the step face increase, which is not consistently the case in this study. Generally the high pressures, at $h = 15$ mm, increase with discharge but at $h = 55$ mm, where the lower pressures occur, the mean pressures vary considerably with discharge.

3. DESIGN AND STUDY OF A NARROW EXPERIMENTAL STEPPED SPILLWAY

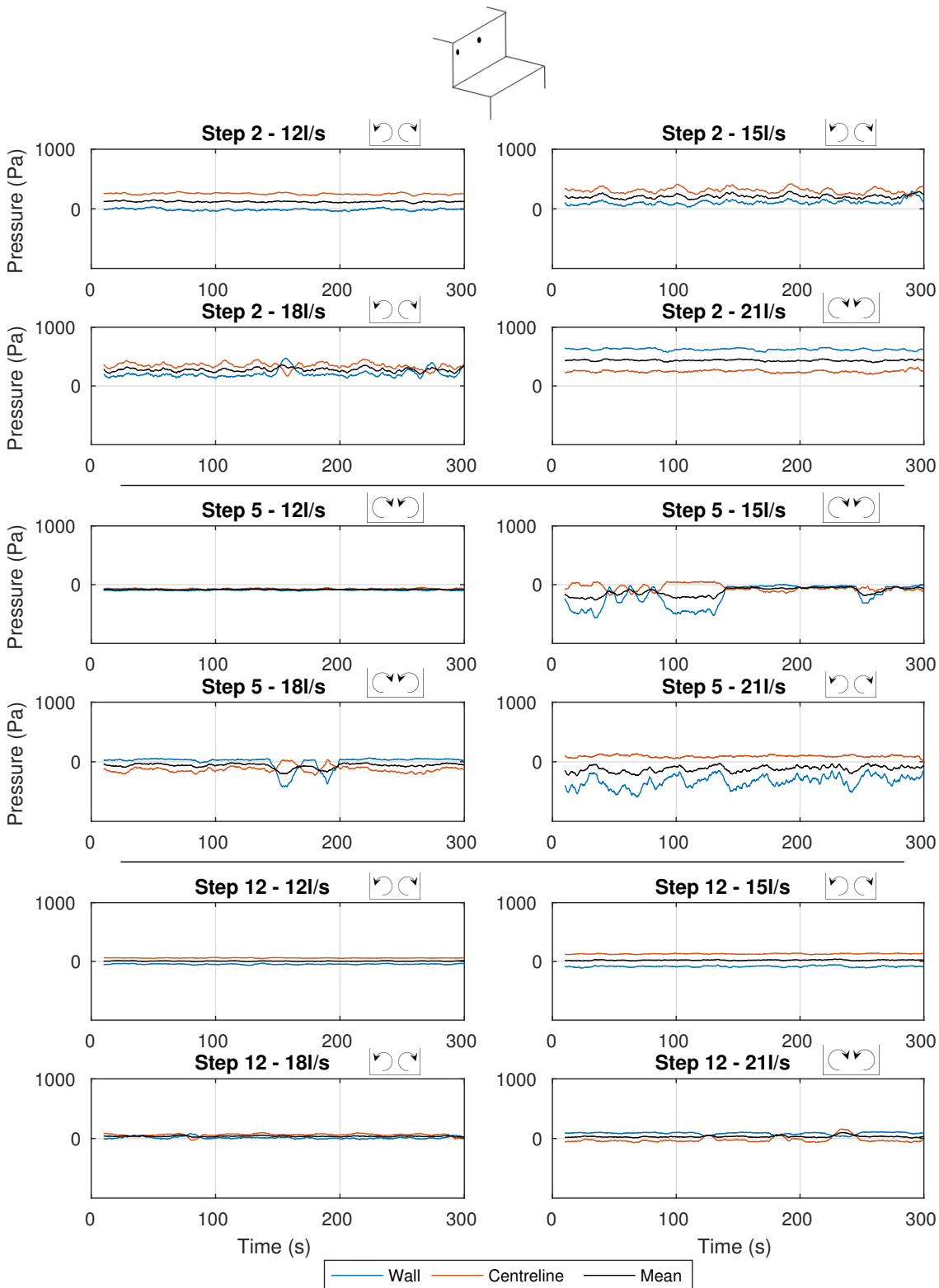


Figure 3.17: 10 second moving averages of the pressure acting at the centreline and close to the wall, at the top of the vertical step faces. Data is shown at steps 2, 5 and 12 for varying flow rates

The differences in the pressure readings on the vertical step face, between the wall and

centreline, are much less than on the horizontal step face. It is also noticeable that the difference between the pressures at the centreline and the wall becomes much less in the aerated region. The lowest pressures occur at step 5 close to the inception point. At step 12, sub-atmospheric pressures occur and the pressures are lower than step at 2. It is thought that the non-aerated region is at most risk of cavitation and plucking damage due to the protection provided by the cushioning effect of air in the fully aerated region. These results suggest that this might not be the case, as the pressures are lower in the fully aerated region than they are in the non-aerated region. The pressures recorded in these experiments are not low enough to cause cavitation damage, however, in prototype spillways this might not be the case. The experimentally measured pressures in this study may be low enough to cause plucking damage, however. This highlights how useful accurate CFD modelling of prototype stepped spillways could be to reservoir engineers to identify regions within the spillway which are at risk of plucking or cavitation damage. This is considered further in chapter 6.

As with the horizontal step faces, to analyse how flow rate affects pressures, only the data for $Q = 12 - 18$ l/s is considered. At the bottom of the step the mean pressure generally increases with discharge as does the pressure at the top of the step at step 2. At $h = 55$ mm for steps 5 and 12, however, there does not appear to be a correlation between the mean pressure and the flow rate. This disagrees with the findings of Amador et al. (2009) and Sánchez-Juny and Dolz (2005) who show that the mean pressure, on the vertical step face, increases with Q in the fully aerated region. Amador et al. (2009) also shows, using experimental modelling, that the pressure fluctuations at the top of the vertical step decrease in the fully aerated region and that the fluctuations increase with flow rate. This is not the case in this study as there is not much variation in the pressure fluctuations and they do not appear to be affected by the step number or the flow rate. Again, any differences between the trends shown in this data, and those shown in other studies, may be due to the complexity of the cross-stream vortices and vortex switching.

Figure 3.18 shows the generalised pressure patterns which occur on the step faces according to the direction of circulation of the cross-stream vortices (assuming symmetry around the centreline of the spillway). It can be seen that the highest pressures on the horizontal step face, and the lowest pressures on the vertical step face, are found at the position across the channel width where the cross-stream vortices impinge on the horizontal step face. Although the resolution of this image is very low, it will be useful to compare to pressure contours

3. DESIGN AND STUDY OF A NARROW EXPERIMENTAL STEPPED SPILLWAY

produced using numerical modelling.

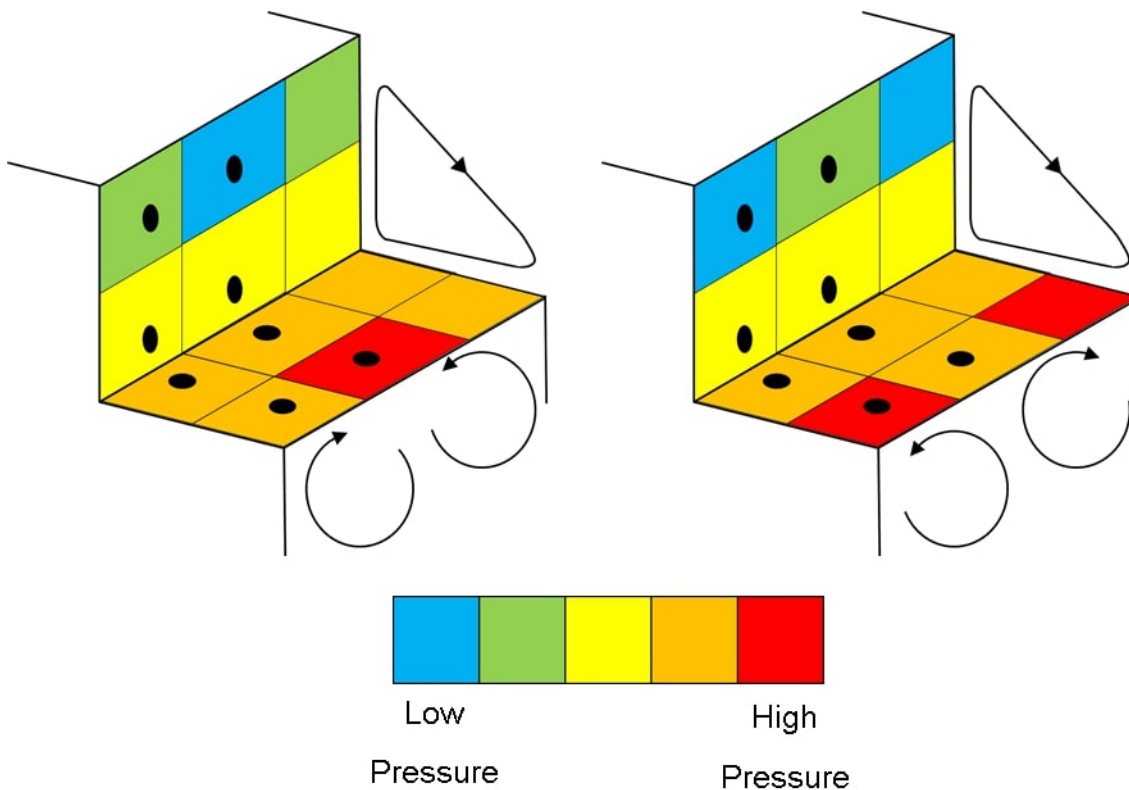


Figure 3.18: Experimentally observed pressure patterns on the step faces according to the direction of circulation of the cross-stream vortices

3.5.3.3 Spillway Side Wall

To the best of the authors knowledge, Winter et al. (2010) is the only other study to experimentally investigate the pressures acting at the wall of a stepped spillway. Making direct comparisons between the results of that study and those of the current study, however, is difficult due to a number of differences between the experiments. In the study by Winter et al. (2010), the slope of the spillway is approximately 1:2.4 and pressure measurements were taken at the third and fourth step of an 8 step cascade with a long, sloped approach channel. Measurements were taken with either a smooth or rough approach and there is no reference to whether the flow was aerated with either approach. Furthermore, the cross-stream vortices observed in the current study affect the pressure profiles, further reducing the comparability of the two studies.

Figure 3.20 shows the mean pressures and standard deviations of the pressures acting on the spillway side wall. The measurement positions are referred to as 1-4 as shown in figure

3.20. Positions 1, 3 and 4 fall within the recirculation zone of the step whereas position 2 is located in the main flow, above the pseudo-bottom. Note that the moving averages at the wall have not been included, as they have for the vertical and horizontal step faces. This is because the pressure data at the wall does not allow the variation in pressure across the width of the channel, due to the effect of the cross-stream vortices, to be compared.

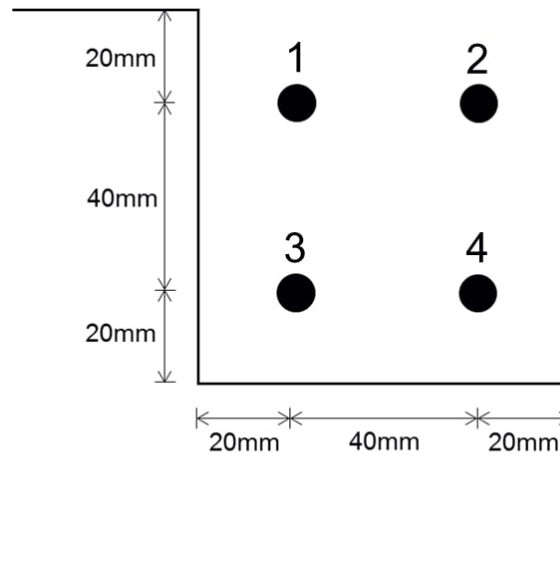


Figure 3.19: Numbered pressure measurement positions at the wall

Firstly consider the lower two pressure measurement positions at $h = 20$ mm (positions 3 and 4). Generally the pressures are higher at position 4, which agrees with the findings of Winter et al. (2010). It is noticeable, however, that, again, the direction of circulation of the vortices affects the pressure. The pressure at position 4 is significantly higher at the steps where the vortex impinges close to the wall (steps 2 and 12 for $Q = 12 - 18$ l/s and step 5 for $Q = 21$ l/s.) In the opposite cases, where the cross-stream vortices impinge at the centreline of the spillway, there is little difference between the pressures at positions 3 and 4.

3. DESIGN AND STUDY OF A NARROW EXPERIMENTAL STEPPED SPILLWAY

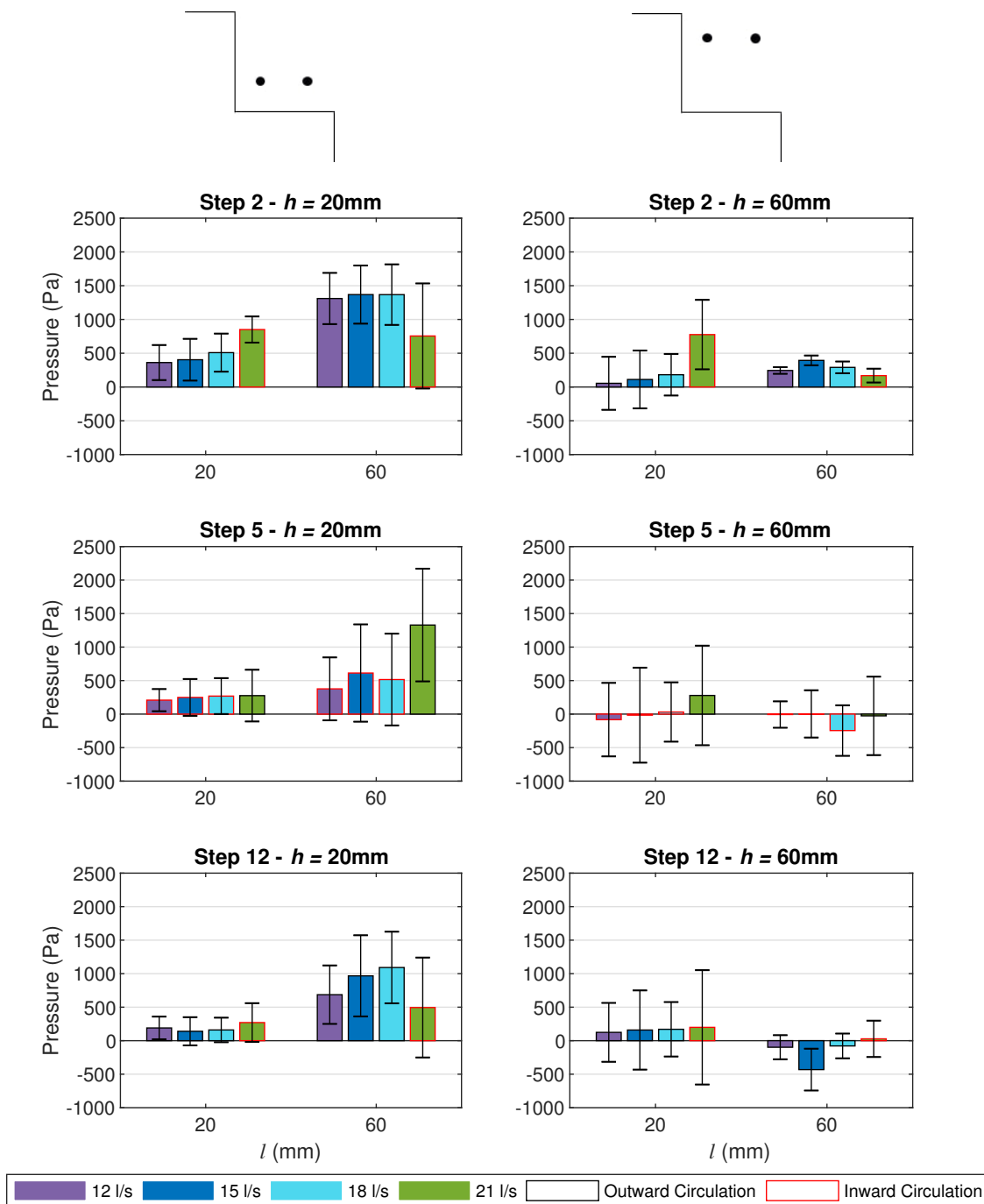


Figure 3.20: Mean pressure acting on the wall \pm standard deviation. h is the distance up the vertical step face from the inside step corner and l is the distance along the horizontal step face from the inside step corner. These dimensions are detailed in figure 3.4b

Now compare the pressure measurements at $l = 20$ mm (positions 1 and 3). At steps 2 and 5, the pressure is lower at position 1 for 12 - 18 l/s however at 21 l/s the mean pressure at positions 1 and 3 is roughly similar. At step 12, in the fully aerated region, the pressure

at positions 1 and 3 is roughly similar at all flow rates. On the horizontal and vertical step faces, the pressure data at 21 l/s shows a different pattern than at the other flow rates due to the difference in the direction of circulation of the cross-stream vortices. Here, however, this does not appear to be the case, as the same pattern is shown at steps 2 and 5 with opposite circulation directions and the same pattern of pressure is shown at step 12 for all flow rates.

In order to assess the effect of air entrainment on the pressures acting on the side walls, it is only possible to compare discharges of 12 - 18 l/s at steps 2 and 12. This is due to the difference in the direction of circulation of the cross-stream vortices at different steps and for different flow rates. At positions 3 and 4 there is a slight reduction in the pressures at step 12 in the fully aerated region. At position 1 the pressure is small and there does not appear to be a significant difference between the pressures in the aerated and non-aerated regions.

Position 2 is located in the main flow, so is less likely to be affected by vorticity in the step cavity. Direct comparisons can, therefore, be made at all steps and for all flow rates. At step 2, for all flow rates, the pressure is above atmospheric pressure, relatively small and with low fluctuations in the pressure. At steps 5 and 12 the pressures reduce and some extremely low pressures, relative to other pressures measured in this study, can be observed. Dong et al. (2010) and McGee (1988) show that the presence of air bubbles can reduce the pressures acting on solid boundaries, however, the results of this study show that very low pressures may occur in the fully aerated region at the wall, above the pseudo-bottom. In the design and maintenance of stepped spillway it is common practice to only protect upstream steps from plucking, but these results suggest that in some cases this may not be sufficient. Further investigation into this should be conducted. High pressure fluctuations can contribute to plucking damage by vibrating masonry blocks (Winter et al., 2010). The fluctuations in pressure at steps 5 and 12 are also higher than at step 2. This is further evidence that masonry blocks in the downstream, aerated regions of stepped spillways may be at risk of plucking damage.

The pressure fluctuations are generally highest at position 4. This is where the vortices impact the step during outward circulation, however high fluctuations also occur at this position during inward circulation. The pressure fluctuations at position 4 also tend to be higher at steps 5 and 12 than they are at step 2. The pressure fluctuations at position 1, close to the top of the step, show a similar pattern to position 4. As observed in figure 3.20, the standard deviation is relatively large and increases slightly at steps 5 and 12. At position 3, close to

3. DESIGN AND STUDY OF A NARROW EXPERIMENTAL STEPPED SPILLWAY

the inside step corner, the pressure fluctuations are relatively low and do not vary significantly at different flow rates or steps. Position 2, above the pseudo-bottom, shows extremely small pressure fluctuations at step 2 in the non-aerated region. The SD then increases significantly at step 5 and then decreases slightly at step 12. It is unclear why the pressure fluctuations are so small at step 2 compared with the other steps, however small values of the SD are observed at all flow rates and this result is repeatable at each flow rate.

The pressure measurement described in sections 3.5.3.1, 3.5.3.2 and 3.5.3.3 show that the cross-stream vortices, which have been visually observed, have a significant effect on the pressures across the channel width, especially on the horizontal step faces. At the lower flow rates the direction of circulation of the cross-stream vortices is relatively stable, however, as the flow rate increases, vortex switching occurs. At the higher flow rates the direction of circulation of the cross-stream vortices, at a particular step, is generally opposite to that at the lower flow rates, but some vortex switching occurs. This can be observed visually and also by the moving averages of the pressure data. Vortex switching is investigated further in section 3.5.3.4.

The pressure data also shows that areas of low pressure, which may cause plucking and possibly cavitation damage, are observed on the vertical step faces and on the spillway side walls in the fully aerated region. This region is considered to be protected from low pressures due to the presence of air, however these results show that there may be some situations where this is not the case. This highlights how reliable and accurate numerical modelling techniques could be used to identify at risk areas to help ensure that stepped spillways can be operated safely.

3.5.3.4 Cross-stream Vorticity Direction and Vortex Switching

The data presented in the previous sections of this chapter show that the direction of circulation of the cross-stream vortices remains constant at lower flow rates and vortex switching seldom occurs. At higher flow rates, vortex switching is observed and at even higher flow rates the direction of circulation is predominantly the opposite to that at the lower flow rates, although significant vortex switching may still occur. This behaviour can be observed both visually and by the moving averages of the pressure data on the horizontal step faces.

This data, however, has been collected with only a small number of flow rates. It is not clear at what flow rate the predominant direction of circulation changes, or how sensitive vortex

switching is to varying discharge. In this section, the effect of flow rate on circulation direction and vortex switching is investigated further, using a larger number of flow rates. All of the pressure measurements presented in this section have been recorded at the downstream end of the horizontal step face of step 12.

Figure 3.21 shows the 10 second moving averages of pressure data, for a range of discharges. For each flow rate, two pressure transducers were used to measure the pressure at the wall and the centreline simultaneously. In figure 3.21, the same pattern of symmetry, as observed in figure 3.15, can be seen.

At $Q = 16.5\text{ l/s}$ the pressure is generally higher at the wall, however, during some of the measurement period, the pressure is higher at the centreline. This shows that, over the five minute measurement period, outward circulation dominated but some vortex switching occurred. This is the case for the majority of the flow rates. One direction of cross-stream circulation dominates over the measurement period, but some vortex switching also takes place. At the lower flow rates outward circulation is dominant and at the higher flow rates inward circulation dominates (at step 12, where this data has been measured).

In some cases there is little or no vortex switching, for example at 17.9 l/s and 20.3 l/s . Conversely, in other cases, there does not appear to be a dominant direction of circulation. For example at 18.7 l/s and 19.8 l/s there appears to be almost continuous vortex switching.

In general, more vortex switching appears to occur at the mid range of flow rates. At the lower range of flow rates, the pressure is consistently higher at the wall and at the higher range of flow rates the pressure is consistently higher at the centreline. This is also seen in figure 3.15, as there is little vortex switching observed at 12 l/s and 15 l/s . This trend, however, is only a general trend, as there are a number of cases in which it does not apply. In the lower range of flow rates, at 17.5 l/s and 17.9 l/s , there is little or no vortex switching, however, at 16.5 l/s a significant amount of vortex switching occurs. The most vortex switching occurs at 18.7 l/s and at 19.8 l/s yet between these flow rates, at 19.0 l/s , there is very little vortex switching.

3. DESIGN AND STUDY OF A NARROW EXPERIMENTAL STEPPED SPILLWAY

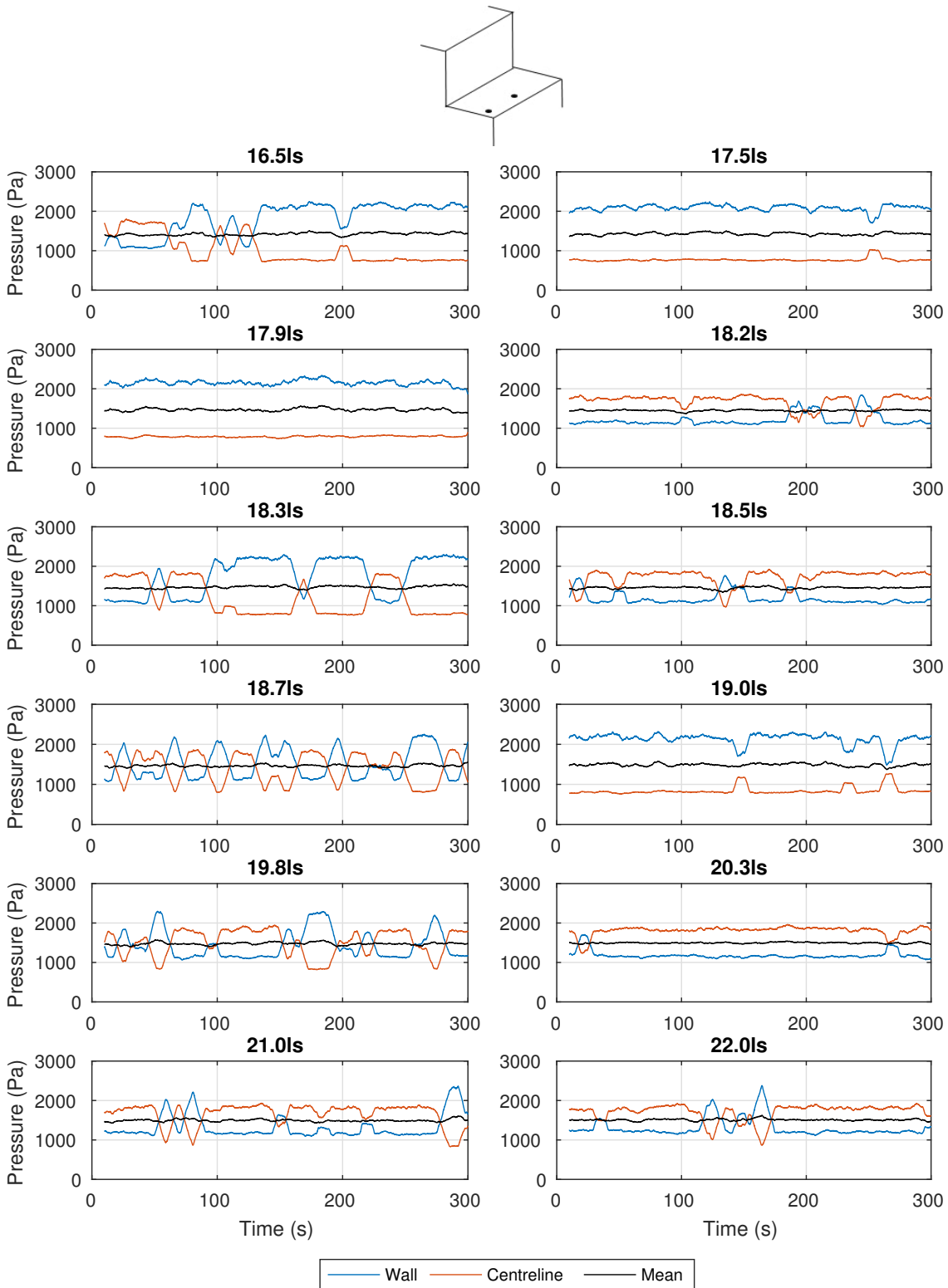


Figure 3.21: 10 second moving averages of the pressure acting at the centreline and close to the wall, at the downstream end of the horizontal step face of step 12. Each flow rate is shown in a separate sub-plot

Figure 3.22 shows the means of the pressures, measured over 300 s, which were used to calculate the moving averages displayed in figure 3.21. It can be seen that, the mean pressures, over a range of flow rates, show a similar symmetry to that observed in figure 3.21. In this case, however, the mean of the pressure at the wall and the centreline, which acts as the line of symmetry, increases gradually as the discharge increases. This is consistent with the findings of Amador et al. (2009) and Sánchez-Juny et al. (2007), who show that the pressures acting on the downstream end of the horizontal step face increase with discharge.

At the lower flow rates, the predominant direction of circulation is relatively consistent, with the higher pressures occurring at the centreline, and a larger difference between the mean pressure at the wall and at the centreline. In the mid range of discharges, the location of the highest mean pressure is not consistent and can change with a small change in the discharge. For example at 18.3 l/s and 19.0 l/s outward circulation dominates whereas at 18.2 l/s and 18.5 l/s inward circulation dominates. The smaller differences between the mean pressures, at these flow rates, also indicate that vortex switching occurs during the measurement period. At the higher flow rates, the mean pressures show that the predominant direction of circulation of the cross-stream vortices is the opposite of that at the lower flow rates.

Figures 3.21 and 3.22 show that vortex switching is highly unpredictable. In general, it occurs more frequently at the intermediate flow rates. However, this is not always the case. In order to better understand the direction of circulation of the cross-stream vortices, and the unpredictable nature of vortex switching, further research should be conducted into these phenomena.

3. DESIGN AND STUDY OF A NARROW EXPERIMENTAL STEPPED SPILLWAY

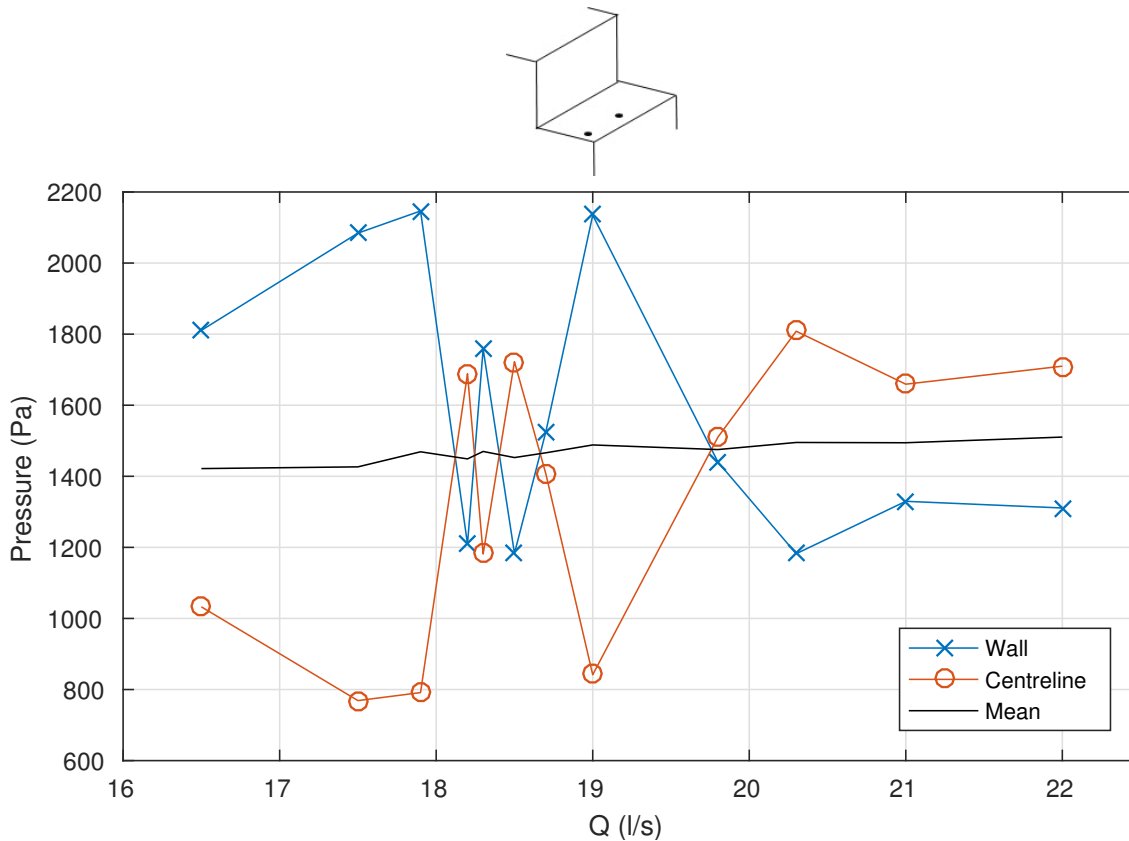


Figure 3.22: Mean pressures acting at the centreline and close to the wall, at the downstream end of the horizontal step face of step 12, for varying flow rates. The flow rates displayed are the same as those displayed in figure 3.21

3.6 Conclusions

An experimental stepped spillway was designed in order to investigate flow depths and pressures during skimming flows and to provide data for validation of CFD models. The spillway is relatively narrow at 150 mm and has been designed such that skimming flow occurs for a range of flow rates

The free-surface was measured using image analysis and average flow depths were calculated. The largest variation in the position of the free-surface is observed directly downstream of the inception point and intense splashing is observed. The depth of the free-surface generally increased with discharge, however, in some positions, this was not the case.

The point of inception varies around a mean position. Its location is recorded by visual observation with a precision of \pm half of the distance between step corners. As the flow rate increases, the inception point generally moves downstream and varies over a larger distance.

Pressures were measured on the spillway side walls and the step faces. On the step

faces pressure measurements were taken at the centreline of the spillway and also close to wall, in order to investigate how the pressure varies across the channel width. Pressures are recorded at three steps: one in the non-aerated region, one close to the inception point and one in the fully aerated, uniform flow region.

A complex pattern of cross-stream vortices are observed in the step cavities, in which each cavity contains two vortices which circulate in opposite directions and meet at the centreline of the channel. The vortices either impinge on the horizontal step face at the centreline of the spillway (inward circulation) or at the wall (outward circulation) and the direction of circulation reverses at each step.

The direction of circulation of the vortices affects the pressures acting across the width of the channel, with the largest effect occurring on the horizontal step face. At the downstream end of the horizontal step face, the pressures are significantly higher at the location where the cross-stream vortices impinge on the step.

Visual observations, as well as analysis of the moving averages of the pressure data, show that the direction of circulation of the cross-stream vortices can sometimes switch between outward and inward circulation, in a process referred to as vortex switching. For the most part, at lower flow rates, each step has a predominant direction of circulation and at the higher flow rates each step has a predominant direction of circulation which is the opposite to that of the lower flow rates. There is a mid range of flow rates in which considerable vortex switching occurs and it is difficult to determine a predominant direction of circulation. However, the behaviour of the vortex switching is extremely unpredictable and in some cases significant vortex switching occurs at the lower and higher flow rates and very little occurs in the mid range of flow rates.

The mean and fluctuating pressures were compared to other studies into the pressures acting on stepped spillways. In certain aspects, the results of this study agree with those found in the literature, however in others they do not. It is difficult to compare the pressure data in this study to that of other studies, due to the complexity introduced by the cross-stream vortices and vortex switching. Any dissimilarities which are observed may be due to these factors.

At the top of the vertical step face, and at the side wall above the pseudo-bottom, much lower mean pressures were observed in the fully aerated region than in the non-aerated region. The cushioning effect of air in the fully aerated region is thought to reduce the occurrence of extremely low pressures and protect the spillway from cavitation and plucking damage.

3. DESIGN AND STUDY OF A NARROW EXPERIMENTAL STEPPED SPILLWAY

These results, however, suggest that, in some circumstances, the fully aerated region may be also be at risk of plucking and cavitation damage.

The cross-stream vortices and vortex switching represent unusual and unexpected flow behaviour in the step cavities which, to the best of the author's knowledge, have not been previously reported (although flows which exhibit some similar behaviour have been reported, as discussed in section 3.4.1). It remains to be seen, however, whether this behaviour would occur in stepped spillways of different geometries and whether the cross-stream vorticity can be predicted using numerical modelling. These aspects are investigate further, using both experimental and numerical modelling, in chapters 6 and 7.

CHAPTER 4

Numerical Modelling Theory

4. NUMERICAL MODELLING THEORY

4.1 Introduction

The Navier-Stokes (NS) equations are the governing equations of fluid flows. The NS equations consist of non-linear partial differential equations, for which analytical solutions are only available for a handful of cases. Therefore, in order to solve the NS equations for a wide range of fluid flows, numerical models are required, which are solved using an iterative process. Numerical modelling of fluid flows is often known as computational fluid dynamics (CFD).

In order to solve the NS equations numerically, they must be converted into discrete functions, in a process known as discretisation. In the finite volume method (discussed in section 4.5), the continuous domain which is to be modelled is divided into a number of discrete control volumes. The NS equations are then solved numerically at each control volume. At the limits of the domain, boundary conditions, such as walls, inlets or outlets, are defined to match the conditions of the physical fluid flow which is to be modelled.

This chapter describes the specific numerical models used in this project, as well as some of the general concepts of numerical modelling of fluid flows. There are a range of solvers available for CFD modelling. In this project, ANSYS Fluent v17.2 has been used for all CFD simulations.

4.2 Governing Equations

The behaviour of the motion of fluids can be described through the laws of conservation of mass, momentum and energy, which together form the NS equations. Conservation of mass is described by the continuity equation, which is given by

$$\frac{\partial \rho}{\partial t} + \nabla \cdot (\rho \mathbf{u}) = 0 \quad (4.1)$$

where ρ is the fluid density and $\mathbf{u} = (u, v, w)$ is the fluid velocity vector. For incompressible fluids there is no variation in density so equation (4.1) becomes

$$\nabla \cdot \mathbf{u} = 0. \quad (4.2)$$

Conservation of momentum is derived from Newton's 2nd law, which states that the rate of change of momentum of an object (e.g. a fluid particle) is directly proportional to the resultant

force applied to the object and is in the direction of the resultant forces. The momentum equation describes the change in momentum of a fluid and has terms for transience, advection, diffusion, pressure and body forces, such as gravity. The momentum equation is given by

$$\rho \left(\underbrace{\frac{\partial \mathbf{u}}{\partial t}}_{\text{Transience}} + \underbrace{(\mathbf{u} \cdot \nabla) \mathbf{u}}_{\text{Advection}} \right) - \underbrace{\mu \nabla^2 \mathbf{u}}_{\text{Diffusion}} = - \underbrace{\nabla p}_{\text{Pressure}} + \underbrace{\rho \mathbf{F}}_{\text{Body Forces}} \quad (4.3)$$

where μ is the dynamic viscosity, p is pressure and F represents any body forces acting on the fluid, which is typically $F = (0, 0, g)$ where g is the acceleration due to gravity.

Conservation of energy is concerned with the temperature of the flow. This project assumes that constant temperature occurs in skimming flows over stepped spillway so, therefore, the equations of conservation of energy do not need to be considered.

4.3 Multiphase Numerical Models

In this section, three mesh based multiphase models, which are investigated in this research project, are described. In the following multiphase models, the volume fraction of a particular phase, k , within a computational cell is denoted by α_k . In a particular cell, three possibilities exist: either the cell is completely full of phase k so that $\alpha_k = 1$, the cell is completely empty of phase k so that $\alpha_k = 0$, or the cell contains more than one phase, including phase k , so that $0 < \alpha_k < 1$.

4.3.1 VOF Model

The VOF model is a multiphase free-surface modelling approach which assumes that the phases are immiscible, so that if more than one phase is present within a cell then that cell contains a free-surface. A single momentum equation is solved for the fluid mixture so the phases cannot move relative to one another within a computational cell. For these two reasons the VOF model would have to model each air bubble individually in order to explicitly predict air entrainment. This would require a computation mesh with a high enough density of cells to resolve each air bubble. The computational cost that this would incur is unfeasible for a large number of bubbles (such as in aerated flows over stepped spillway) with current computational resources. Therefore, the VOF model is unable to predict air entrainment in its standard form.

4. NUMERICAL MODELLING THEORY

Note that, although the VOF model is unable to model air entrainment in its standard form, it is commonly used to model open channel free-surface flows, as described in chapter 2. The model has been investigated in this research project for the purpose of comparison and contrast with other multiphase numerical models.

In the VOF model, if $0 < \alpha_k < 1$ in a particular cell, then this cell is assumed to contain an interface between two fluids. The position of each cell containing an interface gives a coarse representation of the position of the free-surface. The position of the free-surface within each cell is then calculated. A common method used to calculate the position of the free-surface is a piecewise linear interpolation scheme.

The VOF model was described by Hirt and Nichols (1981). The continuity equation for the volume fraction of phase k is

$$\frac{1}{\rho_k} \left[\frac{\partial}{\partial t} (\alpha_k \rho_k) + \nabla \cdot (\alpha_k \rho_k \mathbf{u}_k) = 0 \right] \quad (4.4)$$

where \mathbf{u}_k and ρ_k are the velocity and density of phase k respectively. By dividing by ρ_k , the volume fraction of the fluid, rather than the mass, is conserved. Summing the volume fraction of each phase gives

$$\sum_{k=1}^n \alpha_k = 1 \quad (4.5)$$

which is used to calculate the volume fraction of the final phase so that equation (4.4) need only be solved $n - 1$ times.

One momentum equation is solved for the domain, with all phases sharing the velocity field. The momentum equation is

$$\frac{\partial}{\partial t} (\rho_m \mathbf{u}) + \nabla \cdot (\rho_m \mathbf{u} \mathbf{u}) = -\nabla p + \nabla \cdot (\boldsymbol{\tau} + \boldsymbol{\tau}^T) + \rho_m \mathbf{g} + F_s \quad (4.6)$$

where p is the pressure, $\boldsymbol{\tau}$ is the viscous stress tensor, $\boldsymbol{\tau}^T$ is the turbulent stress tensor and F_s is the surface tension. ρ_m is the volume fraction averaged density which is calculated by

$$\rho_m = \sum_{k=1}^n \alpha_k \rho_k. \quad (4.7)$$

Other properties, such as viscosity, are calculated in the same manner.

In the VOF model, the volume fraction in each cell gives a coarse representation of the position of the free-surface, i.e. if $0 < \alpha < 1$ in a particular cell then that cell contains a free-

surface. In order to determine the profile of the free-surface within each of these computational cells, an interface capturing scheme must be used. There are a range of interface capturing schemes available, however, all VOF simulations in this project have utilised the Piecewise Linear Interface Construction (PLIC) method, known as the Geometric Reconstruction Scheme in ANSYS Fluent. In ANSYS Fluent, the Geometric Reconstruction Scheme uses an explicit approach when capturing the free-surface (ANSYS, 2013).

The PLIC was developed by Youngs (1982). The PLIC method assumes that the interface has a linear profile within each cell (surfaces in 3D and lines in 2D). In each cell the normal vector to the interface, n_i is computed using the gradient of α . The fluid interface is calculated as the surface or line which has the normal vector n_i and splits the cell by the volume fraction, α .

4.3.2 Eulerian Multiphase Model

The Eulerian multiphase model is not specifically a free-surface modelling technique and models both phases individually. As such, a free-surface profile is not required to be captured in cells containing more than one phase. Aeration, therefore, can be predicted with cell sizes larger than the individual air bubbles. In the Eulerian multiphase model, momentum and continuity equations are solved for each phase and additional terms are included in the momentum equation to describe the interaction between phases. By solving separate momentum equations for each phase, the phases are able to move at relative velocities to one another. This allows the dispersion of one phase within another, so air entrainment can be modelled. The Eulerian multiphase model is described in detail by Ishii and Hibiki (2010) and Drew and Passman (2006).

For a phase, k , the continuity equation is

$$\frac{\partial}{\partial t}(\alpha_k \rho_k) + \nabla \cdot (\alpha_k \rho_k \mathbf{u}_k) = 0. \quad (4.8)$$

Note that equation (4.8) contains a transient term for density, like in the equation for compressible conservation of mass (equation 4.1). Although both phases are considered incompressible, so that their individual densities are constant, as the volume fraction of each phase can vary within a cell, the phase averaged density can also vary.

4. NUMERICAL MODELLING THEORY

The momentum equation for phase k is

$$\frac{\partial}{\partial t}(\alpha_k \rho_k \mathbf{u}_k) + \nabla \cdot (\alpha_k \rho_k \mathbf{u}_k \mathbf{u}_k) = -\nabla(\alpha_k p) + \nabla \cdot [\alpha_k (\boldsymbol{\tau}_k + \boldsymbol{\tau}_k^T)] + \alpha_k \rho_k \mathbf{g} + M \quad (4.9)$$

where $\boldsymbol{\tau}_k$ and $\boldsymbol{\tau}_k^T$ are the viscous stress and turbulent stress tensors for phase k respectively. The pressure field, p is shared by all phases. M is used to describe the interaction between phases, whereby

$$M = M_D + M_L + M_{VM} + M_{WL} + M_{TD}. \quad (4.10)$$

M_D is the drag force, M_L is a lift force, M_{VM} is a virtual mass force, M_{WL} is a wall lubrication force and M_{TD} is a turbulent dispersion force.

Drag Force

The drag force is the force exerted on, or by, a dispersed particle as it moves through the surrounding fluid. The drag force is given by

$$M_D = \frac{3\alpha_d \rho_c C_D}{4d_d} |\mathbf{u}_c - \mathbf{u}_d| (\mathbf{u}_c - \mathbf{u}_d) \quad (4.11)$$

where the subscripts c and d refer to the continuous and dispersed phases respectively, d_d is the dispersed phase particle diameter (air bubble diameter in aerated flows) and C_D is a drag coefficient. Throughout this project, the Schiller Naumann drag law has been implemented where

$$C_D = \frac{24(1 + 0.15Re_r^{0.687})}{Re_r} \quad (4.12)$$

for $Re_r \leq 1000$ and

$$C_D = 0.44 \quad (4.13)$$

for $Re_r > 1000$. Re_r is the relative Reynolds number between phases, which is given by

$$Re_r = \frac{\rho_c |\mathbf{u}_c - \mathbf{u}_d| d_d}{\mu_c}. \quad (4.14)$$

Lift Force

If the dispersed phase travels through a continuous phase which is in shearing motion then the particles of the dispersed phase (air bubbles in aerated water flows) experience a force

that is transverse to the direction of motion. This is known as the lift force and is described by Drew and Passman (2006).

Virtual Mass Force

When an object accelerates, it experiences what is known as a virtual mass, similar to the way that the acceleration due to gravity causes objects to experience weight. If a dispersed phase accelerates through a continuous phase then it will accelerate some of the continuous phase, resulting in the virtual mass force. The virtual mass force is also described by Drew and Passman (2006).

Wall Lubrication Force

The wall lubrication force is used specifically for liquid gas flows. In certain flows the near wall gas fraction is reduced close to the wall. To model this, an artificial wall lubrication force is used which tends to push gas bubbles away from the walls. A range of wall lubrication force models are described by Lubchenko et al. (2018).

Turbulent Dispersion Force

The turbulent dispersion force describes the interphase turbulent momentum transfer and is also described by Drew and Passman (2006).

An investigation into the effect of M_L , M_{VM} and M_{WL} was conducted and it was found that, for both spillways considered in this project, these interaction forces had a negligible effect on the solution. Simulations including the turbulent dispersion force were attempted, however, for both spillways investigated in this project, a converged solution could not be achieved. For these reasons, all Eulerian model results presented in this project utilise the drag force only, so this phase interaction model has been described in more detail than the other phase interaction models.

4.3.3 Mixture Model

The mixture model (sometimes known as the algebraic slip model), similarly to the VOF model, solves only one momentum equation for the fluid mixture. However, in the mixture model,

4. NUMERICAL MODELLING THEORY

phases are allowed to move at different velocities through the use of an algebraic relationship to describe the relative velocity between the phases. The model assumes that the relative velocity between the phases is small and that local equilibrium is achieved over small length scales. Like the Eulerian model, the mixture model is not specifically a free-surface modelling technique so can also predict air entrainment with cell sizes larger than individual air bubbles.

The mixture model is described in detail by Manninen et al. (1996) and Ishii and Hibiki (2010). In the model both the continuity and momentum equations are solved for the fluid mixture and are obtained by summing the single phase equations over all phases. The continuity equation for the mixture is

$$\frac{\partial \rho_m}{\partial t} + \nabla \cdot (\rho_m \mathbf{u}_m) = 0. \quad (4.15)$$

where \mathbf{u}_m is the mixture velocity at the centre of mass and is defined as

$$\mathbf{u}_m = \frac{1}{\rho_m} \sum_{k=1}^n \alpha_k \rho_k \mathbf{u}_k. \quad (4.16)$$

The momentum equation for the mixture is given by

$$\frac{\partial}{\partial t} (\rho_m \mathbf{u}_m) + \nabla \cdot (\rho_m \mathbf{u}_m \mathbf{u}_m) = -\nabla p + \nabla \cdot (\tau_m + \tau_m^T) + \nabla \cdot \tau_{Dm} + \rho_m \mathbf{g} + M_m \quad (4.17)$$

where τ_m , τ_m^T and τ_{dm} represent the average viscous stress, the turbulent stress and the diffusion stress for the mixture respectively. M_m is the mixture momentum source which includes the influence of surface tension and depends on the geometry of the interface. However, in many practical applications M_m is ignored (Manninen et al., 1996). The diffusion stress arises when summing the single phase equations over the mixture and is defined as

$$\tau_{Dm} = - \sum_{k=1}^n \alpha_k \rho_k \mathbf{u}_{mk} \mathbf{u}_{mk}. \quad (4.18)$$

Here \mathbf{u}_{mk} is known as the diffusion velocity and represents the velocity of phase k relative to the centre of mass of the mixture such that

$$\mathbf{u}_{mk} = \mathbf{u}_k - \mathbf{u}_m. \quad (4.19)$$

The diffusion term in (4.17), $\nabla \cdot \tau_{Dm}$, represents momentum diffusion due to the relative motions of the phases. The volume fraction equation is based on the continuity equation for

a single phase. The phase velocity is replaced using equation (4.19) and it is assumed that densities are constant and phase changes do not occur

$$\frac{\partial}{\partial t} \alpha_k + \nabla \cdot (\alpha_k \mathbf{u}_m) = -\nabla \cdot (\alpha_k \mathbf{u}_{mk}). \quad (4.20)$$

In order to solve equations (4.17) and (4.20) the diffusion velocity, \mathbf{u}_{mk} must be calculated. This is done via the relative velocity between the dispersed and continuous phases (also known as the slip velocity) which is defined as

$$\mathbf{u}_{ck} = \mathbf{u}_k - \mathbf{u}_c \quad (4.21)$$

where \mathbf{u}_{ck} is the relative velocity and \mathbf{u}_c is the velocity of the continuous phase. For a dispersed phase, p , the diffusion velocity can then be expressed by

$$\mathbf{u}_{mp} = \mathbf{u}_{cp} - \sum_{k=1}^n \frac{\alpha_k \rho_k}{\rho_m} \mathbf{u}_{ck}. \quad (4.22)$$

The relative velocity is calculated by

$$\mathbf{u}_{ck} = \frac{\rho_k d_d^2}{18 \mu_c f_{drag}} \frac{\rho_k - \rho_m}{\rho_k} \left[\mathbf{g} - (\mathbf{u}_m \cdot \nabla) \mathbf{u}_m - \frac{\partial \mathbf{u}_m}{\partial t} \right] \quad (4.23)$$

where μ_c is the the viscosity of the continuous phase, d_d is the bubble diameter of the dispersed phase and f_{drag} is a drag function. The Schiller Naumann drag function has also been used for all mixture model simulations in this project.

4.3.4 Summary

In this research project, the three multiphase models described in this section are used to model skimming flows over two stepped spillways, in both 2D and 3D. The VOF model is not expected to predict air entrainment, however, it is a commonly used approach to model free-surface flows. Therefore, it will provide a useful benchmark with which to compare the mixture and Eulerian model results to, with specific focus on the ability of these models to capture additional details of the aerated flows.

4. NUMERICAL MODELLING THEORY

4.4 Turbulence Modelling

This section discusses turbulent flows and associated modelling techniques, with focus on the turbulence modelling techniques employed in this project. A more comprehensive outline the concepts discussed in this section can be found in Pope (2001) and Wilcox et al. (1998).

Turbulent flows are characterised by chaotic and unsteady fluid motion in three dimensions. They display distinct rotational patterns known as turbulent eddies. The size of these eddies varies significantly and the largest eddies extract energy from the mean flow. The large eddies then transfer energy to the smaller eddies and in the smallest eddies viscous dissipation converts turbulent energy into internal energy. The largest eddies are to scale with the mean flow, whereas the smallest eddies are significantly smaller.

The Reynolds number, Re , can be used to determine whether a fluid flow is turbulent or not. Re is given by

$$Re = \frac{\rho UL}{\mu} \quad (4.24)$$

where L is a known length scale within the fluid domain. The NS equations are non-linear as the advection term is quadratic (the second term in equation (4.3)). As the Reynolds number increases, the effect of this non-linearity increases and at high Reynolds numbers the advection term dominates and the flow is fully turbulent. At low Reynolds numbers, viscous effects dominate and steady laminar flow occurs. At intermediate Reynolds numbers both the advection and viscous terms have an important effects on the flow. This is known as the laminar-turbulent transition.

The NS equations can be used to predict turbulent flows directly by using Direct Numerical Simulation (DNS). However, the time and space scales of the smallest turbulent eddies are several orders of magnitude smaller than the flow domain. In order to fully resolve all of the turbulent eddies, an extremely large number of mesh elements, and an extremely small time step, are required. This requires an unfeasible computational cost for complex domain geometries at anything other than low Reynolds numbers (Balakumar, 2015).

However, for engineering applications, the details of all of the turbulent eddies are rarely required and it is the effect of turbulence on the mean flow that is of most importance. Therefore, simplified turbulence models can be used to predict the effect of turbulence on the mean flow for a significantly lower computational cost.

One method used to model turbulent flows is Large Eddy Simulation (LES). In LES, the lar-

ger eddies are directly resolved whereas eddies smaller than the mesh are modelled. This is much less computationally expensive than DNS, however, still very computationally expensive for many complex geometries and engineering applications.

The turbulence modelling in this project has been conducted using Reynolds Averaged Navier Stokes (RANS) turbulence models, in which models are used to approximate the turbulent characteristics of the flow at all scales.

4.4.1 RANS Models

In RANS turbulence models, the instantaneous velocity, \mathbf{U} , is split into its mean and fluctuating components by

$$\mathbf{U} = \mathbf{u} + \mathbf{u}' \quad (4.25)$$

where \mathbf{u} is the mean velocity and \mathbf{u}' is the fluctuating component. This process is known as the Reynolds decomposition. The instantaneous pressure can also be expressed in this manner.

The instantaneous pressure and velocity in the continuity and momentum equations can be replaced by their Reynolds decompositions to give the Reynolds averaged incompressible continuity and momentum equations:

$$\frac{\partial \rho \mathbf{u}_i}{\partial x_i} = 0 \quad (4.26)$$

and

$$\rho \frac{\partial \mathbf{u}_i}{\partial t} + \rho \frac{\partial}{\partial x_j} [(\mathbf{u}_j \mathbf{u}_i + \overline{\mathbf{u}'_j \mathbf{u}'_i})] = -\frac{\partial p}{\partial x_j} + \frac{\partial}{\partial x_j} \mu \left(\frac{\partial \mathbf{u}_i}{\partial x_j} + \frac{\partial \mathbf{u}_j}{\partial x_i} \right) + \rho \mathbf{g}. \quad (4.27)$$

p is the average pressure, ρ is the fluid density and μ is the dynamic viscosity of the fluid. The term $\overline{\mathbf{u}'_i \mathbf{u}'_j}$ on the left-hand side of equation (4.27) has the same structure as a stress tensor so can be taken to the right-hand side of the equation and absorbed into stress to give

$$\rho \frac{\partial \mathbf{u}_i}{\partial t} + \rho \frac{\partial \mathbf{u}_j \mathbf{u}_i}{\partial x_j} = -\frac{\partial p}{\partial x_j} + \frac{\partial}{\partial x_j} \left[\mu \left(\frac{\partial \mathbf{u}_i}{\partial x_j} + \frac{\partial \mathbf{u}_j}{\partial x_i} \right) - \tau_{ij} \right] + \rho \mathbf{g} \quad (4.28)$$

where $\tau_{ij} = \overline{\mathbf{u}'_i \mathbf{u}'_j}$ and is known as the Reynolds stress tensor.

The RANS equations are time averaged over a time period which is large when compared with the turbulent fluctuations but small compared with the mean flow time scales. This is why time derivative terms appear in equations (4.26) - (4.28) and allows RANS modelling to be used for transient simulations. Note that turbulence models which use time dependent RANS equations are sometimes referred to as Unsteady Reynolds Averaged Navier Stokes

4. NUMERICAL MODELLING THEORY

(URANS) models, however, in this project they will be referred to as RANS models.

4.4.1.1 Eddy Viscosity Models

The Reynolds stress term in (4.28) contains unknown fluctuating velocity components. In order to close the system of governing equations, the Reynolds stresses must be related to the known mean flow variables using new equations. These equations are known as turbulence models.

A common method to close the system of governing equations is through the Boussinesq eddy viscosity (sometimes referred to as turbulent viscosity) hypothesis. The eddy viscosity hypothesis assumes that mixing and momentum transfer through turbulence is analogous to mixing and momentum transfer through molecular diffusion. The turbulent momentum transfer is modelled using the concept of eddy viscosity, μ_t , which reduces the closure problem to finding the closure equations for the eddy viscosity. In eddy viscosity models the Reynolds stress is calculated by

$$\tau_{ij} = -\rho \overline{u'_i u'_j} = 2\mu_t S_{ij} - \frac{2}{3}\rho k \delta_{ij} \quad (4.29)$$

where k is the turbulent kinetic energy which is given by

$$k = \frac{1}{2} \overline{u'_i u'_i} \quad (4.30)$$

and S_{ij} is the mean rate of strain tensor given by

$$S_{ij} = \frac{1}{2} \left(\frac{\partial u_i}{\partial x_j} + \frac{\partial u_j}{\partial x_i} \right). \quad (4.31)$$

There are a number of methods used to relate the eddy viscosity to the other computed mean flow variables, including zero equation models (also known as algebraic eddy viscosity models), one equation models and two equation models. Two equation models are by far the most widely used eddy viscosity closure. In eddy viscosity models, the Reynolds stresses are modelled assuming an isotropic Newtonian constitutive equation. This assumption is valid for many flows and two equation eddy viscosity models have been shown to provide accurate solutions for a wide range of turbulent flow conditions in domains with complex geometries.

In the two equation models, the turbulent kinetic energy, k , and the turbulent length scale, l_t , must be determined by transport equations. Most models solve a transport equation for k

directly, however, l_t is determined from a transport equation for a different, related, variable. A different variable is used to determine l_t , depending on the turbulence model being employed. The transport equations for the two equation models also make use of empirically derived constants.

In this project a range of two equation eddy viscosity models have been investigated, in conjunction with the various multiphase modelling approaches, in order to determine their accuracy in predicting turbulent skimming flows over stepped spillways. The eddy viscosity models used in this project are described in this section.

$k - \epsilon$ Models

In the $k - \epsilon$ turbulence models the eddy viscosity is calculated by

$$\mu_t = C_\mu \rho \frac{k^2}{\epsilon} \quad (4.32)$$

Different $k - \epsilon$ models define C_μ by different methods. ϵ is the turbulent energy dissipation and is given by

$$\epsilon = \nu \overline{\frac{\partial \mathbf{u}'_i}{\partial x_j} \frac{\partial \mathbf{u}'_i}{\partial x_j}} \quad (4.33)$$

The $k - \epsilon$ models, as the name would suggest, solve transport equations for k and ϵ . The turbulent length scale is related to the turbulent energy dissipation by

$$l_t = \frac{k^{3/2}}{\epsilon} \quad (4.34)$$

Standard $k - \epsilon$ Model

The standard $k - \epsilon$ model is described by Launder and Spalding (1983). This was the first two equation eddy viscosity model to be developed, however, has now generally been superseded by other $k - \epsilon$ and two equation models, which overcome some of its limitations. In the standard $k - \epsilon$ model, C_μ is an empirically derived constant. The transport equation for k is

$$\frac{\partial(\rho k)}{\partial t} + \frac{\partial(\rho k \mathbf{u}_i)}{\partial x_i} = \frac{\partial}{\partial x_j} \left[\left(\mu + \frac{\mu_t}{\sigma_k} \right) \frac{\partial k}{\partial x_j} \right] + G_k - \rho \epsilon \quad (4.35)$$

4. NUMERICAL MODELLING THEORY

where G_k is the generation of turbulence due to mean velocity gradients and is defined as

$$G_k = 2\mu_t S_{ij} S_{ij}. \quad (4.36)$$

The transport equation for ϵ is defines as

$$\frac{\partial(\rho\epsilon)}{\partial t} + \frac{\partial(\rho\epsilon\mathbf{u}_i)}{\partial x_i} = \frac{\partial}{\partial x_j} \left[\left(\mu + \frac{\mu_t}{\sigma_\epsilon} \right) \frac{\partial\epsilon}{\partial x_j} \right] + C_{1\epsilon} \frac{\epsilon}{k} G_k - C_{2\epsilon} \rho \frac{\epsilon^2}{k} \quad (4.37)$$

The empirical constants used in the standard $k - \epsilon$ turbulence model are:

$$C_\mu = 0.09 \quad \sigma_k = 1 \quad \sigma_\epsilon = 1.3 \quad C_{1\epsilon} = 1.42 \quad C_{2\epsilon} = 1.68$$

RNG $k - \epsilon$ Model

The Renormalisation-group (RNG) $k - \epsilon$ turbulence model is a modification to the standard $k - \epsilon$ model and is described by Yakhot et al. (1992). The model uses statistical techniques, known as RNG theory, to derive the $k - \epsilon$ equation and the corresponding coefficients directly from the NS equations rather than from empirical data (Pope, 2001). One of the main features of the RNG $k - \epsilon$ model is that it accounts for low Reynolds numbers, whereas the standard $k - \epsilon$ model is strictly a high Reynolds number model. This is achieved by the use of an effective viscosity term in both the k and ϵ transport equations. Although the RNG $k - \epsilon$ model accounts for low Reynolds numbers, it must be used in conjunction with an appropriate near wall treatment method. This is discussed further in section 4.4.2.

The transport equation for the k given by

$$\frac{\partial(\rho k)}{\partial t} + \frac{\partial(\rho k \mathbf{u}_i)}{\partial x_i} = \frac{\partial}{\partial x_j} \left(\mu_{eff} \psi_k \frac{\partial k}{\partial x_j} \right) + G_k - \rho \epsilon \quad (4.38)$$

where $\mu_{eff} = \mu + \mu_t$ is the effective viscosity.

The transport equation for ϵ is given by

$$\frac{\partial(\rho\epsilon)}{\partial t} + \frac{\partial(\rho\epsilon\mathbf{u}_i)}{\partial x_i} = \frac{\partial}{\partial x_j} \left(\mu_{eff} \psi_\epsilon \frac{\partial\epsilon}{\partial x_j} \right) + C_{1\epsilon} \frac{\epsilon}{k} G_k + C_{2\epsilon} \rho \frac{\epsilon^2}{k} - R. \quad (4.39)$$

Another key difference between the standard $k - \epsilon$ model and the RNG $k - \epsilon$ model is the

addition of the term for R in the latter model, with

$$R = \frac{C_\mu \rho \eta^3 (1 - \eta/\eta_0) \epsilon^2}{1 + \beta \eta^3} \frac{1}{k} \quad (4.40)$$

where $\eta \equiv (k\sqrt{2S_{ij}S_{ij}})/\epsilon$. The constants used in the RNG $k - \epsilon$ turbulence model, other than β which is derived empirically, are derived from RNG theory. The constants are:

$$\begin{aligned} C_\mu &= 0.0845 & C_{1\epsilon} &= 1.42 & C_{2\epsilon} &= 1.68 & \psi_k &= 1.39 \\ \psi_\epsilon &= 1.39 & \eta_0 &= 4.382 & \beta &= 0.012 \end{aligned}$$

In areas of high strain $\eta > \eta_0$. This causes R to be negative and therefore make a positive contribution to the transport equation of ϵ . This increases the turbulent dissipation rate, ϵ , which reduces k and, therefore, the effective viscosity. Conversely, in areas of low strain, where $\eta < \eta_0$, R is positive so makes a negative contribution to the transport equation, increasing the effective viscosity. The RNG $k - \epsilon$ model, therefore, is more accurate than the standard $k - \epsilon$ model for rapidly strained flows and swirling flows where there is high streamline curvature.

Realizable $k - \epsilon$ Model

The Realisable $k - \epsilon$ model was introduced by Shih et al. (1995). The model is based on realisability, whereby the model is required to insure positivity of the Reynolds stress components on the diagonal and Schwartz's inequality on non-diagonal components (Mohammadi and Pironneau, 1993). These mathematical constraints are consistent with the physics of turbulent flows. In order to ensure realisability, the model uses a variable C_μ , which varies depending on the mean flow and the turbulence. C_μ is defined by

$$C_\mu = \frac{1}{A_0 + A_s \frac{kU^*}{\epsilon}} \quad (4.41)$$

where

$$U^* \equiv \sqrt{S_{ij}S_{ij} + \tilde{\Omega}_{ij}\tilde{\Omega}_{ij}}, \quad (4.42)$$

$$\tilde{\Omega}_{ij} = \Omega_{ij} - 2\epsilon_{ijk}\omega_k \quad (4.43)$$

and

$$\Omega_{ij} = \overline{\tilde{\Omega}_{ij}} - \epsilon_{ijk}\omega_k. \quad (4.44)$$

4. NUMERICAL MODELLING THEORY

$\overline{\Omega_{ij}}$ is the mean rate of rotation when viewed in a rotating reference frame with the angular velocity ω_k . $A_0 = 4.0$ and $A_s = \sqrt{6} \cos \phi$ where

$$\phi = \frac{1}{3} \cos^{-1}(\sqrt{6W}), \quad W = \frac{S_{ij}S_{jk}S_{ki}}{\sqrt{S_{ij}S_{ij}}^3}$$

In the Realizable $k - \epsilon$ model the transport equation for k is identical to that of the standard $k - \epsilon$ model. The transport equation for ϵ is obtained from the dynamic equation for the mean-square vorticity fluctuations. The transport equation is given by

$$\frac{\partial(\rho\epsilon)}{\partial t} + \frac{\partial(\rho\epsilon\mathbf{u}_i)}{\partial x_i} = \frac{\partial}{\partial x_j} \left[\left(\mu + \frac{\mu_t}{\sigma_\epsilon} \right) \frac{\partial \epsilon}{\partial x_j} \right] + C_1 \rho \epsilon \sqrt{2S_{ij}S_{ij}} - C_2 \rho \frac{\epsilon^2}{k + \sqrt{(\mu/\rho)\epsilon}} \quad (4.45)$$

where

$$C_1 = \max \left[0.43, \frac{\eta}{(\eta + 5)} \right] \quad (4.46)$$

The constants used in this turbulence model are:

$$\sigma_k = 1.0 \quad \sigma_\epsilon = 1.2 \quad C_2 = 1.42 \quad A_0 = 4.0$$

Shih et al. (1995) showed the Realisable $k - \epsilon$ model to perform more accurately than the standard $k - \epsilon$ model for a variety of flows including flows over backwards facing steps, boundary layer flows and channel flows.

$k - \omega$ Models

The $k - \omega$ models solve transport equations for k and ω , the specific dissipation rate, rather than k and ϵ . ω is related to k and ϵ by

$$\omega = \frac{\epsilon}{k} \quad (4.47)$$

and can, therefore, be used to calculate l_t using equation (4.34). In the $k - \omega$ models the turbulent viscosity is calculated by

$$\mu_t = \rho k / \omega. \quad (4.48)$$

Standard $k - \omega$ model

The standard $k - \omega$ model is described in detail by Wilcox (1991) and Wilcox et al. (1998).

The transport equation for k is

$$\frac{\partial(\rho k)}{\partial t} + \frac{\partial(\rho k \mathbf{u}_i)}{\partial x_i} = \frac{\partial}{\partial x_j} \left[(\mu + \sigma_k \mu_t) \frac{\partial k}{\partial x_j} \right] + G_k - \beta^* \rho k \omega \quad (4.49)$$

and the transport equation for ω is

$$\frac{\partial(\rho \omega)}{\partial t} + \frac{\partial(\rho \omega \mathbf{u}_i)}{\partial x_i} = \frac{\partial}{\partial x_j} \left[(\mu + \sigma_\omega \mu_t) \frac{\partial \omega}{\partial x_j} \right] + \gamma \frac{\omega}{k} G_k - \beta \rho k \omega^2. \quad (4.50)$$

The empirical constants used in this turbulence model are:

$$\sigma_k = 0.5 \quad \sigma_\omega = 0.5 \quad \beta^* = 0.072 \quad \beta = 0.09 \quad \gamma = 0.52$$

The $k - \omega$ model is numerically robust in the viscous sublayer near the wall and does not require wall damping functions (Bardina et al., 1997). The model has been shown to give more accurate predictions the near wall region than $k - \epsilon$ models but performs less well further from the wall in the free stream region (Bardina et al. (1997) and Menter (1992)).

Shear Stress Transport (SST) $k - \omega$ Model

The SST $k - \omega$ model is described by Menter (1994) and is essentially a hybrid of the $k - \epsilon$ and $k - \omega$ models. Blending functions are used to change between each model depending on the distance from the wall. Close to the wall the $k - \omega$ model dominates and further from the wall, in the free stream, the $k - \epsilon$ model dominates. This allows each model to be used in the areas in which it performs best.

The turbulent viscosity is

$$\mu_t = \frac{\rho a_1 k}{\max(a_1 \omega, F_2 \sqrt{2 S_{ij} S_{ij}})} \quad (4.51)$$

where a_1 is an empirical constant and F_2 is a blending function which is calculated by

$$F_2 = \tanh \left[\left[\max \left(\frac{2\sqrt{k}}{\beta^* \omega y}, \frac{500\nu}{y^2 \omega} \right) \right]^2 \right] \quad (4.52)$$

4. NUMERICAL MODELLING THEORY

In this blending function, y is the distance to the next surface and $\nu = \mu/\rho$ is the kinematic viscosity.

The transport equation for k is similar to the standard $k - \omega$ model but with a blending function applied to G_k :

$$\frac{\partial(\rho k)}{\partial t} + \frac{\partial(\rho k \mathbf{u}_i)}{\partial x_i} = \frac{\partial}{\partial x_j} \left[(\mu + \sigma_k \mu_t) \frac{\partial k}{\partial x_j} \right] + \tilde{G}_k - \beta^* \rho k \omega \quad (4.53)$$

with

$$\tilde{G}_k = \min(G_k, 10\beta^* \rho k \omega). \quad (4.54)$$

the transport of ω is also similar to but with extra term on the right hand side of the equation

$$\frac{\partial(\rho \omega)}{\partial t} + \frac{\partial(\rho \omega \mathbf{u}_i)}{\partial x_i} = \frac{\partial}{\partial x_j} \left[(\mu + \sigma_\omega \mu_t) \frac{\partial \omega}{\partial x_j} \right] + \gamma \frac{\omega}{k} G_k - \beta \rho k \omega^2 + 2(1 - F_1) \rho \sigma_{\omega 2} \frac{1}{\omega} \frac{\partial k}{\partial x_i} \frac{\partial \omega}{\partial x_i} \quad (4.55)$$

where F_1 is a blending function and is given by

$$F_1 = \tanh \left\{ \left\{ \min \left[\max \left(\frac{\sqrt{k}}{\beta^* \omega y}, \frac{500\nu}{y^2 \omega} \right), \frac{4\rho \sigma_{\omega 2} k}{CD_{k\omega} y^2} \right] \right\}^4 \right\}. \quad (4.56)$$

$CD_{k\omega}$ is given by

$$CD_{k\omega} = \max \left(2\rho \sigma_{\omega 2} \frac{1}{\omega} \frac{\partial k}{\partial x_i} \frac{\partial \omega}{\partial x_i}, 10^{-10} \right) \quad (4.57)$$

Constants are blended between the regions near wall and far from wall values using

$$\phi = F_1 \phi_1 + (1 - F_1) \phi_2 \quad (4.58)$$

where ϕ represents the constants σ_k , σ_ω , γ and β .

The empirical constants used in this turbulence model are:

$$\begin{array}{lllll} \sigma_{k1} = 0.85 & \sigma_{k2} = 1 & \sigma_{\omega 1} = 0.5 & \sigma_{\omega 2} = 0.856 & \gamma_1 = 0.556 \\ \gamma_2 = 0.44 & \beta_1 = 0.075 & \beta_2 = 0.0828 & \beta^* = 0.09 & a_1 = 0.31 \end{array}$$

4.4.1.2 Reynolds Stress Models

Reynolds stress models do not utilise the eddy viscosity hypothesis and instead solve full transport equations for the Reynolds stresses. This requires six transport equations for Reynolds stresses, plus one equation for turbulent dissipation, resulting in seven total equations

which must be solved. This obviously requires a significantly larger computational cost than the two equation eddy viscosity models. However, by solving the Reynolds stresses directly, the eddy viscosity assumption, and therefore the isotropic constitutive equation assumption, is not required. This allows Reynolds stress models to more accurately predict turbulent flows with strong anisotropy, such as flows involving separation and stratified buoyant flows.

In this project, Reynolds stress turbulence models are only considered very briefly and the investigation into modelling turbulence in skimming flows over stepped spillways focuses mainly on the two equation eddy viscosity models described above. For this reason a full description of the Reynolds stress turbulence models is not given here. Full details of the model can be found in Launder et al. (1975).

4.4.2 Near Wall Treatment for Turbulent Flows

Turbulent flows close to a solid boundary behave differently from turbulent flows in the free-stream, as the no slip condition causes the flow velocity to be zero at the wall. The Reynolds number close to a wall is, therefore, small relative to the Reynolds number in the free stream. In the free stream, the viscous stresses are small compared to the Reynolds stresses, however, close to the wall the viscous stresses dominate.

When considering near wall turbulence, two dimensionless numbers, y^+ and u^+ , are used in order to represent the perpendicular distance from the wall and the the velocity perpendicular to the wall respectively. u^+ is defined as

$$u^+ = \frac{u}{u_\tau} \quad (4.59)$$

where u_τ is the shear velocity, given by

$$u_\tau = \sqrt{\frac{\tau_w}{\rho}} \quad (4.60)$$

and τ_w is the wall shear stress. y^+ is defined as

$$y^+ = \frac{y u_\tau}{\nu} \quad (4.61)$$

where y is the perpendicular distance from the wall.

The near wall region in turbulent flows can be divided into several sub-regions (figure 4.1),

4. NUMERICAL MODELLING THEORY

depending on the distance from the wall. Far away from the wall there is the outer region, where the velocity has a flat profile and turbulent stresses dominate. The outer region is found at approximately $y^+ \geq 350$. Adjacent to the wall there is the inner region, which is then divided into three layers.

Next to the wall is a very thin viscous sub-layer where the viscous stresses dominate and the velocity profile is approximately linear such that

$$u^+ = y^+. \quad (4.62)$$

The viscous sub-layer extends to $y^+ \approx 5$.

Further from the wall there is the logarithmic layer, where both viscous and turbulent stresses are important. The velocity profiles in this region follow a logarithmic profile such that

$$u^+ = \frac{1}{\kappa} \ln(Ey^+) \quad (4.63)$$

where κ is the empirically derived von Karman's constant ($= 0.4187$) and E is another empirical constant ($= 9.7397$). The logarithmic layer extends approximately from $y^+ \geq 30$.

From $5 < y^+ < 30$ there is a buffer layer where neither the linear or logarithmic velocity profiles apply. The cross-over point between where the linear and logarithmic velocity profiles are found to be most accurate is at $y^+ = 11.225$. Therefore it is common to assume a linear profile up to $y^+ = 11.225$ and a logarithmic profile above $y^+ = 11.225$. Errors will increase, however, outside of the above stated ranges of y^+ for the viscous sub-layer and the logarithmic layer.

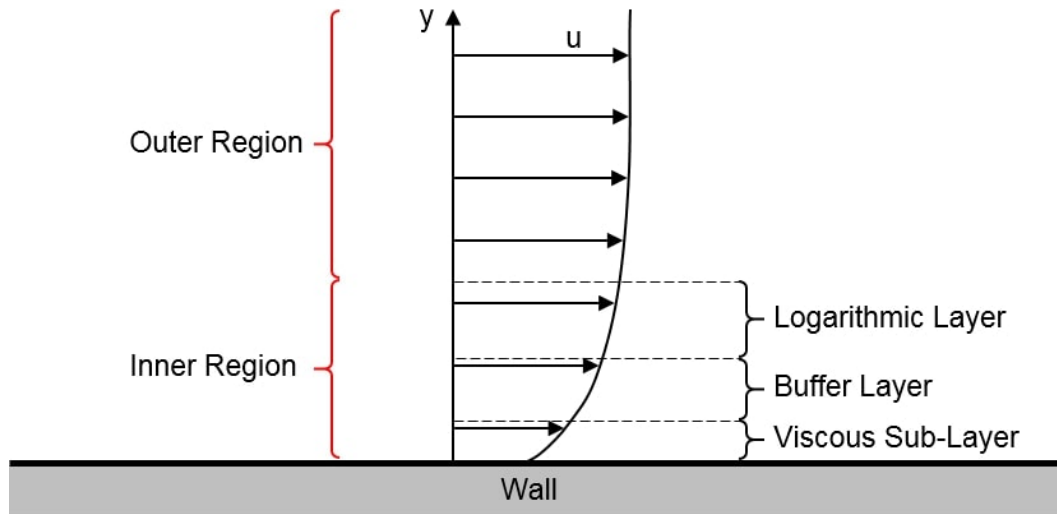


Figure 4.1: Schematic of the various layers of near wall turbulent flows

Modelling the turbulence near the wall, therefore, has added complexity. There are generally two methods in by which this is done. One method is the wall function approach. Wall functions are semi-empirical relationships which are used to describe the viscosity affected region near the wall. In the wall function approach, only the fully turbulent region is directly modelled and wall functions are used to specify the flow behaviour close to the wall. A major drawback of the wall function approach is that it requires the cell nodes closest to the solid boundary to be in the fully turbulent region, generally requiring the y^+ value of the wall adjacent cell node to be greater than 30. If the near wall mesh nodes have y^+ values less than 30, then the viscosity affected region is modelled using a turbulence model designed only for the fully turbulent region, causing errors in the solution.

The second method used to model turbulence in the near wall region is the near wall modelling approach, in which the near wall region is directly modelled using modifications to the turbulence model, which allow the viscosity affected region to be predicted. The drawback of this approach is that the mesh adjacent to the wall must be fine enough to fully resolve the viscosity affected region. This requires a small y^+ value for the wall adjacent cell (generally recommended as ≈ 1) as well as a sufficient number of cells across the viscosity affected region.

Both of these methods of predicting near wall turbulence have specific and distinct requirements for the mesh resolution adjacent to a solid boundary. However, during mesh generation, these specific requirements may not be known. One method to ensure that the correct mesh

4. NUMERICAL MODELLING THEORY

resolution is used is to generate a mesh and calculate a solution. The y^+ values at the walls can then be examined and used to modify the original mesh so that the correct near wall refinement is achieved. A problem with this method is that, if an unsuitable mesh is used for the initial solution, then the flow velocities, and therefore y^+ values, may be predicted inaccurately, so that the obtained requirements for the mesh modifications may be incorrect. This process may require a number of iterations which may be time consuming and computationally expensive.

Another problem is that for complex geometries, or in situations where the flow velocity adjacent to a wall varies significantly over a small distance, then it may be difficult to produce a mesh which has a consistent near wall resolution for the near wall modelling approach being implemented.

In order to overcome these problems, near wall treatment methods have been developed which are insensitive to the mesh resolution adjacent to the wall. One of these methods is scalable wall functions. Scalable wall functions make use of standard wall functions, however a limiting value, y_{lim} is applied to y^+ to ensure that wall functions are used only in the fully turbulent region. If the y^+ value of the cell node adjacent to the wall is greater than y_{lim} , then a standard wall function approach is used. If, however, the y^+ value of the cell node is less than y_{lim} , then y_{lim} is used instead.

Another wall treatment approach which is insensitive to the value of y^+ at the wall adjacent cell node is enhanced wall treatment (EWT). In the EWT approach, both the wall function and the near wall modelling approaches are employed, depending on the y^+ value of the wall adjacent cell node. For the $k - \epsilon$ models, ANSYS Fluent uses two-layer approach when near wall modelling is required with use of EWT. The two-layer approach subdivides the flow into the viscosity affected region and the fully turbulent region. In the viscosity affected region, a one equation model, described by Wolfshtein (1969), is implemented and in the fully turbulent region the $k - \epsilon$ model in question is used in its normal way. The $k - \omega$ models are able to resolve the entire turbulent boundary layer when near wall modelling is required in EWT.

4.5 The Finite Volume Method

In order to solve the NS equations, they must be discretised in both time and space. The three most commonly used methods to do this are the finite difference method, the finite element method and the finite volume method (FVM). Most CFD solvers utilise the FVM, which is described below.

The FVM is described in detail by Eymard et al. (2000) and Versteeg and Malalasekera (2007). In the FVM, the computational domain is split into a finite number of control volumes, known as cells, using a mesh. At the centroid of each cell there is a node point, where variables are stored. Figure 4.2 shows a schematic of the FVM. The cell under consideration has the node P and has neighbours W and E to the "west" and "east" respectively. Cells P and W are connected by surface w and cells P and E are connected by surface e. Transport equations are integrated over the control volume for P and then converted to surface integrals, using the divergence theorem, so that the fluxes through surfaces can be calculated.

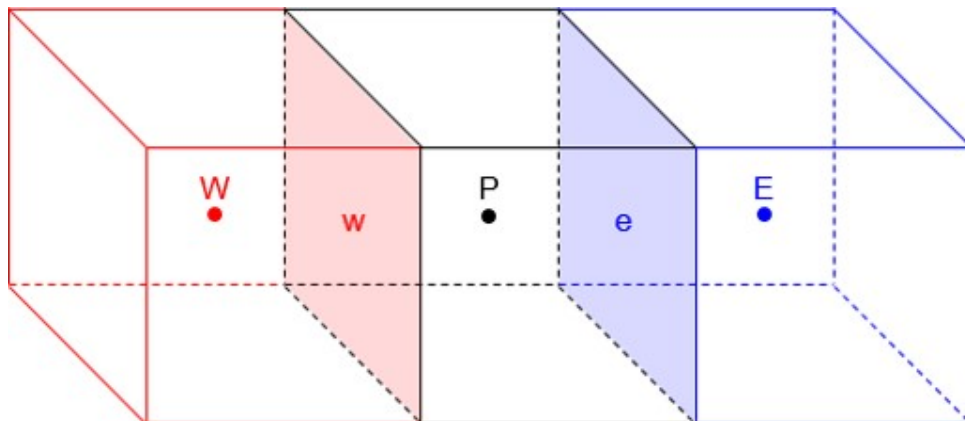


Figure 4.2: Schematic of the FVM with reference to node P. Nodes W and E are connected to node P by faces w and e respectively

The FVM has a number of advantages. It can be easily implemented on both structured and unstructured meshes, which makes the method suitable for complex geometries. High gradients of a flow variable on a computational grid can cause discontinuities. These discontinuities are not problematic in the FVM, due to the integral formulation used in the method. The FVM is inherently conservative, which is particularly advantages for fluid flows.

Within a particular cell, the conservation of a flow variable, such as velocity, is the balance between the various mechanisms which may change the value of the flow variable within the cell. The rate of change of the variable over time is the sum of the net rates of change of

4. NUMERICAL MODELLING THEORY

convection, diffusion and generation within the cell. Conservation is applied over each cell so, therefore, global conservation is observed.

In order to solve a particular fluid flow using the finite volume method, the following steps are undertaken:

- The governing equations are integrated over all of the computational cells within the domain
- The resulting integral equations are discretised into a system of algebraic equations.
- Iterative methods are used to solve the algebraic equations

4.6 Numerical Modelling Error

Errors are an inherent part of all CFD simulations and can occur in a number of forms. It is important that these errors are understood and, if possible, reduced or eliminated so that numerical solutions to fluid flow problems can be viewed with confidence. The main sources of error which occur in CFD modelling are discussed below.

Physical Approximation Errors These errors occur because the physical approximations used in numerical models do not represent the physical processes exactly. This may be due to a lack of understanding of the physical process involved or simplification of the physical processes in order for it to be modelled using the computational resources available. Physical approximation errors are quantified using validation studies. Validation of the physical approximations used in numerical models is the goal of much research into CFD methods. Errors caused by other factors, which are discussed below, must be identified and minimised in order for meaningful conclusions to be drawn from these validation studies.

Discretisation Errors These errors are caused by the discrete approximation of continuous solutions (Eça and Hoekstra, 2006). Discretisation error may be caused by the mesh or time step sizes used in a simulation. Increasing the mesh resolution, or decreasing the time step size, can reduce the numerical error, with the assumption that as the grid size, $h \rightarrow 0$, or the time step size, $\Delta t \rightarrow 0$, the numerical solution approaches the exact solution (Freitas, 2002).

However, reducing the grid size also increases the computational cost and may improve the solution to a level of accuracy beyond that which is required. For example, a more refined

mesh (or smaller time step) may require a 25% increased computational cost but only improve a solution of velocity from 20 m/s to 20.1 m/s. This increase in accuracy may not be worth the increased computational cost. Therefore, the aim of CFD modelling should be to minimise numerical errors to an acceptable level, while also minimising computational cost. In this project, the spatial and temporal discretisation errors are analysed using methods described in detail in Chapter 5 and Appendix A.

Iterative Convergence Error These errors occur due to the fact that the iterative methods used to solve the problem use a finite number of iterations. These can be minimised by choosing appropriate convergence criteria for the solution, and ensuring that these criteria are met. The convergence of a solution is determined by examination of the solution residuals. Numerical models calculate variables by making discrete approximations to continuous equations. The continuous solutions equal zero but the discrete approximation will give a non-zero value, known as the residual. The lower the value of the residual is, the closer the discrete approximation is to the true value and, at each iteration, the residual value will become closer to zero if the solution is converging.

In steady state simulations, convergence should be assessed by ensuring that either the residuals for each variable have reached a sufficiently low value, or that the residuals have plateaued and that there is only minimal variation in the residual values at each iteration. If a residual plateaus at a value which is deemed to high to be acceptable, then the solution methods, domain or mesh may need to be modified. Convergence in steady state solutions can also be monitored by observation of one or more variables in a certain location within the domain, to ensure that a steady state is achieved.

Convergence in transient simulations or more complex, as convergence criteria must be met at each time step. The convergence assessment methods used for steady state simulations must be applied at each time step. In transient simulations it is often difficult to ensure a residual reaches a specific value. For this reason it is often common to set a residual target which is relative to the residual value after the first iteration of each time step.

User Error This is caused by incorrect use of CFD software, for example the incorrect use of a turbulence model or inappropriate boundary conditions. User error can manifest in different ways, such as a lack of convergence. However, a converged solution may still be found but

4. NUMERICAL MODELLING THEORY

the the solution found may not be accurate. For this reason, user errors are often difficult to identify. User error is minimised by training as well as practice and experience. User error may also be introduced intentionally to reduce computational cost at the expense of accuracy, maybe in the preliminary design phase of a project.

Computer Round-Off Error These errors occur due to the finite accuracy at which numbers can be stored. Generally these errors are insignificant when compared with other sources of error and do not need to be addressed.

4.7 Assumptions and Limitations

Compressibility

Both the air and water phases are treated as incompressible in all numerical modelling presented in this project. Water has a very low compressibility and is therefore almost universally treated as incompressible. Air, however, has a higher compressibility than water, although it is usually treated as incompressible at velocities less than around Mach 0.3 (≈ 370 km/h). To confirm whether this assumption is valid a simulation was conducted, using the Eulerian model, in which the air phase was treated as an ideal gas, allowing variable density. The velocity, air volume fraction and pressure results were found to show negligible differences to those of a simulation that treated both phases as incompressible, but was otherwise identical.

Steady State Solutions

All simulations were calculated transiently until a steady state was achieved, whereby there was negligible variation in the flow variables over time. This was confirmed through analysis of monitor point data in all simulations. More detailed analysis was conducted on a handful of simulations to confirm that steady state behaviour in the monitor points was representative of steady state behaviour throughout the domain. Some transient behaviour, however, was observed with the VOF model in combination with the SST $k - \omega$ turbulence model. This is discussed in detail in the relevant chapters of this thesis.

No-Slip Conditions at Solid Boundaries

A no-slip boundary condition has been used at all solid boundaries in the numerical modelling conducted in this project. This is due to the fact that the surfaces of both experimental stepped spillways which have been modelled are constructed from smooth transparent plastic. It is therefore assumed that the surface roughness is negligible and does not need to be accounted for in the numerical models.

Air Bubble Diameter

The range of air bubble diameters for all Eulerian model simulations was set to between 0.09 mm and 9.99 mm. The average bubble diameter is defined using the Sauter mean diameter, an estimation of the mean size of a given particle distribution, based on the volume to surface area ratio of particles within the defined range (Filippa et al., 2012). Matos (1999) investigated the range of bubble sizes found in the aerated region of one of the experimental stepped spillways which is numerically modelled in this project. It was found, using high speed photography, that the bubbles in the aerated region of an experimental stepped spillway ranged from less than 1 mm to around 4 mm. The other spillway that has been modelled in this project has the same step height (80 mm). Therefore, the range of bubble sizes used for the Eulerian model was deemed to be a reasonable assumption.

For mixture model simulations conducted in chapter 5, the air bubble diameter was also set to between 0.09 mm and 9.99 mm. For all mixture model simulations conducted in chapter 6, however, the bubble diameter was set at a constant 0.1 mm.

Phase Interaction Modelling with the Eulerian model

Only the drag force phase interaction model has been implemented during Eulerian multiphase modelling, as discussed in section 4.3.2.

Bubble Breakage and Coalescence

In the mixture and Eulerian models, the bubble breakage and coalescence models were not included. Sensitivity analysis was conducted which showed that including the bubble breakage or coalescence models, with either the mixture or Eulerian model, had a negligible effect on the solution.

4. NUMERICAL MODELLING THEORY

Turbulence Modelled for Fluid Mixture

The turbulence has been modelled for the fluid mixture, for all Eulerian model results presented in this project. An investigation was conducted to compare simulation results with the turbulence modelled for the fluid mixture and also per phase. Little variation was found between the velocity and air volume fraction results. Therefore, it was decided that the additional computational cost incurred by modelling turbulence separately for each phase was not justifiable.

4.8 Solver Settings

Table 4.1 shows a summary of key solver settings used for numerical modelling conducted in this project.

Table 4.1: Summary of key solver settings used for numerical modelling conducted in this project

| Solver Setting | VOF Model | Eulerian Model | Mixture Model |
|---------------------------------------|-----------------------------|-----------------------------|-----------------------------|
| Pressure-Velocity Coupling | SIMPLE | Phase Coupled SIMPLE | SIMPLE |
| Advection Discretisation | Second Order Upwind | Second Order Upwind | Second Order Upwind |
| Diffusion Discretisation | Least Squares Cell Based | Least Squares Cell Based | Least Squares Cell Based |
| Transient Discretisation | First Order Implicit | First Order Implicit | First Order Implicit |
| Volume Fraction Discretisation | Geometric Reconstruction | First Order Upwind | First Order Upwind |

CHAPTER 5

Two-Dimensional Numerical Model Study of a
Large Experimental Stepped Spillway

5. TWO-DIMENSIONAL NUMERICAL MODEL STUDY OF A LARGE EXPERIMENTAL STEPPED SPILLWAY

This chapter describes a numerical study of a large scale, experimental stepped spillway. Comprehensive two-dimensional (2D) modelling of the spillway, using a range of multiphase and turbulence models, is conducted for a number of flow rates. The velocities, air volume fractions (AVFs) and flow depths are validated against experimental data and number of methods of identifying the location of the inception point are investigated.

The VOF model is not expected to predict air entrainment, for the reasons outlined in chapter 4. However, the model has been shown to be able to predict certain flow features of skimming flows over stepped spillways accurately. The VOF model is a commonly used free-surface modelling technique and has, therefore, been included in this investigation for comparison with other multiphase numerical models. The Eulerian and mixture models however, are expected to be able to predict air entrainment.

5.1 Experimental Set-Up

Experimental data on air concentrations, velocities and inception point locations have been provided for this part of the project by Professor Jorge Matos from the Instituto Superior Tecnico (IST) of the University of Lisbon. The data was collected from a large scale experimental stepped spillway, located at the National Laboratory of Civil Engineering (LNEC) in Lisbon. The design of the experimental spillway and the collection of the data was not part of this project.

The spillway is 2900 mm high from crest to toe and 1000 mm wide. The crest of the spillway follows U.S. Army Corps of Engineers, Waterways Experimental Station (WES) spillway profile. This comprises an upstream smooth region followed by 11 steps of increasing size. There are then 33 uniform steps of $h_s = 80\text{mm}$ and $l_s = 60\text{mm}$, giving a slope of 1V:0.75H, and a chute angle, $\theta \approx 53^\circ$. The geometry of the numerical domain used to model the experimental spillway is detailed in figure 5.2.

In the experiments, skimming flow is observed at all flow rates considered in this chapter. A non-aerated region, inception point, aerated region and recirculating vortices in the step cavities can be clearly observed. 3D behaviour is observed in the step cavities of the experimental spillway (Matos et al., 1999). However, the spillway is more than six times wider than, and has more than double the number of steps of, the experimental stepped spillway studied in chapter 3. This significantly larger domain size would make a comprehensive, transient, 3D

study of the stepped spillway at the LNEC unfeasible, due to the extremely high computation cost that would be required. However, the flow above the step cavity is found to be essentially 2D (Bombardelli et al., 2011). In addition to this, Bombardelli et al. (2011) and Meireles et al. (2014) used 2D numerical modelling to accurately predict velocity profiles and flow depths in the non-aerated region of the same experimental spillway that is modelled in this study. For these reasons it was judged that 2D numerical modelling of the 3D spillway would be a useful approach for studying the flow characteristics above the pseudo-bottom. A 3D study of a small upstream section of the spillway is also conducted in order to investigate 3D behaviour in the spillway. This is discussed in chapter 7.

5.1.1 Instrumentation

Air concentrations were measured using a conductivity probe. The conductivity probe contains two wires which have tips that are a few millimetres apart. An electric current is applied to the probe and, in the presence of water, the current is conducted between the two wires. If an air bubble comes into contact with either of the wires, then the current is interrupted and the presence of air is recorded. The ratio of time when the current is interrupted to total measurement time is used to calculate the air concentration.

Velocities were measured using a back-flushing Pitot tube, which measures the difference between the stagnation pressure and the static pressure. The stagnation pressure is measured at the end of the Pitot tube and the static pressure is measured at a port several diameters downstream. The velocity is then calculated by

$$u = \sqrt{\frac{2\Delta p}{\rho_w(1 - \lambda_T C)}} \quad (5.1)$$

where u is the velocity, Δp is the difference between the total pressure head and the static pressure head, C is the local air concentration and λ_T is a tapping coefficient, which is required due to the non-homogeneous nature of the air-water flow approaching the stagnation point of the Pitot tube. $\lambda_T = 1$ is an acceptable tapping coefficient to use for values of C up to 0.7 (Matos et al., 2002). Above $C = 0.7$, using $\lambda_T = 1$ in equation (5.1) causes the velocity to be considerably underestimated. Note that the experimental velocity data included in this project is all at water depths where $C \leq 0.7$. C is the time averaged air concentration value obtained from the conductivity probe measurements. Continual back-flushing of the Pitot tube

5. TWO-DIMENSIONAL NUMERICAL MODEL STUDY OF A LARGE EXPERIMENTAL STEPPED SPILLWAY

was used to ensure that there was only water present in both the static pressure ports and the total head ports.

All measurements were taken in a line perpendicular to the pseudo-bottom. Each line is located at a step corner and measurements are made at specific distances from the pseudo-bottom. The number of measurement points at each step varies, depending on the flow depth and the reliability of the data close to the free-surface (discussed further below). Sensitivity analysis of the 3D nature of the flow above the steps was conducted using the conductivity probe and the back flushing Pitot tube. The time averaged flow characteristics (over 90 s) were found to be essentially 2D (Bombardelli et al., 2011). Therefore, at each measurement location, the velocity and AVFs were measured simultaneously at channel widths 100 mm either side of the spillway centreline (Matos, 1999). These positions were deemed close enough to the centreline so that there would be no wall effects, yet far enough away from one another so that the presence of the instruments in the flow would not affect one another.

Measuring velocities close to the free-surface is difficult, as waviness of the free-surface profile and turbulence of the flow causes the back-flushing Pitot tube to only be submerged for part of the time. This means the velocity recorded will be an average of the time the instrument is submerged and the time that it is not. Equation 5.1 accounts for this, however, the waviness of the free-surface has a high frequency compared to the response time of the Pitot tube. In certain cases the velocity data close to the free-surface was deemed to be inaccurate and not included in the data set, for example, if the measured velocity was greater than the maximum potential velocity. There are, therefore, fewer velocity data points at each step location than the corresponding air concentration data. Both velocities and air concentrations were recorded for 90 seconds. Due to time constraints on the original project, data is available for a different number of steps at each flow rate considered.

Figure 5.1 shows photographs of skimming flow over the stepped spillway at the LNEC, with instrumentation locations indicated. Further details of the experimental spillway, instrumentation and calibration can be found in Matos and Frizell (2000), Matos (2000), Bombardelli et al. (2011) and Meireles et al. (2012).

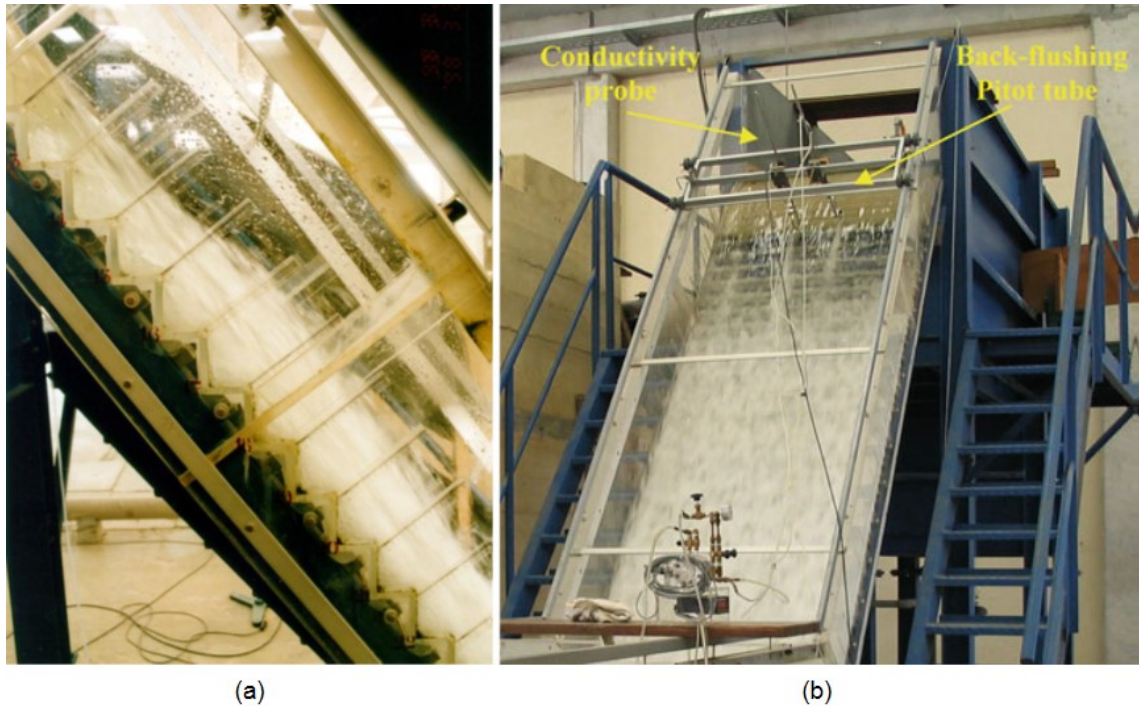


Figure 5.1: Skimming flow over the stepped spillway at the LNEC: (a) view from the side of the spillway (image taken from Matos and Meireles (2014)); (b) view from in front of the spillway with the conductivity probe and back flushing Pitot tube indicated (image taken from Bombardelli et al. (2011))

5.2 Modelling Procedure

The VOF, mixture and Eulerian multiphase models were investigated in conjunction with the Realisable $k - \epsilon$, RNG $k - \epsilon$ and SST $k - \omega$ RANS turbulence models. Further investigation was conducted using the Eulerian model in combination with the standard $k - \epsilon$, the standard $k - \omega$ and the Reynolds Stress RANS turbulence models. ANSYS Fluent v17.2 was used for all numerical modelling conducted in this chapter. Numerical models were run transiently until a steady state was achieved, at which time negligible unsteady behaviour was observed in flow variables. As such, instantaneous numerical values are presented in this chapter, as they are equivalent to time averaged values.

All numerical modelling conducted in this chapter utilised enhanced wall treatment (EWT) apart from the grid convergence study, which utilised scalable wall functions. Both of these wall treatments are insensitive to y^+ , as described in chapter 4. The insensitivity of these wall treatment approaches to y^+ is important, as the recirculating vortices in the step cavities cause y^+ values acting on the step faces to vary significantly over small distances. Although

5. TWO-DIMENSIONAL NUMERICAL MODEL STUDY OF A LARGE EXPERIMENTAL STEPPED SPILLWAY

both EWT and scalable wall functions are insensitive to y^+ , it is commonly considered that y^+ values should not exceed 300. For all numerical modelling conducted in this chapter, no y^+ values acting on the step faces exceed 150 and the vast majority of y^+ values are below 100.

5.2.1 Domain

Figure 5.2 shows the numerical domain that has been used throughout this study. The inlet leads to a larger reservoir, which in turn leads to the WES curve. This is then followed by the spillway steps, a short horizontal section and then the outlet. The top of the domain generally follows the same profile as the bottom of the domain, so that a structured mesh could be easily constructed. The exception to this is above the WES curve, where the top of the domain follows a different profile due to the changing gradient of the WES curve. The 2D simulations in this study consist of a domain which has a 10 mm width consisting on one cell and symmetry boundary conditions at either side. Details of the 3D domain are found in section 7.5.

In this study, unlike in chapters 3 and 6, the stream-wise distance along the chute is given by s rather than x . x is defined as length along the pseudo-bottom from the first step corner. In this case, s is defined as the distance from the maximum height of the spillway crest, along the WES curve and the pseudo-bottom. Between the maximum height of the spillway crest and the upstream corner of the first 80 mm \times 60 mm step (step 12), s follows a curve, due to the variable gradient, and downstream of this point, s follows a straight line. The pseudo-bottom becomes a straight line at $s = 440$ mm. z is defined as the perpendicular distance from the pseudo-bottom. Throughout this study the flow depth refers the value of z at a particular position. Step numbers refer to the step cavity and the step corner of the vertical edge immediately downstream of the step cavity. For example, velocity data labelled at step 20 is measure along z at the step corner which joins steps 20 and 21, where steps are numbered from upstream to downstream.

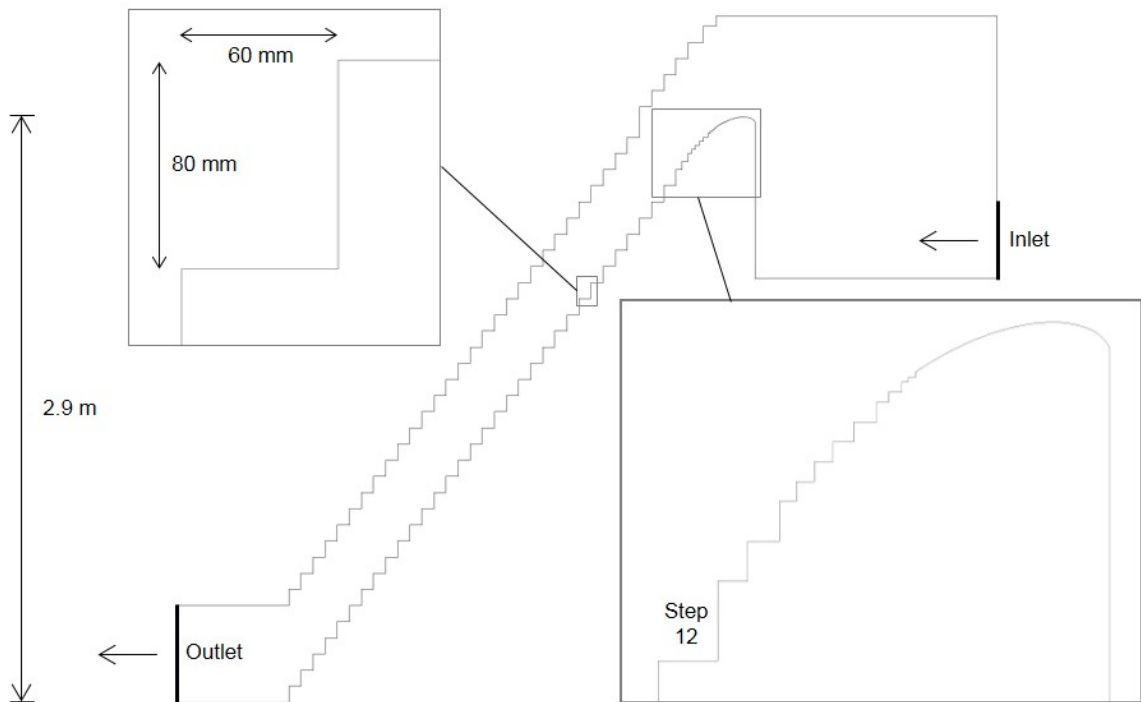


Figure 5.2: Numerical domain detailing the inlet, crest, steps and outlet. s is defined as the distance from the maximum height of the spillway crest, along the WES curve and the pseudo-bottom. The corner of step 11 is located at $s = 440$ mm

5.2.2 Numerical Error

In order to ensure that the discretisation errors (discussed in chapter 4) are minimised, and do not have a significant effect on the numerical solutions, grid convergence and time step independence studies were conducted. The methodologies and results of these studies are detailed below.

5.2.2.1 Grid Convergence

The Grid Convergence Index (GCI) has been used to assess the numerical error due to mesh size, and also to determine whether solutions fall within the asymptotic range, whereby the solution shows negligible change with increased grid refinement. The GCI, described by Roache (1994), is a method of determining the numerical error due to the mesh size, which is based on the Richardson extrapolation. The GCI method requires solutions produced using three separate meshes of increasing mesh refinement. The results of these solutions are then used to assess whether the solutions are independent of the mesh size. The mesh sizes used

5. TWO-DIMENSIONAL NUMERICAL MODEL STUDY OF A LARGE EXPERIMENTAL STEPPED SPILLWAY

in this study are detailed in table 5.1. The Horizontal and vertical step faces refer to the 80 mm × 60 mm steps from step 11 onward.

Table 5.1: Numbers of cells and cell sizes for meshes used in the grid convergence study

| Mesh | Vertical Step Face | | Horizontal Step Face | | Total Number of Cells |
|--------|--------------------|----------------|----------------------|----------------|-----------------------|
| | Number of cells | Cell Size (mm) | Number of Cells | Cell Size (mm) | |
| Mesh 1 | 32 | 2.50 | 24 | 2.50 | 529530 |
| Mesh 2 | 40 | 2.00 | 32 | 1.88 | 934068 |
| Mesh 3 | 48 | 1.67 | 40 | 1.50 | 1445014 |

In the GCI method, hg is a measure of the refinement of the grid, for example, a dimension of a cell. The grid refinement ratio r is then calculated by $r = hg_3/hg_2 = hg_2/hg_1$. In this study, hg will be defined using the size of the cells in the step cavities. In order to make use of hanging nodes for grid refinement (discussed below), the number of cells along both the vertical and horizontal step faces must be multiples of 4. Therefore, r varies depending on whether the the vertical or horizontal dimensions of the cell are considered and the value of r between meshes 1 and 2 is not equal to that at meshes 2 and 3. The values of r range from 1.2 to 1.33, so a mean value of 1.258 has been used for r in the grid convergence analysis.

f_i is the value of a variable produced by Mesh i . The observed convergence rate, ρ_g , is given by

$$\rho_g = \frac{\ln\left(\frac{|f_3 - f_2|}{|f_2 - f_1|}\right)}{\ln r} \quad (5.2)$$

The grid convergence index is the calculated by

$$GCI = \frac{Fs|e|}{r^{\rho_g} - 1} \times 100 \quad (5.3)$$

where Fs is a factor of safety, often taken as 1.25, and e is the error between the two grids. Note that the value of the GCI is multiplied by 100 to convert it into a percentage error. e is calculated by

$$e = \frac{f_i - f_{i-1}}{f_{i-1}}. \quad (5.4)$$

If the solutions for the three meshes investigated are in the asymptotic range then

$$GCI_{23} \approx r^{\rho_g} GCI_{12}. \quad (5.5)$$

Equation (5.5) can be rearranged to produce

$$\frac{GC_{I_{23}}}{r^{p_g} GC_{I_{12}}} \approx 1. \quad (5.6)$$

The left hand side of equation (5.6) will be referred to as the asymptotic verification (AV) so that, for solutions to be in the asymptotic range, $AV \approx 1$.

In this study, all grid convergence analysis has been conducted using the Realisable $k - \epsilon$ model with scalable wall functions, at $Q - 180$ l/s. Figure 5.3 shows the GCI values of the velocities with the Eulerian model. The majority of the values of $GC_{I_{23}}$ are below 10%, with many falling below 5%. At the lowest values of z the values of the GCI errors are slightly higher. At most steps these values are still relatively low, however in some cases the values of the GCI errors are above 20%. Figure 5.4 shows the AV values for the Eulerian model. It can be seen the all of the values of AV are close to 1, so the solution can be assumed to be in the asymptotic range. At the lower values of z , the AV values are slightly further from 1. This corresponds to the higher values of the GCI errors observed at these depths. The AV values in these positions are still reasonably close to 1, however. Further details on the grid convergence analysis conducted for this study, including details on the AVFs and the VOF and mixture models, can be found in appendix A. The results of this grid convergence analysis have concluded that the model solutions are independent of grid refinement at meshes 2 and 3, so mesh 2 has been used for all 2D numerical modelling in this study.

5. TWO-DIMENSIONAL NUMERICAL MODEL STUDY OF A LARGE EXPERIMENTAL STEPPED SPILLWAY

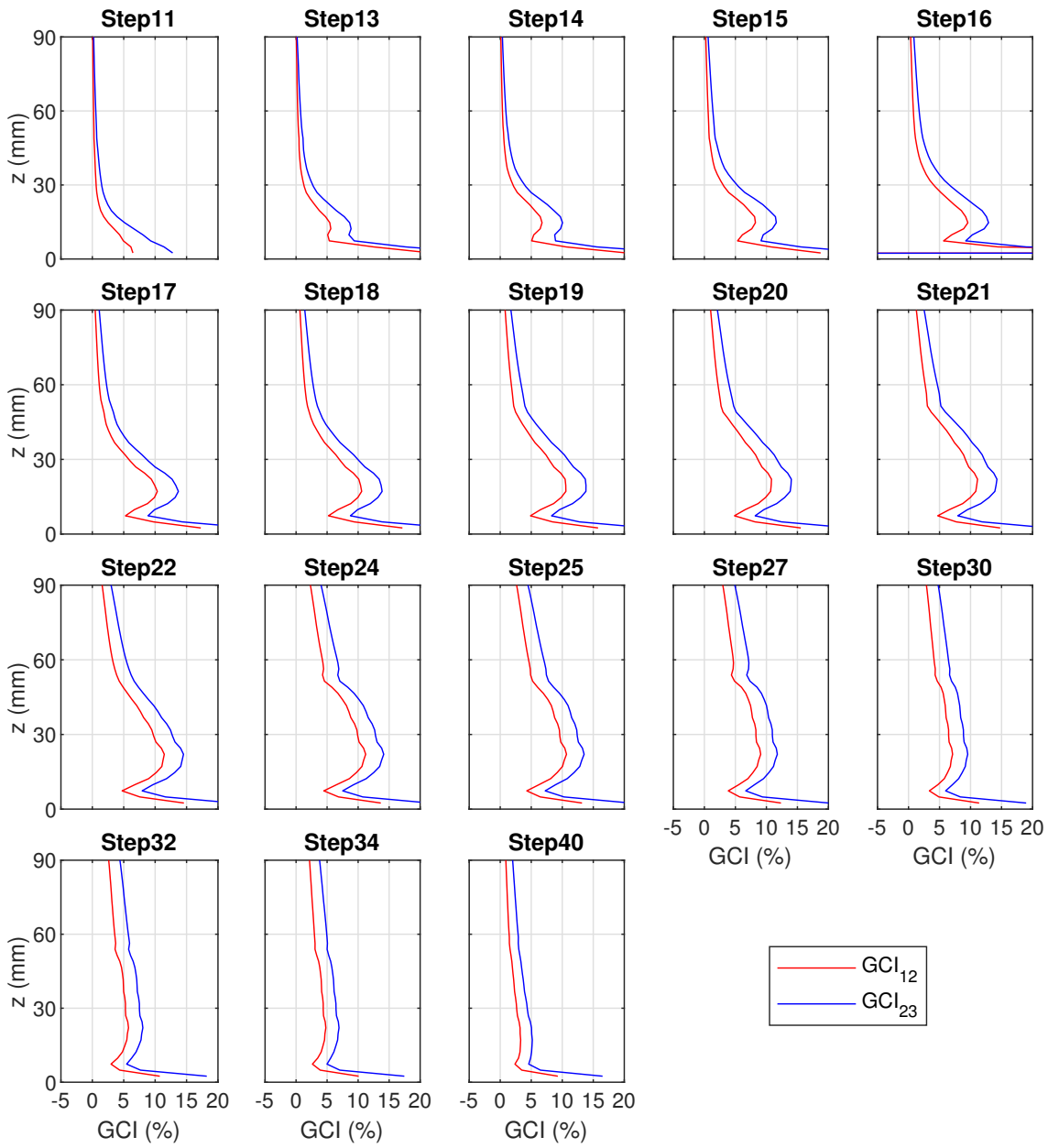


Figure 5.3: Grid convergence index percentage error of velocity at numerous locations above the pseudo-bottom. The solutions were calculated for three meshes, using the Eulerian model with the Realisable $k - \epsilon$ model, at $Q = 180$ l/s

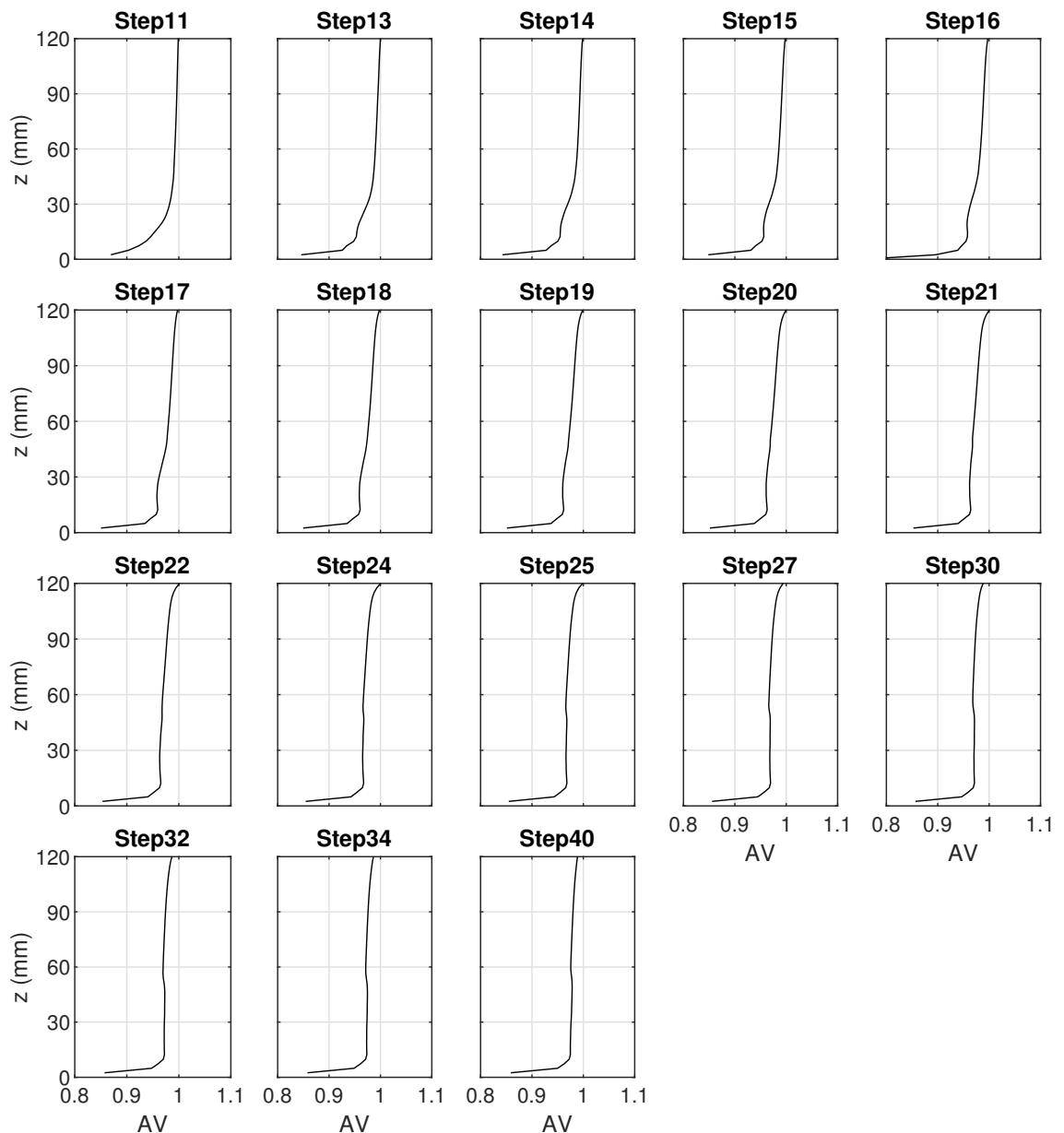


Figure 5.4: Asymptotic verification of velocity at numerous locations above the pseudo-bottom. The solutions were calculated for three meshes, using the Eulerian model with the Realisable $k - \epsilon$ model, at $Q = 180$ l/s

Figure 5.5 shows the final mesh that resulted from the mesh independence study, which has been used throughout the next stages of the study. In order to reduce computational costs, hanging nodes have been used to refine the mesh in the areas of most importance. At the steps and the WES curve there are two levels of refinement using hanging nodes. Each level of refinement doubles the number of cells along the edge in question. This is why the numbers of cells along the step faces are all multiples of four. There is also one level of refinement at the inlet and close to the free-surface in the reservoir. The mesh is relatively

5. TWO-DIMENSIONAL NUMERICAL MODEL STUDY OF A LARGE EXPERIMENTAL STEPPED SPILLWAY

coarse towards the top of the domain and toward the outlet. This is due to the fact that these areas are not of interest in this study and do not affect the flow in the areas of interest. The mesh is also coarse in the approach reservoir, as the velocities in this region are low and the flow field is less complex to predict.

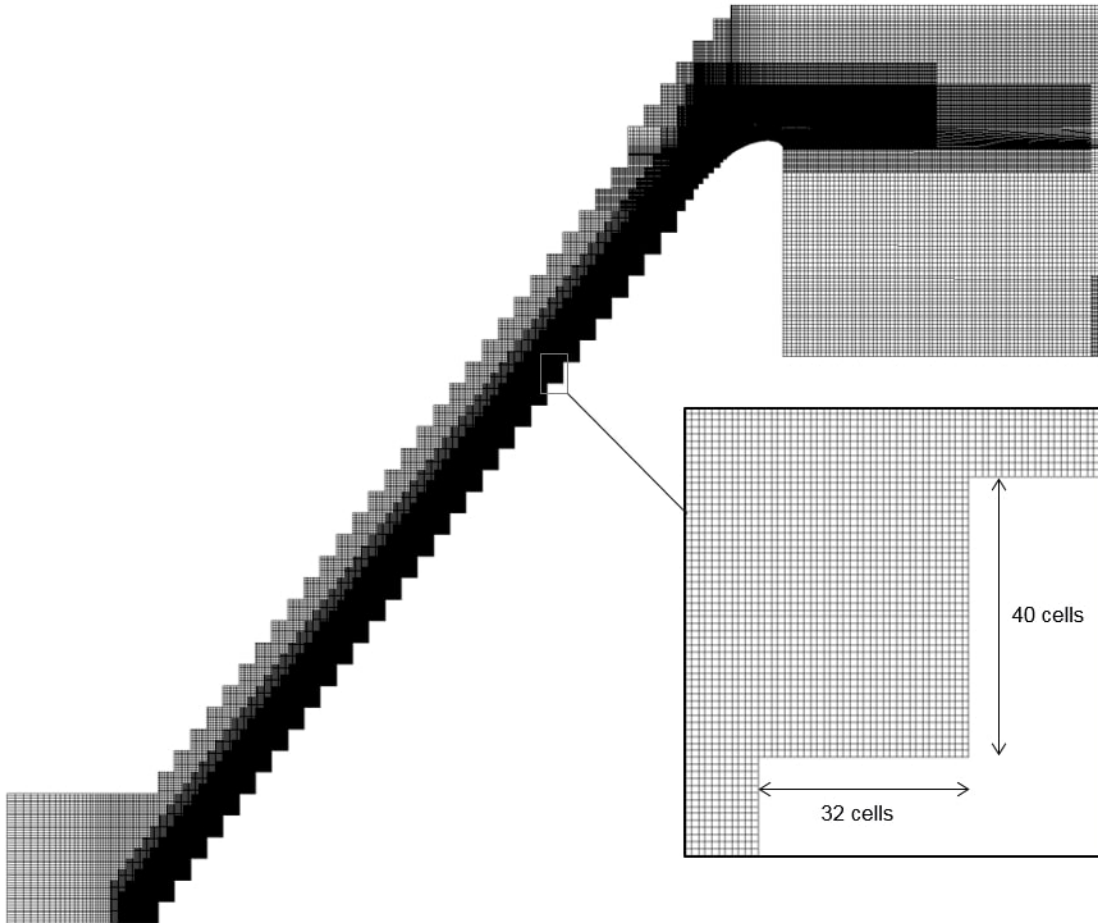


Figure 5.5: Diagram of 2D mesh used for numerical modelling of the stepped spillway at the LNEC. The mesh is refined at the steps, the WES curve and at the inlet. The rest of the domain is relatively coarse in order to reduce the computational cost of simulations. The total number of cells in the domain is 934068

5.2.2.2 Time Step Independence

In order to ensure that the model solutions are independent of the time step used in the simulations, a time step independence study was conducted, whereby solutions for different time steps were compared in order to determine the error. In all cases, initial simulations, including mesh independence, were conducted using the largest time step that was possible while still producing a fully converged solution. For the VOF and mixture models this value was 1×10^{-3} s and for the Eulerian model this was 1×10^{-4} s. In order to make a meaningful comparison

of the solutions for different time steps, the time steps considered must be relatively different from one another. In this study it was decided that halving the time step would be sufficient. Therefore, for the VOF and mixture models, time steps of 1×10^{-3} s and 5×10^{-4} were used and for the Eulerian model, time steps of 1×10^{-4} s and 5×10^{-5} s were used. Further details on the time step independence study for the VOF and mixture models models can be found in Appendix A.

Figures 5.6 and 5.7 show the velocity and AVF solutions for the Eulerian model at the two time steps investigated. It can be seen that the two time steps produce almost identical velocity and AVF profiles other than at steps 34 and 40, where there is only a small difference between the predicted AVFs. This data, along with the VOF and mixture model data detailed in Appendix A, indicate that the solutions are not significantly affected by reducing the time step from the larger of the two time steps investigated. Therefore, for the remainder of this study, a time step of 1×10^{-3} has been used for the VOF and mixture models and 1×10^{-4} has been used for the Eulerian model.

5. TWO-DIMENSIONAL NUMERICAL MODEL STUDY OF A LARGE EXPERIMENTAL STEPPED SPILLWAY

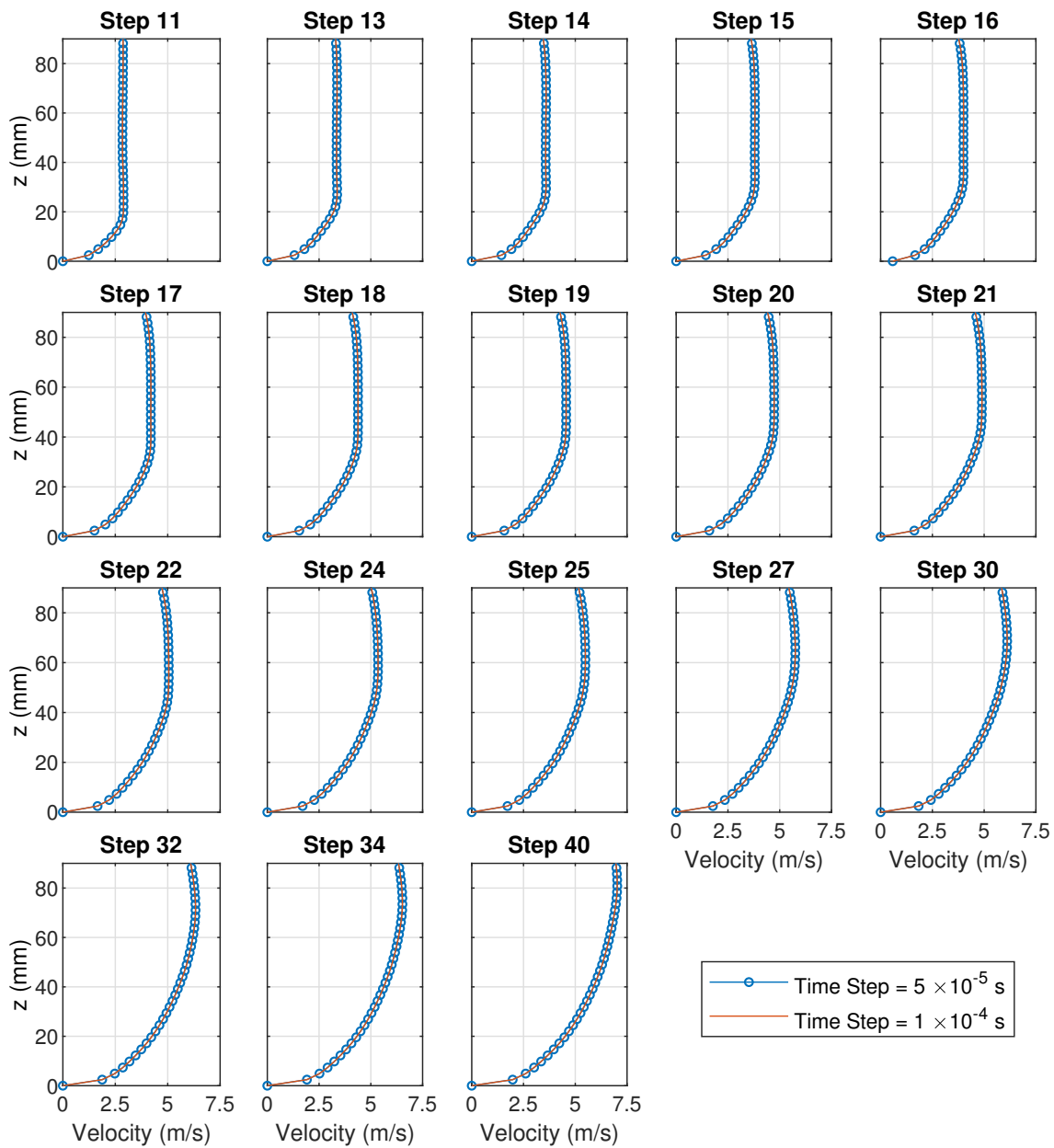


Figure 5.6: Velocity profiles at different time steps for the Eulerian model with the SST $k - \omega$ turbulence model. $Q = 180$ l/s

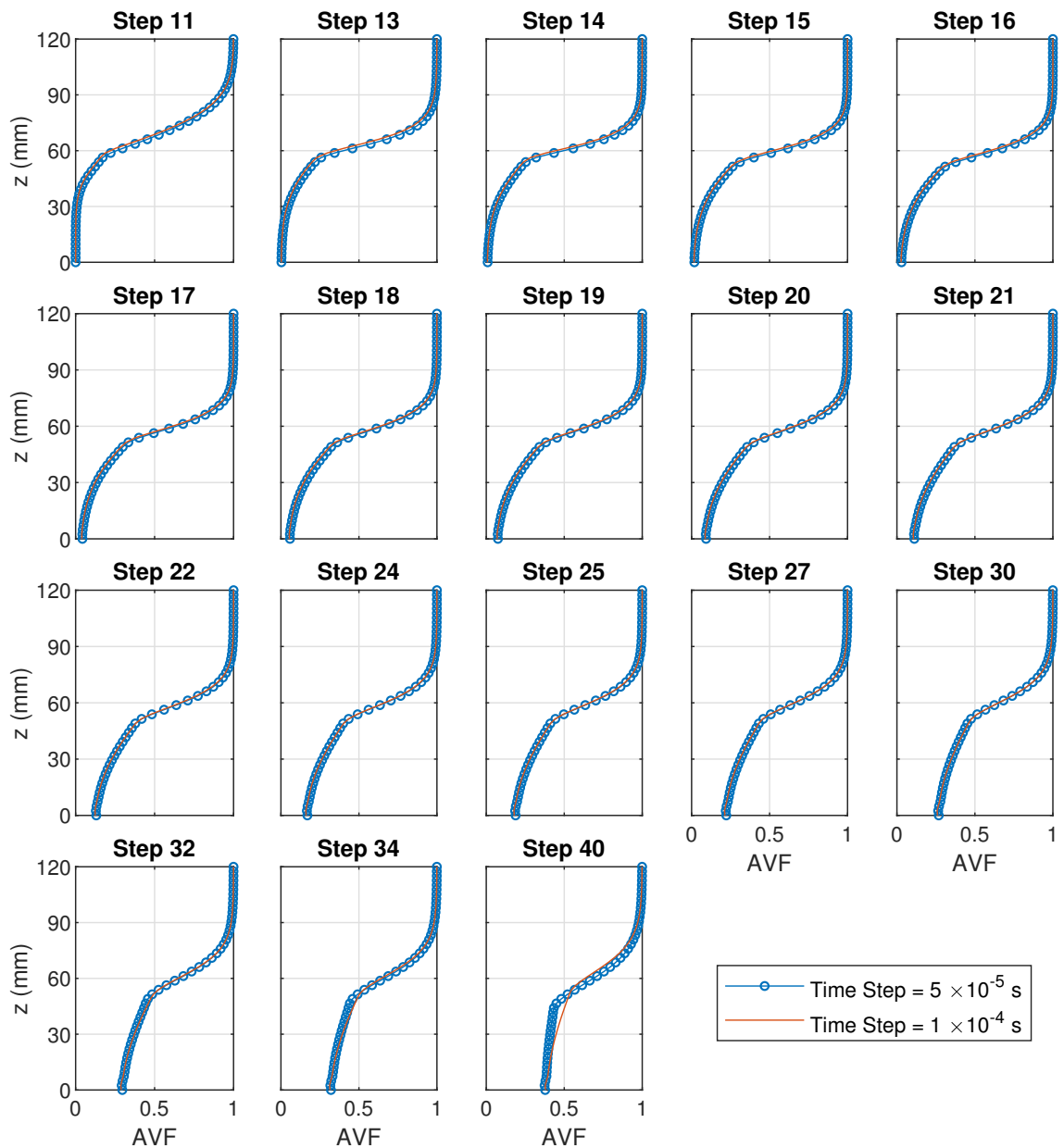


Figure 5.7: AVF profiles at different time steps for the Eulerian model with the SST $k - \omega$ turbulence model. $Q = 180$ l/s

5.2.3 Transient Behaviour

All numerical simulations performed for this project have been conducted transiently, however, for the majority of simulations a steady state is reached whereby the transient fluctuations in variables are negligible. Simulations of the narrow stepped spillway at the university of Leeds, using the VOF model with the SST $k - \omega$ turbulence model, found transient fluctuations in the free-surface position (chapter 6). In order to ascertain whether transient effects are observed,

5. TWO-DIMENSIONAL NUMERICAL MODEL STUDY OF A LARGE EXPERIMENTAL STEPPED SPILLWAY

when using the VOF and SST $k - \omega$ models, to simulate flows over the experimental spillway at the LNEC, flow properties at different time steps have been compared.

Figures 5.8 and 5.9 show velocity and AVF profiles respectively, from 8.0 - 10.2 s, for the VOF model with the SST $k - \omega$ model. It can be seen that the velocity and AVF profiles are almost identical at each time step so no transient effects are observed. Therefore no time averaging of the results is required and all of the CFD results presented in this chapter represent a single time step.

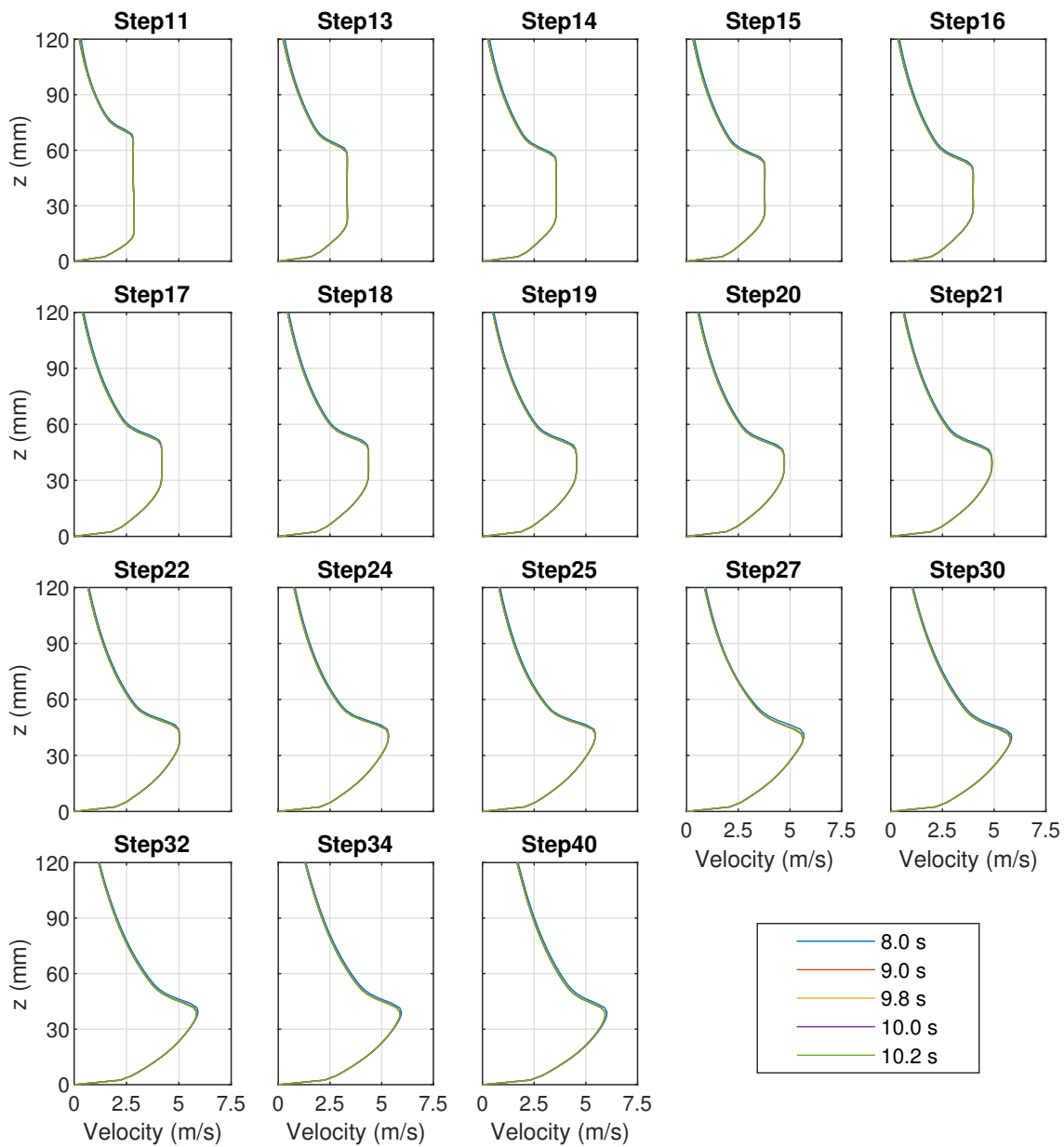


Figure 5.8: Velocity profiles at $Q = 180$ l/s for the VOF and SST $k - \omega$ models at various time steps

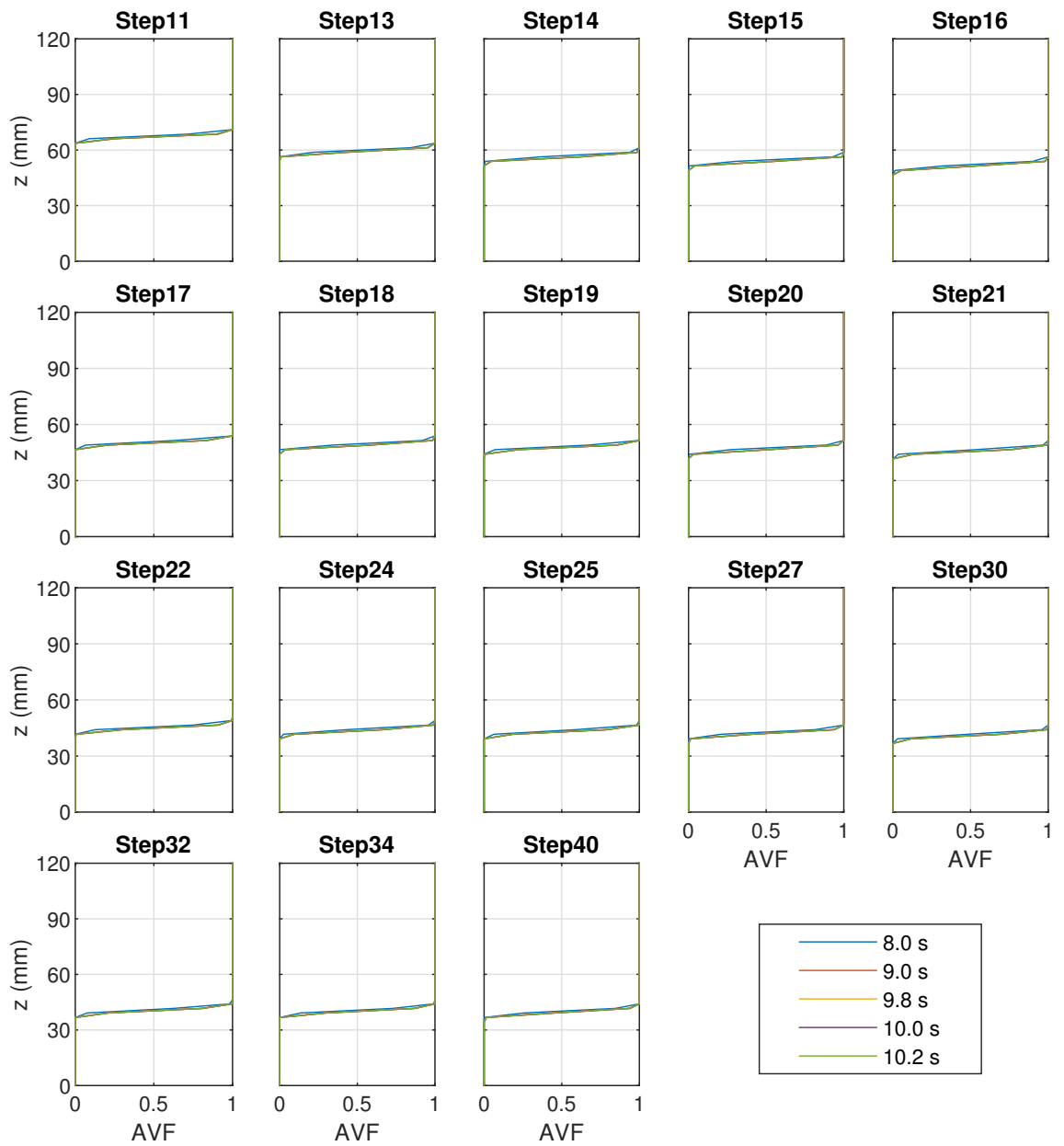


Figure 5.9: Air volume fraction profiles at $Q = 180$ l/s for the VOF and SST $k - \omega$ models at various time steps

5.3 Results and Discussion of a 2D Numerical Modelling Study of Skimming Flow over the LNEC Stepped Spillway

5.3.1 Experimental Inception Point Locations

Two methods were used to determine the location of the inception point in the experiments. The first method defines the location of the inception point as the position where the turbulent boundary layer (TBL) intersects the free-surface, as shown in figure 2.1. For the definition of the inception point, the free-surface is defined as the equivalent clear water depth, d , which is given by

$$d = \int_{z=0}^{y_{90}} (1 - AVF) dz \quad (5.7)$$

where z is measured perpendicular to the pseudo-bottom and y_{90} is the value of z at which the AVF is 0.9. Note that y_{90} is used to define in the flow depth in the z coordinate. This is because this study defines z as the perpendicular distance from the pseudo-bottom, however, convention from other studies, including Matos (2000) and Boes and Hager (2003a), is to define this location as y_{90} . The AVF is the time averaged value obtained from the conductivity probe measurements. d is slightly lower than y_{90} due to waviness at the free-surface and entrapped air close to the free-surface. The depth of the TBL is defined as the depth at which the velocity is equal to 99% of the maximum velocity (Bombardelli et al., 2011). Note that the instantaneous inception point varies around a mean position. The AVF and velocity data used to calculate d and the depth of the TBL are time averaged over 90 s. This results in a time averaged inception point location.

The second method used to determine the location of the inception point is by visual observation. The visually observed inception point is defined as *"the vertical edge immediately upstream of the step cavity where a continuous presence of white water or air bubbles was noticed from above and also through both sidewalls along the entire flume width"* (Meireles et al., 2012). Figure 5.10 shows the view of the visually observed inception point from the side of the experimental spillway.

The inception point location determined by the intersection of the boundary layer and d will be referred to as IP1 and the inception point determined by visual observation will be referred to as IP2. Note that both IP1 and IP2 are always located at a step corner and, throughout this study, IP1 and IP2 will refer only to the experimental inception point locations. Table 5.2

5.3 Results and Discussion of a 2D Numerical Modelling Study of Skimming Flow over the LNEC Stepped Spillway

details the step numbers and distances along the chute at which IP1 and IP2 occur for the flow rates considered in this study.

Table 5.2: Locations of experimental inception points

| Q (l/s) | IP1 | | IP2 | |
|---------|-------------|----------|-------------|----------|
| | Step Number | s (mm) | Step Number | s (mm) |
| 100 | 14 | 740 | 15 | 840 |
| 140 | 16 | 940 | 17 | 1040 |
| 180 | 18 | 1140 | 20 | 1340 |
| 200 | 19 | 1240 | 21 | 1440 |



Figure 5.10: View of the visually observed inception point (IP2) from the side of the experimental spillway. The darker regions indicate the presence of air bubbles

5. TWO-DIMENSIONAL NUMERICAL MODEL STUDY OF A LARGE EXPERIMENTAL STEPPED SPILLWAY

5.3.2 Velocity Profiles

Figures 5.13 - 5.19 show velocity profiles calculated using the VOF, mixture and Eulerian models in combination with the Realisable $k - \epsilon$, RNG $k - \epsilon$ and SST $k - \omega$ turbulence models. The corresponding experimental data is also shown. At each flow rate, data is shown for a different number of steps, to correspond to the experimental data that was available. Table 5.3 gives details of the multiphase model and the flow rate in each of the figures (5.13 - 5.19).

The locations of IP1 and IP2 are detailed by the colour of the title of the the plot for each step. IP1 is denoted by a green title, IP2 is denoted by an orange title and the other steps have black titles. For example, in figure 5.13, IP1 is located at step 18 and IP2 is located at step 20. Note that, at 200 l/s no experimental data is shown at step 21, as it was not available. The numerical data for this step has been included to indicate the location of IP2. Numerical modelling was initially conducted for $Q = 180$ l/s. It was found that the mixture model did not predict the velocities, AVFs or flow depths (figures 5.15, 5.25 and 5.34) accurately so further flow rates were not simulated using the mixture model.

Table 5.3: Details of figures showing velocity profiles

| Figure | Multiphase Model | Flow Rate (l/s) |
|--------|------------------|-----------------|
| 5.11 | VOF | 100 |
| 5.12 | VOF | 140 |
| 5.13 | VOF | 180 |
| 5.14 | VOF | 200 |
| 5.15 | Mixture | 180 |
| 5.16 | Eulerian | 100 |
| 5.17 | Eulerian | 140 |
| 5.18 | Eulerian | 180 |
| 5.19 | Eulerian | 200 |

5.3.2.1 VOF Model

The VOF model shows the same general velocity profile pattern at all flow rates (figures 5.11 - 5.14). In the upstream region of the spillway all turbulence models predict the experimental velocities accurately and there is little difference between the velocities predicted by the three turbulence models. At all steps, the velocities suddenly reduce at a certain value of z . This is due to the sharp interface between the two phases in the VOF model. The air has a lower velocity than the water, so above the free-surface there is a sudden reduction in the velocity.

5.3 Results and Discussion of a 2D Numerical Modelling Study of Skimming Flow over the LNEC Stepped Spillway

The mixture and Eulerian models have a smooth transition between the phases so no sudden decrease in velocity is observed.

Moving further downstream, approaching IP1, the velocities predicted by the two $k - \epsilon$ models remain close to one another, but begin to diverge from the velocities predicted by the SST $k - \omega$ model. All turbulence models, however, predict the velocities reasonably accurately in this region.

Moving downstream of IP2, into the fully aerated region, the two $k - \epsilon$ models underestimate the experimental velocities and the discrepancy between the experimental and numerical data increases at each downstream step. The SST $k - \omega$ model, however, predicts the velocities accurately at all steps for the lower values of z . At a certain depth the numerical velocity decreases and the experimental velocities are not predicted accurately. This is due to the difference in the velocity of the air and the water, as discussed above. The standard VOF model cannot model air entrainment so flow bulking is not predicted. In the fully aerated region, where significant flow bulking occurs, the VOF model underestimates the depth of flow so the velocities are only predicted accurately up to the depth of flow predicted by the VOF model. Note that at 100 l/s the SST $k - \omega$ model predict the velocities slightly less accurately in the far downstream region of the spillway than at the other flow rates. They are still reasonably accurate, however.

5. TWO-DIMENSIONAL NUMERICAL MODEL STUDY OF A LARGE EXPERIMENTAL STEPPED SPILLWAY

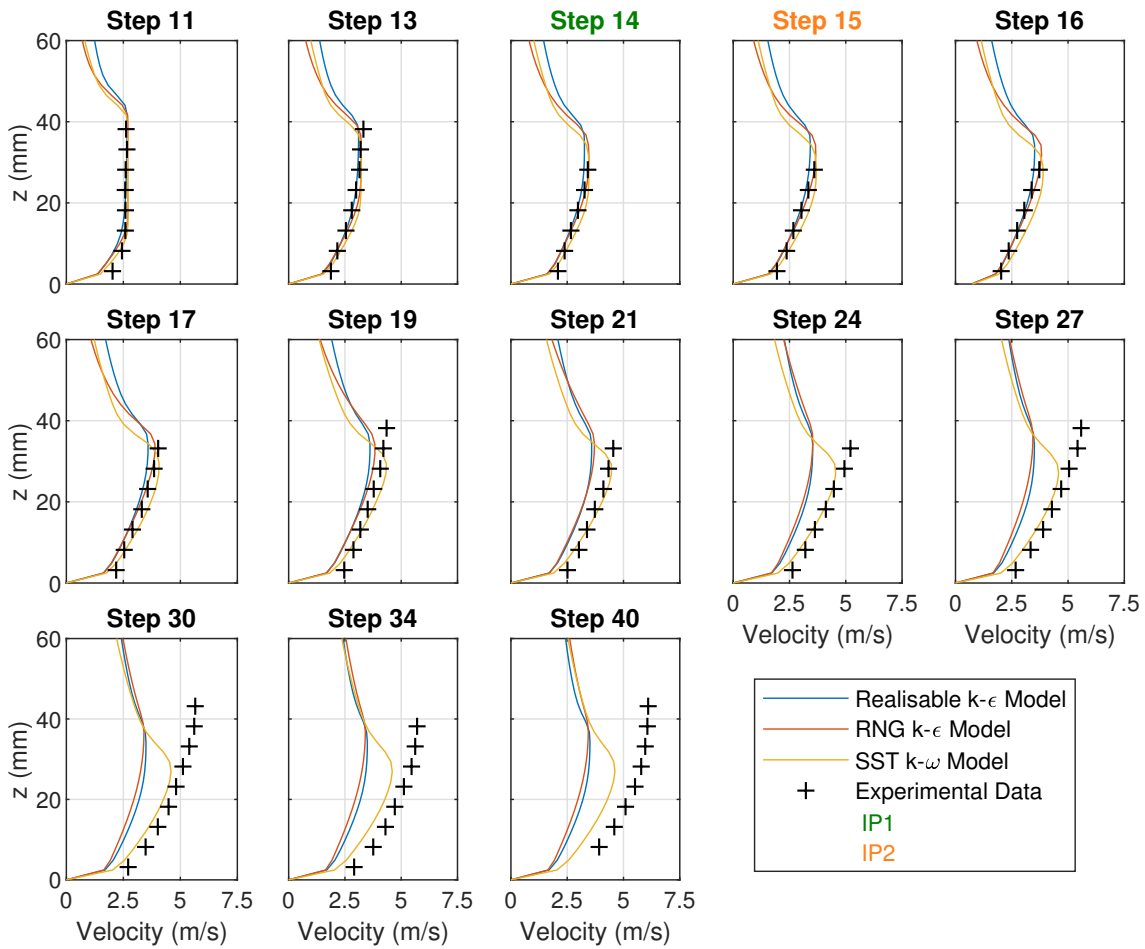


Figure 5.11: Comparison of experimental and numerical velocity profiles for $Q = 100$ l/s. Numerical data is shown for the VOF model with various turbulence models. The experimental inception point locations, IP1 and IP2, are indicated by the colour of the title of the subplots

5.3 Results and Discussion of a 2D Numerical Modelling Study of Skimming Flow over the LNEC Stepped Spillway

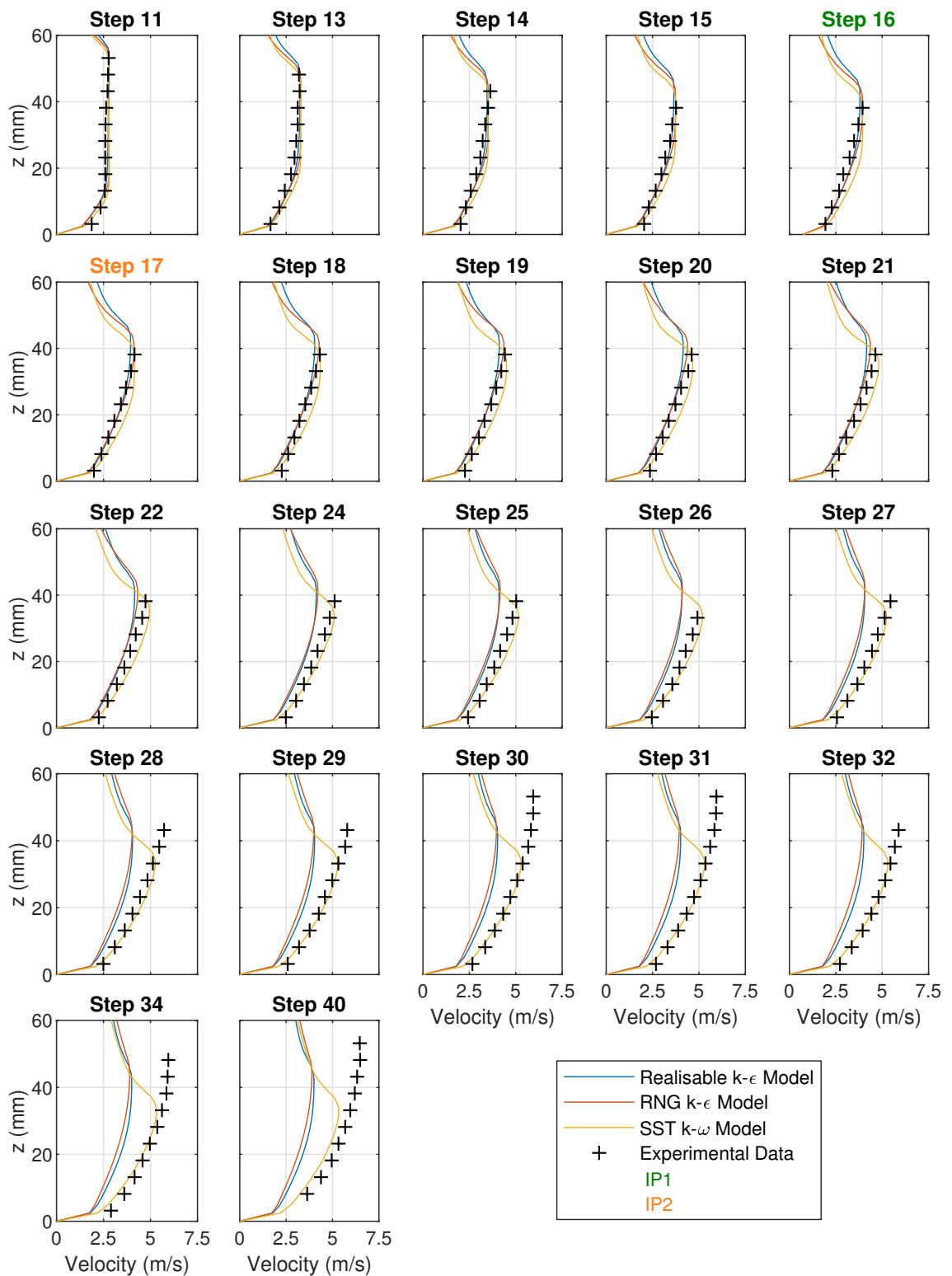


Figure 5.12: Comparison of experimental and numerical velocity profiles for $Q = 140$ l/s. Numerical data is shown for the VOF model with various turbulence models. The experimental inception point locations, IP1 and IP2, are indicated by the colour of the title of the subplots

5. TWO-DIMENSIONAL NUMERICAL MODEL STUDY OF A LARGE EXPERIMENTAL STEPPED SPILLWAY

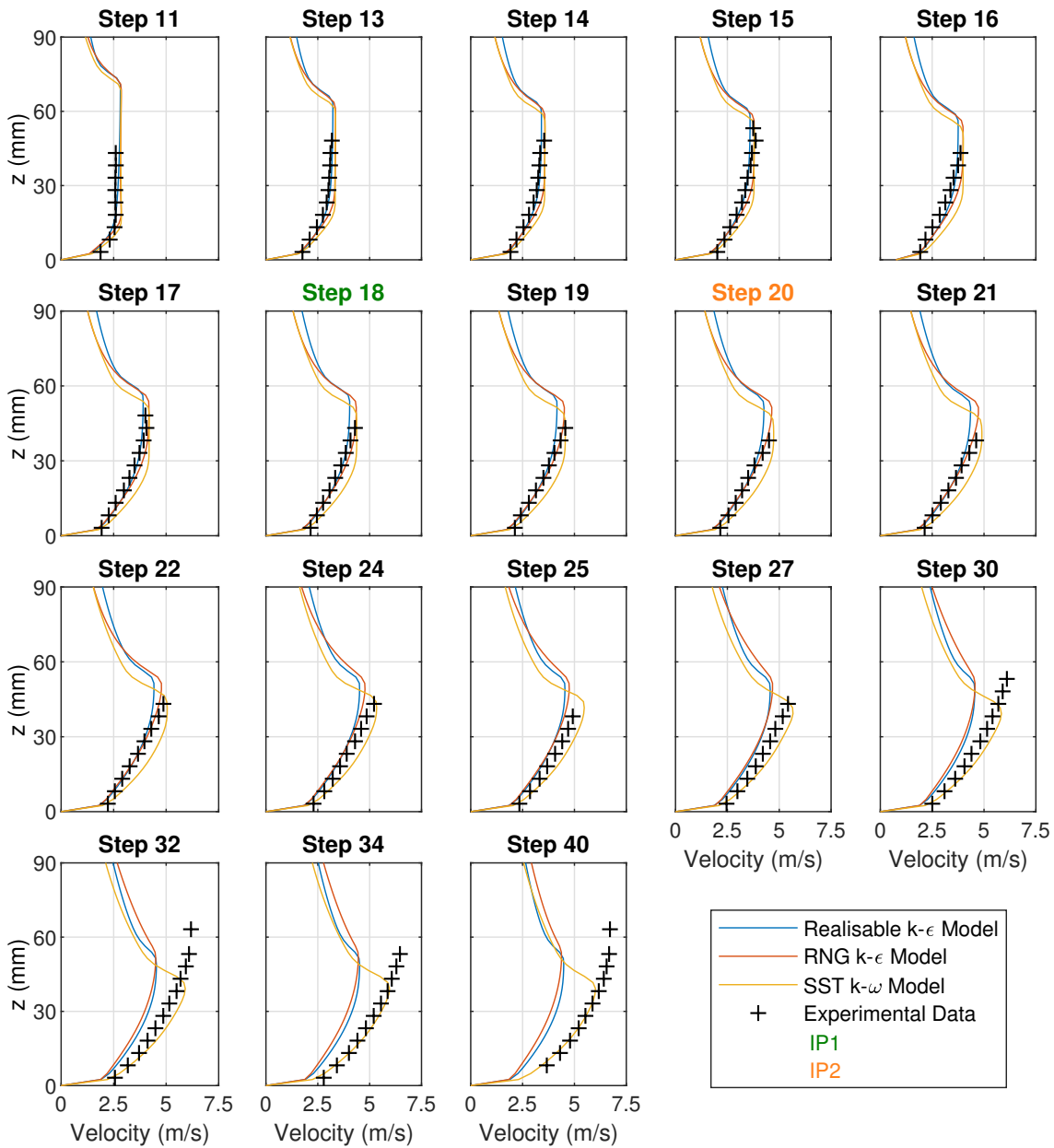


Figure 5.13: Comparison of experimental and numerical velocity profiles for $Q = 180$ l/s. Numerical data is shown for the VOF model with various turbulence models. The experimental inception point locations, IP1 and IP2, are indicated by the colour of the title of the subplots

5.3 Results and Discussion of a 2D Numerical Modelling Study of Skimming Flow over the LNEC Stepped Spillway

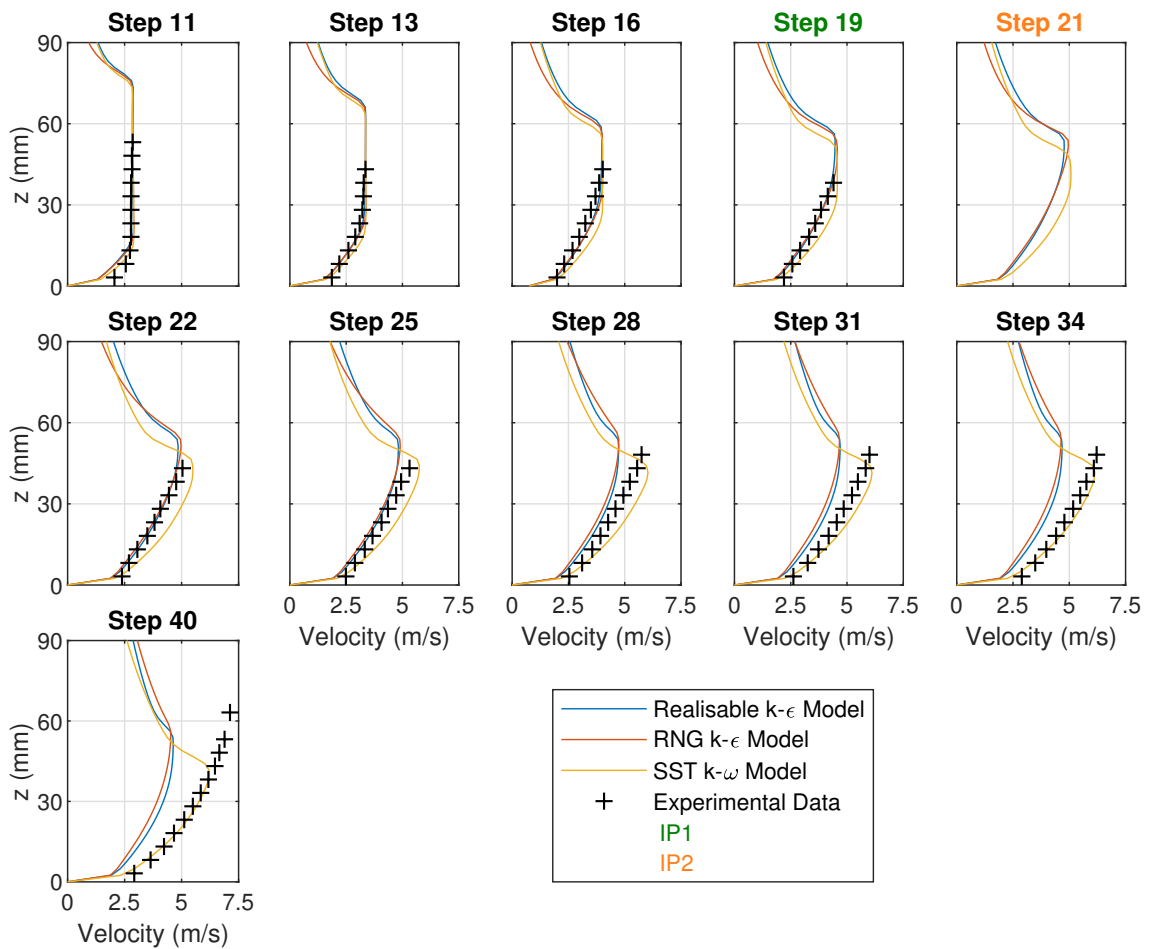


Figure 5.14: Comparison of experimental and numerical velocity profiles for $Q = 200$ l/s. Numerical data is shown for the VOF model with various turbulence models. The experimental inception point locations, IP1 and IP2, are indicated by the colour of the title of the subplots

5.3.2.2 Mixture Model

The mixture model (figures 5.15) data shows some similarities to the VOF model data. In the upstream region, the three turbulence models produce very similar data and predict the velocities well. Moving downstream, the $k - \epsilon$ models remain similar to one another and begin to diverge from the SST $k - \omega$ model. However, in the far downstream region, all of the turbulence models underestimate the velocities significantly. This shows the mixture model is not able to predict the velocities in the fully aerated region accurately, in combination with any of the turbulence models investigated.

5. TWO-DIMENSIONAL NUMERICAL MODEL STUDY OF A LARGE EXPERIMENTAL STEPPED SPILLWAY

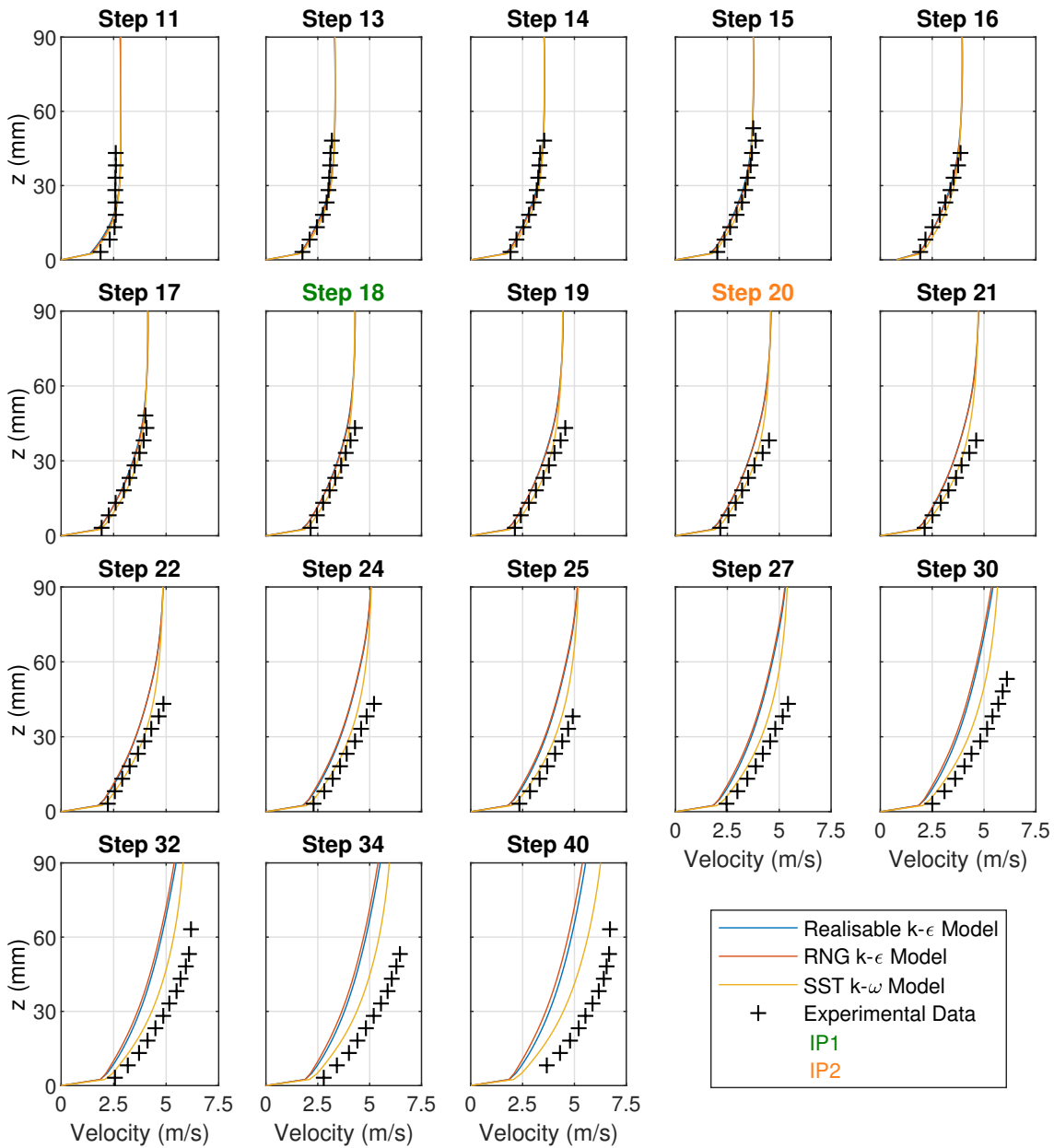


Figure 5.15: Comparison of experimental and numerical velocity profiles for $Q = 180$ l/s. Numerical data is shown for the mixture model with various turbulence models. The experimental inception point locations, IP1 and IP2, are indicated by the colour of the title of the subplots

5.3.2.3 Eulerian Model

The Eulerian model (figures 5.16 - 5.19) also shows similar behaviour to the VOF model and the same general pattern of velocity profiles at each step. Again, in the upstream region of the spillway, all of the turbulence models predict the velocities accurately and the $k-\epsilon$ models diverge from the SST $k-\omega$ model further downstream. The two $k-\epsilon$ models underestimate the

5.3 Results and Discussion of a 2D Numerical Modelling Study of Skimming Flow over the LNEC Stepped Spillway

velocities significantly in the downstream area of the spillway and the SST $k-\omega$ model predicts the velocities accurately. The Eulerian model does predict air entrainment and flow bulking, however. With the SST $k-\omega$ model the velocities are predicted accurately for the entire flow depth at all steps. Note that, like the VOF model, the Eulerian model underestimates the velocities slightly in the far downstream region of the spillway at $Q = 100$ l/s. The velocities are still predicted reasonably accurately, however.

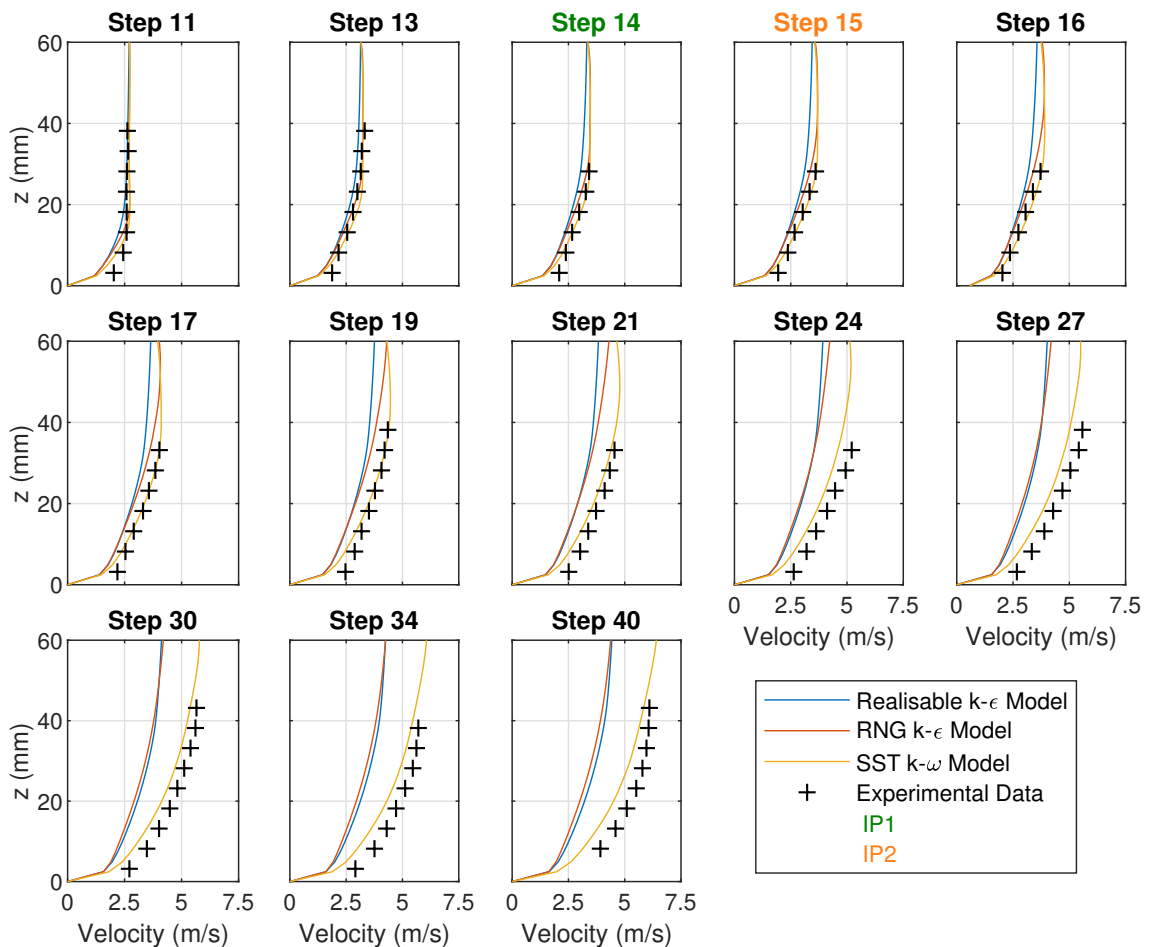


Figure 5.16: Comparison of experimental and numerical velocity profiles for $Q = 100$ l/s. Numerical data is shown for the Eulerian model with various turbulence models. The experimental inception point locations, IP1 and IP2, are indicated by the colour of the title of the subplots

5. TWO-DIMENSIONAL NUMERICAL MODEL STUDY OF A LARGE EXPERIMENTAL STEPPED SPILLWAY

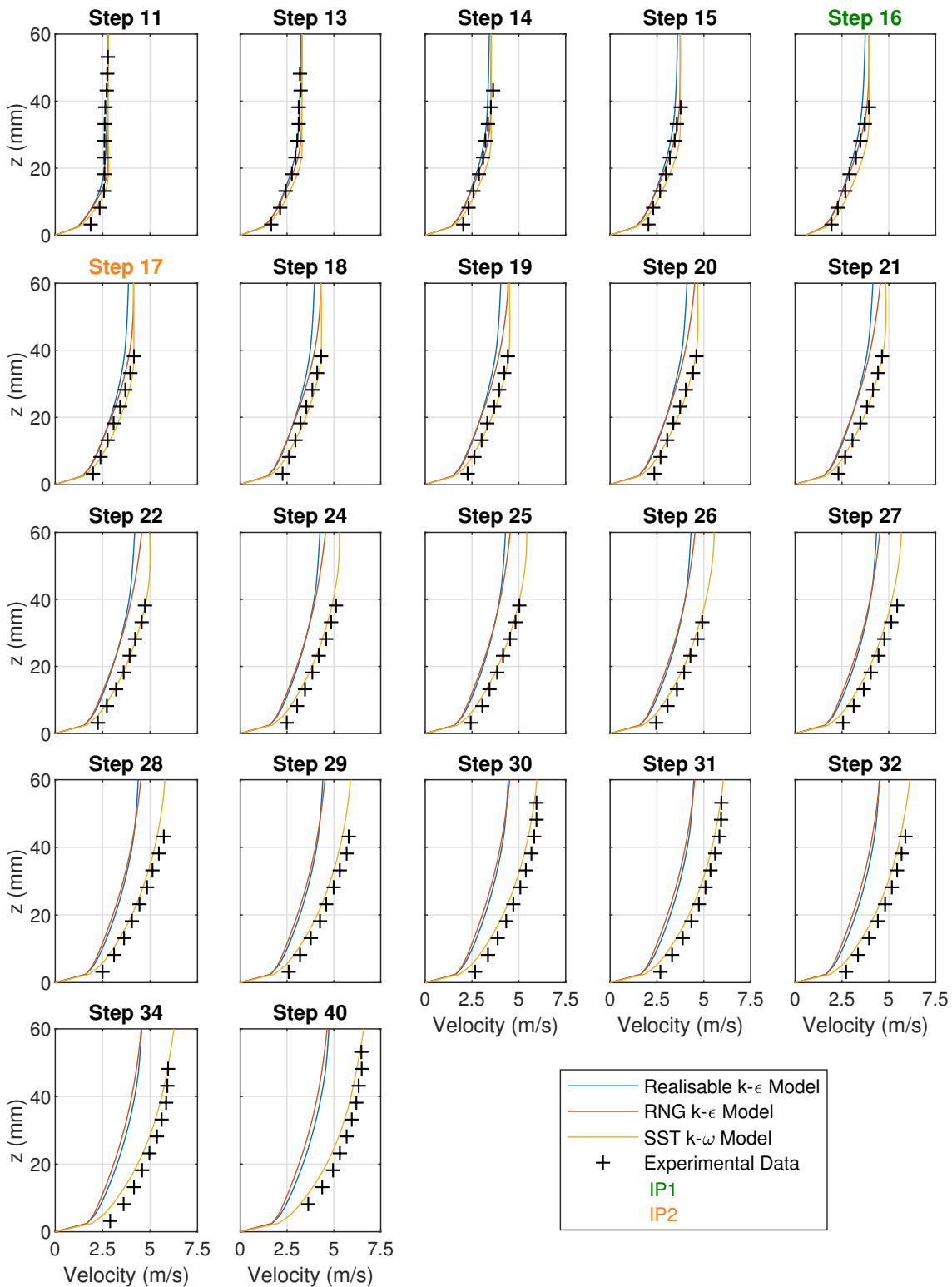


Figure 5.17: Comparison of experimental and numerical velocity profiles for $Q = 100$ l/s. Numerical data is shown for the Eulerian model with various turbulence models. The experimental inception point locations, IP1 and IP2, are indicated by the colour of the title of the subplots

5.3 Results and Discussion of a 2D Numerical Modelling Study of Skimming Flow over the LNEC Stepped Spillway

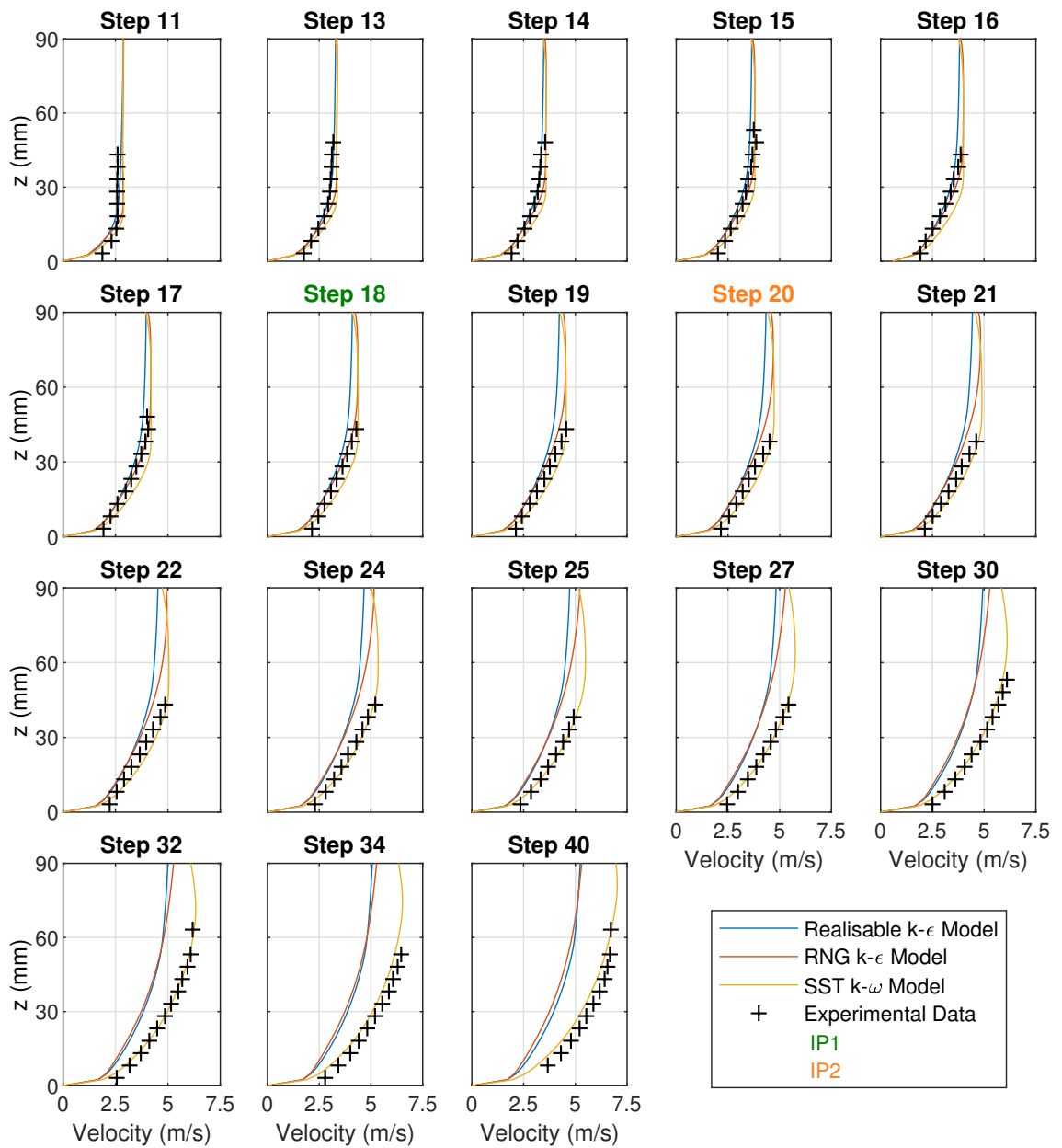


Figure 5.18: Comparison of experimental and numerical velocity profiles for $Q = 100$ l/s. Numerical data is shown for the Eulerian model with various turbulence models. The experimental inception point locations, IP1 and IP2, are indicated by the colour of the title of the subplots

5. TWO-DIMENSIONAL NUMERICAL MODEL STUDY OF A LARGE EXPERIMENTAL STEPPED SPILLWAY

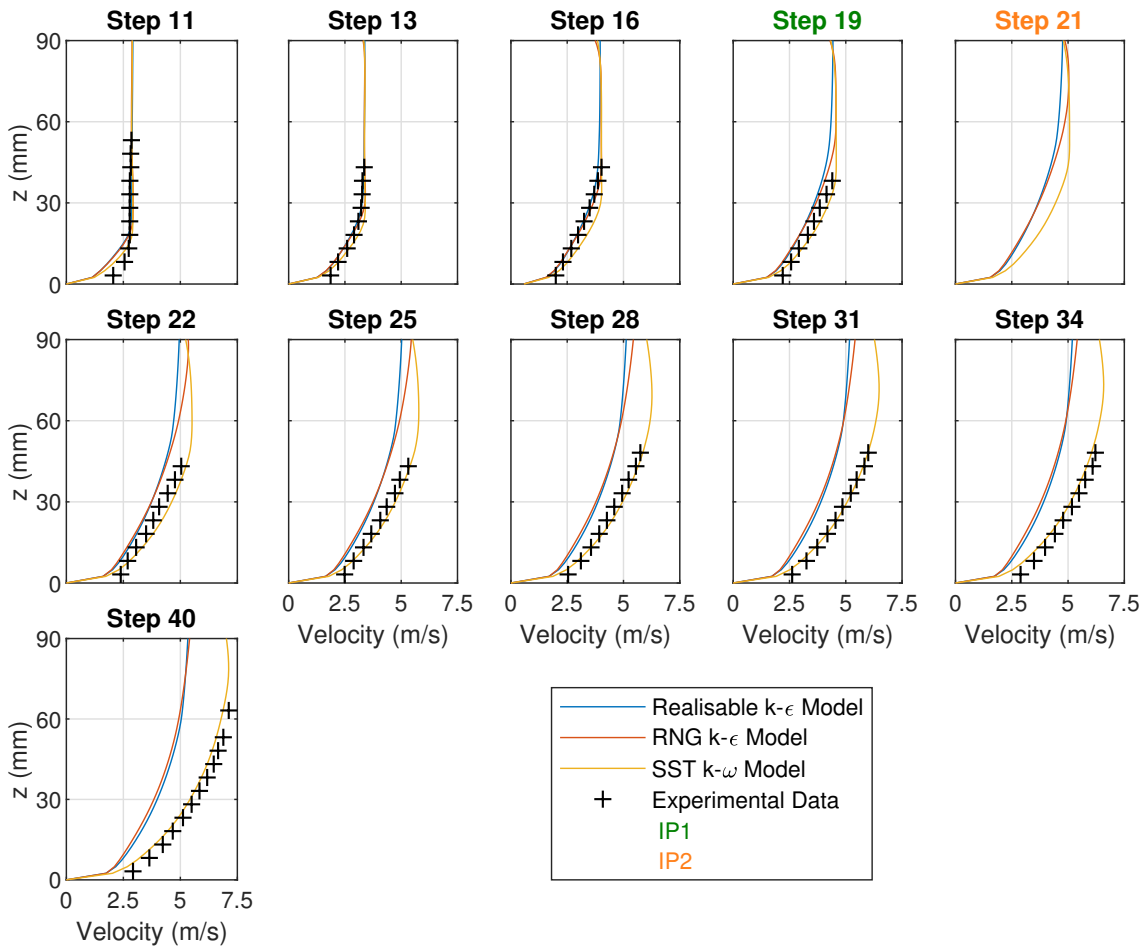


Figure 5.19: Comparison of experimental and numerical velocity profiles for $Q = 100$ l/s. Numerical data is shown for the Eulerian model with various turbulence models. The experimental inception point locations, IP1 and IP2, are indicated by the colour of the title of the subplots

5.3.2.4 Percentage Error

To help further understand the performance of the numerical models, the percentage errors between the experimental data and the numerical data, for the SST $k - \omega$ model with the VOF and Eulerian models, at different locations in the flow are presented and discussed. Note that only the SST $k - \omega$ model has been considered for the percentage errors, as this model has consistently produced more accurate results than the other turbulence models investigated. The percentage error (PE) is calculated by

$$PE = \frac{|Numerical\ data - Experimental\ data|}{Experimental\ data} \times 100 \quad (5.8)$$

Figures 5.20 shows the PEs between the experimental data and the VOF model with SST $k - \omega$ model for all flow rates. At all discharges the PEs are high at large values of z in the

5.3 Results and Discussion of a 2D Numerical Modelling Study of Skimming Flow over the LNEC Stepped Spillway

downstream region of the spillway. This is due to the fact that the VOF model underestimates the flow depth in this region, as discussed in section 5.3.2.1. In the other areas of the spillway, the velocities are predicted reasonably well, with the majority of the PEs below 20% and many below 10%. At $Q = 100$ l/s the PEs are slightly higher in the far downstream region than at the other flow rates, as discussed in section 5.3.2.1. In general, however, the velocities are predicted reasonably well. It is also noticeable that some of the velocities close to the pseudo-bottom, at $z = 3.2$ mm, are also predicted less accurately at $Q = 100$ l/s than the other flow rates.

5. TWO-DIMENSIONAL NUMERICAL MODEL STUDY OF A LARGE EXPERIMENTAL STEPPED SPILLWAY

| Q = 100 l/s | | | | | | | | | | | | | Q = 140 l/s | | | | | | | | | | | | |
|-------------|--------|------|----------------|------|------|------|----------------|------|------|------|----------|------|-------------|--------|-------------------|------|------|------|------|------|------|------|------|------|------|
| Step Number | z (mm) | | | | | | | | | | | | Step Number | z (mm) | | | | | | | | | | | |
| | 3.2 | 8.2 | 13.2 | 18.2 | 23.2 | 28.2 | 33.2 | 38.2 | 43.2 | 48.2 | 53.2 | 63.2 | | 3.2 | 8.2 | 13.2 | 18.2 | 23.2 | 28.2 | 33.2 | 38.2 | 43.2 | 48.2 | 53.2 | 63.2 |
| 11 | 20.8 | 4.5 | 3.5 | 4.3 | 4.3 | 3.3 | 1.1 | 2.6 | | | | | 11 | 14.4 | 0.1 | 6.7 | 7.5 | 7.3 | 7.1 | 6.3 | 4.5 | 1.6 | 0.7 | 0.6 | |
| 13 | 11.4 | 6.7 | 10.2 | 11.5 | 7.1 | 2.2 | 0.5 | 12.6 | | | | | 13 | 1.9 | 9.7 | 17.2 | 15.3 | 11.0 | 7.4 | 4.8 | 4.9 | 1.8 | 0.5 | | |
| 14 | 12.8 | 2.6 | 9.3 | 10.0 | 5.2 | 1.4 | | | | | | | 14 | 9.8 | 6.6 | 14.0 | 15.4 | 12.8 | 9.0 | 4.5 | 0.2 | 3.6 | | | |
| 15 | 8.3 | 3.5 | 10.9 | 11.2 | 8.6 | 2.4 | | | | | | | 15 | 11.4 | 8.4 | 12.4 | 14.5 | 14.9 | 8.4 | 4.9 | 0.8 | | | | |
| 16 | 0.5 | 12.0 | 14.2 | 15.7 | 12.6 | 4.4 | | | | | | | 16 | 5.7 | 17.2 | 17.7 | 22.4 | 18.0 | 12.9 | 6.1 | 0.2 | | | | |
| 17 | 13.9 | 1.9 | 7.5 | 7.8 | 9.4 | 5.5 | 6.2 | | | | | | 17 | 4.2 | 9.7 | 14.0 | 16.5 | 14.2 | 11.0 | 4.7 | 0.8 | | | | |
| 18 | | | | | | | | | | | | | 18 | 13.2 | 2.8 | 9.3 | 14.0 | 13.7 | 10.5 | 5.5 | 1.0 | | | | |
| 19 | 20.4 | 6.1 | 2.4 | 6.3 | 9.0 | 6.4 | 7.3 | 33.2 | | | | | 19 | 12.2 | 3.7 | 8.8 | 12.9 | 11.6 | 11.0 | 6.6 | 0.1 | | | | |
| 20 | | | | | | | | | | | | | 20 | 13.9 | 3.4 | 9.9 | 13.3 | 12.5 | 11.5 | 5.1 | 1.3 | | | | |
| 21 | 18.8 | 7.0 | 0.3 | 4.3 | 4.3 | 2.9 | 13.8 | | | | | | 21 | 11.0 | 5.8 | 11.2 | 11.6 | 11.6 | 10.6 | 8.2 | 1.1 | | | | |
| 22 | | | | | | | | | | | | | 22 | 6.8 | 5.7 | 7.9 | 9.7 | 11.2 | 11.3 | 7.8 | 1.2 | | | | |
| 24 | 19.1 | 8.6 | 2.8 | 2.1 | 1.5 | 8.3 | 24.2 | | | | | | 24 | 13.4 | 2.5 | 3.2 | 6.1 | 7.6 | 6.2 | 4.8 | 7.9 | | | | |
| 25 | | | | | | | | | | | | | 25 | 10.3 | 1.6 | 5.4 | 7.9 | 10.1 | 9.0 | 6.6 | 5.8 | | | | |
| 26 | | | | | | | | | | | | | 26 | 10.2 | 0.7 | 3.0 | 6.4 | 8.3 | 7.2 | 5.5 | | | | | |
| 27 | 18.9 | 10.7 | 7.8 | 4.6 | 5.3 | 9.8 | 26.4 | 41.5 | | | | | 27 | 12.8 | 1.5 | 1.4 | 5.3 | 5.4 | 5.8 | 1.7 | 12.1 | | | | |
| 28 | | | | | | | | | | | | | 28 | 9.3 | 0.4 | 3.4 | 6.3 | 6.5 | 4.9 | 2.3 | 12.4 | 32.9 | | | |
| 29 | | | | | | | | | | | | | 29 | 11.7 | 1.4 | 0.8 | 1.9 | 4.1 | 2.5 | 0.9 | 16.2 | 33.9 | | | |
| 30 | 19.4 | 13.6 | 10.0 | 8.3 | 7.3 | 10.9 | 25.2 | 40.1 | 47.0 | | | | 30 | 13.8 | 5.7 | 1.5 | 0.8 | 1.8 | 0.9 | 1.8 | 15.3 | 33.0 | 42.6 | 48.1 | |
| 31 | | | | | | | | | | | | | 31 | 13.8 | 3.7 | 1.1 | 1.0 | 1.6 | 1.1 | 1.2 | 14.1 | 32.7 | 41.8 | 47.3 | |
| 32 | | | | | | | | | | | | | 32 | 14.7 | 4.8 | 2.4 | 0.4 | 0.5 | 0.2 | 2.7 | 15.2 | 32.8 | | | |
| 34 | 24.6 | 19.8 | 15.7 | 12.6 | 12.6 | 16.3 | 27.4 | 39.4 | | | | | 34 | 19.5 | 11.0 | 6.9 | 3.6 | 2.5 | 3.7 | 5.5 | 17.5 | 32.7 | 40.8 | | |
| 40 | | 22.9 | 20.8 | 18.8 | 18.6 | 20.6 | 30.3 | 41.0 | 46.8 | | | | 40 | | 11.4 | 11.4 | 10.7 | 8.8 | 8.9 | 10.9 | 22.1 | 36.8 | 45.2 | 49.7 | |
| Q = 180 l/s | | | | | | | | | | | | | Q = 200 l/s | | | | | | | | | | | | |
| 11 | 15.4 | 1.2 | 9.7 | 10.3 | 10.6 | 10.7 | 10.3 | 9.0 | 8.9 | | | | 11 | 23.7 | 9.2 | 2.0 | 4.3 | 4.1 | 4.0 | 3.8 | 3.5 | 1.6 | 1.2 | 0.3 | |
| 13 | 3.1 | 12.2 | 16.9 | 17.6 | 13.9 | 10.6 | 9.1 | 7.8 | 7.4 | 5.3 | | | 13 | 8.4 | 7.8 | 10.8 | 11.7 | 8.6 | 4.6 | 3.1 | 2.5 | 0.0 | | | |
| 14 | 4.1 | 12.5 | 16.5 | 19.2 | 16.7 | 11.9 | 9.3 | 7.7 | 6.7 | 1.0 | | | 14 | | | | | | | | | | | | |
| 15 | 9.0 | 6.6 | 15.0 | 16.9 | 15.5 | 12.5 | 8.8 | 4.6 | 2.9 | 1.7 | 1.2 | | 15 | | | | | | | | | | | | |
| 16 | 7.3 | 23.5 | 26.7 | 25.2 | 23.4 | 17.6 | 13.0 | 6.4 | 3.4 | | | | 16 | 3.8 | 16.6 | 19.0 | 20.7 | 19.7 | 14.6 | 8.4 | 3.6 | 0.4 | | | |
| 17 | 0.0 | 16.6 | 22.4 | 21.1 | 21.3 | 18.4 | 12.2 | 6.6 | 3.2 | 4.5 | | | 17 | | | | | | | | | | | | |
| 18 | 8.1 | 10.0 | 17.8 | 20.5 | 21.1 | 17.9 | 13.4 | 7.3 | 1.9 | | | | 18 | | | | | | | | | | | | |
| 19 | 5.7 | 14.0 | 18.1 | 20.0 | 17.9 | 16.6 | 12.2 | 5.1 | 0.1 | | | | 19 | 8.6 | 7.3 | 13.7 | 14.0 | 15.5 | 14.9 | 9.7 | 3.8 | | | | |
| 20 | 5.2 | 10.0 | 16.2 | 19.8 | 20.4 | 18.3 | 11.2 | 4.9 | | | | | 20 | | | | | | | | | | | | |
| 21 | 2.8 | 13.5 | 17.6 | 19.2 | 17.7 | 17.3 | 12.0 | 5.8 | | | | | 21 | | | | | | | | | | | | |
| 22 | 5.1 | 13.4 | 20.0 | 22.0 | 19.5 | 18.2 | 14.7 | 8.5 | 3.5 | | | | 22 | 11.4 | 7.9 | 14.1 | 14.0 | 14.9 | 15.5 | 11.2 | 6.2 | 0.6 | | | |
| 24 | 5.5 | 6.0 | 11.6 | 14.8 | 15.9 | 12.9 | 11.7 | 9.2 | 2.1 | | | | 24 | | | | | | | | | | | | |
| 25 | 6.3 | 5.8 | 9.7 | 12.9 | 12.6 | 11.7 | 11.1 | 10.1 | | | | | 25 | 11.5 | 4.9 | 9.7 | 13.5 | 12.7 | 13.3 | 10.7 | 10.1 | 3.3 | | | |
| 26 | | | | | | | | | | | | | 26 | | | | | | | | | | | | |
| 27 | 8.5 | 3.9 | 8.0 | 10.4 | 11.8 | 11.0 | 11.9 | 8.9 | 1.7 | | | | 27 | | | | | | | | | | | | |
| 28 | | | | | | | | | | | | | 28 | 10.2 | 1.1 | 6.5 | 10.4 | 12.0 | 12.0 | 10.5 | 9.6 | 5.2 | 8.5 | | |
| 29 | | | | | | | | | | | | | 29 | | | | | | | | | | | | |
| 30 | 7.2 | 3.6 | 7.1 | 9.1 | 11.1 | 9.2 | 8.7 | 7.6 | 1.8 | 22.5 | 36.7 | | 30 | | | | | | | | | | | | |
| 31 | | | | | | | | | | | | | 31 | 10.1 | 0.3 | 4.9 | 7.1 | 8.7 | 9.9 | 8.6 | 8.4 | 2.8 | 13.6 | | |
| 32 | 7.4 | 3.1 | 6.5 | 9.8 | 11.0 | 10.4 | 10.5 | 7.2 | 1.1 | 22.6 | 35.2 | 46.9 | 32 | | | | | | | | | | | | |
| 34 | 13.4 | 2.7 | 0.3 | 4.1 | 4.9 | 4.7 | 3.7 | 1.2 | 7.0 | 26.3 | 37.8 | | 34 | 16.2 | 4.2 | 1.3 | 4.5 | 6.4 | 6.0 | 6.0 | 5.3 | 0.3 | 16.7 | | |
| 40 | | 6.7 | 4.2 | 1.6 | 0.5 | 0.4 | 0.4 | 2.8 | 12.1 | 27.9 | 37.0 | 46.1 | 40 | 14.2 | 4.9 | 1.3 | 2.3 | 2.7 | 2.7 | 2.0 | 0.1 | 5.8 | 22.1 | 35.5 | 47.1 |
| PE > 30 | | | 20 < PE ≤ 30 | | | | 10 < PE ≤ 20 | | | | PE ≤ 10 | | | | No Data Available | | | | | | | | | | |

Figure 5.20: Velocity percentage error between the experimental data and the VOF model with the SST $k - \omega$ model, at all flow rates. The colour of each cell represents the range of values that the PE falls within. These ranges are defined in the key of the figure

Figure 5.21 shows the PEs between the experimental data and the Eulerian model, with the SST $k - \omega$ model, for all flow rates. It is noticeable that the highest PEs occur, for all flow rates, at $z = 3.175$ mm. This is also where reasonably high PE values are found for the VOF model (figure 5.20). This may be due to the accuracy of the experimental velocity measurements in these positions. The back-flushing Pitot tube, used to take velocity measurements,

5.3 Results and Discussion of a 2D Numerical Modelling Study of Skimming Flow over the LNEC Stepped Spillway

is orientated parallel to the pseudo-bottom, pointing upstream. Figure 5.22 shows numerical velocity vectors at a step. The location of the first measurement point, at $z = 3.175$ mm, is indicated in the figure. It can be seen that, at $z = 3.175$ mm, the velocity vectors are not parallel to the pseudo-bottom due to the deflection of the flow caused by the impact on the step corner. The flow in this position is not aligned in the same direction as the back-flushing Pitot tube. This will produce less accurate velocity measurements than at higher values of z , where the flow is more closely orientated with the Pitot tube. So although the highest PE values occur at $z = 3.175$ mm for both the VOF and Eulerian models, this should be viewed with caution as the experimental velocities in these locations may not be as accurate as in other locations. At all other values of z the Eulerian model, with the SST $k - \omega$ turbulence model, predicts the velocities extremely accurately. The vast majority of the PEs are less than 10% and there are only a handful of PE values above 20%.

5. TWO-DIMENSIONAL NUMERICAL MODEL STUDY OF A LARGE EXPERIMENTAL STEPPED SPILLWAY

| Q = 100 l/s | | | | | | | | | | | | | Q = 140 l/s | | | | | | | | | | | | |
|-------------|--------|------|------|------|------|------|------|------|------|------|------|------|-------------|--------|------|------|------|------|------|------|------|------|------|------|------|
| Step Number | z (mm) | | | | | | | | | | | | Step Number | z (mm) | | | | | | | | | | | |
| | 3.2 | 8.2 | 13.2 | 18.2 | 23.2 | 28.2 | 33.2 | 38.2 | 43.2 | 48.2 | 53.2 | 63.2 | | 3.2 | 8.2 | 13.2 | 18.2 | 23.2 | 28.2 | 33.2 | 38.2 | 43.2 | 48.2 | 53.2 | 63.2 |
| 11 | 30.8 | 11.8 | 0.5 | 5.3 | 5.2 | 3.9 | 1.8 | 3.4 | | | | | 11 | 25.5 | 8.1 | 2.4 | 8.0 | 8.5 | 7.8 | 6.8 | 5.1 | 2.3 | 1.4 | 0.5 | |
| 13 | 24.3 | 1.2 | 2.2 | 6.5 | 6.6 | 2.8 | 1.1 | 2.6 | | | | | 13 | 13.0 | 2.2 | 9.4 | 10.4 | 10.6 | 8.4 | 5.4 | 5.1 | 2.0 | 3.5 | | |
| 14 | 25.7 | 5.9 | 0.4 | 2.5 | 1.8 | 1.0 | | | | | | | 14 | 22.8 | 1.1 | 6.1 | 8.7 | 10.1 | 9.2 | 4.9 | 0.2 | 3.2 | | | |
| 15 | 20.9 | 4.8 | 1.6 | 2.6 | 2.6 | 0.7 | | | | | | | 15 | 23.8 | 0.6 | 4.2 | 6.8 | 9.8 | 7.3 | 5.2 | 0.6 | | | | |
| 16 | 13.1 | 2.1 | 3.9 | 5.5 | 4.4 | 1.3 | | | | | | | 16 | 8.1 | 8.3 | 8.6 | 13.4 | 11.3 | 10.1 | 5.9 | 0.3 | | | | |
| 17 | 25.7 | 7.0 | 2.4 | 2.2 | 0.1 | 0.2 | 0.2 | | | | | | 17 | 17.6 | 1.0 | 4.7 | 7.3 | 6.2 | 5.6 | 3.0 | 0.1 | | | | |
| 18 | | | | | | | | | | | | | 18 | 25.6 | 5.8 | 0.0 | 4.5 | 4.9 | 3.4 | 2.2 | 0.1 | | | | |
| 19 | 31.4 | 14.9 | 7.6 | 4.2 | 1.8 | 1.7 | 0.4 | 0.9 | | | | | 19 | 24.5 | 5.1 | 0.7 | 3.1 | 2.3 | 2.7 | 1.6 | 0.9 | | | | |
| 20 | | | | | | | | | | | | | 20 | 26.0 | 5.7 | 0.1 | 3.0 | 2.6 | 2.1 | 1.2 | 0.9 | | | | |
| 21 | 30.1 | 16.1 | 10.0 | 6.6 | 6.6 | 4.5 | 3.6 | | | | | | 21 | 23.4 | 3.6 | 0.9 | 1.2 | 1.4 | 0.8 | 0.5 | 0.6 | | | | |
| 22 | | | | | | | | | | | | | 22 | 19.9 | 4.0 | 2.3 | 0.8 | 0.7 | 1.0 | 0.8 | 0.3 | | | | |
| 24 | 30.3 | 17.5 | 12.4 | 11.6 | 10.2 | 12.3 | 11.9 | | | | | | 24 | 25.4 | 11.6 | 6.7 | 4.3 | 3.0 | 4.4 | 4.0 | 4.3 | | | | |
| 25 | | | | | | | | | | | | | 25 | 22.6 | 10.9 | 4.8 | 2.8 | 0.9 | 2.0 | 2.1 | 1.2 | | | | |
| 26 | | | | | | | | | | | | | 26 | 22.5 | 10.1 | 7.1 | 4.1 | 2.5 | 3.4 | 2.6 | | | | | |
| 27 | 28.4 | 17.3 | 14.6 | 11.1 | 10.5 | 10.4 | 11.6 | 10.2 | | | | | 27 | 24.7 | 10.8 | 8.5 | 5.0 | 4.9 | 4.2 | 5.5 | 6.4 | | | | |
| 28 | | | | | | | | | | | | | 28 | 21.6 | 9.0 | 6.5 | 3.9 | 3.5 | 4.5 | 4.1 | 5.5 | 6.2 | | | |
| 29 | | | | | | | | | | | | | 29 | 23.3 | 10.3 | 8.4 | 7.3 | 5.1 | 5.8 | 6.1 | 7.8 | 5.9 | | | |
| 30 | 26.5 | 17.4 | 13.6 | 11.5 | 9.1 | 8.0 | 7.7 | 7.5 | 5.0 | | | | 30 | 24.7 | 13.7 | 10.0 | 7.8 | 6.5 | 6.6 | 6.1 | 6.6 | 5.4 | 4.5 | 2.1 | |
| 31 | | | | | | | | | | | | | 31 | 24.3 | 11.4 | 9.0 | 6.9 | 5.9 | 5.5 | 4.7 | 4.5 | 4.6 | 3.1 | 0.9 | |
| 32 | | | | | | | | | | | | | 32 | 24.6 | 11.8 | 9.6 | 7.5 | 6.2 | 5.9 | 5.2 | 4.8 | 4.4 | | | |
| 34 | 28.7 | 20.4 | 16.0 | 12.3 | 10.9 | 10.4 | 8.1 | 5.6 | | | | | 34 | 28.4 | 17.1 | 13.2 | 9.8 | 8.2 | 8.3 | 7.0 | 6.4 | 3.9 | 1.6 | | |
| 40 | | 20.0 | 17.5 | 14.9 | 13.6 | 11.5 | 9.5 | 7.1 | 4.2 | | | | 40 | | 16.7 | 16.6 | 15.7 | 13.3 | 12.5 | 11.4 | 10.8 | 9.2 | 8.8 | 6.1 | |
| Q = 180 l/s | | | | | | | | | | | | | Q = 200 l/s | | | | | | | | | | | | |
| 11 | 27.0 | 8.0 | 3.4 | 10.1 | 11.9 | 12.2 | 11.5 | 9.9 | 9.6 | | | | 11 | 33.8 | 17.1 | 4.1 | 3.4 | 4.9 | 5.0 | 4.9 | 4.5 | 2.2 | 1.8 | 0.4 | |
| 13 | 17.5 | 4.5 | 9.1 | 12.4 | 13.4 | 11.9 | 10.1 | 8.2 | 7.5 | 5.3 | | | 13 | 21.9 | 0.5 | 3.4 | 6.5 | 7.8 | 5.7 | 3.9 | 3.0 | 0.4 | | | |
| 14 | 17.7 | 4.9 | 9.0 | 12.7 | 14.1 | 12.4 | 10.1 | 8.0 | 6.7 | 0.9 | | | 14 | | | | | | | | | | | | |
| 15 | 21.6 | 0.4 | 7.4 | 9.8 | 11.0 | 11.5 | 9.4 | 4.9 | 3.0 | 1.8 | 1.4 | | 15 | | | | | | | | | | | | |
| 16 | 6.2 | 15.3 | 18.0 | 17.2 | 17.4 | 15.3 | 13.1 | 6.7 | 3.4 | | | | 16 | 9.3 | 9.0 | 11.1 | 13.3 | 14.0 | 12.5 | 8.7 | 4.2 | 0.1 | | | |
| 17 | 13.8 | 8.4 | 13.6 | 12.7 | 14.0 | 13.8 | 11.0 | 6.7 | 3.3 | 4.5 | | | 17 | | | | | | | | | | | | |
| 18 | 21.0 | 1.9 | 8.9 | 11.7 | 13.1 | 11.9 | 10.7 | 7.0 | 2.0 | | | | 18 | | | | | | | | | | | | |
| 19 | 18.7 | 5.3 | 8.9 | 10.8 | 9.5 | 9.6 | 8.0 | 3.9 | 0.2 | | | | 19 | 21.3 | 0.7 | 5.1 | 5.6 | 7.6 | 8.0 | 5.9 | 3.1 | | | | |
| 20 | 18.4 | 1.3 | 6.8 | 10.3 | 11.4 | 10.3 | 5.7 | 2.5 | | | | | 20 | | | | | | | | | | | | |
| 21 | 16.2 | 4.3 | 7.8 | 9.4 | 8.4 | 8.7 | 5.1 | 2.0 | | | | | 21 | | | | | | | | | | | | |
| 22 | 18.3 | 3.9 | 9.7 | 11.6 | 9.7 | 9.0 | 6.8 | 3.3 | 1.8 | | | | 22 | 23.7 | 0.8 | 4.6 | 4.5 | 5.8 | 6.7 | 3.6 | 1.4 | 1.0 | | | |
| 24 | 18.5 | 3.2 | 1.6 | 4.6 | 5.8 | 3.3 | 2.7 | 1.8 | 1.4 | | | | 24 | | | | | | | | | | | | |
| 25 | 19.2 | 3.6 | 0.3 | 2.7 | 2.6 | 1.9 | 1.6 | 1.9 | | | | | 25 | 23.7 | 4.1 | 0.0 | 3.5 | 2.9 | 3.7 | 1.5 | 2.0 | 1.3 | | | |
| 26 | | | | | | | | | | | | | 26 | | | | | | | | | | | | |
| 27 | 21.0 | 5.5 | 2.1 | 0.1 | 1.5 | 0.9 | 1.7 | 0.5 | 1.1 | | | | 27 | | | | | | | | | | | | |
| 28 | | | | | | | | | | | | | 28 | 22.3 | 7.8 | 3.2 | 0.3 | 1.8 | 2.0 | 0.6 | 0.0 | 1.7 | 1.7 | | |
| 29 | | | | | | | | | | | | | 29 | | | | | | | | | | | | |
| 30 | 19.8 | 6.0 | 3.0 | 1.4 | 0.5 | 1.3 | 1.7 | 1.6 | 2.4 | 2.5 | 3.4 | | 30 | | | | | | | | | | | | |
| 31 | | | | | | | | | | | | | 31 | 22.0 | 9.1 | 4.7 | 2.8 | 1.3 | 0.3 | 1.5 | 1.3 | 3.1 | 2.4 | | |
| 32 | 19.9 | 6.6 | 3.7 | 0.7 | 0.4 | 0.1 | 0.3 | 1.2 | 0.3 | 1.1 | 1.0 | 1.2 | 32 | | | | | | | | | | | | |
| 34 | 24.9 | 11.7 | 9.1 | 5.7 | 4.8 | 4.7 | 5.2 | 5.7 | 4.9 | 4.9 | 4.9 | | 34 | 27.1 | 12.6 | 7.8 | 5.0 | 3.2 | 3.5 | 3.2 | 3.0 | 4.3 | 2.8 | | |
| 40 | | 14.8 | 12.2 | 9.5 | 8.0 | 6.5 | 6.4 | 6.3 | 5.9 | 4.4 | 3.4 | 0.4 | 40 | 24.2 | 11.9 | 8.4 | 4.9 | 4.1 | 3.7 | 3.6 | 4.1 | 4.4 | 4.0 | 4.5 | 3.5 |

Figure 5.21: Velocity percentage error between the experimental data and the Eulerian model with the SST $k - \omega$ model, at all flow rates. The colour of each cell represents the range of values that the PE falls within. These ranges are defined in the key of the figure

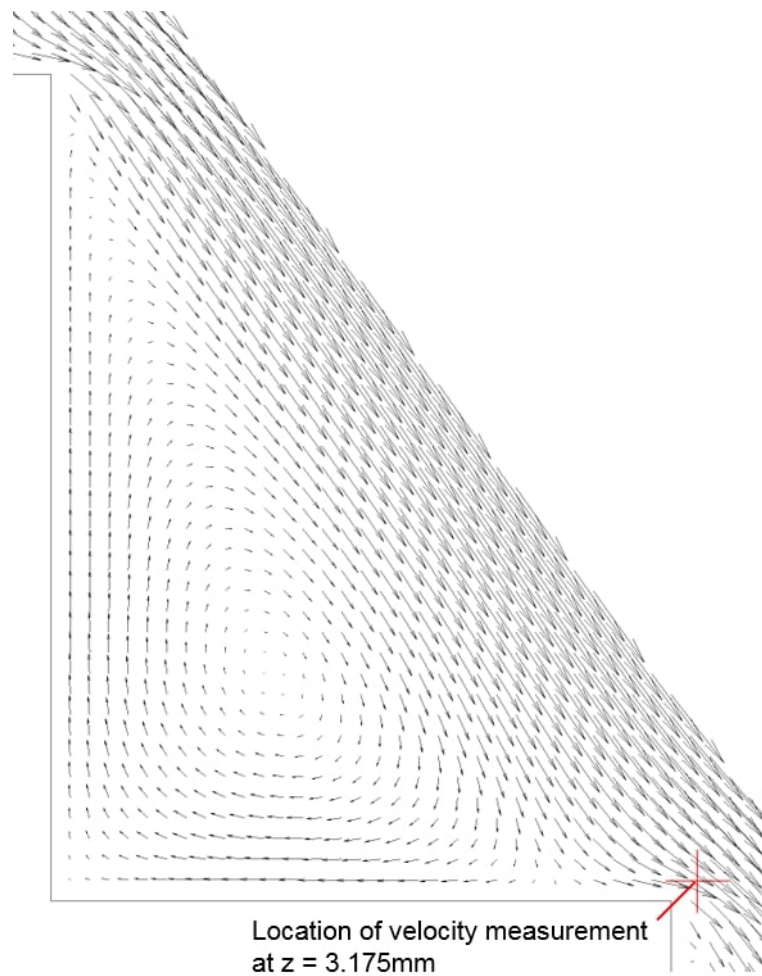


Figure 5.22: Velocity vectors close to a step corner for the Eulerian model with the SST $k - \omega$ model at $Q = 180$ l/s. The location of the velocity measurement closest to the pseudo-bottom, at $z = 3.175$ mm, is indicated in the diagram

5.3.2.5 Summary

At all flow rates, the velocities in the upstream region of the spillway have been accurately predicted by all models. In the downstream, fully aerated, region the two $k - \epsilon$ turbulence models underestimate the velocities in all cases. There is little difference between the velocities predicted by the two $k - \epsilon$ models for all multiphase models. The SST $k - \omega$ model predicts the velocities extremely accurately with the Eulerian model. With the VOF model the velocities are only predicted accurately up to the depth of flow predicted by the VOF model. Both the VOF and Eulerian models produce the least accurate results at $z = 3.175$ mm, however, the experimental velocity measurements in these positions may not be as accurate as at other values of z .

5. TWO-DIMENSIONAL NUMERICAL MODEL STUDY OF A LARGE EXPERIMENTAL STEPPED SPILLWAY

5.3.3 Air Volume Fraction Profiles

Figure 5.23 shows the AVF contours produced by the three multiphase models in combination with the SST $k-\omega$ turbulence model. Streamlines at step 34 are also shown. Each multiphase model shows the recirculating vortex in the step cavity. No air entrainment is predicted by the VOF model, as would be expected due to the reasons described in chapter 4. Both the mixture and Eulerian models show air entrainment, with the AVFs increasing further downstream. The non-aerated region is visible upstream, where no air is found in the step cavities. Further downstream air is transported into the step cavities and the entire flow is aerated. These two models, however, predict the onset of air entrainment to be near the spillway crest, which is further upstream than observed in the experiments.

The reason for this is hypothesised as follows: neither the Eulerian or mixture models are specifically free-surface modelling approaches and, as such, do not capture a free-surface in the same manner that the the VOF model does. In physical stepped spillways, air entrainment begins when turbulence close to the free-surface overcomes buoyancy and surface tension forces (Zhang and Chanson, 2017). The effects of surface tension are modelled in the mixture model, and a surface tension model can be applied to the Eulerian model. However, in each model, there is no numerically defined free-surface at which to apply surface tension to. Free-surfaces in these multiphase models are assumed to be at sub-grid scales and are, therefore, considered using models which predict the interaction between a dispersed and continuous phase. Surface tension effects, therefore, must be applied to the free-surface of the bubbles or droplets, which are not specifically modelled. The effect of this is that surface tension cannot be applied to the free-surface between air and water in the non-aerated region. Therefore, turbulence close to the free-surface only needs to overcome buoyancy forces for air to be entrained into the flow. This results in lower turbulent forces being required for free-surface aeration to occur, than would be required in physical free-surface flows.

The Eulerian and mixture models predict turbulence close to the boundary between air and water in the upstream region of the spillway. This level of turbulence appears to be sufficient to entrain a small amount of air into the flow, as observed in figure 5.23. The AVFs predicted by the numerical models are discussed further below.

5.3 Results and Discussion of a 2D Numerical Modelling Study of Skimming Flow over the LNEC Stepped Spillway

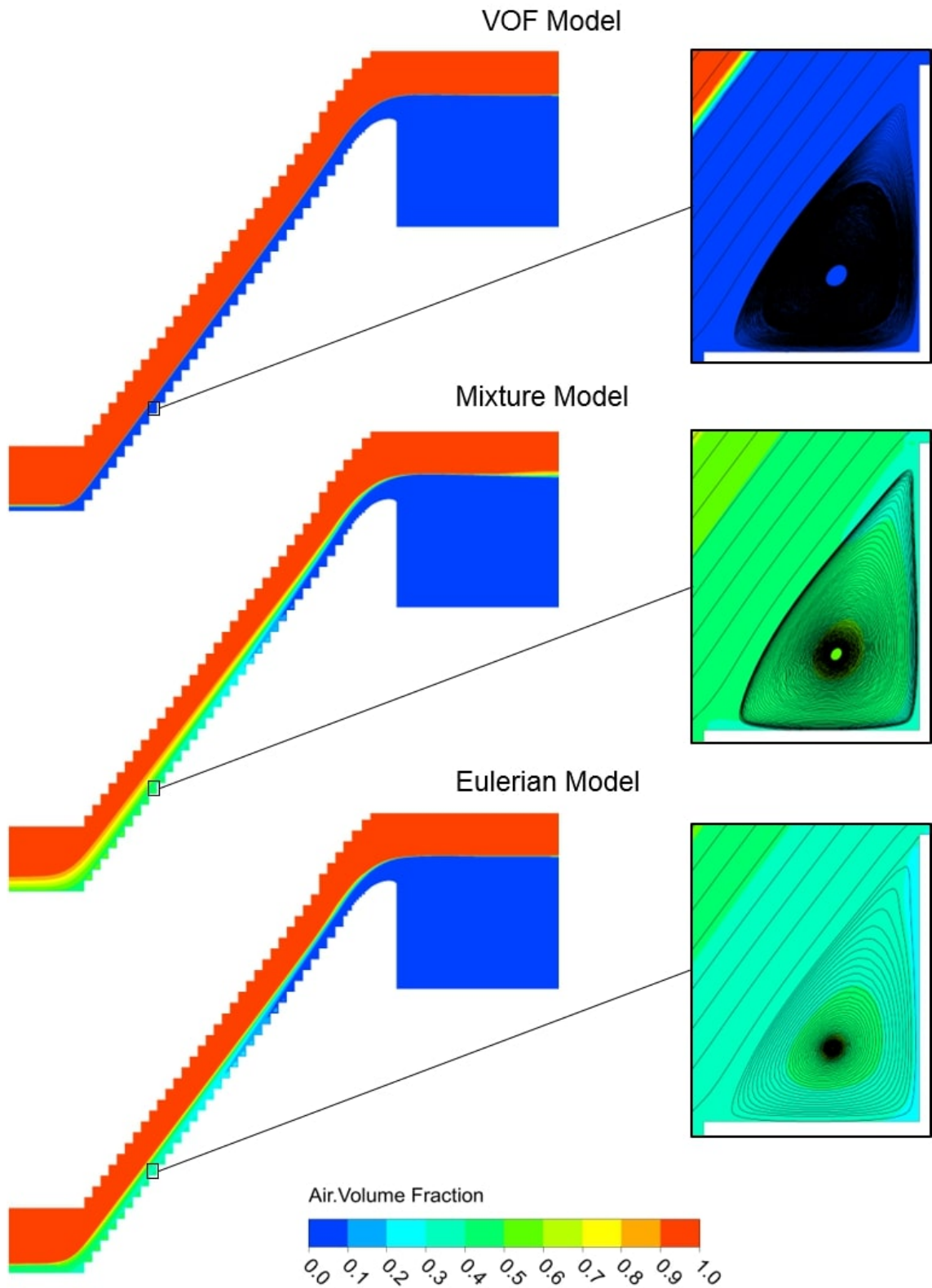


Figure 5.23: Air volume fraction contours of the stepped spillway at the LNEC from the VOF, mixture and Eulerian models, at $Q = 180$ l/s. Streamlines are shown at step 34. The SST $k - \omega$ turbulence model was used in each case

5. TWO-DIMENSIONAL NUMERICAL MODEL STUDY OF A LARGE EXPERIMENTAL STEPPED SPILLWAY

Figures 5.24 - 5.29 show AVF profiles of the VOF, mixture and Eulerian models in combination with the Realisable $k-\epsilon$, RNG $k-\epsilon$ and SST $k-\omega$ turbulence models. The corresponding experimental data are also shown in the figures. Table 5.4 details the multiphase model and flow rate shown in each figure. As with the velocity data, the locations of IP1 and IP2 are indicated by the colour of the plot titles.

Table 5.4: Details of figures showing air volume fraction profiles

| Figure | Multiphase Model | Flow Rate (l/s) |
|--------|------------------|-----------------|
| 5.24 | VOF | 180 |
| 5.25 | Mixture | 180 |
| 5.26 | Euler | 100 |
| 5.27 | Euler | 140 |
| 5.28 | Euler | 180 |
| 5.29 | Euler | 200 |

5.3.3.1 Experimental Data

The experimental data shows the same pattern of AVF profiles for all discharges. Close to the spillway crest, in the non-aerated region, the AVF is 0 at the pseudo-bottom and for the majority of the flow depth. The AVF then increases rapidly to a value of 1. This sudden increase in the AVF represents the sharp free-surface in the non-aerated region. Although there is a sharp free-surface in this region, there are some experimental AVFs in this area with a value between 0 and 1. This is due to the fact that the experimental data are time averaged values, so that entrapped air and waviness in the free-surface result in AVFs between 0 and 1. Note that although the experimental data represents time averaged values, instantaneous numerical data is suitable for comparison, as negligible transient effects are observed in the numerical data.

Approaching IP1, the experimental AVF is greater than 0 for a larger depth. This is attributed to the entrapped air in the wavy free-surface and also entrained air close to the inception point, due to the difference between the instantaneous and time averaged inception point locations (Bombardelli et al., 2011).

Moving downstream from IP1, the AVF at the pseudo-bottom begins to increase from 0 as entrained air is transported throughout the flow depth and into the step cavities. In the fully aerated region the AVF increases with depth more gradually due to the entrained air. In the far downstream region there is little variation in the AVF profiles from one step to the next.

5.3 Results and Discussion of a 2D Numerical Modelling Study of Skimming Flow over the LNEC Stepped Spillway

5.3.3.2 VOF Model

Figure 5.24 shows the AVF profiles for the VOF model and the experimental data at $Q = 180$ l/s. In the upstream region of the spillway, all of the turbulence models produce similar results, however, further downstream the SST $k - \omega$ model diverges from the two $k - \epsilon$ models (which remain relatively close to one another). This is similar to the pattern observed in the velocity profiles. Upstream of IP1, all three turbulence models predict the AVF profiles reasonably well. The numerical data show a slightly sharper increase in the AVF than the experimental data. This is due to the time averaging of the experimental data, as discussed above. In the aerated region, none of the turbulence models predict the AVFs accurately, as would be expected, due to the fact that air entrainment is not predicted by the VOF model. Similar results are shown for all discharges, so only the data for $Q = 180$ l/s has been displayed here. Data for the remaining flow rates can be found in appendix A. Note that, in figure 5.24, at $AVF = 0$ and $AVF = 1$, the numerical AVF values are exactly 0 and 1, so overlap one another.

5. TWO-DIMENSIONAL NUMERICAL MODEL STUDY OF A LARGE EXPERIMENTAL STEPPED SPILLWAY

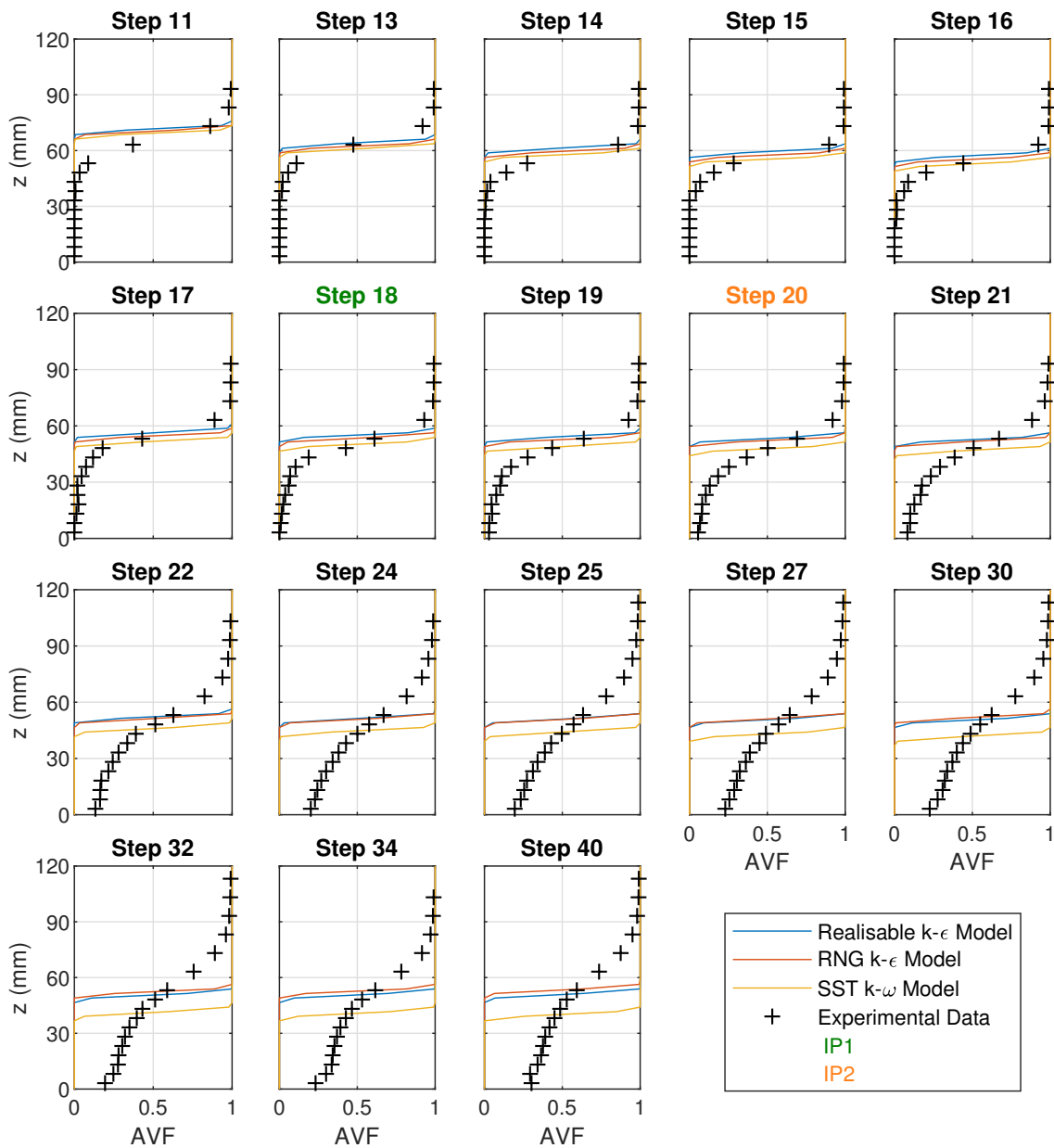


Figure 5.24: Comparison of experimental and numerical air volume fraction profiles for $Q = 180$ l/s. Numerical data is shown for the VOF model with various turbulence models. The experimental inception point locations, IP1 and IP2, are indicated by the colour of the title of the subplots. Note that at $AVF = 0$ and $AVF = 1$, the numerical AVF values are exactly 0 and 1 so overlap one another

5.3.3.3 Mixture Model

With the mixture model (figure 5.25), all of turbulence models predict almost the identical results. In a small number of locations the AVF profiles are predicted reasonably well, for example the lower depths of steps 22 - 30. In the majority of positions, however, the AVF profiles are not predicted accurately.

5.3 Results and Discussion of a 2D Numerical Modelling Study of Skimming Flow over the LNEC Stepped Spillway

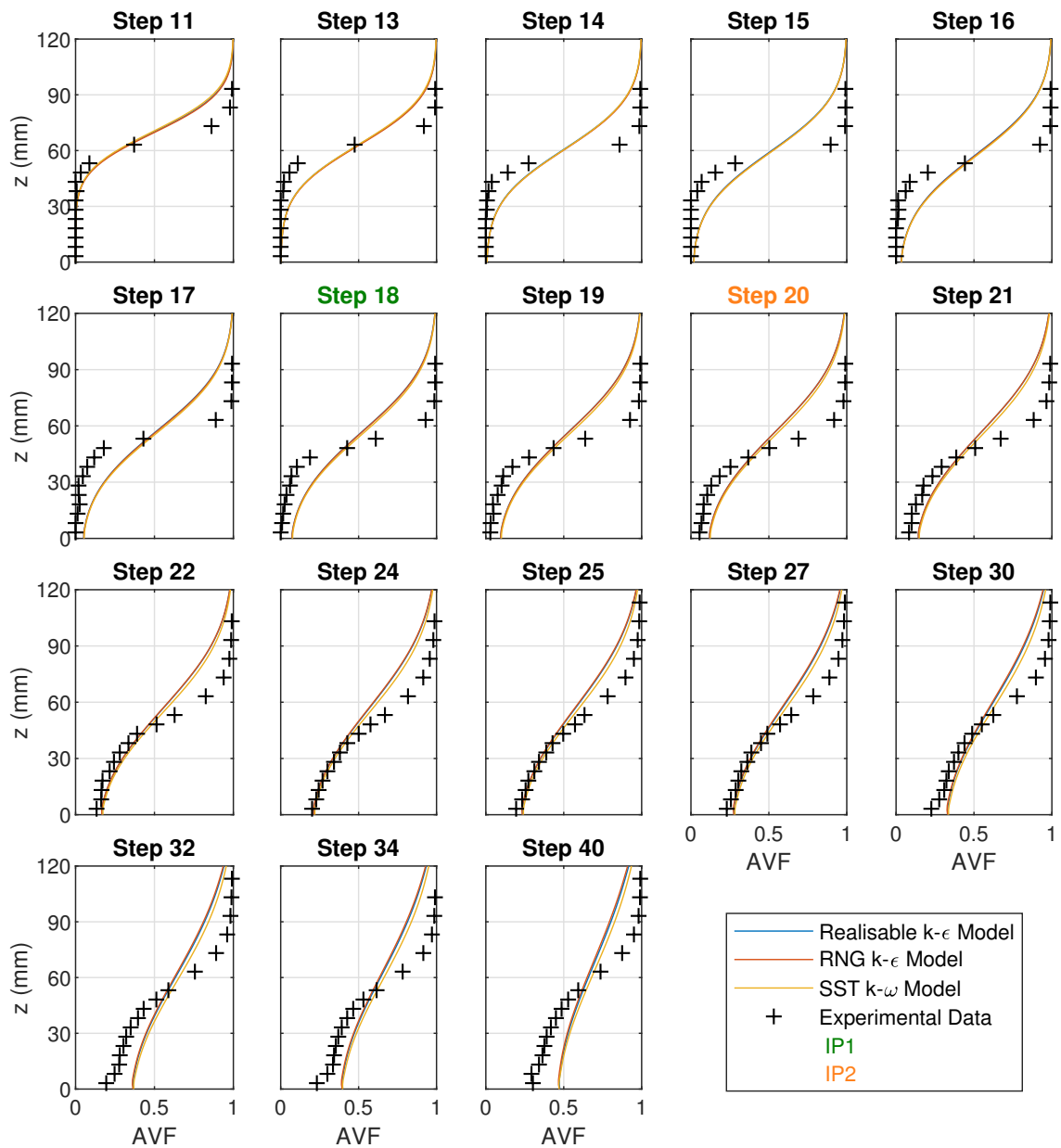


Figure 5.25: Comparison of experimental and numerical air volume fraction profiles for $Q = 180$ l/s. Numerical data is shown for the mixture model with various turbulence models. The experimental inception point locations, IP1 and IP2, are indicated by the colour of the title of the subplots

5.3.3.4 Eulerian Model

Again the Eulerian model shows similar behaviour for all flow rates. In the upstream region of the spillway, the three turbulence models produce approximately similar results, however, there is a small difference in the Realisable $k - \epsilon$ results. Further downstream the SST $k - \omega$ model diverges from the two $k - \epsilon$ models (which largely agree with one another).

Upstream of IP1, the Eulerian model predicts the AVFs reasonably well. This may be

5. TWO-DIMENSIONAL NUMERICAL MODEL STUDY OF A LARGE EXPERIMENTAL STEPPED SPILLWAY

slightly misleading however. Experimental values of the AVF between 0 and 1 in this region are caused by time averaging in the experiments, however in the Eulerian model this isn't the case, as an instantaneous value is displayed.

In the Eulerian model, air entrainment begins at the crest of the spillway (figure 5.23). There is a narrow layer at the free-surface where the AVF is between 0 and 1, due to the air entrainment at the crest of the spillway. So although the Eulerian model predicts the AVFs reasonably well upstream of IP1, it is due to different behaviour and should be viewed with caution. This is of little importance, however, as the AVFs in the non-aerated region are not as important to reservoir engineers as in the aerated region, because no air entrainment takes place. The depth of flow in the non-aerated region and the location of the inception point are of more interest.

Approaching IP1, the Eulerian models overestimate the AVF at the pseudo-bottom. This is again a consequence of the entrainment of air beginning at the spillway crest so a small amount of air is transported to the pseudo-bottom further upstream than in the experiments. A short distance downstream of IP2 all three turbulence models predict the AVF at the Pseudo-bottom accurately. Downstream of this point the two $k - \epsilon$ models predict the AVFs reasonably well, however, the SST $k - \omega$ model produces significantly more accurate results. The accuracy of the SST $k - \omega$ model shows that the entrainment of air at the spillway crest appears to have a negligible effect on the AVFs in the aerated region.

5.3 Results and Discussion of a 2D Numerical Modelling Study of Skimming Flow over the LNEC Stepped Spillway

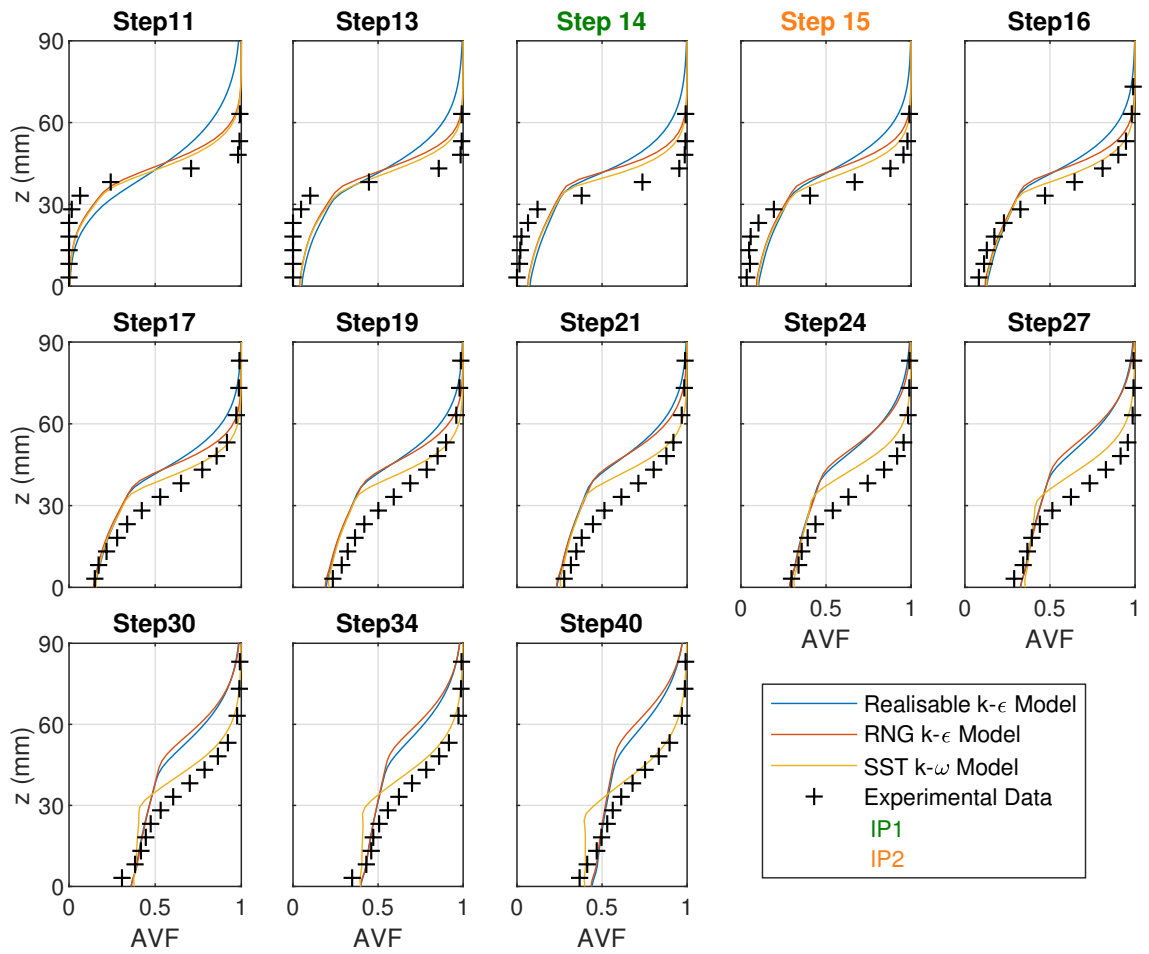


Figure 5.26: Comparison of experimental and numerical air volume fraction profiles for $Q = 100$ l/s. Numerical data is shown for the Eulerian model with various turbulence models. The experimental inception point locations, IP1 and IP2, are indicated by the colour of the title of the subplots

5. TWO-DIMENSIONAL NUMERICAL MODEL STUDY OF A LARGE EXPERIMENTAL STEPPED SPILLWAY

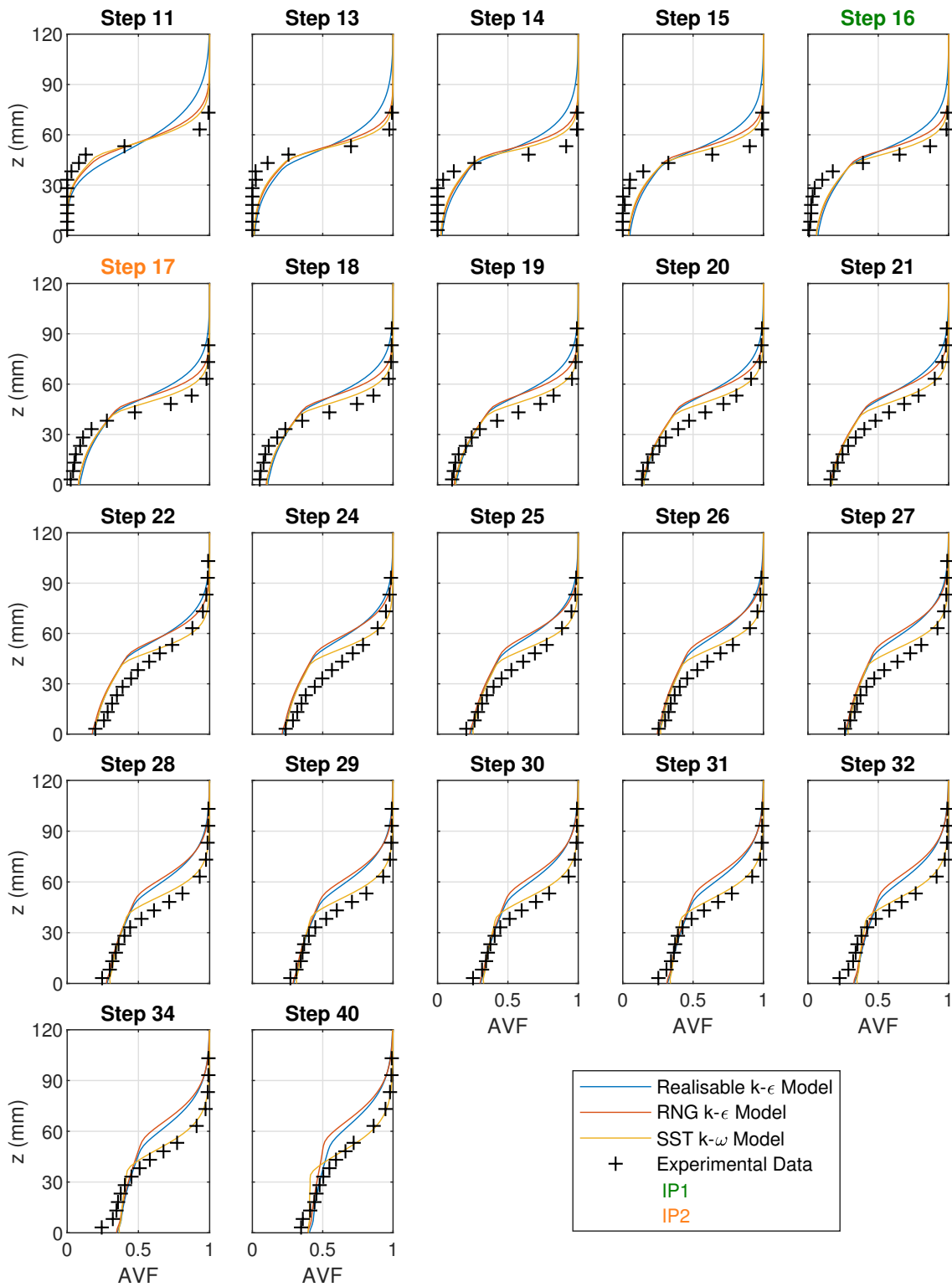


Figure 5.27: Comparison of experimental and numerical air volume fraction profiles for $Q = 140$ l/s. Numerical data is shown for the Eulerian model with various turbulence models. The experimental inception point locations, IP1 and IP2, are indicated by the colour of the title of the subplots

5.3 Results and Discussion of a 2D Numerical Modelling Study of Skimming Flow over the LNEC Stepped Spillway

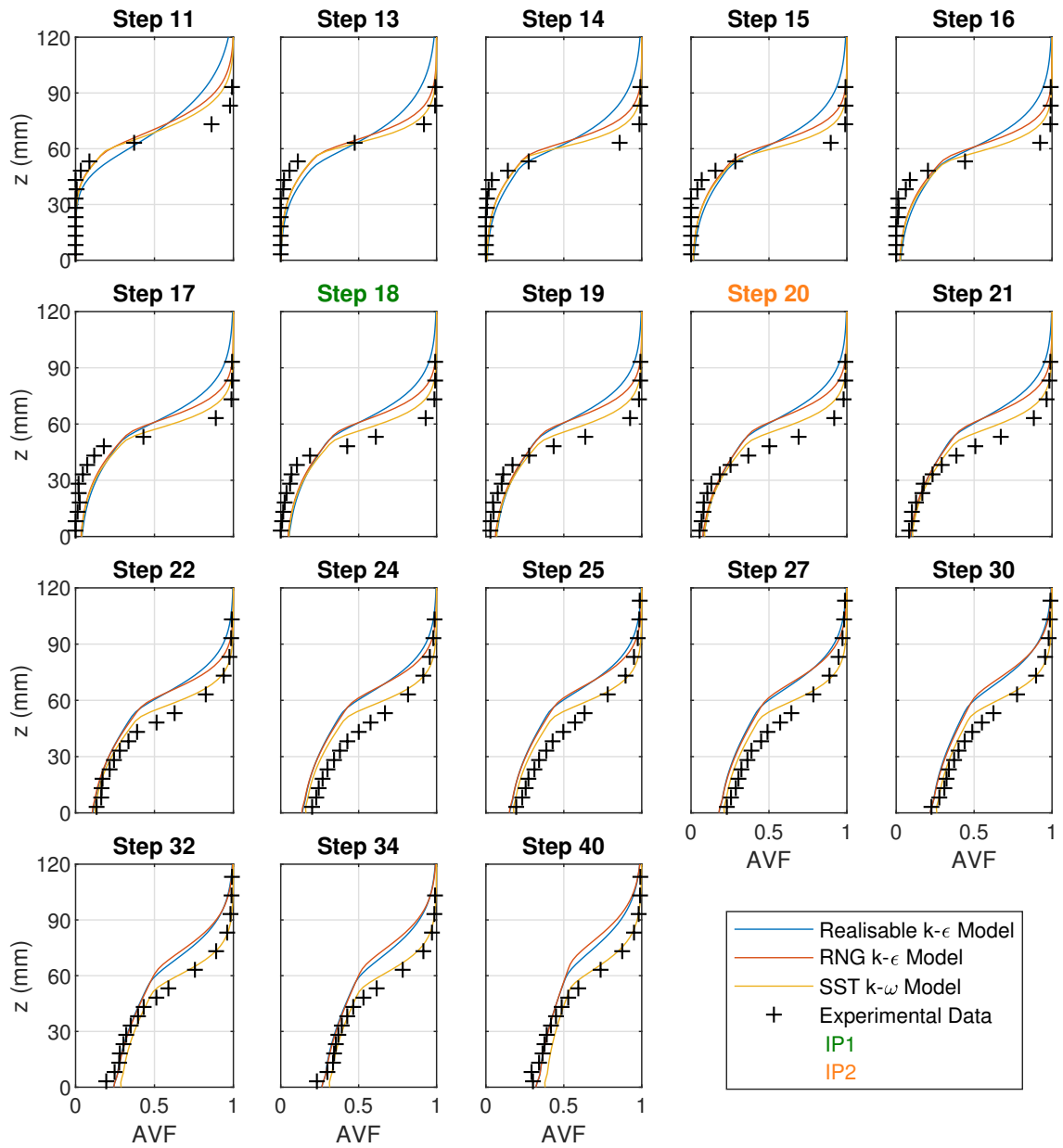


Figure 5.28: Comparison of experimental and numerical air volume fraction profiles for $Q = 180$ l/s. Numerical data is shown for the Eulerian model with various turbulence models. The experimental inception point locations, IP1 and IP2, are indicated by the colour of the title of the subplots

5. TWO-DIMENSIONAL NUMERICAL MODEL STUDY OF A LARGE EXPERIMENTAL STEPPED SPILLWAY

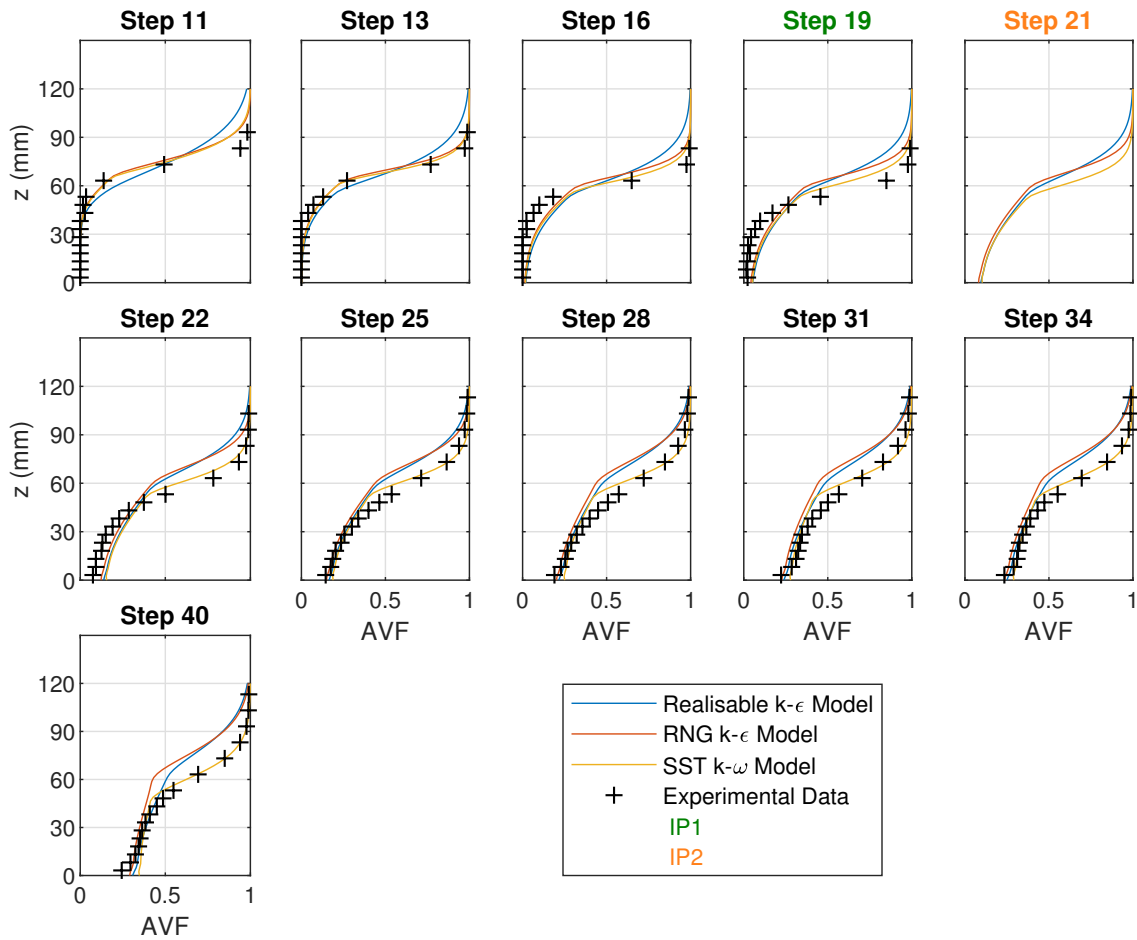


Figure 5.29: Comparison of experimental and numerical air volume fraction profiles for $Q = 200$ l/s. Numerical data is shown for the Eulerian model with various turbulence models. The experimental inception point locations, IP1 and IP2, are indicated by the colour of the title of the subplots

5.3.3.5 Quantification of Errors between the Numerical and Experimental AVF Data

The percentage error has not been calculated for the AVFs as all of the results lie between 0 and 1. Experimental values ranging from 0 to 1 in the denominator of equation (5.8) cause the values of percentage error to vary significantly depending on the experimental AVF, which produces misleading results. As the results are bounded between 0 and 1, however, the absolute error can be used to quantify the accuracy of the numerical models in predicting AVFs. The absolute error is calculated by

$$\text{Error} = \text{Numerical data} - \text{Experimental data} \quad (5.9)$$

Figure 5.30 shows the absolute error between the experimental data and the numerical data, for the Eulerian model with the SST $k-\omega$ model, as this combination of multiphase model and

5.3 Results and Discussion of a 2D Numerical Modelling Study of Skimming Flow over the LNEC Stepped Spillway

turbulence model produced the most accurate results. The VOF and Mixture have not been considered as they did not predict the AVFs accurately. The corresponding experimental AVFs are also shown in the figure so that the total AVF at each location can be observed. It can be seen that the error is extremely small in most cases. The majority of error values are below 0.1, there is only one value above 0.3 (step 14 at $Q = 100$ l/s) and there are very few values above 0.2. This shows that the Eulerian model with the SST $k - \omega$ model predicts the air volume fractions accurately.

5.3 Results and Discussion of a 2D Numerical Modelling Study of Skimming Flow over the LNEC Stepped Spillway

5.3.3.6 Summary

The VOF model does not predict air entrainment, so is not appropriate for modelling AVFs in the aerated region. The mixture model does predict air entrainment, however did not produce accurate results with any of the turbulence models considered. The Eulerian model with the SST $k - \omega$ model, however, produces accurate predictions of the air volume fractions in both the aerated and non-aerated regions. The two $k - \epsilon$ models also produced reasonably accurate results with the Eulerian model. The Eulerian and mixture models predict the onset of air entrainment to occur at the crest of the spillway, which is not the case in the experimental models. However, this appears to have little effect on the AVFs in the aerated region, as the Eulerian model with the SST turbulence model predicted the AVFs in this region accurately.

5.3.4 Flow Depths

Figures 5.32 - 5.34 show the experimental and numerical free-surface data for the VOF, Eulerian and mixture models at each flow rate. Each figure shows the experimental and numerical profiles of y_{90} and the equivalent clear water depth, d . Upstream of the inception point, in the non-aerated region, d may represent a more accurate value for the flow depth than y_{90} , due to the waviness of the free-surface in this region. Figure 5.31 shows a schematic of both y_{90} and d in the non-aerated region, where waves are observed at the experimental free-surface. It can be seen that, due to the shape of the waves, y_{90} is close to the peaks of the wave and will overestimate the average flow depth. d , on the other hand, appears at the midpoint between the wave peaks and troughs, so will therefore give a more accurate representation of the average flow depth in this region. In the aerated region, however, the entrained air causes significant flow bulking so d does not accurately represent the flow depth and y_{90} can be considered the more accurate method to define the free-surface. After IP2 there is a jump in the experimental values of y_{90} for all flow rates. This is due to flow bulking. In all the numerical models, the profile of y_{90} is relatively smooth and there is no obvious increase in depth at the inception point.

5. TWO-DIMENSIONAL NUMERICAL MODEL STUDY OF A LARGE EXPERIMENTAL STEPPED SPILLWAY

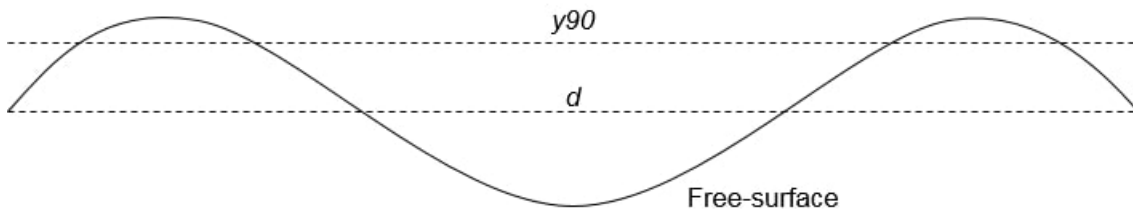


Figure 5.31: Schematic of y_{90} and d in the non-aerated region, in relation to the experimental free-surface where waves are observed

The VOF model shows the same general behaviour for all flow rates. For each turbulence model, the profiles of y_{90} and d are almost identical. This is to be expected as no air entrapment or entrainment occurs in the VOF model, so no flow bulking occurs. Although some waves, with a very small amplitude, are visible at the free-surface, a steady state flow is achieved in the simulations so the waves are stationary. This means that, at a specific measurement location, the waviness of the free-surface would not cause any difference between d and y_{90} . The small differences between y_{90} and d which are observed in figure 5.32 are due to a very small diffuse layer observed at the free-surface in the VOF model.

In the non-aerated region, all turbulence models underestimate y_{90} slightly but predict d accurately. In the aerated region, the SST $k - \omega$ model predicts d reasonably well, whereas, the two $k - \epsilon$ models overestimate the equivalent clear water depth. All turbulence models underestimate y_{90} significantly in the aerated region, which is to be expected as the VOF model does not predict air entrainment, so flow bulking does not take place in this numerical model.

5.3 Results and Discussion of a 2D Numerical Modelling Study of Skimming Flow over the LNEC Stepped Spillway

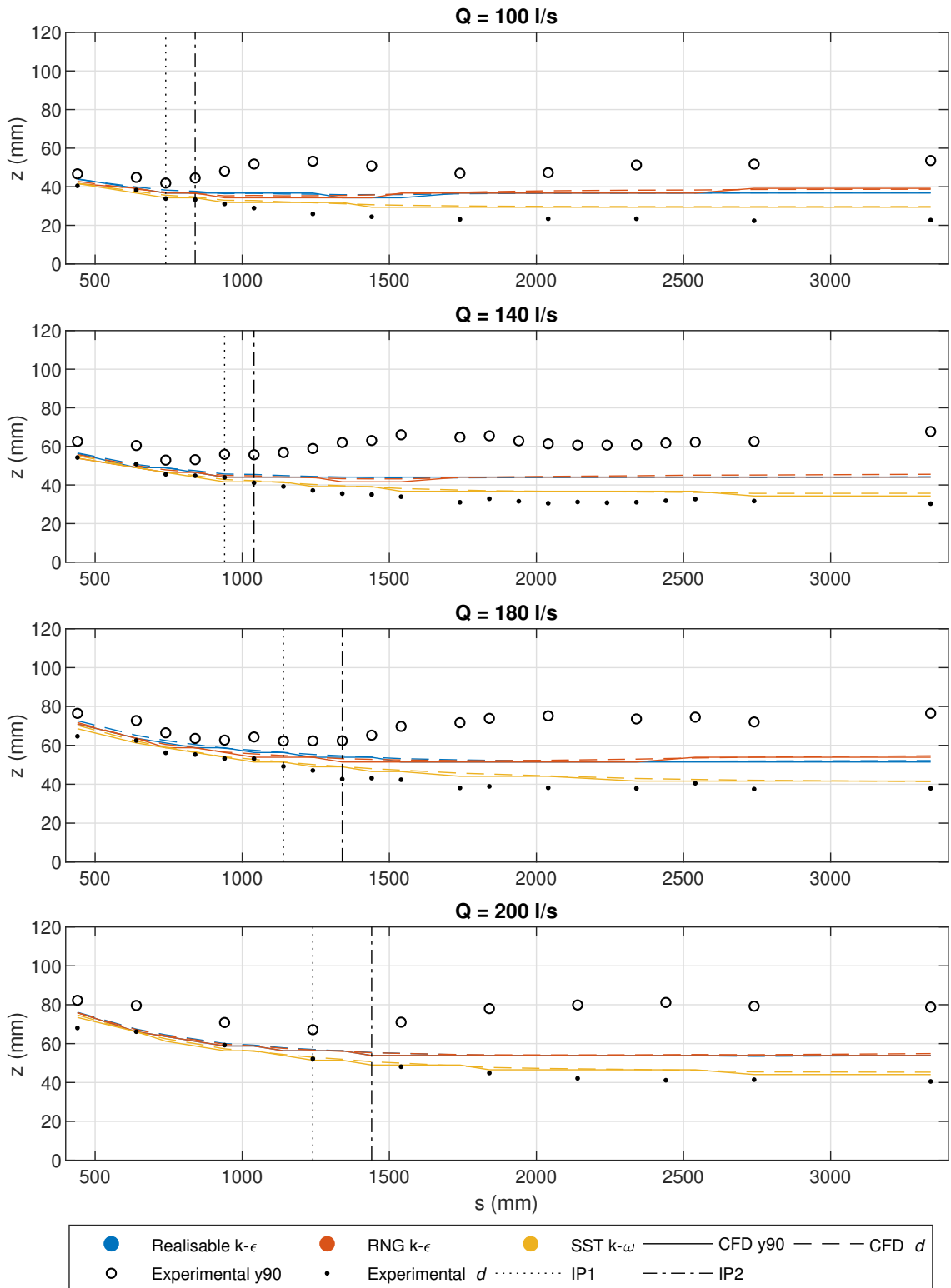


Figure 5.32: Experimental and numerical y_{90} and equivalent clear water depth profiles for the VOF model, with various turbulence models, at all flow rates investigated

The Eulerian model also shows the same behaviour for each flow rate. Unlike the VOF

5. TWO-DIMENSIONAL NUMERICAL MODEL STUDY OF A LARGE EXPERIMENTAL STEPPED SPILLWAY

model, there is a significant difference between d and y_{90} due to air entrainment. In the non-aerated region, all turbulence models predict d accurately, with the SST $k - \omega$ model being slightly more accurate than the two $k - \epsilon$ models. y_{90} is overestimated by all turbulence models in this region, however the SST $k - \omega$ model is still reasonably accurate. This is a consequence of the location of the onset of air entrainment in the Eulerian model. A small amount of flow bulking is predicted in the upstream region of the spillway, which results in the flow depth being slightly overestimated. In the aerated region the SST $k - \omega$ model predicts both y_{90} and d accurately. The two $k - \epsilon$ models overestimate both d and y_{90} in this region. The mixture model predicts d accurately but significantly overestimates y_{90} at all locations, with all turbulence models.

5.3 Results and Discussion of a 2D Numerical Modelling Study of Skimming Flow over the LNEC Stepped Spillway

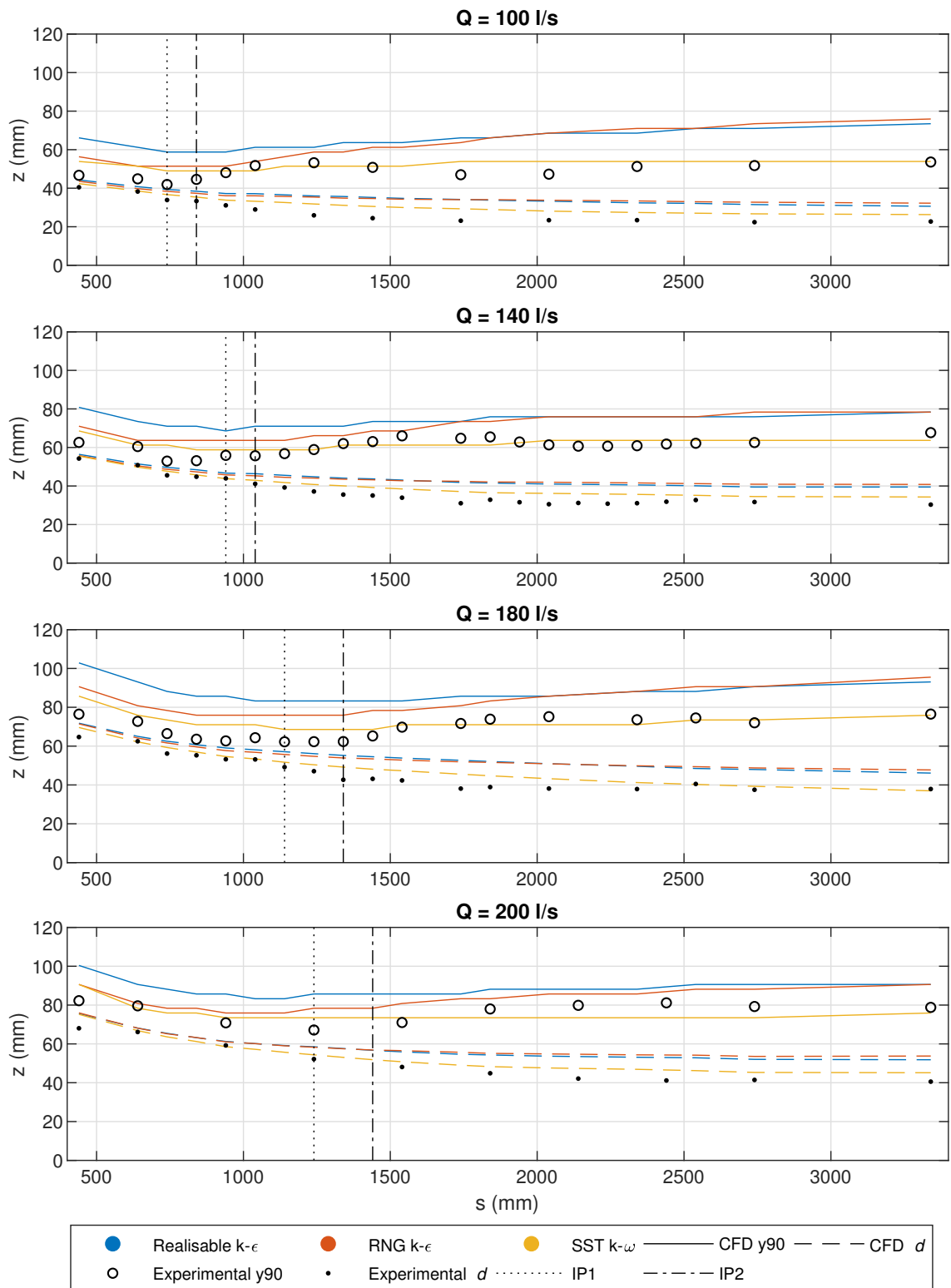


Figure 5.33: Experimental and numerical y_{90} and equivalent clear water depth profiles for the Eulerian, with various turbulence models, model at all flow rates investigated

5. TWO-DIMENSIONAL NUMERICAL MODEL STUDY OF A LARGE EXPERIMENTAL STEPPED SPILLWAY

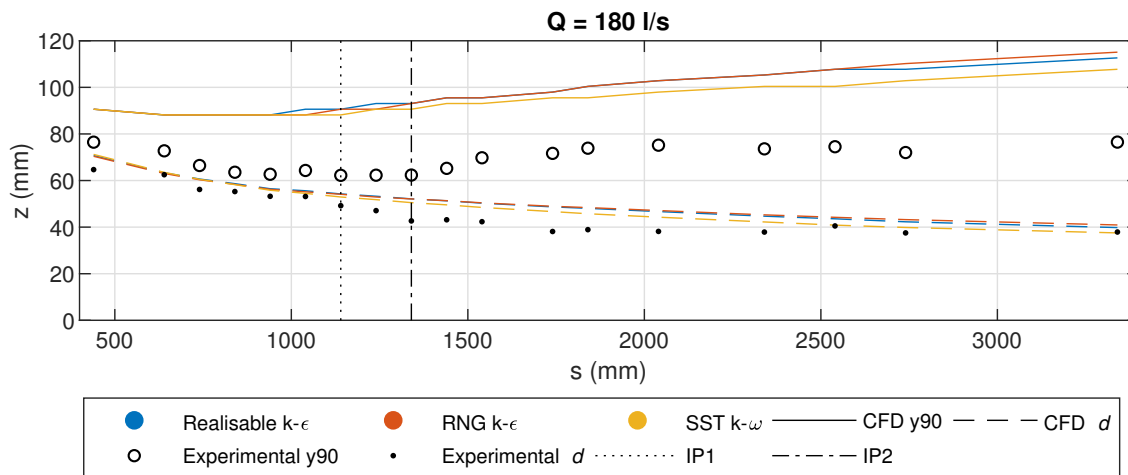


Figure 5.34: Experimental and numerical y_{90} and equivalent clear water depth profiles for the mixture model, with various turbulence models, at 180 l/s, the only flow rate investigated with this multiphase model

5.3.5 Further Turbulence Models

All of the turbulence models considered so far have been variations on the standard $k - \omega$ and $k - \epsilon$ models. In this section the standard $k - \omega$ and $k - \epsilon$ and the Reynolds stress turbulence models are also investigated, in order to consider the impact of turbulence model selection in more detail. The Eulerian model is the most accurate multiphase model at predicting velocities, AVFs and flow depths, so simulations with these further turbulence models have been conducted with the Eulerian model at $Q = 180$ l/s. The data from these turbulence models is compared with the Realisable $k - \epsilon$ and the SST $k - \omega$ models.

5.3.5.1 Standard $k - \omega$ Model

Figures 5.35 and 5.38 show velocity and AVF profiles with the standard $k - \omega$ model. It can be seen that the velocity profiles for the standard $k - \omega$ model and the SST $k - \omega$ model are almost identical at all positions. In the upstream region of the spillway, the AVFs for the $k - \omega$ and SST $k - \omega$ models differ by a small amount, however, further downstream the profiles are, again, almost identical. Note that, as the AVFs are so similar, and the flow depth is defined using the AVFs (y_{90} and d), it can be assumed that there is also very little difference in the flow depth between the two turbulence models. The similarity between the results produced by the standard $k - \omega$ and SST $k - \omega$ turbulence models is discussed further in section 5.3.5.4.

5.3 Results and Discussion of a 2D Numerical Modelling Study of Skimming Flow over the LNEC Stepped Spillway

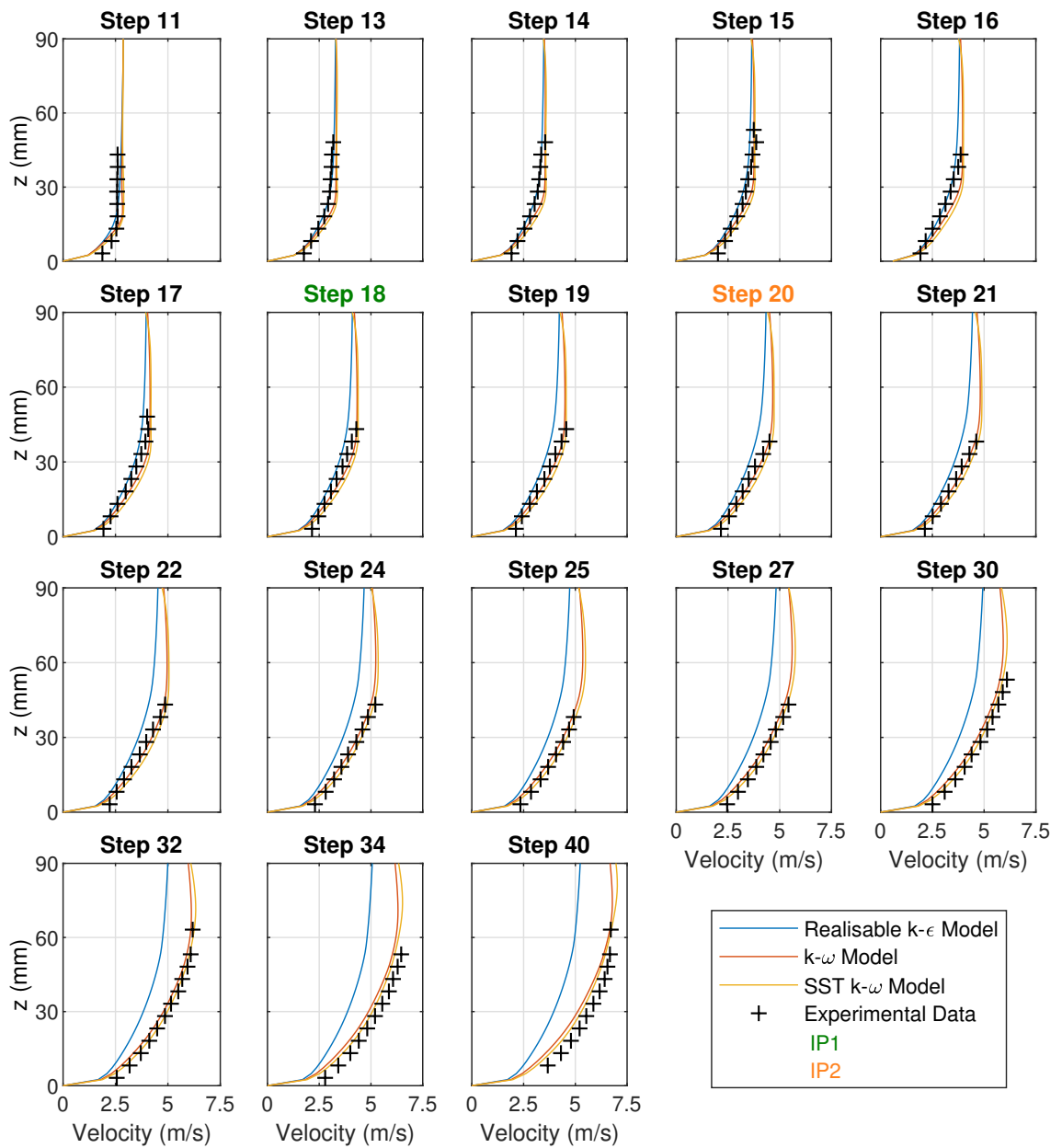


Figure 5.35: Comparison of experimental and numerical velocity profiles for $Q = 180$ l/s. Numerical data is shown for the Eulerian model with various turbulence models, including the standard $k - \omega$ model. The experimental inception point locations, IP1 and IP2, are indicated by the colour of the title of the subplots

5. TWO-DIMENSIONAL NUMERICAL MODEL STUDY OF A LARGE EXPERIMENTAL STEPPED SPILLWAY

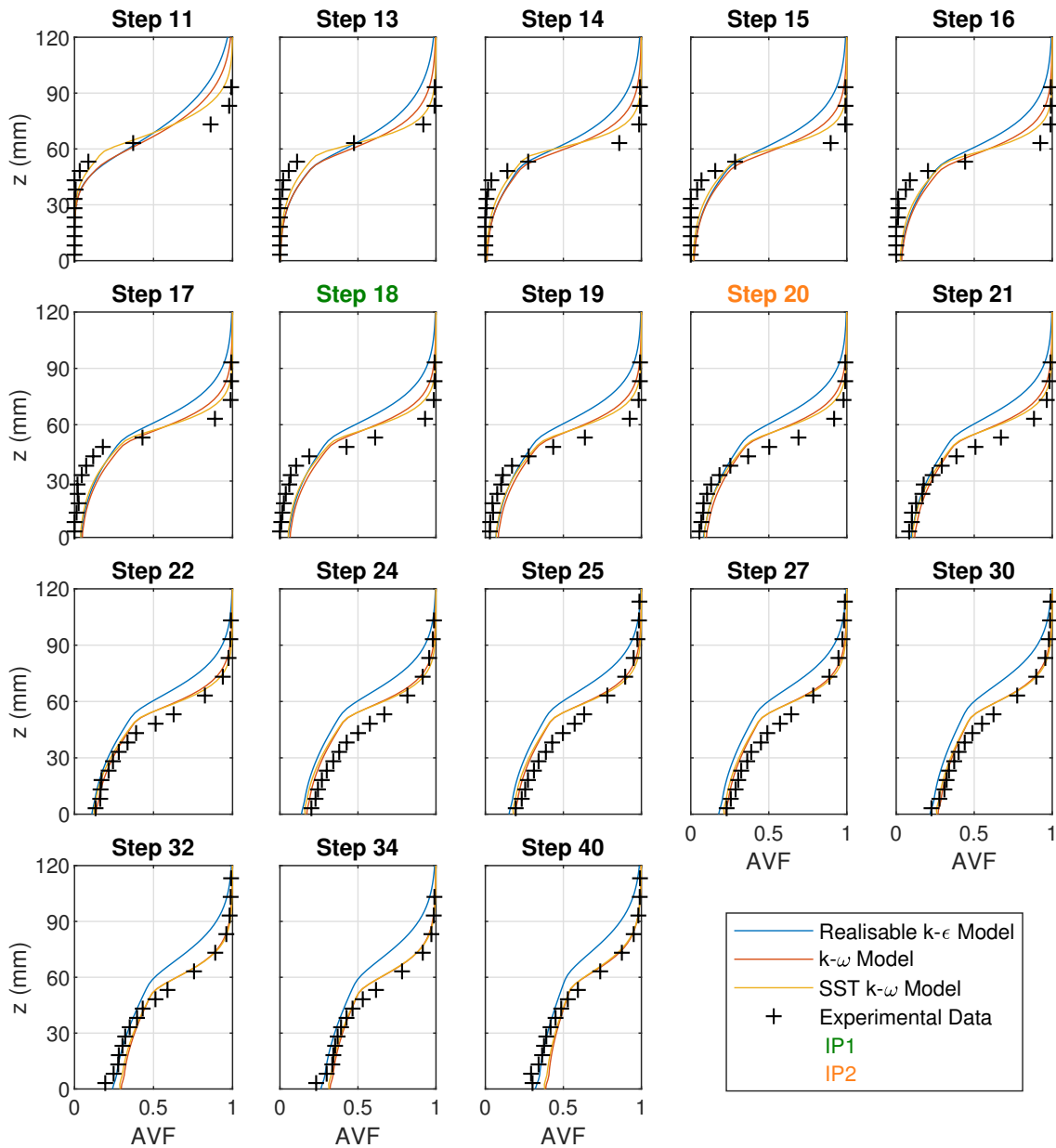


Figure 5.36: Comparison of experimental and numerical air volume fraction profiles for $Q = 180$ l/s. Numerical data is shown for the Eulerian model with various turbulence models, including the standard $k - \omega$ model. The experimental inception point locations, IP1 and IP2, are indicated by the colour of the title of the subplots

5.3.5.2 Standard $k - \epsilon$ Model

Figures 5.37 and 5.38 show velocity and AVF profiles for the standard $k - \epsilon$ model. The standard $k - \epsilon$ and Realisable $k - \epsilon$ have produced almost identical velocity profiles at all locations. In the upstream region of the spillway the AVF of the $k - \epsilon$ model are almost identical to the SST $k - \omega$ model but still similar to the Realisable $k - \epsilon$ model. Further downstream the $k - \epsilon$ profiles diverge from the SST $k - \omega$ model and become almost identical to those of the

5.3 Results and Discussion of a 2D Numerical Modelling Study of Skimming Flow over the LNEC Stepped Spillway

Realisable $k - \epsilon$ model. This is the same as the pattern of AVF profiles shown by the RNG $k - \epsilon$ model (section 5.3.3.4). Again, it can be assumed that the similarity of the AVF profiles between the three $k - \epsilon$ models produces a similar free-surface position. These results show that the three $k - \epsilon$ models considered here produce very similar solutions for velocities, AVFs and flow depths.

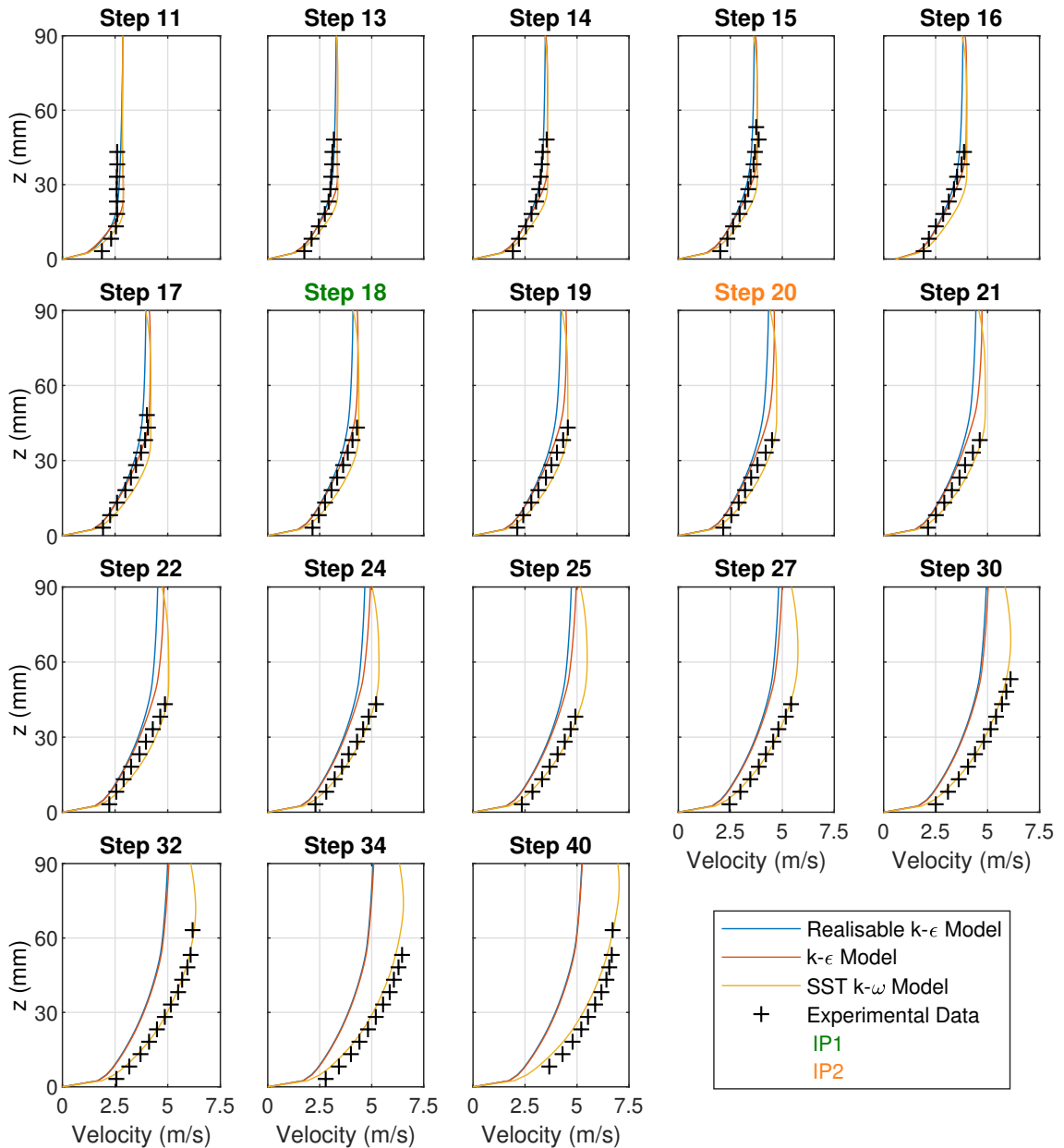


Figure 5.37: Comparison of experimental and numerical velocity profiles for $Q = 180$ l/s. Numerical data is shown for the Eulerian model with various turbulence models, including the standard $k - \epsilon$ model. The experimental inception point locations, IP1 and IP2, are indicated by the colour of the title of the subplots

5. TWO-DIMENSIONAL NUMERICAL MODEL STUDY OF A LARGE EXPERIMENTAL STEPPED SPILLWAY

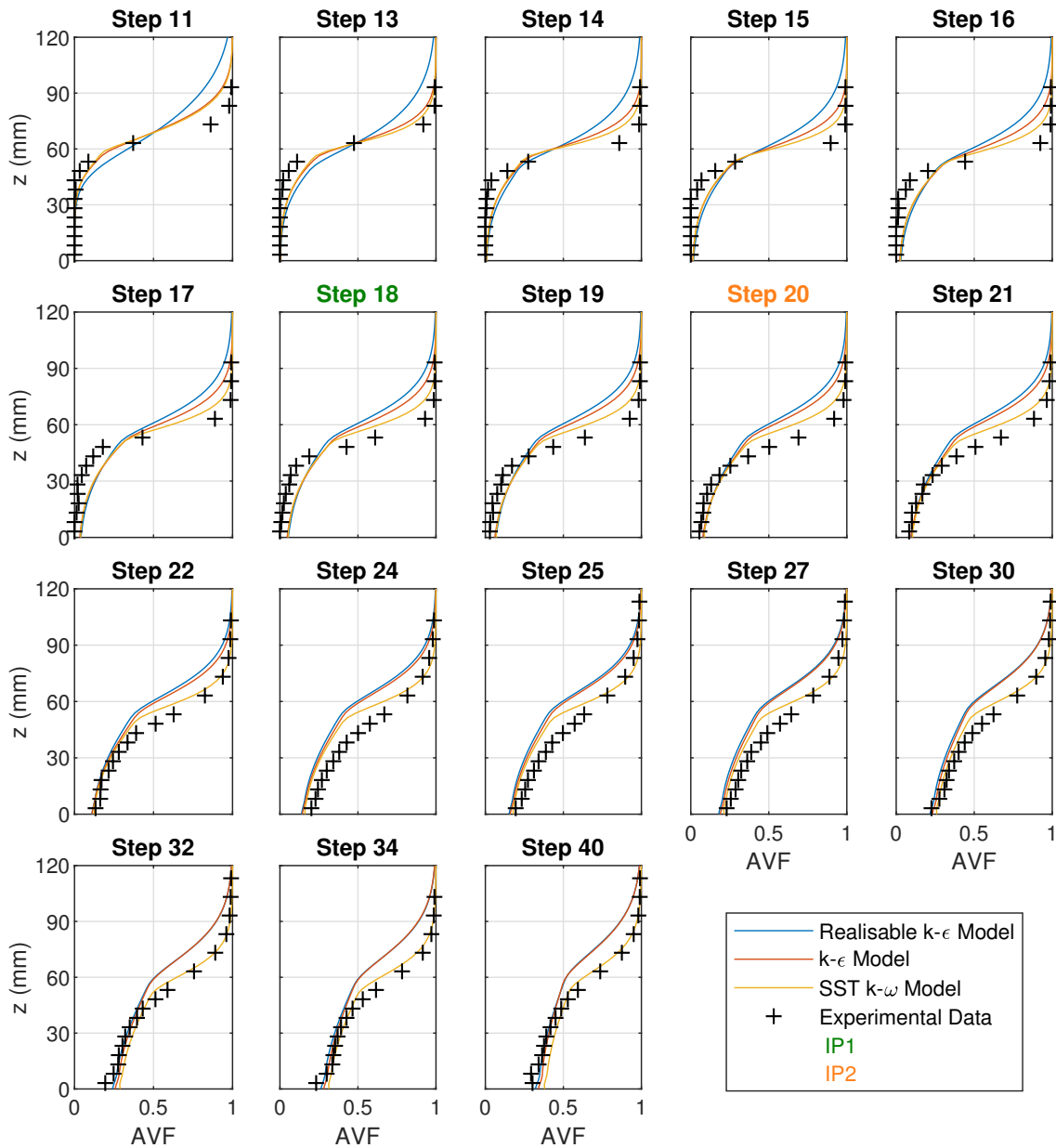


Figure 5.38: Comparison of experimental and numerical air volume fraction profiles for $Q = 180$ l/s. Numerical data is shown for the Eulerian model with various turbulence models, including the standard $k - \epsilon$ model. The experimental inception point locations, IP1 and IP2, are indicated by the colour of the title of the subplots

5.3.5.3 Reynolds Stress Model

Figures 5.39 - 5.41 show velocity, AVF and y_{90} profiles for the Reynolds stress turbulence model. In the upstream region of the spillway the Reynolds stress model predicts the velocities accurately and shows similar results to the other turbulence models. Moving downstream, the Reynolds stress model diverges from the other turbulence models and underestimates the flow velocities significantly. The Reynolds stress model also predicts the AVFs inaccurately at

5.3 Results and Discussion of a 2D Numerical Modelling Study of Skimming Flow over the LNEC Stepped Spillway

each step. At some steps, the AVF is predicted accurately at the lower values of z , however, in general, the AVFs differ significantly from the experimental data. As there is little similarity between the Reynolds stress AVFs and the other turbulence models, no assumptions can be made about the free-surface position. Figure 5.41 shows that the Reynolds stress model overestimates y_{90} significantly at all locations. This data shows that the Reynolds stress model does not appear to be suitable to model aerated flows over stepped spillways.

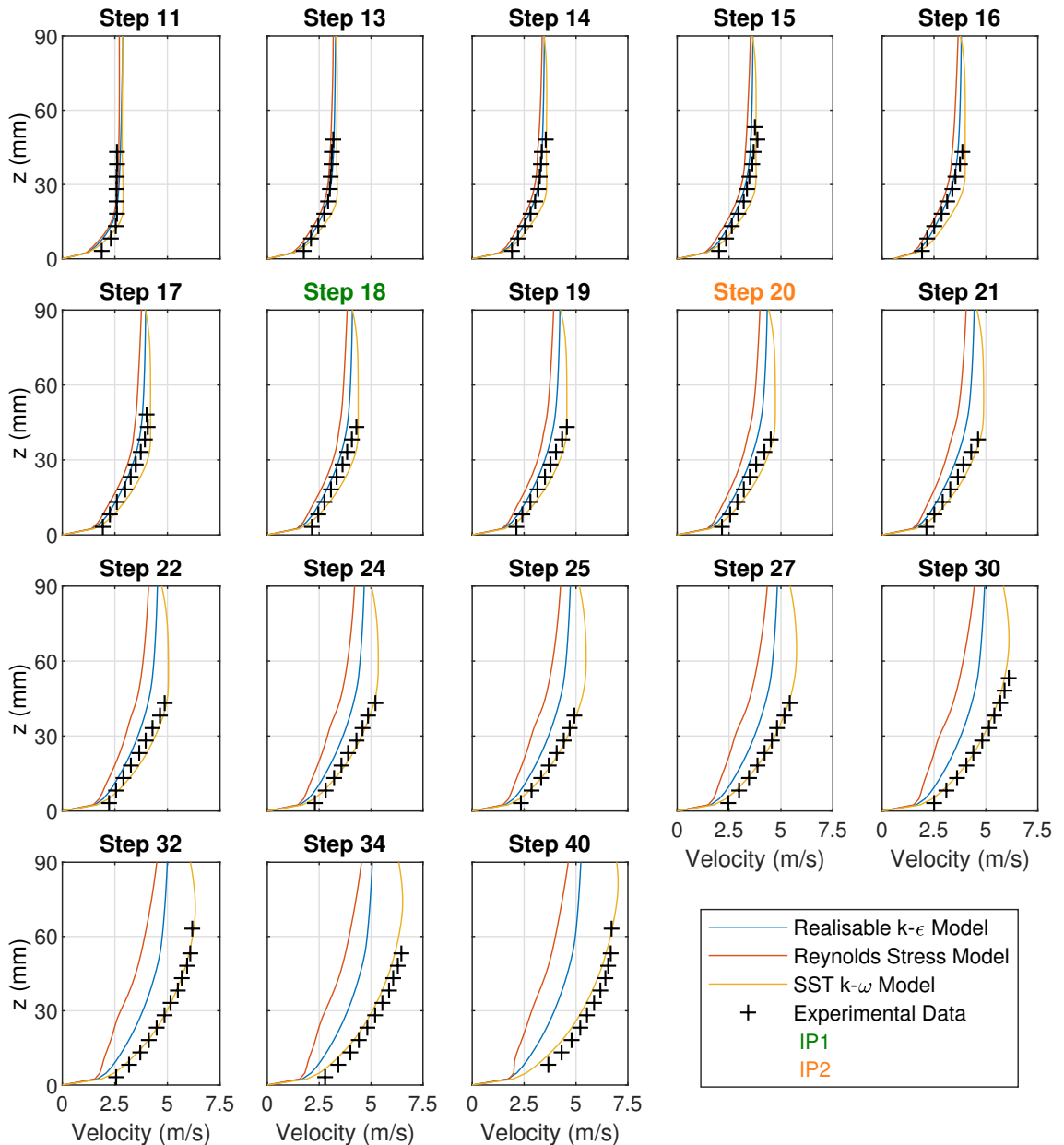


Figure 5.39: Comparison of experimental and numerical velocity profiles for $Q = 180$ l/s. Numerical data is shown for the Eulerian model with various turbulence models, including the Reynolds stress model. The experimental inception point locations, IP1 and IP2, are indicated by the colour of the title of the subplots

5. TWO-DIMENSIONAL NUMERICAL MODEL STUDY OF A LARGE EXPERIMENTAL STEPPED SPILLWAY

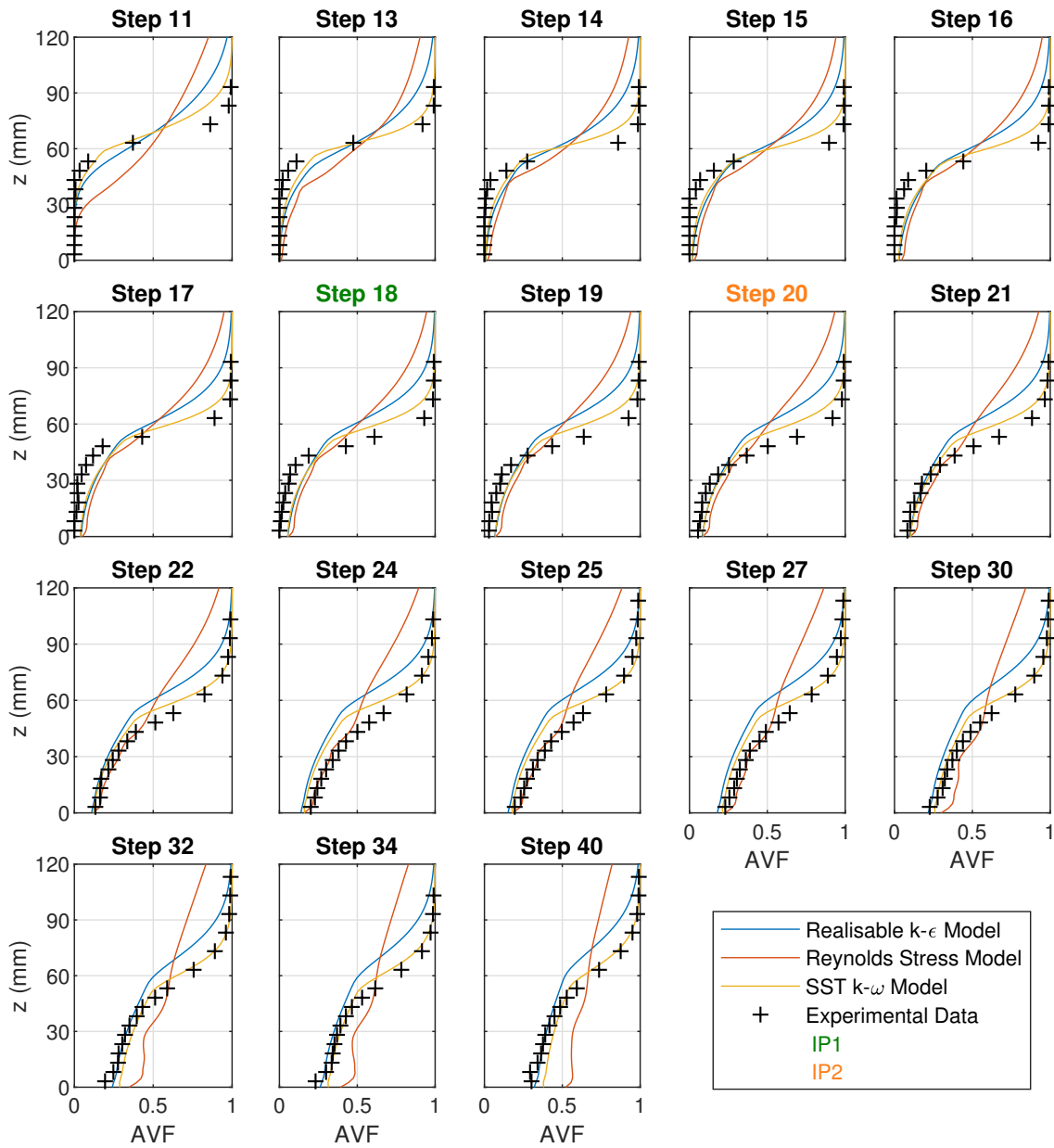


Figure 5.40: Comparison of experimental and numerical air volume fraction profiles for $Q = 180$ l/s. Numerical data is shown for the Eulerian model with various turbulence models, including the Reynolds stress model. The experimental inception point locations, IP1 and IP2, are indicated by the colour of the title of the subplots

5.3 Results and Discussion of a 2D Numerical Modelling Study of Skimming Flow over the LNEC Stepped Spillway

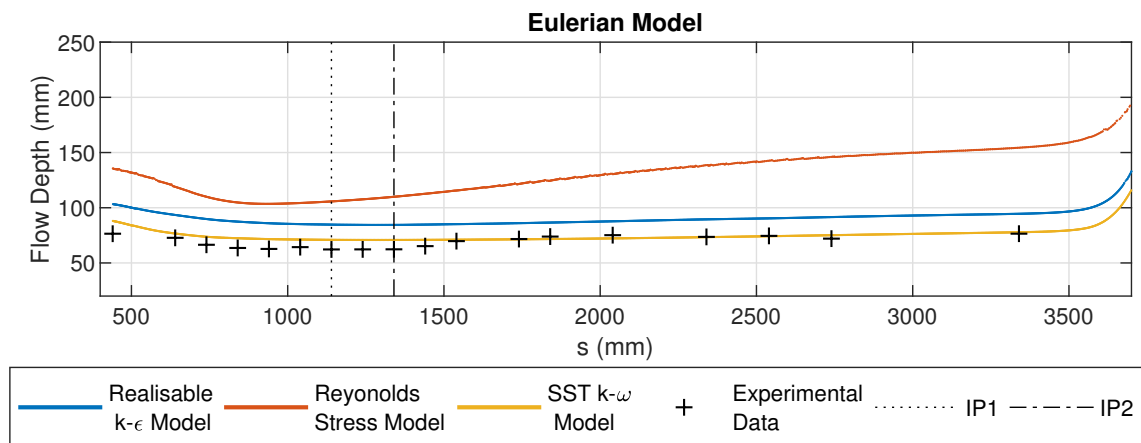


Figure 5.41: Comparison of experimental and numerical y_{90} profiles for $Q = 180$ l/s. Numerical data is shown for the Eulerian model with various turbulence models, including the Reynolds stress model

5.3.5.4 Comparison of $k - \epsilon$ and $k - \omega$ Turbulence Models

Generally, the three $k - \epsilon$ models produce extremely similar results to one another, which agrees with the findings of Bayon et al. (2018), as do the the two $k - \omega$ models. All of the turbulence models in combination with the Eulerian model predict the velocities well in the upstream region of the spillway. Further downstream, the two $k - \omega$ models predict the velocities and the AVFs accurately, whereas the three $k - \epsilon$ models underestimate the velocities and do not predict the AVFs as accurately. The SST $k - \omega$ model blends between the $k - \omega$ model in the near wall region and the $k - \epsilon$ model in the free stream (Menter, 1994). As the $k - \omega$ and SST $k - \omega$ models produce such similar results, it follows that it is the behaviour of the turbulence model in the near wall region which affects the accuracy of the velocity and AVF results away from the wall, above the steps. There are three distinct ways in which the flow above the pseudo-bottom interacts with the wall in the stepped spillway: (i) at the smooth section of the WES curve, (ii) at the step corners and (iii) through mixing with the recirculating vortices in the step cavities, which are in contact with the step faces. The $k - \epsilon$ models produce similarly accurate results to the $k - \omega$ models in the upstream region of the spillway, so it is likely that the differences observed between the results of the $k - \epsilon$ models and the $k - \omega$ models are caused further downstream than the smooth section of the WES curve.

A number of studies into numerical modelling of turbulent flows over a backwards facing step, including Anwar-ul Haque et al. (2007), Pozarlik et al. (2008) and Wilcox et al. (1998), have shown that $k - \epsilon$ turbulence models underestimate the reattachment length whereas the $k - \omega$ models predict the reattachment length significantly more accurately. Chen et al. (2002)

5. TWO-DIMENSIONAL NUMERICAL MODEL STUDY OF A LARGE EXPERIMENTAL STEPPED SPILLWAY

also shows that the $k - \epsilon$ model, with the VOF model, underestimates the experimental reattachment length of a recirculating vortex in a step cavity of a stepped spillway under skimming flow conditions.

Figure 5.42 shows contours of turbulent kinetic energy (k), with streamlines also displayed, at step 33 for the Eulerian model, with all $k - \epsilon$ and $k - \omega$ turbulence models investigated, at $Q = 180$ l/s. It can be seen from the streamlines that the two $k - \omega$ models predict a longer reattachment length than the three $k - \epsilon$ models, which agrees with the findings of the studies into flows over a backwards facing step. The effect of the shorter reattachment length predicted by the $k - \epsilon$ models is that the main flow impacts on a larger area of the horizontal step face than in the $k - \omega$ model simulations. This generates higher values of turbulent kinetic energy (and resulting turbulence) throughout the flow and particularly at the step corners and along the pseudo-bottom. These higher values of turbulence in the $k - \epsilon$ models act to dissipate energy and reduce the velocities compared with the $k - \omega$ models. This may also affect the transport of air, resulting in the differences observed in the AVF profiles. The high turbulence along the pseudo-bottom will also increase mixing between the flow over the steps and the recirculating vortices in the step cavities, which may also contribute to the observed differences in the velocity and AVF profiles.

5.3 Results and Discussion of a 2D Numerical Modelling Study of Skimming Flow over the LNEC Stepped Spillway

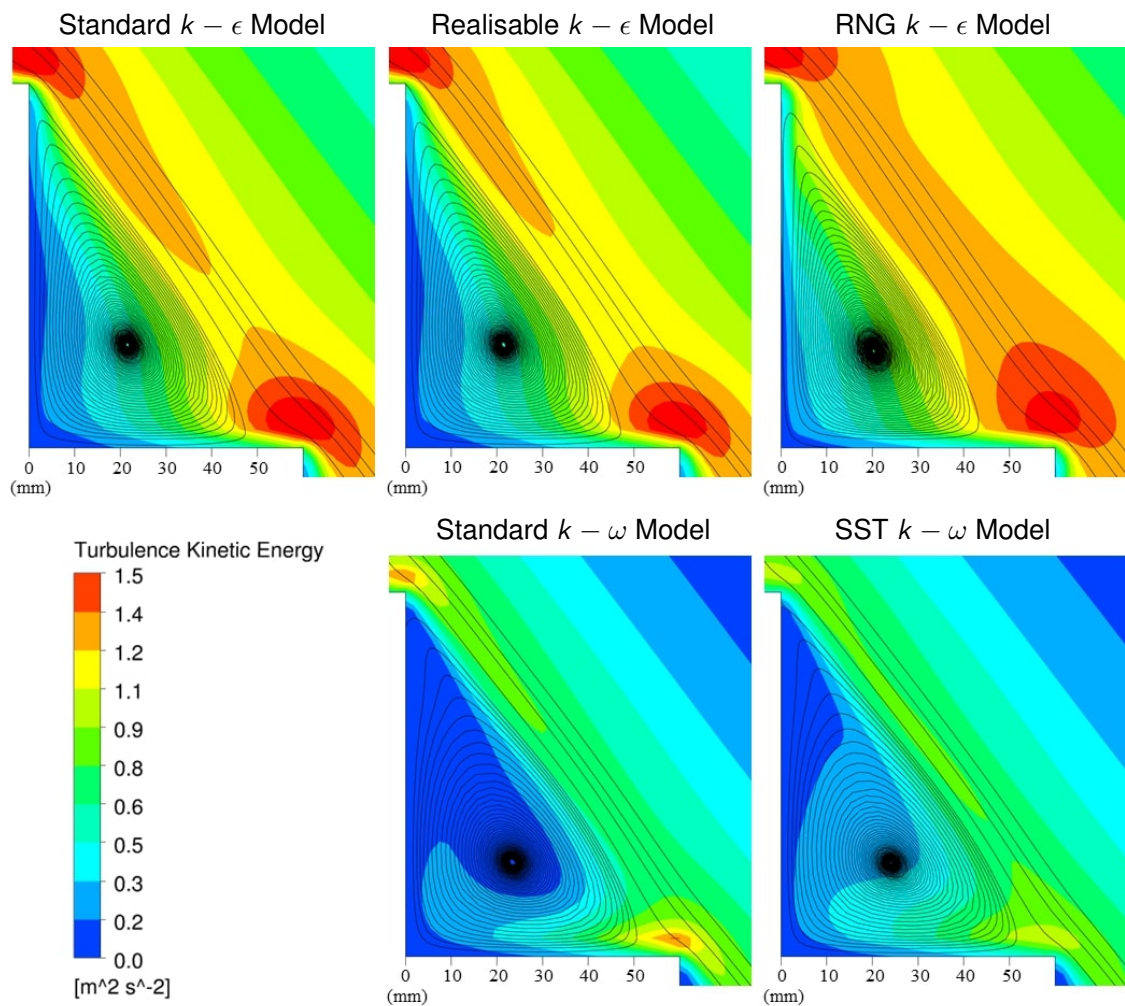


Figure 5.42: Contours of turbulent kinetic energy (k), with streamlines also displayed, at step 33 for the Eulerian model with a range of turbulence model for $Q = 180$ l/s, highlighting the similarity between the $k - \epsilon$ and $k - \omega$ models respectively

5.3.6 Inception Point

The location of the inception point can be defined using a variety of methods, as discussed in chapter 2. This section will investigate whether some of these methods can be used in conjunction with numerical modelling, to accurately predict the location of the inception point.

5.3.6.1 Intersection of the Turbulent Boundary Layer and the Free-Surface

This first technique used to identify the location of the inception point is by determining the location of the intersection of the free-surface and the TBL, the same method by which IP1 is defined in the experimental data (section 5.3.1). As in the experimental data, the free-surface

5. TWO-DIMENSIONAL NUMERICAL MODEL STUDY OF A LARGE EXPERIMENTAL STEPPED SPILLWAY

is defined as the equivalent clear water depth, d , and the TBL is defined as the depth at which the velocity is 99% of the maximum velocity.

Figure 5.43 shows the TBL and d for the VOF model with the Realisable $k - \epsilon$, the RNG $k - \epsilon$ and the SST $k - \omega$ models, for all four flow rates. The location of IP1 and IP2 are also shown. Note that the TBL will never meet the free-surface. The maximum velocity occurs at the free-surface, therefore 99% of the maximum velocity will always appear below the free-surface. Therefore the intersection of d and the TBL is deemed to be the position where the two lines, representing d and the TBL, become parallel. After this it is assumed that the TBL has reached the free-surface.

It can be seen that, in each case, the SST $k - \omega$ model predicts the inception point to be further downstream than the experimental data. However, the two $k - \epsilon$ models become parallel at, or just downstream of, IP2. Experimentally, the intersection of d and the TBL is at IP1. The $k - \epsilon$ models, therefore, predict the intersection further downstream than the experiments. However, they consistently predict the location of IP2 accurately for all flow rates. So, although the intersection of d the TBL is predicted too far downstream, this method of identifying the inception point, using the VOF model with the two $k - \epsilon$ models, would still potentially provide a useful tool for reservoir engineers.

Between $Q = 100$ l/s and $Q = 180$ l/s the Realisable $k - \epsilon$ model shows the TBL to decrease in depth slightly and then increase again, which is unrealistic as the TBL will increase in depth from a solid boundary. This may be a result of the method used to define the TBL, however, as this does not happen with the RNG $k - \epsilon$ model, this model may be considered the more reliable of the two $k - \epsilon$ models in identifying the inception point as the intersection of d and the TBL.

5.3 Results and Discussion of a 2D Numerical Modelling Study of Skimming Flow over the LNEC Stepped Spillway

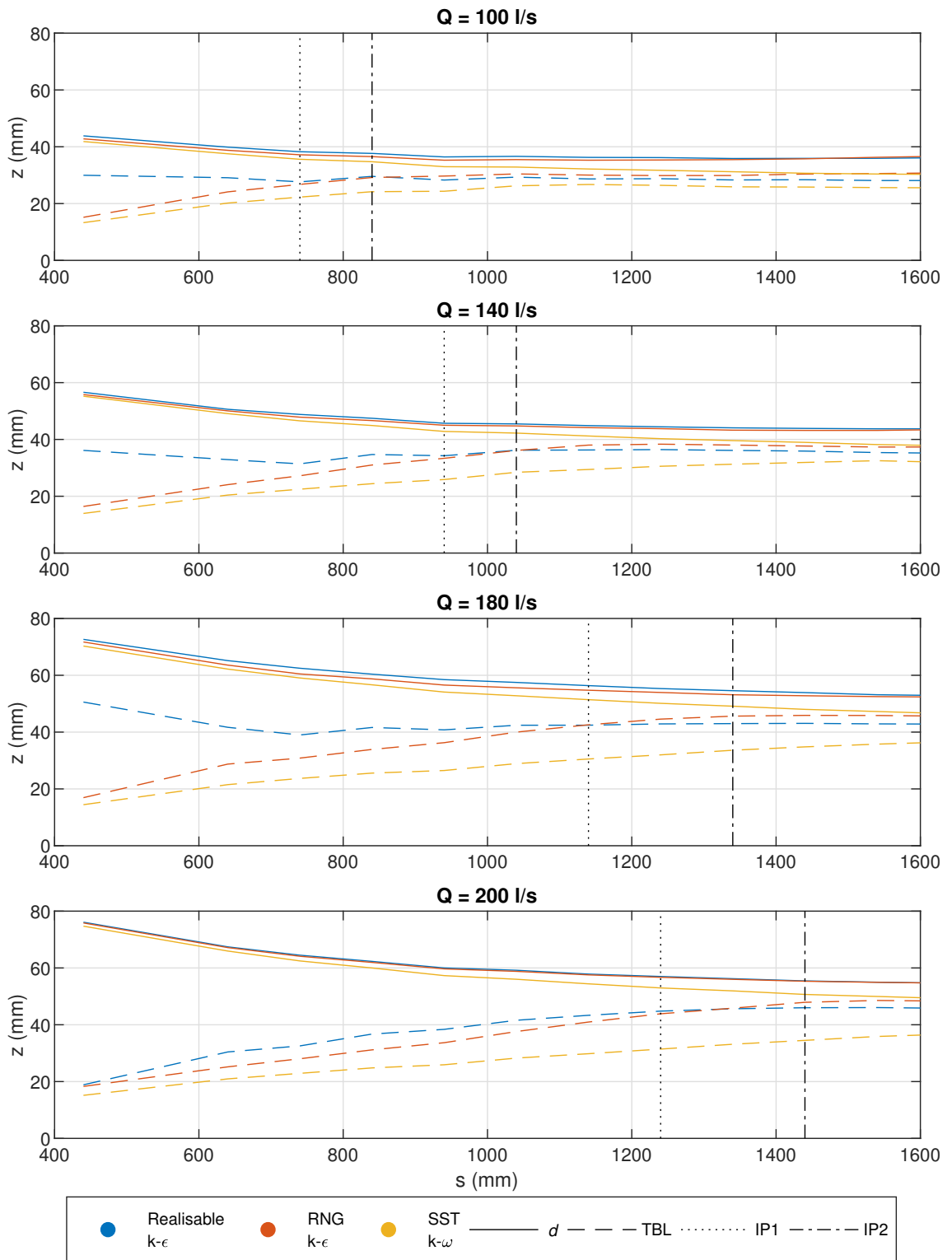


Figure 5.43: Equivalent clear water depth and turbulent boundary layer for the VOF model, with various turbulence models, at all flow rates considered. The locations of IP1 and IP2 are also indicated

Figure 5.44 shows d and the TBL for the Eulerian model. As with the VOF model, the SST

5. TWO-DIMENSIONAL NUMERICAL MODEL STUDY OF A LARGE EXPERIMENTAL STEPPED SPILLWAY

$k - \omega$ model predicts the intersection of d and the TBL to be significantly further downstream than the experiments. The two $k - \epsilon$ models, however, predict the location of IP1 accurately at all flow rates. Similarly to the VOF model, the RNG $k - \epsilon$ model can be considered to be the more reliable of the two $k - \epsilon$ models, as at some flow rates the Realisable $k - \epsilon$ model show the TBL to decrease in depth moving downstream, which is unrealistic.

5.3 Results and Discussion of a 2D Numerical Modelling Study of Skimming Flow over the LNEC Stepped Spillway

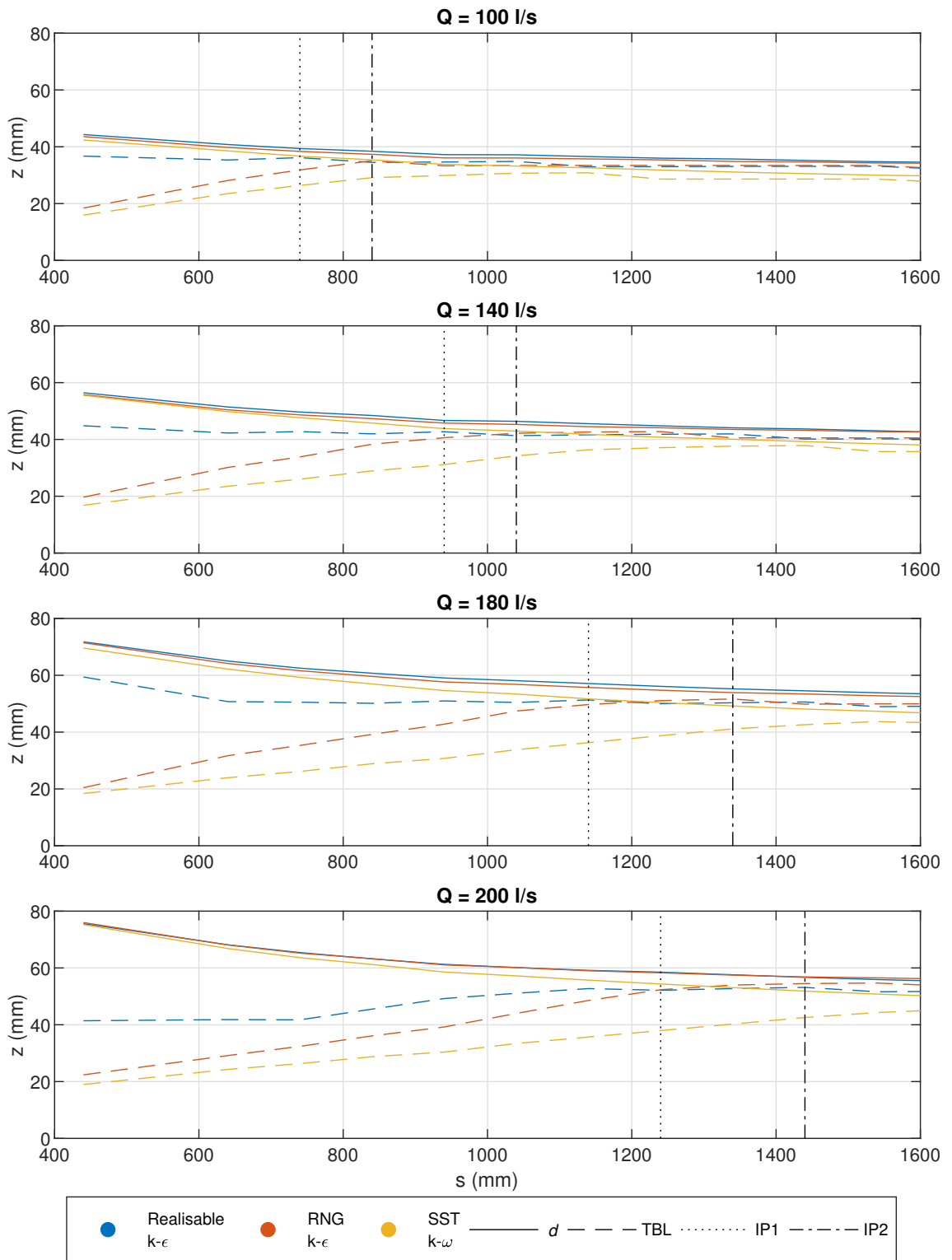


Figure 5.44: Equivalent clear water depth and turbulent boundary layer for the Eulerian model, with various turbulence models, at all flow rates considered. The locations of IP1 and IP2 are also indicated

Figure 5.45 shows d and the TBL for the mixture model at $Q = 180$ l/s. The location of

5. TWO-DIMENSIONAL NUMERICAL MODEL STUDY OF A LARGE EXPERIMENTAL STEPPED SPILLWAY

IP1 is predicted accurately with all turbulence models. This data is for only a single flow rate however, so further flow rates would need to be investigated to confirm the mixture models accuracy at predicting the intersection of d and the TBL. Note that, although the mixture model predicts IP1 well at $Q = 180$ l/s using this method, the mixture model does not generally make accurate predictions of the flow velocities, depths or AVF profiles. Therefore it has not been considered further in this study.

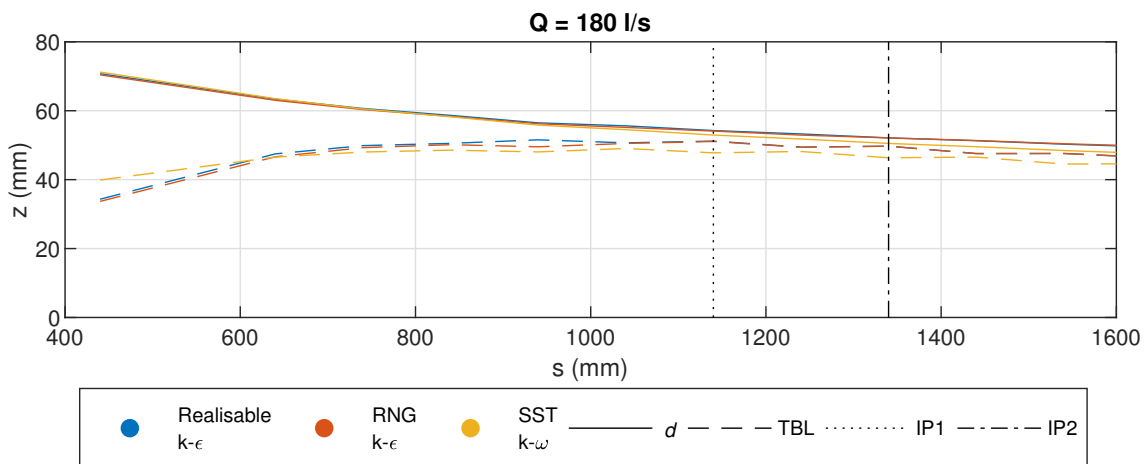


Figure 5.45: Equivalent clear water depth and turbulent boundary layer for the mixture model, with various turbulence models, at $Q = 180$ l/s. The locations of IP1 and IP2 are also indicated

5.3.6.2 Visual Inspection

Many authors, including Chanson and Toombes (2002) and Meireles et al. (2012), have used visual inspection of the onset of air entrainment to identify the location of the inception point. The inception point identified by visual inspection for the experimental data included in this study is defined by the specific criterion: *"the vertical edge immediately upstream of the step cavity where a continuous presence of white water or air bubbles was noticed from above and also through both sidewalls along the entire flume width"*. Visual inspection of AVF contours has been carried out in order to examine if the inception point location can be accurately predicted using numerical modelling. The VOF model does not predict air entrainment so has not been considered in this method.

Figure 5.46 shows AVFs close to the inception point, at each flow rate, for the Eulerian model with the SST $k - \omega$ turbulence model. IP1 and IP2 are shown in each case. At all discharges the same behaviour is shown. The AVF is below 0.1 in all step cavities upstream of IP1. Between IP1 and IP2 the step cavities contain some small "bubbles" of an AVF between

5.3 Results and Discussion of a 2D Numerical Modelling Study of Skimming Flow over the LNEC Stepped Spillway

0.1 and 0.2, which is always restricted to the centre of the step cavity and doesn't touch either of the step faces. The step cavity directly downstream of IP2 is mostly, or completely, filled with an AVF of 0.1 - 0.2. The contour of 0.1 - 0.2 AVF reaches the horizontal step face and is very close to, or touching, the vertical step face. At all flow rates the Eulerian model, with the SST $k - \omega$ model, has shown similarly accurate contours of air volume fraction around IP1 and IP2. Although this may not be the most clearly definable method to identify the location of the inception point in the numerical models, it still may provide another useful tool for reservoir engineers.

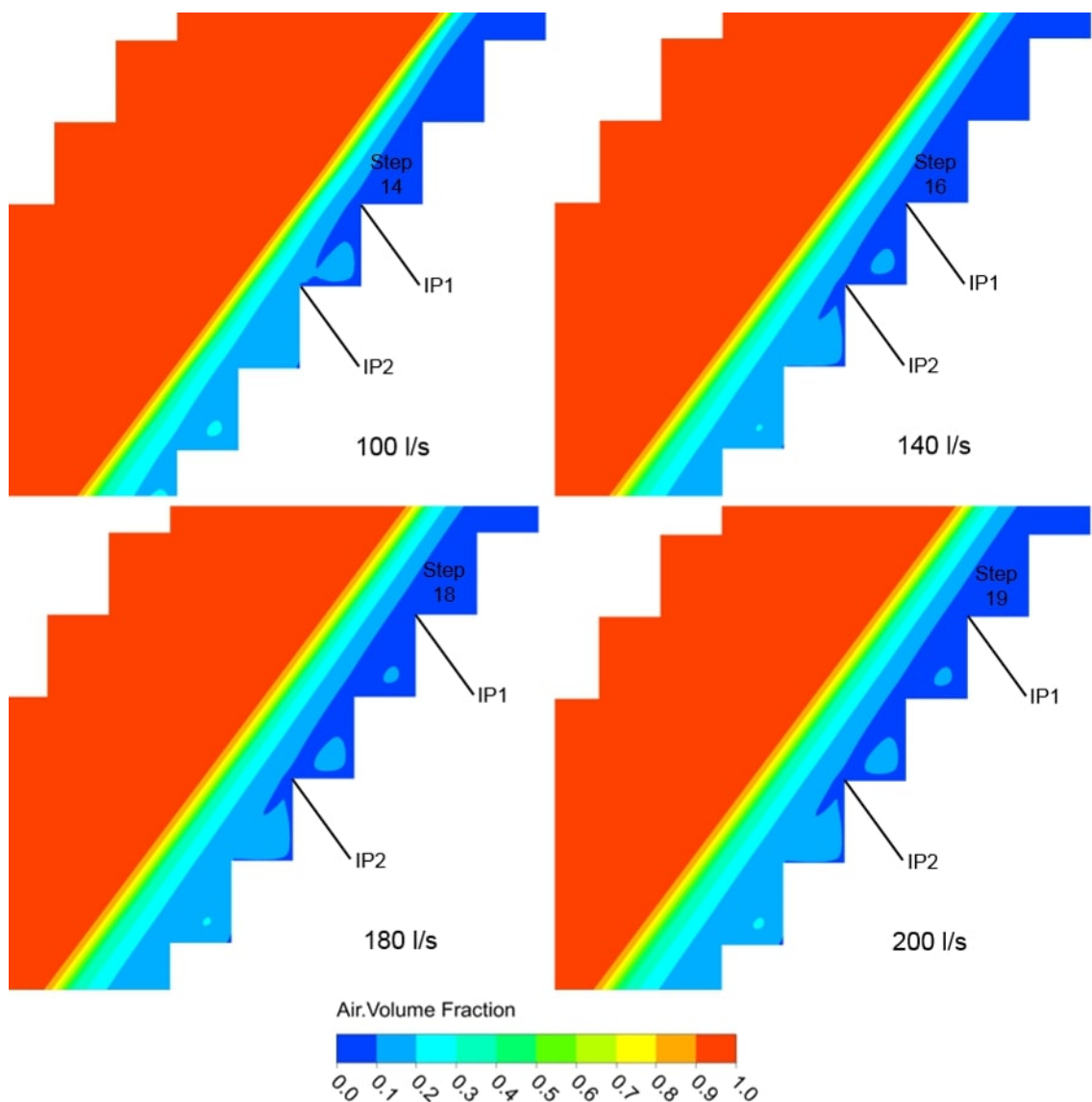


Figure 5.46: Contours of air entrainment at the inception point for the Eulerian model with the SST $k - \omega$ model. The locations of IP1 and IP2, at each flow rate, are indicated in the figure

5. TWO-DIMENSIONAL NUMERICAL MODEL STUDY OF A LARGE EXPERIMENTAL STEPPED SPILLWAY

5.3.6.3 Depth Averaged Air Volume Fraction

Bung (2011) defines the inception point as the location where the depth averaged air concentration, C_{mean} , is equal to 0.2, based on experimental findings by Matos (2000) and Boes and Hager (2003a). As with the method of visual inspection, this method cannot be used with the VOF model as there is no air entrainment predicted by the model.

Figure 5.47 shows the experimental and numerical values of C_{mean} at different values of s , for the four flow rates considered. C_{mean} , as defined by Boes and Hager (2003a), is calculated by

$$C_{mean} = \frac{1}{y_{90}} \int_{z=0}^{y_{90}} AVF(z) dz \quad (5.10)$$

The same general pattern is shown at each flow rate. Upstream of IP2 the numerical C_{mean} overestimates the experimental value slightly. At IP2 the numerical and experimental values of C_{mean} are in close agreement. Downstream of IP2 the numerical model underestimates the value of C_{mean} , and further downstream the numerical and experimental values become closer to one another. Note that at $Q = 200$ l/s the numerical model slightly underestimates C_{mean} at the far upstream section of the spillway, however the same general pattern as the other flow rates is observed.

The error between the numerically predicted and experimental C_{mean} values can be explained by considering the numerically predicted AVF and y_{90} profiles. Upstream of the inception point the Eulerian model, with the SST $k - \omega$ model, overestimates y_{90} . This is due to the fact that, in this region of the spillway, the numerical model overestimates the AVFs due to the small amount of air entrainment which occurs close to the free-surface, as discussed in section 5.3.3.

Downstream of the inception point, the numerical C_{mean} values underestimate the experimental values. This is due to a combination of small errors in the prediction of the AVF profiles and y_{90} in this region. Downstream of the inception point the numerical model underestimates the AVFs, particularly between $z = 30$ mm and $z = 60$ mm (figures 5.26 - 5.30). The y_{90} values are also underestimated slightly downstream of the inception point, for example, between steps 22 and 28 at $Q = 140$ l/s (figure 5.33). Although the Eulerian model with the SST $k - \omega$ model predicts the AVFs and y_{90} values well in this region, the combination of small errors in the prediction of these variables results in a significant error in the numerically predicted and experimentally measured values of C_{mean} . Despite this error, the results of this investigation

5.3 Results and Discussion of a 2D Numerical Modelling Study of Skimming Flow over the LNEC Stepped Spillway

show that the Eulerian model with the SST $k-\omega$ model is able to predict AVFs and flow depths accurately in the aerated region.

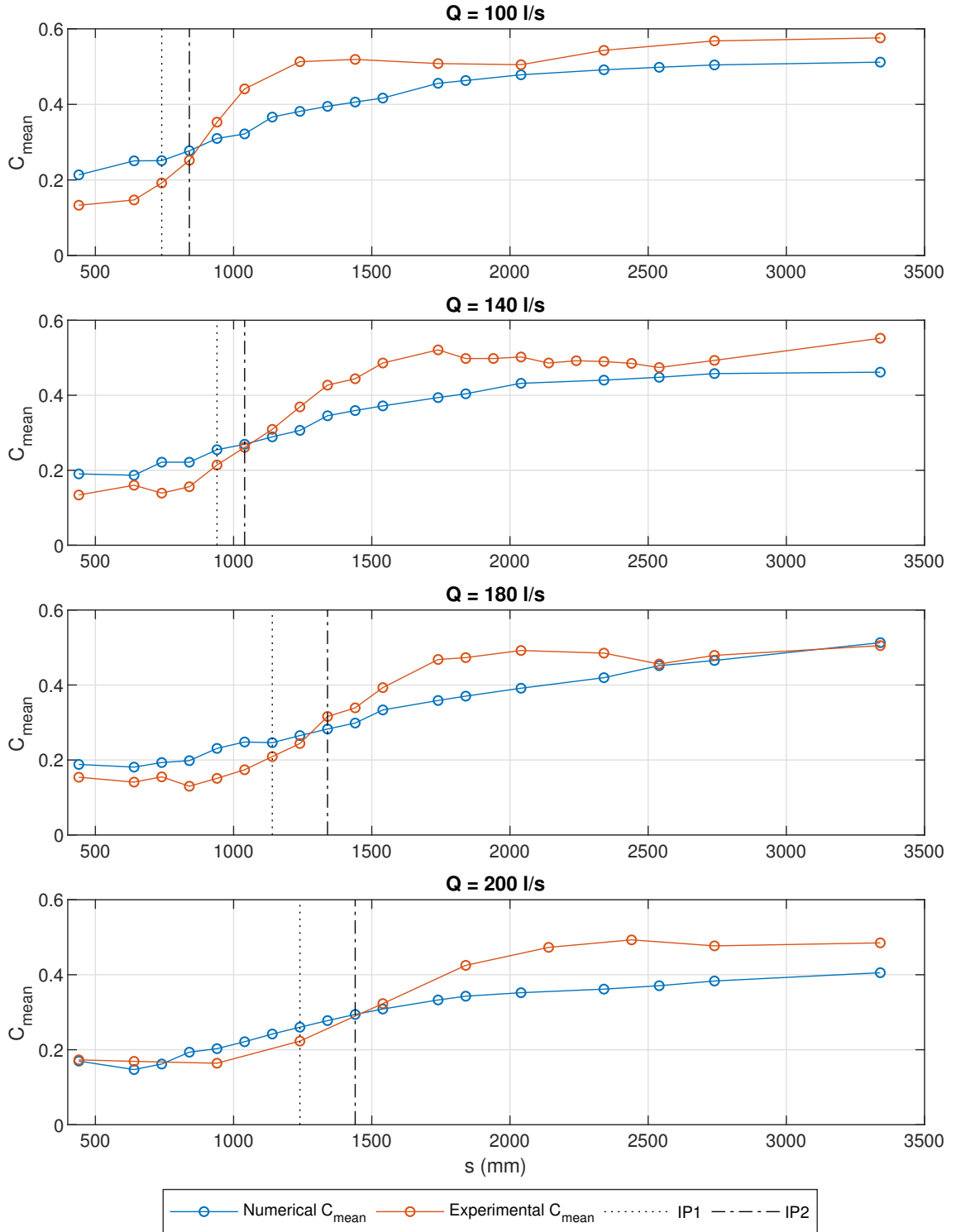


Figure 5.47: Numerical and experimental depth averaged AVFs for all flow rates. The numerical data is shown for the Eulerian multiphase model with the SST $k-\omega$ turbulence model

5. TWO-DIMENSIONAL NUMERICAL MODEL STUDY OF A LARGE EXPERIMENTAL STEPPED SPILLWAY

The value of C_{mean} of 0.2 at the inception point corresponds experimentally to IP1, as can be seen in figure 5.47. The numerical value of C_{mean} , however, is consistently slightly larger than 0.2 at IP1. This result is not surprising since, as previously discussed, the onset of air entrainment appears further upstream than in the experiments, so the numerically predicted value of C_{mean} at the inception point will be slightly higher than the experimental value. Although the numerical model overestimates C_{mean} at IP1, there appears to be roughly the same error at each flow rate. This poses the question: is there a different value of C_{mean} that can be used to predict the location of the inception point using the Eulerian model with the SST $k - \omega$ turbulence model?

Table 5.5 shows the values of C_{mean} at IP1 and IP2 for the Eulerian model with the SST $k - \omega$ model for all flow rates. At both IP1 and IP2 there is reasonable consistency in the values of C_{mean} . At IP1 the mean depth averaged AVF, across the four flow rates investigated, is 0.2530 and the range is 0.0139, which is 5% of the mean. At IP2 the mean depth averaged AVF is 0.2808, with a range of 0.0248, 9% of the mean. This shows considerable consistency and seems to be a reliable method to identify both IP1 and IP2 using the Eulerian model with the SST $k - \omega$ model. For reservoir engineers to use this method with confidence, a large set of experimental and numerical data could be used to create a standard C_{mean} value at the inception point. The inception point could then be defined in the numerical model as the step corner where the C_{mean} is closest to this standard value.

Table 5.5: Depth averaged air volume fractions at IP1 and IP2 for different discharges

| Q (l/s) | Depth Averaged AVF | |
|---------|--------------------|--------|
| | IP1 | IP2 |
| 100 | 0.2511 | 0.2772 |
| 140 | 0.2547 | 0.2693 |
| 180 | 0.2462 | 0.2826 |
| 200 | 0.2601 | 0.2941 |

5.3.6.4 Air Volume Fraction at the Pseudo-Bottom

Boes and Hager (2003a) found the location of the inception point, by visual observation of the surface flow conditions, to correspond with the location where the AVF at the pseudo-bottom is equal to 0.01. Again, only the Eulerian model has been considered in this analysis. Like with the depth averaged AVF, the AVF at the pseudo-bottom reaches 0.01 much further upstream than IP1 and IP2, due to the onset of air entertainment at the crest of the spillway. Therefore,

5.3 Results and Discussion of a 2D Numerical Modelling Study of Skimming Flow over the LNEC Stepped Spillway

again, the values of the AVF at the pseudo-bottom have been recorded for the Eulerian model with the SST $k - \omega$ model at IP1 and IP2 and are shown in table 5.6. At IP1 the mean value is 0.0600 with a range of 0.0158, 25 % of the mean. At IP2 the mean value is 0.0891 with a range of 0.0162, 18 % of the mean. Therefore, although there is a reasonable agreement on the AVF at the pseudo-bottom at IP1 and IP2, there is significantly less consistency than the depth averaged AVF.

Table 5.6: Pseudo-bottom air volume fractions at IP1 and IP2 for different discharges

| Q (l/s) | AVF at Pseudo-Bottom | |
|---------|----------------------|--------|
| | IP1 | IP2 |
| 100 | 0.0695 | 0.0993 |
| 140 | 0.0625 | 0.0831 |
| 180 | 0.0541 | 0.0878 |
| 200 | 0.0537 | 0.0860 |

5.3.7 Prototype Scale Numerical Modelling

The Eulerian model with the SST $k - \omega$ model has been shown to be able to predict the velocities, AVFs, flow depths and inception point locations in the experimental spillway accurately. However, as discussed by Chanson (2013a), a numerical model must be validated against physical data sets at prototype scale in order for the model to be fully trusted to be able to predict prototype scale flows accurately.

Prototype physical model data was not available for this research project. However, the experimental model data can be scaled up to give an indication of the magnitudes of flow variables at prototype scale. The LNEC stepped spillway was numerically modelled at a geometric scale 15 times larger (scale factor, λ , of 15) than the experimental stepped spillway, giving a step height of 1200 mm, which is of sufficient size to represent a prototype scale spillway.

The numerical modelling was conducted in 2D using the Eulerian model with the SST $k - \omega$ model. The numerical domain and mesh was scaled by a factor of 15 in all geometric dimensions. The number of computational cells in each step, and across the channel width, remained the same as the mesh used to model the experimental scale spillway. Symmetry boundary conditions were used at either side of the computational domain. Froude similitude was used to define the prototype scale flow rate, with reference to the 180 l/s experimental flow rate. A Froude number, Fr , of 0.677 resulted in a width averaged flow rate, q , of 0.18 m²/s

5. TWO-DIMENSIONAL NUMERICAL MODEL STUDY OF A LARGE EXPERIMENTAL STEPPED SPILLWAY

in the experimental scale spillway and 10.45 m²/s in the scaled up spillway. The experimental scale AVFs are dimensionless so do not require scaling and the velocities are scaled using Froude similarity by

$$u_p = \sqrt{\lambda} u_{sm} \quad (5.11)$$

where u_p is the velocity in the prototype scale spillway and u_{sm} is the velocity in the experimental scale spillway.

Figure 5.48 shows the velocities predicted by the prototype scale numerical model, the scaled experimental velocities and the scaled numerical velocities predicted by the Eulerian model with the SST $k - \omega$ model at experimental scale at $Q = 180$ l/s. It can be seen that, throughout the spillway, the prototype scale numerical data is in very close agreement with the scaled experimental and numerical velocities.

5.3 Results and Discussion of a 2D Numerical Modelling Study of Skimming Flow over the LNEC Stepped Spillway

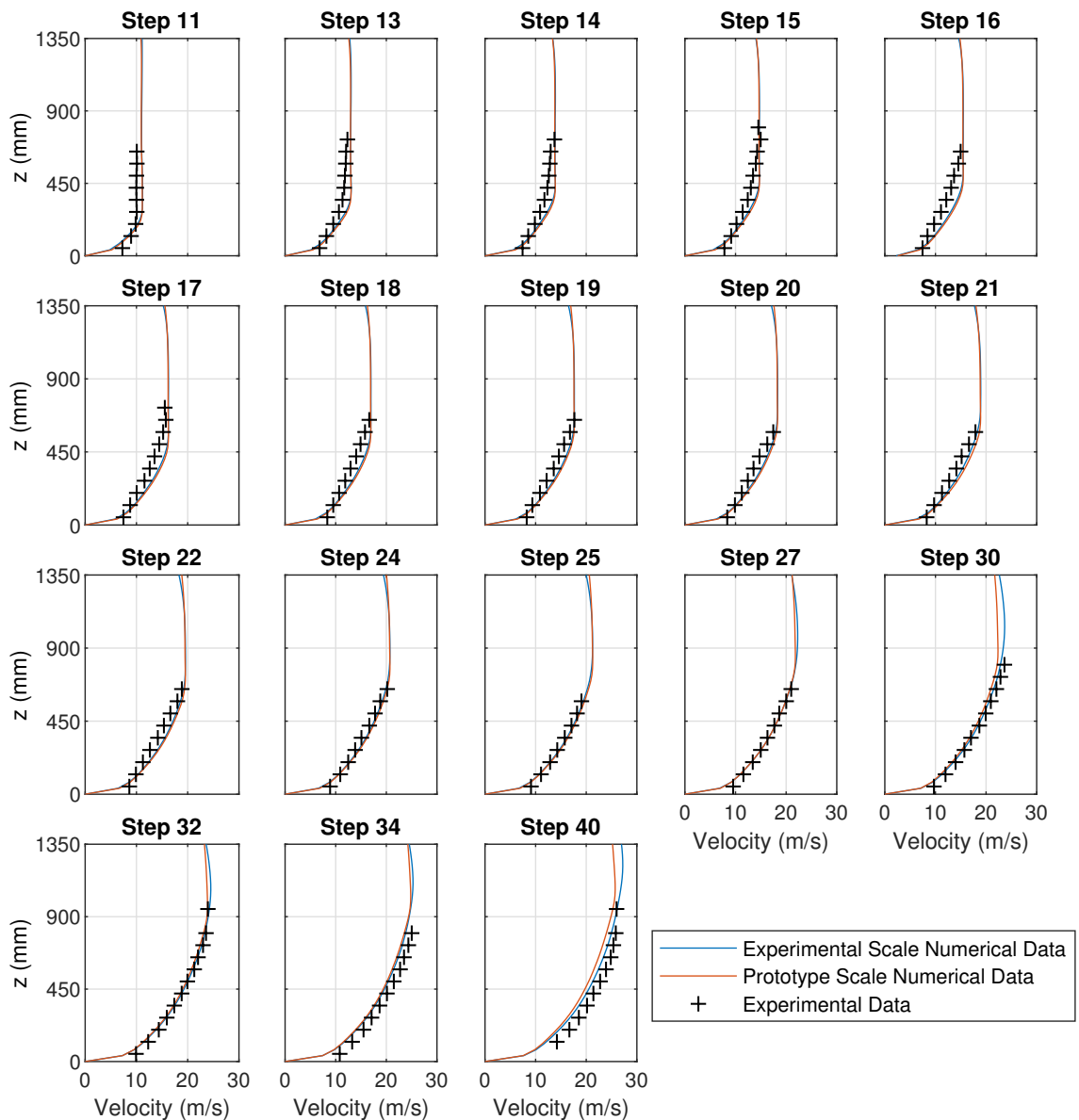


Figure 5.48: Numerical and experimental velocities at prototype scale with $\lambda = 15$. The experimental scale physical and numerical data is scaled using Froude similarity. The Eulerian model with the SST $k - \omega$ model was used for numerical modelling

Figure 5.49 shows the AVFs predicted by the prototype scale numerical model, the experimental AVFs and the scaled numerical AVFs predicted by the Eulerian model with the SST $k - \omega$ model at experimental scale at $Q = 180$ l/s. Note that, although the AVFs are not scaled, the z coordinate at which they are compared is scaled by λ to ensure geometric similarity between the models. There is a greater disparity between the numerically predicted AVFs than there is between the numerically predicted velocities, however, they are still similar to one another and the prototype scale numerical AVFs are in reasonably close agreement

5. TWO-DIMENSIONAL NUMERICAL MODEL STUDY OF A LARGE EXPERIMENTAL STEPPED SPILLWAY

with the experimental AVFs.

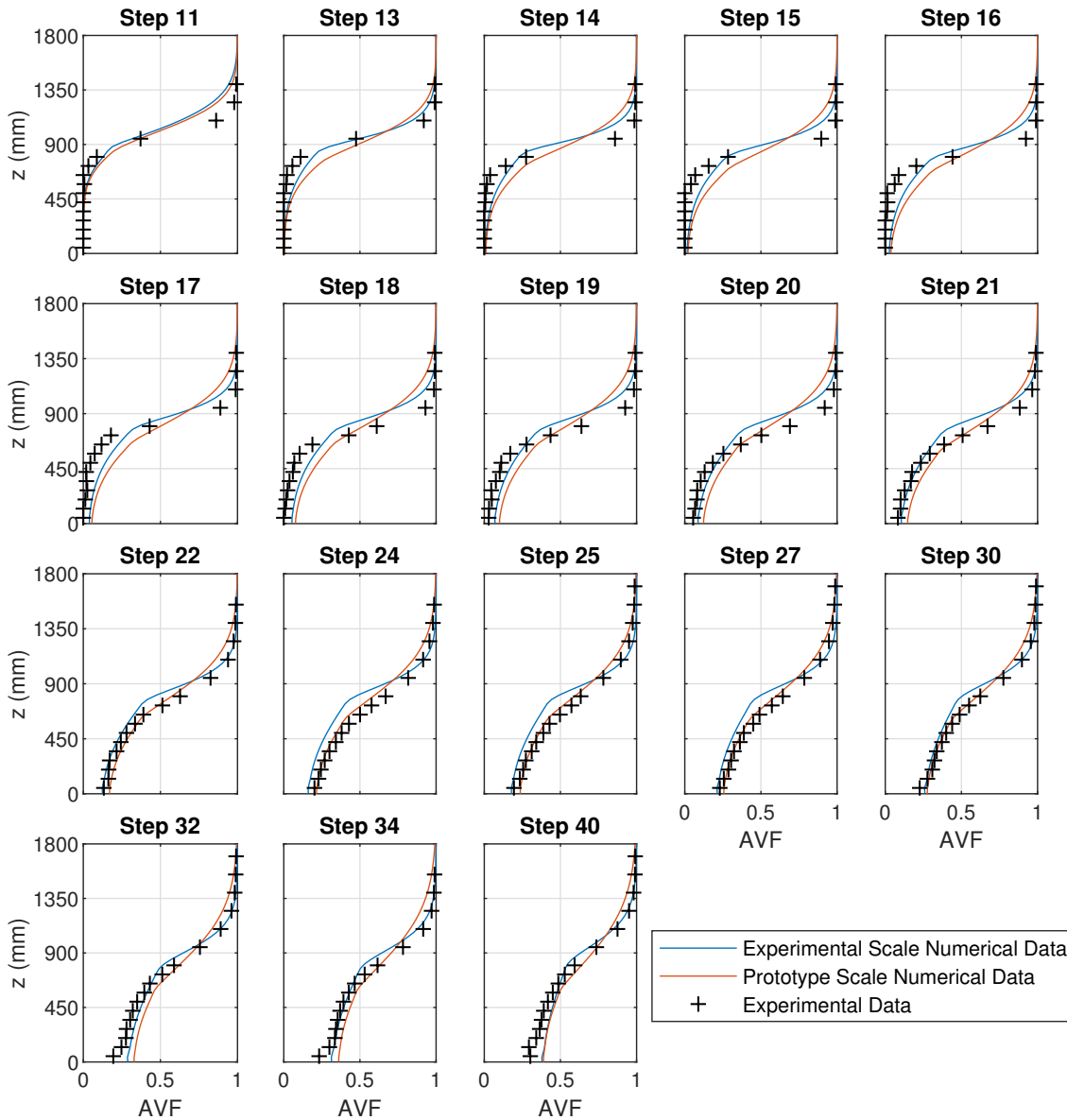


Figure 5.49: Numerical and experimental AVFs at prototype scale with $\lambda = 15$. The Eulerian model with the SST $k - \omega$ model was used for numerical modelling

Numerical modelling, using the Eulerian model with the SST $k - \omega$ model, was conducted in 2D at a geometric scale 15 times larger than the experimental scale spillway. The numerical model predicts velocities which are in close agreement with the scaled numerical and physical velocities and also predicts AVFs which are in reasonably close agreement with the experimental scale numerical and physical data. These results are promising and indicate that the Eulerian model with the SST $k - \omega$ model has the potential to accurately predict velocities and AVFs above the steps at prototype scale spillways. However, full validation of the numer-

ical models against prototype scale physical data sets is required in order for certainty in the numerical model's ability to predict flow features in skimming flows over prototype stepped spillways. Froude scaling has been used in this investigation, however, for full dynamic similarity in air water flows Reynolds and Weber similarity are also required.

5.4 Conclusions

A comprehensive 2D numerical study of a large scale experimental stepped spillway has been conducted using the VOF, mixture and Eulerian multiphase models in combination with the Realisable $k - \epsilon$, RNG $k - \epsilon$ and SST $k - \omega$ turbulence models.

Four flow rates were modelled using the VOF and Eulerian models. The Eulerian model with the SST $k - \omega$ model was found to show very close agreement with the experimental velocities, AVFs and flow depths and was the most accurate combination of multiphase and turbulence model. The location of the inception point was also predicted accurately using several methods of identification. To the best of the author's knowledge, this is the first time the Eulerian model has been used to accurately predict such a wide range of flow variables in complex free-surface aerated flows. This suggests that the Eulerian model has the potential to be used as a reliable tool for predicting skimming flows over stepped spillway. A further implication of these findings is that the Eulerian model may also be able to accurately predict other free-surface flows in which air entrainment is important.

The VOF model and SST $k - \omega$ model made some accurate predictions, however, due to the model's inability to predict air entrainment, it is limited in scope for modelling air-water flows. Both the VOF and Eulerian models made some reasonably accurate predictions using the two $k - \epsilon$ turbulence model, however the SST $k - \omega$ model was found to be the most accurate turbulence model. The mixture model was found to predict velocities, AVFs and flow depths inaccurately with all turbulence models, so only one flow rate was modelled using the mixture model.

The standard $k - \epsilon$, standard $k - \omega$ and Reynold's stress turbulence models were also investigated, in combination with the Eulerian multiphase model. The Reynolds stress model did not predict velocities, AVFs or flow depths accurately. It was found that the standard $k - \epsilon$ model produced very similar solutions to the Realisable and RNG $k - \epsilon$ models and the standard $k - \omega$ model produced extremely similar results to the SST $k - \omega$ model. As the SST

5. TWO-DIMENSIONAL NUMERICAL MODEL STUDY OF A LARGE EXPERIMENTAL STEPPED SPILLWAY

$k - \omega$ model is a blend between the $k - \omega$ model near the wall and the $k - \epsilon$ model in the free stream, these results suggest that it is the behaviour of the turbulence models near the wall which cause the differences observed between the turbulence models. The $k - \epsilon$ models predict a shorter reattachment length of the recirculating vortices in the step cavities than the $k - \omega$ models. The shorter reattachment length generates significantly more turbulence along the pseudo-bottom which may be the cause of the less accurate prediction of the flow characteristics above the pseudo-bottom.

In order to determine whether the numerical models are able to accurately predict the location of the inception point, the intersection of the equivalent clear water depth and the TBL was identified for all multiphase and turbulence models. The VOF model, with the $k - \epsilon$ turbulence models, was found to consistently overestimate the location of the intersection of d and the TBL. The predicted position of the intersection, however, is also consistently close to the experimental location of the inception point by visual inspection. Although the location of the intersection is overestimated, the consistency of the results means that this method of identifying the location of the inception point may be a useful tool for reservoir engineers. The Eulerian model, with the $k - \epsilon$ turbulence models, was found to predict the location of the intersection of d and the TBL extremely accurately, however the SST $k - \omega$ model predicted the intersection to occur much further downstream. Several other methods of identifying the location of the inception point were investigated using the Eulerian model with the SST $k - \omega$ turbulence model. It was found that the inception point location can be reliably identified by visual inspection of the AVF contours and also by the depth averaged AVF. The value of the depth averaged AVF at the inception point in the numerical model, however, is slightly higher than that found in other experimental studies.

Numerical modelling of the LNEC stepped spillway was conducted at a geometric scale 15 times larger than the experimental spillway, in order to investigate the numerical model's ability to predict skimming flows at prototype scale. The numerical modelling was conducted using the Eulerian model with the SST $k - \omega$ model and velocities and AVFs were compared to scaled experimental and numerical data. The velocities were in close agreement and the AVFs were in reasonably close agreement. These results are promising and suggest that the Eulerian model with the SST $k - \omega$ model has the potential to accurately predict skimming flows at prototype scale. However, full validation against prototype scale physical data sets is required in order to confirm this.

CHAPTER 6

Three-dimensional Numerical Model Study of a
Narrow Stepped Spillway at the University of
Leeds

6.1 Introduction

This chapter presents an in-depth, 3D numerical model study of the University of Leeds stepped spillway, which is described in chapter 3. In chapter 5, the VOF Eulerian and mixture models were investigated in 2D. In the experimental stepped spillway which is modelled in this chapter, however, complex 3D vortex structures are observed in the step cavities, and the free-surface has a 3D profile. In this chapter, numerical modelling is extended to 3D in order to investigate the ability of the different numerical models to predict the 3D flow behaviour observed in the experimental spillway.

Free-surface aeration is challenging to model numerically. In chapter 5, it was demonstrated that the Eulerian multiphase model is able to accurately predict a number of important flow features of aerated skimming flow over stepped spillways, including air volume fraction (AVF) profiles and velocities, in 2D. This chapter will investigate whether 3D numerical modelling using the Eulerian model can also accurately predict the pressures acting on the step faces and side walls, the flow depths and the complex 3D vortex structures observed in the experimental stepped spillway. A number of methods to identify the location of the inception point in the numerical models are also considered.

The VOF model is unable to predict air entrainment, for the reasons described in chapter 4. This was demonstrated in chapter 5. Despite this, the VOF model is able to accurately predict certain flow features in aerated flows, such as velocities, as also demonstrated in chapter 5. The VOF model remains the most common numerical modelling approach for free-surface flow and, as such, is used in this study for comparison and contrast with other multiphase models which are able to predict air entrainment.

In chapter 5, the mixture model was shown to be able to predict air entrainment. However, the model was unable to predict AVFs, or other flow features, such as velocity, as accurately as other multiphase models. The mixture model, however, is also investigated in this chapter, again, for comparison with other multiphase models.

6.2 Modelling Procedure

The VOF, mixture and Eulerian multiphase models are investigated in conjunction with the Realisable $k - \epsilon$, RNG $k - \epsilon$ and SST $k - \omega$ RANS turbulence models. In chapter 5, the SST $k - \omega$ model was generally found to be the most accurate of these RANS turbulence models.

However, as different flow parameters are investigated in this chapter, and 3D behaviour is also observed, several RANS models have been implemented so that comparisons between the turbulence models can be made.

The numerical models are implemented in the same manner as in chapter 5. All modelling is conducted using ANSYS Fluent v17.2 and all models are run transiently, until a steady state is achieved, whereby there is negligible variation in flow variables over time. There is one exception to this, where a steady state solution is not achieved. This case is described in detail in section 6.3.5. In this case, time averaged values are used for comparison with the experimental data, which is also time averaged.

All numerical modelling in this chapter utilises enhanced wall treatment (EWT), which is insensitive to y^+ (described in chapter 4). This insensitivity to y^+ is important in predicting skimming flows, as the recirculating vortices cause y^+ values within the step cavities to vary significantly over short distances, when a mesh of constant density is used. Despite EWT's insensitivity to y^+ , it is generally considered that y^+ values should be below 300. For all numerical modelling conducted in this chapter, most of the y^+ values on the step faces and spillway side walls are below 100, and no y^+ values above 150 are found.

6.2.1 Domain

The 3D domain and mesh used for numerical modelling is shown in figure 6.1, as viewed from the side. More details on the mesh are found in section 6.2.2.1. In the numerical domain, the outflow end box of the experimental spillway (figure 3.3) was not included, as this region is not of interest to this project. The outlet of the domain consists of a pressure outlet at the vertical boundary, at the end of the outflow channel. The inflow end box of the experimental spillway (figure 3.3) was modelled with a rectangular cross-section, rather than as a cylinder, so that a structured computational mesh could be easily constructed. Only the topmost section of the inflow end box is included in the domain. The rectangular cross-section has the same width as the main channel, a length of 200 mm and the velocity inlet boundary condition is located 300 mm below the approach channel. The top boundary of the domain follows the same profile as the bottom boundary, again to aid in the construction of a structured mesh. A pressure outlet boundary condition is used at the top of the domain. The spillway is modelled in 3D and, as the spillway is symmetrical about the centreline, only half of the channel width is modelled, with a symmetry boundary condition used at the centreline of the spillway. This halves the

6. THREE-DIMENSIONAL NUMERICAL MODEL STUDY OF A NARROW STEPPED SPILLWAY AT THE UNIVERSITY OF LEEDS

number of computational cells in the domain, significantly reducing the computational cost of numerical modelling. The spillway steps and side walls are modelled using a wall boundary condition.

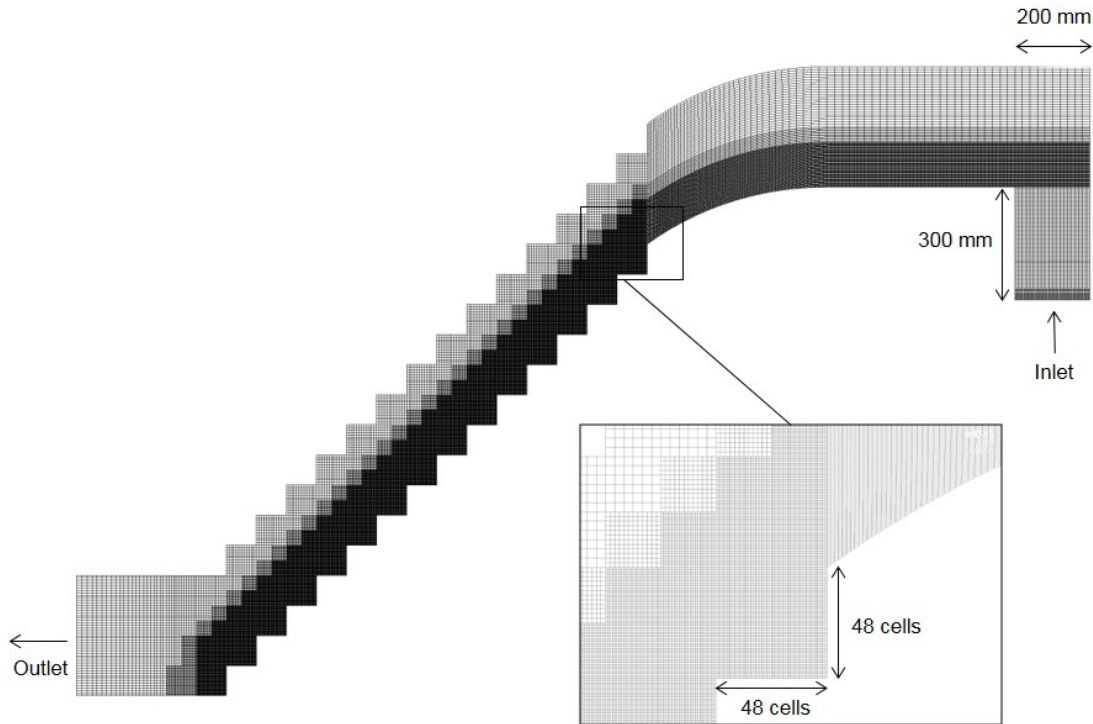


Figure 6.1: Diagram of the 3D domain and mesh used for numerical modelling of the experimental stepped spillway at the University of Leeds. The mesh is refined at the steps, inlet and approach channel in order to reduce the computational cost of simulations. The total number of cells within the domain is 4243488

6.2.2 Numerical Error

Grid convergence and time step independence studies have been conducted in order to quantify and minimise the discretisation errors which are discussed in chapter 4. Grid convergence analysis has been conducted using the Eulerian, VOF and mixture models, all in combination with the Realisable $k - \epsilon$ turbulence mode. Although the SST $k - \omega$ was found to generally be more accurate than the Realisable $k - \epsilon$ model in chapter 5, transient behaviour was observed in the free-surface profile when the VOF model was used with the SST $k - \omega$ model (discussed further in section 6.3.5). The transient behaviour may have added complications in the analysis of the grid convergence with the VOF model, so the Realisable $k - \epsilon$ model was used instead. Analysis of the Eulerian model is presented in this chapter. Similar results were found for the VOF and mixture models, which are presented in appendix A. All

grid convergence analysis is conducted at a flow rate of $Q = 15$ l/s.

6.2.2.1 Grid Convergence

The grid convergence index (GCI) method has been used to assess the numerical error due to mesh resolution. This method is described in detail in chapter 5 and appendix A. Details of the three computational meshes used in the study are presented in table 6.1.

Table 6.1: Numbers of cells and cell sizes for meshes used in the grid convergence study

| Mesh | Step Faces | | Half Channel Width | | Total Number of Cells |
|--------|-----------------|----------------|--------------------|----------------|-----------------------|
| | Number of cells | Cell Size (mm) | Number of Cells | Cell Size (mm) | |
| Mesh 1 | 32 | 2.50 | 32 | 2.34 | 1261760 |
| Mesh 2 | 48 | 1.67 | 48 | 1.56 | 4243488 |
| Mesh 3 | 64 | 1.25 | 64 | 1.17 | 9630848 |

Pressure

Figure 6.2 shows pressure data for meshes 1, 2 and 3, at different locations within the cavities of steps 2, 5 and 12. The strong agreement between all three meshes can be seen, with only marginal differences observed at certain points. The GCI data and asymptotic verification (AV) data at each location is also presented. On the horizontal step face of step 5, it can be seen that the pressures predicted by all three meshes are extremely similar. The GCI errors are small and the AV values are close to 1 at all locations other than at the far downstream end of the step. The large GCI error and the low AV value are caused by a large difference between the pressures predicted with meshes 1 and 2 at $l = 78.4$ mm. However, the pressure data on the horizontal step face of step 2 generally demonstrate that the solutions are independent of grid resolution.

On the vertical step face of step 12, the pressure profiles predicted with the three meshes are also very similar, however, there are large GCI errors at certain positions and the AV values differ from 1 significantly towards the top of the step. These results are a consequence of the GCI method. The pressure profiles predicted with the three meshes can be observed to be extremely similar at most locations. A result of this is that, the difference in pressure between meshes 1 and 2, at a particular position, may be very similar to the difference in pressure between meshes 2 and 3. As discussed in appendix A, this causes denominator of equation (5.3) to be small, which in turn produces a large GCI error. The AV values differ

6. THREE-DIMENSIONAL NUMERICAL MODEL STUDY OF A NARROW STEPPED SPILLWAY AT THE UNIVERSITY OF LEEDS

from 1 because the solution is not within the asymptotic range. This is caused by a smaller difference in pressure between meshes 1 and 2 than between meshes 2 and 3 which is the opposite trend than would be required for the solutions to be in the asymptotic range.

The large GCI errors, and AV values which are not close to 1, are caused by the fact that the pressures predicted with the three meshes are extremely similar. At a particular position the differences in the pressures predicted by the three meshes may produce GCI and AV values which suggest that grid convergence has not been achieved. However, the magnitude of these differences are small and refinement of the mesh has not resulted in any significant difference in the pressure profiles, which demonstrates that the solution is independent of grid refinement.

At the wall of step 2, in figure 6.2, the pressures predicted with the three meshes are, again, very similar. The GCI errors are generally small, however, at the higher values of l they are larger. The same trend is shown by the AV values, which are close to 1 at the lower values of l but are further from 1 at the higher values of l . It can be seen that, at the higher values of l , the pressure predicted with mesh 1 differs slightly from the pressure data for meshes 2 and 3, which are extremely similar. This similarity in the pressures predicted with meshes 2 and 3 suggests that further refinement of the computational mesh would not have a meaningful effect on the pressures predicted in this location.

The GCI approach is a useful method for quantifying the numerical errors caused by mesh resolution. However, in certain cases, as demonstrated above, the GCI errors and AV values may produce misleading results. It is important, when analysing grid convergence, that all of the data is considered in order to ascertain whether further refinement of the computational mesh is required to minimise numerical error.

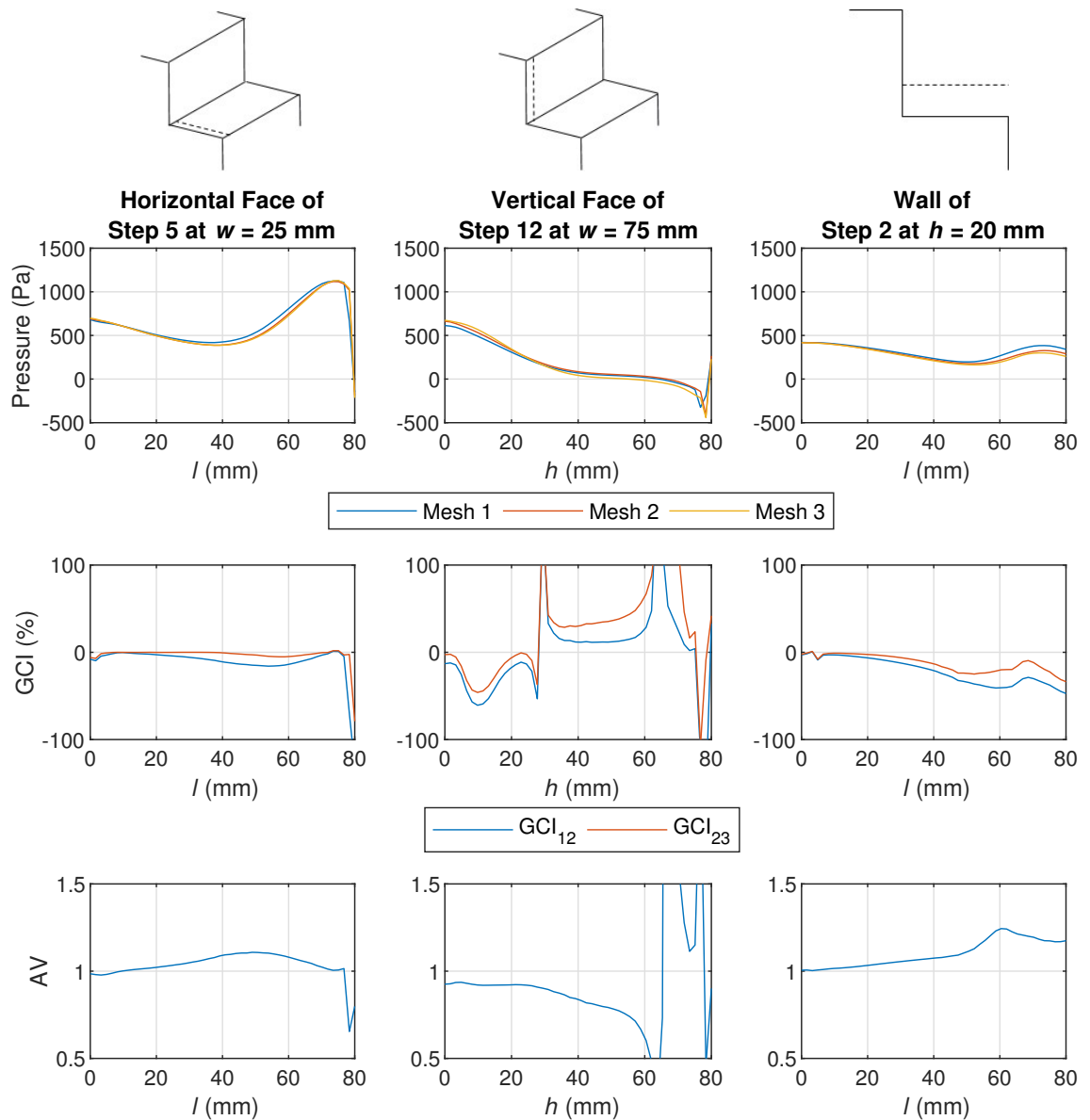


Figure 6.2: Grid convergence pressure data for three meshes at several locations within the spillway, calculated using the Eulerian multiphase model with the Realisable $k - \epsilon$ turbulence model. The pressure data, grid convergence index error and asymptotic verification values are displayed

Flow Depths

Figure 6.3 shows the flow depths for the three meshes, as well as the GCI errors and AV values, at the centreline of the spillway. Generally, the depths predicted with meshes 2 and 3 are reasonably close to one another and those predicted with mesh 1 are slightly further away. The GCI errors are reasonably small in the majority of locations, especially GCI_{23} . Between $x = 200$ mm and $x = 400$ mm, and at the far downstream region of the spillway, the errors are

6. THREE-DIMENSIONAL NUMERICAL MODEL STUDY OF A NARROW STEPPED SPILLWAY AT THE UNIVERSITY OF LEEDS

extremely large. It can be seen that in these positions the difference in flow depth between meshes 1 and 2 is similar to that between 3 and 4. For the reasons discussed above this produces a large GCI error.

Throughout the spillway the AV values are close to 1, which demonstrates that the solutions are within the asymptotic range. Although there is a noticeable difference in the flow depths predicted with meshes 2 and 3, the difference is generally small the fact that the data falls within the asymptotic range suggests that further refinement of the computational grid would not have a significant effect on the flow depths predicted by the numerical model.

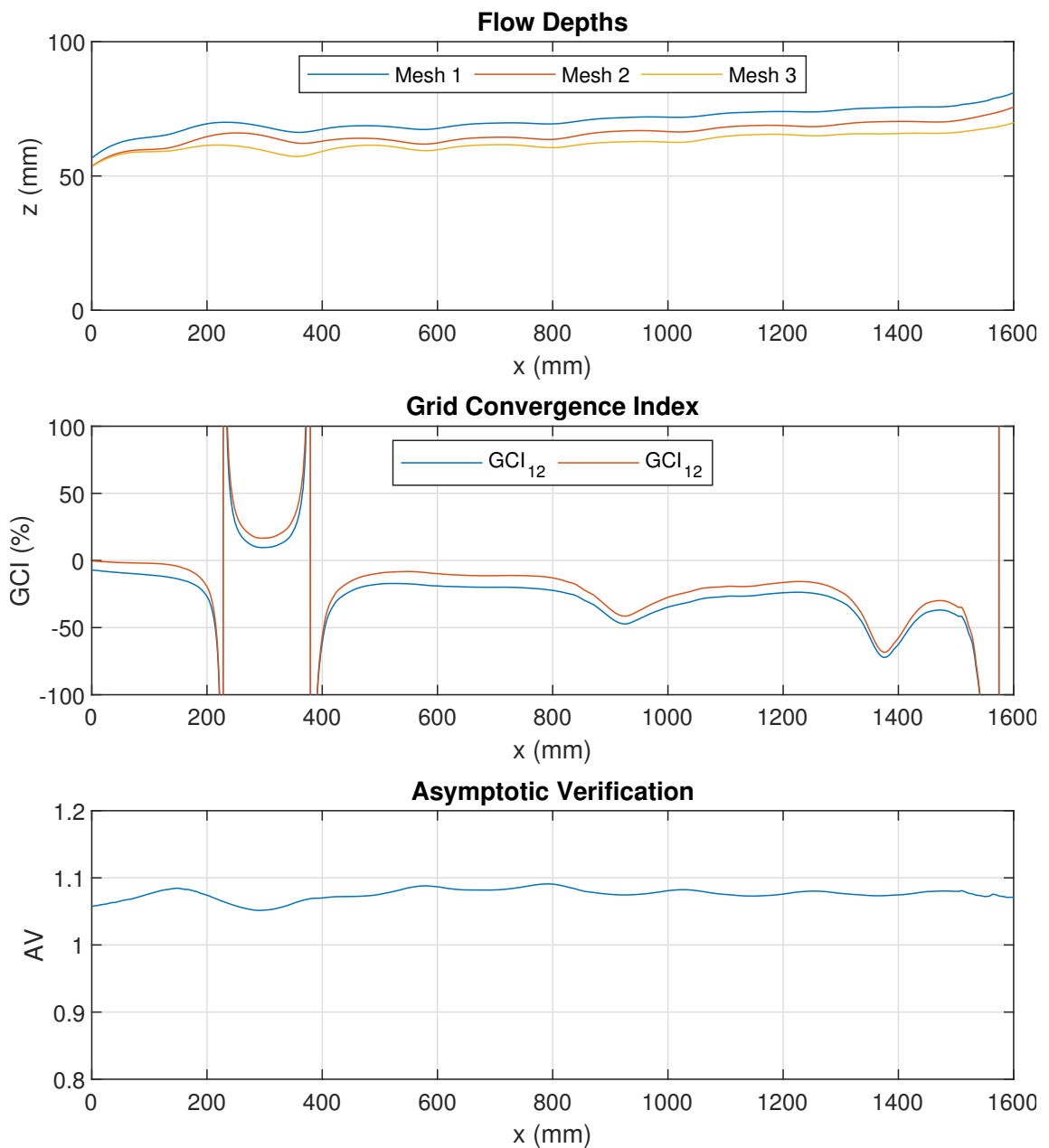


Figure 6.3: Grid convergence flow depth data for three meshes, calculated using the Eulerian multiphase model with the Realisable $k - \epsilon$ turbulence model. The pressure data, grid convergence index error and asymptotic verification values are displayed. Flow depths are displayed at the centreline of the spillway

Figures 6.2 and 6.3 support the case that pressures and flow depths are judged to be independent of the grid resolution. The velocities above the steps were also investigated and showed grid independence. The VOF and mixture models also produced similarly mesh independent results (see appendix B). Therefore, mesh 2 has been used for all subsequent numerical modelling presented in this chapter.

Figure 6.1 shows the computational mesh as viewed from the side. As in chapter 5, the

6. THREE-DIMENSIONAL NUMERICAL MODEL STUDY OF A NARROW STEPPED SPILLWAY AT THE UNIVERSITY OF LEEDS

mesh has been refined near the steps, along the approach channel and at the inlet. This allows a coarser mesh to be used in less critical areas, which significantly reduces the computational cost required for numerical modelling.

6.2.2.2 Time Step Independence

As all simulations have been conducted transiently, a time step independence study was conducted in order to ensure that the time step used for numerical modelling did not affect the solution. Simulations were conducted using the Eulerian, VOF and mixture models in combination with the Realisable $k - \epsilon$ turbulence model. Again, the Realisable $k - \epsilon$ model was used to analyse time step independence due to the transient behaviour observed in the free-surface predicted by the VOF model with the SST $k - \omega$ mode (section 6.3.5). The Eulerian model results are presented in this chapter and the VOF and mixture model results are presented in appendix B. Modelling was conducted at a flow rate of $Q = 15$ l/s, using time steps of 1×10^{-3} s and 5×10^{-4} s.

Figure 6.4 shows the pressures predicted using the two time steps investigated, in the same locations that were considered in the grid convergence analysis. Figure 6.5 shows the flow depths predicted by the numerical model, using the two different time steps investigated, at the centreline of the spillway. Both figures show that the pressures and flow depths predicted using the two different time steps are almost identical. The VOF and mixture models also produced near identical results when these two different time steps are used to calculate the solution. Therefore, a time step of 1×10^{-3} s has been used for all subsequent numerical modelling presented in this chapter.

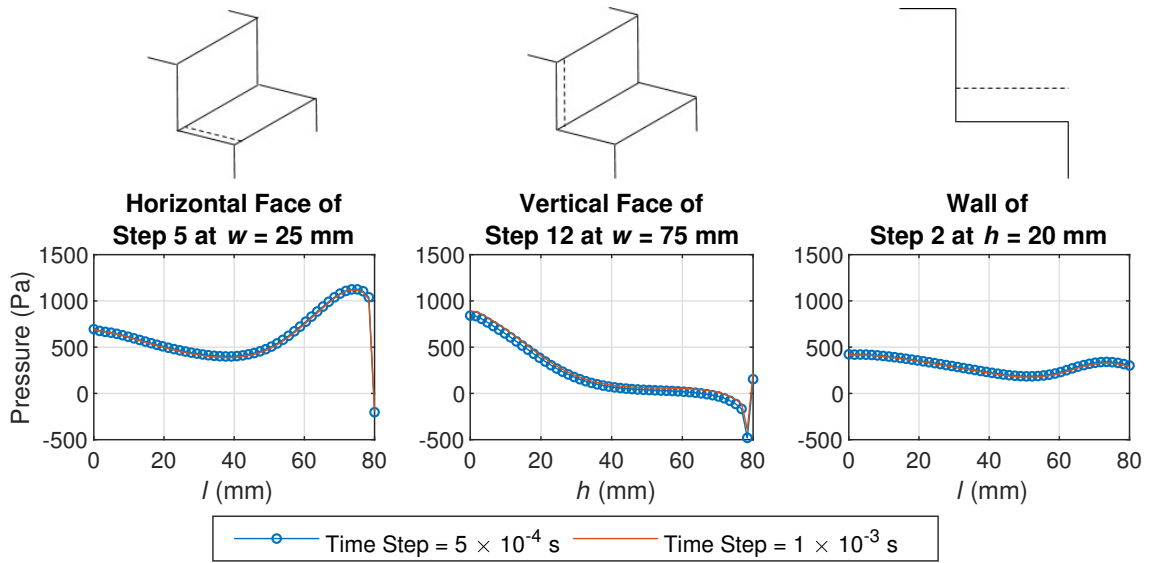


Figure 6.4: Pressure data at several locations within the spillway, calculated using two different time steps. The Eulerian multiphase model with the Realisable $k - \epsilon$ turbulence model was used for numerical modelling

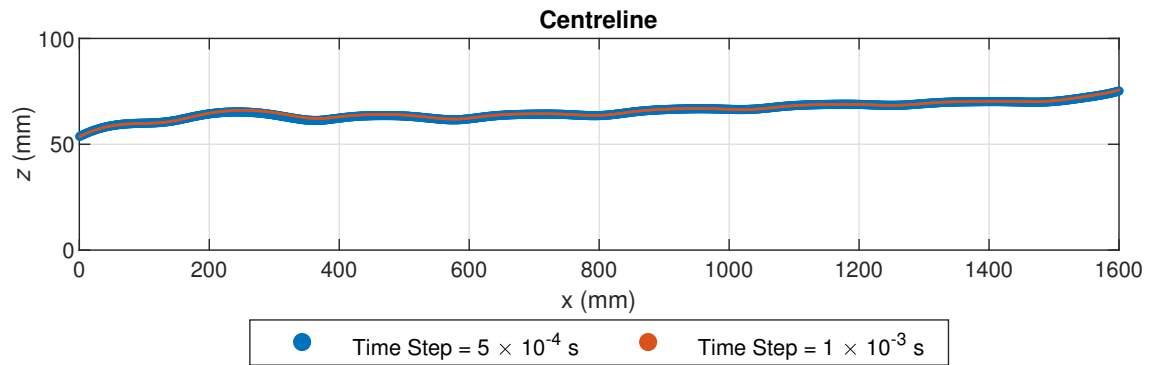


Figure 6.5: Flow depth data calculated using two different time steps. The Eulerian multiphase model with the Realisable $k - \epsilon$ turbulence model was used for numerical modelling. Flow depths are displayed at the centreline of the spillway

6.3 Results and Discussion of a 3D Numerical Modelling Study of Skimming Flow over the University of Leeds Stepped Spillway

This section presents the results of 3D numerical modelling of the University of Leeds stepped spillway, using the VOF, mixture and Eulerian models in combination with three RANS turbulence models. The solutions have been judged to be independent of grid resolution and time step size by the analysis conducted in section 6.2.2.

The 3D behaviour and air entrainment predicted by the numerical models is analysed, as is the time dependent behaviour predicted by the VOF model with the SST $k - \omega$ model. The Numerically predicted pressures acting on the spillway steps and side walls, and the flow depths at the spillway wall and centreline, are compared to the experimentally measured data. The last part of this section considers a number of methods for predicting the location of the inception point.

6.3.1 3D Free-Surface Profiles

Due to the relatively narrow width of the channel, significant wall effects can be observed across the entire width of the the channel, in both the experiments and the numerical models. Figure 6.6 shows isosurfaces of an AVF of 0.9 for all three multiphase models, with the SST $k - \omega$ turbulence model. The isosurfaces represent y_{90} and can be considered the numerical free-surfaces. It can be seen that, in all three multiphase models, at around the third step the free-surface increases in depth significantly at the wall. It can be seen that downstream of this position all three multiphase models show significant variation in the flow depth across the channel width and the free-surface profile is distinctly 3D.

The VOF model predicts that, in the downstream section of the spillway, there is "splashing" which is created close to the wall and meets at the centreline of the spillway. 3D free-surface profiles are predicted by all turbulence models and at all flow rates. The splashing, however, is only predicted by the VOF model with the SST $k - \omega$ model. Isosurfaces of y_{90} for the other flow rates considered are shown in appendix B. Further analysis of the variation in flow depth across the width of the channel is conducted in section 6.3.7.

6.3 Results and Discussion of a 3D Numerical Modelling Study of Skimming Flow over the University of Leeds Stepped Spillway

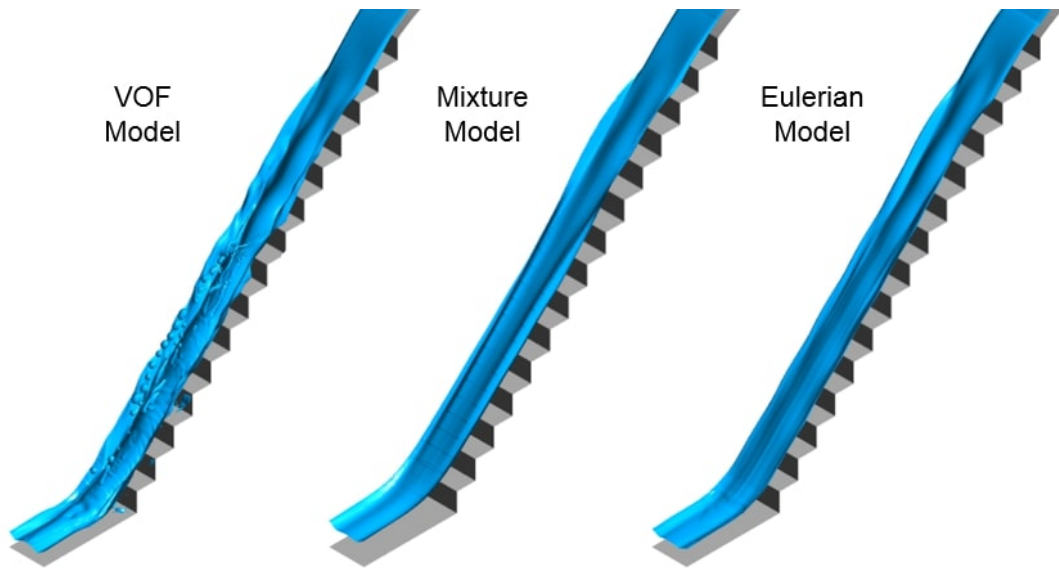


Figure 6.6: Isosurfaces at air volume fractions of 0.9 for the VOF, mixture and Eulerian multiphase models, with the SST $k - \omega$ turbulence model, at $Q = 15$ l/s. The images are mirrored at the centreline of the spillway due to the symmetry boundary condition used centreline

Figure 6.7 shows the experimental stepped spillways from the side and from the front of the steps. It can be seen that significant splashing takes place in a similar location to that predicted by the VOF model. This shows that the VOF model with the SST $k - \omega$ model is able to capture an aspect of time dependent splashing behavior that is consistent with that observed in the experiments. This splashing is not observed in the mixture or Eulerian models. A potential reason for this may be that the VOF model has a sharp free-surface between air and water, whereas both the mixture and Eulerian models have diffuse layers of increasing AVF. These diffuse layers may prevent individual "splashes" of water forming, whereas the sharp free-surface in the VOF model may allow them to form. The splashing predicted by the VOF model with the SST $k - \omega$ model is discussed further in section 6.3.5.

6. THREE-DIMENSIONAL NUMERICAL MODEL STUDY OF A NARROW STEPPED SPILLWAY AT THE UNIVERSITY OF LEEDS

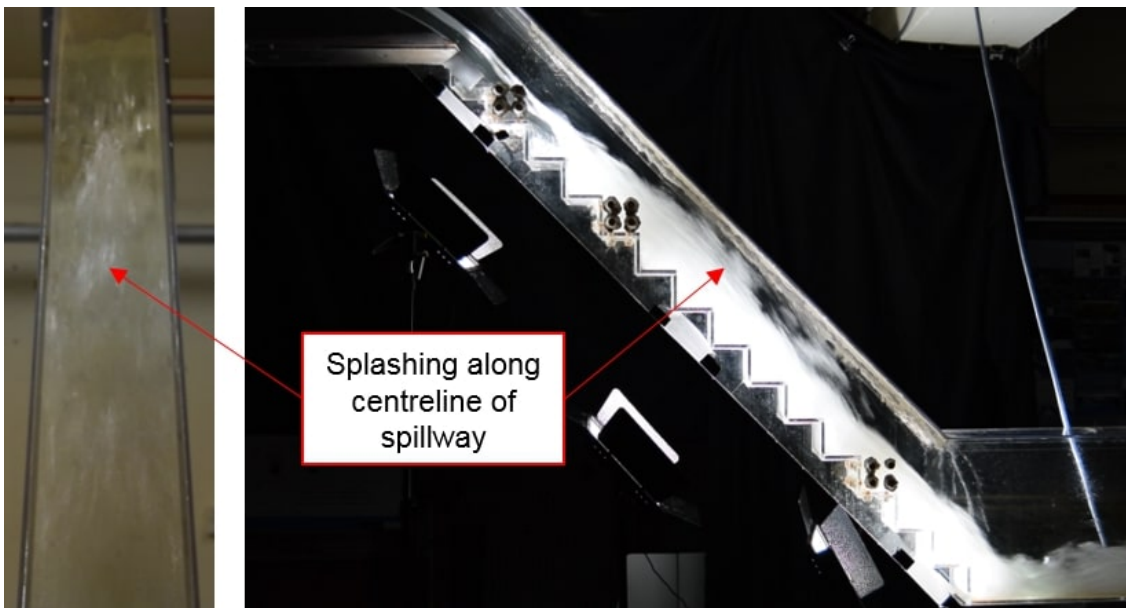


Figure 6.7: Images showing splashing occurring at the centreline of the experimental stepped spillway. Splashing can be observed from in front of the spillway as well as from the side of the spillway

6.3.2 Air Entrainment

Figure 6.8 shows AVF contours at the centreline of the spillway for the VOF, mixture and Eulerian multiphase models, at $Q = 15$ l/s. In each case, data for the Realisable $k - \epsilon$ turbulence model has been displayed. The AVF contours show very similar results to those of the LNEC stepped spillway shown in chapter 5. No air entrainment is shown in the VOF model. This is to be expected for the reasons described in chapter 4. The mixture and Eulerian models do show air entrainment. For both models, the non-aerated region is visible in the upstream region of the spillway where no air is present in the step cavities. Further downstream air is transported into the step cavities and the entire flow becomes aerated.

Similarly to the numerical models of the LNEC stepped spillway, the onset of air entrainment in the Eulerian and mixture models appears to be at the crest of the spillway. The mixture model predicts some air entrainment even further upstream, which can be seen by the diffuse free-surface. It is hypothesised that the air entrainment, predicted by the Eulerian and mixture models, close to the spillway crest is a consequence of the implementation of surface tension in these two models. This is discussed further in Chapter 5. It was demonstrated in chapter 5 that the Eulerian model with the SST $k - \omega$ predicts the AVFs above the steps in the fully aerated region accurately. This suggests that entrainment of air at the crest of the spillway does not significantly affect the AVF profiles in the fully aerated region. The AVF contours in

6.3 Results and Discussion of a 3D Numerical Modelling Study of Skimming Flow over the University of Leeds Stepped Spillway

figure 6.8 are displayed at the centreline of the spillway. Similarly to the free-surface, there is also some variation in the AVFs across the width of the channel. This is discussed further in section 6.3.8.

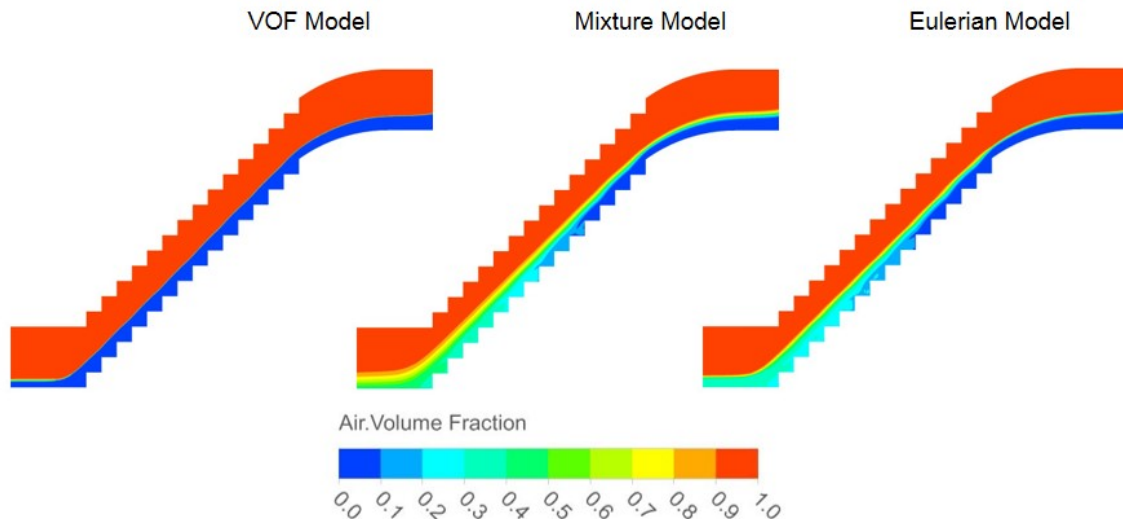


Figure 6.8: Contours of air volume fraction for the the VOF, mixture and Eulerian models at $Q = 15$ l/s. The contours are displayed at the spillway centreline and data for the Realisable $k - \epsilon$ turbulence model has been displayed in each case

6.3.3 Cross-Stream Vortices

Figure 6.9 shows streamlines seeded within the step cavities of steps 7 and 8 from four different view points. Figure 6.9 (a) shows a 3D view of the steps, figure 6.9 (b) shows a view from the side of the steps, figure 6.9 (c) shows a view from behind the steps and figure 6.9 (d) shows a view from beneath the steps. The data shown was calculated using the Eulerian multiphase model with the SST $k - \omega$ turbulence model. These images have been shown as an example of the flow conditions within the steps and a similar pattern of streamlines is shown for all combinations of multiphase and turbulence model and at all flow rates.

The streamlines in figure 6.9 (a) show that, as in the experimental model, the flow within the step cavities is not uniform across the channel width. At step 7, there are two vortices within the step cavity which are orientated diagonally from the centreline at the upstream end of the horizontal step face, to the wall at the downstream end of the horizontal step face. At step 8, there are also two vortices, however, they have the opposite orientation, which is diagonal from the wall at the upstream end of the horizontal step face, to the centreline at the downstream end of the horizontal step face. This alternating pattern of diagonally oriented

6. THREE-DIMENSIONAL NUMERICAL MODEL STUDY OF A NARROW STEPPED SPILLWAY AT THE UNIVERSITY OF LEEDS

vortices can also be clearly seen in figure 6.9, the view from beneath the steps.

In chapter 3, the vortices within the step cavities were described as stream-wise vortices and cross-stream vortices, depending on their orientation. This is due to the fact that the vortices within in the step cavities of the experimental model were viewed in 2D planes, from either the side of the spillway or from behind the steps. Figure 6.9 (b) shows the view of the streamlines from the side of the spillway. From this viewpoint, the streamlines show stream-wise vortices similar to those observed in the experimental model and depicted in figure 3.9. Figure 6.9 (c) shows the view of the streamlines from behind the spillway. From this viewpoint, the streamlines clearly show the cross-stream vortices, which change direction at each step, similar to those observed in the experimental model and shown in figure 3.8. However, it is clear from figure 6.9 (a) that there is no distinction between the stream-wise and cross-stream vortices and, in fact, they are the same vortices which are 3D and are orientated diagonally across the horizontal step face, with the direction depending on the step number. This pattern of vortices, which are not orientated in the direction of the main flow, will continue to be referred to as cross-stream vortices.

6.3 Results and Discussion of a 3D Numerical Modelling Study of Skimming Flow over the University of Leeds Stepped Spillway

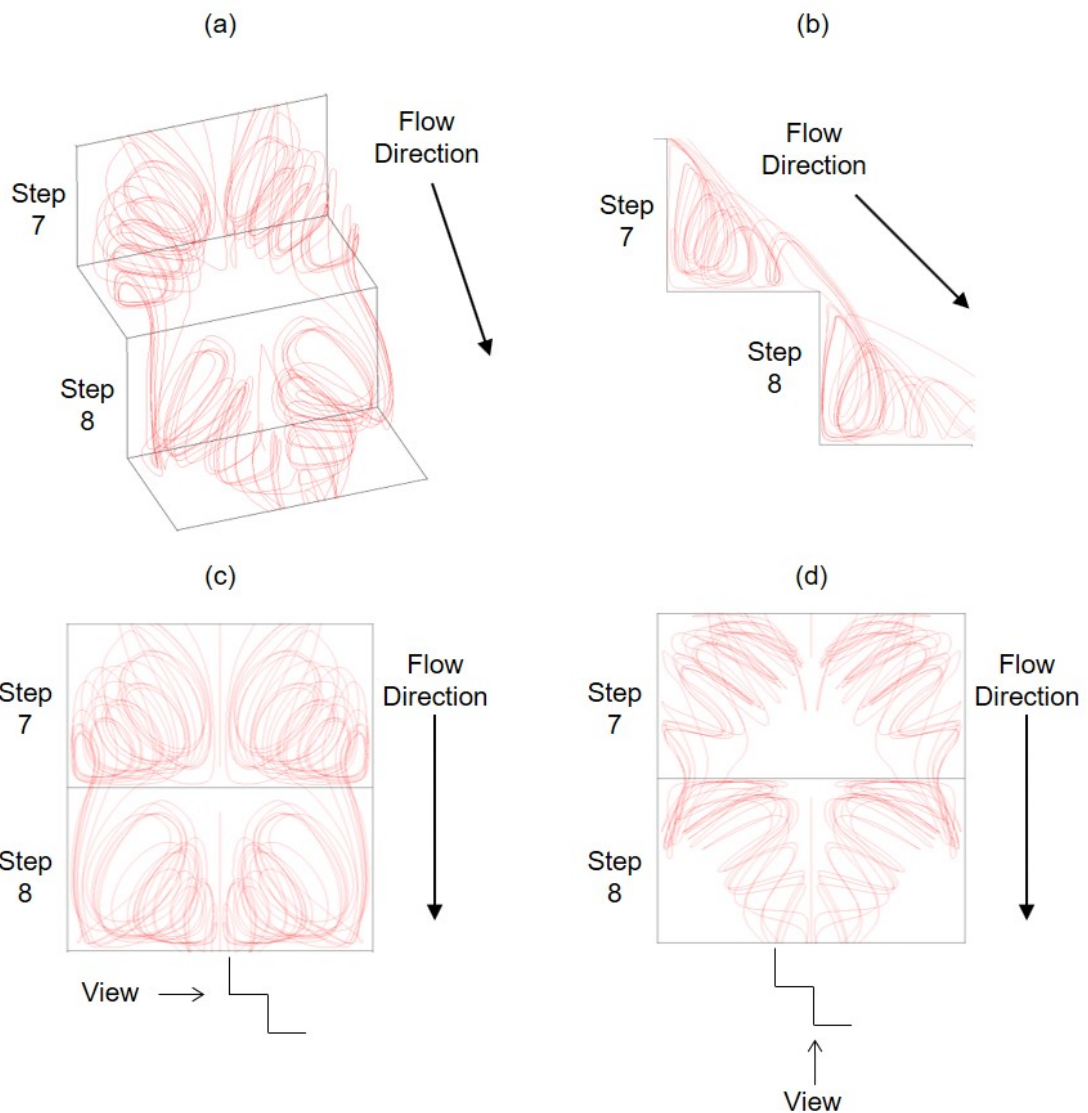


Figure 6.9: Numerical streamlines at steps 7 and 8 from four different view points: (a) 3D view of the steps; (b) view from the side of the steps; (c) view from behind the steps; (d) view from beneath the steps. The step geometry is displayed in black and the streamlines are displayed in red. The streamlines are shown for the Eulerian model with the SST $k - \omega$ model

Figure 6.10 shows pressure contours acting on the step faces of steps 7 and 8, and streamlines seeded within the step cavities, for various combinations of multiphase and turbulence models, at $Q = 12$ l/s. Again, these images have been used as an example of the flow conditions within the steps and a similar pattern of pressure profiles and streamlines can be observed for all combinations of multiphase and turbulence model and at all flow rates.

The cross-stream vortices in the numerical models affect the pressure distributions on the step faces, similarly to the experimental model. The high pressures on the horizontal step

6. THREE-DIMENSIONAL NUMERICAL MODEL STUDY OF A NARROW STEPPED SPILLWAY AT THE UNIVERSITY OF LEEDS

faces are localised in the locations where the cross-stream vortices impinge on the step face. The pressure acting on the vertical step faces are also affected by the direction of circulation of the cross-stream vortices, however, as in the experimental model, to a lesser extent than the horizontal step faces.

On the horizontal step faces, there are large pressure differentials across a relatively short distance. In masonry stepped spillways, this difference in pressure may act across a single masonry block, so that a high pressure at one end of a block and a low pressure at the other end of the block may cause the masonry block to rotate out of position, as described by Winter et al. (2010).

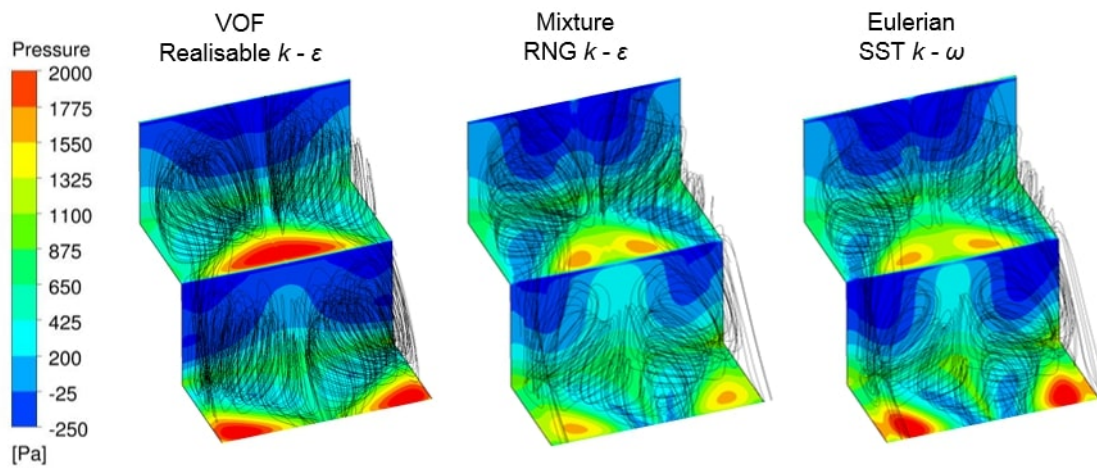


Figure 6.10: Numerical pressure profiles and streamlines at steps 7 and 8 for various numerical models at $Q = 12$ l/s

Figure 6.11 shows the pressures acting on all of the step faces for the VOF, mixture and Eulerian models with the SST $k - \omega$ turbulence model at $Q = 15$ l/s. It can be seen from the pressure contours that the pattern of cross-stream vortices begins at step 1 and alternates in direction at each step throughout the length of the spillway. This agrees with the experimental findings detailed in chapter 3.

At all flow rates, all of the numerical models show the same direction of circulation of the cross-stream vortices, whereby inward circulation occurs at the odd numbered steps and outward circulation occurs at the even numbered steps. This matches the predominant direction of circulation of the cross-stream vortices in the experimental spillway at $Q = 12, 15$ and 18 l/s. At $Q = 21$ l/s, however, the predominant direction of circulation of the experimental cross-stream vortices is the opposite to that at the lower flow rates. This is not predicted by the

6.3 Results and Discussion of a 3D Numerical Modelling Study of Skimming Flow over the University of Leeds Stepped Spillway

numerical models and the direction of circulation of the cross-stream vortices at each step is the same for all flow rates. It is unclear why the predominant direction of circulation of the cross-stream vortices in the experimental models is different at $Q = 21$ l/s. The fact that it is not observed in the numerical models suggests that it may be caused by transient flow conditions in the experimental spillway.

In the experimental spillway, vortex switching was observed, whereby the direction of circulation of the cross-stream vortices at each step changes unpredictably over time. Vortex switching occurred more frequently at the higher flow rates. No Vortex switching was observed in any of the numerical models. This is, perhaps, unsurprising as no transient effects are observed in the numerical models (other than in one specific case which is discussed in section 6.3.5) and vortex switching is a time dependent phenomenon. The cause of vortex switching in the experimental spillway is unclear. Again, the fact that the numerical models do not predict vortex switching may indicate that it is caused by time dependent flow behaviour within the spillway.

6.3.4 The Effect of Air Entrainment on Pressure

Figure 6.11 also shows the effect that air entrainment has on the pressures acting on the step faces, in the numerical models. In the VOF model, no air entrainment occurs and it can be seen that the pressures acting on the step faces remain reasonably similar throughout the spillway. In the mixture and Eulerian models, however, air entrainment does occur and the pressures in the downstream, aerated region are different to those in the upstream, non-aerated region.

On the horizontal step faces the high pressures are lower in the aerated region than in the non-aerated region. This effect is much more pronounced in the mixture model than in the Eulerian model, however, with different turbulence models the Eulerian model predicts a greater reduction in the pressures on the horizontal step faces in the aerated region. This agrees with the experimental data reported in chapter 3, which show that the high pressures on the horizontal step faces were lower in the presence of air. This also agrees with the findings of Amador et al. (2009), Sánchez-Juny and Dolz (2005) and Sánchez-Juny et al. (2000) who show that the presence of air in the flow acts to reduce pressures.

On the vertical step faces, however, the mixture and Eulerian models show that the presence of air has little effect on the low pressures acting on the step faces. This also agrees with

6. THREE-DIMENSIONAL NUMERICAL MODEL STUDY OF A NARROW STEPPED SPILLWAY AT THE UNIVERSITY OF LEEDS

the experimental findings reported in chapter 3. These results, however, disagree with the findings of McGee (1988) and Dong et al. (2010) who show that, albeit for different hydraulic structures, aeration of the flow acts to increase low pressures which may cause cavitation or plucking damage. Although the presence of air in the flow does not act to increase the low pressures on the vertical step faces, in experimental and prototype stepped spillways, the cushioning effect that air bubbles have on the collapse of cavitation vapour bubbles may protect the spillway from cavitation damage. This is not the case for plucking damage however, and the results of this project suggest that masonry spillways may still be at risk of plucking damage in both the aerated and non-aerated regions, due to the low pressures found throughout the spillway. This is discussed further in section 6.3.6.

It is suggested by Vischer et al. (1982) and Wood (1984) that it is the added compressibility of the aerated flow that reduces the pressure of the collapsing cavitation vapour bubbles and protects a solid surface from cavitation damage. Figure 6.11 shows that the presence of air in the mixture and Eulerian models reduces the high pressures on the horizontal step faces. In both of these models, the air and water phases have both been treated as incompressible fluids. This shows that it is not only the compressibility of aerated flow which reduces pressures acting on a solid surface. However, the compressibility of the aerated flow may still be a factor in reducing high pressures. It is unclear what effect the air has to reduce pressures in the numerical models.

6.3 Results and Discussion of a 3D Numerical Modelling Study of Skimming Flow over the University of Leeds Stepped Spillway

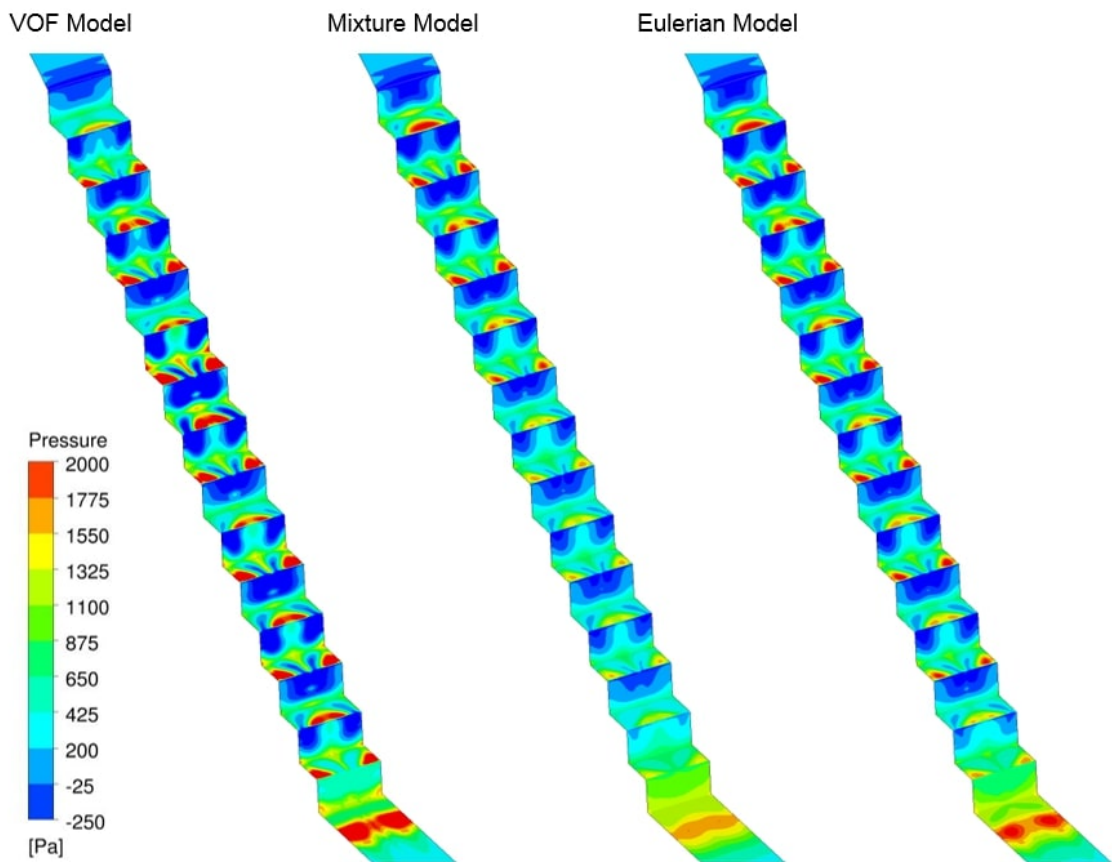


Figure 6.11: Numerical pressures acting on all of the step faces for the VOF, mixture and Eulerian models at $Q = 15$ l/s. Data for the SST $k - \omega$ turbulence model is displayed in each case

Figure 6.12 shows the pressures acting on the spillway side wall for the three multiphase models which have been investigated, at $Q = 15$ l/s. In each case, data for the Realisable $k - \epsilon$ model has been displayed. For each multiphase model, it can be seen that the pattern of pressure alternates at each step, due to the alternating pattern of cross-stream vortices. It can also be seen that, at the even numbered steps, there is a high and low pressure region which results in a large difference in pressure over a relatively small distance. Like on the horizontal step faces, this may cause masonry blocks to rotate out of position in the manner described by Winter et al. (2010).

The VOF model shows very little change in the high pressure regions down the length of the spillway. The magnitudes of pressure in the low pressure regions reduce down the spillway up to step 14, where they are slightly higher. The decrease in the pressures in the low pressure regions may be due to the acceleration of the flow down the spillway increasing the velocity of the vortices within the step cavities. The increase in pressure at step 14 may

6. THREE-DIMENSIONAL NUMERICAL MODEL STUDY OF A NARROW STEPPED SPILLWAY AT THE UNIVERSITY OF LEEDS

be due to the proximity of this step to the outlet channel.

The mixture and Eulerian models show a small decrease in the high pressures moving down the spillway. This agrees with the experimental findings, although, due to the limited number of steps that experimental measurements were taken at, and the alternating direction of circulation of the cross-stream vortices, comparisons of the experimental pressures in aerated and non-aerated regions of the spillway could only be made between steps 2 and 12.

In the mixture and Eulerian models, the pressures in the low pressure regions increase further downstream in the fully aerated region. This suggests that the entrainment of air into the flow acts to increase low pressures, helping to protect the spillway from cavitation or plucking damage. The numerical pressures acting on the spillway walls are compared to the experimental data in section 6.3.6.

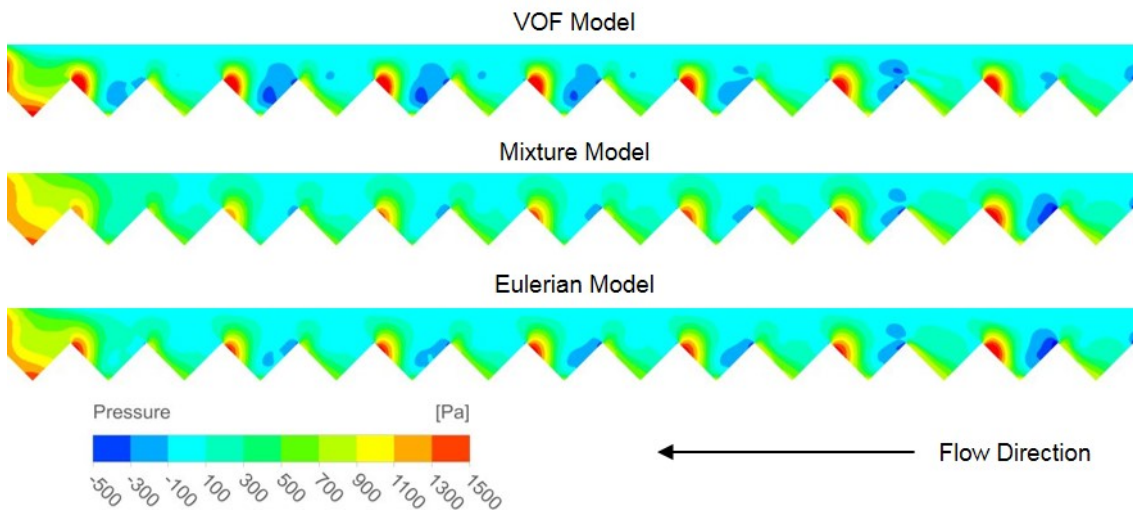


Figure 6.12: Numerical pressures acting on the spillway side wall for the VOF, mixture and Eulerian models at $Q = 15$ l/s. Data for the Realisable $k - \epsilon$ turbulence model is displayed in each case

6.3.5 Unsteady Behaviour

The splashing observed in the downstream section of the VOF model with the SST $k - \omega$ model causes transience in the free-surface. Although all simulations in this research project have been run transiently, this is the only case where a steady state has not been achieved and transient effects can be observed. It should be noted that no transient effects were observed in the pressures acting on the spillway steps or side walls in this case. No transient effects were observed in the free-surface of the 2D simulations using the VOF model with the SST $k - \omega$ model in chapter 5. This suggests that the splashing is a result of wall effects in the

6.3 Results and Discussion of a 3D Numerical Modelling Study of Skimming Flow over the University of Leeds Stepped Spillway

relatively narrow stepped spillway which is considered in this chapter.

Figure 6.13 shows contours of AVF at the centreline and the wall for three different time steps and figure 6.14 shows isosurface of y_{90} for the same three time steps, for the VOF model with the SST $k - \omega$ model. It can be seen that the splashing occurs at the centreline of the spillway and not at the wall, although transient effects are observed in the free-surface position at the wall. At 7.00 s there are a small number of large splashes visible. At 7.02 s these splashes have moved downstream slightly, as would be expected. At 8.50 s, however, there are a larger number of much smaller splashes. This shows that splashing is occurring, and moving downstream transiently, but also that the splashing occurs in an irregular manner and the "pattern" of splashes also varies over time. Note that the splashing that can be observed in figures 6.13 and 6.14 only occurs at $Q = 12$ l/s and $Q = 15$ l/s. At $Q = 18$ l/s and $Q = 21$ l/s there is some transience observed in the free-surface position, but splashing does not occur and there is less variation in the free-surface position over time than at the lower flow rates. It is unclear why this is the case, however, as splashing occurs at all flow rates in the experimental model.

6. THREE-DIMENSIONAL NUMERICAL MODEL STUDY OF A NARROW STEPPED SPILLWAY AT THE UNIVERSITY OF LEEDS

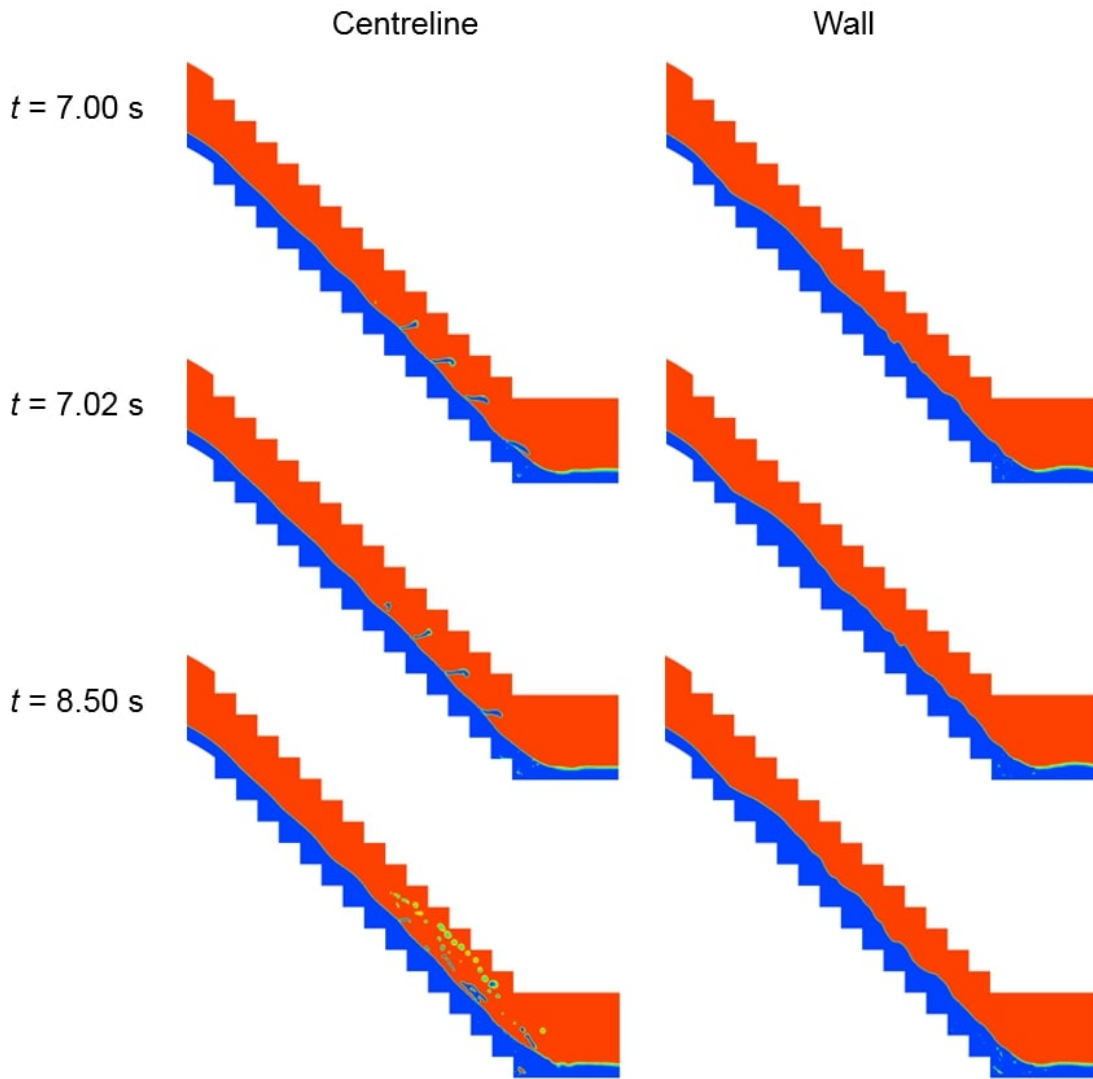


Figure 6.13: Contours of air volume fraction, at the centreline of the spillway and at the wall, for different values of t , for the VOF model with the SST $k - \omega$ model, at $Q = 15$ l/s

6.3 Results and Discussion of a 3D Numerical Modelling Study of Skimming Flow over the University of Leeds Stepped Spillway

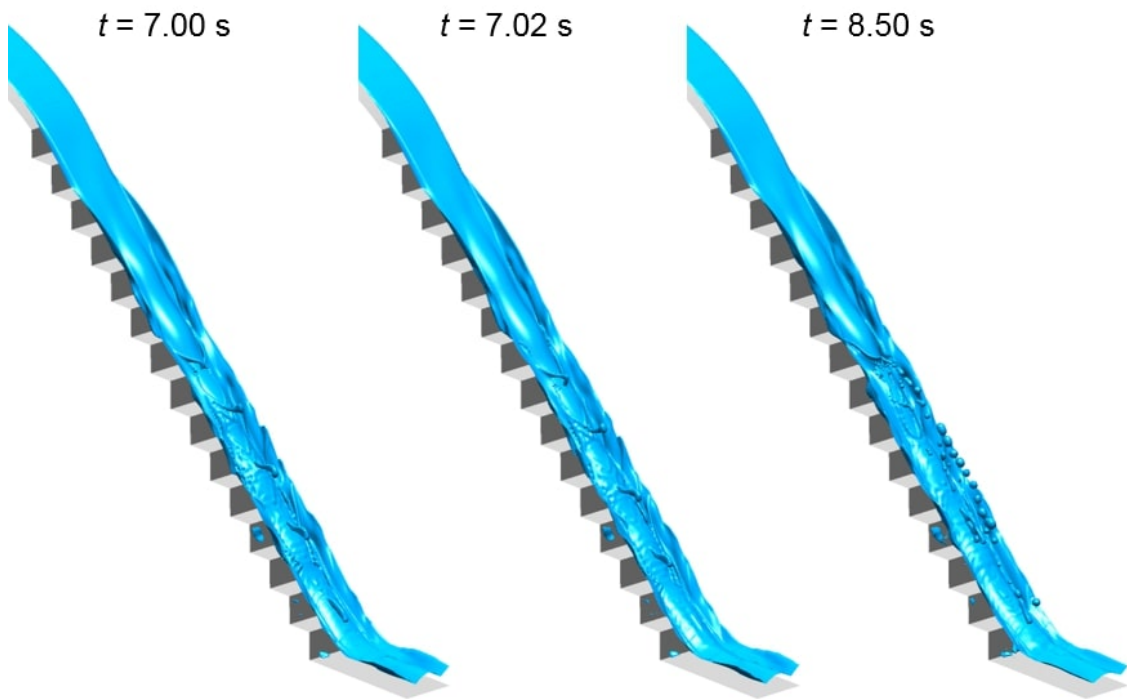


Figure 6.14: Isosurfaces of an air volume fraction of 0.9 for different values of t , for the VOF model with the SST $k - \omega$ model, at $Q = 15$ l/s

Figure 6.15 shows the mean free-surface position, \pm the standard deviation, for the VOF model with the SST $k - \omega$ model, at the centreline and at the wall. The mean and standard deviation are calculated using data at 0.01 s intervals, over a 5.00 s period. Firstly, note that at around $x = 1650$ mm there is a sudden decrease in the free-surface position at both the centreline and the wall. This is due to the fact that a small bubble of air is trapped in the cavity of the final step. The free-surface of this bubble has caused the free-surface profile to be distorted in this position. However, the effect of the transient splashing on the mean free-surface can still be observed.

At the wall there is a very little variation in the free-surface, up to roughly $x = 200$ mm, where there is a sudden increase in the flow depth. Downstream of this point, the standard deviation is slightly larger, showing that there is some variation in the flow depth at the wall over time.

At the centreline there is very little transient variation in the free-surface depth up to approximately $x = 800$ mm. Downstream of this point the standard deviation is extremely high due to the splashing in this area of the spillway. As transient effects are observed in the free-surface predicted by the VOF model with the SST $k - \omega$ model, the mean free-surface

6. THREE-DIMENSIONAL NUMERICAL MODEL STUDY OF A NARROW STEPPED SPILLWAY AT THE UNIVERSITY OF LEEDS

position, taken over 5 s, will be used to compare the numerically predicted flow depth to the experimental data. Note that the free-surface for the VOF model with the SST $k - \omega$ model is the only case in this research project that mean values are presented for numerical data. Instantaneous numerical values have been used in all other cases as no other transient behaviour has been observed, so, as such, instantaneous values are equivalent to time averaged values.

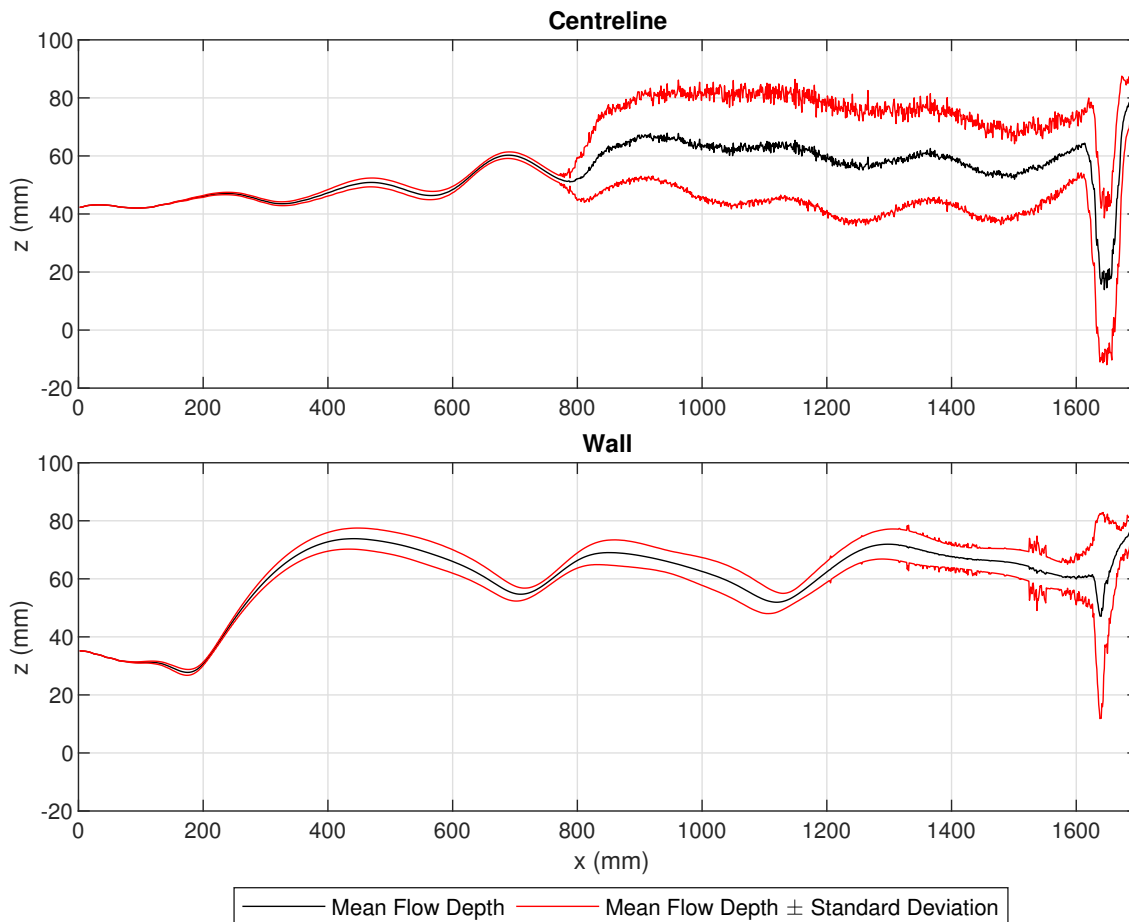


Figure 6.15: Mean flow depth \pm the standard deviation for the VOF model with the SST $k - \omega$ model. The mean and standard deviation are calculated using data at 0.01 s over a 5.00 s period

6.3.6 Pressures Acting on the Step Faces and Spillway Side Walls

In chapter 3, experimental pressures were measured at various locations on the step faces and side walls of the spillway. Measurements were made at individual points on the horizontal and vertical step faces, at both the centreline and close to the wall, and also at a number of points on the side wall of the spillway. Pressures were recorded at steps 2, 5 and 12, as these steps represented locations in the non-aerated region, close to the inception point and in the

6.3 Results and Discussion of a 3D Numerical Modelling Study of Skimming Flow over the University of Leeds Stepped Spillway

aerated region, for the flow rates investigated. The predominant direction of circulation of the cross-stream vortices, in experimental model, at steps 2 and 12 is the opposite of at step 5. These measurements, therefore, allowed the effect that the cross-stream vortices have on pressure to be analysed. In this section, numerical pressure profiles, in lines which intersect the experimental measurement locations, are compared to the experimental pressure data. This section only discusses the pressures acting on the spillways step faces or side walls, as pressures in other locations were not considered.

The experimentally measured pressures vary over time. Therefore, the mean pressures and standard deviations are used to indicate the average magnitude of the pressure as well as the variation in pressure at each measurement location. Almost no transience is observed in the numerical pressures on the spillway steps or side walls, so the numerical models are unable to predict the pressure variations within the spillway. The transient variation in the experimental pressure at a certain location are used as an indication of whether the error between the numerical pressure and the experimental mean pressure is within a reasonable range.

6.3.6.1 Horizontal Step Face

Figures 6.16 - 6.19 show the experimental and numerical pressures acting on the horizontal step faces for the four flow rates investigated. Firstly consider the discharges of $Q = 12 - 18$ l/s (figures 6.16 - 6.18), as, at these discharges, the predominant direction of circulation of the cross-stream vortices in the experiments agrees with that of the numerical data.

It can be seen that, in all cases the numerical data shows the same general pattern of pressure as the experimental data. At steps 2 and 12 there is little variation in the pressure across the length of the step at the centreline, whereas, at the wall the pressure is significantly larger at the downstream end of the step. This pattern of pressure is due to the direction of circulation of the cross-stream vortices, as discussed in chapter 3. At step 5 the opposite pattern is shown and at the centreline the pressure is larger at the downstream end of the step.

For $Q = 12 - 18$ l/s the experimental pressures are generally predicted well by the CFD models. In many cases, there is a large variation in the pressures predicted by the different numerical models at the downstream ends of the horizontal step faces, but this corresponds to large fluctuations in the experimental pressure. Close to the wall at step 2 most of the

6. THREE-DIMENSIONAL NUMERICAL MODEL STUDY OF A NARROW STEPPED SPILLWAY AT THE UNIVERSITY OF LEEDS

numerical models underestimate the pressure. The VOF and Eulerian model, with the SST $k-\omega$ model, however, predict the pressure reasonably accurately, especially at the downstream end of the step. The pressures are also underestimated slightly by most of the numerical models at the downstream end of step 5, close to the wall. In this position the Realisable $k-\epsilon$ model, with all multiphase models, predicts the pressure reasonably accurately.

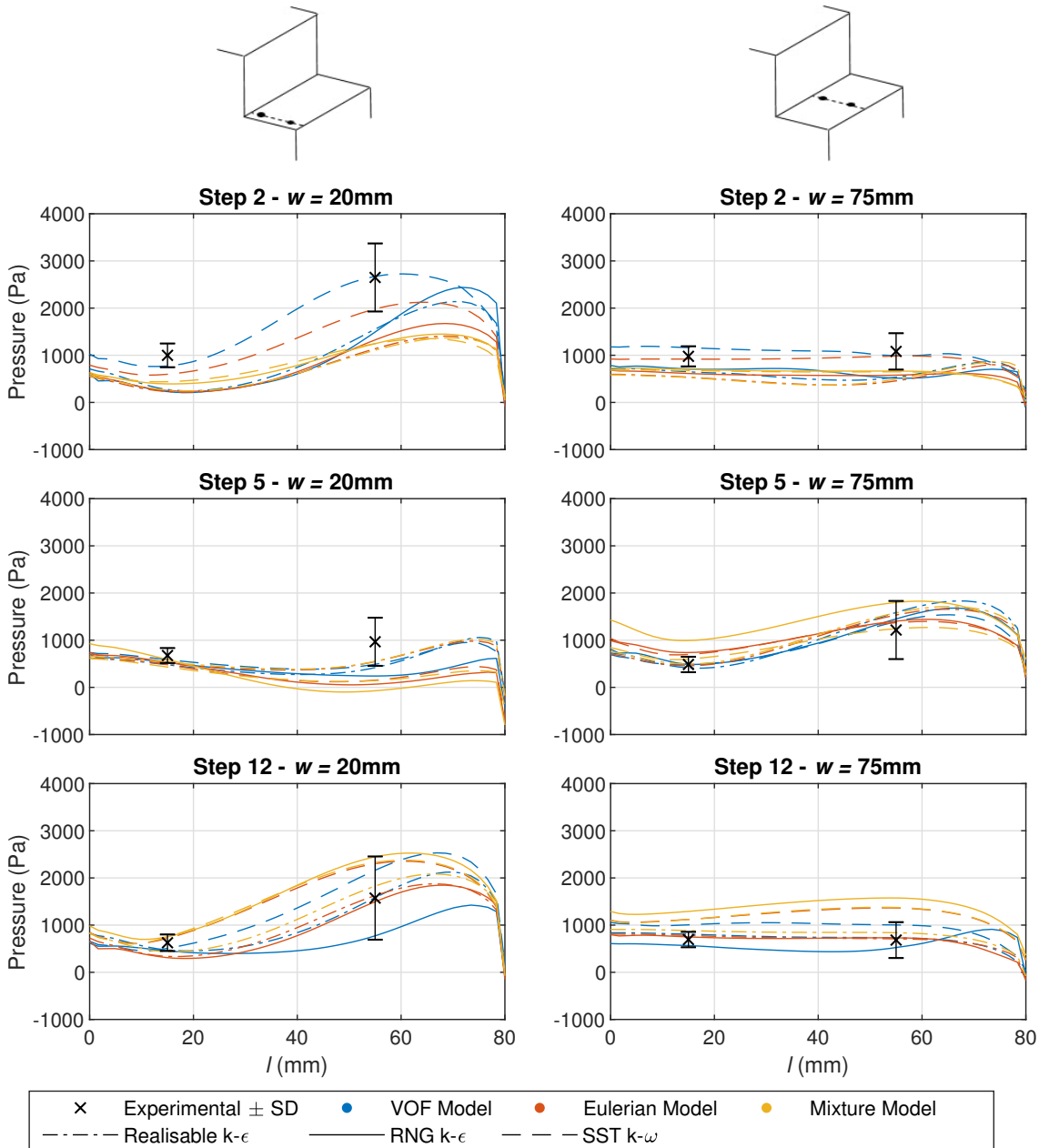


Figure 6.16: Experimental and numerical pressures acting on the horizontal step faces of steps 2, 5 and 12, at $Q = 12$ l/s. All combinations of multiphase and turbulence models are displayed. w is the distance across the channel width from the spillway side wall and l is the distance along the horizontal step face from the inside step corner. These dimensions are detailed in figure 3.4a

6.3 Results and Discussion of a 3D Numerical Modelling Study of Skimming Flow over the University of Leeds Stepped Spillway

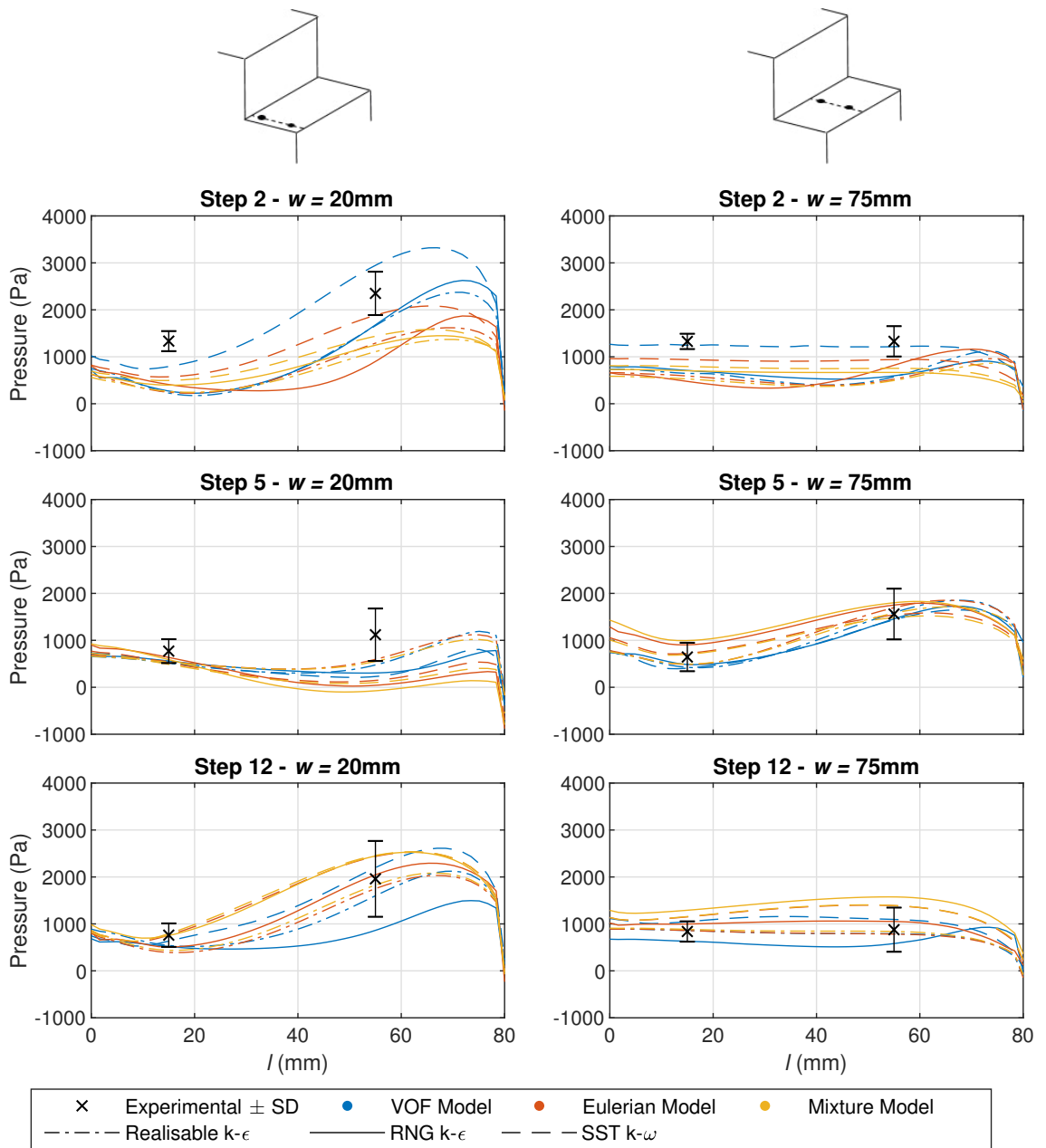


Figure 6.17: Experimental and numerical pressures acting on the horizontal step faces of steps 2, 5 and 12, at $Q = 15$ l/s. All combinations of multiphase and turbulence models are displayed. w is the distance across the channel width from the spillway side wall and l is the distance along the horizontal step face from the inside step corner. These dimensions are detailed in figure 3.4a

6. THREE-DIMENSIONAL NUMERICAL MODEL STUDY OF A NARROW STEPPED SPILLWAY AT THE UNIVERSITY OF LEEDS

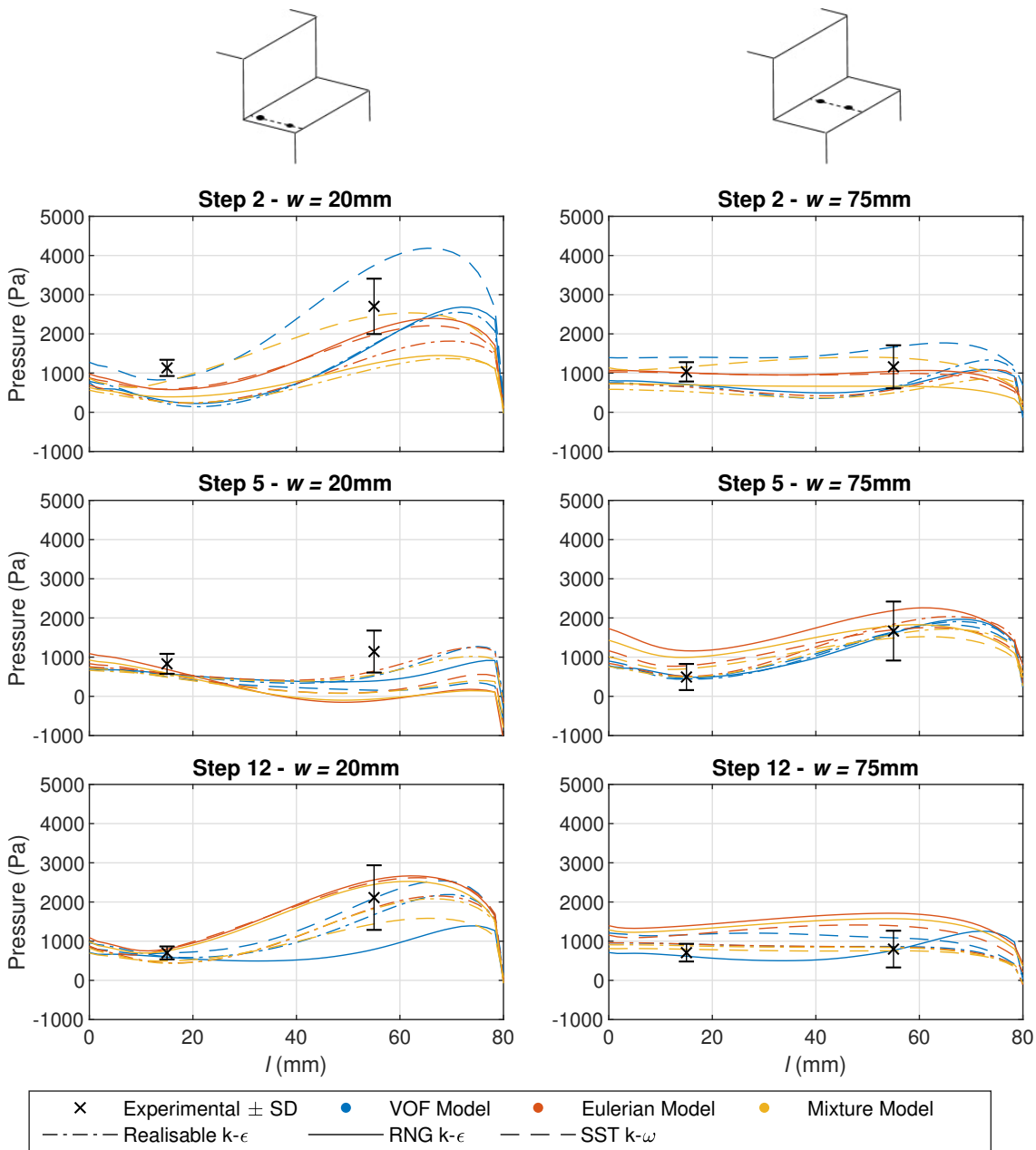


Figure 6.18: Experimental and numerical pressures acting on the horizontal step faces of steps 2, 5 and 12, at $Q = 18$ l/s. All combinations of multiphase and turbulence models are displayed. w is the distance across the channel width from the spillway side wall and l is the distance along the horizontal step face from the inside step corner. These dimensions are detailed in figure 3.4a

Figure 6.19 shows the experimental and numerical pressures acting on the horizontal step faces at $Q = 21$ l/s. At this flow rate, the predominant direction of circulation of the cross-stream vortices in the experimental spillway is the opposite of the lower flow rates, and frequent vortex switching is observed. In the numerical models, however, this is not the case. The direction of circulation of the cross-stream vortices is the same as at the lower flow rates,

6.3 Results and Discussion of a 3D Numerical Modelling Study of Skimming Flow over the University of Leeds Stepped Spillway

and no vortex switching occurs.

This can be seen by the data presented in figure 6.19, at steps 2 and 5. Although the magnitude of pressure is predicted accurately by some of the numerical models, the general pattern of pressure predicted by the numerical models is the opposite of the experimental pressure pattern. At the downstream end of the steps the experimental pressures are highest at the centreline at step 2 and at the wall at step 5, whereas, the numerical pressures are highest at the wall at step 2 and the centreline at step 5. This is due to the difference in the direction of circulation of the cross-stream vortices. This makes it impossible to directly compare the numerical and experimental pressure magnitudes at these steps.

At step 12, the experimental pressures show the same pattern at the wall and the centreline. This is due to vortex switching and is discussed in chapter 3. In chapter 3, analysis of the moving averages of the experimental pressures at the downstream end of the horizontal step faces allowed the direction of circulation of the cross-stream vortices at a particular time to be identified. Therefore, the numerical pressures can be compared to the experimental pressure at a time when the direction of circulation of the cross-stream vortices was known to be the same in both the experimental and numerical models.

6. THREE-DIMENSIONAL NUMERICAL MODEL STUDY OF A NARROW STEPPED SPILLWAY AT THE UNIVERSITY OF LEEDS

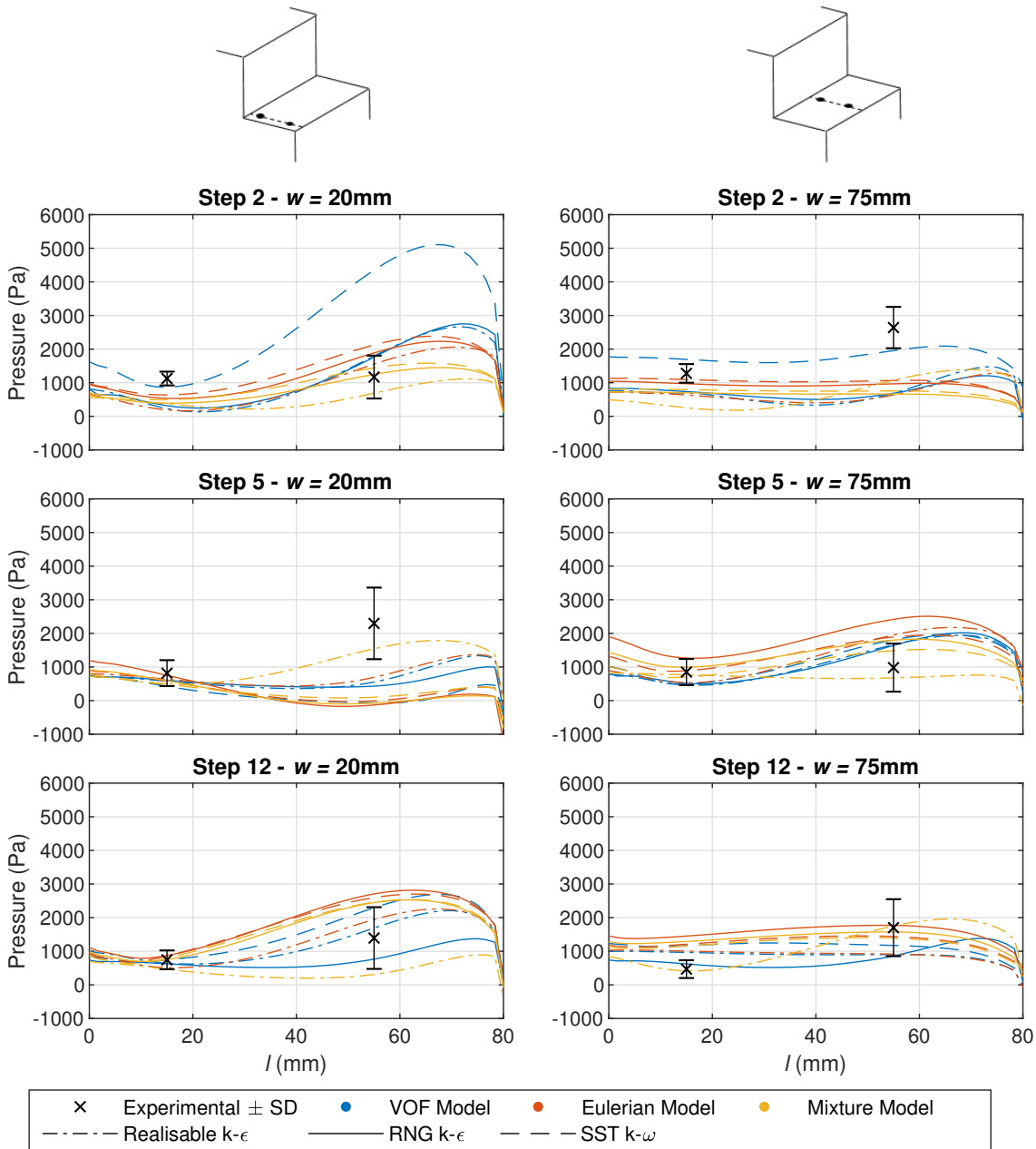


Figure 6.19: Experimental and numerical pressures acting on the horizontal step faces of steps 2, 5 and 12, at $Q = 21$ l/s. All combinations of multiphase and turbulence models are displayed. w is the distance across the channel width from the spillway side wall and l is the distance along the horizontal step face from the inside step corner. These dimensions are detailed in figure 3.4a

Figure 6.20 shows the numerical pressure data acting on the horizontal step face of step 12, at $Q = 21$ l/s. The experimental pressure at the downstream end of the step is also displayed. The experimental mean and standard deviation is calculated over a 10 s period, from 152.0245 s. Figure 3.15 clearly shows that, over this time period, vortex switching has caused the direction of circulation of the experimental cross-stream vortices to match those in

6.3 Results and Discussion of a 3D Numerical Modelling Study of Skimming Flow over the University of Leeds Stepped Spillway

the numerical model.

It can be seen that the majority of the numerical models predict the pressures accurately at both the wall and the centreline. This suggests that, although the numerical models do not predict the predominant direction of circulation of the cross-stream vortices accurately at $Q = 21$ l/s, the magnitudes of pressures are predicted accurately, as is the localisation of high and low pressures caused by the cross-stream vortices. The numerical models can, therefore, be used in order to gain an understanding of the pressure patterns and magnitudes on the horizontal step faces at all flow rates.

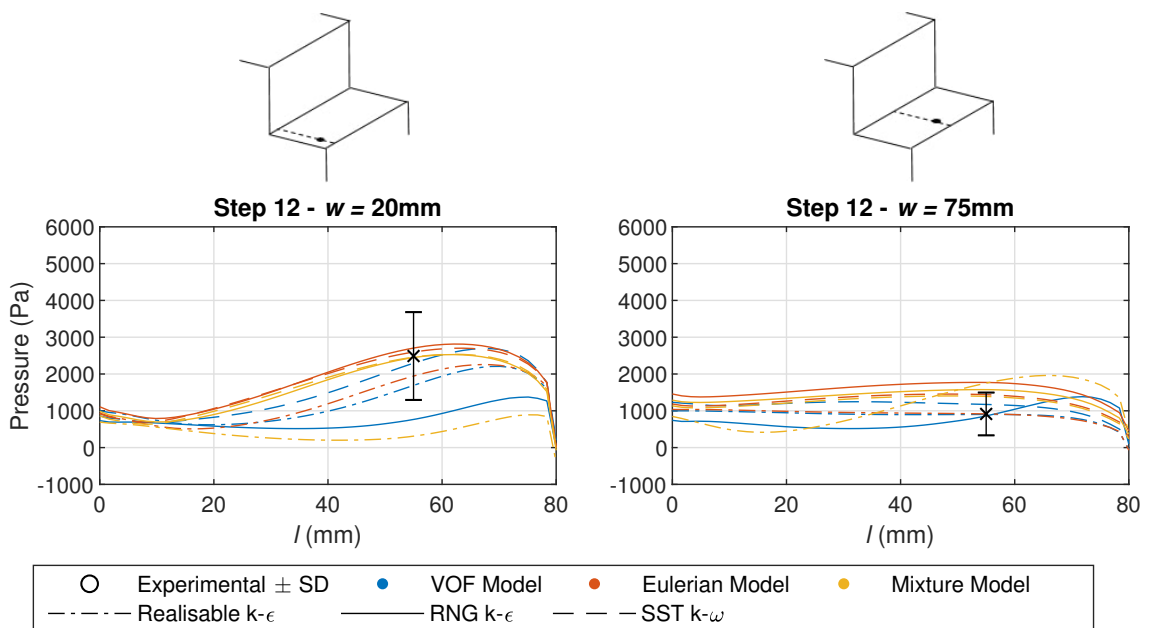


Figure 6.20: Experimental and numerical pressures acting on the horizontal step face of step 12, at $Q = 21$ l/s. The experimental mean pressure and standard deviation are calculated using only the data measured between 152.0245 s and 162.0245 s, when the moving averages, shown in figure 3.15, indicate that vortex switching has occurred and the direction of circulation of the cross-stream vortices is the same as that predicted by the CFD models. Experimental data is also only shown at $l = 55$ mm, the downstream end of the step. All combinations of multiphase and turbulence models are displayed. w is the distance across the channel width from the spillway side wall and l is the distance along the horizontal step face from the inside step corner. These dimensions are detailed in figure 3.4a

6.3.6.2 Vertical Step Face

Figures 6.21 - 6.24 show the experimental and numerical pressures acting on the vertical step faces for the four flow rates investigated. Again, consider the flow rates of $Q = 12 - 18$ l/s first, as, at these discharges, the predominant direction of circulation of the cross-stream vortices in the experiments matches that of the numerical models.

Unlike on the horizontal faces, there is not a significant difference in the pressure patterns

6. THREE-DIMENSIONAL NUMERICAL MODEL STUDY OF A NARROW STEPPED SPILLWAY AT THE UNIVERSITY OF LEEDS

between the centreline of the spillway and the wall. This is because, as shown in chapter 3, the cross-stream vortices affect the pressures across the width of the channel on the vertical step faces to a lesser extent than on the horizontal step faces. This can also be observed in figures 6.10 and 6.11.

The numerical pressures in all locations tend to decrease as h increases, up to the top of the step where there is a sudden decrease in the pressure. At some locations the magnitude of this decrease in pressure varies for different numerical models. As the experimental pressures could not be measured in these locations, due to the manner in which the spillway was constructed, the numerical models in these locations cannot be validated. The low pressures in these regions may have an important effect on the occurrence of cavitation or plucking. Further investigation, therefore, is required in order to determine whether the numerical models accurately predict the low pressures in these regions.

The numerical models generally predict the pressures on the vertical step faces accurately. There are only a small number of cases where the pressure are not predicted accurately. Close to the wall at step 12, many of the numerical models underestimate the pressure at $h = 55$ mm. At $Q = 15$ and 18 l/s the pressures are underestimated by all numerical models close to the wall at step 5 and, at $Q = 15$ l/s, the pressures at the centreline of step 2 are slightly underestimated by all of the numerical models.

6.3 Results and Discussion of a 3D Numerical Modelling Study of Skimming Flow over the University of Leeds Stepped Spillway

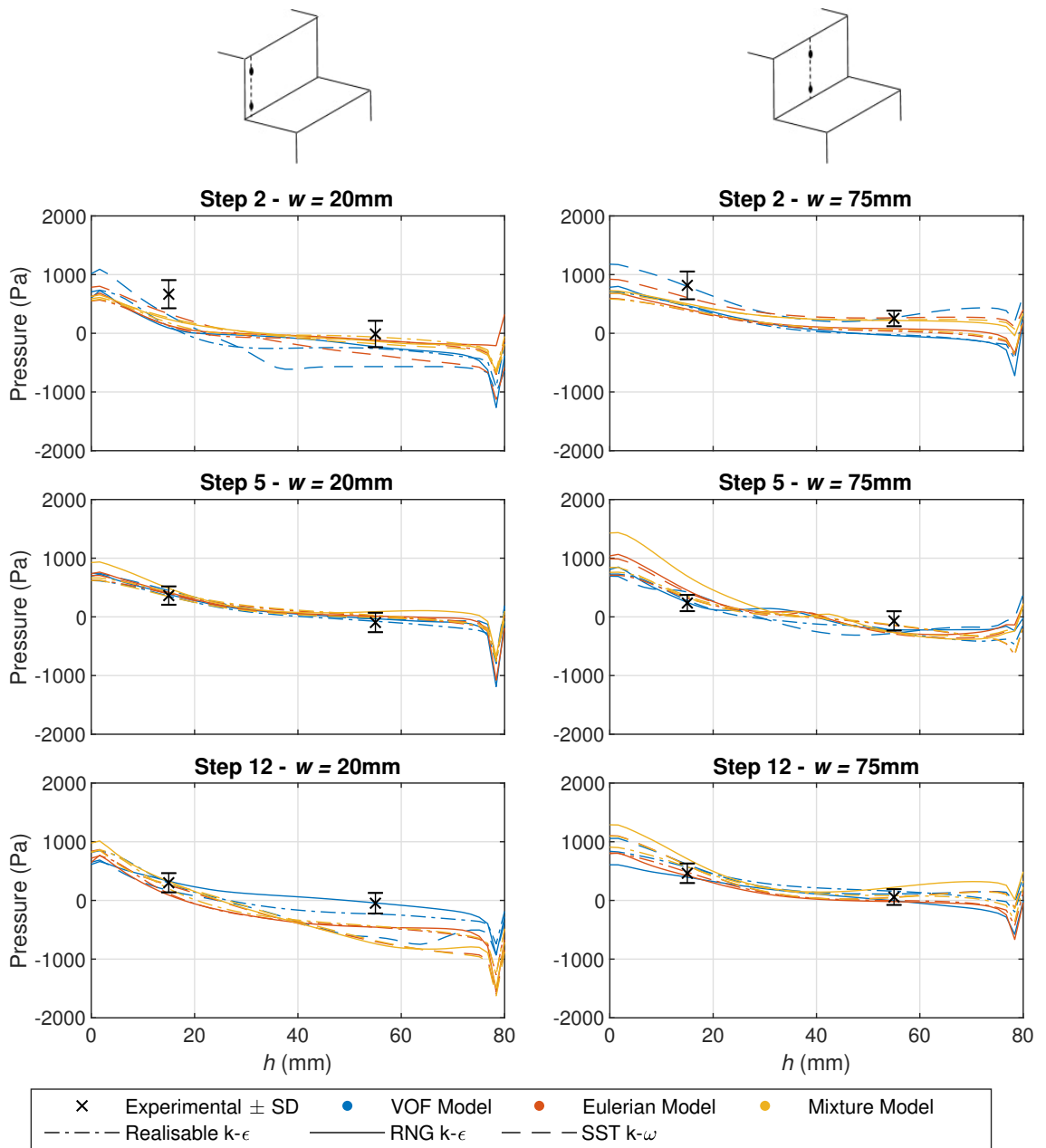


Figure 6.21: Experimental and numerical pressures acting on the vertical step faces of steps 2, 5 and 12, at $Q = 12$ l/s. All combinations of multiphase and turbulence models are displayed. w is the distance across the channel width from the spillway side wall and h is the distance up the vertical step face from the inside step corner. These dimensions are detailed in figure 3.4a

6. THREE-DIMENSIONAL NUMERICAL MODEL STUDY OF A NARROW STEPPED SPILLWAY AT THE UNIVERSITY OF LEEDS

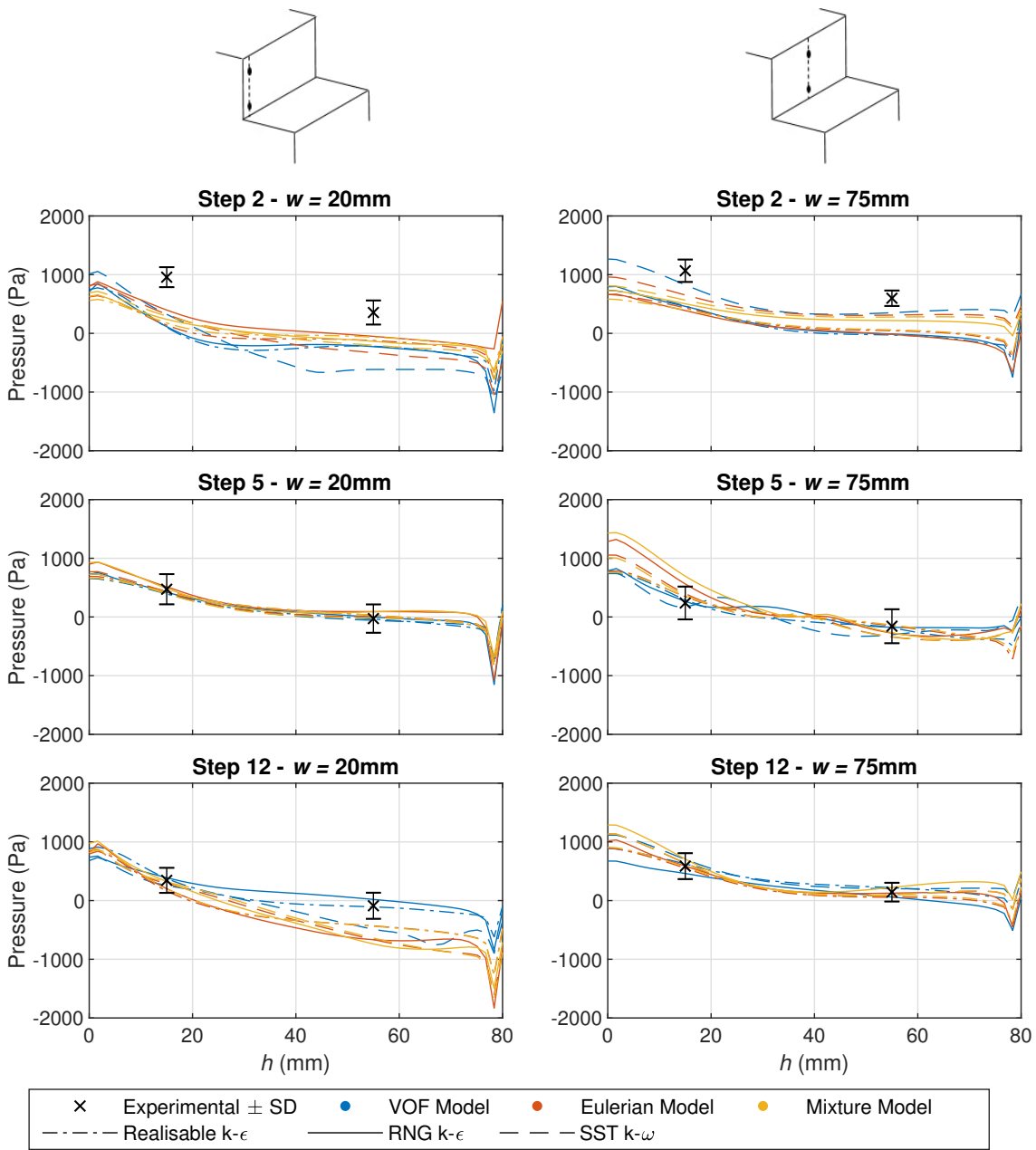


Figure 6.22: Experimental and numerical pressures acting on the vertical step faces of steps 2, 5 and 12, at $Q = 15$ l/s. All combinations of multiphase and turbulence models are displayed. w is the distance across the channel width from the spillway side wall and h is the distance up the vertical step face from the inside step corner. These dimensions are detailed in figure 3.4a

6.3 Results and Discussion of a 3D Numerical Modelling Study of Skimming Flow over the University of Leeds Stepped Spillway

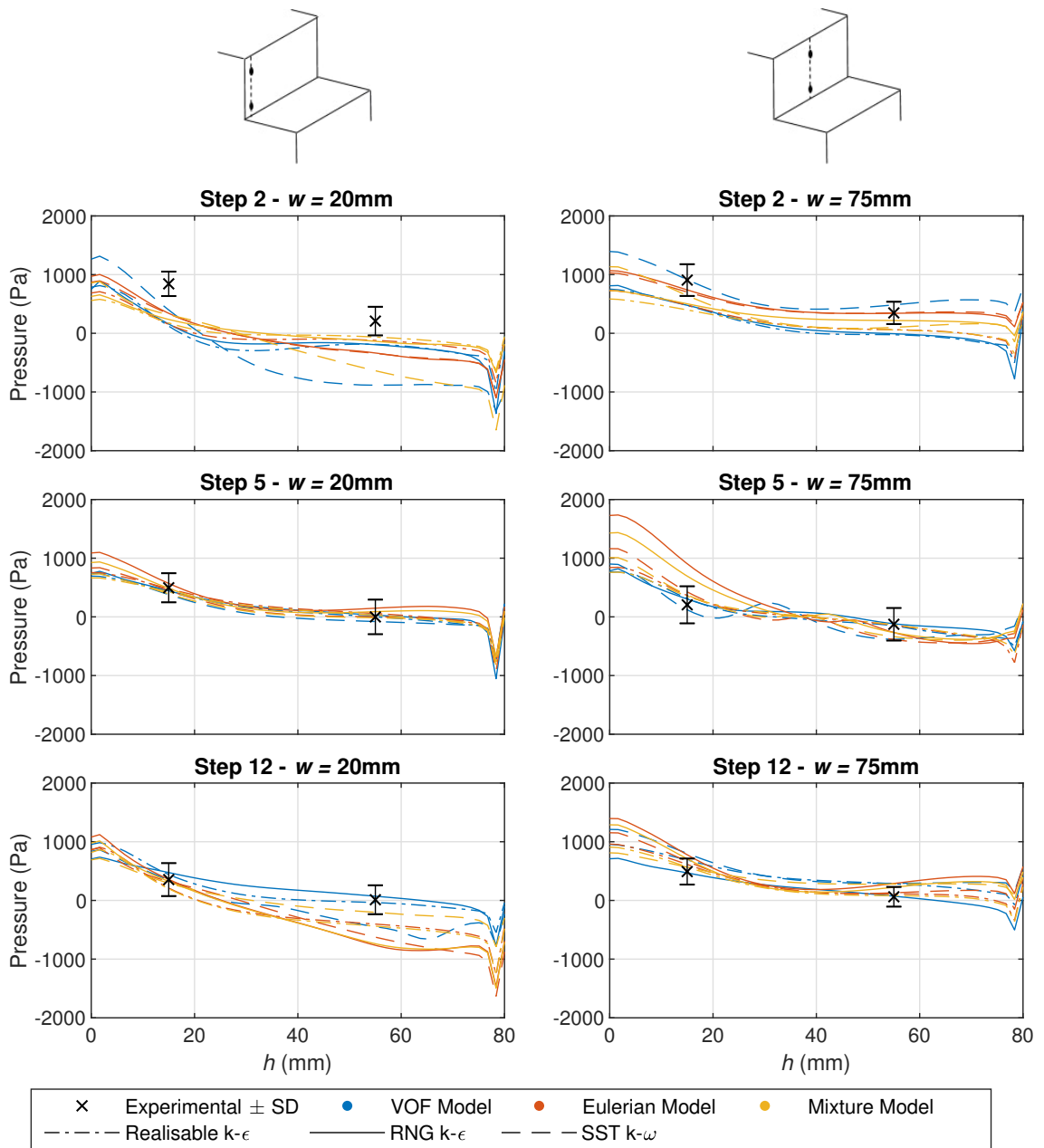


Figure 6.23: Experimental and numerical pressures acting on the vertical step faces of steps 2, 5 and 12, at $Q = 18$ l/s. All combinations of multiphase and turbulence models are displayed. w is the distance across the channel width from the spillway side wall and h is the distance up the vertical step face from the inside step corner. These dimensions are detailed in figure 3.4a

Figure 6.24 shows the experimental and numerical pressures acting on the vertical step faces at $Q = 21$ l/s. As on the horizontal step faces, the predominant direction of circulation of the experimental cross-stream vortices is the opposite to the numerical data at this flow rate. However, as the direction of circulation of the cross-stream vortices does not have a significant effect on the pressures acting on the vertical step face, across the width of the channel, the

6. THREE-DIMENSIONAL NUMERICAL MODEL STUDY OF A NARROW STEPPED SPILLWAY AT THE UNIVERSITY OF LEEDS

experimental pressures are predicted reasonably accurately by the numerical model. As with the lower flow rates, the pressures are underestimated by all numerical models close to the wall at step 5 and by some of the numerical models close to the wall at the top of step 12.

Although the pressures are predicted well at $Q = 21$ l/s, the cross-stream vortices in the numerical models circulate in the opposite direction to the experimental model. Therefore, the numerical data is again compared to the experimental data at a time when the direction of circulation of the cross-stream vortices was the same as in the numerical models.

6.3 Results and Discussion of a 3D Numerical Modelling Study of Skimming Flow over the University of Leeds Stepped Spillway

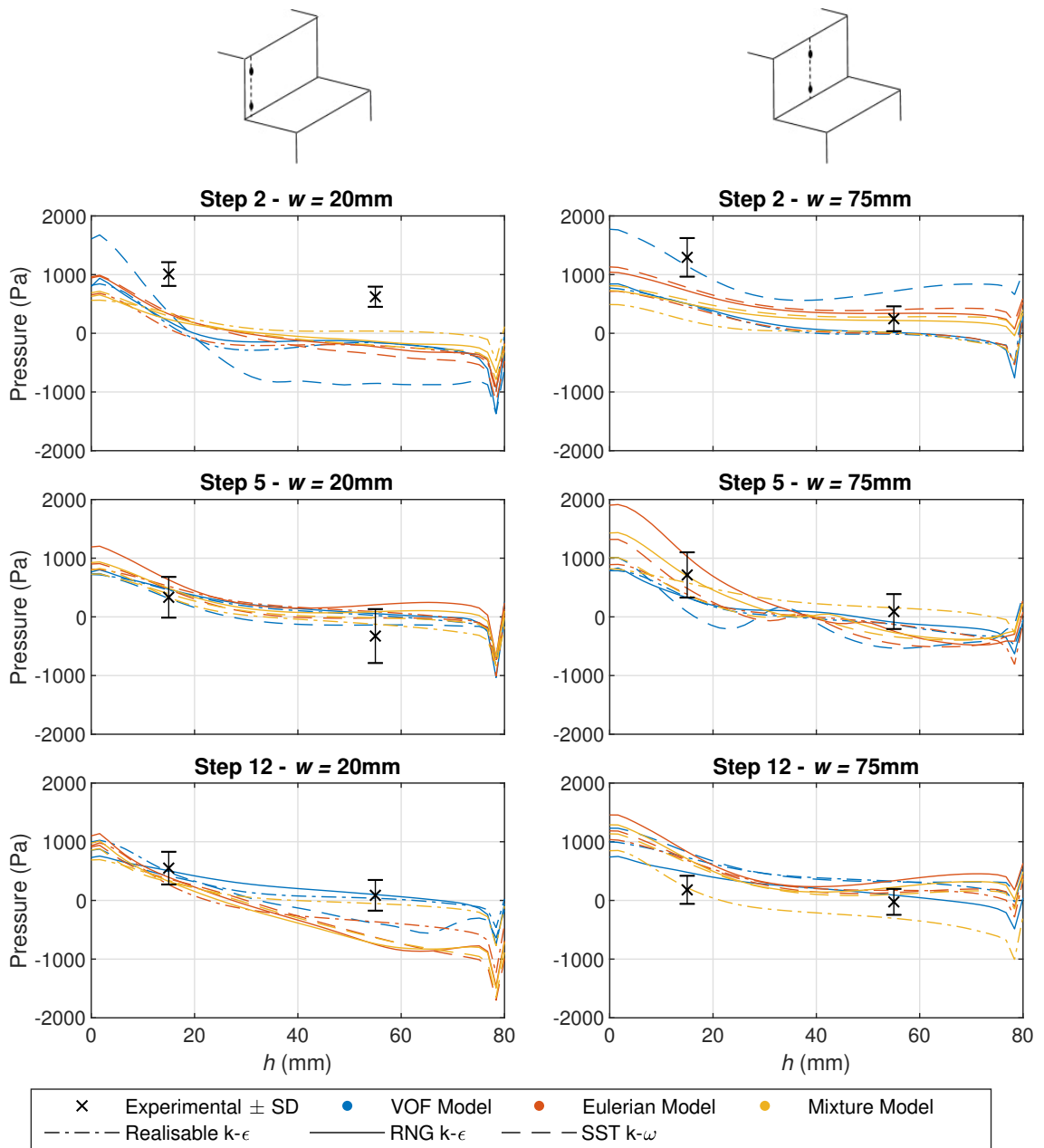


Figure 6.24: Experimental and numerical pressures acting on the vertical step faces of steps 2, 5 and 12, at $Q = 21$ l/s. All combinations of multiphase and turbulence models are displayed. w is the distance across the channel width from the spillway side wall and h is the distance up the vertical step face from the inside step corner. These dimensions are detailed in figure 3.4a

Figure 6.25 shows the numerical pressure data acting on the vertical step face of step 12, at $Q = 21$ l/s. The experimental pressure at $h = 55$ mm is also displayed. The experimental mean and standard deviation is calculated over a 10 s period from 234.1488 s. Figure 3.17 clearly shows that, over this time period, vortex switching has caused the direction of circulation of the experimental cross-stream vortices to match those in the numerical model.

6. THREE-DIMENSIONAL NUMERICAL MODEL STUDY OF A NARROW STEPPED SPILLWAY AT THE UNIVERSITY OF LEEDS

It can be seen that there is very little difference between the experimental pressures shown in figure 6.25 and those shown in the corresponding locations in figure 6.24. Again the pressures are predicted accurately by most numerical models at the top of the step at the centreline, whereas close to the wall a number of the models underestimate the pressure.

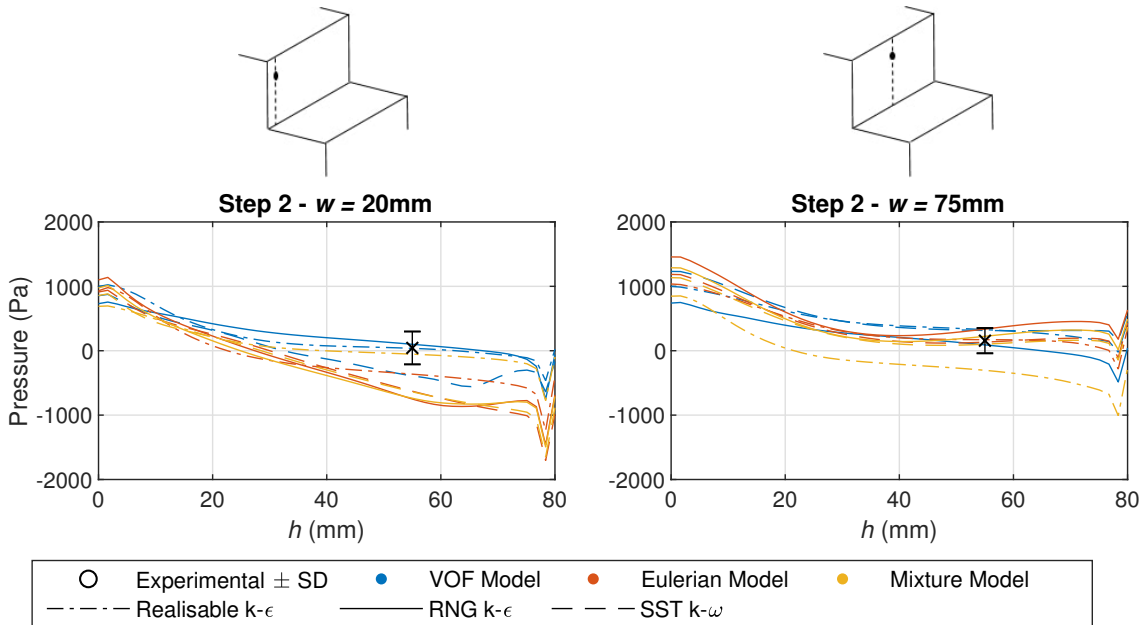


Figure 6.25: Experimental and numerical pressures acting on the vertical step face of step 12, at $Q = 21$ l/s. The experimental mean pressure and standard deviation are calculated using only the data measured between 234.1488 s and 244.1488 s, when the moving averages, shown in figure 3.17, indicate that vortex switching has occurred and the direction of circulation of the cross-stream vortices is the same as that predicted by the CFD models. Experimental data is also only shown at $h = 55$ mm, the top of the step. All combinations of multiphase and turbulence models are displayed. w is the distance across the channel width from the spillway side wall and l is the distance along the horizontal step face from the inside step corner. These dimensions are detailed in figure 3.4a

6.3.6.3 Wall

Figures 6.26 - 6.29 show the experimental and numerical pressures acting on the spillway side walls for the four flow rates investigated. Again consider $Q = 12 - 18$ l/s first, due to the direction of circulation of the cross-stream vortices.

In the experimental data, different directions of circulation of the cross-stream vortices at each step can be seen at $h = 20$ mm. At steps 2 and 12, where outward circulation dominates, the experimental pressure at $l = 60$ mm is significantly higher than at $l = 20$ mm. At step 5, where inward circulation dominates, there is smaller difference in pressure between, $l = 20$ mm and $l = 60$ mm, although the pressure is still slightly higher at $l = 60$ mm. At $h = 60$ mm, however, the experimental pressure patterns are similar at each step and do not indicate the

6.3 Results and Discussion of a 3D Numerical Modelling Study of Skimming Flow over the University of Leeds Stepped Spillway

direction of circulation of the cross-stream vortices.

The numerical data also shows different pressure patterns at the spillway side wall, according to the direction of circulation of the cross-stream vortices. At steps 2 and 12, similar patterns of pressure are shown which are different from those at step 5. This is the case at both $h = 20$ mm and $h = 60$ mm. The differences in pressure patterns are more clear in the numerical data, as entire profiles can be displayed, rather than the pressures at specific locations, as is the case for the experimental data.

In general the numerical models predict the pressures acting on the side walls well. Similarly to the step faces, in certain locations there is a large variation in the pressures predicted by the different numerical models, however, these locations tend to correspond to large variations in the experimental pressures. The experimental pressures are predicted less accurately at only a small number of locations. At $h = 20$ mm and $l = 60$ mm the pressure is underestimated by a number of the numerical models at steps 2 and 5. At $h = 60$ mm and $l = 60$ mm, which is located above the pseudo-bottom, the pressures are predicted less well at 15 l/s, but reasonably well at 12 and 18 l/s.

The numerical models predict reasonably low pressures on the spillway side walls in both the aerated and non-aerated region and also match the experimental data well. This suggests that the spillway side walls may be at risk of plucking, and potentially cavitation, damage throughout the spillway.

6. THREE-DIMENSIONAL NUMERICAL MODEL STUDY OF A NARROW STEPPED SPILLWAY AT THE UNIVERSITY OF LEEDS

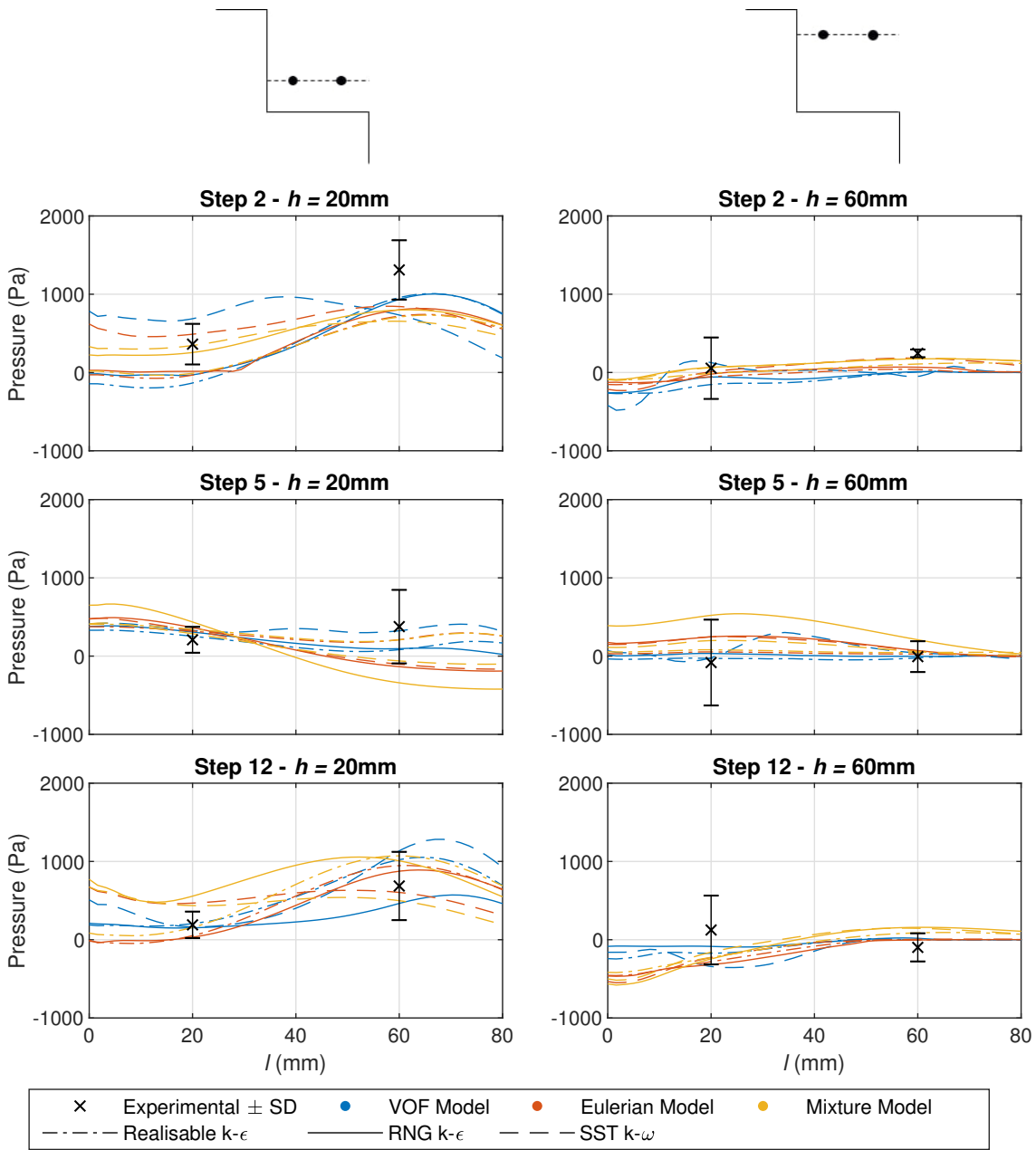


Figure 6.26: Experimental and numerical pressures acting on the wall at steps 2, 5 and 12, at $Q = 12$ l/s. All combinations of multiphase and turbulence models are displayed. h is the distance up the vertical step face from the inside step corner and l is the distance along the horizontal step face from the inside step corner. These dimensions are detailed in figure 3.4a

6.3 Results and Discussion of a 3D Numerical Modelling Study of Skimming Flow over the University of Leeds Stepped Spillway

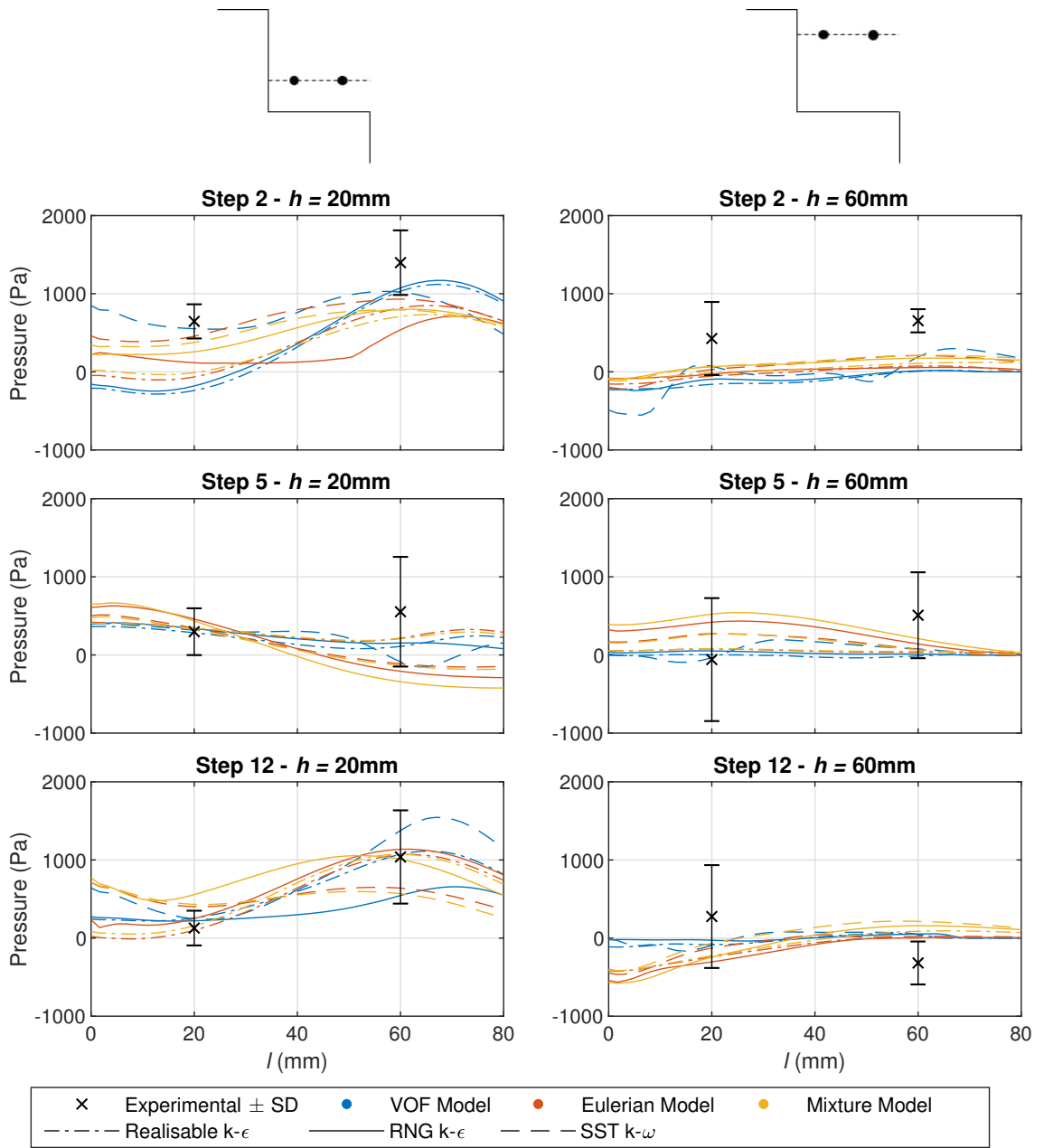


Figure 6.27: Experimental and numerical pressures acting on the wall at steps 2, 5 and 12, at $Q = 15$ l/s. All combinations of multiphase and turbulence models are displayed. h is the distance up the vertical step face from the inside step corner and l is the distance along the horizontal step face from the inside step corner. These dimensions are detailed in figure 3.4a

6. THREE-DIMENSIONAL NUMERICAL MODEL STUDY OF A NARROW STEPPED SPILLWAY AT THE UNIVERSITY OF LEEDS

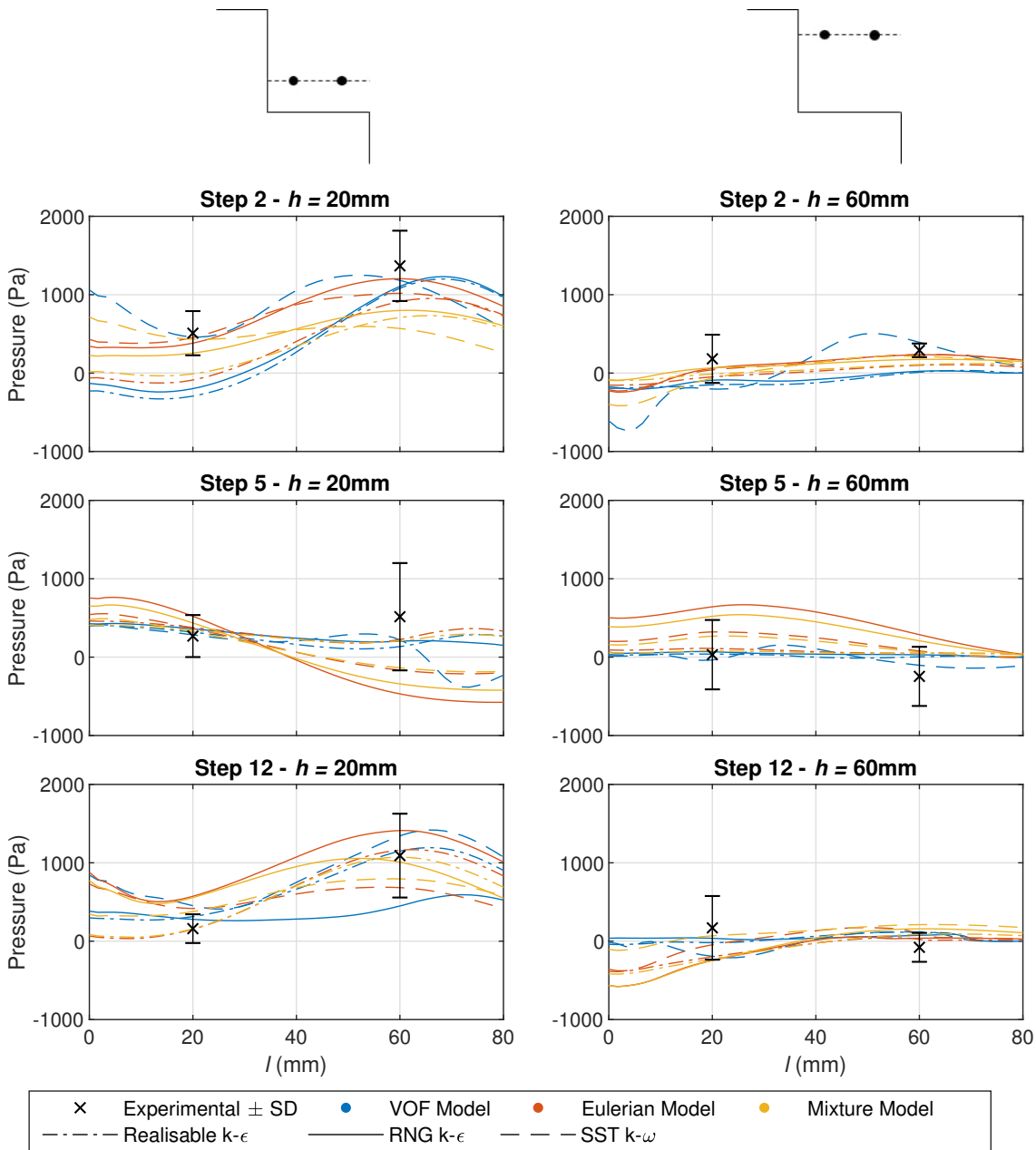


Figure 6.28: Experimental and numerical pressures acting on the wall at steps 2, 5 and 12, at $Q = 18$ l/s. All combinations of multiphase and turbulence models are displayed. h is the distance up the vertical step face from the inside step corner and l is the distance along the horizontal step face from the inside step corner. These dimensions are detailed in figure 3.4a

At $Q = 21$ l/s the predominant direction of circulation of the cross-stream vortices in the experimental model is the opposite to that of the lower flow rates and the numerical models at all flow rates. This can be observed in the experimental data at $h = 20$ mm. There is a significantly larger difference in the experimental pressures between $l = 20$ mm and $l = 60$ mm at step 5 than at steps 2 and 12. This trend is the opposite of the lower flow rates and is

6.3 Results and Discussion of a 3D Numerical Modelling Study of Skimming Flow over the University of Leeds Stepped Spillway

due to the direction of circulation of the cross-stream vortices.

The numerical models predict some of the experimental pressures accurately however these results should be viewed with caution, due to the differences in the flow conditions between the experimental and numerical models. Unlike on the step faces, it is not possible to determine the direction of circulation of the cross-stream vortices by analysis of the experimental pressures acting on the spillway side wall. Therefore, the numerical pressures on the side walls cannot be directly compared to experimental pressures at $Q = 21$ l/s.

6. THREE-DIMENSIONAL NUMERICAL MODEL STUDY OF A NARROW STEPPED SPILLWAY AT THE UNIVERSITY OF LEEDS

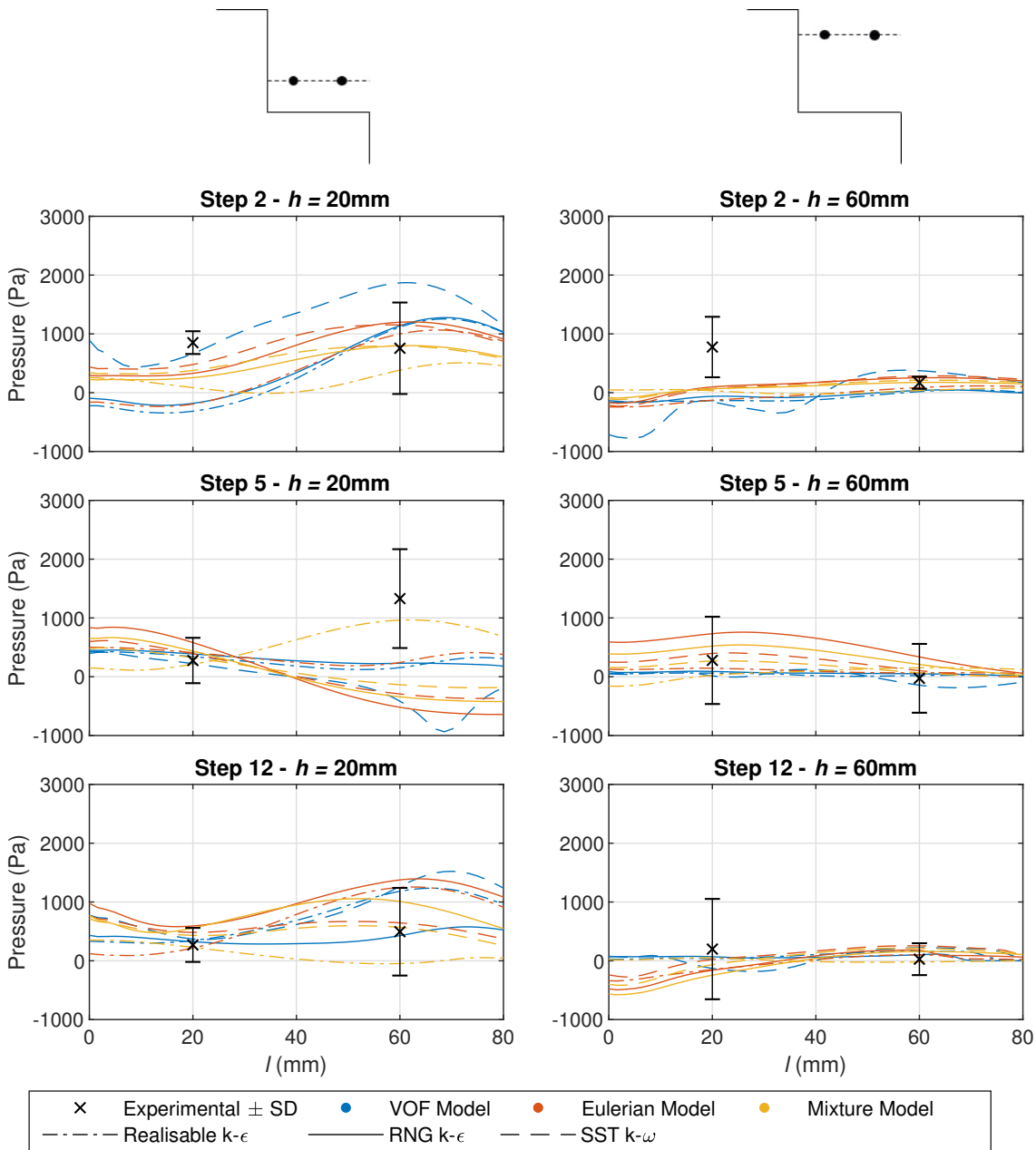


Figure 6.29: Experimental and numerical pressures acting on the wall at steps 2, 5 and 12, at $Q = 21$ l/s. All combinations of multiphase and turbulence models are displayed. h is the distance up the vertical step face from the inside step corner and l is the distance along the horizontal step face from the inside step corner. These dimensions are detailed in figure 3.4a

6.3.6.4 Summary

Numerical pressure data for a range of multiphase and turbulence models has been compared to experimental pressures on the step faces and side walls of steps 2, 5 and 12. The standard deviation of the experimental pressures are used to indicate the variation in pressure over

6.3 Results and Discussion of a 3D Numerical Modelling Study of Skimming Flow over the University of Leeds Stepped Spillway

time. No transience was observed in the numerical pressures so the numerical models are unable to predict the transient pressure fluctuations.

At $Q = 12 - 18$ l/s, the cross-stream vortices circulate in the same direction in both the numerical models and the experiments. At these flow rates the experimental pressures are generally predicted accurately by all of the numerical models. In some locations there are relatively large variations in the pressures predicted by the numerical models, however, these locations correspond to large variations in the experimental pressures in most cases.

At $Q = 21$ l/s, the predominant direction of circulation of the cross-stream vortices in the experiments is the opposite of that in the numerical models, so direct comparison of the numerical and experimental pressures may be misleading. On the step faces, the the numerical pressures at $Q = 21$ l/s were compared to experimental pressures at times when vortex switching had caused the experimental cross-stream vortices direction to match that of the numerical models. At these times, the numerical models were found to predict the experimental models accurately.

In general, all of the numerical models have been shown to predict the pressures reasonably well. However, as no time dependent behaviour is observed in the pressures predicted by the numerical models, the fluctuations in pressure which are observed in the experimental spillway cannot be modelled. This has an important impact on the use of numerical modelling to assess the risk of cavitation or plucking damage to a stepped spillway. A numerical model may predict minimum pressures which are above the vapour pressure of water. However, in the prototype structure the the pressure fluctuations may result in pressures low enough cause cavitation to occur. The numerical model may still be of use, however, as pressure contours can be used to identify low pressure regions, which may be at risk of cavitation damage. This is not always possible using experimental models due to restrictions on measurement locations. The pressure fluctuations observed in physical models also have an effect on plucking damage as they cause vibrations which can cause masonry blocks to move or be removed from the spillway surface. Again, numerical modelling can still be used to identify low pressure regions which may be at risk of plucking damage.

In chapter 5, the Eulerian model with the SST $k - \omega$ was shown to be the most accurate combination of multiphase model for predicting velocities and AVFs above the steps as well as the flow depths. This is not the case for the pressures acting on the step faces of the University of Leeds stepped spillway, as no combination of multiphase model and turbulence

6. THREE-DIMENSIONAL NUMERICAL MODEL STUDY OF A NARROW STEPPED SPILLWAY AT THE UNIVERSITY OF LEEDS

model stands out as the superior numerical model. All of the numerical models generally show good agreement with the experimental data, however, all models show inaccuracies in certain locations.

The numerical models are also unable to predict the occurrence of vortex switching. However, vortex switching appears to be unpredictable. Its cause, and the conditions under which it may occur, are not understood so further research is required to determine when, or if, vortex switching may occur in stepped spillways in service. When vortex switching does occur, the flow structures within the step cavities remain similar, but the direction of circulation of the cross-stream vortices swaps at each step. The numerical models do predict cross-stream vortices so may, therefore, provide a useful tool for identifying vortex structures within stepped spillways, and their associated effect on pressure, even if vortex switching does occur.

6.3.7 Flow Depths

Flow depths in the experiments are measured from the side of the spillway and recorded as the highest point observed by the camera. As such, a limitation of this experimental approach is that it is not feasible to determine if the recorded free-surface value was that at the wall, centreline or somewhere in between. The experimental flow depths will, therefore, be compared to the numerical data both at the centreline of the spillway and at the wall. In all cases y_{90} has been used to define the numerical free-surface.

6.3.7.1 Flow Depth at the Centreline

Firstly the numerically predicted flow depths at the centreline of the spillway will be considered. Figures 6.30 - 6.33 show the experimental mean free-surface profiles \pm the standard deviation, as well as the numerically predicted free-surface profiles at the centreline of the spillway, for the four flow rates investigated.

The VOF model with the two $k - \epsilon$ models underestimates the depth of the free-surface at all locations. The VOF model with the SST $k - \omega$ model underestimates the flow depth in the upstream region of the spillway, however, in the downstream region of the spillway the numerically predicted free-surface appears to agree with the experimental data reasonably well. This result, in fact, is misleading. At $Q = 12$ and 15 l/s, this is due to the splashing which is observed in the numerical model. Time averaging of the splashes causes the flow depth to appear higher than the depth of the main body of water. At $Q = 18$ and 21 l/s no splashing

6.3 Results and Discussion of a 3D Numerical Modelling Study of Skimming Flow over the University of Leeds Stepped Spillway

occurs in the numerical model. There is significant variation in the flow depth across the channel width and the depth at the centreline is significantly higher than that predicted by the other turbulence models. This higher flow depth, however, appears to be a result of the wall effects and are not due to flow bulking caused by air entrainment, as is the case in the experimental flow depths. Note that at $Q = 12 - 18$ l/s the VOF model with the SST $k - \omega$ model predicts a significant decrease in the flow depth at around $x = 1650$ mm. This is due to an air bubble which is trapped in the cavity of step 15. The true flow depth in this position is similar to the flow depth further upstream, as observed in figure 6.13.

The Eulerian model generally predicts the free-surface reasonably accurately at all positions and with all turbulence models, however, at the higher flow rates, the Realisable $k - \epsilon$ and SST $k - \omega$ turbulence models slightly underestimate the flow depth in the middle region of the spillway. These results are similar to the findings of chapter 5, although, in chapter 5 there was a larger difference in the free-surface profiles between the SST $k - \omega$ model and the two $k - \epsilon$ models.

The mixture model shows similar free-surface profiles for all turbulence models. The flow depth is accurately predicted close to the crest of the spillway. The flow depth then increases, but slightly further upstream than in the experimental data. Downstream of this point, the flow depths are predicted reasonably well by all turbulence models. In the far downstream region of the spillway, where the experimental flow depth reduces, at $Q = 12$ l/s, 15 l/s and 18 l/s the flow depths are slightly overestimated. This is dissimilar to the results found in chapter 5 where the mixture model significantly overestimated the flow depth with all turbulence models. These different findings may be due to the the complex free-surface profile caused by the narrow channel width of the University of Leeds spillway, and, possibly, due to the different step geometries of the two spillways investigated in this project.

The Eulerian and mixture models are able to predict the free-surface profile at the centreline of the spillway reasonably accurately. The VOF model, however, underestimates the flow depth as no flow bulking due to air entrainment is predicted. These results, however, do not provide full validation of the numerical models as the flow depths vary across the width of the channel. The numerically predicted flow depths at the wall of the spillway are compared to the experimental data in the following section.

6. THREE-DIMENSIONAL NUMERICAL MODEL STUDY OF A NARROW STEPPED SPILLWAY AT THE UNIVERSITY OF LEEDS

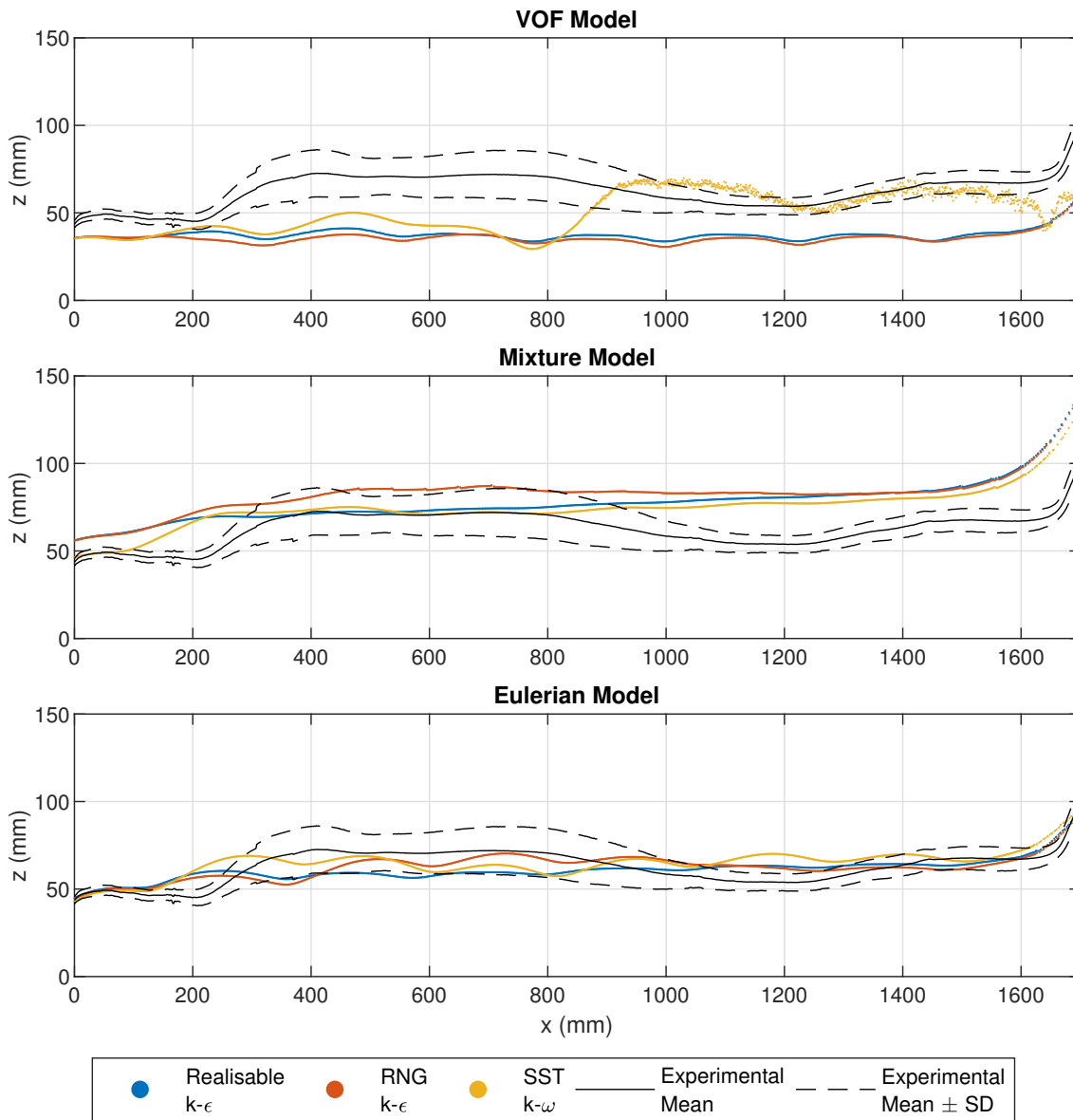


Figure 6.30: Comparison of experimental and numerical flow depths for $Q = 12$ l/s. The experimental mean flow depth \pm the standard deviation is displayed. The numerical flow depths are calculated at the centreline of the spillway, for all combinations of multiphase and turbulence model

6.3 Results and Discussion of a 3D Numerical Modelling Study of Skimming Flow over the University of Leeds Stepped Spillway

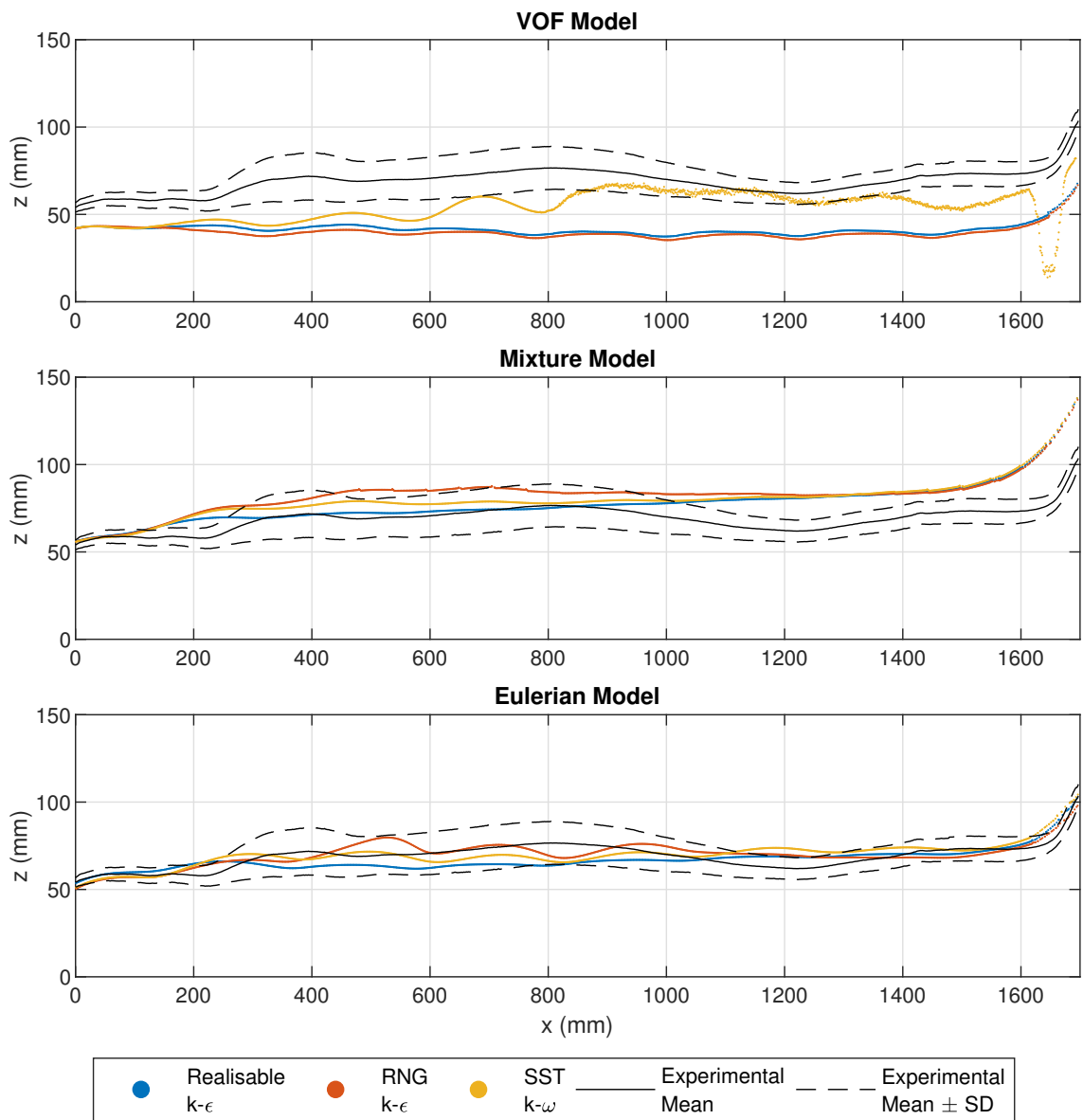


Figure 6.31: Comparison of experimental and numerical flow depths for $Q = 15$ l/s. The experimental mean flow depth \pm the standard deviation is displayed. The numerical flow depths are calculated at the centreline of the spillway, for all combinations of multiphase and turbulence model

6. THREE-DIMENSIONAL NUMERICAL MODEL STUDY OF A NARROW STEPPED SPILLWAY AT THE UNIVERSITY OF LEEDS

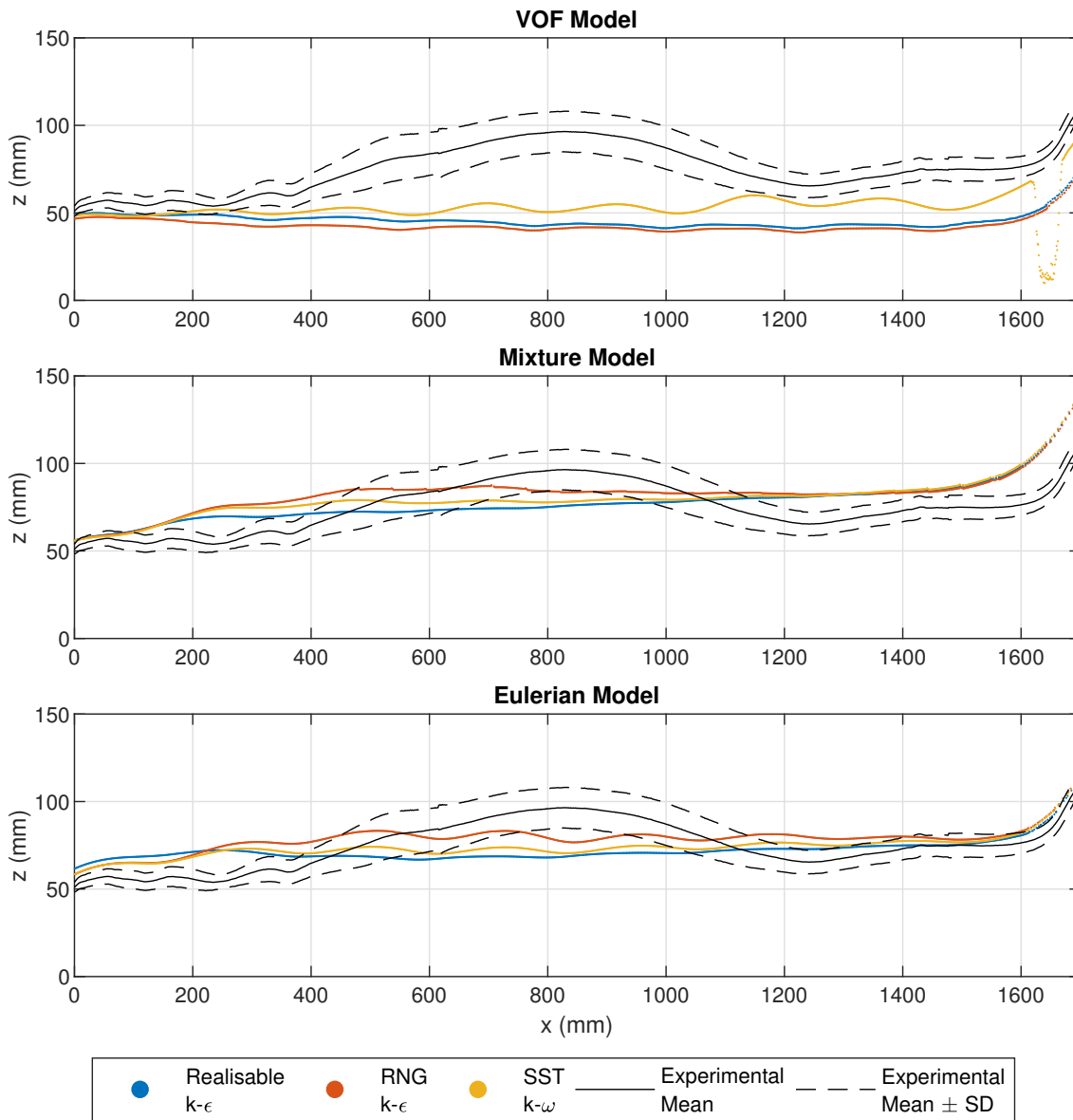


Figure 6.32: Comparison of experimental and numerical flow depths for $Q = 18$ l/s. The experimental mean flow depth \pm the standard deviation is displayed. The numerical flow depths are calculated at the centreline of the spillway, for all combinations of multiphase and turbulence model

6.3 Results and Discussion of a 3D Numerical Modelling Study of Skimming Flow over the University of Leeds Stepped Spillway

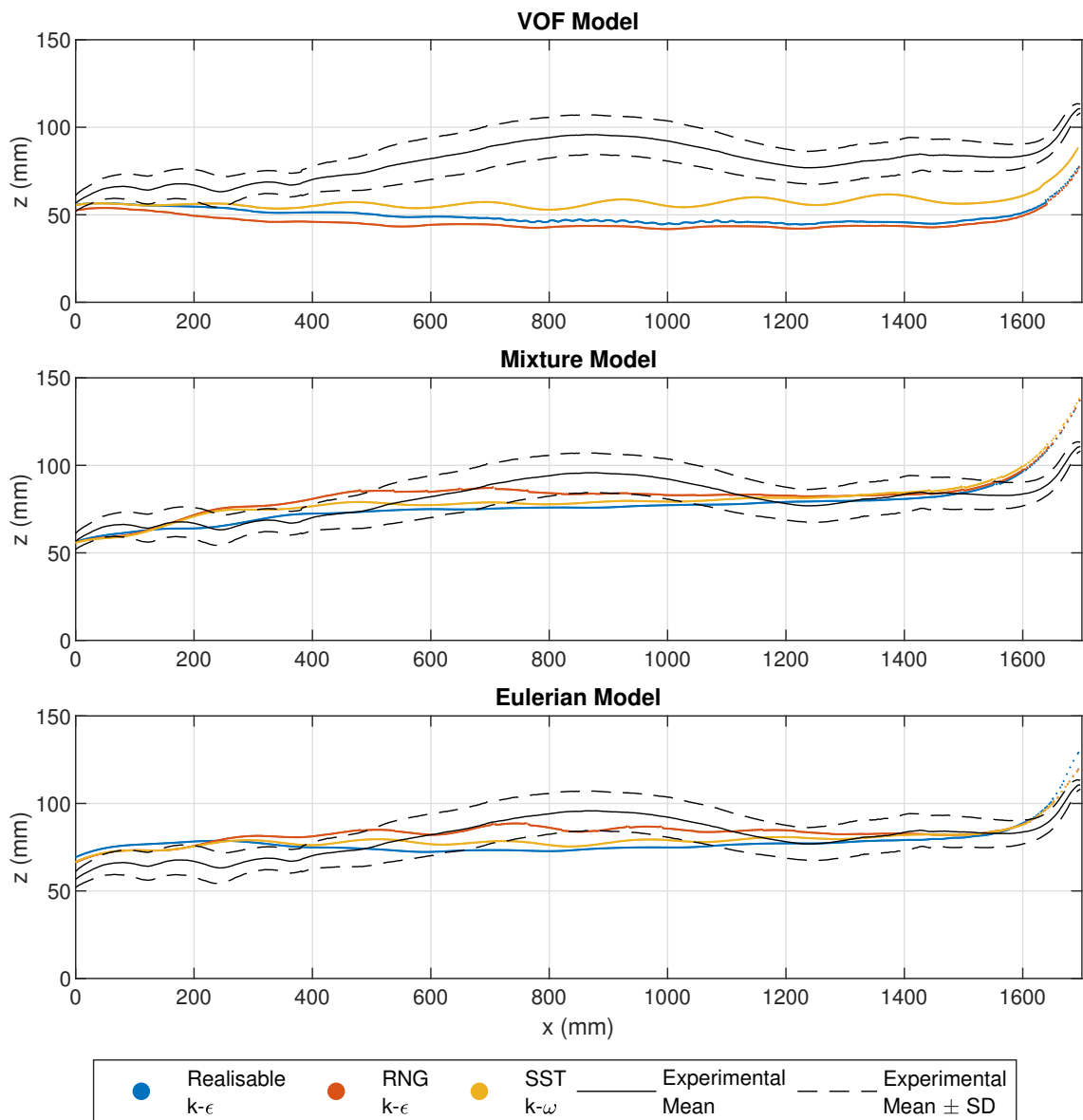


Figure 6.33: Comparison of experimental and numerical flow depths for $Q = 21$ l/s. The experimental mean flow depth \pm the standard deviation is displayed. The numerical flow depths are calculated at the centreline of the spillway, for all combinations of multiphase and turbulence model

6.3.7.2 Flow Depth at the Wall

Figures 6.34 - 6.37 show the experimental mean free-surface profiles \pm the standard deviation, as well as the numerical free-surface profiles at the wall of the spillway, for the four flow rates investigated.

At approximately $x = 250$ mm, there is a distinct sudden increase in the experimental free-surface profiles. This increase is predicted by the majority of the numerical models at the wall. In chapter 3, this increase in flow depth was attributed to flow bulking caused by aeration of

6. THREE-DIMENSIONAL NUMERICAL MODEL STUDY OF A NARROW STEPPED SPILLWAY AT THE UNIVERSITY OF LEEDS

the flow. The numerical models predict a distinct sudden increase in flow depth at the wall but not at the centreline. This suggests that wall effects, caused by the relatively narrow channel width, also contribute to the increase in flow depth. The exact difference in the flow depth between the wall and centreline at this location was difficult to observe in the experimental spillway, due to the highly turbulent and transient nature of the free-surface and inception point location, as well as splashing close to the inception point. It is likely that flow bulking also contributes to the increase in flow depth, as the experimentally observed inception point location correspond to the location where the increase in flow depth occurs.

At $Q = 12$ l/s and $Q = 15$ l/s, the numerical models all tend to predict the sudden increase in flow depth at the correct value of x . At $Q = 18$ l/s and $Q = 21$ l/s, however, the numerical models predict the sudden increase in flow depth further upstream than the experimental data. In fact, the numerical models predict the sudden increase in flow depth at approximately the same position, $x \approx 250$ mm, for all flow rates. The reason for this is unclear, however.

Similarly to at the centreline, the VOF model with the two $k - \epsilon$ models underestimates the flow depth at all locations. The SST $k - \omega$ model underestimates the flow depth in the upstream region of the spillway but predicts a higher, more accurate flow depth further downstream. This is not due to time averaging of the splashing, as discussed above, as the splashing only occurs at the centreline of the spillway. It is also not due to flow bulking, as is the case in the experimental model. At the wall, the free-surface shows significant transient behaviour and wall effects cause the flow depth to be significantly higher than at the centreline. This can be observed in figures 6.6 and 6.14.

It is to be expected that the VOF model underestimates the flow depth in the aerated region, due to the fact the the VOF model does not predict air entrainment, so no flow bulking occurs, as is observed in chapter 5. The VOF model also underestimates the flow depth in the non-aerated region, although it is more accurate than in the aerated region. This, again, is similar to the results observed in chapter 5. However, in chapter 5 this is attributed to the fact that the experimental free-surface is defined as y_{90} , and transient waviness at the free-surface may cause y_{90} to be slightly higher than in the numerical data, which is confirmed by the fact that the VOF model predicts the equivalent clear water depth, d , accurately at the LNEC stepped spillway. This cannot be the case for the experimental data presented here, as the free-surface is not defined as y_{90} , but rather as the maximum fluid depth observed by the camera. The standard deviation from the mean experimental flow depth is displayed in the

6.3 Results and Discussion of a 3D Numerical Modelling Study of Skimming Flow over the University of Leeds Stepped Spillway

figures, which would account for unsteady waviness in the free-surface.

Experimental error may be a reason why the VOF model appears to underestimate the flow depths in the non-aerated region. The the calibration of the orifice plate, which is used to measure the flow rates, has an error of $\pm 2.5\%$. A difference in the flow rate between the numerical and experimental model would result in a difference in the flow depth. There will also be some experimental error in the measurement of the free-surface, which may affect the results. The use of image analysis to measure flow depth is less developed than more established flow depth measurement techniques, such as through analysis of the AVFs. Further investigation into flow depth measurement through image analysis could be undertaken in order to fully quantify the experimental uncertainty associated with this measurement technique.

The Eulerian model generally predicts the flow depths at the wall reasonably accurately with the RNG $k - \epsilon$ and SST $k - \omega$ turbulence models at all locations. The Realisable $k - \epsilon$ model tends to predict a lower flow depth than the other turbulence models and underestimates the experimental flow depth in the middle region of the spillway, where the increase in flow depth is observed. The RNG $k - \epsilon$ model predicts the increase in depth reasonably well, however, slightly too far upstream at the higher flow rates, as discussed above. The SST $k - \omega$ model is discussed in more detail below.

The mixture model predicts the flow depth reasonably accurately close to the crest of the spillway. The RNG $k - \epsilon$ and SST $k - \omega$ models overestimate the sudden increase in flow depth significantly, whereas, the Realisable $k - \epsilon$ model is more accurate. Downstream of this point the flow depths are predicted reasonably accurately by all turbulence models. In the far downstream region, like at the centreline, the flow depth is slightly overestimated at all flow rates other than $Q = 21$ l/s.

6. THREE-DIMENSIONAL NUMERICAL MODEL STUDY OF A NARROW STEPPED SPILLWAY AT THE UNIVERSITY OF LEEDS

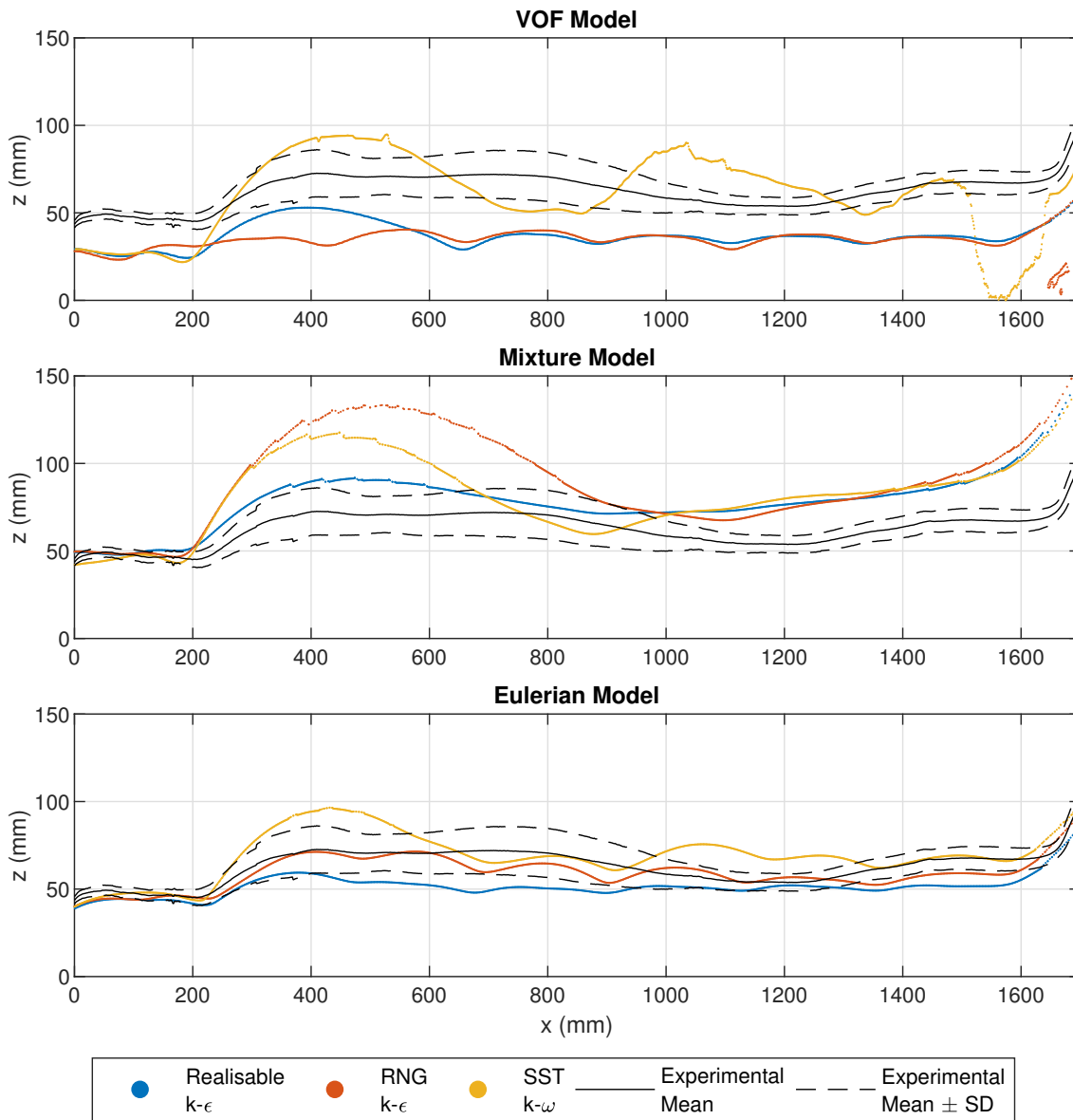


Figure 6.34: Comparison of experimental and numerical flow depths for $Q = 12$ l/s. The experimental mean flow depth \pm the standard deviation is displayed. The numerical flow depths are calculated at the wall of the spillway, for all combinations of multiphase and turbulence model

6.3 Results and Discussion of a 3D Numerical Modelling Study of Skimming Flow over the University of Leeds Stepped Spillway

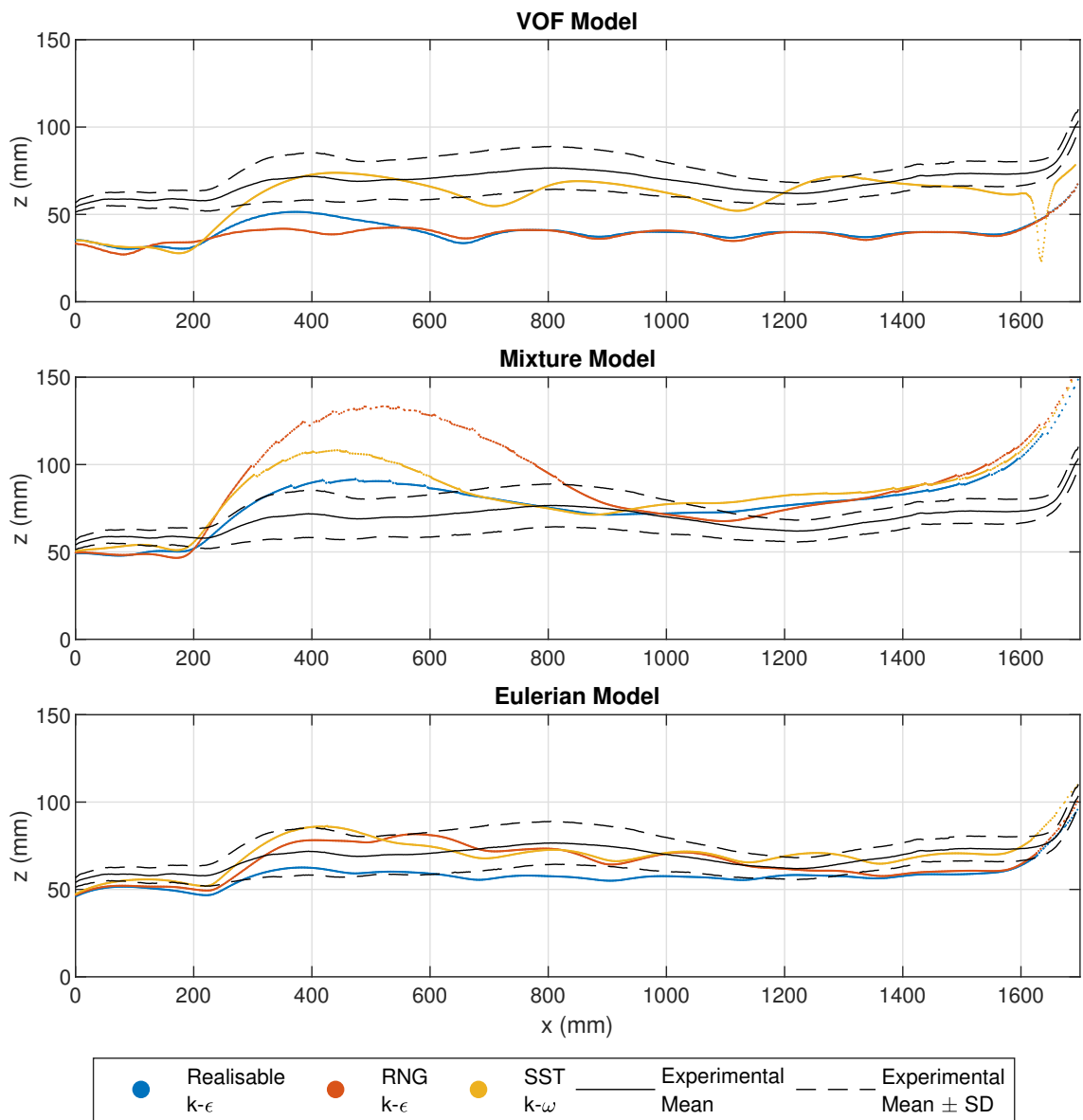


Figure 6.35: Comparison of experimental and numerical flow depths for $Q = 15$ l/s. The experimental mean flow depth \pm the standard deviation is displayed. The numerical flow depths are calculated at the wall of the spillway, for all combinations of multiphase and turbulence model

6. THREE-DIMENSIONAL NUMERICAL MODEL STUDY OF A NARROW STEPPED SPILLWAY AT THE UNIVERSITY OF LEEDS

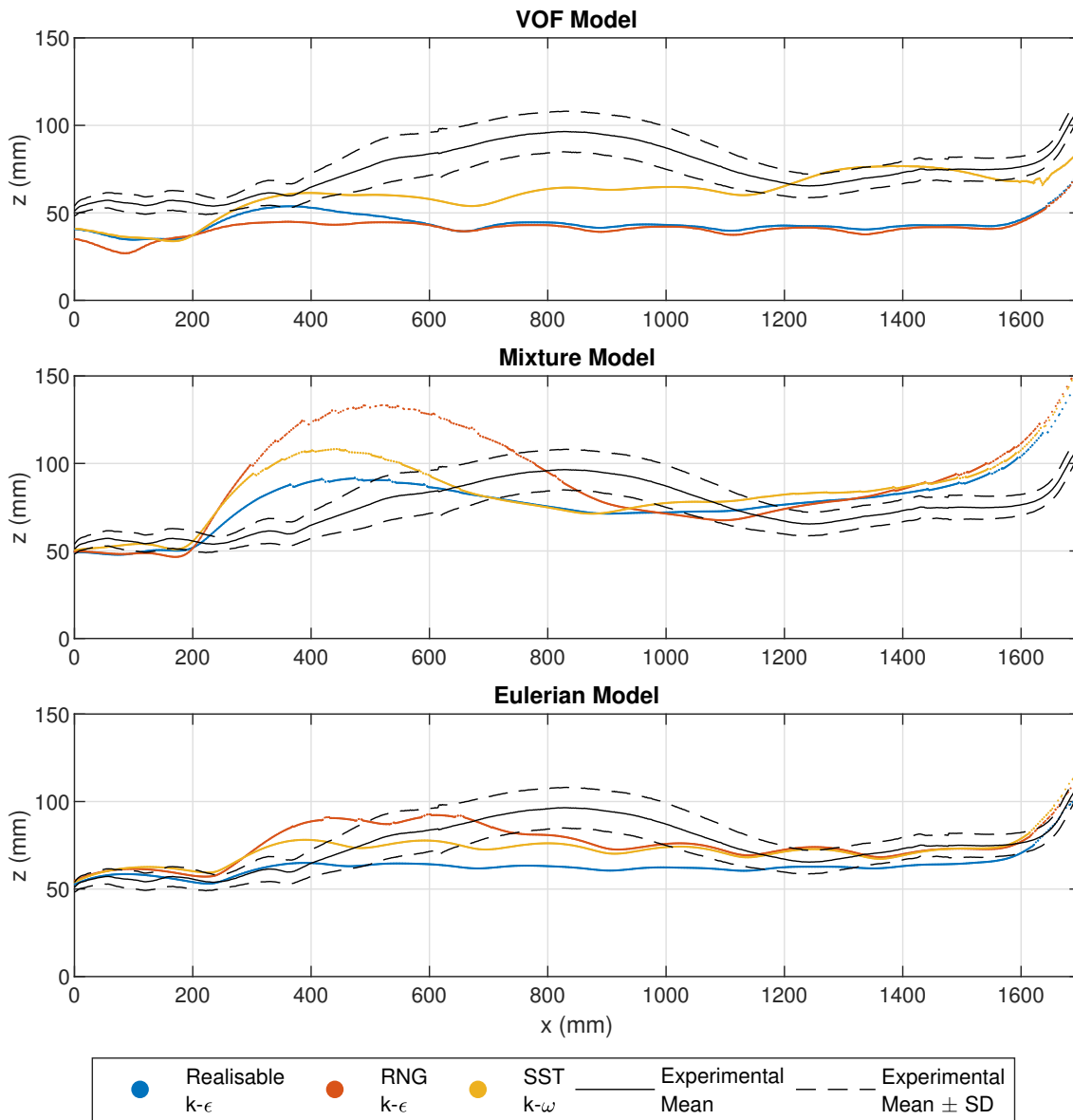


Figure 6.36: Comparison of experimental and numerical flow depths for $Q = 18$ l/s. The experimental mean flow depth \pm the standard deviation is displayed. The numerical flow depths are calculated at the wall of the spillway, for all combinations of multiphase and turbulence model

6.3 Results and Discussion of a 3D Numerical Modelling Study of Skimming Flow over the University of Leeds Stepped Spillway

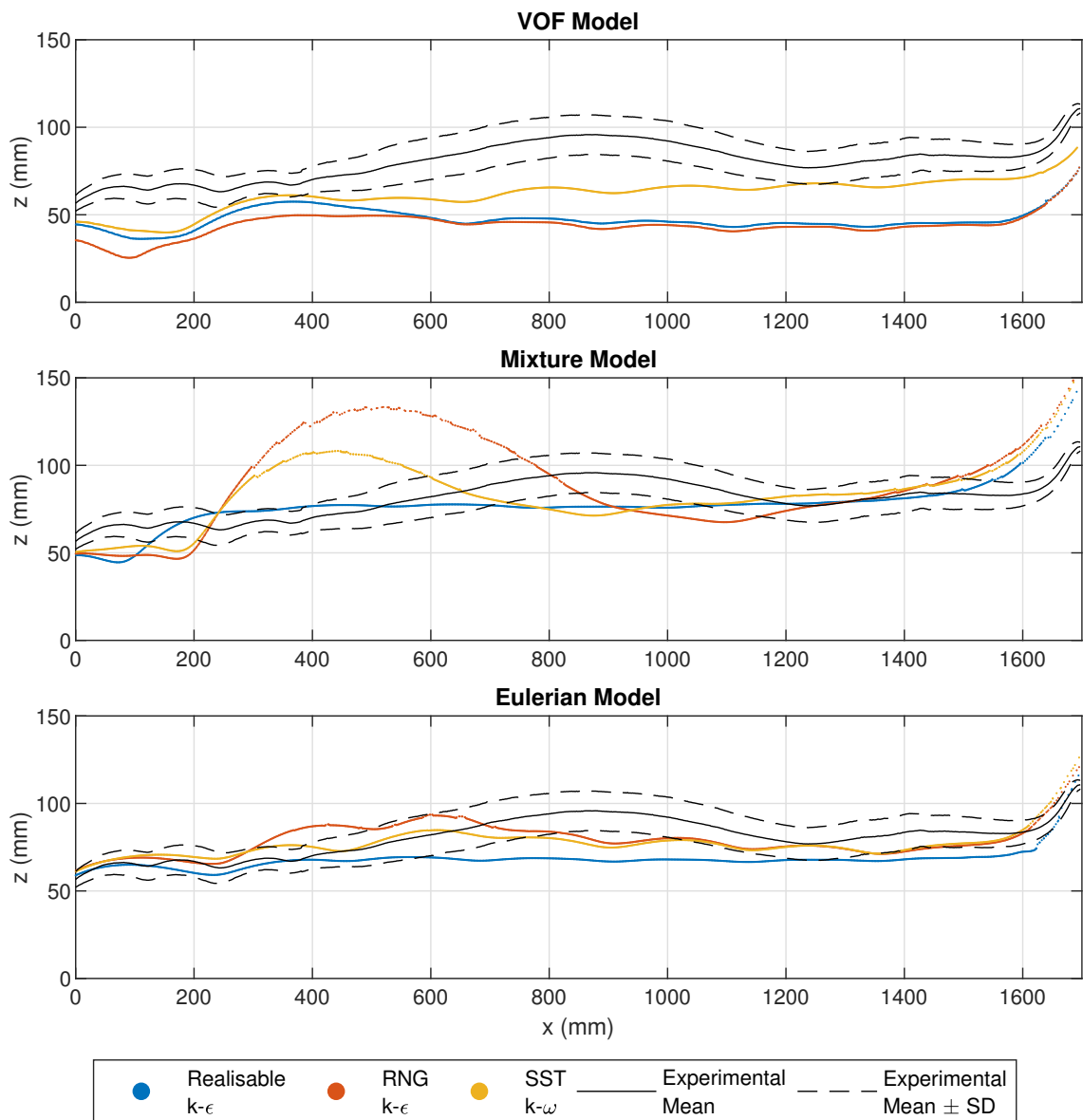


Figure 6.37: Comparison of experimental and numerical flow depths for $Q = 21$ l/s. The experimental mean flow depth \pm the standard deviation is displayed. The numerical flow depths are calculated at the wall of the spillway, for all combinations of multiphase and turbulence model

6.3.7.3 Comparison of Numerically Predicted Flow Depths at the Wall and the Centreline

The Eulerian model has been found to be the most accurate multiphase model at predicting the flow depths at both the centreline and at the wall. In this section the numerically predicted free-surface profiles at the wall and centreline are compared to one another, as well as to the experimental flow depths. Figure 5.33 shows the free-surface profiles, predicted by the Eulerian model with the SST $k - \omega$ model, at both the centreline and the wall, as well as the Experimental free-surface profiles, for each flow rate investigated. The SST $k - \omega$ turbulence

6. THREE-DIMENSIONAL NUMERICAL MODEL STUDY OF A NARROW STEPPED SPILLWAY AT THE UNIVERSITY OF LEEDS

model was chosen as this turbulence model has performed well at predicting the free-surface at both the wall and centreline in this chapter, and also was shown, in chapter 5, to be the most accurate turbulence model, when used in conjunction with the Eulerian model, at predicting the flow depths at the LNEC stepped spillway.

Generally the flow depths are predicted reasonably accurately at both the wall and the centreline. Other than at the sudden increase in flow depth, the Eulerian model predicts similar flow depths at the wall and at the centreline. In chapter 5 the Eulerian model predicted a smooth free-surface, whereas, it can be seen in figure 6.38 that there are waves in the free-surface. The wavelength of these waves is approximately equal to two step lengths (≈ 226 mm) other than where the sudden increase in flow depth at the wall occurs. There are several possibilities for the cause of the waves in the free-surface. It may be due to the shallower slope of the spillway, the cross-stream vortices, the significant wall effects caused by the narrow channel width or a combination of these reasons.

6.3 Results and Discussion of a 3D Numerical Modelling Study of Skimming Flow over the University of Leeds Stepped Spillway

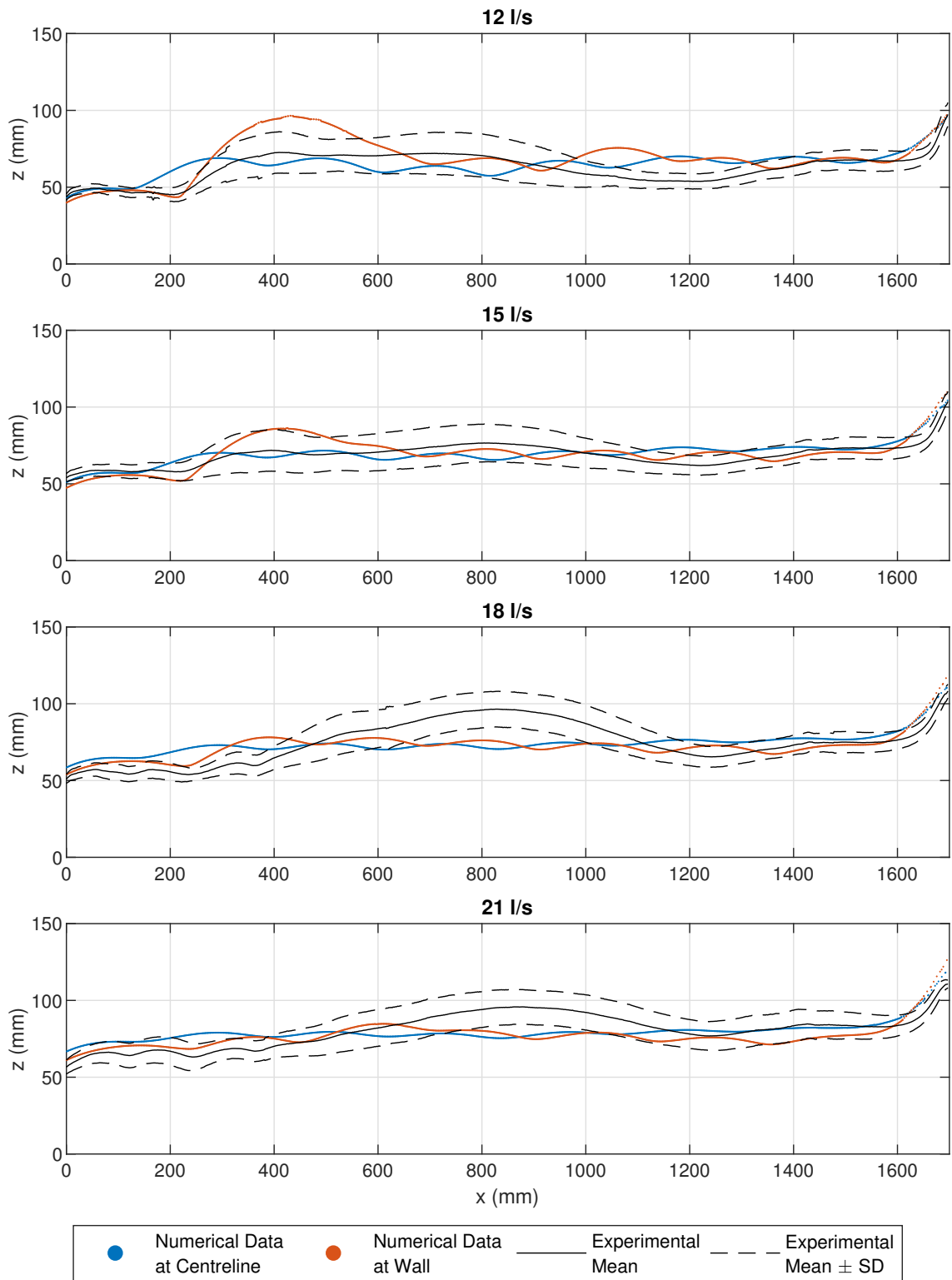


Figure 6.38: Comparison of experimental and numerical flow depths for the Eulerian model with the SST $k - \omega$ model, at all flow rates investigated. The experimental mean flow depth is displayed and the numerical flow depths at both the centreline and at the wall of the spillway are displayed

6. THREE-DIMENSIONAL NUMERICAL MODEL STUDY OF A NARROW STEPPED SPILLWAY AT THE UNIVERSITY OF LEEDS

6.3.7.4 Summary

In chapter 5, the numerically predicted free-surface profiles were compared to experimentally measured flow depths at individual points along the length of the spillway. The numerical modelling was conducted in 2D and the experimental measurements were taken at the centreline of the spillway, where wall effects were minimal. In this chapter, the numerically predicted flow depths were compared to full experimental free-surface profiles. The numerical modelling in this chapter was conducted in 3D and, due to the relatively narrow channel width, the free-surface profiles varied significantly across the width of the channel. For this reason, the numerically predicted flow depths at both the wall and the centreline of the spillway were compared to experimentally measured free-surface profiles.

The Eulerian model accurately predicted d in the non-aerated region and y_{90} in the aerated region, with the SST $k - \omega$ turbulence model, at the LNEC stepped spillway. The two $k - \epsilon$ models produced less accurate results than the SST $k - \omega$ model, however. The flow depths in the University of Leeds spillway were generally predicted reasonably well by both the Eulerian model with both the SST $k - \omega$ and RNG $k - \epsilon$ turbulence models. The Realisable $k - \epsilon$ model underestimated the flow depths at the wall slightly, however, was reasonably accurate at the centreline. Overall, taking into account the results from chapter 5 and this chapter, the Eulerian model with the SST $k - \omega$ model is the most accurate combination of multiphase model and turbulence model at predicting flow depths in skimming flows over stepped spillways.

The VOF model does not predict flow bulking caused by air entrainment so, therefore, underestimates the free-surface in the aerated region. Despite this, numerical modelling was conducted using the VOF model for comparison with other multiphase numerical models, as the VOF model is commonly employed for free-surface modelling and is able to predict certain flow features, such as the recirculating vortices, accurately.

The mixture model predicts air entrainment so might be expected to predict the flow depth in the aerated region more accurately than the VOF model. In chapter 5 the mixture model significantly overestimated the flow depth at all locations and with all turbulence models. The flow depths at the centreline of the University of Leeds spillway, however, were generally predicted reasonably well by the mixture model. At the wall however, the mixture model was less accurate.

Neither the Eulerian or mixture models specifically model a free-surface, as the VOF model does. Despite this, by considering y_{90} as the numerical free-surface, both of these multiphase

6.3 Results and Discussion of a 3D Numerical Modelling Study of Skimming Flow over the University of Leeds Stepped Spillway

models are able to predict 3D free-surface profiles caused by the interaction between the flow and the wall. The mixture model is less accurate than the Eulerian model, however.

Differences between the numerically predicted and experimentally measured free-surface profiles may also be due to small differences in the boundary conditions. The process of recirculating the flow in the experimental spillway may have a relatively small effect on the inflow boundary, which may result in the more transient nature of the flow observed in the experimental model. Predicting the transient nature of the flow is challenging and further research into this area is required. In order to match the inlet boundary conditions in the numerical and experimental models exactly would require further, extremely controlled, investigation, which is outside the remit of this project.

6.3.8 Inception Point

In chapter 5, four methods for defining the inception point in the numerical data were investigated for the spillway at the LNEC. These four methods are also investigated for the spillway at the University of Leeds.

6.3.8.1 Intersection of the Turbulent Boundary Layer and the free-surface

Figures 6.39 - 6.41 show the equivalent clear water depths and the depths of the turbulent boundary layers, for all multiphase and turbulence models, at all of the flow rates investigated. The experimentally defined inception points, including the precision error (described in chapter 3), are also indicated in the figures.

Firstly, it can be seen that the equivalent clear water depths show similar behaviour to the y_{90} profiles shown in section 6.3.7. In both the VOF model and Eulerian model results, d shows a wavy profile due to the locations of the step corners. In the mixture model d increases significantly with the RNG $k - \epsilon$ and SST $k - \omega$ turbulence models at approximately $x = 100$ mm, but not with the Realisable $k - \epsilon$ model.

Like in chapter 5, the intersection of the turbulent boundary layer and the equivalent clear water depth will be defined as the location where the profiles for d and the TBL become parallel to one another. In some cases d and the TBL do not become parallel, due to the pattern of waves in the the equivalent clear water depth and also waviness of the TBL. In the cases where d and the TBL do not become parallel, the intersection of the two lines will be defined as the point where the two lines are closest to one another.

6. THREE-DIMENSIONAL NUMERICAL MODEL STUDY OF A NARROW STEPPED SPILLWAY AT THE UNIVERSITY OF LEEDS

Generally the location of the inception point is predicted reasonably well by all multiphase models and turbulence models. However, there are inconsistencies in the accuracy of each model in predicting the distance to the inception point (L_i). For example the VOF model with the SST $k - \omega$ model overestimates L_i significantly at $Q = 15$ l/s but slightly underestimates L_i at 21 l/s.

6.3 Results and Discussion of a 3D Numerical Modelling Study of Skimming Flow over the University of Leeds Stepped Spillway

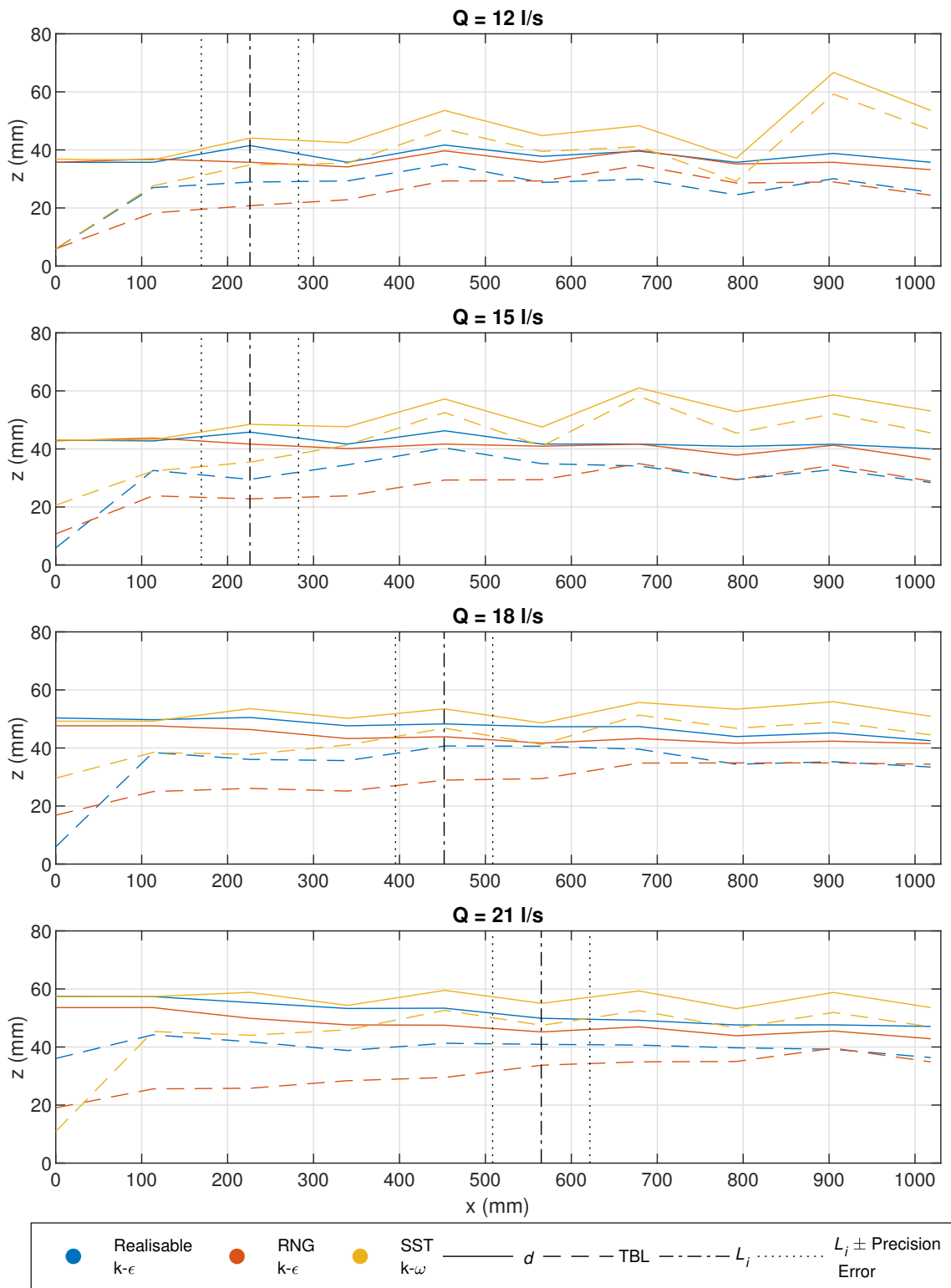


Figure 6.39: Equivalent clear water depth and turbulent boundary layer for the VOF model, with various turbulence models, at all flow rates considered. The experimental locations of L_i and the precision error are also indicated

6. THREE-DIMENSIONAL NUMERICAL MODEL STUDY OF A NARROW STEPPED SPILLWAY AT THE UNIVERSITY OF LEEDS

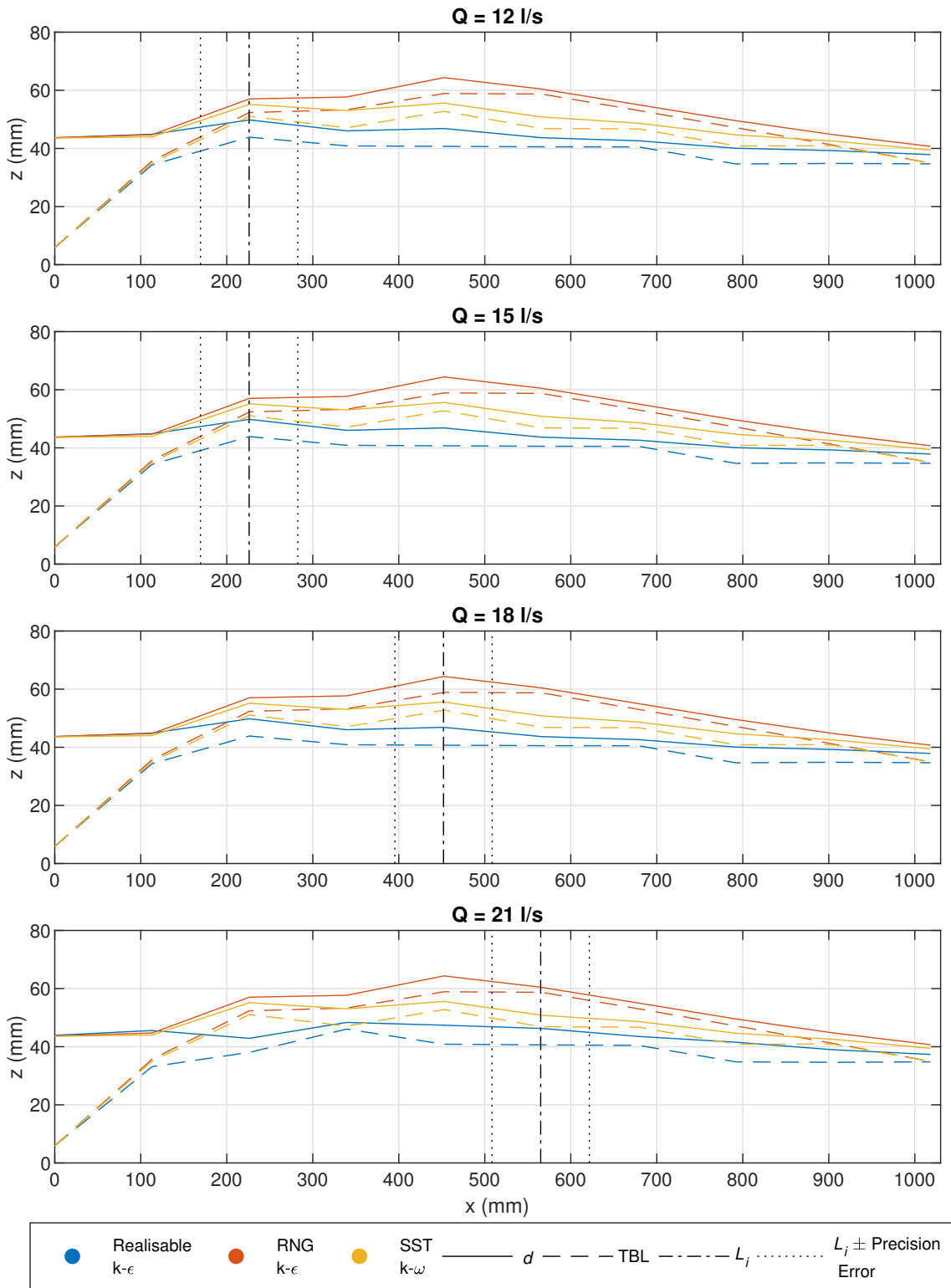


Figure 6.40: Equivalent clear water depth and turbulent boundary layer for the mixture model, with various turbulence models, at all flow rates considered. The experimental locations of L_i and the precision error are also indicated

6.3 Results and Discussion of a 3D Numerical Modelling Study of Skimming Flow over the University of Leeds Stepped Spillway

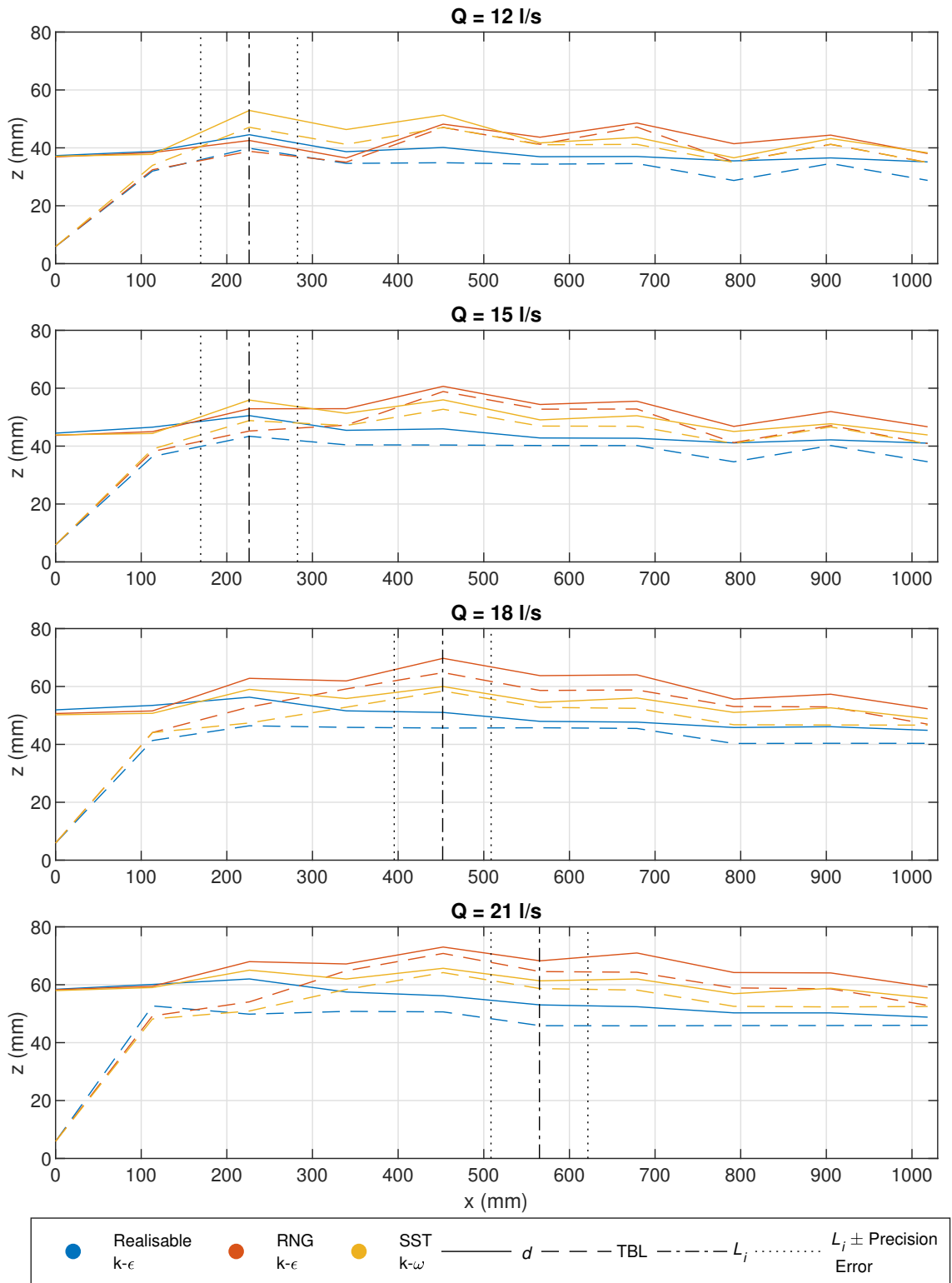


Figure 6.41: Equivalent clear water depth and turbulent boundary layer for the Eulerian model, with various turbulence models, at all flow rates considered. The experimental locations of L_i and the precision error are also indicated

The wall effects, caused by the relatively narrow channel width, are likely a major reason

6. THREE-DIMENSIONAL NUMERICAL MODEL STUDY OF A NARROW STEPPED SPILLWAY AT THE UNIVERSITY OF LEEDS

for the inconsistencies observed in the accuracy of each model in predicting L_j . It has been shown in sections 6.3.1 and 6.3.7 that y_{90} varies significantly across the channel width, due to wall effects. Therefore, d may also vary significantly across the channel width.

Figure 6.42 shows velocity contours, at planes parallel to the pseudo-bottom and at different values of z for the Eulerian model with the SST $k - \omega$ model, at $Q = 18$ l/s. It can be seen that, at $z = 0$ mm, the pattern of velocity matches the cross-stream vortices and varies across the channel width, and also at each step. At $z = 50$ mm, strong wall effects can be observed and the velocity varies significantly across the width of the channel. At $z = 25$ mm, the velocity contour shows wall effects and also some effects from the cross-stream vortices, again causing a variation in the velocity across the channel width. The depth of the TBL is defined using the velocity profiles, and it can be seen, from figure 6.42, that the velocity, and therefore the depth of the TBL, varies across the channel width. Note that, the effect that the cross-stream vortices have on the velocity profiles is likely the cause of the wave pattern in the depth of the TBL, as discussed above. As the pattern of cross-stream vortices, and therefore the effect that they have on the velocity profiles, changes at each step, the depth of the TBL may increase and decrease as x increases.

Both d and the TBL vary across the channel width. The profiles shown in figures 6.39 - 6.41 are taken at the centreline of the spillway, however different profiles, and, therefore, different values for L_j , would be predicted at different values of w . For these reasons, this data should be viewed with caution when drawing conclusions on the reliability of these numerical models in predicting the location of the inception point by the intersection of the TBL and the equivalent clear water depth.

6.3 Results and Discussion of a 3D Numerical Modelling Study of Skimming Flow over the University of Leeds Stepped Spillway

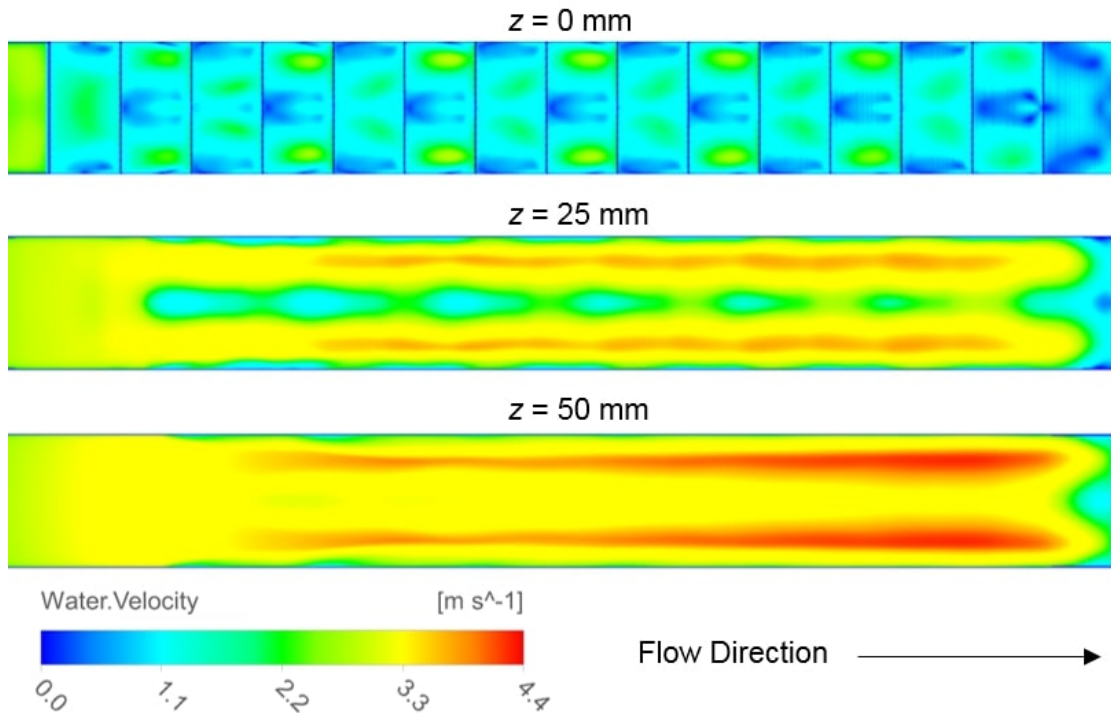


Figure 6.42: Velocity contours at planes parallel to the pseudo-bottom at different values of z for the Eulerian multiphase model with the SST $k - \omega$ turbulence model, at $Q = 18$ l/s

6.3.8.2 Visual Inspection

The experimentally defined location of the inception point for the University of Leeds spillway is the step corner immediately upstream of the step cavity that has a continuous presence of air bubbles when viewed from the side walls. Figure 6.43 shows contours of air volume fraction for the Eulerian model with the SST $k - \omega$ model at all of the flow rates investigated. Again strong wall effects are observed so, for each flow rate, AVF contours have been shown at $w = 0$ mm (the wall), $w = 37.5$ mm and $w = 75$ mm (the centreline). The experimentally observed inception point locations (IP) are also indicated.

It can be seen that, at each flow rate, an AVF of 0.1-0.2 is transported into the step cavities slightly further upstream at $w = 37.5$ mm than at the wall or the centreline. At most flow rates, the inception point by visual inspection of air entrainment into the step cavities is predicted well. At $w = 37.5$ mm an AVF of 0.1-0.2 is, at least partly, present in the step cavity directly downstream of the experimentally observed inception point. At the wall and the centreline and AVF of 0.1-0.2 is present in the step cavity within two steps of the experimentally observed inception point.

6. THREE-DIMENSIONAL NUMERICAL MODEL STUDY OF A NARROW STEPPED SPILLWAY AT THE UNIVERSITY OF LEEDS

The exception to this is at $Q = 15$ l/s, where the numerical model predicts air to be transported into the step cavities further downstream than was observed experimentally. This, however, is likely due to the fact that the experimentally observed inception point is located in the same position as at 12 l/s. The numerical data predicts air to be entrained into the step cavities further downstream as Q increases. At 15 l/s, an AVF of 0.1-0.2 is transported into the step cavities further downstream than at $Q = 12$ l/s, but further upstream than at $Q = 18$ l/s. This is to be expected as the inception point moves downstream with increasing discharge (Chanson, 2002). A possible explanation for the difference in the experimental and numerical inception point locations at $Q = 15$ l/s, is that the experimental method to define the inception point is only precise to \pm half of the distance between step corners (56.57 mm). Although the inception location by observation of the AVF contours is less accurate at $Q = 15$ l/s than at the other flow rates, it is still reasonably accurate.

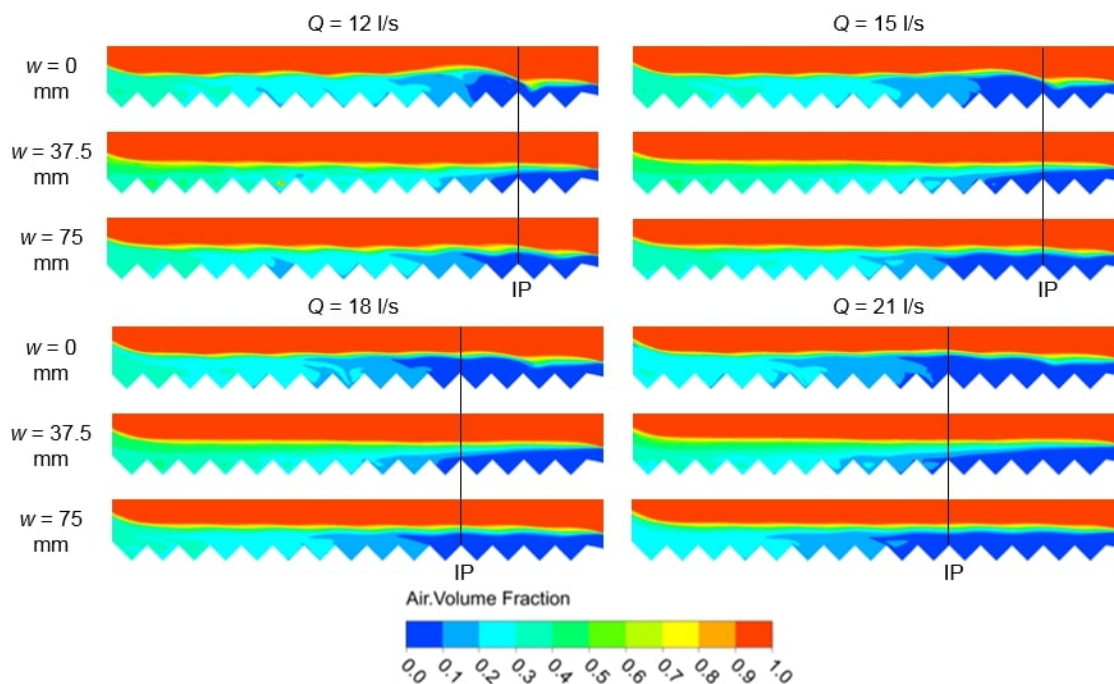


Figure 6.43: Contours of air volume fraction for the Eulerian multiphase model, with the SST $k - \omega$ turbulence model, at each flow rate investigated. The contours of air volume fraction are shown at $w = 0$ mm (wall), $w = 37.5$ mm and $w = 75$ mm (centreline). The locations of the experimentally defined inception points (IP) are also indicated

6.3 Results and Discussion of a 3D Numerical Modelling Study of Skimming Flow over the University of Leeds Stepped Spillway

6.3.8.3 Depth Averaged Air Volume Fraction and Air Volume Fraction at the Pseudo-Bottom

Bung (2011) defines the inception point as the location where the depth averaged air concentration, C_{mean} , is equal to 0.2, based on experimental findings by Matos (2000) and Boes and Hager (2003a). Boes and Hager (2003a) found the location of the inception point by visual observation of the surface flow conditions to correspond with the location where the air concentration at the pseudo-bottom is equal to 0.01. In chapter 5, it was shown that these methods could be used to predict the inception point locations in the Eulerian model with the SST $k - \omega$ model, using slightly higher values than 0.2 and 0.01. Analysis of C_{mean} , however, was shown to be the more reliable of these two methods.

Figures 6.44 and 6.45 show C_{mean} and the AVF at the pseudo-bottom respectively, across the channel width for the Eulerian model with the SST $k - \omega$ model at $Q = 18$ l/s. The data shown in the figures are recorded at $x = 452$ mm (step 5), the experimentally recorded inception point. It can be seen that both C_{mean} and the AVF at the pseudo-bottom vary significantly across the channel width. This is due to the relatively narrow width of the channel causing wall boundary effects to impact the entire channel width. It is unclear which value of w , if any, should be considered most reliable for defining the location of the inception point using these methods. Therefore, this spillway geometry is not suitable to investigate whether the numerical models can accurately predict the inception point location by analysis of C_{mean} or the AVF at the pseudo-bottom.

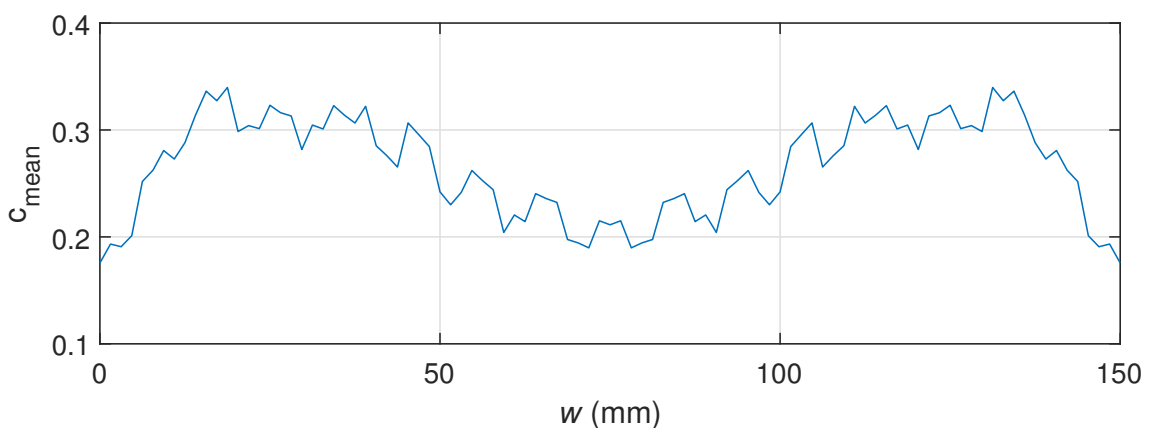


Figure 6.44: The depth averaged air volume fraction (C_{mean}) across the channel width for the Eulerian multiphase model, with the SST $k - \omega$ turbulence model, at $Q = 18$ l/s. C_{mean} is calculated at $x = 452$ mm (step 5), the experimentally observed inception point at $Q = 18$ l/s

6. THREE-DIMENSIONAL NUMERICAL MODEL STUDY OF A NARROW STEPPED SPILLWAY AT THE UNIVERSITY OF LEEDS

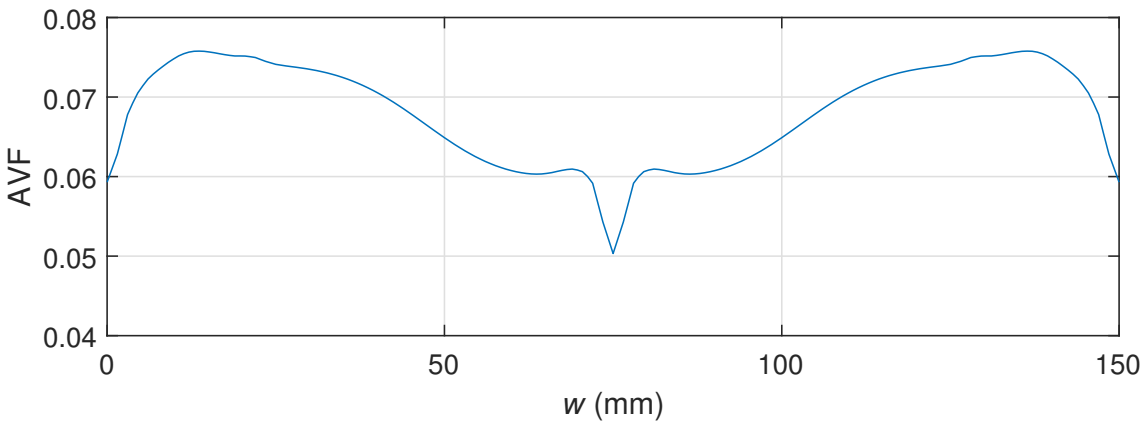


Figure 6.45: The air volume fraction at the pseudo-bottom, across the channel width for the Eulerian multiphase model, with the SST $k - \omega$ turbulence model, at $Q = 18$ l/s. The AVF is recorded at $x = 452$ mm (step 5), the experimentally observed inception point at $Q = 18$ l/s

6.4 Conclusions

A comprehensive 3D numerical study of the University of Leeds experimental stepped spillway has been conducted using the VOF, mixture and Eulerian multiphase models, in conjunction with the Realisable $k - \epsilon$, RNG $k - \epsilon$ and SST $k - \omega$ turbulence models. The pressures, flow depths and inception point locations were investigated, as well as the occurrence of cross-stream vortices in the step cavities. As in chapter 5, the Eulerian model predicts air entrainment and is shown to be able to accurately predict a number of flow features, including the complex pattern of cross-stream vortices in the step cavities, the associated effect on the pressure patterns and the flow depths at the wall and the centreline of the spillway.

The VOF model does not predict air entrainment, whereas the mixture and Eulerian models do. Similarly to chapter 5, the Eulerian and mixture models predict that a small amount of air is entrained into the flow close to the spillway crest, further upstream than is observed in the experimental models. The same reasons as described in chapter 5 are hypothesised as the cause of this aeration close to the spillway crest.

All numerical models predicted 3D cross-stream vortices in each step cavity, with the direction of the cross-stream vortices alternating at each step. This agreed with the patterns of vortices which were observed in the experimental spillway. At $Q = 21$ l/s, however, the numerical models predicted that the cross-stream vortices circulated in the same directions as the lower flow rates, whereas, in the experimental spillway the predominant direction of circulation of the cross-stream vortices, at $Q = 21$ l/s, was the opposite to that at the lower

flow rates.

The VOF model in combination with the SST $k - \omega$ model predicts a transient free-surface profile, with splashing occurring at the centreline of the spillway at the lower flow rates. Other than this, only negligible transient behaviour was observed in any of the numerical models. Therefore, the numerical models did not predict vortex switching or the pressure fluctuations which were observed in the experimental model.

In both the Eulerian and mixture models, as well as in the experimental model, air entrainment was shown to reduce the high pressures on the horizontal step faces, but did not have a significant effect on the low pressures acting on the vertical step faces. These low pressure regions may still be protected from cavitation damage in the aerated region, as the presence of air may act to cushion the collapse of vapour bubbles. Air entrainment of the flow, however, does not appear to protect the spillway from plucking damage as low pressure regions are observed throughout the spillway on both the step faces and the spillway side walls.

The numerical models predict the pressure patterns caused by the cross-stream vortices accurately, although at $Q = 21$ l/s they do not predict the direction of circulation of the cross-stream vortices correctly. Significant vortex switching occurs at this flow rate, which is not predicted by the numerical models. The numerical models generally predict the magnitudes of pressure reasonably well, however, in some locations they are less accurate. The numerical models predict pressures which differ from one another significantly in certain locations, however, these locations often correspond to large pressure fluctuations in the experimental data, so the dissimilar numerical pressures all fall within the experimental standard deviation.

At the top of the vertical step faces, the numerical models predict a highly localised low pressure region. Experimental pressure data is not available in these locations, however, so further research is required to validate the numerically predicted pressures at the top of the vertical step faces.

The numerical models are unable to predict the experimental pressure fluctuations, or vortex switching, as these are both transient effects. However, the numerical models are able to predict cross-stream vortices and their associated effects on pressure, so the numerical models may still provide a useful tool for predicting complex flow structures and pressure distributions within stepped spillways.

The experimental free-surface measurement technique is unable to distinguish between the flow depth at the wall and the at the centreline of the spillway. Therefore the numerical

6. THREE-DIMENSIONAL NUMERICAL MODEL STUDY OF A NARROW STEPPED SPILLWAY AT THE UNIVERSITY OF LEEDS

data at both the wall and centreline was compared to the experimental data. The free-surface, in both the experiments and numerical models, is more complex in the University of Leeds stepped spillway than the LNEC stepped spillway, due to the significant wall effects, which are observed in both the experimental and numerical models, caused by the relatively narrow channel width.

Despite this, the Eulerian model was able to predict the free-surface profiles reasonably well, especially with the SST $k - \omega$ turbulence model. This combination of multiphase and turbulence model also predicted the LNEC spillway flow depths accurately. The Eulerian model, however, tended to slightly underestimate the flow depth in the middle section of the spillway. The VOF model generally underestimated the flow depth, although the SST $k - \omega$ model predicted slightly higher flow depths due to transient behaviour, splashing and wall effects. Flow bulking due to air entrainment, however, was not predicted. The mixture model predicted the free-surface position accurately in some locations, however tended to overestimate the flow depth in the downstream region of the spillway.

In the same manner as in chapter 5, four methods of identifying the inception point location were investigated. The wall effects, which are observed in the numerical and physical models, caused the depth averaged AVFs, and the AVFs at the pseudo-bottom, to vary significantly across the channel width, so these methods could not be used to identify the location of the inception point. Some reasonable predictions of the inception point location were made by considering the position where the TBL intersects the equivalent clear water depth, and by visual observation of the AVF contours. However, the wall effects caused by the narrow channel width also influenced these methods. Therefore, it may be more appropriate to investigate the identification of location of the inception point using numerical models by considering wider channels, in which wall effects are not as significant, as was conducted in chapter 5.

CHAPTER 7

Study into the Occurrence of Cross-Stream
Vortices in Stepped Spillways of Varying
Geometry

7. STUDY INTO THE OCCURRENCE OF CROSS-STREAM VORTICES IN STEPPED SPILLWAYS OF VARYING GEOMETRY

7.1 Introduction

Visual observations of the 150 mm wide stepped spillway at the University of Leeds showed cross-stream vortices within the step cavities. These observations were verified by pressure measurements on the step faces. The cross-stream vortices were also observed in numerical simulations of the spillway. This chapter describes investigations into the occurrence of cross-stream vorticity in stepped spillways with varying geometries.

The stepped spillway at the LNEC was modelled in 2D and numerical models were able to accurately predict velocities and AVFs above the pseudo-bottom as well as the flow depths and inception point locations. 2D modelling was considered to be suitable for modelling the flow above the step cavities, as Bombardelli et al. (2011) found the flow above the steps to be essentially 2D from comparison of experimentally measured velocities and AVFs at different verticals across the channel width. Matos et al. (1999), on the other hand, found that there was a 3D structure to the flow within the step cavities. This chapter also describes an investigation into the 3D behaviour within the step cavities of the LNEC spillway.

7.2 Cross-Stream Vorticity in Channels of Varying Width

This section describes an investigation into the occurrence of cross-stream vortices in spillways with 80 mm \times 80 mm steps, in common with the experimental stepped spillway at the University of Leeds, but of varying widths. In order to reduce computational costs, the spillways in this section consist of only 5 steps. The inlet and approach channel have the same geometry as the simulations of the experimental stepped spillway, with only the widths altered. In all cases the computation mesh has been constructed such that it has the same mesh density as the computational mesh used to model the experimental stepped spillway, which is described in chapter 6.

Figure 7.1 shows pressure contours on the step faces, and streamlines within the step cavities, of a spillway of width $W = W_0 \times 2$, where W_0 is the width of the experimental stepped spillway (150 mm) and W is the width of the spillway being considered (150 \times 2 = 300 mm in this case). Data is shown for the Eulerian model with a range of turbulence models. Note that, as in chapter 6, only half of the spillway width has been modelled and a symmetry boundary condition has been used at the centreline of the spillway.

For all turbulence models, other than the Realisable $k - \epsilon$ model, it can be seen that

7.2 Cross-Stream Vorticity in Channels of Varying Width

the pattern of cross-stream vortices, and associated pressure profiles on the step faces, is repeated across the channel width so that there are four vortices across the channel width rather than the two that are observed in the experiments. The direction of circulation of the cross-stream vortices also changes direction at each step. The Realisable $k - \epsilon$ model does not show the same distinct pattern of cross-stream vortices, however there does appear to be some variation in the vortex structures and pressure profiles across the channel width. This variation also appears to have the same wavelength as the cross-stream vortices which occur with the other turbulence models.

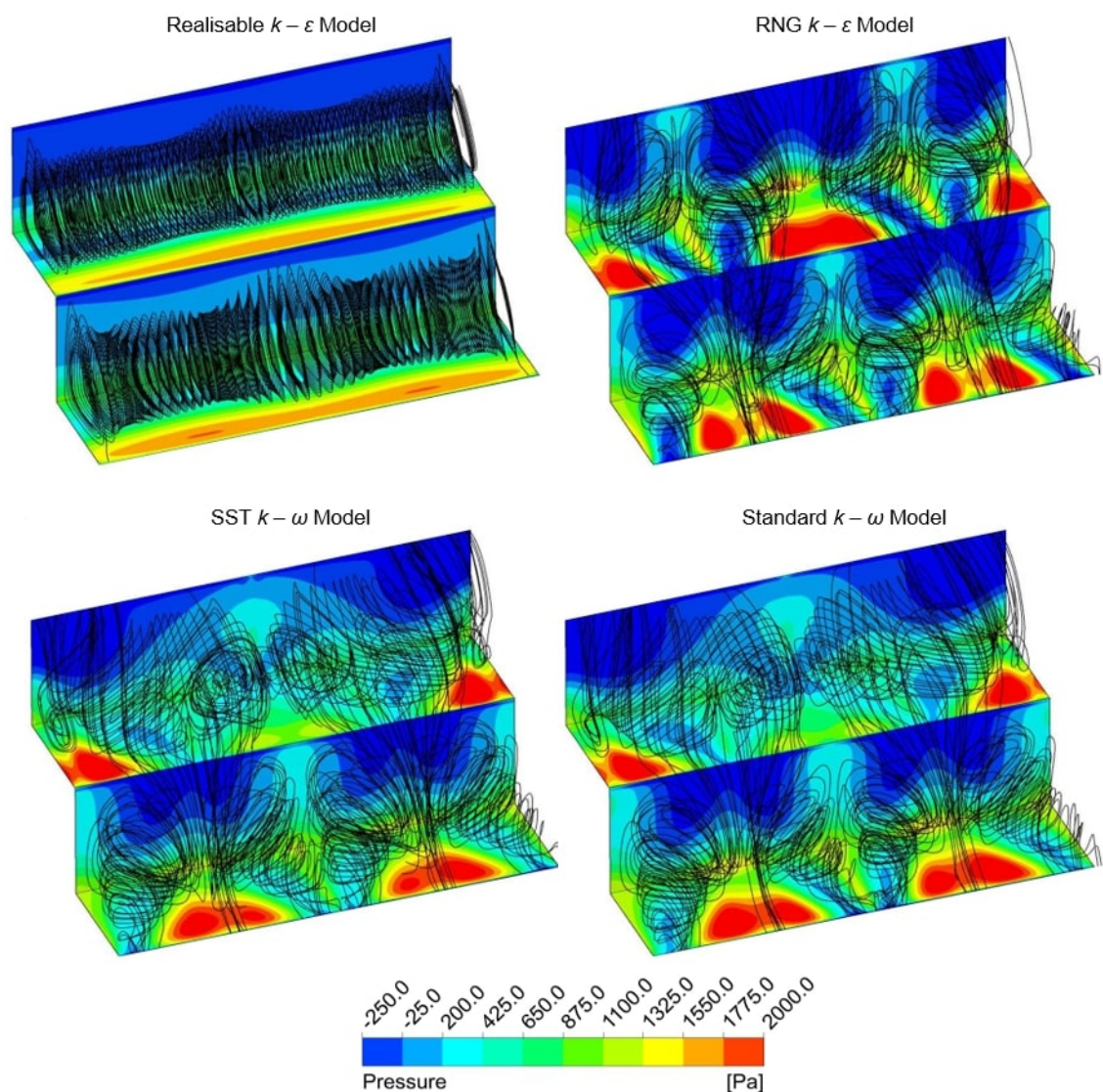


Figure 7.1: Pressure contours and streamlines of a 300 mm wide spillway for the Eulerian model with a range of turbulence models. Each image shows steps 2 and 3 of the spillway

Figure 7.2 shows pressure contours and streamlines for the same spillway geometry as

7. STUDY INTO THE OCCURRENCE OF CROSS-STREAM VORTICES IN STEPPED SPILLWAYS OF VARYING GEOMETRY

shown in figure 7.1 for the VOF model with the Realisable $k - \epsilon$ and SST $k - \omega$ turbulence models. It can be seen that both turbulence models show the distinct repeated pattern of cross-stream vortices across the channel width. The Realisable $k - \epsilon$ model does not show as strong a pattern of cross-stream vortices when used in conjunction with the Eulerian model, however, the model does predict the pattern of cross-stream vortices when used in combination with the VOF model. It is unclear why this is the case. Despite this, it is clear that the numerical data generally shows that, when the channel width of the experimental spillway is doubled, the pattern of cross-stream vortices repeats across the channel width. This suggests that the occurrence of these cross-stream vortices are not due to the relatively narrow width of the experimental spillway.

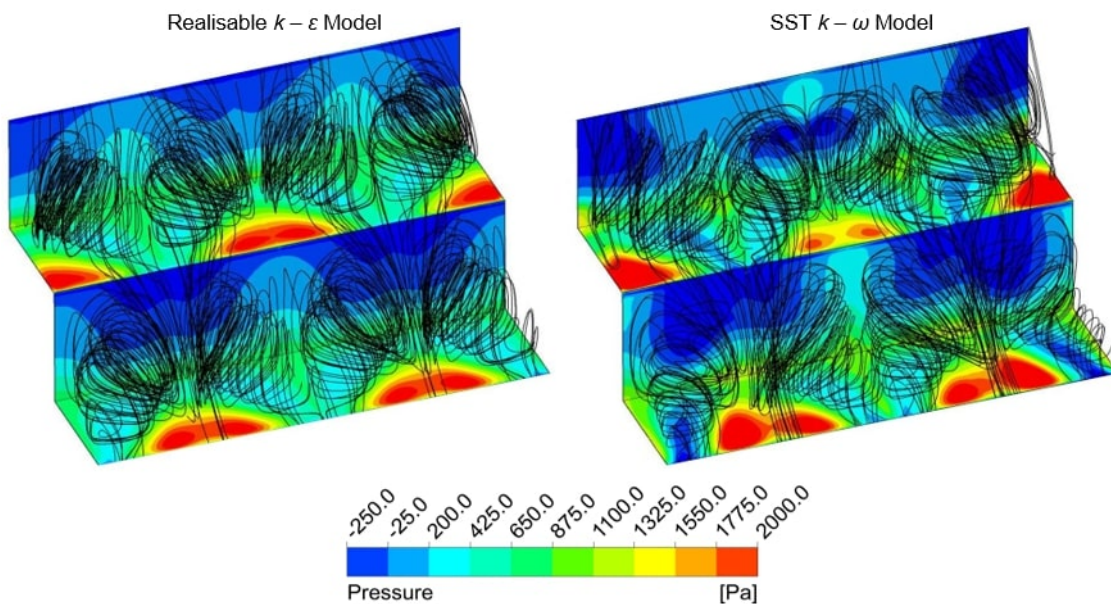


Figure 7.2: Pressure contours and streamlines of a 300 mm wide spillway for the VOF model with two different turbulence models. Each image shows steps 2 and 3 of the spillway

Significant wall effects were observed in the experimental stepped spillway as well as the associated numerical models. In order to ascertain whether the cross-stream vortices are caused by the wall boundary condition at the side of the spillway, simulations were conducted with different boundary conditions at the spillway wall. Figure 7.3 shows pressure contours and streamlines for three combinations of multiphase and turbulence model, with a symmetry boundary condition at each side of the spillway. Figure 7.4 shows pressure contours and streamlines for the VOF model with two different turbulence models, with periodic boundary conditions at each side of the spillway. Note that the actual numerical domain used in these

7.2 Cross-Stream Vorticity in Channels of Varying Width

simulations is 150 mm wide, however, the figures display a 300 mm wide spillway. This is due to the fact that it is the same mesh and domain used for the simulations shown in figures 7.1 and 7.2 so the data shown has been reflected in the same plane for clarity of comparison.

It can be seen that, with both symmetry and periodic boundary conditions, the repeated pattern of cross-stream vortices occurs. This strongly suggests that the occurrence of these vortices, in both the numerical and experimental models, is caused by the geometry of the steps and the channel width, rather than the the boundary conditions which are imposed at the walls of the spillway. Note that the VOF model with the Realisable $k - \epsilon$ model and the periodic boundary conditions does show the repeated pattern of cross-stream vortices, but again the vortices are not as distinct as in other cases.

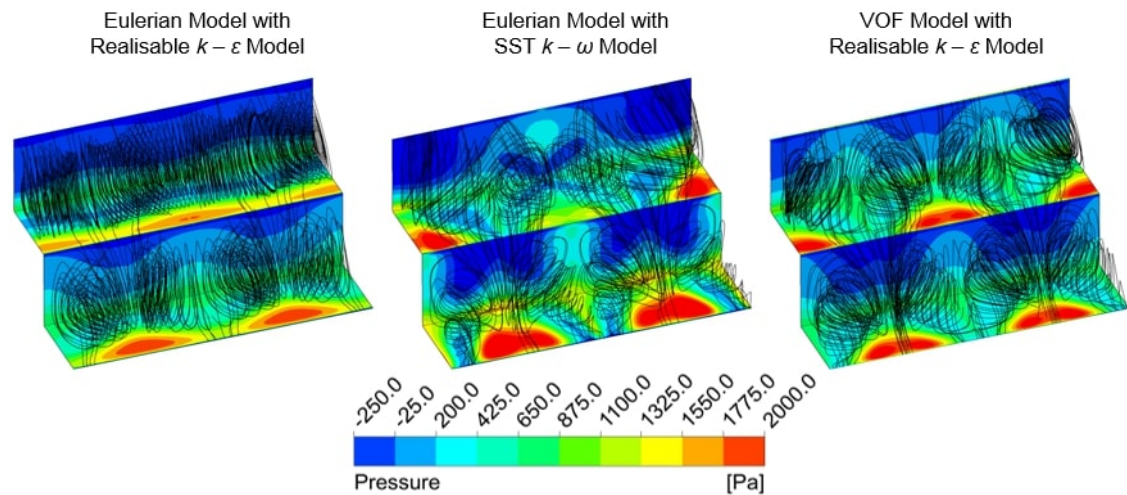


Figure 7.3: Pressure contours and streamlines of a 300 mm wide spillway for various multiphase and turbulence models with symmetry boundary conditions at the spillway walls. Each image shows steps 2 and 3 of the spillway

7. STUDY INTO THE OCCURRENCE OF CROSS-STREAM VORTICES IN STEPPED SPILLWAYS OF VARYING GEOMETRY

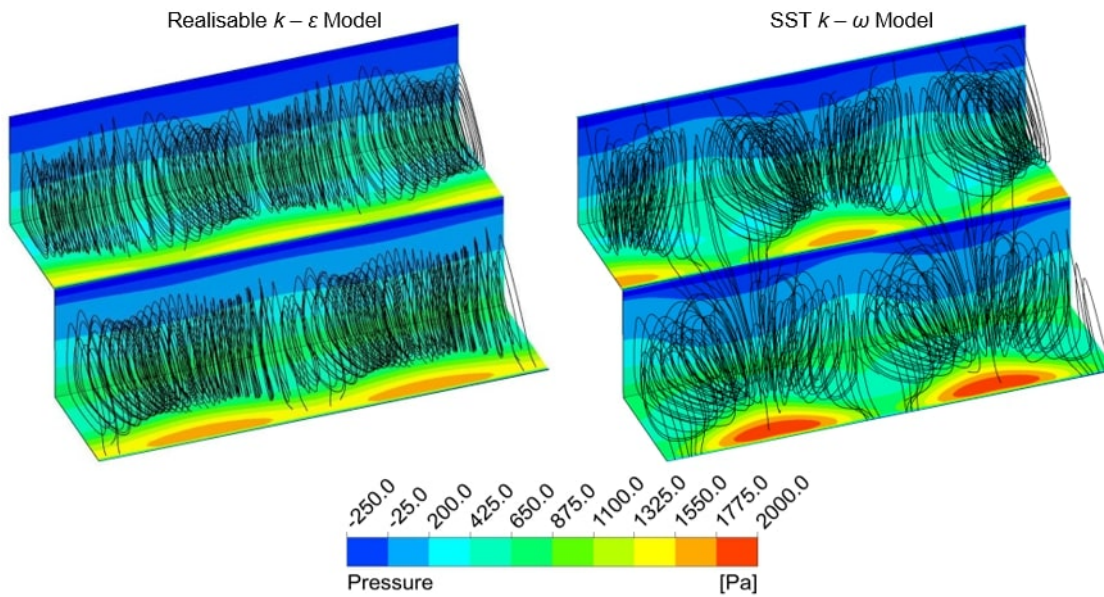


Figure 7.4: Pressure contours and streamlines of a 300 mm wide spillway for the VOF model with two different turbulence models with periodic boundary conditions at the spillway walls. Each image shows steps 2 and 3 of the spillway

Figure 7.5 shows pressure contours and streamlines for three different spillways of increasing width. At each width, the VOF model with the Realisable $k - \epsilon$ model has been used, and at $W_0 \times 2.5$ the VOF model with the SST $k - \omega$ model has also been used. In each case, symmetry boundary conditions are used at the spillway walls. At $W_0 \times 2.5$, the Realisable $k - \epsilon$ model shows some cross-stream vorticity, however, as in figures 7.1 and 7.4, the vortices are not as distinct as with the other turbulence models. The SST $k - \omega$ model does show strong cross-stream vorticity at $W_0 \times 2.5$. At $W_0 \times 2.5$ the pattern of cross-stream vortices is repeated 3 times. At $W_0 \times 3$ the pattern of cross-stream vortices is also repeated 3 times, but with each cross-stream vortex spread over a greater width of the spillway. At $W_0 \times 3.5$ there are 4 repetitions of the pattern of cross-stream vortices. These results show that, as the width of the spillway increases, the cross-stream vortices spread out over a greater width until a certain value of W , at which an additional repetition of the cross-stream vortex pattern occurs across the channel width.

7.2 Cross-Stream Vorticity in Channels of Varying Width

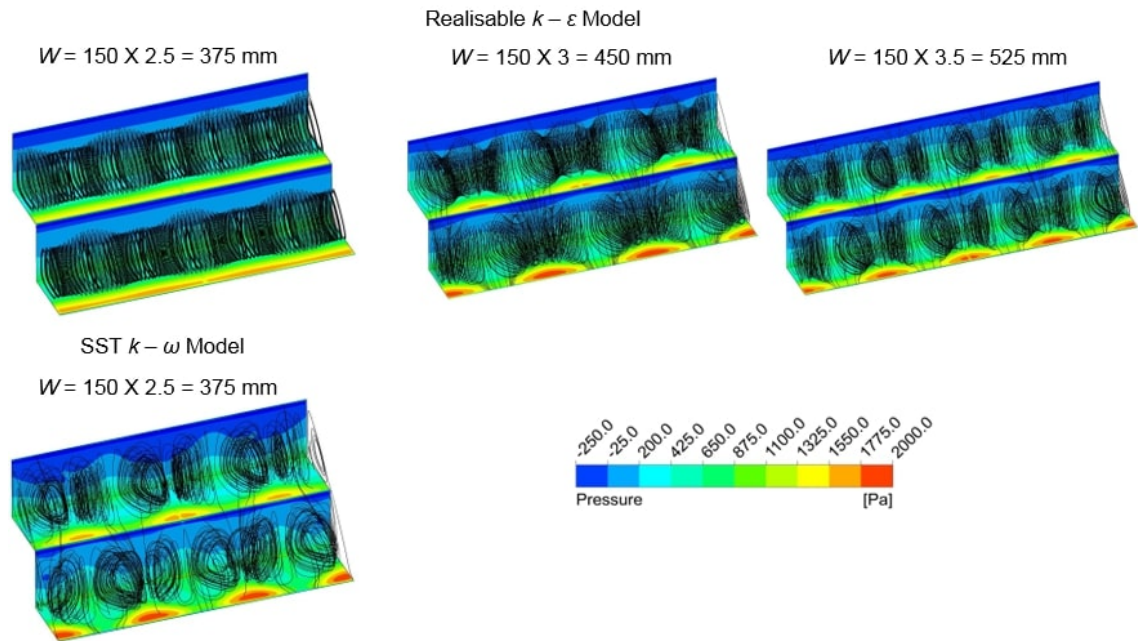


Figure 7.5: Pressure contours and streamlines of spillways of varying widths for the VOF model. Symmetry boundary conditions have been used at the spillway walls for all cases

Figure 7.6 shows pressure contours and streamlines of a 1000 mm wide spillway for the VOF model with the Realisable $k - \epsilon$ model. Symmetry boundary conditions are used at either side of the spillway. In this case there is no reflection of the data, and the 1000 mm width was modelled. There are 7 repetitions of the cross-stream vortex pattern across the channel width. This shows that, for a range of spillway widths, the repeated pattern of cross-stream vortices appears to occur.

7. STUDY INTO THE OCCURRENCE OF CROSS-STREAM VORTICES IN STEPPED SPILLWAYS OF VARYING GEOMETRY

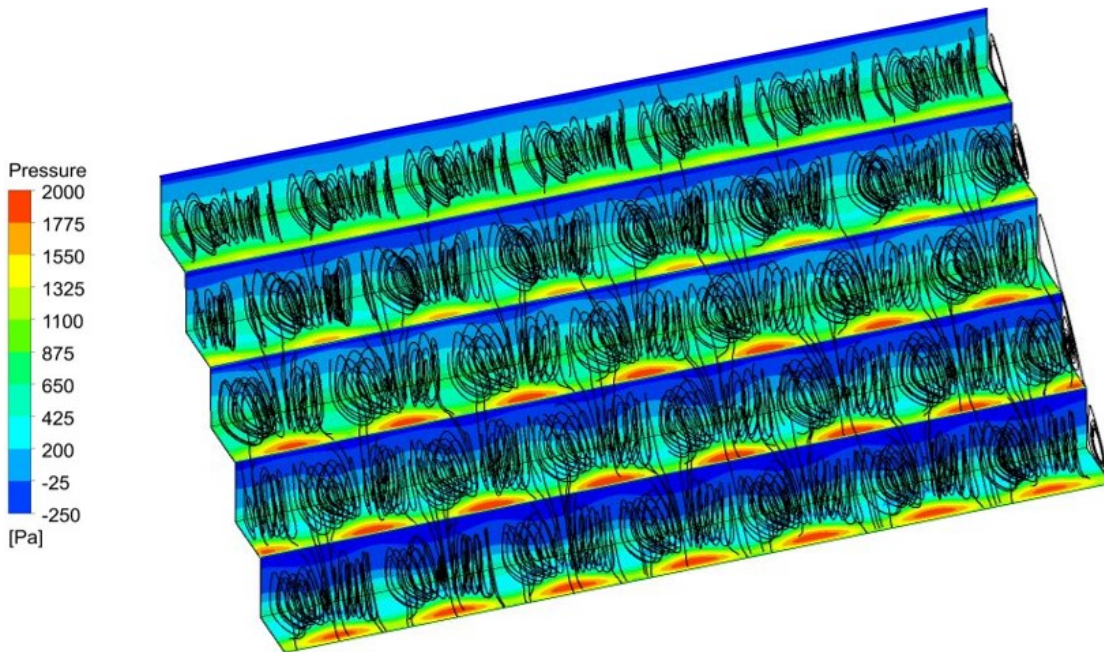


Figure 7.6: Pressure contours and streamlines of a 1000 mm wide spillway for the VOF model with the Realisable $k - \epsilon$ turbulence model. Symmetry boundary conditions are used at either side of the spillway

This numerical investigation into cross-stream vorticity in channels of varying widths has shown that, in most cases, there are distinct cross-stream vortices which repeat across the channel width. When the Realisable $k - \epsilon$ turbulence model is used, however, this is not always the case and the cross-stream vortices appear to be significantly less distinct in some cases. It is not only the geometry of the model which effects this behaviour with the Realisable $k - \epsilon$ model. Figures 7.1 and 7.2 show images of the vortices in the step cavities for simulations with the Realisable $k - \epsilon$, which are identical other than the multiphase model which has been used. The prediction of cross-stream vortices using the Realisable $k - \epsilon$ model is unpredictable and not consistent with different multiphase models or step geometries. Therefore, when investigating cross-stream vortices in stepped spillway, it may be more appropriate to use turbulence models other than the Realisable $k - \epsilon$ model.

7.3 Experimental and Numerical Investigation into Cross-Stream Vorticity in a Spillway of Modified Step Size

The previous section shows that numerical simulations of spillways of varying widths, but identical step height and length as the experimental stepped spillway, predict that the pattern of cross-stream vortices repeats as the width of the spillway increases. Experimental modelling of the spillways of different widths would allow these numerical results to be confirmed, however, the width of the experimental spillway cannot be altered. The ratio of step height to channel width, on the other hand, can be modified by the installation of extra steps.

In each step cavity of the experimental spillway, a transparent plastic block was installed to create a 150 mm wide spillway, consisting of 30 steps, with a step height and length of 40 mm. The resultant spillway has a step geometry with double the channel width to step height ratio as the original experimental spillway. The spillway was also numerically modelled using the Eulerian multiphase model with the SST $k - \omega$ turbulence model. The numerical model used a mesh with the same mesh density as the mesh used to model the experimental stepped spillway. Due to symmetry, half of the channel width was modelled, with a wall boundary condition at one side of the domain and a symmetry boundary condition at the other.

Figure 7.7 shows pressure contours and streamlines of the numerical solution at steps 2 and 3 for $Q = 15$ l/s. The repeated pattern of cross-stream vortices can be seen, which change direction at each step and affect the pressures across the width of the channel. This is the same pattern as observed in the numerical model data in the previous section.

7. STUDY INTO THE OCCURRENCE OF CROSS-STREAM VORTICES IN STEPPED SPILLWAYS OF VARYING GEOMETRY

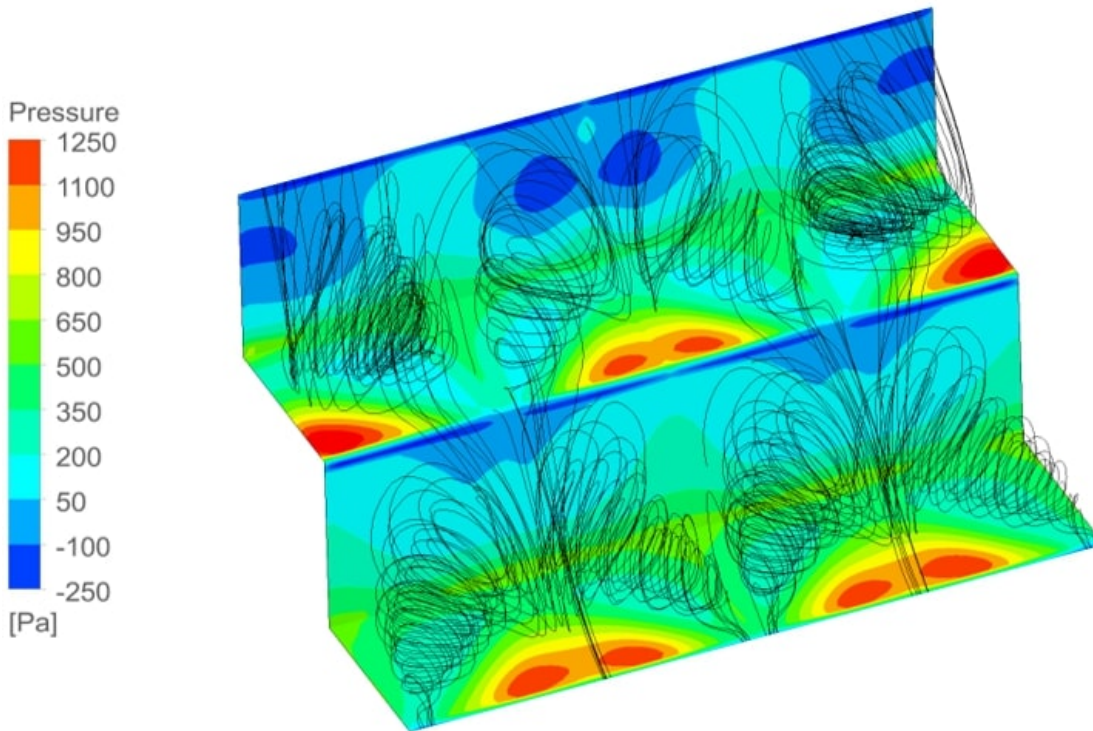


Figure 7.7: Pressure contours and streamlines of the 40 mm step height spillway, at steps 2 and 3, for the Eulerian multiphase model with the SST $k - \omega$ turbulence model

In the experimental spillway, the repeated pattern of cross-stream vortices could be clearly observed, such that the flow within the step cavities resembled that in figure 7.7. It was also noticeable that vortex switching, whereby the direction of circulation of the cross-stream vortices change direction at irregular time intervals (described in chapter 3), occurred significantly more frequently than in the 80 mm steps, and at all flow rates which produced skimming flow. A potential reason for this is that the phenomenon within the flow which causes vortex switching may be more likely to occur as there are more cross-stream vortices in each step cavity. This is speculation, however, and further research would be required to identify the cause of vortex switching. Pressure measurements were not taken with the 40 mm steps due to the fact that the 40 mm steps prevented pressure measurements being taken at half of the locations on the step faces.

Figure 7.8 shows numerical pressure contours and streamlines viewed from above step 2, as well as the experimental flow viewed from below step 12. Although different steps are shown, the direction of circulation is the same in each image, and is more clearly viewed further downstream in the experimental stepped spillway due to the presence of air bubbles.

7.3 Experimental and Numerical Investigation into Cross-Stream Vorticity in a Spillway of Modified Step Size

Figure 7.9 shows numerical pressure contours and streamlines viewed from above step 3, as well as the experimental flow viewed from below, again at step 12. The experimental flow is shown at the same step but at a different time, when vortex switching had caused the direction of circulation of the cross-stream vortices to match that of the numerical image shown. This step was chosen as the installation of the 40 mm blocks resulted in the flow being more easily observed from below at the even numbered steps.

In each figure, red arrows have been used to identify the similarities between the numerical and experimental images. In both figures, the curved shape of the vortices is identifiable by the lighter region of bubbles towards the top of the experimental image. There is one central curve in figure 7.8 and two curves at either side of the step in figure 7.9. It should be noted that, although the experimental images in figures 7.8 and 7.9 do not show the cross-stream vortex structures as clearly as the numerical images, when the spillway is directly viewed in real time, the cross-stream vortices clearly show the same structures that are observed in the numerical images.

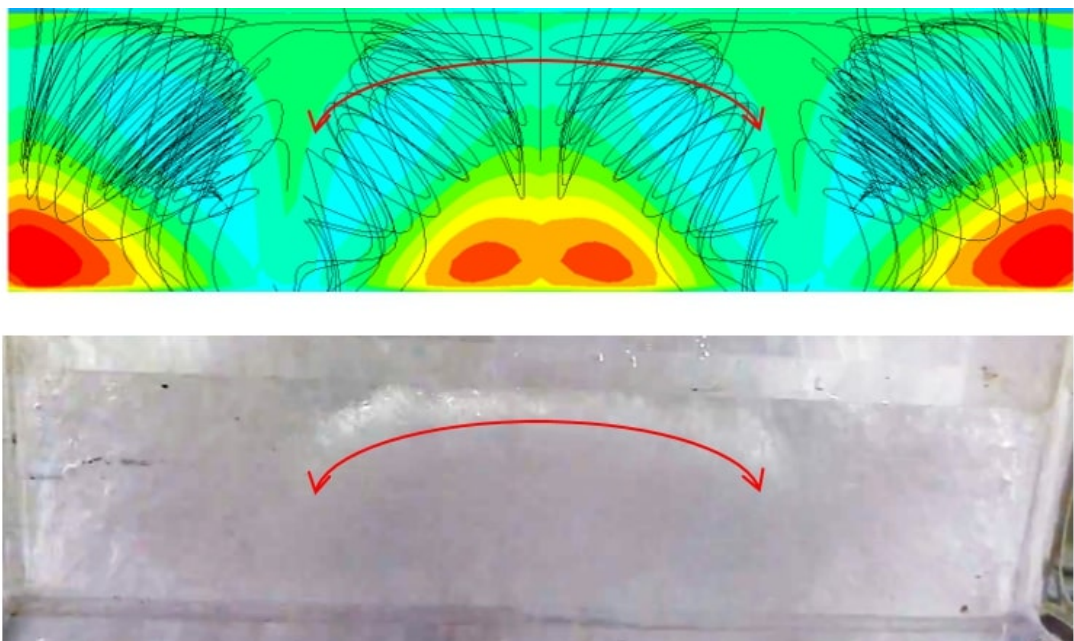


Figure 7.8: Numerical and experimental representation of cross-stream vortices. The numerical data is shown at step 2 and the experimental data is shown at step 12, at a time when the cross-stream vortex pattern matched that of the numerical data displayed in the figure

7. STUDY INTO THE OCCURRENCE OF CROSS-STREAM VORTICES IN STEPPED SPILLWAYS OF VARYING GEOMETRY

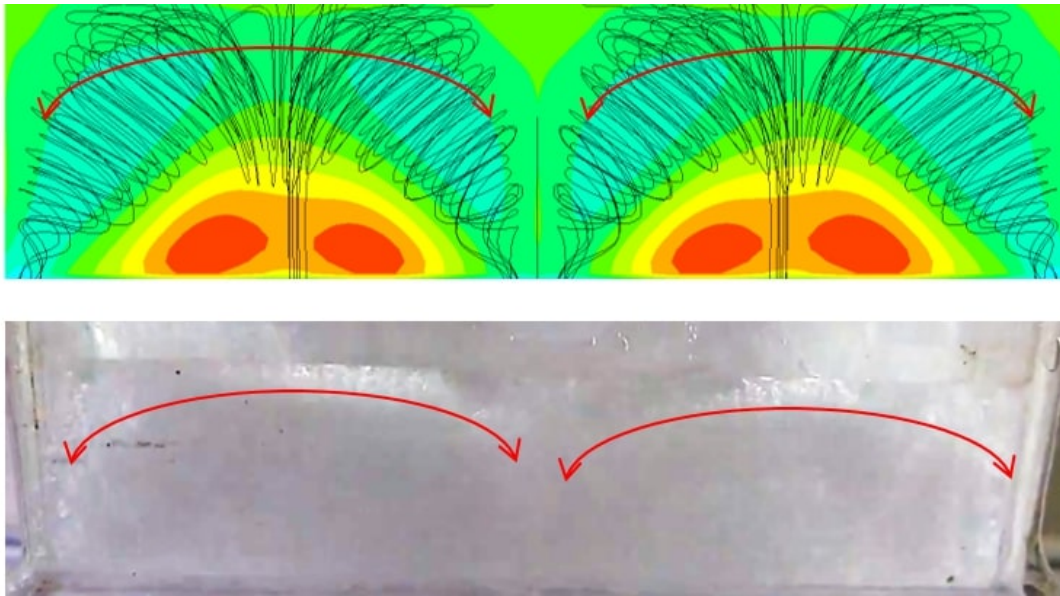


Figure 7.9: Numerical and experimental representation of cross-stream vortices. The numerical data is shown at step 3 and the experimental data is shown at step 12, at a time when the cross-stream vortex pattern matched that of the numerical data displayed in the figure

7.4 Cross-Stream Vorticity in Stepped Spillways of Varying Slope

Experimental and numerical modelling has shown that cross-stream vortices occur in spillways of varying widths, with a 1H:1V slope. In order to determine whether cross-stream vortices occur in stepped spillways of different slopes, numerical modelling of spillways of varying slopes was conducted. Four spillways of slopes 2H:1V, 3H:2V, 2H:3V and 1H:2V were modelled, each with a step height of 80 mm and a channel width of 150 mm. As in section 7.2, only 5 steps were modelled to reduce computational cost. For slopes 2H:1V and 3H:2V the same inflow and approach as the numerical models of the experimental spillway were used. For slopes 2H:3V and 1H:2V, however, the approach curve was modified to prevent jet deflection, whereby the flow jets over the first several steps. Simulations were conducted using the Eulerian model with the SST $k - \omega$ model and the meshes were created in order to retain the same mesh density as the mesh used for numerical modelling of the experimental stepped spillway. As before, half of the channel width was modelled, with a wall boundary condition at one side of the domain and a symmetry boundary condition at the other.

Figure 7.10 shows pressure contours and streamlines at steps 2 and 3, for the four slopes investigated. At 3H:2V and 2H:3V, the streamlines clearly show the occurrence of cross-stream vortices and the effect of the vortices on the pressures acting on the step faces. This

7.4 Cross-Stream Vorticity in Stepped Spillways of Varying Slope

is, perhaps, unsurprising since these slopes are reasonably similar to the 1H:1V slope, in which cross-stream vortices have been observed both numerically and experimentally.

At 2H:1V the cross-stream vortices and associated effect on the pressures can be observed, however their direction of flow appears to be more in line with the main flow direction than at 3H:2V, 1H:1V or 2H:3V. Lopes et al. (2017) showed that, on a 2H:1V slope, an alternating vortex structure occurs, which is similar to the cross-stream vortices observed in this study and the pressure patterns on the step faces also show the same trend. The numerical streamlines shown in the study by Lopes et al. (2017) resemble those of the 2H:1V spillway shown here. Lopes et al. (2017) also showed that for spillways of identical step height and length, the alternating pattern occurred on a 500 mm wide spillway but not on a 300 mm wide spillway. This study has shown that at 1H:1V the cross-stream vortices occur regardless of the channel width. The findings of Lopes et al. (2017) suggest, however, that at shallower slopes, such as 2H:1V, the width of the channel may have an effect on the occurrence of cross-stream vortices.

At 1H:1V no cross-stream vortices are observed. The streamlines and pressures are similar at both steps displayed and also at the other steps which are not displayed in figure 7.10.

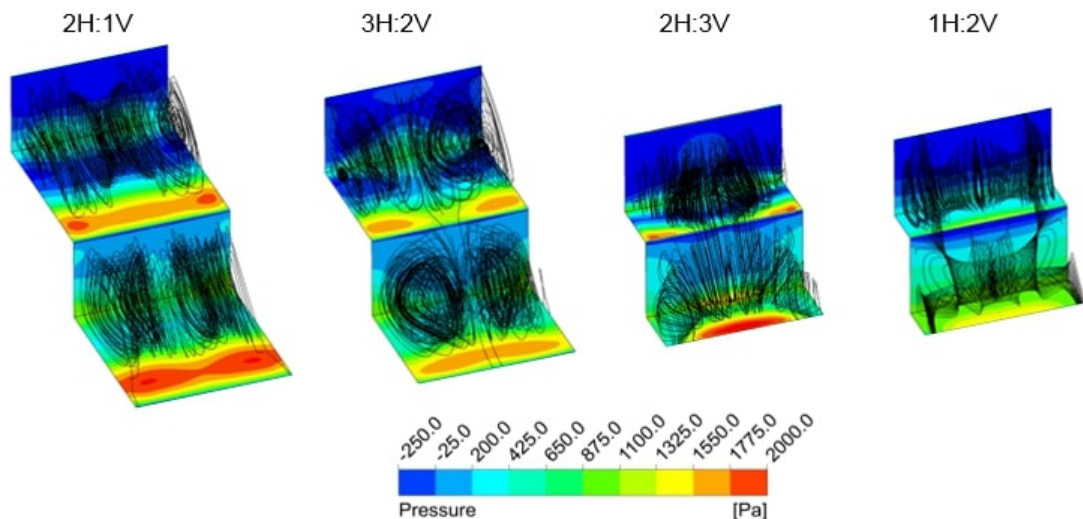


Figure 7.10: Pressure contours and streamlines of spillways of varying slope angles for the Eulerian model with the SST $k - \omega$ model turbulence. Each spillway is 150 mm wide and each image shows steps 2 and 3 of the spillway

7.5 Investigation into 3D behaviour in the LNEC Stepped Spillway

Chapter 5 described an in-depth investigation into 2D numerical modelling of the experimental stepped spillway at the LNEC. 2D modelling was found to be able to accurately predict velocities and AVFs above the pseudo-bottom, as well as the flow depths and inception point locations. In the step cavities, however, 3D patterns of vortices have been observed experimentally in the narrow stepped spillway at the University of Leeds (chapter 3). This chapter has also shown that 3D vorticity is predicted by numerical models of stepped spillways with a range of widths and step geometries. Matos et al. (1999) reported 3D flow behaviour in the step cavities of the experimental stepped spillway at the LNEC. Bombardelli et al. (2011), however, reports that the flow is essentially 2D in the above the steps. In order to investigate the 3D behaviour in the LNEC stepped spillway further, 3D modelling of the spillway has been conducted.

7.5.1 Modelling Procedure

The 3D modelling was conducted over the first 17 steps only (the first seven 60 mm by 80 mm steps), in order to reduce the domain size and, therefore, the computational cost. The LNEC spillway is symmetrical about the centreline. Two simulations were conducted: one using a symmetry boundary condition at both the centreline and the wall and another with a symmetry boundary condition at the centreline and a wall boundary condition at the wall. In the step cavities, the mesh consists of 140 cells over the 500 mm domain width, giving a cell width of 3.57 mm. The mesh is refined in the regions close to the steps in the same manner as shown in figure 5.5 and the mesh has a total number of cells of 15,622,008.

For the flow rate investigated, the experimental inception point defined by the intersection of the turbulent boundary layer and the equivalent clear water depth was found to be at step 18. The inception point defined by visual observation was found to be at step 20. The numerical model domain, therefore, incorporates almost all of the non-aerated region.

All 3D modelling has been conducted using the VOF model, as the Eulerian model is more computationally expensive than the VOF model and, for this domain, requires a time step one tenth the size of that required for VOF model. 3D simulations using the Eulerian model were, therefore, unfeasible as they require a computational cost an order of magnitude higher than the VOF model. The VOF model was considered applicable for this study as it predicts the

7.5 Investigation into 3D behaviour in the LNEC Stepped Spillway

velocities accurately in the region of the spillway covered by the 3D domain. It also shows the same 3D behaviour as the Eulerian model, as described in chapter 6. 3D simulations were conducted with $Q = 180$ l/s using the SST $k - \omega$ turbulence model, as this turbulence model has been shown to predict the velocities most accurately.

7.5.2 3D Flow Structures in the Step Cavities

Matos et al. (1999) shows that the vortices within the step cavities are 3D, by examination of the deformation of wool fibres attached to the step faces and side walls. However, the structure of these 3D vortices is not reported. Figure 7.11 (Matos and Meireles, 2014) shows a photograph of the back of the steps at the LNEC chute, with wool fibres fixed in position so that the 3D structure of the flow within the step cavities could be observed. The turbulent structures within the step cavities (observed by the wool fibres and air bubbles) are not uniform across the channel width, demonstrating that there is 3D behaviour within the step cavities. It is not clear from figure 7.11, however, whether these 3D structures resemble the cross-stream vortices observed in the experimental and numerical models in this project.



Figure 7.11: Flow with attached wool fibres at the LNEC stepped spillway, viewed from below the chute. Image taken from Matos and Meireles (2014)

Figure 7.12 shows pressure contours on the full size steps as well as streamlines, seeded

7. STUDY INTO THE OCCURRENCE OF CROSS-STREAM VORTICES IN STEPPED SPILLWAYS OF VARYING GEOMETRY

in the step cavities for the numerically modelled section of the LNEC spillway. A repeated pattern of cross-stream vortices, which change direction at each consecutive step, can be observed. Cross-stream vortices were clearly observed in the University of Leeds stepped spillway with both 40 mm and 80 mm steps, and pressure measurements on the 80 mm steps verified these observations. These cross-stream vortices were also predicted accurately by the Eulerian model with SST $k - \omega$ model, (as well as other combinations of multiphase and turbulence models), for both step sizes. It is reasonable to assume, therefore, that the pattern of cross-stream vortices shown in figure 7.12, with the wall boundary condition, represents the flow structures within the step cavities of the LNEC experimental spillway reasonably accurately.

Regular patterns of vorticity which alternate at subsequent steps have also been reported by Lopes et al. (2017) and Toro et al. (2017). These results, in combination with the results of this project, strongly suggest that a regular pattern of cross-stream vortices, which alternate at each step, may occur in a wide range of stepped spillways in use at reservoirs. Furthermore, those involved with the design and operation of stepped spillways may be unaware of the occurrence of these vortices, and the associated effects on the pressure on the step faces.

The cross-stream vortices observed in figure 7.12 occur whether symmetry or wall boundary conditions are used, which agrees with the findings of chapter 6. This is further evidence that the occurrence of the cross-stream vortices is due to the geometry of the steps, rather than the boundary condition used at the wall. The pattern of vortices begins one step further downstream when symmetry planes are used, however, suggesting that the interaction between the flow and the wall does have some effect on the instigation of the cross-stream vortices.

7.5 Investigation into 3D behaviour in the LNEC Stepped Spillway

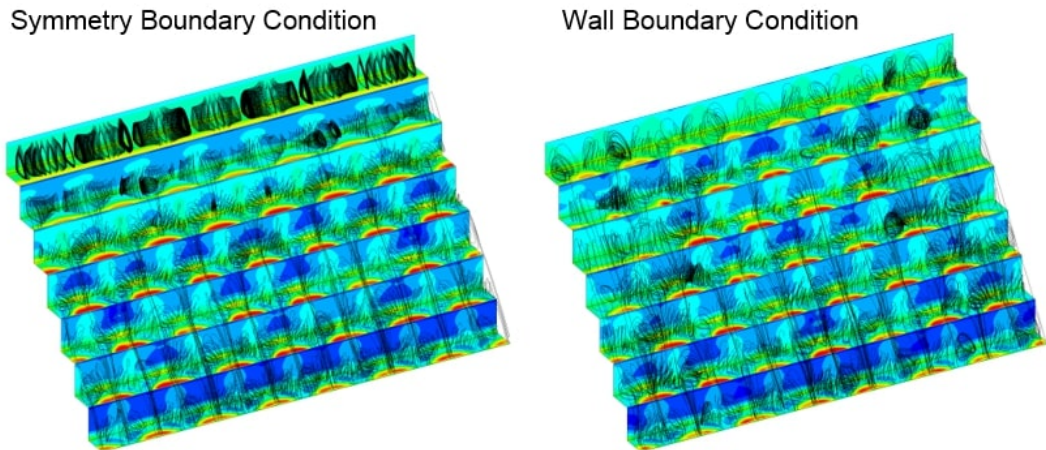


Figure 7.12: Pressure contours and stream lines of a three dimensional model of the first 17 steps of the LNEC stepped spillway. The VOF model with the SST $k - \omega$ model is used in each case and $Q = 180$ l/s

Although strong 3D behaviour is observed across the channel width, 2D simulations of the flow characteristics above the steps have produced predictions of flow variables, such as velocities and AVFs, in close agreement with the experimental data. In order to determine whether these 3D cross-streams also affect the bulk flow above the step cavities, the velocities and flow depths in the 3D models have been investigated. Note that the AVFs have not been investigated due to the fact that the VOF model does not predict air entrainment and all of the steps in the 3D simulations are within the non-aerated region.

7.5.3 Velocities

Figure 7.13 shows velocity contours at planes parallel to the pseudo-bottom, at depths of 15 mm, 30 mm and 45 mm. It can be seen that the velocities above the steps vary across the channel width in a regular repeating pattern of alternating high and low velocities, which has the same wavelength as the cross-stream vortices. This shows that the cross-stream vortices have an effect on the flow characteristics above the pseudo-bottom. With both symmetry and wall boundary conditions, the variation in velocity across the channel is higher at depths closer to the pseudo-bottom. The symmetry boundary condition results show that the alternating pattern of velocities begin at approximately the same position across the channel width, and at all depths. The wall boundary condition results, however, show that the alternating velocities begin further upstream at the centreline of the spillway than at the wall, which is due to the no slip wall boundary condition causing lower velocities close to the wall. At the higher values of z , the difference between the centreline and the wall reduces significantly.

7. STUDY INTO THE OCCURRENCE OF CROSS-STREAM VORTICES IN STEPPED SPILLWAYS OF VARYING GEOMETRY

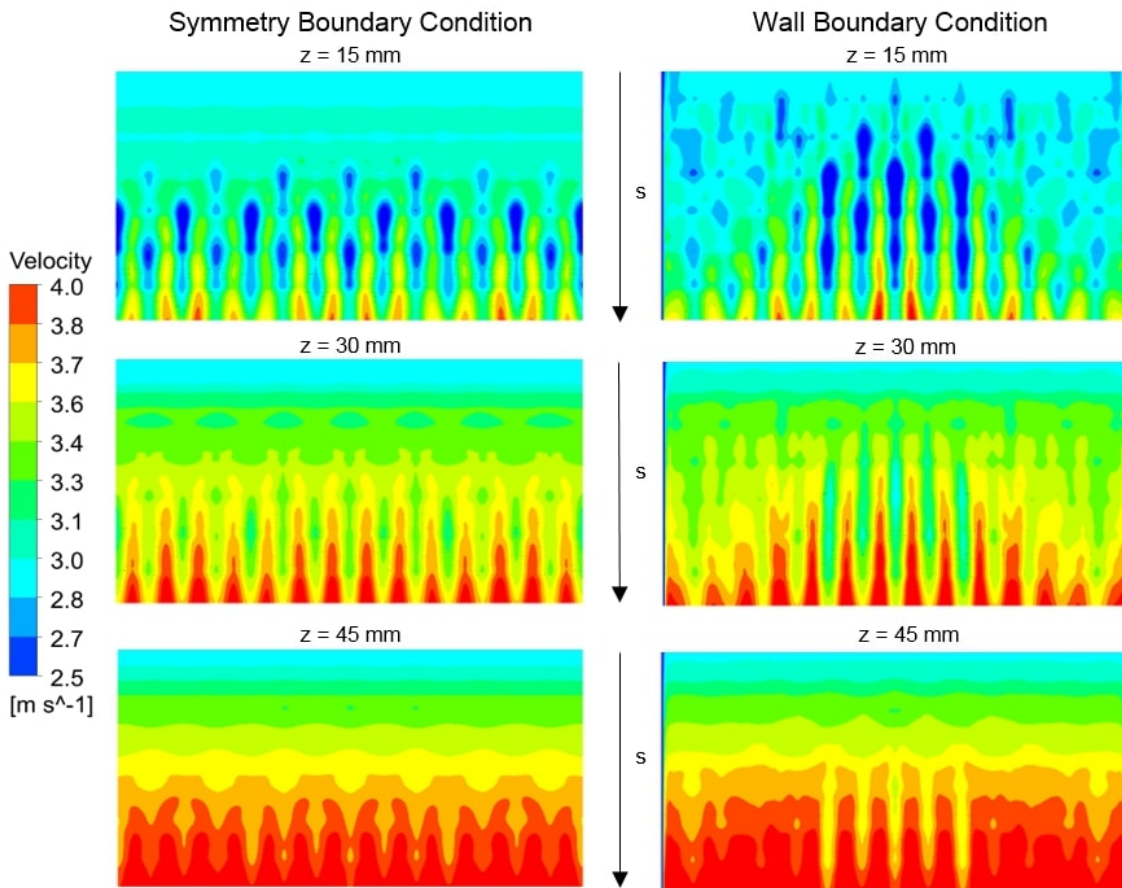


Figure 7.13: Velocity contours above steps 11 to 17, parallel to the pseudo-bottom, at different values of z for the simulations of the upstream section of the LNEC spillway. Data is displayed for the VOF model with the SST $k - \omega$ model at $Q = 180$ l/s

Figures 7.14 and 7.15 compare velocity profiles with the experimental data at different steps for both the symmetry and wall boundary conditions. Velocity profiles are shown for $w = 500$ mm (the centreline), for $w = 571$ mm and the width averaged velocity. The 2D velocity data for the VOF model with the SST $k - \omega$ model are also shown. The pattern of cross-stream vortices repeats seven times across the 1000 mm channel width, giving a wavelength of approximately 142 mm. The centreline was chosen as the velocities are symmetric about this position. $w = 571$ mm was chosen as this position is half a wavelength from the centreline so might be expected to show the largest variation in velocity from the centreline.

Both figures show almost identical behaviour. At steps 11 and 13, all numerical velocity profiles are extremely close to one another and agree well with the experimental data. At step 14 the velocity at $w = 500$ mm is less than the other predicted numerical data at the lower values of z . Then at step 15 the velocity at $w = 571$ mm is slightly less than the other predicted

7.5 Investigation into 3D behaviour in the LNEC Stepped Spillway

numerical data at the lower values of z . This pattern repeats at each step, which corresponds to the alternation direction of the cross-stream vortices at each step. At higher depths, all of the numerical velocity profiles converge and show similar results. The difference in the velocities at $w = 500$ mm and $w = 571$ mm matches the velocity contours shown in figure 7.13. At all steps, the width averaged velocity and the 2D velocity are similar and predict the experimental data reasonably accurately. This shows that the alternating pattern of low velocities at each step does not have a great effect on the average velocity across the width of the channel.

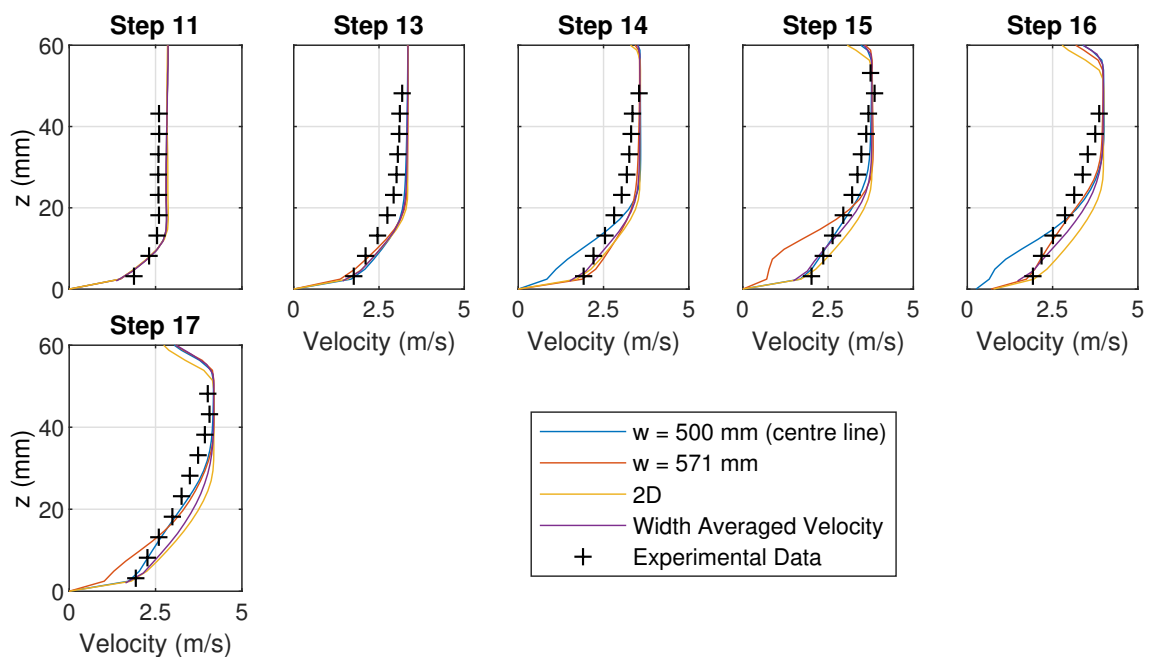


Figure 7.14: Numerical velocity profiles at different channel widths of the 3D simulation of the upstream region of the LNEC spillway using symmetry boundary conditions at the spillway walls. The width averaged, 2D and experimental velocity profiles are also shown

7. STUDY INTO THE OCCURRENCE OF CROSS-STREAM VORTICES IN STEPPED SPILLWAYS OF VARYING GEOMETRY

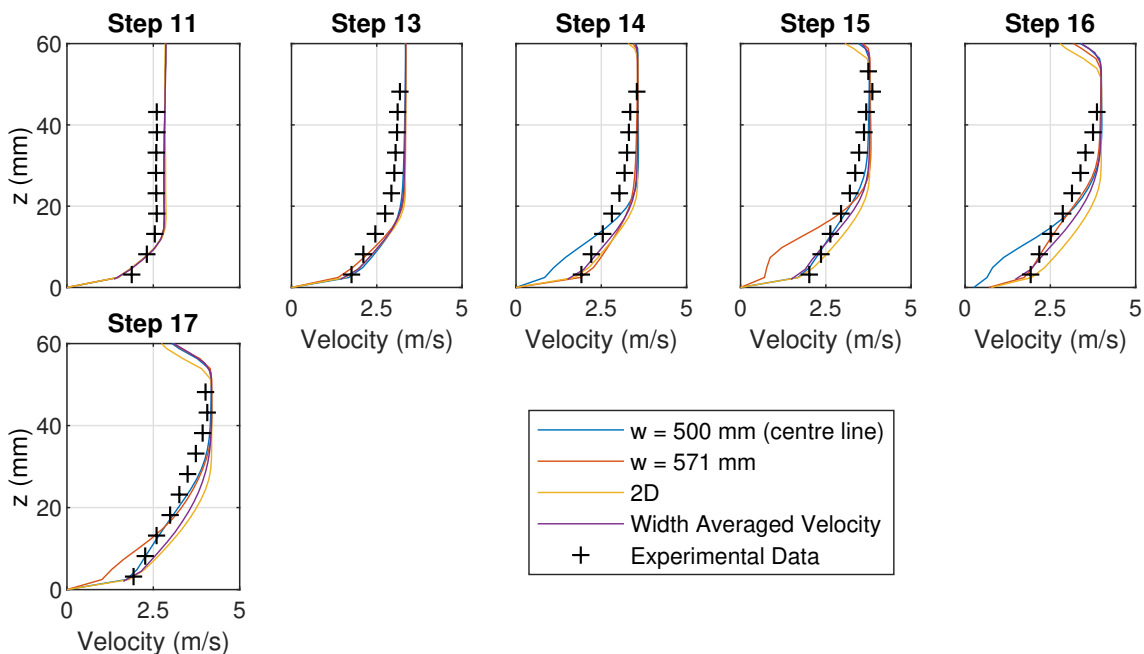


Figure 7.15: Numerical velocity profiles at different channel widths of the 3D simulation of the upstream region of the LNEC spillway using wall boundary conditions at the spillway walls. The width averaged, 2D and experimental velocity profiles are also shown

Figure 7.16 shows the velocities across the width of the channel, at increasing values of z , at step 14, for the simulation with symmetry boundary conditions at either side of the spillway. The mean velocity and standard deviation are shown and the positions of $w = 500$ mm and $w = 571$ mm are also indicated. It can be seen that, at all depths, the velocities follow a sinusoidal wave across the width of the channel. The variation in the velocity across the width of the channel reduces significantly as the depth increases, in common with figures 7.13 - 7.15.

At $z = 4$ mm and $z = 17$ mm, most of the velocity values fall within the standard deviation from the mean. The lowest velocities (including the velocity at $w = 571$ mm) fall below this range, however, these positions account for only a small proportion of the width of the channel. Therefore, these low velocities do not significantly affect the average velocity across the width of the channel. At the lower values of z there appears to be two modes to the wave. Both $w = 500$ mm and $w = 571$ mm appear in a trough of the wave, however, at $w = 500$ mm the trough is at a higher velocity than at $w = 571$ mm. As the depth increases the second mode disappears.

At step 15 the velocity profiles show a very similar wave pattern, but with the peaks and troughs of the wave patterns translated by 71 mm (half a wavelength), due to the alternating pattern of cross-stream vortices. With wall boundary conditions the velocity profiles also show

7.5 Investigation into 3D behaviour in the LNEC Stepped Spillway

a similar wave pattern, but with distinct wall effects next to the solid boundary. These results are shown in appendix C.

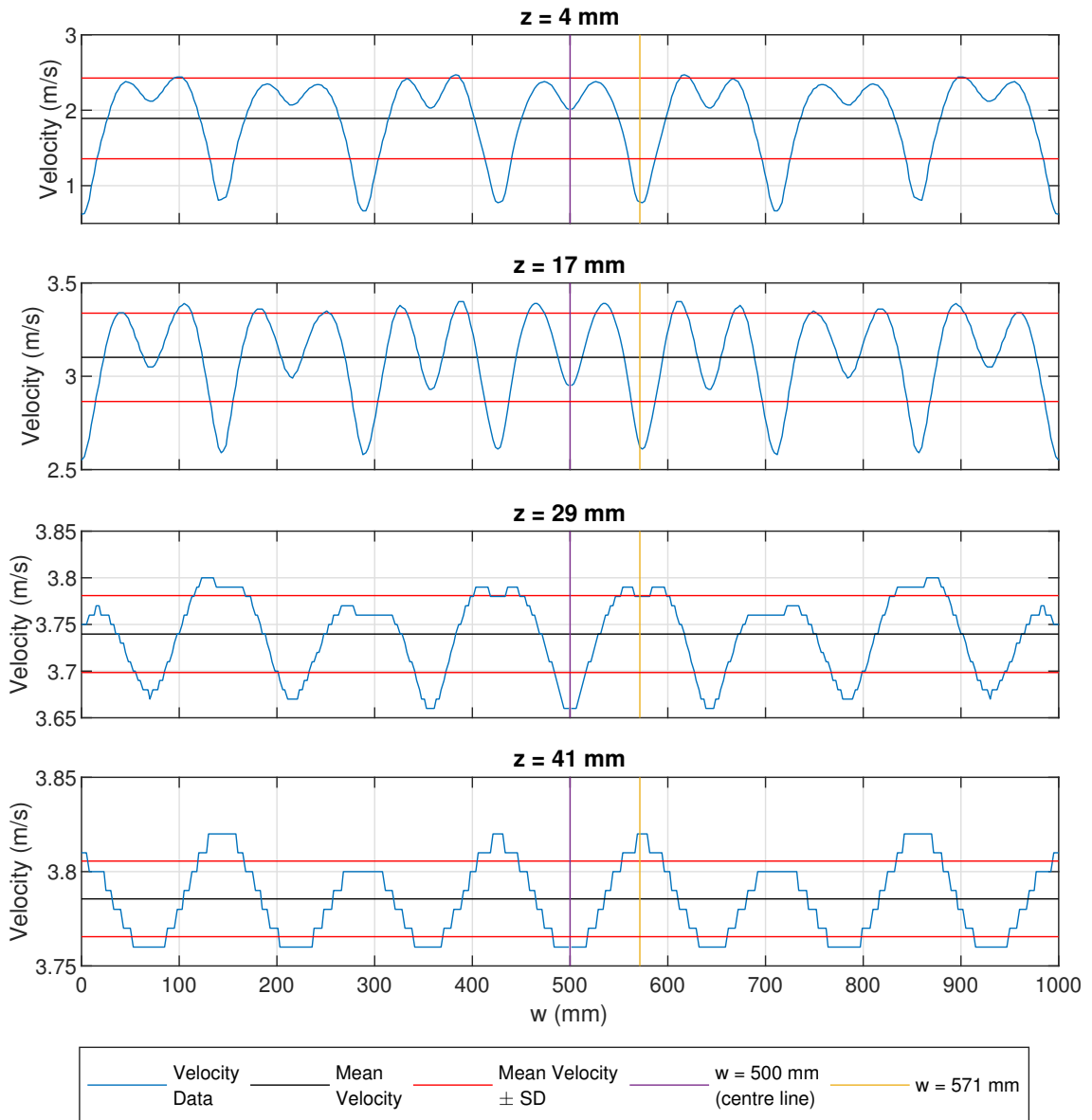


Figure 7.16: Velocity profiles across the channel width of step 14, at different values of z , for the 3D simulation of the upstream section of the LNEC spillway using symmetry boundary conditions. The mean velocity and standard deviation are also shown and the locations of $w = 500$ mm and $w = 571$ mm are indicated

This variation in the velocities across the width of the channel would suggest that the 2D modelling of the velocities will result in the loss of some important 3D flow effects. However, 2D modelling has been shown to accurately predict the experimental velocities. A potential reason for this is that the experimental velocities are time averaged, whereas the numerical data represents an single time step, as no transient behaviour is observed in the numerical

7. STUDY INTO THE OCCURRENCE OF CROSS-STREAM VORTICES IN STEPPED SPILLWAYS OF VARYING GEOMETRY

models. In chapter 3, vortex switching was observed in the University of Leeds experimental spillway, whereby, the direction of circulation of the cross-stream vortices, at a particular step, changes direction unpredictably over time. When 40 mm steps were used the pattern of cross-stream vortices was repeated and vortex switching was observed to occur significantly more frequently (section 7.3). This suggests that more repetitions of the pattern of cross-stream vortices induce vortex switching to occur more frequently.

There are significantly more repetitions of the pattern of cross-stream vortices in the numerical models of the LNEC spillway than in the University of Leeds stepped spillway. Vortex switching may occur in the experimental LNEC spillway frequently enough so that time averaged velocity measurements do not record the variation in velocity caused by the occurrence of the cross-stream vortices. This may be the reason for the 2D flow behaviour above the steps described by Bombardelli et al. (2011).

The results of this section have shown that although the cross-stream vortices appear to affect the velocities across the width of the channel, any significant variation in velocity is localised and does not significantly affect the width averaged velocities. These variations in velocity are not observed in the time averaged experimental data, possibly due to vortex switching, so 2D numerical modelling is a suitable approach to predict the time averaged velocities above the steps.

Figure 7.17 shows pressure contours and streamlines on steps 14-17 for a section of the channel width covering two repetitions of the pattern of cross-stream vortices, from $w = 500$ mm to $w = 784$ mm. In the locations where the cross-stream vortices reach the downstream end of the horizontal step faces, the streamlines show that fluid is ejected from the step cavities into the main flow above the pseudo-bottom. The locations of these ejections of fluid from the step cavities correspond to the locations where the lower velocities are observed in figures 7.13 - 7.16. The flow velocity in the step cavities is significantly lower than above the pseudo-bottom, so it appears that it is the ejection of fluid from the step cavities which causes the observed reduction in velocity in the flow above the steps. These fluid ejections from the step cavities can also be observed in other images of pressure contours and streamlines within the step cavities which have been presented in this project.

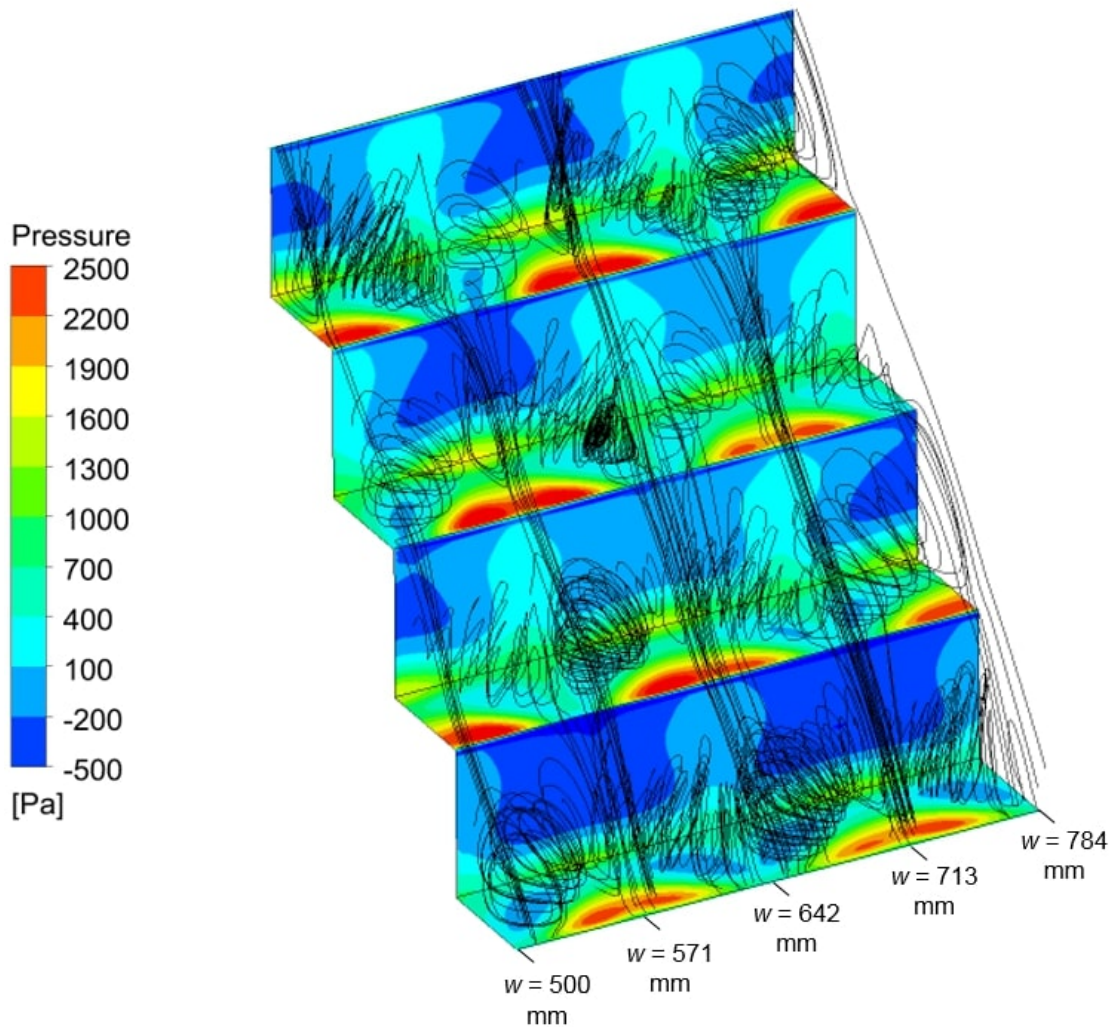


Figure 7.17: Pressure contours and streamlines on steps 14-17 from $w = 500$ mm to $w = 784$ mm, for the 3D simulation of the upstream section of the LNEC spillway using symmetry boundary conditions.

7.5.4 Free-Surface Profiles

Although Bombardelli et al. (2011) states that the flow above the steps is essentially 2D, Matos and Meireles (2014) shows that the free-surface upstream of the inception point is 3D. Figure 7.18, taken from Matos and Meireles (2014), shows the free-surface deformations upstream of the inception point at the LNEC spillway, as well as a probe tip used to measure the flow depth. The two images show two instants in time and are viewed from upstream of the probe tip. In image (a) the probe tip is practically submerged, whereas in image (b) the probe tip is above the free-surface. This shows that the free-surface profile varies over time. Free-surface deformations can also be observed across the width of the channel, in both images

7. STUDY INTO THE OCCURRENCE OF CROSS-STREAM VORTICES IN STEPPED SPILLWAYS OF VARYING GEOMETRY

(a) and (b), which demonstrates that the free-surface profile varies across the width of the channel. Chanson (2013b) records surface scars directly upstream of the inception point at the Hinze dam in Australia, which are believed to be caused by elongated hairpin vortices generated by boundary friction. Hunt and Kadavy (2010) observed 3D undulations to the free-surface profile immediately upstream of the inception point, which was thought to be due to the turbulent boundary layer approaching the free-surface. Meireles et al. (2012) describe free-surface unsteadiness upstream of the inception point due to turbulence. This unsteadiness may contribute to the free-surface profile varying across the channel width, as well as in time.

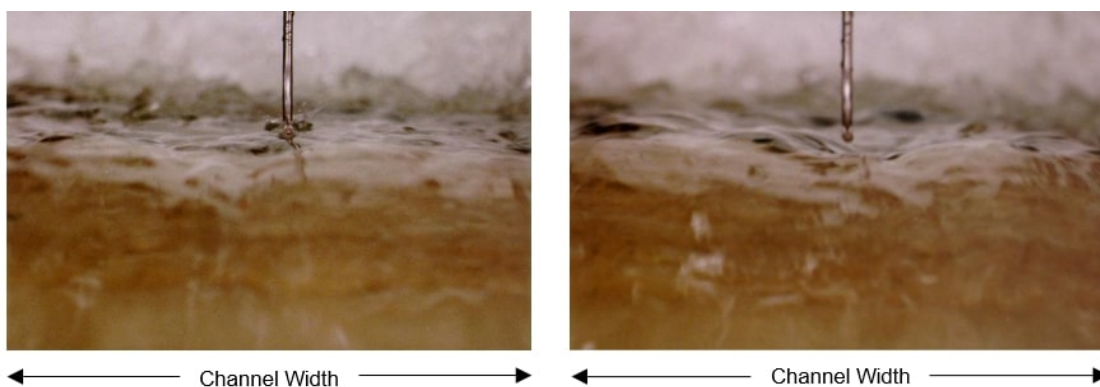


Figure 7.18: Free-surface deformation upstream of the inception point at the LNEC stepped spillway in two instances in time. The images are viewed from upstream of the probe tip. In each image a probe tip, used to measure the flow depth, can be observed. In image (a) the probe tip is practically submerged and in image (b) the probe tip is above the free-surface. Images taken from Matos and Meireles (2014)

Figure 7.19 shows the flow depths above steps 11-17 across the entire channel width for the simulation using wall boundary conditions at either side of the spillway. The corresponding 2D flow depths are also indicated at the centreline of the spillway. Wall effects can be observed, however, it should be noted that the significance of these wall effects appear exaggerated in figure 7.19 due to the different scales used on the x and y axes. At step 11, the free-surface is constant across the width of the channel, other than adjacent to the walls. At step 13, there is a small variation in the flow depth across the channel width and then at each subsequent step the variation in free-surface profile increases. This agrees with the findings of the studies described above.

Figure 7.20 shows the same data as figure 7.19, but for the simulation using symmetry boundary conditions at either side of the spillway. The free-surface profiles show a similar pattern to figure 7.19, but no wall effects are observed. At steps 14 and 15 the free-surface deformations show a regular wavy pattern across the width of the channel, with the same

7.5 Investigation into 3D behaviour in the LNEC Stepped Spillway

wavelength as the pattern of cross-stream vortices. Furthermore, the waviness in the free-surface profile at step 15 is offset from step 14 by half a wavelength, in accordance with the alternating pattern of the cross-stream vortices. The wavy free-surface profiles at steps 14 and 15 are also present in figure 7.19, however the wall effects make the wavelength of the free-surface waves difficult to identify.

At steps 16 and 17 the wavy pattern is not as clear. This may be due to the fact that the free-surface profile is being affected by one of the mechanisms described above, although no hairpin vortices were observed in the numerical models. At these steps, however, there does appear to be some regularity to the free-surface profile which may correspond to the wavelength of the cross-stream vortices. Figures 7.19 and 7.20 suggest that the cross-stream vortices affect the free-surface profiles upstream of the inception point and may contribute to the surface deformations observed by Hunt and Kadavy (2010), Chanson (2013b), Matos and Meireles (2014) and others.

The 2D flow depths agree well with the 3D flow depths at the centreline of the spillway with wall boundary conditions. This shows that 2D numerical modelling is an appropriate approach to predict the flow depths at the centreline of the spillway, providing that the spillway is sufficiently wide so that no significant wall effects are observed at the centreline of the spillway. The 2D flow depths also agree reasonably well with the 3D flow depths at the centreline of the spillway with symmetry boundary conditions, although there is a greater error than between the 2D model and wall boundary condition model. The reasons for this, however, is unclear as the 2D model also used symmetry boundary conditions at the spillway sidewalls.

7. STUDY INTO THE OCCURRENCE OF CROSS-STREAM VORTICES IN STEPPED SPILLWAYS OF VARYING GEOMETRY

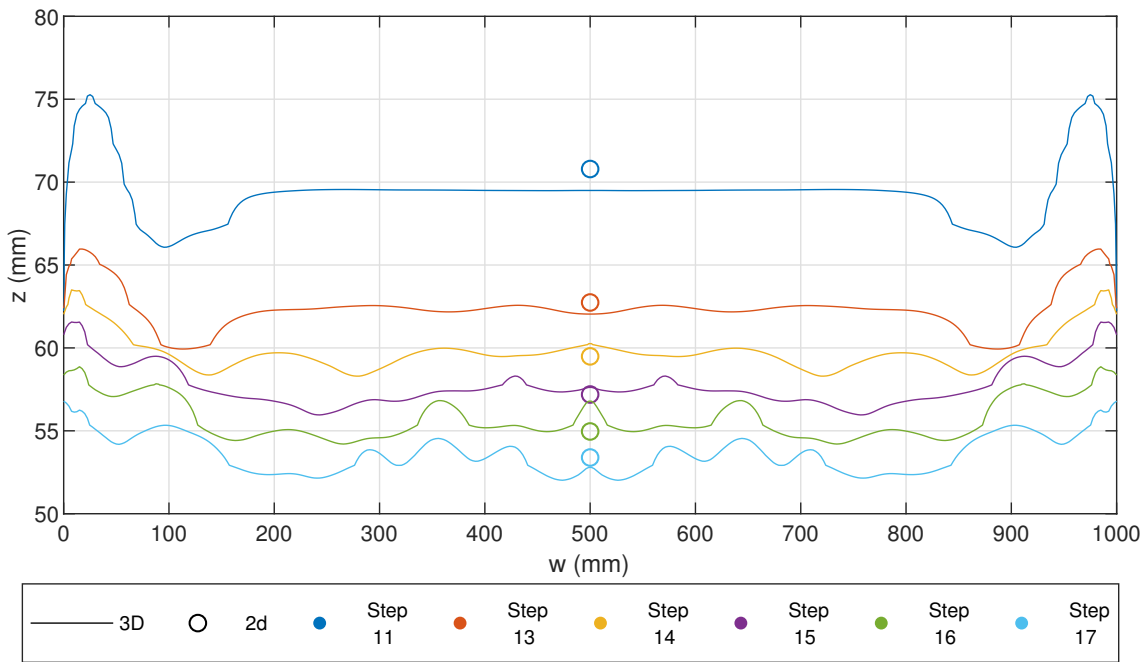


Figure 7.19: Free-surface profiles across the channel width of for the 3D simulation of the upstream section of the LNEC spillway using wall boundary conditions, at different steps. The 2D free-surface depth is also shown at $w = 500$ mm

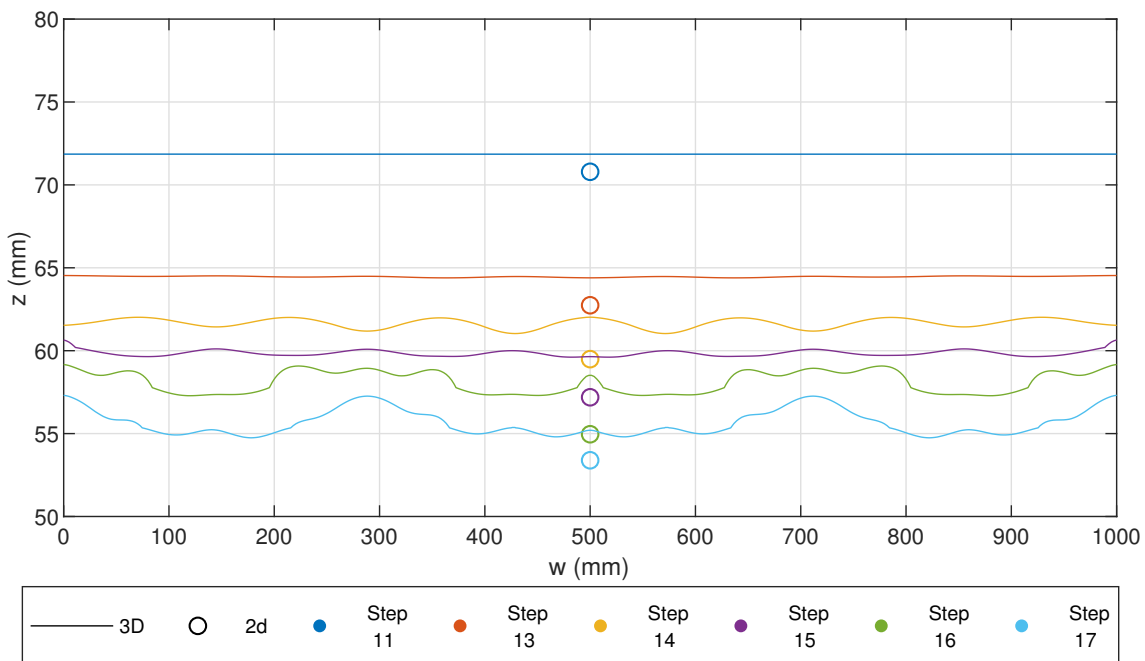


Figure 7.20: Free-surface profiles across the channel width of for the 3D simulation of the upstream section of the LNEC spillway using symmetry boundary conditions, at different steps. The 2D free-surface depth is also shown at $w = 500$ mm

7.5.5 Numerical Velocities and Air Volume Fractions Above the Steps of a 3D Stepped Spillway

3D modelling of the upstream section of the LNEC stepped spillway has shown that cross-stream vortices occur in the step cavities and effect the velocities in the bulk flow above the pseudo-bottom. The VOF model was used for this modelling, as the Eulerian model required an unfeasible computational cost. The effect of cross-stream vorticity on the AVFs within the spillway could not be analysed as no air entrainment is predicted by the VOF model.

In order to investigate the effect of cross-stream vorticity on the AVFs above the pseudo-bottom, a spillway with the same geometry as the University of Leeds stepped spillway but double the width ($W = W_0 \times 2 = 300 \text{ mm}$) was modelled using the Eulerian model. The width of the spillway was doubled so that the pattern of cross-stream vortices was repeated across the channel width, similarly to the 3D models of the LNEC stepped spillway. The SST $k - \omega$ turbulence model was used and either side of the spillway consisted of a symmetry plane. The repeated pattern of cross-stream vortices, similar to those shown in section 7.2 was observed in the step cavities. This modelling also allows the effect of cross-stream vortices on the velocities to be analysed throughout the length of the spillway, in both the non-aerated and aerated regions.

Figure 7.21 shows velocity contours at planes parallel to the pseudo-bottom at different values of z . The results are very similar to those shown in figure 7.13 in that the velocities vary across the channel width with the same wavelength as the cross-stream vortices and that, as the depth increases, the variation in velocity decreases. Figure 7.21 also shows that the variation in velocity occurs throughout the length of the spillway in both the aerated and non-aerated regions.

7. STUDY INTO THE OCCURRENCE OF CROSS-STREAM VORTICES IN STEPPED SPILLWAYS OF VARYING GEOMETRY

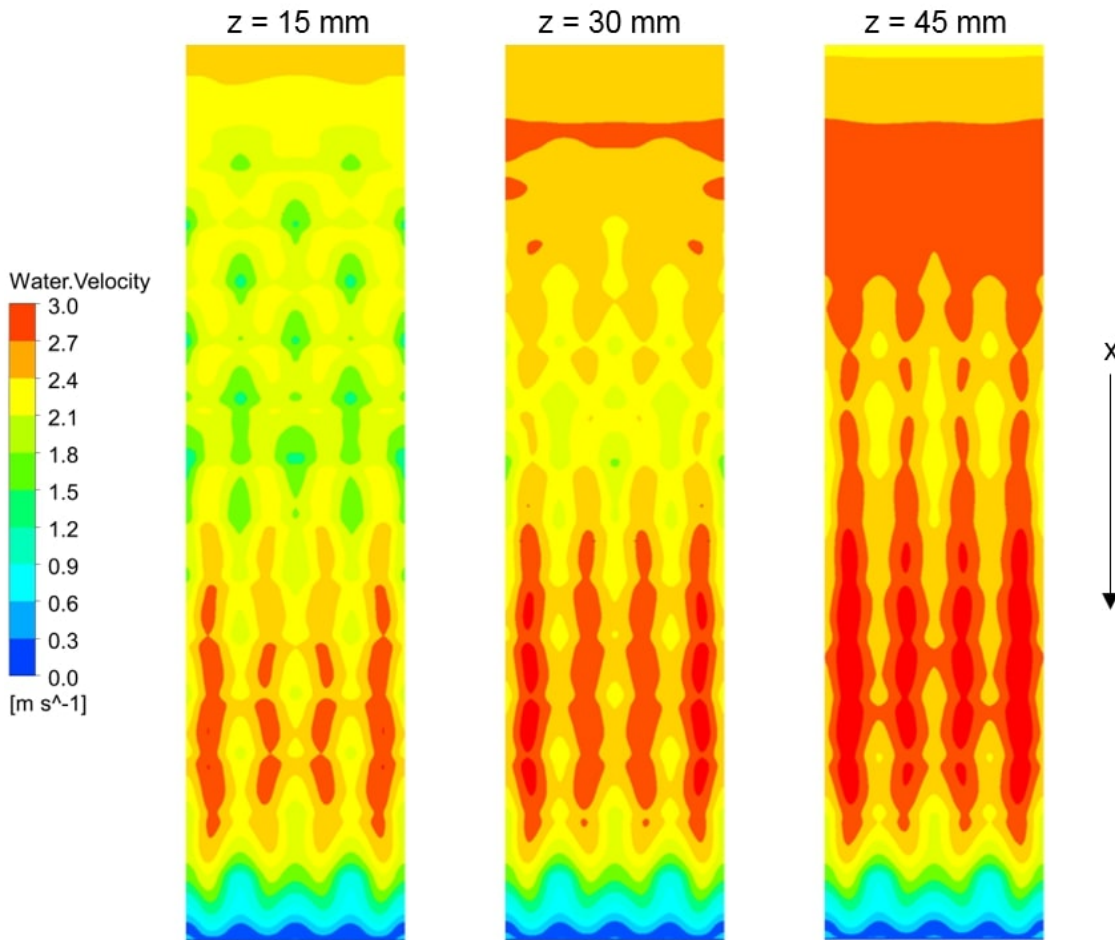


Figure 7.21: Velocity contours above the steps, parallel to the pseudo-bottom, at different values of z for the simulations of the 300 mm wide University of Leeds spillway geometry. Data is displayed for the Eulerian model with the SST $k - \omega$ model, at $Q = 180$ l/s

Figure 7.22 shows the velocity profiles at different channel widths as well as the width averaged velocity at all 15 steps. As in figures 7.14 and 7.15, velocity profiles have been shown at the centreline ($w = 150$ mm) and a width half a wavelength away from the centreline ($w = 75$ mm). Again, the results are relatively similar to those shown in figures 7.14 and 7.15. In the first few steps there is very little variation in the velocity profiles. Then there is an alternating pattern of low velocity between $w = 150$ mm and $w = 75$ mm, at the lower values of z . This matches the alternating direction of circulation of the cross-stream vortices. At the higher values of z the variation in the velocities between the different positions across the channel width reduces.

7.5 Investigation into 3D behaviour in the LNEC Stepped Spillway

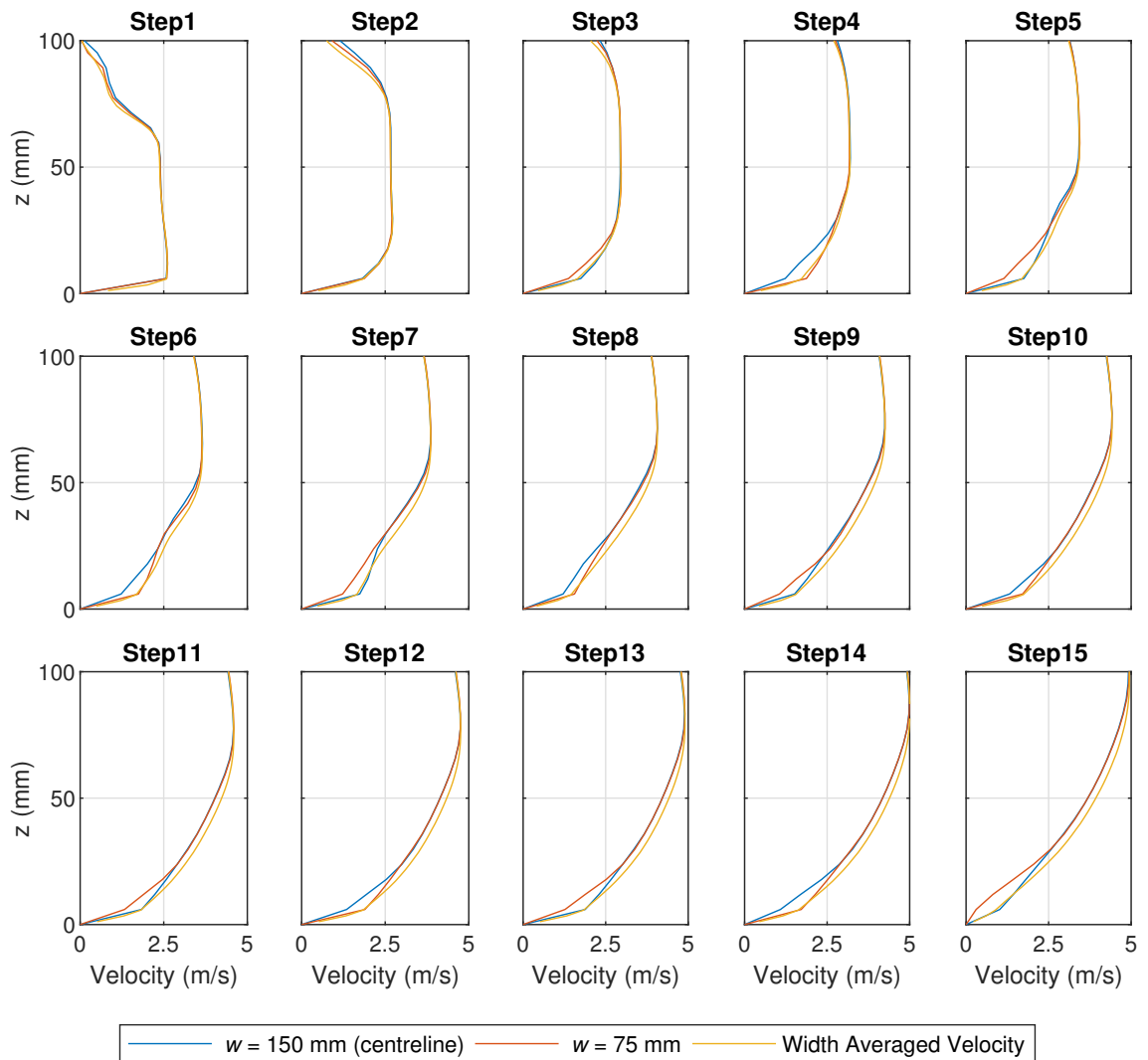


Figure 7.22: Numerical velocity profiles at different channel widths of the simulation of the 300 mm wide University of Leeds spillway geometry. The width averaged velocity profiles are also shown

Figure 7.23 shows contours of AVF at planes parallel to the pseudo-bottom at different values of z . It can be seen that, unlike the velocity contours, there is very little variation in the AVF across the channel width. Figure 7.24 shows AVF profiles at the same locations as the velocity profiles in figure 7.22, as well as the width averaged AVF profiles. Again, it can be seen that there is very little variation in the AVFs at different channel widths and at each value of w the AVF profiles are almost identical. It appears, therefore, that cross-stream vortices in the step cavities have very little effect on the aeration of the flow. A potential reason for this is that air is drawn into the flow at the free-surface whereas the cross-stream vortices originate below the pseudo-bottom so the effect on the flow caused by the cross-stream vortices may not affect the entrainment of air into the flow.

7. STUDY INTO THE OCCURRENCE OF CROSS-STREAM VORTICES IN STEPPED SPILLWAYS OF VARYING GEOMETRY

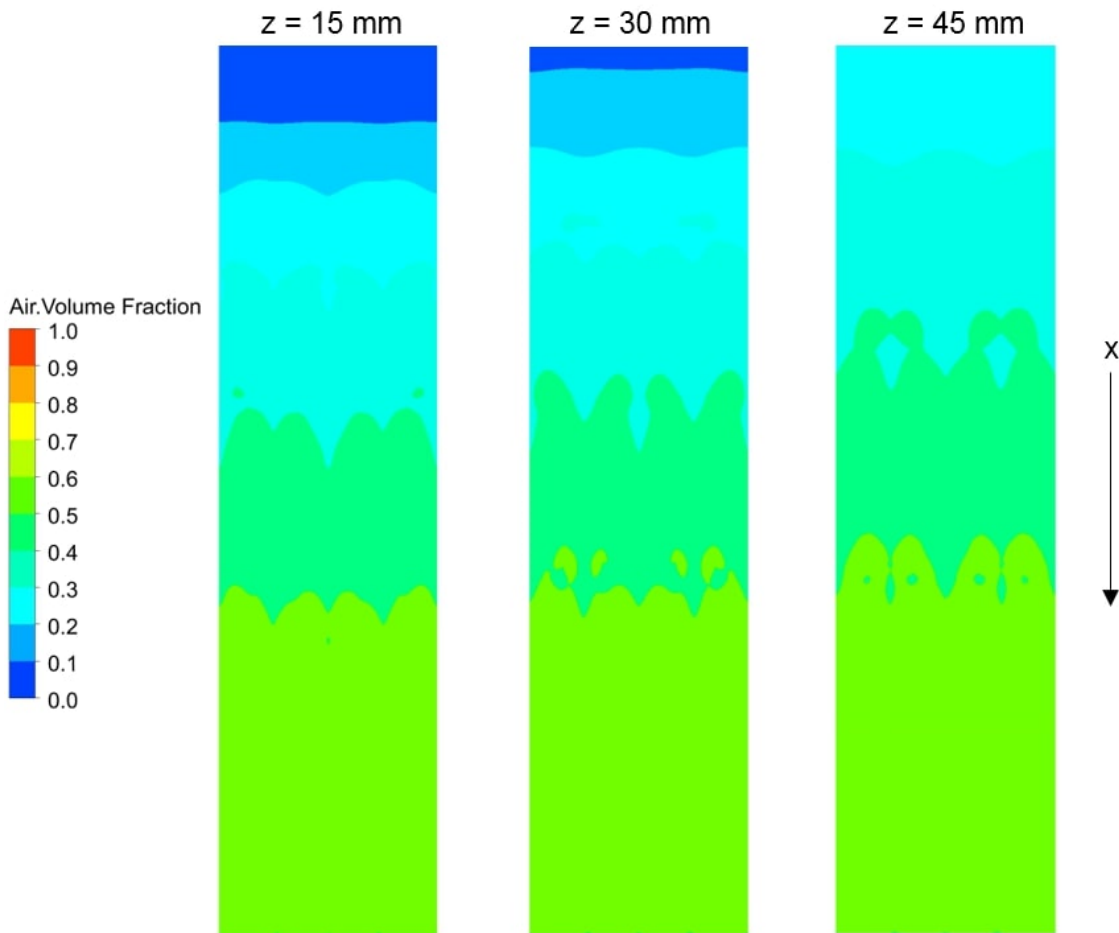


Figure 7.23: Air volume fraction contours above the steps, parallel to the pseudo-bottom, at different values of z for the simulations of the 300 mm wide University of Leeds spillway geometry. Data is displayed for the Eulerian model with the SST $k - \omega$ model, at $Q = 180 \text{ l/s}$

7.6 Prediction of Cross-Stream Vortices

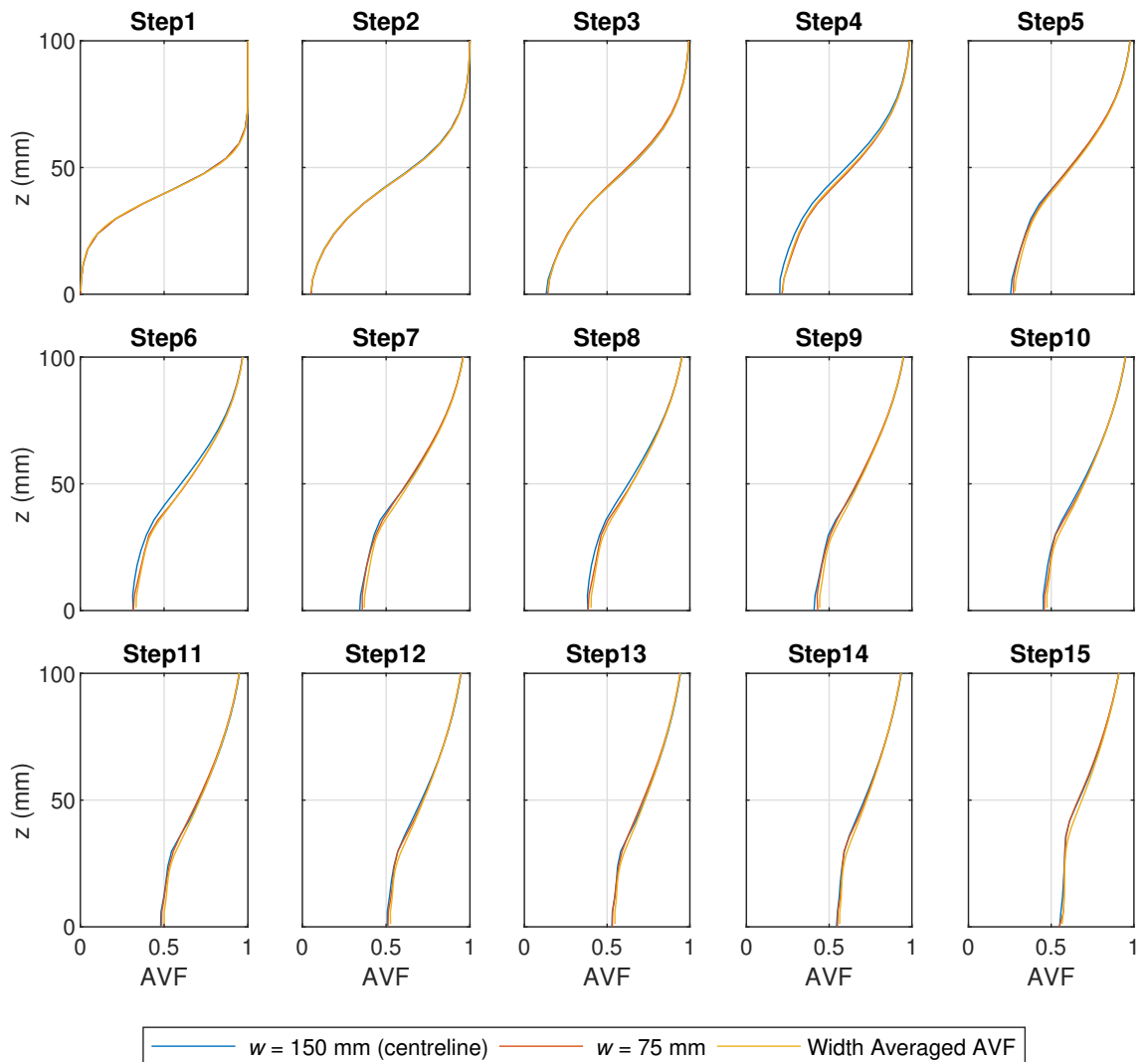


Figure 7.24: Numerical air volume fraction profiles at different channel widths of the simulation of the 300 mm wide University of Leeds spillway geometry. The width averaged air volume fraction profiles are also shown

7.6 Prediction of Cross-Stream Vortices

The results of this investigation into cross-stream vortices in stepped spillways of varying geometry strongly suggest that cross-stream vortices occur in a range of stepped spillways, and that as the width of the channel increases, the number of repetitions of the cross-stream vortices, N , increases. For the design of stepped spillways, it would be useful for engineers to be able to accurately predict N . In this section, a method for predicting N , based on the spillway width and step height, is presented.

Further simulations, other than those which have previously been discussed, were conducted for spillways with step heights and lengths of 80 mm. Channel widths were defined as

7. STUDY INTO THE OCCURRENCE OF CROSS-STREAM VORTICES IN STEPPED SPILLWAYS OF VARYING GEOMETRY

multiples of the step height and the Eulerian model, with the SST $k - \omega$ model, was used for numerical modelling. Table 7.1 displays N and the wavelength of the cross-stream vortices, λ_w , for all of the 3D spillway geometries investigated in this research project. The 80:80 steps refer to the unmodified University of Leeds spillway, the 80:60 steps refer to the LNEC spillway and the 40:40 steps refer to the modified University of Leeds spillway. It can be seen that, at $W/h_s = 1$, $N = 0$. In this simulation cross-stream vortices were not observed. This shows that there is a minimum channel width required for cross-stream vortices to form.

Table 7.1: Data on the number of repetition's of the cross-stream vortices, and their associated wavelengths, which were observed in the three step geometries investigated in this project

| Ratio of Step Height to Step Length, $h_s:l_s$ | Channel Width, W (mm) | W/h_s | Number of Repetitions, N | Wavelength, λ_w (mm) |
|--|-------------------------|---------|----------------------------|------------------------------|
| 80:80 | 80 | 1 | 0 | N/A |
| | 120 | 1.5 | 1 | 120 |
| | 150 | 1.875 | 1 | 150 |
| | 160 | 2 | 1 | 160 |
| | 200 | 2.5 | 1 | 200 |
| | 240 | 3 | 2 | 120 |
| | 280 | 3.5 | 2 | 140 |
| | 300 | 3.75 | 2 | 150 |
| | 320 | 4 | 2 | 160 |
| | 375 | 4.6875 | 3 | 125 |
| | 450 | 5.6250 | 3 | 150 |
| | 525 | 6.5625 | 4 | 131.25 |
| 80:60 | 1000 | 12.5 | 7 | 142.86 |
| 40:40 | 150 | 3.75 | 2 | 75 |

Figure 7.25 shows N against W for the three step height to step length ratios investigated in this project. The figure also displays a line representing $W/\sqrt{\pi}h_s$. It can be seen that the majority of the data points are close to $W/\sqrt{\pi}h_s$. The exceptions to this are the 40 mm by 40 mm steps and the 80 mm by 80 mm steps at $W = 80$ mm, which falls below the minimum value of W required for cross-stream vortices to form.

At $W = 1000$ mm, the 80 mm by 80 mm steps and the 80 mm by 60 mm steps have the same number of repetitions of the cross-stream vortices. This suggests that N may be independent of the step length. However, there is only one data point which does not have a channel slope of 1H:1V, so further investigation is required to confirm this. Not all of the observed values of N fall on the line of $W/\sqrt{\pi}h_s$, due to the fact that N must be a positive

integer.

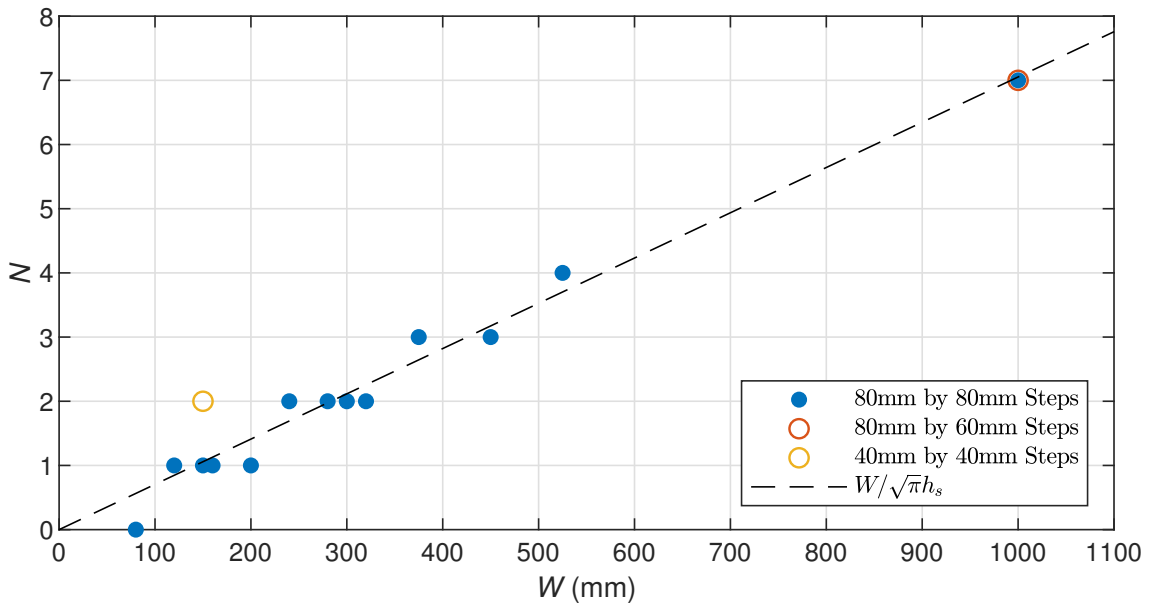


Figure 7.25: N against W for the three step geometries investigated in this project. A line representing $W/\sqrt{\pi}h_s$ is also displayed

Figure 7.26 shows N against W/h_s for the three step geometries investigated. Again, $W/\sqrt{\pi}h_s$ is displayed on the plot. In this case, the value of N for the 40 mm by 40 mm steps is close to $W/\sqrt{\pi}h_s$.

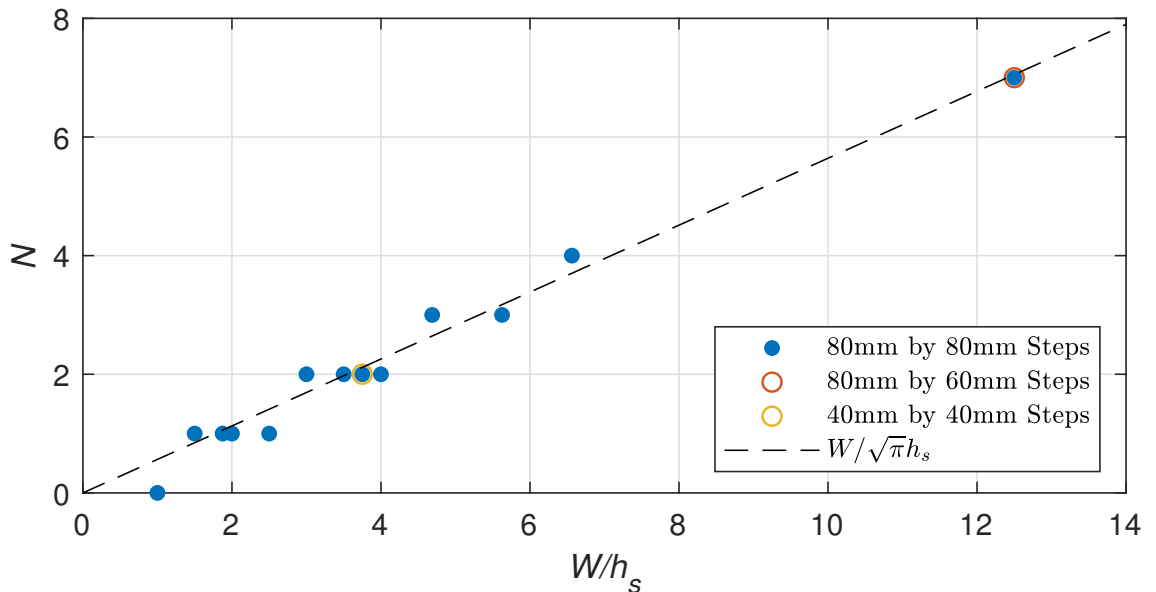


Figure 7.26: N against W/h_s for the three step geometries investigated in this project. A line representing $W/\sqrt{\pi}h_s$ is also displayed

Based on the results displayed in figures 7.25 and 7.26, the following expression can be

7. STUDY INTO THE OCCURRENCE OF CROSS-STREAM VORTICES IN STEPPED SPILLWAYS OF VARYING GEOMETRY

used to predict N :

$$N = \left\lceil \frac{W}{\sqrt{\pi}h_s} \right\rceil \quad (7.1)$$

for

$$W \geq 1.5h_s \quad (7.2)$$

where $\lceil x \rceil$ denotes that x is rounded to the nearest integer. Equation (7.2) represents the minimum value of W required for cross-stream vortices to occur, based on the spillway width investigated in this project. The actual limiting value of W may be less than $1.5h_s$.

Table 7.2 shows the values of N observed in the numerical and experimental modelling conducted in this project, as well as the values of N predicted using equation (7.1). It can be seen that N is predicted accurately by equation (7.1) for all cases which are wide enough for cross-stream vortices to occur.

It is interesting that N can be accurately predicted using a relationship which contains $\sqrt{\pi}$. This may be a coincidence, however, $\sqrt{\pi}$ may play a fundamental role in the formation of the cross-stream vortices. It is not clear, as of yet, whether this is the case. Research into the relationship between $\sqrt{\pi}$ and the formation of the cross-stream vortices is ongoing, however, the identification of this relationship is beyond the remit of this research project.

Table 7.2: Data on the number of repetition's of the cross-stream vortices, which were observed in the three step geometries investigated in this project, and the values of N predicted by equation (7.25)

| Ratio of Step Height to Step Length, $h_s:l_s$ | Channel Width, W (mm) | W/h_s | Number of Repetitions, N | $\left\lceil \frac{W}{\sqrt{\pi}h_s} \right\rceil$ |
|--|-------------------------|---------|----------------------------|--|
| 80:80 | 80 | 1 | 0 | 1 |
| | 120 | 1.5 | 1 | 1 |
| | 150 | 1.875 | 1 | 1 |
| | 160 | 2 | 1 | 1 |
| | 200 | 2.5 | 1 | 1 |
| | 240 | 3 | 2 | 2 |
| | 280 | 3.5 | 2 | 2 |
| | 300 | 3.75 | 2 | 2 |
| | 320 | 4 | 2 | 2 |
| | 375 | 4.6875 | 3 | 3 |
| | 450 | 5.6250 | 3 | 3 |
| | 525 | 6.5625 | 4 | 4 |
| | 1000 | 12.5 | 7 | 7 |
| 80:60 | 1000 | 12.5 | 7 | 7 |
| 40:40 | 150 | 3.75 | 2 | 2 |

7.6 Prediction of Cross-Stream Vortices

The prediction of N also allows the wavelength of the cross-stream vortices to be calculated by

$$\lambda_w = \frac{W}{N} = \frac{W}{\left\lfloor \frac{W}{\sqrt{\pi}h_s} \right\rfloor} \quad (7.3)$$

Figure 7.27 shows λ_w/h_s against W/h_s for the wavelengths calculated by equation (7.3), as well as the wavelengths observed in the numerical and experimental models. A line representing $\sqrt{\pi}$ is also displayed. The observed wavelength match those predicted by equation (7.27), as would be expected due to the fact that equation (7.1) predicted N correctly. It can also be seen that as the width of the channel increases, the wavelengths predicted by equation (7.27) tend toward $\sqrt{\pi}h_s$. This suggests that the "natural" wavelength of the cross-stream vortices is $\sqrt{\pi}h_s$.

At the lower values of W , there is a greater variation in the wavelengths of the cross-stream vortices. This is due to the fact that, at narrower channel widths, the width of the channel has a larger effect on the wavelength of the cross-stream vortices. When N is small, if W increases past a certain threshold to increase N by 1, then the wavelength of each repetition of the cross-stream vortices must decrease by a relatively large distance in order to fit another wavelength across the channel width. When N is large, however, the wavelength of each repetition of the cross-stream vortices only needs to decrease by a small distance in order to fit another wavelength across the width of the channel.

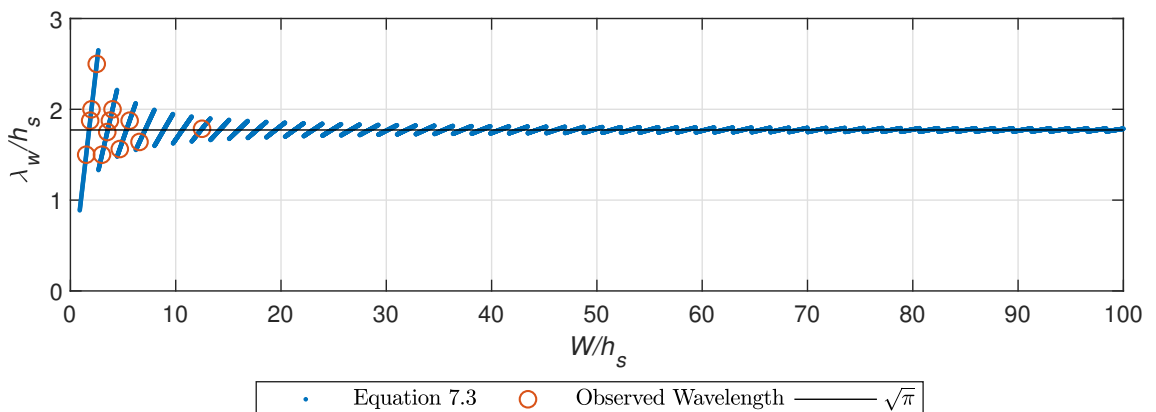


Figure 7.27: λ_w/h_s against W/h_s for the wavelengths calculated by equation (7.3), as well as the wavelengths observed in the numerical and experimental models. A line representing $\sqrt{\pi}$ is also displayed

In this section, relationships have been defined in order to predict the the number of repetitions of the cross-stream vortices, and their wavelength, based on the step height and channel width (equations (7.1) - (7.3)). These relationships match the patterns of cross-stream vortices

7. STUDY INTO THE OCCURRENCE OF CROSS-STREAM VORTICES IN STEPPED SPILLWAYS OF VARYING GEOMETRY

observed in both experimental and numerical modelling conducted in this project. Further research is required, however, in order to confirm the accuracy of these relationships. This should include investigation into spillways with varying slopes.

7.7 Conclusions

An in depth study into the occurrence of cross-stream vortices in spillways of different geometries, and their effect on the flow conditions above the steps, was conducted using both numerical and experimental modelling. Numerical modelling of a spillways of slope 1H:1V, with different channel widths was conducted. It was found that as the channel width increases, the pattern of cross-stream vortices, observed experimentally and numerically in chapters 3 and 6, are repeated across the channel width. At increasing channel widths the vortices become stretched across the channel width until a certain width is reached, at which point an additional repetition of the cross-stream vortices is observed. Cross-stream vortices were also observed when symmetry or periodic boundary conditions were used at the spillway side walls. This shows that cross-stream vortices are caused by the step geometry of the steps and the channel width, rather than the boundary condition which is used at the walls of the spillway

The Realisable $k - \epsilon$ model did predict this repetition of cross-stream vortices, however, in some cases the pattern of vortices was significantly less distinct than in other cases. This phenomenon, however, was unpredictable and inconsistent with different multiphase models and step geometries. This suggests that the Realisable $k - \epsilon$ model should not be used to investigate cross-stream vorticity.

The width of the University of Leeds experimental spillway could not altered in order to experimentally validate the numerical findings of repeated cross-stream vortices in channels of increasing width. Instead, 40 mm \times 40 mm steps were installed, in order to double the channel width to step height ratio. The repeated pattern of cross-stream vortices was observed in both the experiments and the numerical modelling of the modified spillway. It was observed that, in the modified experimental model, vortex switching occurred at a significantly higher frequency than in the unmodified spillway, for all flow rates. Note that no vortex switching was observed in any of the numerical modelling in this project and the causes of the vortex switching are unclear. It is likely, as no transient behaviour is observed in the vortex structures predicted

by the numerical models, that vortex switching is caused by time dependent behaviour in the experimental model.

Relationships are presented which accurately predict the number of receptions of the cross-stream vortices, as well as the wavelengths of the receptions, for a given step height and channel width. These relationships may provide a useful tool for the design and inspection of stepped spillways.

A numerical investigation was also conducted into the occurrence of cross-stream vortices in spillways of varying slope. At 3H:2V and 2H:3V the cross-stream vortices are clearly visible. This shows that they occur for a range of channel slopes. At 2H:1V some cross-stream vorticity can be observed, however the direction of circulation is more in line with the flow direction than at steeper slopes. At 1H:2V no cross-stream vortices were observed.

The LNEC experimental stepped spillway was also numerically modelled in 3D. Modelling of the entire spillway using the Eulerian model required an unfeasible computational cost, so the spillway was modelled up to step 17 using the VOF model. A repeated pattern of cross-stream vortices across the channel width, which alternate direction at each step, was observed in the numerical models. The cross-stream vortices have been observed both numerically and experimentally in the University of Leeds spillway, with both 80 mm \times 80 mm and 40 mm \times 40 mm steps. 3D behaviour was observed experimentally by Matos et al. (1999) within the step cavities of the LNEC spillway. This strongly suggests that the cross-stream vortices which are observed in the numerical models also occur in the experimental LNEC spillway.

The cross-stream vortices were shown to affect the velocities above the pseudo-bottom. The locations where the velocities had a large deviation from the width averaged velocity were highly localised. The width averaged velocity profiles were not significantly affected by the variation in the velocities across the channel width and were in close agreement with the 2D velocity profiles.

The time averaged experimental velocities did not show any of the effects of the cross-stream vorticity and agreed well with both the 2D and the width averaged velocities. This may be due to the fact that significant vortex switching occurs in the experimental model so that the effects of the cross-stream vortices are removed in the averaging process. Further research is required, however, to confirm this hypothesis.

3D undulations in the free-surface profile, directly upstream of the inception point, have been observed by several authors, including Matos and Meireles (2014) and Hunt and Kadavy

7. STUDY INTO THE OCCURRENCE OF CROSS-STREAM VORTICES IN STEPPED SPILLWAYS OF VARYING GEOMETRY

(2010). The cross-stream vortices were shown to cause deformations of the free-surface profile several steps upstream of the inception point. Directly upstream of the inception point the free-surface profiles were more complex, however, the cross-stream vortices may contribute to the complex free-surface profile in this region. The variations in depth across the channel width were small and the 3D flow depths at the centreline matched the 2D flow depths reasonably well.

The effect of cross-stream vorticity on the AVFs above the steps of the LNEC spillway could not be investigated, due to the unfeasible computational cost that was required to model the aerated region using the Eulerian model. In order to investigate the effect of cross-stream vortices on the AVFs above the steps, numerical modelling using the Eulerian model was conducted of a spillway with the same step geometry as the University of Leeds spillway, but with twice the channel width. It was found that the cross-stream vortices had no significant effect on the AVFs above the pseudo-bottom, and there was little variation in the AVFs across the channel width.

Although some 3D effects were found in the velocities and free-surface profiles for the LNEC spillway, these effects are not observed in the time averaged, experimentally measured, velocities and flow depths. Therefore, 2D numerical modelling remains an appropriate method to predict the time averaged velocities, AVFs and flow depths for stepped spillways which are too large to be numerically modelled in 3D.

Cross-stream vortices have been observed in numerical models with a range of geometries, multiphase models and turbulence models. They have also been observed at the University of Leeds spillway with two different step sizes and 3D behaviour was observed within the step cavities of the LNEC stepped spillway (Matos et al., 1999). This strongly suggests that cross-stream vortices may occur within the step cavities of many stepped spillways in operation today, potentially without the knowledge of the spillway designers and operators. The occurrence of cross-stream vortices in stepped spillways which are in service would have an important impact on the pressures acting on the spillway steps and side walls.

CHAPTER 8

Conclusions and Further Work

8. CONCLUSIONS AND FURTHER WORK

8.1 Overview of Research Conducted for this Project

Stepped spillways are a common overflow design for reservoirs, as they dissipate large amounts of energy and produce more air entrainment than smooth spillways. This project has concentrated on skimming flows over stepped spillways, which occur at high flow rates. It is important, for both design and inspection, that the important flow features of skimming flows can be predicted, in order to ensure that the spillway can be operated safely. This is commonly done using experimental models, however, there are limitations to these models, such as scale effects. Numerical modelling has the potential to accurately predict important flow features of skimming flows over stepped spillways. Numerical modelling of free-surface aeration, however, is challenging due to the complex interaction between the air and water.

An experimental stepped spillway was designed at the University of Leeds as part of this project. The spillway was used to investigate the flow depths and the pressures acting on the step faces and side walls. This experimental data was also used for validation of numerical models. The University of Leeds stepped spillway was numerically modelled in 3D and another experimental stepped spillway at the LNEC in Lisbon was numerically modelled in 2D. A range of multiphase and turbulence models were investigated in order to assess their ability in predicting important flow features in skimming flows. A complex pattern of 3D vortices, which are observed in the step cavities, were also investigated, both experimentally and numerically, as part of this research project.

8.2 Key Findings

The key findings of this research project are summarised in this section. Further details of the conclusions drawn from this study are discussed in section 8.3, below. The key findings of this research project are:

- A complex pattern of 3D vortices, referred to as cross-stream vortices, are observed in a relatively narrow experimental stepped spillway. Numerical modelling of the spillway also predicts these vortices. The direction of circulation of these vortices alternates at each consecutive step. The vortices have a significant effect on the pressures acting on the spillway side walls and step faces. At irregular and unpredictable time periods, the direction of circulation of the experimentally observed cross-stream vortices reverses

and the direction of circulation is affected by the flow rate.

Experimental and numerical modelling investigation show that as the width of the channel increases, the pattern of cross-stream vortices repeats across the width of the channel. Numerical modelling also shows that cross-stream vortices occur for a range of channel slopes. The results of the numerical and experimental investigations conducted in this research project strongly suggest that cross-stream vortices may occur in stepped spillways which are in currently in service. Those responsible for the design and operation of these spillways may be unaware of the occurrence of these 3D vortices.

- A range of multiphase models and RANS turbulence models have been investigated as part of this project. The Eulerian multiphase model, in combination with the SST $k - \omega$ turbulence model, is shown to be able to accurately predict a range of important flow features in aerated skimming flows over stepped spillways. The model accurately predicts velocities, air volume fractions (AVFs) and flow depths and is able to predict the location of the inception point using several methods. The model is also able to predict the complex 3D cross-stream vortices as well as the effect that these vortices have on the pressures acting on the step faces and spillway side walls. This research project has shown the the Eulerian model, with the SST $k - \omega$ model, has the potential to be an invaluable tool for the design and inspection of stepped spillways over which skimming flows occur.

The VOF model was shown to be able to predict certain aspects of skimming flows over stepped spillways accurately, including the velocities and pressures. However, the model is limited in its scope for predicting aerated skimming flows, due to its inability to predict air entrainment. The mixture model predicts air entrainment, however, is significantly less accurate than the Eulerian model at predicting almost all of the flow variables investigated. The model did however, predict the cross-stream vortices, and associated pressures, reasonably accurately.

- The pressures acting on the side walls and step faces of a relatively narrow stepped spillway were investigated, both experimentally and numerically. It was found that the complex 3D vortices have a significant effect on the pressures acting on the side walls and step faces and that this may contribute to plucking damage. Air entrainment was

8. CONCLUSIONS AND FURTHER WORK

shown to reduce high pressures acting on the horizontal step faces, but have significantly less impact on the low pressures acting on the vertical step faces. Analysis of the experimental and numerical pressures show that low pressures, which may cause cavitation or plucking damage, occur in both the aerated and non-aerated regions.

8.3 Conclusions

In this section the conclusions of this project, as they relate to the project aims set out in chapter 1, are discussed in further detail. Project aim 2 is discussed first, as the results of this investigation impact the other project aims.

8.3.1 Project Aim 2: Investigate Complex Flow Structures Within the Step Cavities using Experimental and Numerical Methods

Complex vortex structures, referred to as cross-stream vortices, are observed in the step cavities of the relatively narrow experimental stepped spillway, which was designed at the University of Leeds as part of this research project. The spillway has a step height of 80 mm, a slope of 1H:1V and a width of 150 mm. Within each step cavity, two vortices are observed which appear to circulate in a perpendicular direction to the stream-wise recirculating vortices, which are a feature of skimming flows over stepped spillways. At each step, the two vortices circulate in opposite directions to one another and meet at the centreline of the spillway. At each sequential step, the direction of circulation of each vortex reverses, so there is an alternating pattern of vortices which circulate in one direction at the odd numbered steps and the other direction at the even numbered steps. The cross-stream vortices have a significant effect on the pressures acting on the spillway side walls and step faces. It is unclear, as of yet, why the cross-stream vortices occur.

Numerical modelling of the University of Leeds stepped spillway also accurately predicted the alternating pattern of cross-stream vortices, with all multiphase and turbulence models investigated. The numerically predicted vortex structures in the step cavities show that there is no distinction between the cross-stream vortices and the recirculating stream-wise vortices. At each step there are two 3D vortices which are oriented diagonally across the horizontal step face, between the spillway centreline and the wall.

In the experimental model, the cross-stream vortices at each step were observed to re-

verse in direction at each step over time. This phenomenon is referred to as vortex switching and is confirmed by analysis of pressure measurements on the step faces. Vortex switching occurs transiently and is unpredictable. At lower flow rates, vortex switching occurs extremely infrequently and the direction of circulation of the cross-stream vortices is almost constant. As the flow rate increases, vortex switching occurs more frequently. As the flow rate increases further, vortex switching continues to occur, however, the predominant direction of circulation of the cross-stream vortices, at each step, becomes the opposite of that observed at the lower flow rates.

All of the numerical models investigated predict the occurrence of the cross-stream vortices, however, they do not predict vortex switching. All of the numerical models are solved transiently, however, in all cases a steady state is achieved so only negligible time dependent behaviour is observed (there is one exception to this, however, in this case only the free-surface is affected and no transient effects are observed in the cross-stream vortices). This suggests that vortex switching is caused by transient behaviour in the experimental model, however, the specific cause of vortex switching is unclear.

The numerical models predict the same direction of circulation of the cross-stream vortices at all flow rates. This suggests that the reversal in the predominant direction of circulation of the cross-stream vortices at the higher flow rates may also be due to transient behaviour in the experimental model.

In order to investigate how the cross-stream vortices were affected by the width of the channel, smaller steps were installed in the University of Leeds experimental spillway, which doubled the ratio of channel width to step height. It was observed that the pattern of cross-stream vortices repeated across the channel, so that four vortices occur rather than two. This repetition of the cross-stream vortices was also predicted by numerical modelling of this modified spillway. In the modified spillway, vortex switching was observed to occur significantly more frequently than in the unmodified spillway and it also occurred frequently at lower flow rates. Again, vortex switching was not predicted by the numerical models.

3D numerical modelling of the upstream section of a large scale experimental stepped spillway at the LNEC in Lisbon was conducted. The spillway has the same step height as the University of Leeds spillway and is considerably wider at 1000 mm. The numerical modelling predicted a repeated pattern of cross-stream vortices across the width of the channel. In the experimental spillway at the LNEC, 3D behaviour was observed in the step cavities (Matos

8. CONCLUSIONS AND FURTHER WORK

et al., 1999), although the structure of this 3D behaviour was not identified. As numerically predicted cross-stream vortices in the University of Leeds spillway are also confirmed by experimental observations (both in the unmodified and modified steps), the numerical modelling of the LNEC spillway strongly suggests that cross-stream vortices also occur in this experimental stepped spillway. This has further implications, as these results also suggest that cross-stream vortices may occur in many stepped spillways in service today. Those responsible for the design and operation of such spillways may be unaware of the occurrence of the cross-stream vortices or the effect that they have on the pressures acting on the spillway.

3D numerical modelling also showed that the cross-stream vortices have an effect on the velocities above the steps. The numerically predicted velocities are only affected in the region directly above the pseudo-bottom, however. The width averaged velocities are only minimally affected by the cross-stream vortices, as the cross-stream vortices only have a significant effect on the velocities above the steps at specific locations. The experimental, time averaged, velocities do not appear to be affected by the cross-stream vortices. This is potentially due to the fact that vortex switching acts to average out these effects.

Numerical modelling was conducted of stepped spillways with varying geometry in order to investigate the occurrence of cross-stream vortices. Spillways of varying width, but the same step height and slope as the unmodified University of Leeds spillway, were numerically modelled. The results showed that, as the width of the channel increases, the cross-stream vortices spread out across the width of the channel until a certain width is reached, at which point another repetition of the cross-stream vortices occurs. There is a limiting value of W , below which cross-stream vortices do not occur. It was found to be between $1h_s$ and $1.5h_s$.

A relationship was developed to predict the number of repetitions of the cross-stream vortices, N , for a given step height and channel width (equation (7.1)). This relationship accurately predicted the values of N observed in all numerical and experimental modelling. The relationship is also used to predict the wavelength of the cross-stream vortices, λ_w (equation (7.3)). It was found that, as the width of the spillway increases, λ_w tends to $\sqrt{\pi}h_s$. The value of $\sqrt{\pi}h_s$ may be fundamental in the formation of the cross-stream vortices, however, further research is required to confirm this. The relationships developed to predict N and λ_w could provide a valuable tool for reservoir engineers to predict cross-stream vortex structures in stepped spillways.

Numerical modelling of stepped spillways of varying slope was also conducted. In each

case, the step height was constant, at 80 mm, and the step length was varied. The channel width was 150 mm and only one repetition of the cross-stream vortices was observed at this width. At slopes of 2H:1V, 3H:2V and 2H:3V the cross-stream vortices were observed. At a slope of 1H:2V, however, cross-stream vortices did not occur in the step cavities, although the flow structures were not uniform across the channel width. This shows that there are a range of channel slopes at which cross-stream vortices may occur, however, there appears to be a limit to this range.

8.3.2 Project Aim 1: Investigate the Ability of Three Mesh Based Multiphase Models to Predict Air Entrainment, and other Important Flow Characteristics, in Skimming Flows over Stepped Spillways

Comprehensive 2D and 3D modelling of two experimental stepped spillways has been conducted using the Eulerian, VOF and mixture multiphase models. A number of RANS turbulence models were used in conjunction with these multiphase models. The University of Leeds stepped spillway was modelled in 3D and the LNEC stepped spillway was modelled in 2D, as full 3D numerical modelling of this spillway was unfeasible due to its large size. The numerically predicted velocities, AVFs, flow depths and pressures were compared to experimental data, and a number of methods of identifying the location of the inception point in the numerical models were also investigated. None of the numerical models predicted time-dependent behaviour, other than in one specific case in which a transient free-surface was observed.

The Eulerian multiphase model was shown to be able to predict air entrainment in both spillways. The SST $k - \omega$ model was found to be the most accurate turbulence model when used in conjunction with the Eulerian model. The Eulerian model predicted the onset of air entrainment close to the crest of both spillways investigated, significantly further upstream than in the experimental models. The air entrainment in this region, however, is restricted to a small band close to the free-surface. It is hypothesised that the observed aeration, close to the spillway crest, is due the fact that the Eulerian model does not explicitly capture a free-surface, so surface tension cannot be applied at the free-surface in the non-aerated region. The AVFs predicted by the Eulerian model, with the SST $k - \omega$ model, above the steps at the LNEC spillway, however, agreed well with the experimental AVFs in the fully aerated region. This suggests that the numerically predicted air entrainment at the crest of the spillway only has a small effect on the AVF profiles in the aerated region.

8. CONCLUSIONS AND FURTHER WORK

The Eulerian model, with the SST $k - \omega$ and standard $k - \omega$ models, predicted the velocity profiles above the steps at the LNEC stepped spillway accurately. Adjacent to the pseudo-bottom, the velocities are predicted less accurately. However, this location is where the maximum experimental error is expected to occur, due to deflection of the main flow from the step corners affecting the velocity measurements. The Realisable, RNG and standard $k - \epsilon$ models predicted the velocities and AVFs less accurately due to fact that they predicted a shorter reattachment length of the recirculating vortices than the $k - \omega$ turbulence models. The Eulerian model with the SST $k - \omega$ model also predicted the flow depths accurately over both spillways investigated.

The Eulerian model was able to accurately predict the inception point location at the LNEC spillway, as defined as the intersection of the turbulent boundary layer (TBL) and the equivalent clear water depth, d , with both the Realisable $k - \epsilon$ mode and the RNG $k - \epsilon$ model. The SST $k - \omega$ model, however, did not predict the inception point accurately using this method. Despite this, the Eulerian model with the SST $k - \omega$ was able to accurately predict the inception point location using other methods. The locations where air is entrained into the step cavities, by visual inspection of the AVF contours, agreed well with the experimentally recorded inception point locations at both spillway investigated. In the LNEC stepped spillway, analysis of the depth averaged AVFs (C_{mean}) and the AVFs at the pseudo-bottom was shown to be a potentially reliable method for predicting the location of the inception point using the Eulerian model with the SST $k - \omega$ model. The values of the C_{mean} and the AVF at the pseudo-bottom which are used to define the inception point in the numerical model, however, vary slightly in the experimental values due to the small amount of air which is entrained close to the crest of the spillway. In the University of Leeds spillway, definition of the inception point by the intersection of the TBL and d , as well as by analysis of C_{mean} and the AVF at the pseudo-bottom, was complicated due to wall effects caused by the relatively narrow channel width.

The LNEC spillways was numerically modelled, using the Eulerian model with the SST $k - \omega$ model, at a geometric scale 15 times larger than the experimental spillway, in order to represent a prototype scale stepped spillway. The experimental velocity measurements, and numerically predicted velocities at experimental scale, were scaled using Froude similarity so that they could be compared to the prototype scale numerical data. The AVFs were compared directly as they are dimensionless, so do not require scaling. Froude similarity was used to match the flow rates between the experimental and prototype scale models.

There was very close agreement between the prototype scale numerical velocities and the scaled up experimental and lab scale numerical velocities. The AVFs predicted at lab scale and prototype scale differed slightly. However, the predicted AVFs were reasonably close to one another and they both predicted the experimental AVFs with similar accuracy. This shows that the Eulerian model, with the SST $k - \omega$ model, has the potential to accurately predict important flow features of aerated skimming flows over stepped spillways at prototype scale.

The VOF model is unable to predict air entrainment in its standard form, however, the model has been shown to be able to accurately predict a number of important flow features of free-surface hydraulic flows, including in stepped spillways. It is a commonly used free-surface modelling technique, so was investigated in this research project in order to make comparisons with the Eulerian and mixture multiphase models.

As the VOF model does not predict air entrainment it underestimates the flow depth considerably in the aerated region. The model did, however, accurately predict the equivalent clear water depth in the non-aerated region of the LNEC stepped spillway. The VOF model, with the SST $k - \omega$ model, was shown to be able to predict the velocities reasonably accurately in LNEC spillway. However, as the VOF model underestimates the flow depth in the aerated region, the velocities were only predicted accurately up to a certain depth. The VOF model was able to predict the location of the inception point, by the intersection of the TBL and d , reasonably well at the LNEC stepped spillway. Again, the relatively narrow channel width of the University of Leeds stepped spillway complicated the analysis of the inception point. The other methods used to identify the location of the inception point were not investigated using the VOF model, as they consider the entrainment of air, which does not occur in the VOF model.

The mixture model predicted air entrainment at both spillways investigated. Similarly to the Eulerian model, the mixture model predicted the onset of air entrainment close to the crest of the spillway. This is thought to be due to the same reasons as the Eulerian model. At the LNEC stepped spillway, the mixture model, with all turbulence models investigated, did not predict the velocities or AVF profiles accurately and significantly overestimated the flow depth. At the University of Leeds stepped spillway, the flow depths were predicted more accurately, however, not as accurately as those predicted by the Eulerian model. By considering the intersection of the TBL and d , the mixture model accurately predicted the inception point location at the LNEC stepped spillway. However, as with the Eulerian and VOF models, the wall

8. CONCLUSIONS AND FURTHER WORK

effects in the University of Leeds stepped spillway complicated the analysis of the inception point location using this definition. As the mixture model did not predict the AVFs accurately, the other methods of identifying the location of the inception point were not considered for this multiphase model.

All of the numerical models investigated predict the general pattern of pressure, caused by the cross-stream vortices in the University of Leeds spillway, accurately. The numerical models, however, do not predict time dependent behaviour in the pressures acting on the spillway walls or step faces. Therefore, the experimentally measured pressure fluctuations, or the reversals in pressure pattern caused by vortex switching, were not predicted by the numerical models. At the highest flow rate investigated, the predominant direction of circulation of the cross-stream vortices, in the experimental spillway, was the opposite of the lower flow rates. The numerical models did not predict this reversal in the direction of the cross-stream vortices so the numerically predicted pattern of pressure at this flow rate is the opposite to what is observed in the experimental model.

In general, the magnitudes of pressure predicted by the numerical models agree well with the experimental pressure data. However, at certain locations within the spillway, the agreement between the numerical and experimental pressures is not as good. In some locations, especially at the downstream ends of the horizontal step faces, there is a large variation between pressures predicted by the different numerical models. These locations, however, often correspond to large fluctuations in the experimentally measured pressures, so the dissimilar numerical pressures all appear to be reasonably accurate.

At the highest flow rate, at which the predominant direction of circulation of the cross-stream vortices is the opposite to that predicted by the numerical models, the numerical pressures were compared to the experimental pressures, over a time period when vortex switching had caused the direction of circulation of the cross-stream vortices to match in both the numerical and experimental models. At these times the numerical models were found to predict the experimental pressures reasonably accurately.

8.3.3 Project Aim 3: Conduct an Experimental and Numerical Investigation into the Pressures Acting on the Side Walls and Step Faces of Stepped Spillways

The pressures acting on the step faces and side wall of the University of Leeds spillway were analysed, both experimentally and numerically, in order to investigate the risk of plucking and cavitation damage in stepped spillways. Both the numerical and experimental models show that there are large variations in pressure over relatively small distances, especially on the horizontal step faces. This has an important impact on plucking damage as a large differential in pressure across a masonry block may cause the block to rotate out of position, which can contribute to plucking damage (Winter et al., 2010).

The experimental and numerical models show that the high pressures acting on the on the horizontal step faces are lower in the fully aerated region. The low pressures acting on the vertical step faces, however, are largely unaffected by the presence of air in the flow. Previous studies, such as McGee (1988), have shown that, for other hydraulic structures, the presence of air acts to increase low pressures and protect the structure from cavitation damage. The results of this research project suggest that this may not be the case for stepped spillways. The aerated region of the spillway may still be protected from cavitation damage, as the air bubbles may cushion the collapse of vapour bubbles. However, this does not apply to plucking of masonry blocks, so stepped spillways may be at risk of plucking damage in both the aerated and non-aerated region.

The Eulerian and mixture models show that the high pressures acting on the horizontal step faces are reduced when the flow is aerated. It is thought that air entrainment affects pressure due to the increased compressibility of air-water mixture. The air phase in both the Eulerian and mixture models was modelled as incompressible. Therefore, the compressibility of the aerated flow must not be the only factor which affects the pressures acting on the spillway surfaces. The compressibility of the air-water mixture, however, may still contribute to the change in pressure in aerated flows.

The lowest numerical pressures were observed at the top of the vertical step faces, immediately below the step corner. Experimental pressure measurements could not be made in these locations, however, so these numerical results require further validation. The numerical pressures observed in this study were not low enough to cause cavitation vapour bubbles to form. The numerical models, however, do not predict the pressure fluctuations observed in

8. CONCLUSIONS AND FURTHER WORK

the experimental model. Therefore, pressure fluctuations in the experimental model may have resulted in pressures which are low enough to cause cavitation bubbles to form. Stepped spillways of different geometry, or higher discharges, may be more likely to result in sub-vapour pressures occurring at the top of the vertical step faces. The low pressures in these regions may also be low enough for plucking damage to occur.

8.4 Recommendations for Further Research

This research project has identified a complex pattern of cross-stream vortices which occur in the step cavities. In order to better understand these vortices, further research should be conducted. This research should aim to identify the cause of the cross-stream vortices, the limiting geometries in which they may occur and the form that the vortices may take for a given geometry. This research may be conducted both experimentally and numerically, however, investigation into prototype stepped spillways should also be undertaken in order to determine whether cross-stream vortices may occur in stepped spillways which are in service. Further investigation should also be conducted into the role that $\sqrt{\pi}$ plays in the formation of the cross-stream vortices.

The Eulerian model multiphase model with the SST $k - \omega$ model has been shown to be able to accurately predict a range of important flow features in skimming flows over stepped spillways. In order to further prove the model's reliability in predicting aerated skimming flows, validation against a wider range of physical data sets is required. This should include numerical modelling of stepped spillways with varying geometries. Validation of the numerical model with physical data sets measured at prototype scale should also be conducted. The investigation could also be extended to consider other free-surface flows in which air entrainment is important. Investigation should also be conducted, using the Eulerian model, into other turbulence models, such as LES, which may be able to predict the time dependent behaviour observed in the physical stepped spillway models.

The pressures acting on the step faces and side walls of the University of Leeds stepped spillway were shown, both numerically and experimentally, to vary significantly over short distances due to the cross-stream vortices. Low pressures, which may cause cavitation or plucking damage, were also observed in both the aerated and non aerated regions. It is important that the pressures acting in stepped spillway are understood more clearly in order to

8.4 Recommendations for Further Research

ensure the safety of stepped spillways operating under skimming flows. Further experimental investigation should aim to measure pressures acting across a greater area of the step faces and side walls, rather than at a limited number of points, as is the case for this study. This is especially important at the top of the vertical step faces, where extremely low pressures are predicted by the numerical models. This would also allow the numerical models to be validated in these locations. Further research should also be conducted into plucking damage, as this is less well understood than cavitation damage. This research should aim to identify the areas at most risk of plucking damage, as well as the magnitudes of pressures required to remove masonry blocks from the surfaces of the spillway side walls or step faces.

8. CONCLUSIONS AND FURTHER WORK

REFERENCES

- Amador, A., Sánchez-Juny, M., and Dolz, J. (2006). Characterization of the nonaerated flow region in a stepped spillway by piv. *Journal of Fluids Engineering*, 128(6):1266–1273.
- Amador, A., Sánchez-Juny, M., and Dolz, J. (2009). Developing flow region and pressure fluctuations on steeply sloping stepped spillways. *Journal of Hydraulic Engineering*, 135(12):1092–1100.
- ANSYS (2013). *Anslys fluent theory guide*. ANSYS, Inc.
- Anwar-ul Haque, F. A., Yamada, S., and Chaudhry, S. R. (2007). Assessment of turbulence models for turbulent flow over backward facing step. In *Proceedings of the World Congress on Engineering*, volume 2, pages 2–7.
- Aydin, M. and Ozturk, M. (2009). Verification and validation of a computational fluid dynamics (cfd) model for air entrainment at spillway aerators. *Canadian Journal of Civil Engineering*, 36(5):826–836.
- Balakumar, P. (2015). DNS/LES simulations of separated flows at high reynolds numbers. In *Proceedings of the 45th AIAA Fluid Dynamics Conference*, page 2783.
- Bardina, J., Huang, P., and Coakley, T. (1997). Turbulence modeling validation. In *Proceedings of the 28th Fluid dynamics conference*, page 2121. AIAA Paper.
- Batchelor, G. (2000). *An introduction to fluid dynamics*. Cambridge university press.
- Bayon, A., Toro, J. P., Bombardelli, F. A., Matos, J., and López-Jiménez, P. A. (2018). Influence of vof technique, turbulence model and discretization scheme on the numerical simulation of the non-aerated, skimming flow in stepped spillways. *Journal of Hydro-environment Research*, 19:137–149.

REFERENCES

- Boes, R. and Hager, W. (2003a). Two-phase flow characteristics of stepped spillways. *Journal of Hydraulic Engineering*, 129(9):661–670.
- Boes, R. M. and Hager, W. H. (2003b). Hydraulic design of stepped spillways. *Journal of Hydraulic Engineering*, 129(9):671–679.
- Bombardelli, F. A., Meireles, I., and Matos, J. (2011). Laboratory measurements and multi-block numerical simulations of the mean flow and turbulence in the non-aerated skimming flow region of steep stepped spillways. *Environmental Fluid Mechanics*, 11(3):263–288.
- Bung, D. B. (2011). Developing flow in skimming flow regime on embankment stepped spillways. *Journal of Hydraulic Research*, 49(5):639–648.
- Carosi, G. and Chanson, H. (2008). Turbulence characteristics in skimming flows on stepped spillways. *Canadian Journal of Civil Engineering*, 35(9):865–880.
- Chakib, B. (2013). Numerical computation of inception point location for flat-sloped stepped spillway. *International Journal of Hydraulic Engineering*, 2(3):47–52.
- Chamani, M. and Rajaratnam, N. (1999). Characteristics of skimming flow over stepped spillways. *Journal of Hydraulic Engineering*, 125(4):361–368.
- Chamani, M. R. and Rajaratnam, N. (1994). Jet flow on stepped spillways. *Journal of Hydraulic Engineering*, 120(2):254–259.
- Chanson, H. (1994). Comparison of energy dissipation between nappe and skimming flow regimes on stepped chutes. *Journal of hydraulic research*, 32(2):213–218.
- Chanson, H. (2002). *Hydraulics of stepped chutes and spillways*. CRC Press.
- Chanson, H. (2013a). Hydraulics of aerated flows: qui pro quo? *Journal of Hydraulic Research*, 51(3):223–243.
- Chanson, H. (2013b). Interactions between a developing boundary layer and the free-surface on a stepped spillway: Hinze dam spillway operation in January 2013. In *Proceedings of the 8th International Conference on Multiphase Flow*. ICMF.
- Chanson, H. and Gonzalez, C. (2005). Physical modelling and scale effects of air-water flows on stepped spillways. *Journal of Zhejiang University-Science A*, 6(3):243–250.

- Chanson, H. and Toombes, L. (2002). Experimental investigations of air entrainment in transition and skimming flows down a stepped chute. *Canadian Journal of Civil Engineering*, 29(1):145–156.
- Chanson, H. and Toombes, L. (2004). Hydraulics of stepped chutes: The transition flow. *Journal of Hydraulic Research*, 42(1):43–54.
- Chanson, H., Yasuda, Y., and Ohtsu, I. (2002). Flow resistance in skimming flows in stepped spillways and its modelling. *Canadian Journal of Civil Engineering*, 29(6):809–819.
- Chen, Q., Dai, G., and Liu, H. (2002). Volume of fluid model for turbulence numerical simulation of stepped spillway overflow. *Journal of Hydraulic Engineering*, 128(7):683–688.
- Cheng, X. and Chen, X. (2011). Applying improved eulerian model for simulation of air-water flow in a hydraulic jump. In *Proceedings of the 2011 World Environmental and Water Resources Congress, Palm Springs, California*.
- Cheng, X., Chen, Y., and Luo, L. (2006). Numerical simulation of air-water two-phase flow over stepped spillways. *Science in China Series E: Technological Sciences*, 49(6):674–684.
- Christodoulou, G. (1993). Energy dissipation on stepped spillways. *Journal of Hydraulic Engineering*, 119(5):644–650.
- Coombs, R. (2016). A comparison of model techniques at a stepped masonry spillway. *Dams and Reservoirs*, 26(1):19–26.
- Dong, Z., Wu, Y., and Zhang, D. (2010). Cavitation characteristics of offset-into-flow and effect of aeration. *Journal of hydraulic research*, 48(1):74–80.
- Down, P. and Wearing, M. (2012). Physical testing of a stepped masonry spillway. In *Dams: Engineering in a Social and Environmental Context*, pages 302–313. ICE Publishing.
- Drew, D. A. and Passman, S. L. (2006). *Theory of multicomponent fluids*, volume 135. Springer Science & Business Media.
- Dular, M. and Coutier-Delgosha, O. (2009). Numerical modelling of cavitation erosion. *International journal for numerical methods in Fluids*, 61(12):1388–1410.

REFERENCES

- Eça, L. and Hoekstra, M. (2006). On the influence of the iterative error in the numerical uncertainty of ship viscous flow calculations. In *Proceedings of the 26th Symposium on Naval Hydrodynamics*, pages 17–22.
- Environment Agency (2007). Review of 2007 summer floods.
- Environment Agency (2017). Reservoir safety. <http://evidence.environment-agency.gov.uk/FCERM/en/Default/FCRM/Areas/ReservoirSafety.aspx>. Accessed: 22/07/2019.
- Eymard, R., Gallouët, T., and Herbin, R. (2000). Finite volume methods. In *Handbook of numerical analysis*, volume 7, pages 713–1018. Elsevier.
- Felder, S. and Chanson, H. (2009a). Energy dissipation, flow resistance and gas-liquid interfacial area in skimming flows on moderate-slope stepped spillways. *Environmental fluid mechanics*, 9(4):427–441.
- Felder, S. and Chanson, H. (2009b). Turbulence, dynamic similarity and scale effects in high-velocity free-surface flows above a stepped chute. *Experiments in Fluids*, 47(1):1–18.
- Felder, S. and Chanson, H. (2011). Air–water flow properties in step cavity down a stepped chute. *International Journal of Multiphase Flow*, 37(7):732–745.
- Filippa, L., Trento, A., and Álvarez, A. M. (2012). Sauter mean diameter determination for the fine fraction of suspended sediments using a LISST-25x diffractometer. *Measurement*, 45(3):364–368.
- Flow Science Inc. (2002). FLOW-3D user manual.
- Freitas, C. J. (2002). The issue of numerical uncertainty. *Applied Mathematical Modelling*, 26(2):237–248.
- Frizell, K., Renna, F., and Matos, J. (2013). Cavitation potential of flow on stepped spillways. *Journal of Hydraulic Engineering*, 139(6):630–636.
- Gingold, R. and Monaghan, J. (1977). Smoothed particle hydrodynamics: theory and application to non-spherical stars. *Monthly notices of the royal astronomical society*, 181(3):375–389.

- Gonzalez, C. A. and Chanson, H. (2004). Interactions between cavity flow and main stream skimming flows: an experimental study. *Canadian Journal of Civil Engineering*, 31(1):33–44.
- Hirt, C. and Nichols, B. (1981). Volume of fluid (vof) method for the dynamics of free boundaries. *Journal of computational physics*, 39(1):201–225.
- Hunt, S. L. and Kadavy, K. C. (2010). Inception point relationship for flat-sloped stepped spillways. *Journal of Hydraulic Engineering*, 137(2):262–266.
- Husain, S., Muhammed, J., Karunaratna, H., and Reeve, D. (2014). Investigation of pressure variations over stepped spillways using smooth particle hydrodynamics. *Advances in Water Resources*, 66:52–69.
- Ishii, M. and Hibiki, T. (2010). *Thermo-fluid dynamics of two-phase flow*. Springer Science & Business Media.
- Kells, J. and Smith, C. (1991). Reduction of cavitation on spillways by induced air entrainment. *Canadian Journal of Civil Engineering*, 18(3):358–377.
- Kositgittiwong, D., Chinnarasri, C., and Julien, P. (2013). Numerical simulation of flow velocity profiles along a stepped spillway. *Proceedings of the Institution of Mechanical Engineers, Part E: Journal of Process Mechanical Engineering*, 227(4):327–335.
- Lauder, B. E., Reece, G. J., and Rodi, W. (1975). Progress in the development of a reynolds-stress turbulence closure. *Journal of fluid mechanics*, 68(3):537–566.
- Lauder, B. E. and Spalding, D. B. (1983). The numerical computation of turbulent flows. In *Numerical Prediction of Flow, Heat Transfer, Turbulence and Combustion*, pages 96–116. Elsevier.
- Lopes, P., Leandro, J., Carvalho, R. F., and Bung, D. B. (2017). Alternating skimming flow over a stepped spillway. *Environmental Fluid Mechanics*, 17(2):303–322.
- Lopes, P. M. B. (2016). *Free-surface flow interface and air-entrainment modelling in hydraulic structures*. PhD thesis, Universidade de Coimbra, Coimbra.

REFERENCES

- Lubchenko, N., Magolan, B., Sugrue, R., and Baglietto, E. (2018). A more fundamental wall lubrication force from turbulent dispersion regularization for multiphase cfd applications. *International Journal of Multiphase Flow*, 98:36–44.
- Manninen, M., Taivassalo, V., Kallio, S., et al. (1996). On the mixture model for multiphase flow. Technical Research Centre of Finland Finland: VTT Publications.
- Mason, P. and Hinks, J. (2008). Security of stepped masonry spillways: lessons from ulley dam. *Dams and Reservoirs*, 18(1):5–8.
- Matos, J. (1999). *Emulsioneamento de ar e dissipação de energia do escoamento em descarregadores em degraus*. PhD thesis, IST, Lisbon.
- Matos, J. (2000). Hydraulic design of stepped spillways over RCC dams. In *Proceedings of the International Workshop on Hydraulics of Stepped Spillways*, pages 187–194. Balkema Publ.
- Matos, J. and Frizell, K. H. (2000). Air concentration and velocity measurements on self-aerated flow down stepped chutes. In *Proceedings of the 2000 Joint Conference on Water Resources Engineering and Water Resources Planning and Management*.
- Matos, J., Frizell, K. H., André, S., and Frizell, K. W. (2002). On the performance of velocity measurement techniques in air-water flows. In *Hydraulic Measurements and Experimental Methods 2002*, pages 1–11.
- Matos, J. and Meireles, I. (2014). Hydraulics of stepped weirs and dam spillways: Engineering challenges, labyrinths of research. In *Proceedings of the 11th National Conference on Hydraulics in Civil Engineering & 5th International Symposium on Hydraulic Structures: Hydraulic Structures and Society-Engineering Challenges and Extremes*, page 330. Engineers Australia.
- Matos, J., Sánchez, M., Quintela, A., and Dolz, J. (1999). Characteristic depth and pressure profiles in skimming flow over stepped spillways. In *Proceedings of the 28th IAHR Congress*.
- McGee, R. (1988). Prototype evaluation of libby dam sluiceway aeration system. In *Model-Prototype Correlation of Hydraulic Structures*, pages 138–147. ASCE.
- Meireles, I. and Matos, J. (2009). Skimming flow in the nonaerated region of stepped spillways over embankment dams. *Journal of Hydraulic Engineering*, 135(8):685–689.

- Meireles, I., Renna, F., Matos, J., and Bombardelli, F. (2012). Skimming, nonaerated flow on stepped spillways over roller compacted concrete dams. *Journal of Hydraulic Engineering*, 138(10):870–877.
- Meireles, I. C., Bombardelli, F. A., and Matos, J. (2014). Air entrainment onset in skimming flows on steep stepped spillways: an analysis. *Journal of Hydraulic Research*, 52(3):375–385.
- Menter, F. (1992). Influence of freestream values on k-omega turbulence model predictions. *AIAA Journal*, 30(6):1657–1659.
- Menter, F. R. (1994). Two-equation eddy-viscosity turbulence models for engineering applications. *AIAA journal*, 32(8):1598–1605.
- Mohammadi, B. and Pironneau, O. (1993). *Analysis of the k-epsilon turbulence model*. Masson / Springer Verlag.
- Morovati, K., Eghbalzadeh, A., and Javan, M. (2016). Numerical investigation of the configuration of the pools on the flow pattern passing over pooled stepped spillway in skimming flow regime. *Acta Mechanica*, 227(2):353–366.
- Nikseresht, A., Talebbeydokhti, N., and Rezaei, M. (2013). Numerical simulation of two-phase flow on step-pool spillways. *Scientia Iranica*, 20(2):222–230.
- Ohtsu, I., Yasuda, Y., and Takahashi, M. (2004). Flow characteristics of skimming flows in stepped channels. *Journal of hydraulic Engineering*, 130(9):860–869.
- Peters, A., Sagar, H., Lantermann, U., and el Moctar, O. (2015). Numerical modelling and prediction of cavitation erosion. *Wear*, 338:189–201.
- Pfister, M. and Hager, W. (2011). Self-entrainment of air on stepped spillways. *International Journal of Multiphase Flow*, 37(2):99–107.
- Pfister, M., Hager, W., and Minor, H.-E. (2006). Bottom aeration of stepped spillways. *Journal of Hydraulic Engineering*, 132(8):850–853.
- Pope, S. B. (2001). *Turbulent flows*. IOP Publishing.

REFERENCES

- Pozarlik, A., Panara, D., Kok, J., and van der Meer, T. (2008). Heat transfer in a recirculation zone at steady-state and oscillating conditions the back facing step test case. In *Proceedings of the 5th European Thermal-Sciences Conference, Eindhoven, Netherlands, May*, pages 18–22.
- Qian, Z., Hu, X., Huai, W., and Amador, A. (2009). Numerical simulation and analysis of water flow over stepped spillways. *Science in China Series E: Technological Sciences*, 52(7):1958–1965.
- Rajaratnam, N. (1990). Skimming flow in stepped spillways. *Journal of Hydraulic Engineering*, 116(4):587–591.
- Rice, C. and Kadavy, K. (1996). Model study of a roller compacted concrete stepped spillway. *Journal of Hydraulic Engineering*, 122(6):292–297.
- Roache, P. J. (1994). Perspective: a method for uniform reporting of grid refinement studies. *Journal of Fluids Engineering*, 116(3):405–413.
- Sánchez-Juny, M., Bladé, E., and Dolz, J. (2007). Pressures on a stepped spillway. *Journal of hydraulic research*, 45(4):505–511.
- Sánchez-Juny, M. and Dolz, J. (2005). Experimental study of transition and skimming flows on stepped spillways in rcc dams: qualitative analysis and pressure measurements. *Journal of Hydraulic Research*, 43(5):540–548.
- Sánchez-Juny, M., Pomares, J., and Dolz, J. (2000). Pressure field in skimming flow over a stepped spillway. In *Proceedings of the International Workshop on Hydraulics of Stepped Spillways, Zurich. Edited by HE Minor and WH Hager. AA Balkema, Rotterdam*, pages 137–146.
- Shih, T.-H., Liou, W. W., Shabbir, A., Yang, Z., and Zhu, J. (1995). A new $k - \epsilon$ eddy viscosity model for high reynolds number turbulent flows. *Computers & Fluids*, 24(3):227–238.
- Sorensen, R. M. (1985). Stepped spillway hydraulic model investigation. *Journal of hydraulic Engineering*, 111(12):1461–1472.
- Teng, P., Yang, J., and Pfister, M. (2016). Studies of two-phase flow at a chute aerator with experiments and CFD modelling. *Modelling and Simulation in Engineering*, 2016.

- Toro, J. P., Bombardelli, F. A., and Paik, J. (2017). Detached eddy simulation of the nonaerated skimming flow over a stepped spillway. *Journal of Hydraulic Engineering*, 143(9).
- Valero, D. and Bung, D. B. (2015). Hybrid investigations of air transport processes in moderately sloped stepped spillway flows. In *E-Proceedings of the 36th IAHR World Congress*, volume 28.
- Versteeg, H. K. and Malalasekera, W. (2007). *An introduction to computational fluid dynamics: the finite volume method*. Pearson education.
- Vischer, D., Volkart, P., and Sighenthaler, A. (1982). Hydraulic modelling of air slots in open chute spillways. In *Proceedings of the International Conference on Hydraulic Modelling, BHRA Fluid Engineering, Coventry, England*.
- Wilcox, D. (1991). A half century historical review of the k-omega model. In *AIAA Paper*, pages 91–0615.
- Wilcox, D. C. et al. (1998). *Turbulence modeling for CFD*, volume 2. DCW industries La Canada, CA.
- Winter, C., Mason, P., Baker, R., and Ferguson, A. (2010). Guidance for the design and maintenance of stepped masonry spillways. *Environment Agency, London, Report SC080015*.
- Wolfshtein, M. (1969). The velocity and temperature distribution in one-dimensional flow with turbulence augmentation and pressure gradient. *International Journal of Heat and Mass Transfer*, 12(3):301–318.
- Wood, I. (1984). Air entrainment in high speed flows. In *Proceedings of the International Symposium on Scale Effects in Modelling Hydraulic Structures*, volume 4.
- Yakhot, V., Orszag, S., Thangam, S., Gatski, T., and Speziale, C. (1992). Development of turbulence models for shear flows by a double expansion technique. *Physics of Fluids A: Fluid Dynamics*, 4(7):1510–1520.
- Yang, J., Teng, P., and Zhang, H. (2019). Experiments and CFD modeling of high-velocity two-phase flows in a large chute aerator facility. *Engineering Applications of Computational Fluid Mechanics*, 13(1):48–66.

REFERENCES

- Yasuda, Y. and Chanson, H. (2003). Micro-and macro-sopic study of two-phase flow on a stepped chute. In *Proceedings of 30th IAHR Biennial Congress*, volume 500, pages 695–702. THEMA.
- Youngs, D. L. (1982). Time-dependent multi-material flow with large fluid distortion. *Numerical methods for fluid dynamics*.
- Zhan, J., Zhang, J., and Gong, Y. (2016). Numerical investigation of air-entrainment in skimming flow over stepped spillways. *Theoretical and Applied Mechanics Letters*, 6(3):139–142.
- Zhang, G. and Chanson, H. (2017). Self-aeration in the rapidly-and gradually-varying flow regions of steep smooth and stepped spillways. *Environmental Fluid Mechanics*, 17(1):27–46.
- Zhang, J., Chen, J., and Wang, Y. (2012). Experimental study on time-averaged pressures in stepped spillway. *Journal of Hydraulic Research*, 50(2):236–240.

APPENDIX A

Additional Information for Chapter 5

A. ADDITIONAL INFORMATION FOR CHAPTER 5

This appendix contains additional information on the grid convergence and time step independence studies, which were conducted for numerical modelling of the LNEC stepped spillway, as presented in chapter 5. AVF profiles predicted by the VOF model, which were not included in the main text, are also included in this appendix.

A.1 Grid Convergence

This section gives further details and analysis of the grid convergence study which was conducted for numerical modelling of the LNEC stepped spillway. All grid convergence analysis was conducted at a flow rate of $Q = 180$ l/s.

A.1.1 Eulerian Model

A.1.1.1 AVFs

As also described in chapter 5, the grid convergence of a solution is determined using the grid convergence index (GCI). In the GCI method, hg is the dimension of a cell. The grid refinement ratio, r , is then calculated by $r = hg_3/hg_2 = hg_2/hg_1$. f_i is the value of a variable produced by Mesh i . The observed convergence rate, pg , is given by

$$pg = \frac{\ln\left(\frac{|f_3 - f_2|}{|f_2 - f_1|}\right)}{\ln r} \quad (\text{A.1})$$

The grid convergence index is calculated by

$$GCI = \frac{Fs|e|}{r^{pg} - 1} \times 100 \quad (\text{A.2})$$

where Fs is a factor of safety, often taken as 1.25, and e is the error between the two grids. Note that the value of the GCI is multiplied by 100 to convert it into a percentage error. e is calculated by

$$e = \frac{f_i - f_{i-1}}{f_{i-1}}. \quad (\text{A.3})$$

If the solutions for the three meshes investigated are in the asymptotic range then

$$GCI_{23} \approx r^{pg} GCI_{12}. \quad (\text{A.4})$$

Equation (A.4) can be rearranged to produce the asymptotic verification (AV), where

$$AV = \frac{GCI_{23}}{r^{pg} GCI_{12}} \approx 1. \quad (\text{A.5})$$

A.1 Grid Convergence

Figure A.1 shows the GCI errors of the AVFs for the Eulerian model. Note that only the data in the aerated region has been shown. It can be seen that there are some extremely high values of both GCI_{12} and GCI_{23} , more than 1000%, which indicates that grid convergence has not been achieved. This disagrees with the findings of the grid convergence analysis for the velocities, which found that the solutions were independent of the mesh sizes.

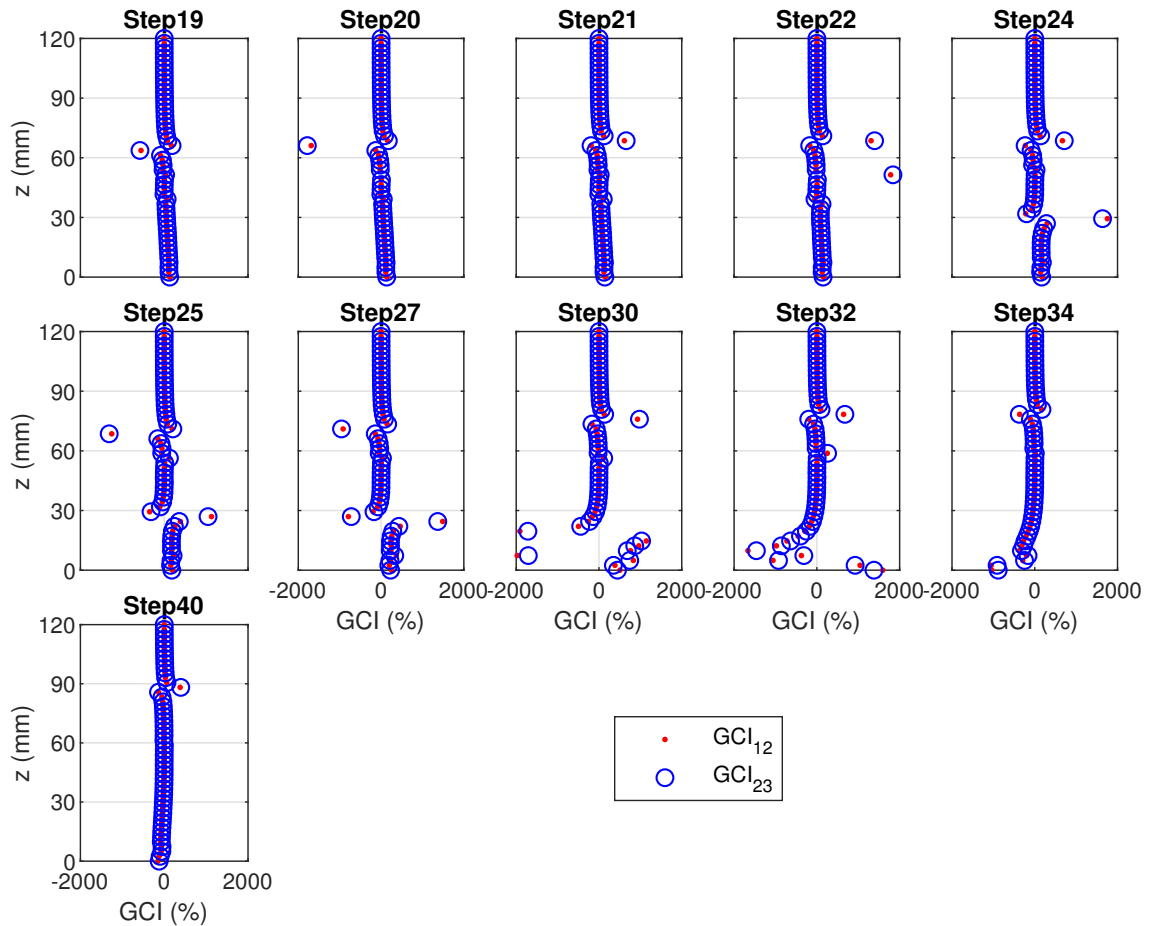


Figure A.1: Grid convergence index percentage error of air volume fraction at numerous locations above the pseudo-bottom. The solutions were calculated for three meshes, using the Eulerian model with the Realisable $k - \epsilon$ model, at $Q = 180$ l/s

In order to investigate the cause of these high GCI values further, the AVF grid convergence of a single data point, $z = 14.7$ mm at step 30, is considered in detail.

The AVFs at this point for each grid are

$$f_1 = 0.2206, \quad f_2 = 0.2482 \quad \text{and} \quad f_3 = 0.2762$$

which gives

A. ADDITIONAL INFORMATION FOR CHAPTER 5

$$|f_2 - f_1| = 0.0276 \quad \text{and} \quad |f_3 - f_2| = 0.0280.$$

These two values are very similar, which indicates that the model solutions are changing linearly with grid refinement and therefore mesh independent solutions have not been achieved.

The affect of this is that

$$\frac{|f_3 - f_2|}{|f_2 - f_1|} = \frac{0.0280}{0.0276} = 1.0144$$

which is close to 1, causing the numerator of eqn. (A.1) to be small and therefore the value of pg to be small:

$$\ln\left(\frac{|f_3 - f_2|}{|f_2 - f_1|}\right) = \ln(1.0144) = 0.0143 \quad \text{so} \quad p = \frac{0.0143}{0.2231} = 0.0641.$$

The low value of pg results in $r^{pg} \approx 1$ so that $r^{pg} - 1$ becomes

$$r^{pg} - 1 = 1.258^{0.06441} - 1 = 1.0145 - 1 = 0.0145.$$

This low value of the denominator in equation (A.2) results in the GCI values becoming extremely high:

$$GCI_{12} = \frac{1.25 \times 0.1251}{0.01445} \times 100 = 1078.45\% \quad \text{and} \quad GCI_{23} = \frac{1.25 \times 0.1128}{0.01445} \times 100 = 972.41\%.$$

Despite these high GCI values, the AV is still relatively close to 1:

$$AV = \frac{GCI_{23}}{r^{pg} GCI_{12}} = \frac{972.441}{1.0145 \times 1078.45} = 0.889$$

which suggests that, although the GCIs are high, the solution still falls within the asymptotic range.

Figure A.2 shows the AV values of the AVFs for the Eulerian model. It can be seen that, in most cases, the values are reasonably close to 1. At the upstream steps, the lower values values of z may be considered outside of the asymptotic range, however the vast majority of values appear to fall within the asymptotic range.

Both the high GCI value, and the AV values which are not close to 1, can both be explained by considering the AVF profiles predicted with the three meshes. Figure A.3 shows the AVF data for each mesh. It can be seen that there is little difference between the AVF profiles predicted with all three meshes. At a certain position, the difference between the AVF

A.1 Grid Convergence

predicted by meshes 1 and 2 may be very similar to the difference between the AVF predicted by meshes 2 and 3. As explained above, this will cause the GCI error to be high. In another position, the difference between the AVF predicted by meshes 1 and 2 may be smaller than the difference between AVF predicted by meshes 2 and 3. This would result in a value of AV which is not close to 1. However, the magnitudes of all these differences are small. Refinement of the computational mesh has not resulted in significant differences in the predicted AVFs, which suggests that further refinement of the computational mesh would not result in an improved solution.

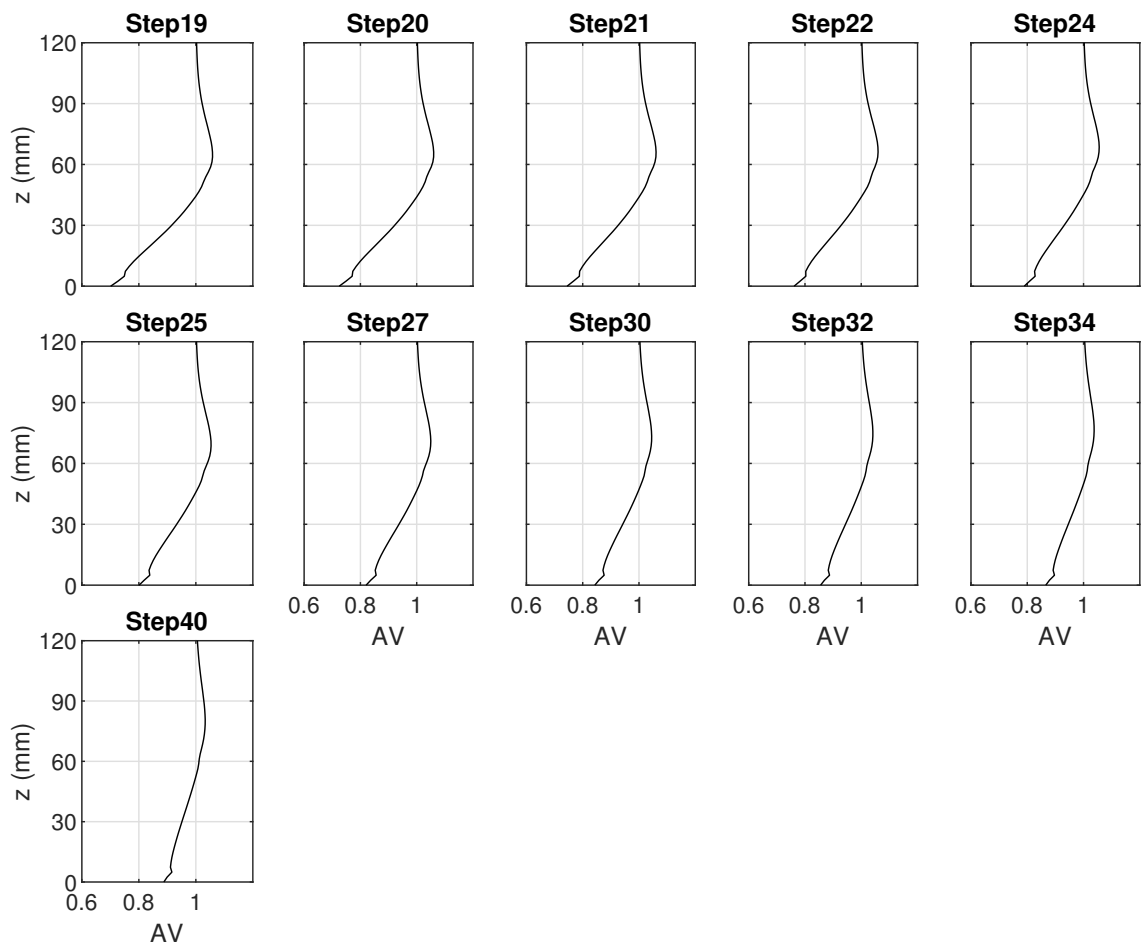


Figure A.2: Asymptotic verification of air volume fraction at numerous locations above the pseudo-bottom. The solutions were calculated for three meshes, using the Eulerian model with the Realisable $k - \epsilon$ model

A. ADDITIONAL INFORMATION FOR CHAPTER 5

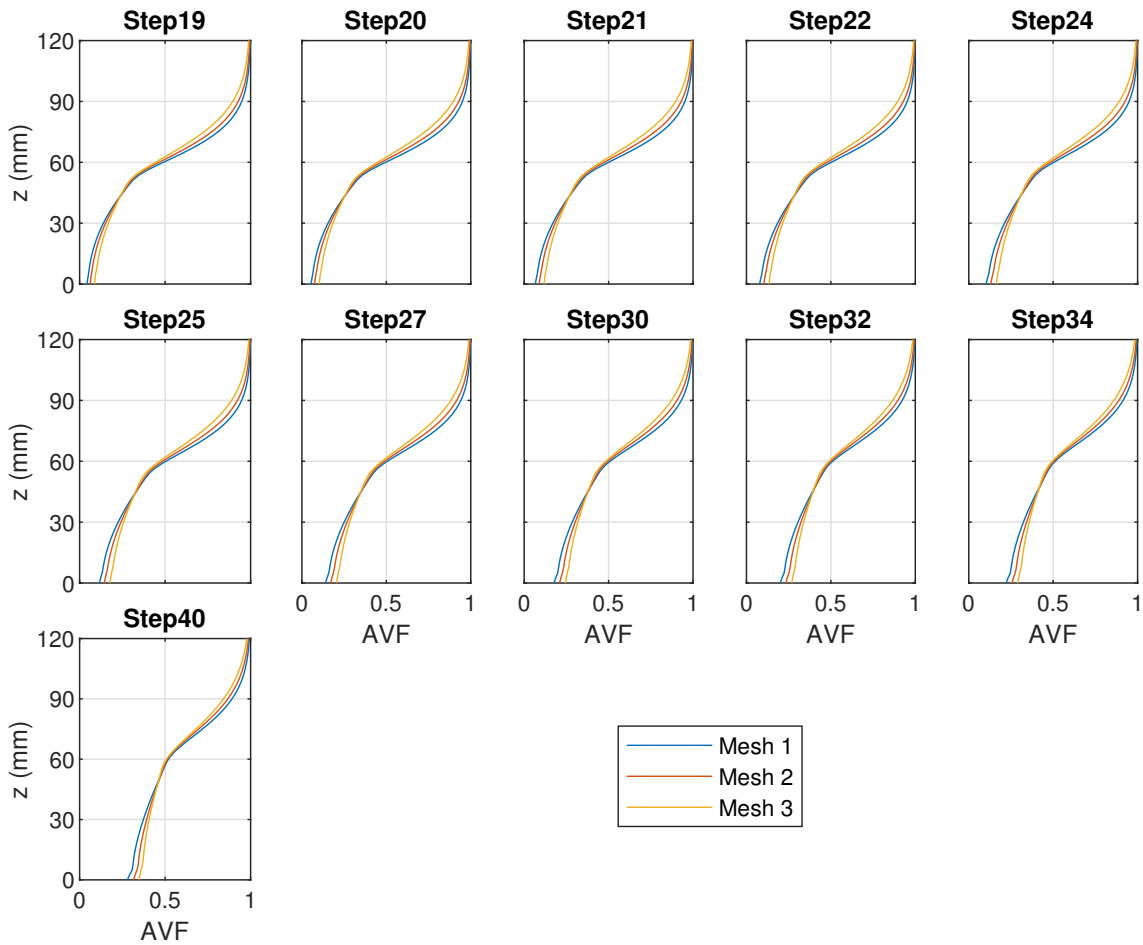


Figure A.3: Air volume fraction data for three meshes at numerous locations above the pseudo-bottom. The solutions were calculated using the Eulerian model with the Realisable $k - \epsilon$ model, at $Q = 180$ l/s

Figure A.4 shows the absolute error between the AVFs predicted by meshes 2 and 3 and the experimental data. The SST $k - \omega$ turbulence model has been used in each case. It can be seen that both meshes produce similarly accurate results. This suggests that the solutions are independent of grid refinement, as there is not a significant difference between the solutions predicted using the two meshes. Therefore, it was decided that mesh 2 was acceptably independent of grid resolution, so was used for all numerical modelling conducted in chapter 5.

The GCI approach is a useful method for analysing numerical error due to the refinement of the computational grid. However, as is demonstrated here, the results can be misleading. It is important, when analysing grid convergence, that all of the data is considered, in order to determine whether further grid refinement is required.

A.1 Grid Convergence

| Step Number | Mesh 2 | | | | | | | | | | | | | Step Number | Mesh 3 | | | | | | | | | | | | | | | | | | | | | | | | | | | | | | |
|-------------|--------|------|------|------|------|------|------|------|------|------|------|------|------|-------------|--------|------|------|------|------|-------|-------|--|-----|-----|------|------|------|------|------|------|------|------|------|------|------|------|------|------|------|------|------|-------|-------|--|--|
| | z (mm) | | | | | | | | | | | | | | z (mm) | | | | | | | | | | | | | | | | | | | | | | | | | | | | | | |
| | 3.2 | 8.2 | 13.2 | 18.2 | 23.2 | 28.2 | 33.2 | 38.2 | 43.2 | 48.2 | 53.2 | 58.2 | 63.2 | 68.2 | 73.2 | 78.2 | 83.2 | 88.2 | 93.2 | 103.3 | 113.3 | | 3.2 | 8.2 | 13.2 | 18.2 | 23.2 | 28.2 | 33.2 | 38.2 | 43.2 | 48.2 | 53.2 | 58.2 | 63.2 | 68.2 | 73.2 | 78.2 | 83.2 | 88.2 | 93.2 | 103.3 | 113.3 | | |
| 11 | 0.0 | 0.0 | 0.0 | 0.1 | 0.2 | 0.5 | 1.1 | 1.8 | 4.7 | 5.0 | 4.1 | 5.3 | 23.4 | 14.2 | 4.9 | | | | | | | | 11 | 0.0 | 0.0 | 0.0 | 0.0 | 0.1 | 0.3 | 0.8 | 1.3 | 4.6 | 5.9 | 7.4 | 0.7 | 28.6 | 22.0 | 12.3 | | | | | | | |
| 13 | 0.3 | 0.5 | 0.8 | 1.3 | 2.1 | 3.3 | 5.1 | 5.9 | 8.6 | 8.9 | 8.3 | 1.9 | 7.7 | 3.3 | 0.2 | | | | | | | | 13 | 0.1 | 0.3 | 0.5 | 0.9 | 1.7 | 3.1 | 5.0 | 6.0 | 9.0 | 9.5 | 8.9 | 3.9 | 14.6 | 9.6 | 3.9 | | | | | | | |
| 14 | 0.8 | 1.1 | 1.6 | 2.4 | 3.5 | 4.5 | 6.6 | 8.5 | 10.1 | 4.1 | 4.3 | 25.9 | 9.5 | 1.5 | 0.4 | | | | | | | | 14 | 0.5 | 0.7 | 1.2 | 1.9 | 3.1 | 4.2 | 6.4 | 8.5 | 10.1 | 4.0 | 4.6 | 27.0 | 15.5 | 5.8 | 1.7 | | | | | | | |
| 15 | 1.7 | 2.1 | 2.7 | 3.7 | 5.1 | 7.0 | 9.6 | 8.7 | 10.1 | 8.1 | 0.6 | 24.2 | 7.9 | 0.9 | 0.5 | | | | | | | | 15 | 1.1 | 1.5 | 2.1 | 3.1 | 4.5 | 6.5 | 9.1 | 8.3 | 9.6 | 5.6 | 0.8 | 26.9 | 12.5 | 3.7 | 0.6 | | | | | | | |
| 16 | 2.8 | 3.4 | 4.2 | 5.5 | 6.0 | 7.9 | 11.0 | 9.9 | 11.7 | 5.2 | 10.8 | 21.3 | 6.6 | 0.6 | 0.6 | | | | | | | | 16 | 2.0 | 2.5 | 3.4 | 4.6 | 5.1 | 7.0 | 10.3 | 9.1 | 11.1 | 4.7 | 11.3 | 24.4 | 10.0 | 2.4 | 0.1 | | | | | | | |
| 17 | 4.0 | 4.7 | 4.3 | 4.4 | 6.8 | 9.4 | 9.7 | 10.7 | 10.9 | 10.0 | 6.9 | 16.9 | 6.3 | 0.6 | 0.6 | | | | | | | | 17 | 2.9 | 3.6 | 3.2 | 3.2 | 5.6 | 8.2 | 8.7 | 9.8 | 10.2 | 9.6 | 7.3 | 19.6 | 9.0 | 1.9 | 0.1 | | | | | | | |
| 18 | 5.4 | 5.4 | 5.7 | 6.3 | 7.1 | 7.5 | 9.8 | 10.2 | 6.4 | 12.4 | 21.7 | 19.4 | 6.0 | 0.6 | 0.6 | | | | | | | | 18 | 4.0 | 3.9 | 4.2 | 4.8 | 5.6 | 6.0 | 8.5 | 9.2 | 5.7 | 12.6 | 22.3 | 21.8 | 8.0 | 1.5 | 0.3 | | | | | | | |
| 19 | 4.1 | 4.9 | 4.2 | 6.2 | 5.3 | 5.5 | 7.8 | 5.8 | 0.3 | 11.0 | 22.1 | 18.2 | 5.5 | 0.6 | 0.5 | | | | | | | | 19 | 2.4 | 3.1 | 2.4 | 4.4 | 3.6 | 3.8 | 6.4 | 4.7 | 1.0 | 11.3 | 22.8 | 20.0 | 7.0 | 1.2 | 0.4 | | | | | | | |
| 20 | 3.3 | 3.1 | 3.1 | 4.6 | 4.5 | 4.7 | 2.7 | 0.4 | 7.3 | 16.0 | 25.5 | 17.1 | 5.2 | 0.6 | 0.6 | | | | | | | | 20 | 1.2 | 1.0 | 1.0 | 2.5 | 2.6 | 2.9 | 1.1 | 1.6 | 8.1 | 16.2 | 26.4 | 18.3 | 6.2 | 1.0 | 0.5 | | | | | | | |
| 21 | 2.3 | 1.7 | 2.9 | 2.0 | 0.2 | 2.2 | 0.2 | 2.3 | 7.4 | 14.9 | 22.3 | 13.3 | 4.0 | 0.0 | 0.7 | | | | | | | | 21 | 0.1 | 0.7 | 0.5 | 0.3 | 1.9 | 0.2 | 1.9 | 3.5 | 8.1 | 15.1 | 23.1 | 14.1 | 4.5 | 0.2 | 0.7 | | | | | | | |
| 22 | 0.9 | 2.6 | 1.5 | 0.4 | 2.6 | 2.6 | 3.0 | 4.8 | 6.2 | 14.1 | 16.9 | 7.4 | 1.5 | 0.7 | 1.0 | 0.9 | | | | | | | 22 | 3.5 | 5.2 | 4.1 | 2.9 | 4.9 | 4.7 | 4.8 | 6.1 | 6.9 | 14.2 | 17.7 | 8.0 | 1.7 | 0.6 | 1.0 | 0.9 | | | | | | |
| 24 | 4.0 | 5.4 | 5.6 | 6.4 | 7.4 | 8.9 | 9.7 | 11.0 | 14.5 | 18.1 | 19.7 | 6.9 | 0.4 | 2.3 | 1.6 | 1.2 | | | | | | | 24 | 7.2 | 8.4 | 8.6 | 9.3 | 10.0 | 11.2 | 11.5 | 12.3 | 15.2 | 18.0 | 20.3 | 7.1 | 0.7 | 2.5 | 1.6 | 1.2 | | | | | | |
| 25 | 1.6 | 4.1 | 5.0 | 5.1 | 6.8 | 7.2 | 8.9 | 9.7 | 12.9 | 16.7 | 15.5 | 3.6 | 2.0 | 2.8 | 2.0 | 1.4 | 1.2 | | | | | | 25 | 4.9 | 7.3 | 8.1 | 8.0 | 9.5 | 9.5 | 10.8 | 11.0 | 13.6 | 16.6 | 16.2 | 3.8 | 2.4 | 3.0 | 2.1 | 1.5 | 1.3 | | | | | |
| 27 | 1.7 | 2.9 | 4.8 | 4.9 | 4.8 | 6.3 | 6.1 | 9.2 | 10.0 | 14.7 | 15.5 | 4.6 | 2.2 | 2.8 | 2.2 | 1.6 | 1.2 | | | | | | 27 | 5.2 | 6.4 | 8.1 | 8.0 | 7.6 | 8.7 | 8.0 | 10.6 | 10.7 | 14.6 | 16.1 | 4.7 | 2.8 | 3.3 | 2.3 | 1.7 | 1.2 | | | | | |
| 30 | 3.4 | 0.2 | 2.3 | 2.3 | 1.9 | 3.2 | 3.6 | 4.7 | 6.7 | 9.7 | 12.0 | 5.0 | 0.0 | 1.3 | 1.3 | 1.1 | 0.9 | | | | | | 30 | 0.3 | 3.8 | 5.8 | 5.6 | 4.9 | 5.6 | 5.5 | 6.2 | 7.5 | 9.8 | 12.6 | 6.0 | 1.0 | 2.0 | 1.6 | 1.2 | 1.0 | | | | | |
| 32 | 9.4 | 5.6 | 3.7 | 4.7 | 4.1 | 4.4 | 3.8 | 1.7 | 0.9 | 4.2 | 7.4 | 3.9 | 0.3 | 0.4 | 0.8 | 0.9 | 0.8 | | | | | | 32 | 5.7 | 2.0 | 0.2 | 1.5 | 1.2 | 1.8 | 1.8 | 0.2 | 0.0 | 4.5 | 8.1 | 4.0 | 0.9 | 1.2 | 1.2 | 1.0 | 0.9 | | | | | |
| 34 | 8.2 | 3.0 | 0.4 | 1.0 | 1.4 | 1.7 | 1.6 | 0.4 | 0.9 | 4.8 | 9.4 | 7.4 | 3.8 | 1.2 | 0.2 | 0.6 | | | | | | | 34 | 4.5 | 0.6 | 3.1 | 2.2 | 1.5 | 0.8 | 0.4 | 1.1 | 1.8 | 5.0 | 9.8 | 7.4 | 2.5 | 0.2 | 0.6 | 0.8 | | | | | | |
| 40 | 7.8 | 10.3 | 6.3 | 5.1 | 5.1 | 5.2 | 4.1 | 2.8 | 1.1 | 1.0 | 5.1 | 4.7 | 2.6 | 1.0 | 0.1 | 0.4 | 0.7 | | | | | | 40 | 4.5 | 7.1 | 3.1 | 2.1 | 2.5 | 2.9 | 2.3 | 1.4 | 0.3 | 1.2 | 4.9 | 4.9 | 1.2 | 0.4 | 0.7 | 0.7 | 0.8 | | | | | |

Error > 0.3

0.2 < Error ≤ 0.3

0.1 < Error ≤ 0.2

Error ≤ 0.1

No Data Available

Figure A.4: Absolute error between numerically predicted and experimentally measure AVFs, for meshes 2 and 3. Numerical results predicted by the Eulerian model with the SST $k - \omega$ turbulence model, at $Q = 180$ l/s. The colour of each cell represents which range of values the error falls within at the corresponding location. These ranges are defined in the key of the figure

A.1.2 VOF Model

For the VOF model, only the velocities are considered, as the VOF model does not predict air entrainment. Figure A.5 shows the GCI values of velocity for the VOF model. There are spikes in both the GCI_{12} and GCI_{23} values at a certain depth at each step. This represents the location of the free-surface, where the different meshes predict slightly different velocity values, as the phase changes from water to air. This does not affect the velocities in the water phase, which are of interest in this study. The GCI values close to the pseudo-bottom are also slightly higher than at other depths, however in most cases still remain reasonably low. The exception to this is step 16, where higher GCI values are observed. However, the vast majority of the of the positions investigated show acceptably low GCI values. This is also evident in figure A.6 which shows the AV values of the velocities for the VOF model. The values close to the pseudo-bottom and at the free-surface are slightly further from 1 than at other depths. Again, the high GCI errors, and values of AV that are not close to 1, are due to the fact that all three meshes predict extremely similar velocity profiles (figure A.7). Therefore, the solutions are considered to be independent of grid refinement.

A. ADDITIONAL INFORMATION FOR CHAPTER 5

A.1.2.1 Velocities

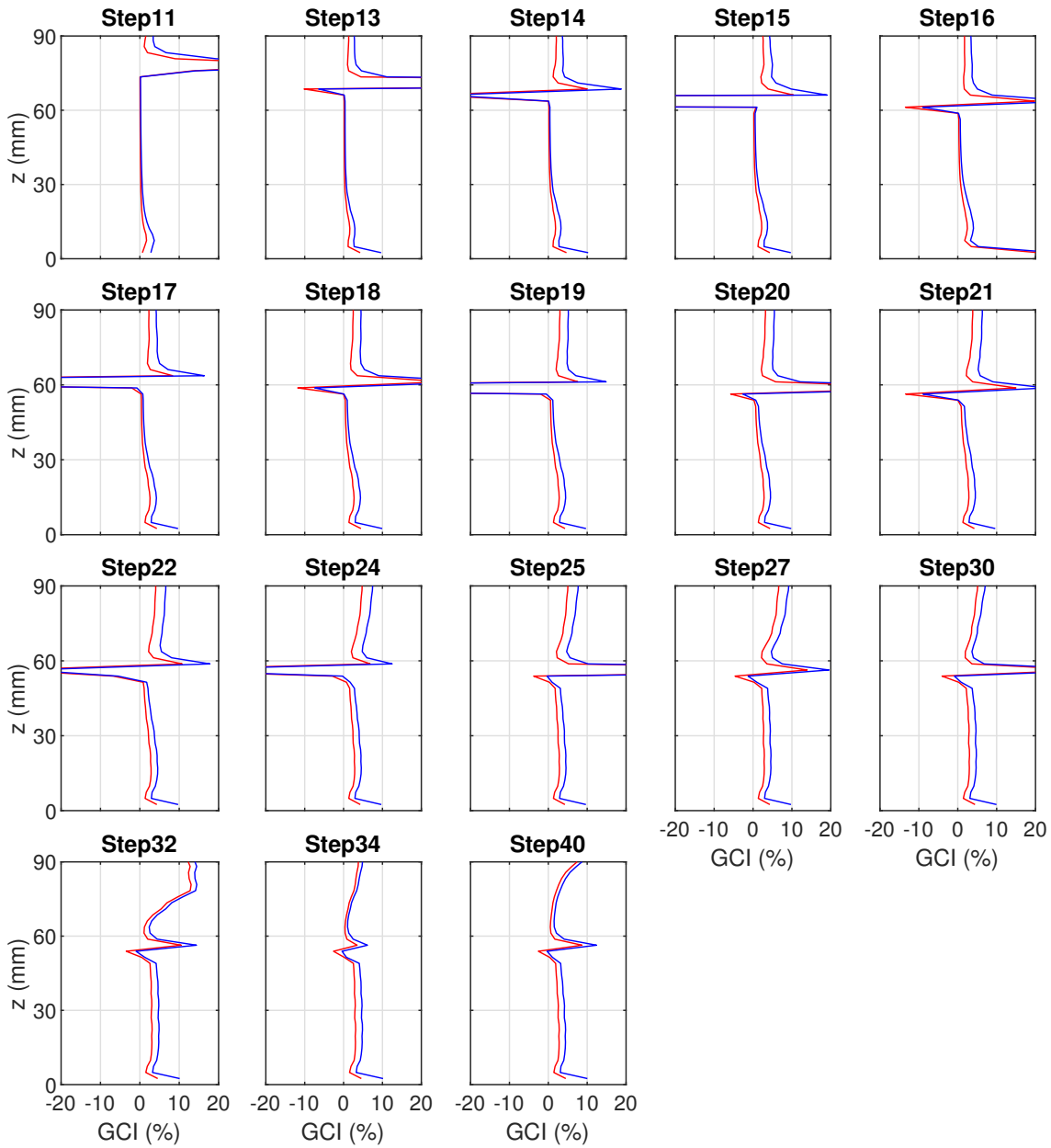


Figure A.5: Grid convergence index percentage error of velocity at numerous locations above the pseudo-bottom. The solutions were calculated for three meshes, using the VOF model with the Realisable $k - \epsilon$ model, at $Q = 180$ l/s

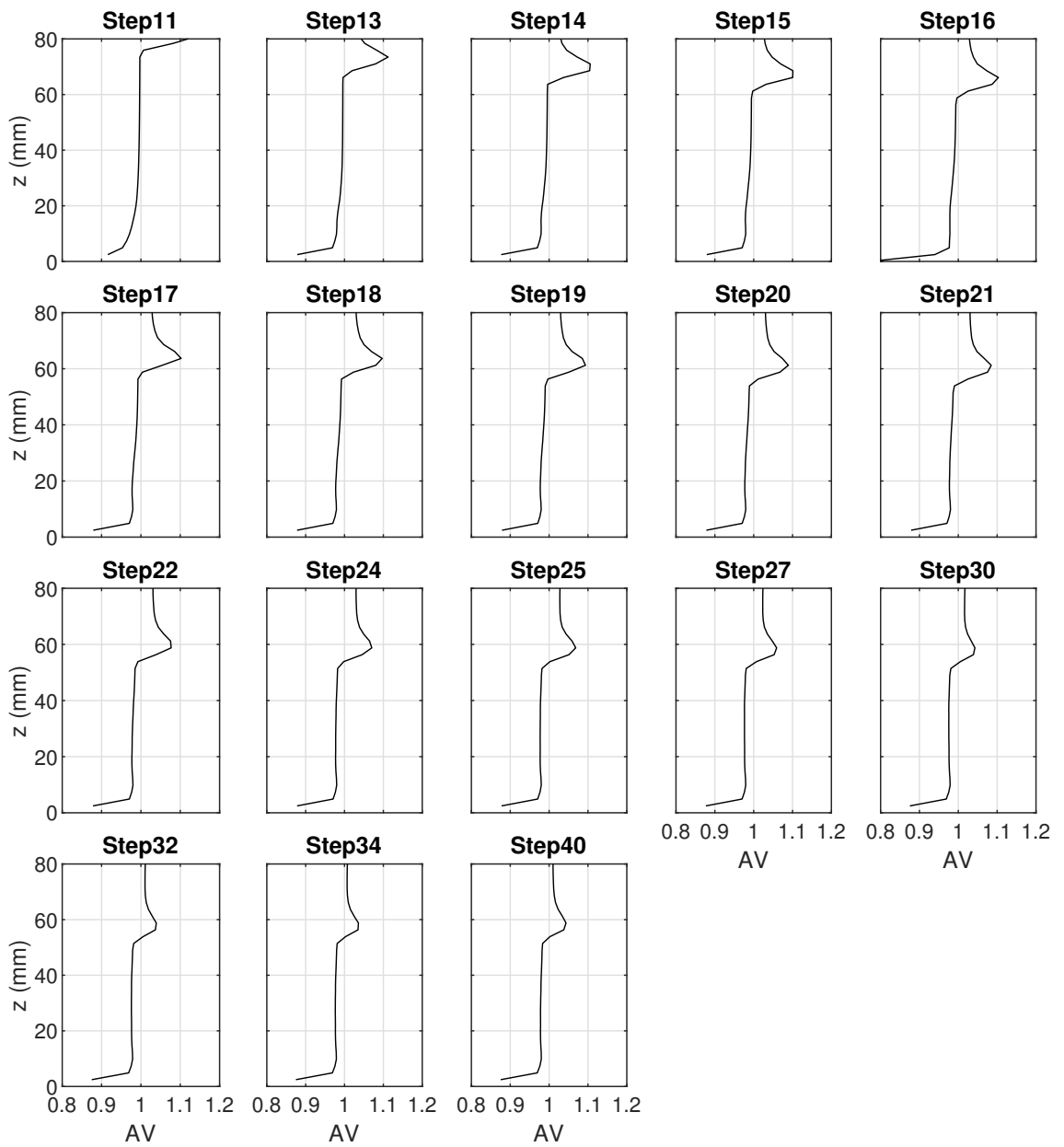


Figure A.6: Asymptotic verification of velocity at numerous locations above the pseudo-bottom. The solutions were calculated for three meshes, using the VOF model with the Realisable $k - \epsilon$ model, at $Q = 180$ l/s

A. ADDITIONAL INFORMATION FOR CHAPTER 5

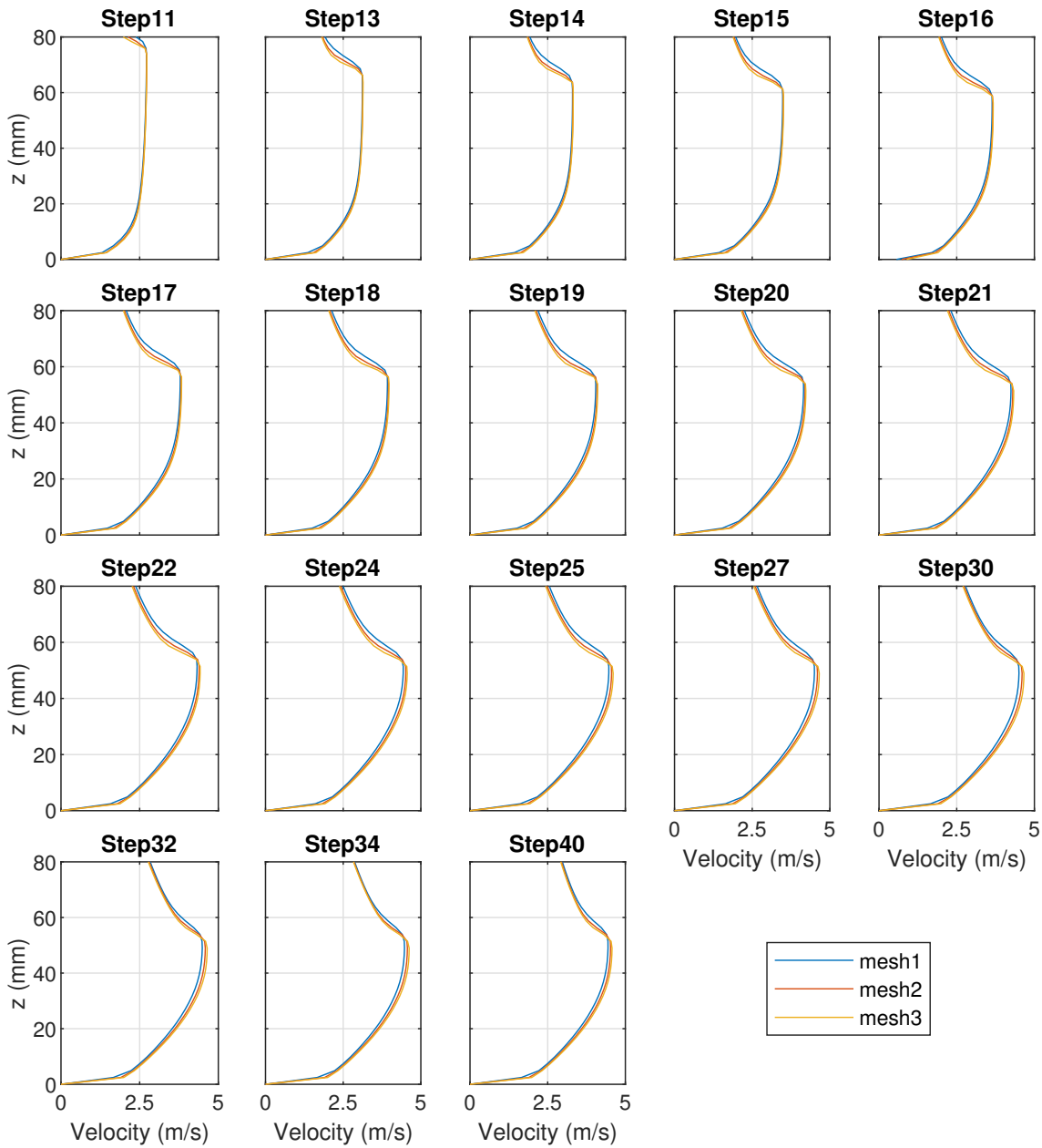


Figure A.7: Velocity data for three meshes at numerous locations above the pseudo-bottom. The solutions were calculated using the VOF model with the Realisable $k - \epsilon$ model, at $Q = 180$ l/s

A.1.3 Mixture Model

A.1.3.1 Velocities

Figures A.8 and A.9 show the GCI values and AV values of the velocities for the mixture model respectively. All of the GCI values are reasonably low, and the AV values are acceptably close to 1 for the velocity solutions to be considered in the asymptotic range.

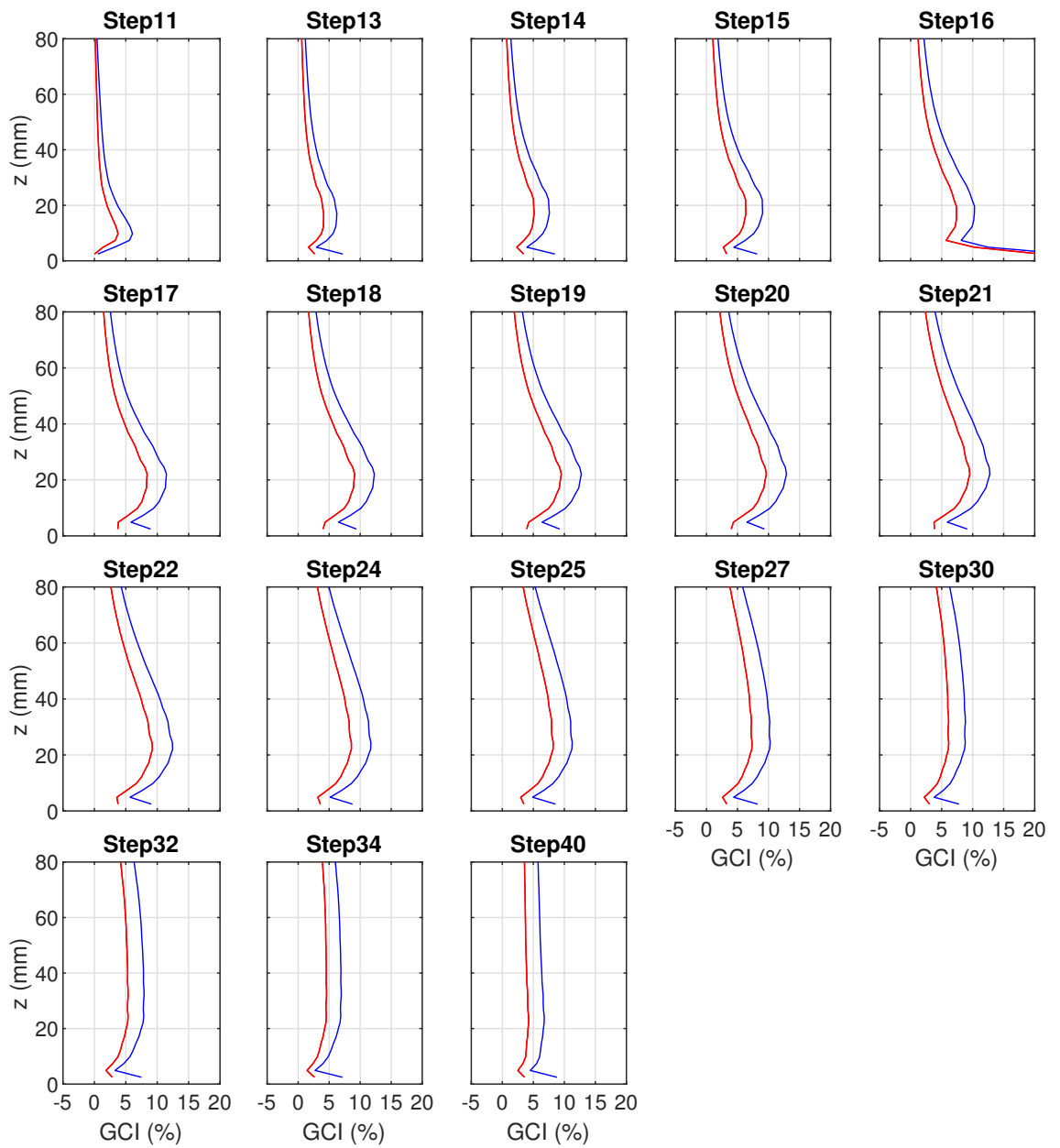


Figure A.8: Grid convergence index error of velocity at numerous locations above the pseudo-bottom. The solutions were calculated for three meshes, using the mixture model with the Realisable $k - \epsilon$ model, at $Q = 180$ l/s

A. ADDITIONAL INFORMATION FOR CHAPTER 5

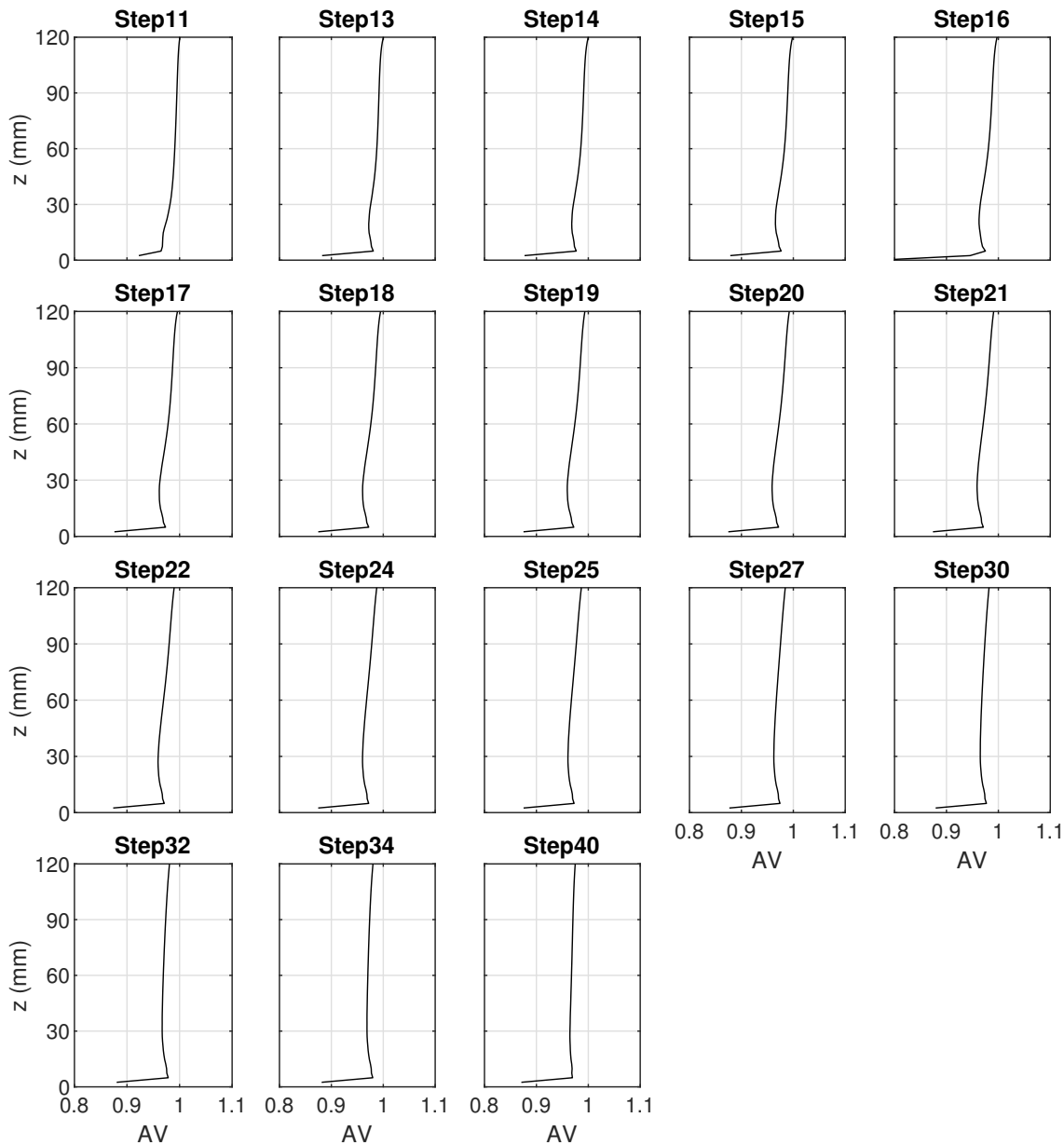


Figure A.9: Asymptotic verification of velocity at numerous locations above the pseudo-bottom. The solutions were calculated for three meshes, using the mixture model with the Realisable $k - \epsilon$ model, at $Q = 180$ l/s

A.1.3.2 AVFs

Figure A.10 shows the GCI values of the AVFs for the mixture model. Some of the GCI values shown are extremely high. This is due to the same reasons that high GCI values were observed in the AVF values for the Eulerian model (section A.1.1.1). Figure A.11 shows the AV values of the AVFs. It can be seen that, although the GCI values are high, in most cases the AV values are reasonably close to 1. Further upstream, the GCI values at the lower depths are further from 1, however. This, again, is due to the reasons described in section A.1.1.1.

A.1 Grid Convergence

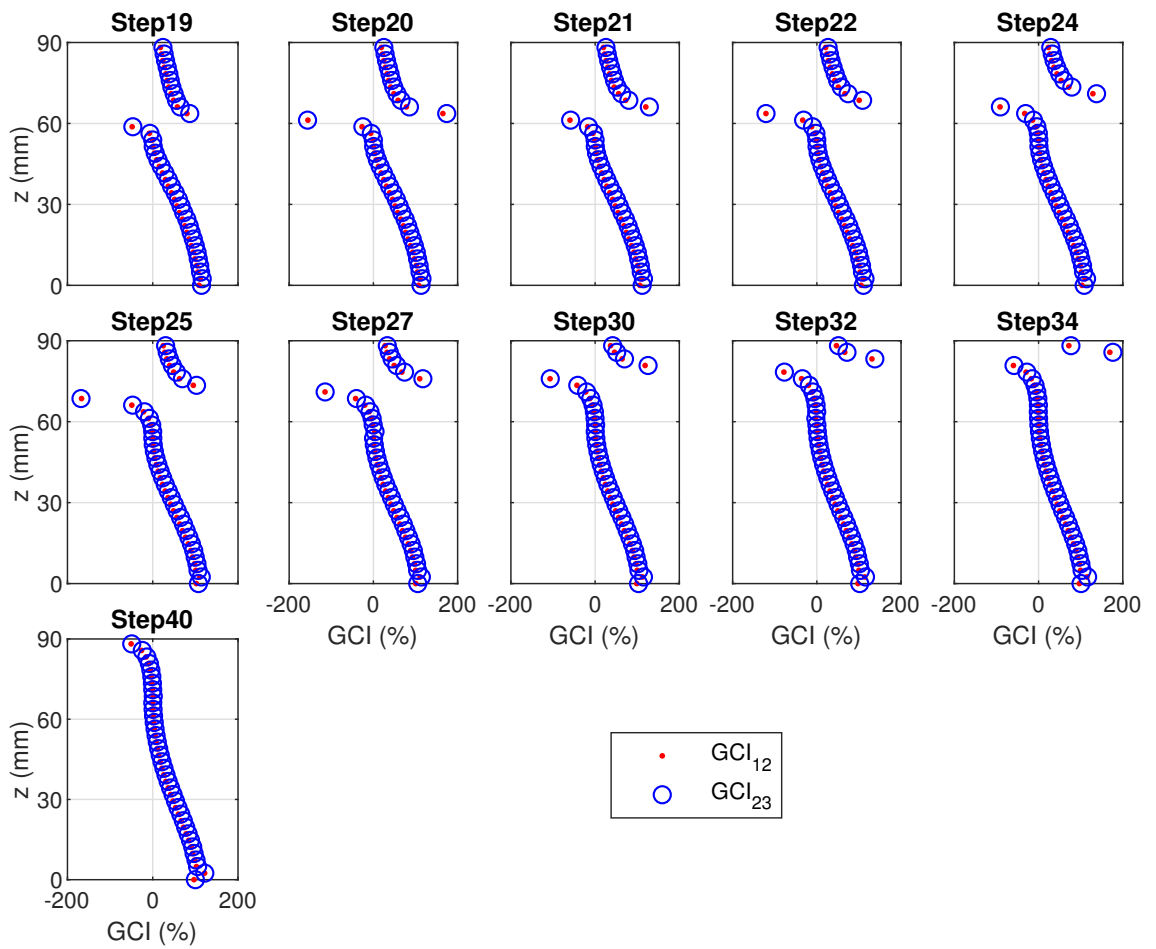


Figure A.10: Grid convergence index error of air volume fraction at numerous locations above the pseudo-bottom. The solutions were calculated for three meshes, using the mixture model with the Realisable $k - \epsilon$ model, at $Q = 180$ l/s

A. ADDITIONAL INFORMATION FOR CHAPTER 5

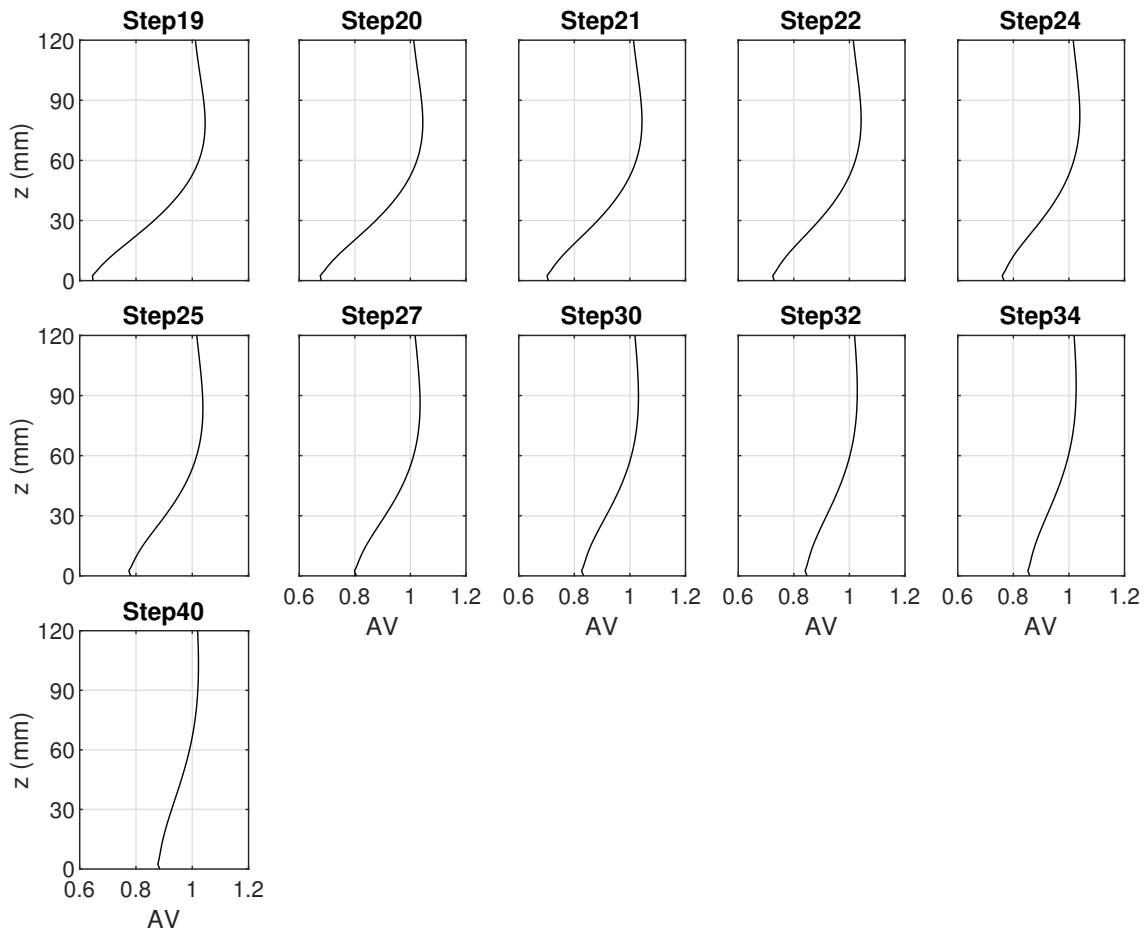


Figure A.11: Asymptotic verification of air volume fraction at numerous locations above the pseudo-bottom. The solutions were calculated for three meshes, using the mixture model with the Realisable $k - \epsilon$ model, at $Q = 180$ l/s

A.2 Time Step Independence

Figures A.12 - A.15 show velocity and AVF profiles for the VOF and mixture models at time steps of 1×10^{-3} and 5×10^{-4} . In all cases the SST $k - \omega$ turbulence model was used. It can be seen that, in all cases, the solutions for different time steps are almost identical. Therefore 1×10^{-3} is an acceptable time step to use for the VOF and mixture models, as reduction of the time step does not significantly alter the solution. All time step size analysis was conducted at a flow rate of $Q = 180$ l/s.

A.2.1 VOF Model

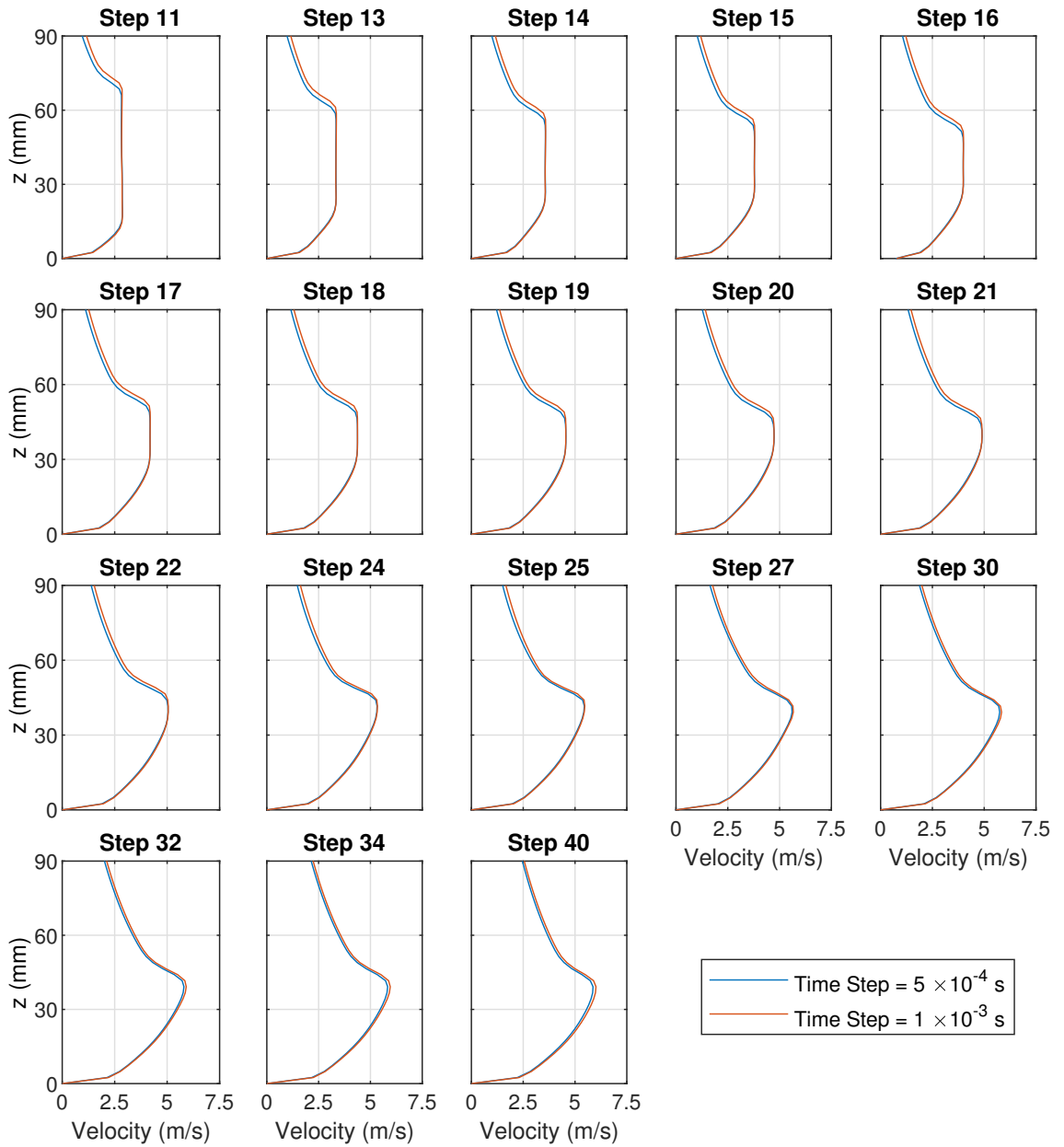


Figure A.12: Velocity profiles calculated using different time steps for the VOF model with the SST $k-\omega$ turbulence model. $Q = 180$ l/s

A. ADDITIONAL INFORMATION FOR CHAPTER 5

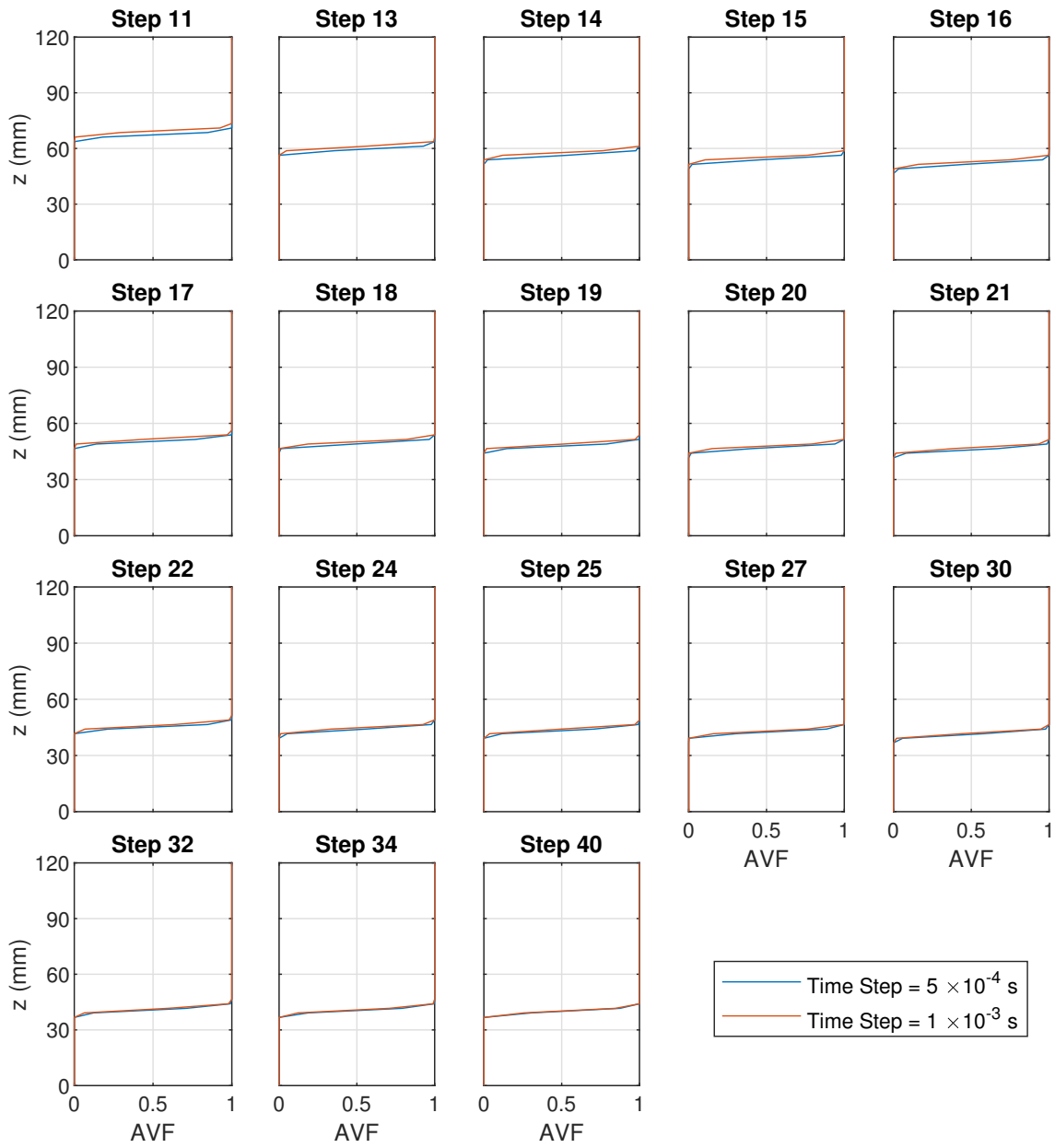


Figure A.13: Air volume fraction profiles calculated using different time steps for the VOF model with the SST $k - \omega$ turbulence model. $Q = 180$ l/s

A.2.2 Mixture Model

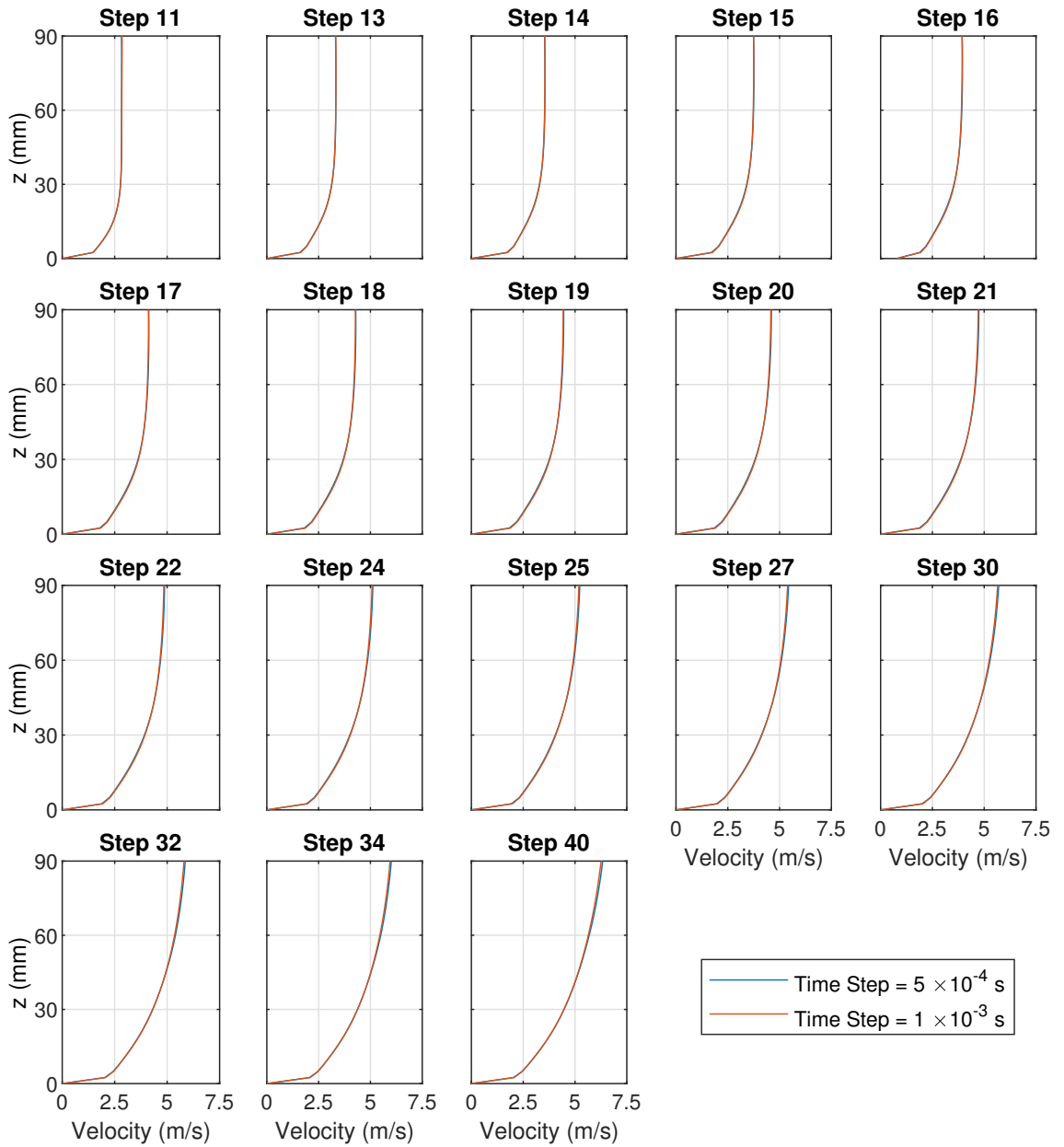


Figure A.14: Velocity profiles calculated using different time steps for the Mixture model with the SST $k - \omega$ turbulence model. $Q = 180$ l/s

A. ADDITIONAL INFORMATION FOR CHAPTER 5

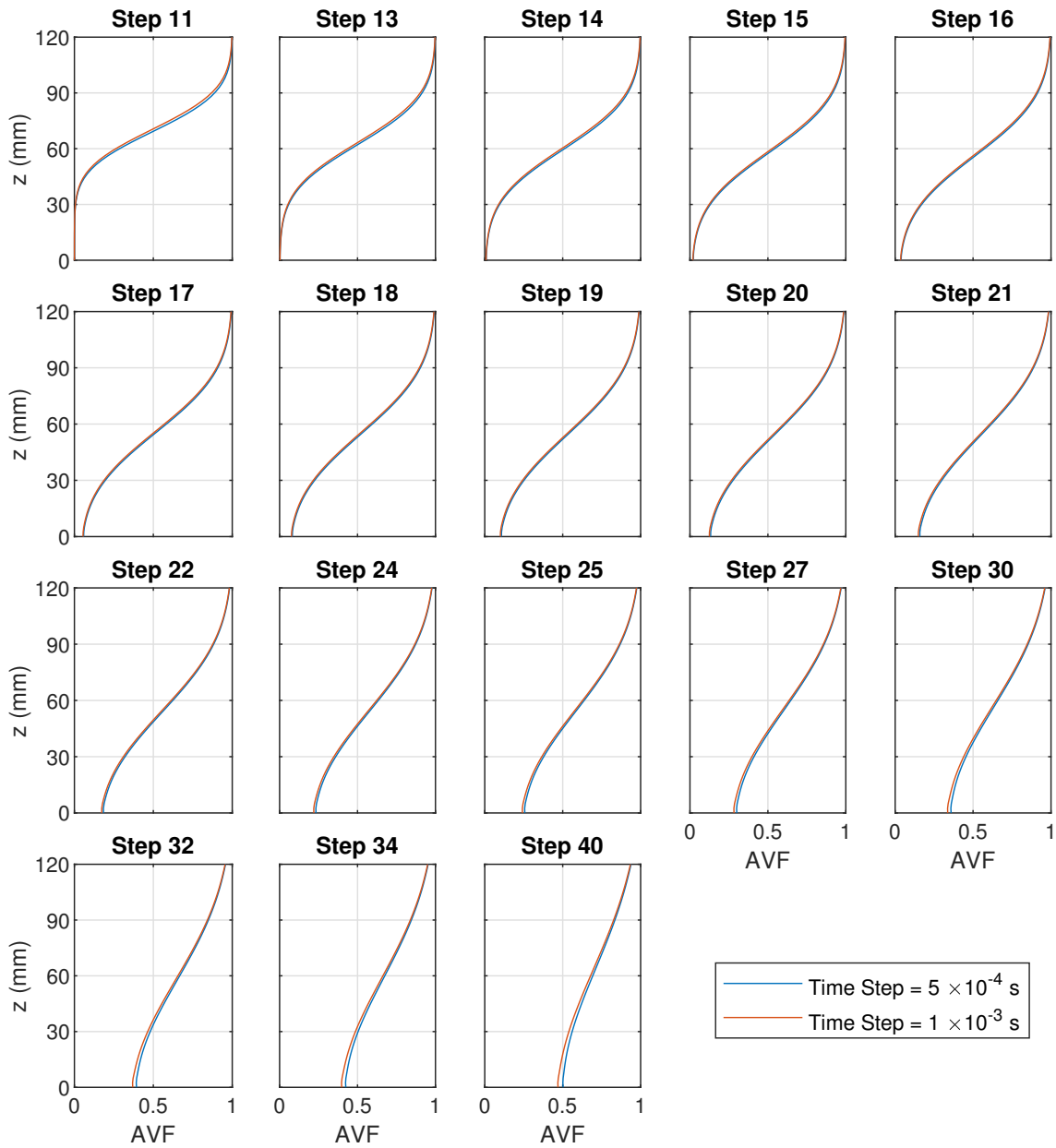


Figure A.15: Air volume fraction profiles calculated using different time steps for the mixture model with the SST $k - \omega$ turbulence model. $Q = 180$ l/s

A.3 VOF Air Volume Fraction Profiles

Figures A.16 - A.18 show the AVF profiles of the VOF model with a range of turbulence models, and the experimental data, for discharges of $Q = 100, 140$ and 200 l/s. It can be seen that the AVF profiles are not predicted accurately as the VOF model does not predict air entrainment. This is discussed further in chapter 5.3.3.2.

A.3 VOF Air Volume Fraction Profiles

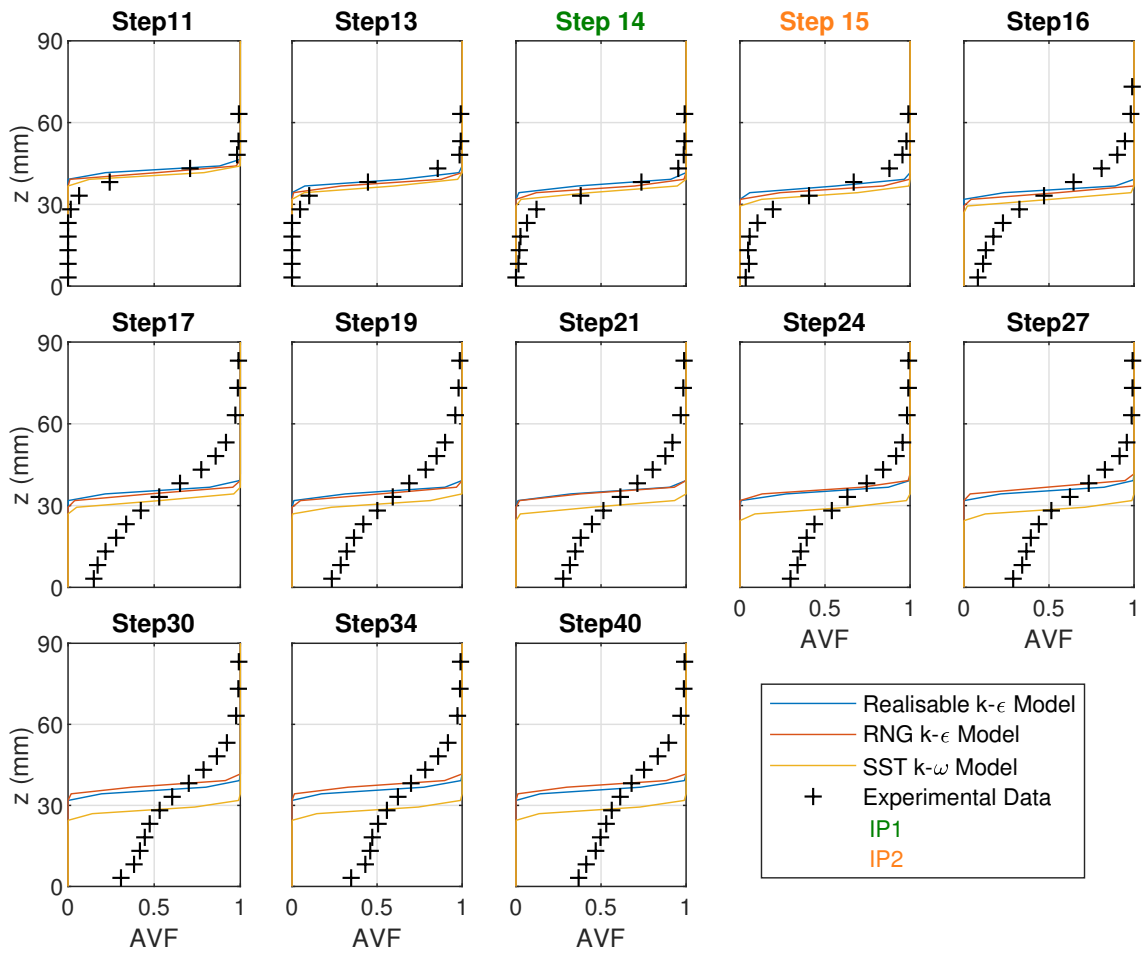


Figure A.16: Comparison of experimental and numerical air volume fraction profiles for $Q = 100$ l/s. Numerical data is shown for the VOF model with various turbulence models. The experimental inception point locations, IP1 and IP2, are indicated by the colour of the title of the subplots. Note that at $AVF = 0$ and $AVF = 1$, the numerical AVF values are exactly 0 and 1 so overlap one another

A. ADDITIONAL INFORMATION FOR CHAPTER 5

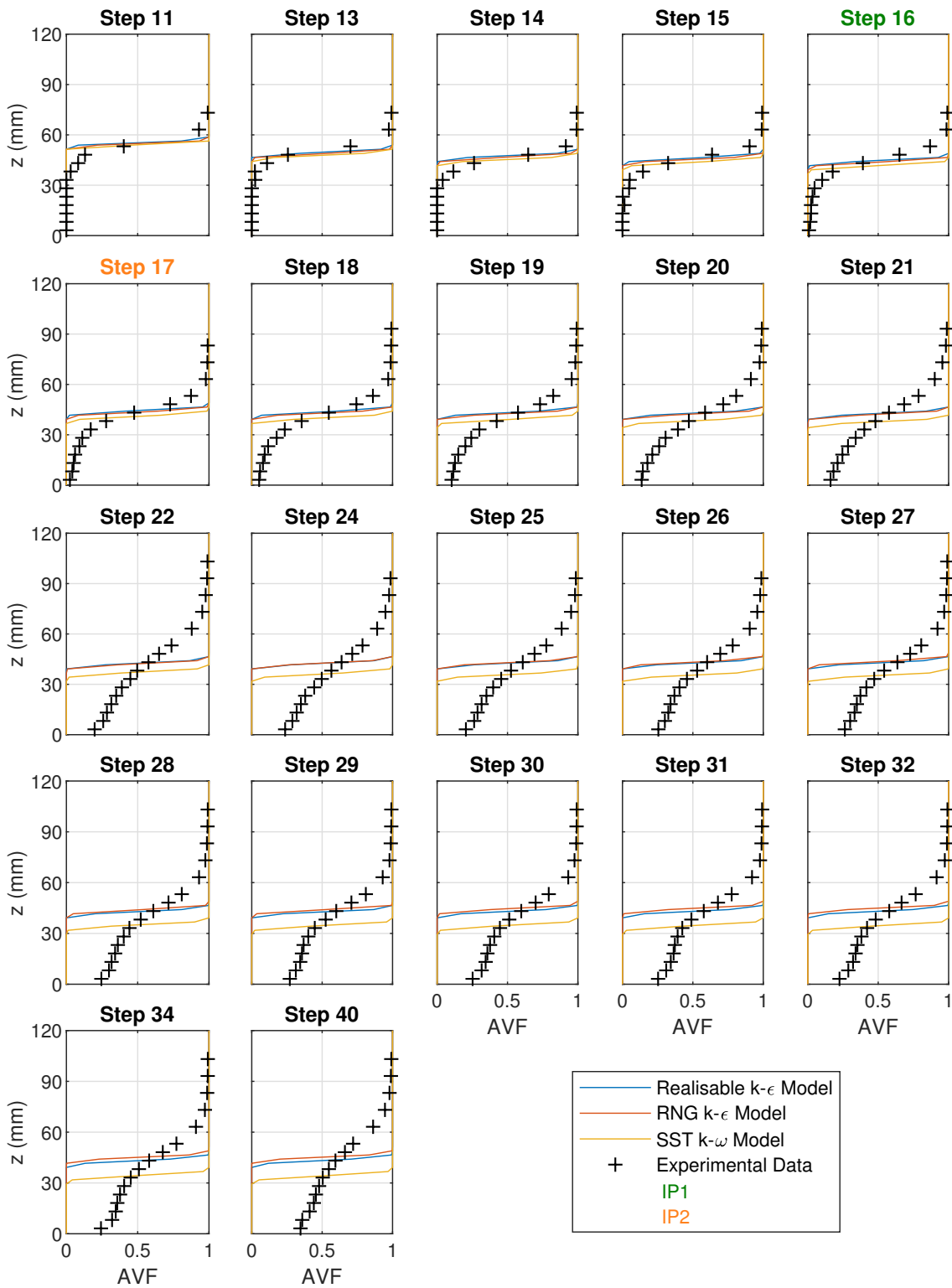


Figure A.17: Comparison of experimental and numerical air volume fraction profiles for $Q = 140$ l/s. Numerical data is shown for the VOF model with various turbulence models. The experimental inception point locations, IP1 and IP2, are indicated by the colour of the title of the subplots. Note that at $AVF = 0$ and $AVF = 1$, the numerical AVF values are exactly 0 and 1 so overlap one another

A.3 VOF Air Volume Fraction Profiles

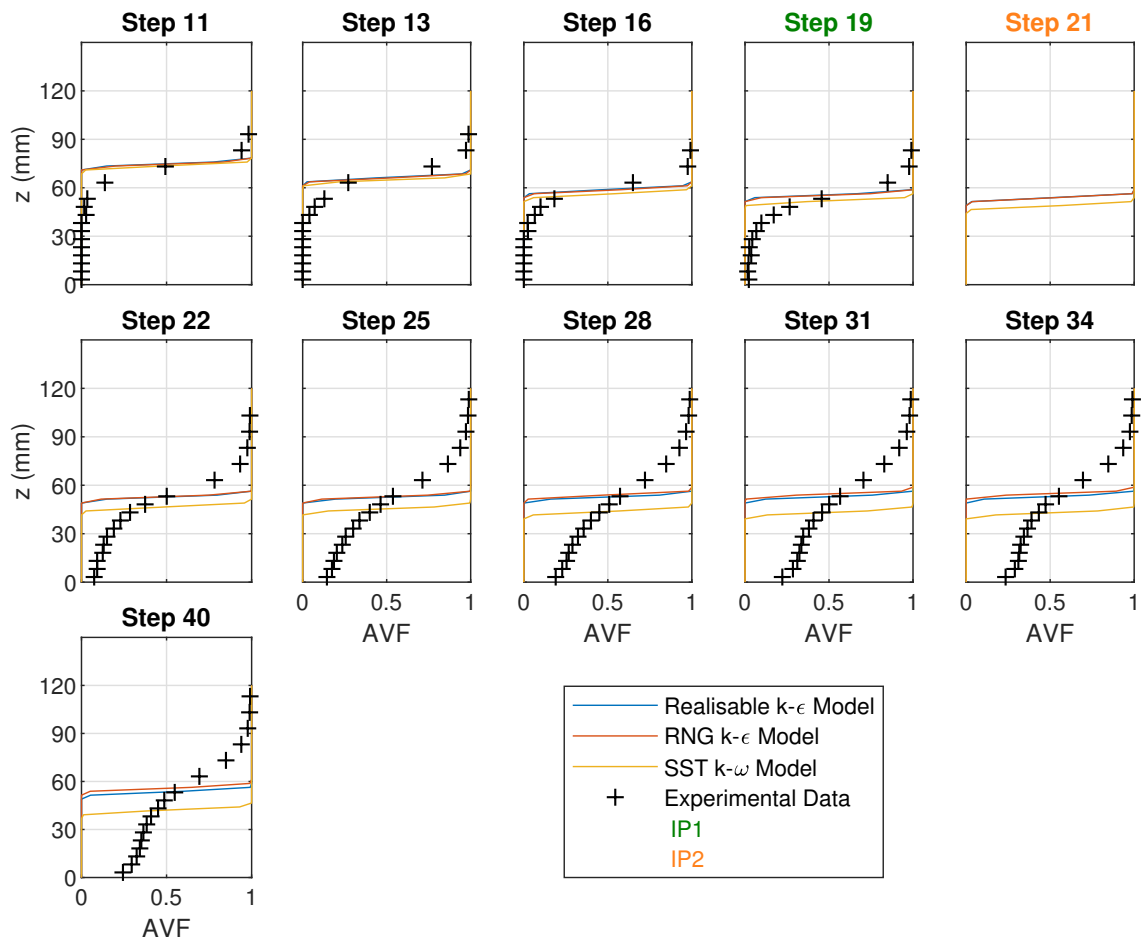


Figure A.18: Comparison of experimental and numerical air volume fraction profiles for $Q = 200$ l/s. Numerical data is shown for the VOF model with various turbulence models. The experimental inception point locations, IP1 and IP2, are indicated by the colour of the title of the subplots. Note that at $AVF = 0$ and $AVF = 1$, the numerical AVF values are exactly 0 and 1 so overlap one another

APPENDIX B

Additional Information for Chapter 6

B. ADDITIONAL INFORMATION FOR CHAPTER 6

This appendix contains additional information on the grid convergence and time step independence studies, which were conducted for numerical modelling of the University of Leeds stepped spillway, as presented in chapter 6.

B.1 Grid Convergence

B.1.1 Pressure

Figures B.1 and B.2 shows pressure data for meshes 1, 2 and 3, at different locations within the cavities of steps 2, 5 and 12, for both the VOF and mixture models, with the Realisable $k - \epsilon$ model. The GCI data and asymptotic verification (AV) data at each location is also presented. The grid convergence results for each multiphase model are similar to those of the Eulerian model, which are presented in chapter 6. The pressure profiles for each mesh are extremely close. In certain positions, the GCI errors are large and the AV values are not close to 1. However, as there is little variation in the pressure profiles for each mesh, further refinement of the computational mesh is unlikely to produce significantly different pressure profiles. This is discussed in more detail in chapter 6.

B.1 Grid Convergence

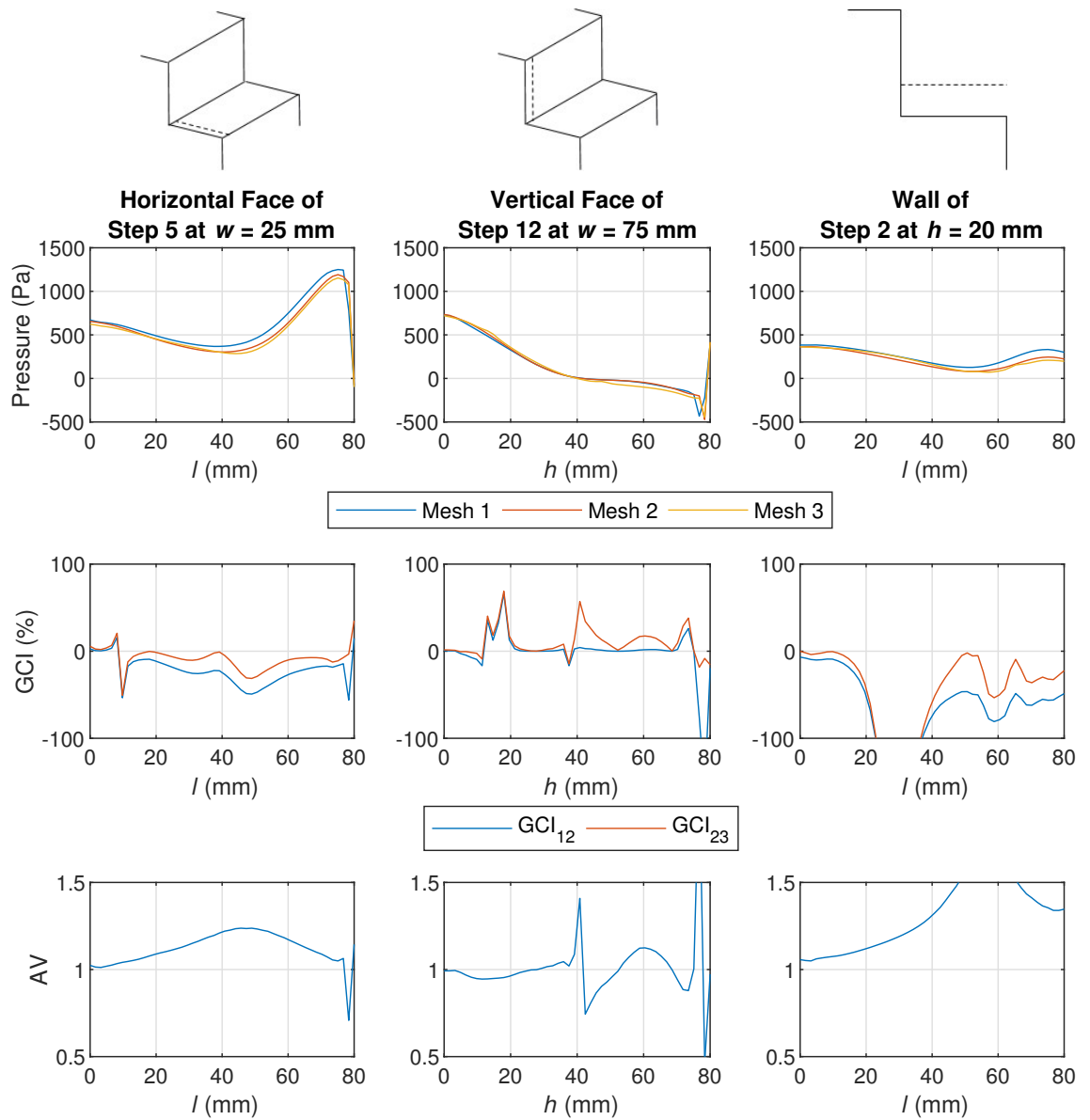


Figure B.1: Grid convergence pressure data for three meshes at several locations within the spillway, calculated using the VOF multiphase model with the Realisable $k - \epsilon$ turbulence model. The pressure data, grid convergence index error and asymptotic verification values are displayed

B. ADDITIONAL INFORMATION FOR CHAPTER 6

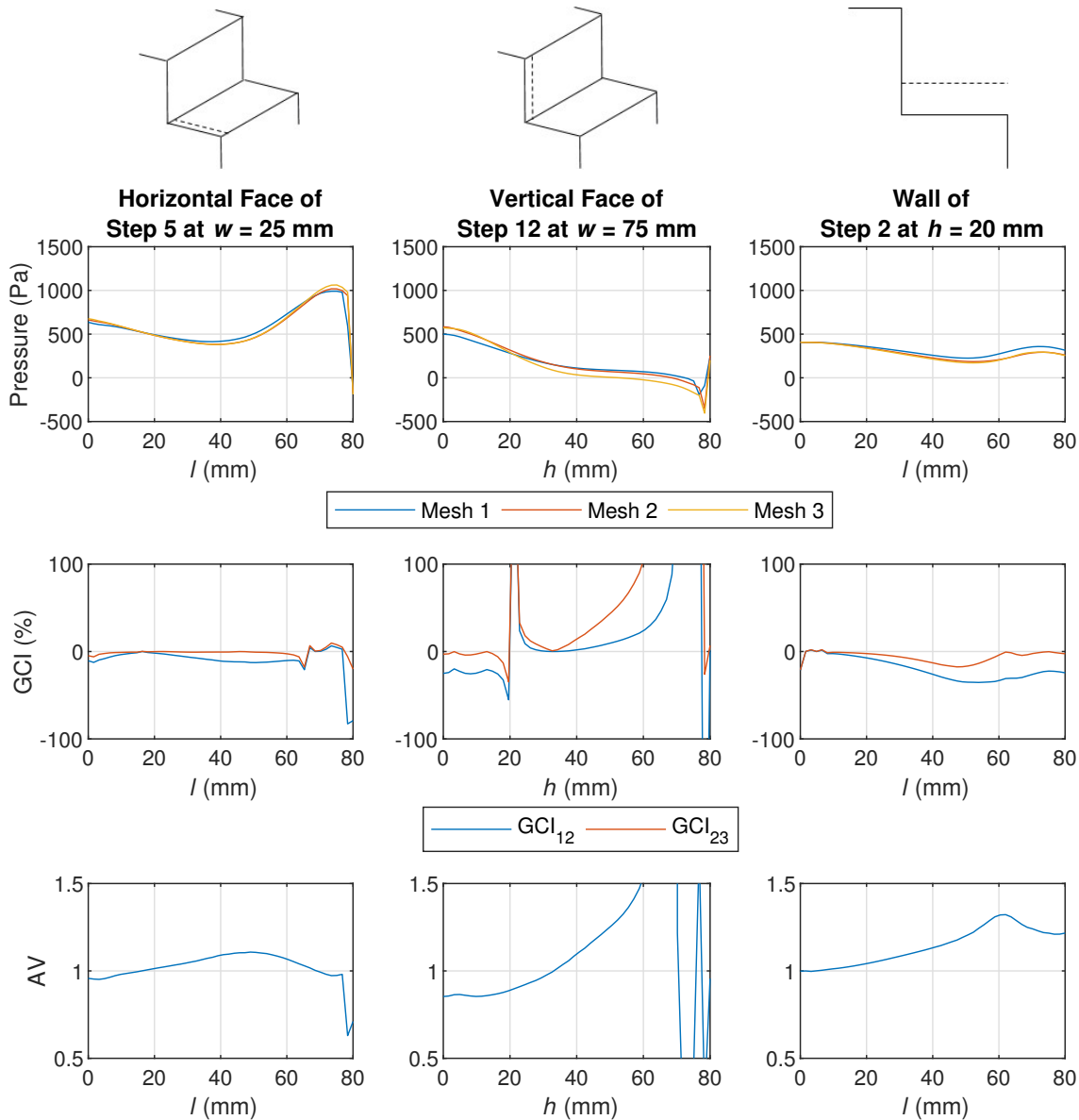


Figure B.2: Grid convergence pressure data for three meshes at several locations within the spillway, calculated using the mixture multiphase model with the Realisable $k - \epsilon$ turbulence model. The pressure data, grid convergence index error and asymptotic verification values are displayed

B.1.2 Flow depths

Figures B.3 and B.4 show the flow depths for the three meshes, as well as the GCI errors and AV values, for the VOF and mixture models with the Realisable $k - \epsilon$ model, at the centreline of the spillway. The flow depth grid convergence results for each multiphase model are also similar to those of the Eulerian model. There is a noticeable difference in the flow depths predicted with the three meshes, and there are extremely large GCI errors in some locations, especially with the mixture model. However, the AV values are very close to 1 in both cases,

B.1 Grid Convergence

which suggests that further refinement of the mesh would not significantly alter the predicted flow depths. Again, refer to chapter 6 for more details on this.

The pressure and flow depth grid convergence results for the VOF and mixture models confirm that mesh 2 was suitable for numerical modelling of the University of Leeds stepped spillway.

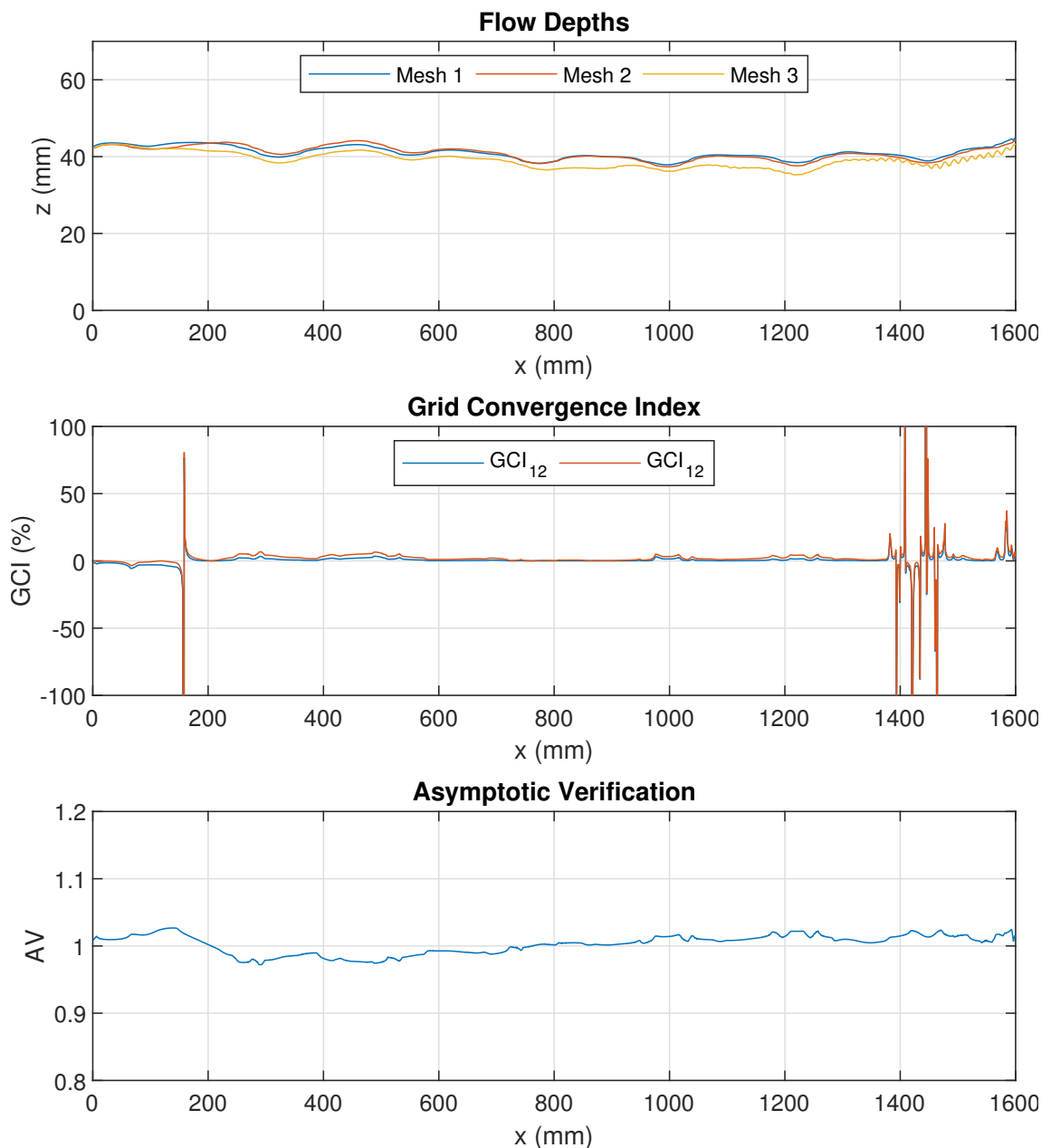


Figure B.3: Grid convergence flow depth data for three meshes, calculated using the VOF multiphase model with the Realisable $k-\epsilon$ turbulence model. The pressure data, grid convergence index error and asymptotic verification values are displayed. Flow depths are displayed at the centreline of the spillway

B. ADDITIONAL INFORMATION FOR CHAPTER 6

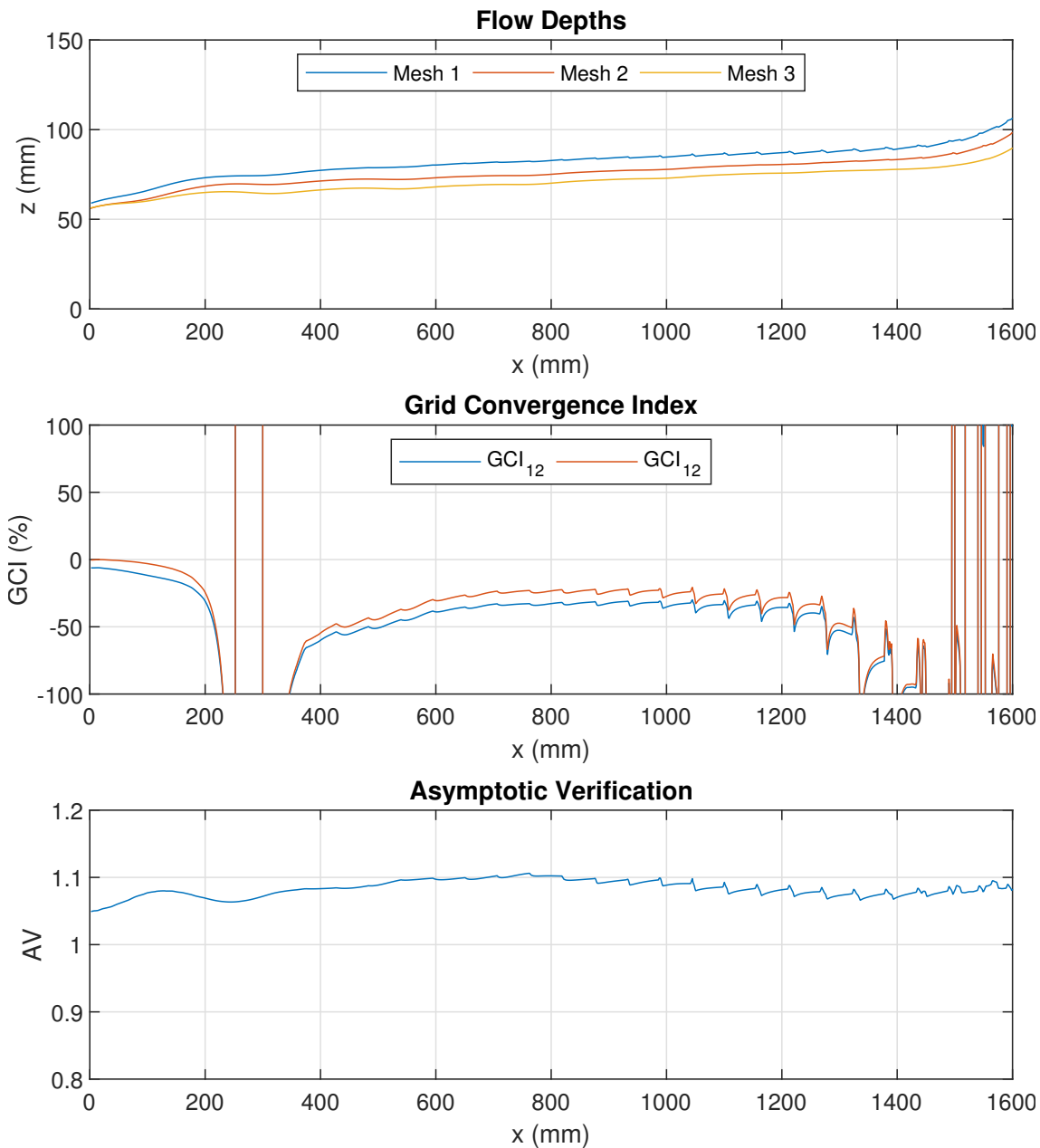


Figure B.4: Grid convergence flow depth data for three meshes, calculated using the mixture multiphase model with the Realisable $k - \epsilon$ turbulence model. The pressure data, grid convergence index error and asymptotic verification values are displayed. Flow depths are displayed at the centreline of the spillway

B.2 Time Step Independence

This section presents data from the time step independence study, which was conducted for numerical modelling of the University of Leeds spillway, for the VOF and mixture models. Modelling was conducted using time steps of 1×10^{-3} s and 5×10^{-4} s and in all cases the Realisable $k - \epsilon$ turbulence model was used.

B.2 Time Step Independence

Figures B.5 and B.6 show the pressures predicted by the VOF and mixture models, using the two time steps investigated, in the same locations that were considered in the grid convergence analysis. Figures B.7 and B.8 show the flow depths predicted by the VOF and mixture models, using the two different time steps investigated, at the centreline of the spillway. All figures show that the pressures and flow depths predicted using the two different time steps are almost identical. Therefore a time step of 1×10^{-3} s was used for numerical modelling of the University of Leeds stepped spillway.

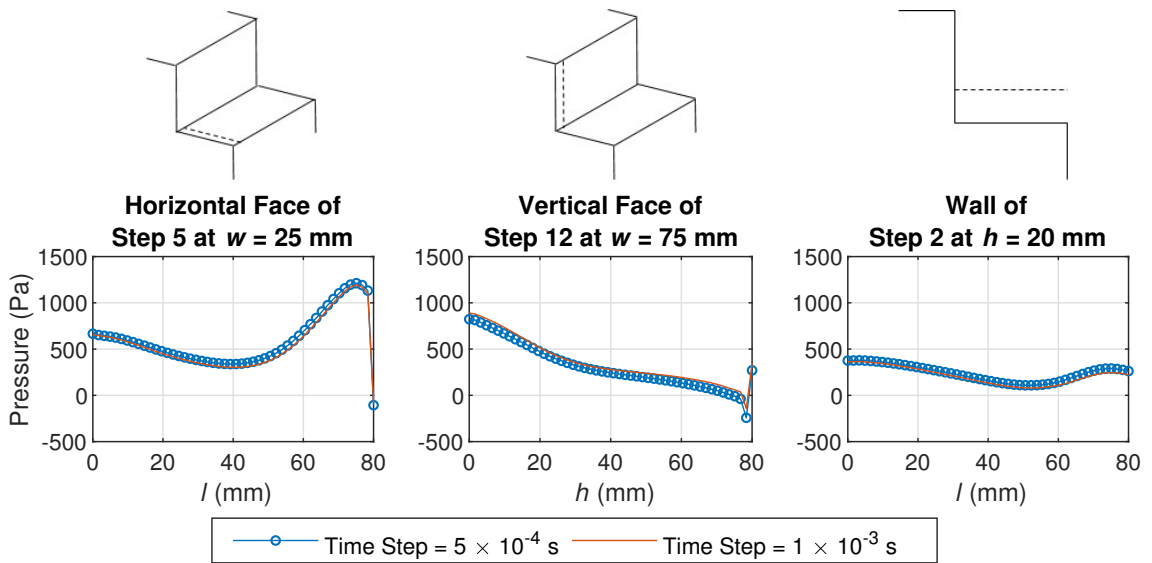


Figure B.5: Pressure data at several locations within the spillway, calculated using two different time steps. The VOF multiphase model with the Realisable $k - \epsilon$ turbulence model was used for numerical modelling

B. ADDITIONAL INFORMATION FOR CHAPTER 6

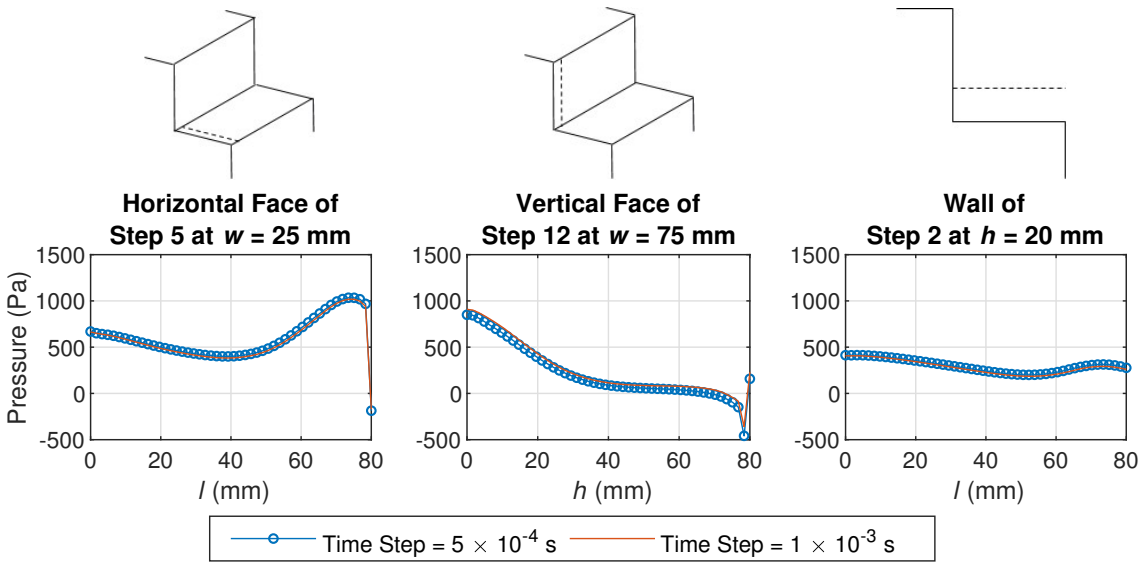


Figure B.6: Pressure data at several locations within the spillway, calculated using two different time steps. The mixture multiphase model with the Realisable $k - \epsilon$ turbulence model was used for numerical modelling

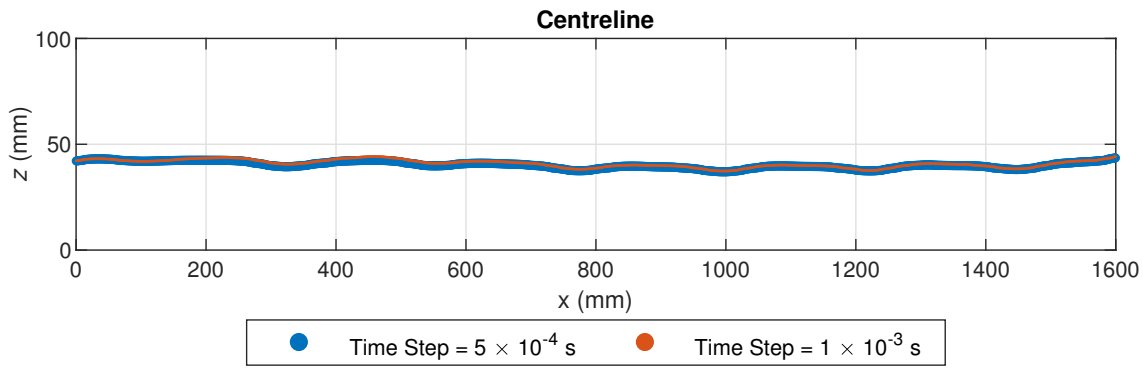


Figure B.7: Flow depth data calculated using two different time steps. The VOF multiphase model with the Realisable $k - \epsilon$ turbulence model was used for numerical modelling. Flow depths are displayed at the centreline of the spillway

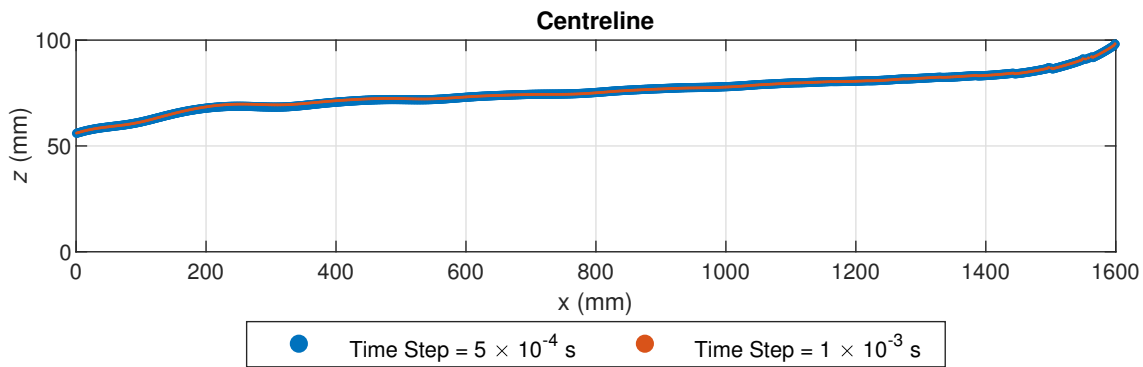


Figure B.8: Flow depth data calculated using two different time steps. The mixture multiphase model with the Realisable $k - \epsilon$ turbulence model was used for numerical modelling. Flow depths are displayed at the centreline of the spillway

B.3 3D Free-Surface Profiles

Figure B.9 shows the isosurfaces of y_{90} for the VOF, mixture and Eulerian models with the Realisable $k - \epsilon$ and RNG $k - \epsilon$ turbulence models at $Q = 15$ l/s. It can be seen that all combinations of multiphase model and turbulence model predicts a 3D free-surface, due to the relatively narrow width of the channel. The transient splashing predicted by the VOF model with the SST $k - \omega$ model (figures 6.6 and 6.14) are not predicted by the VOF model with either of the two $k - \epsilon$ models.

B. ADDITIONAL INFORMATION FOR CHAPTER 6

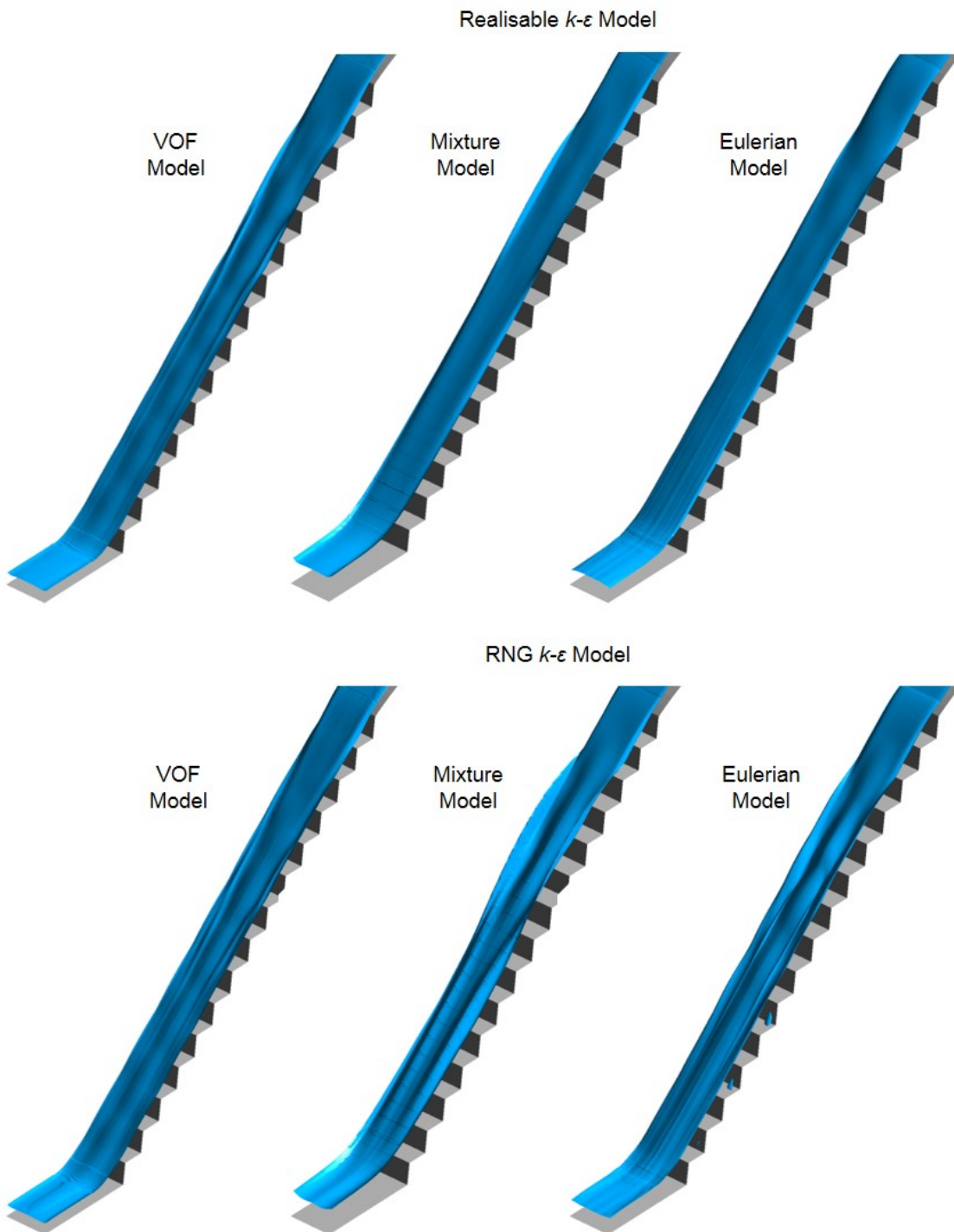


Figure B.9: Isosurfaces at air volume fractions of 0.9 for the VOF, mixture and Eulerian multiphase models, with the Realisable $k-\epsilon$ and RNG $k-\epsilon$ turbulence model, at $Q = 15$ l/s. The images are mirrored at the centreline of the spillway due to the symmetry boundary condition used centreline

APPENDIX C

Additional Information for Chapter 7

C.1 3D Velocity Profiles Above the Steps of the LNEC Stepped Spillway

This appendix contains additional information on the 3D velocity profiles above the steps at the LNEC spillway, as described in chapter 7.

Figure C.1 shows the velocities across the width of the channel, at increasing values of z , at step 15, for the simulation with symmetry boundary conditions at either side of the spillway. Figures C.2 and C.3 show the velocities across the width of the channel, at increasing values of z , at steps 14 and 15, for the simulation with a wall boundary conditions at one side of the spillway and a symmetry boundary condition at the centreline of the spillway. In all figures the mean velocity and standard deviation are shown and the positions of $w=500$ mm and $w=571$ mm are also indicated. It can be seen that at all depths the velocities follow a sinusoidal wave across the width of the channel. The variation in the velocity across the width of the channel reduces significantly as the depth increases, in common with figures 7.13 - 7.15, in chapter 7.

Figures C.1 - C.3 show very similar behaviour to figure 7.16, in chapter 7. In figures C.2 and C.3, significant wall effects can be observed due to the no slip boundary condition used at the wall. It is noticeable that the sinusoidal wave at steps 14 is similar to that at step 15, but with the peaks and troughs of the wave patterns translated by 71 mm (half a wavelength) due to the alternating pattern of cross-stream vortices.

C.1 3D Velocity Profiles Above the Steps of the LNEC Stepped Spillway

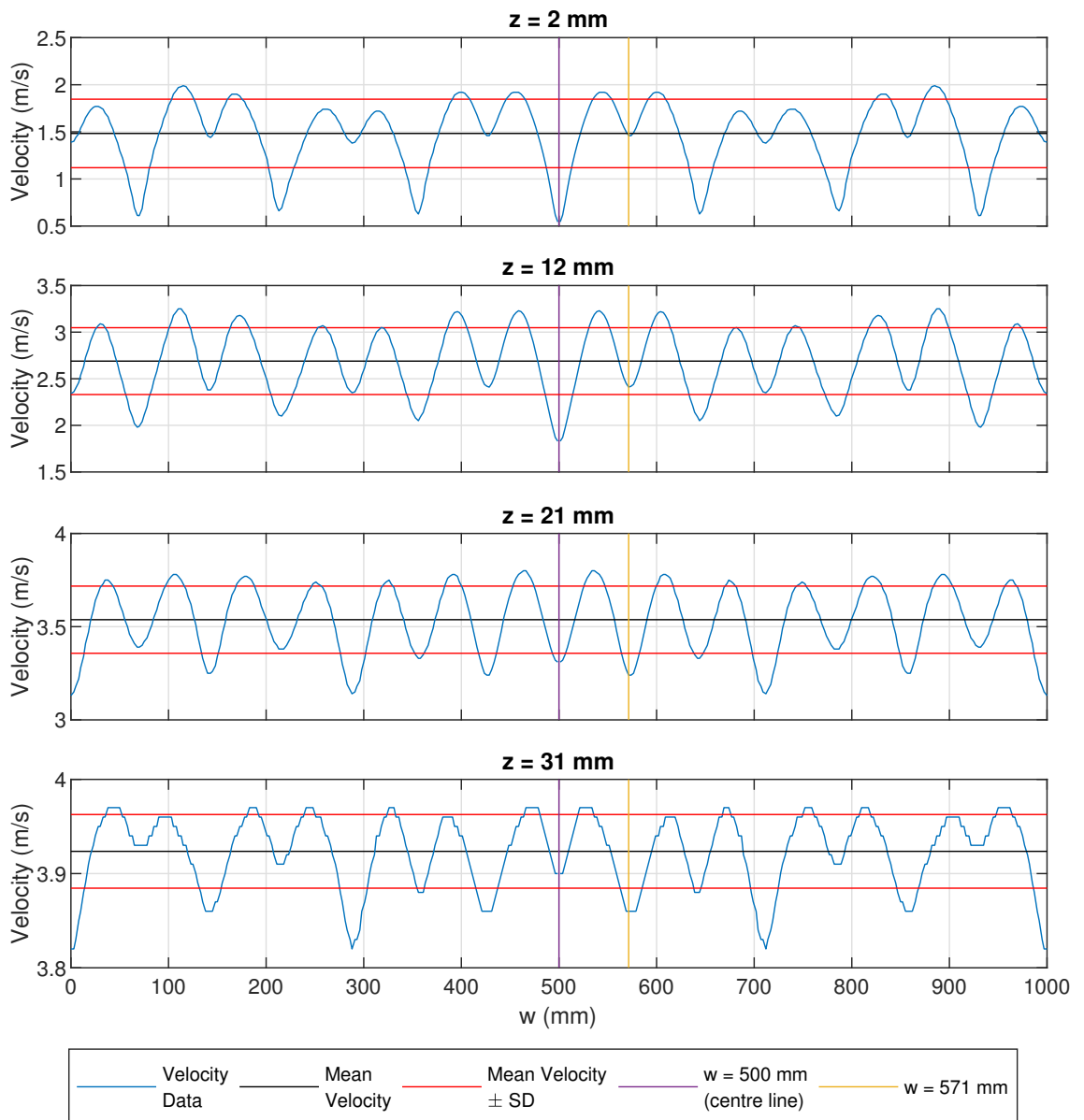


Figure C.1: Velocity profiles across the channel width of step 15, at different values of z , for the 3D simulation of the upstream section of the LNEC spillway using symmetry boundary conditions. The mean velocity and standard deviation are also shown and the locations of $w = 500$ mm and $w = 571$ mm are indicated

C. ADDITIONAL INFORMATION FOR CHAPTER 7

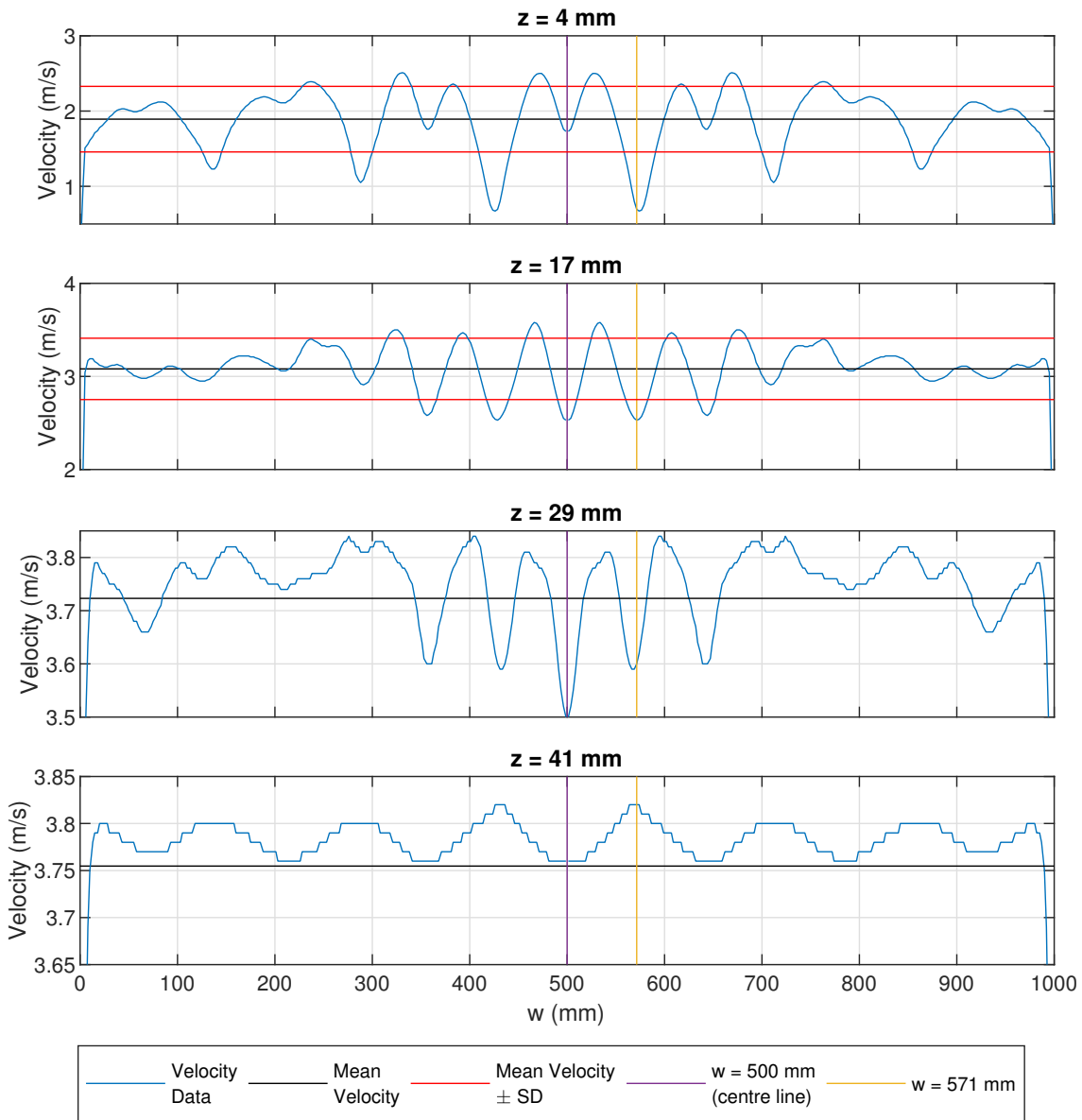


Figure C.2: Velocity profiles across the channel width of step 14, at different values of z , for the 3D simulation of the upstream section of the LNEC spillway using wall boundary conditions. The mean velocity and standard deviation are also shown and the locations of $w=500$ mm and $w=571$ are indicated

C.1 3D Velocity Profiles Above the Steps of the LNEC Stepped Spillway

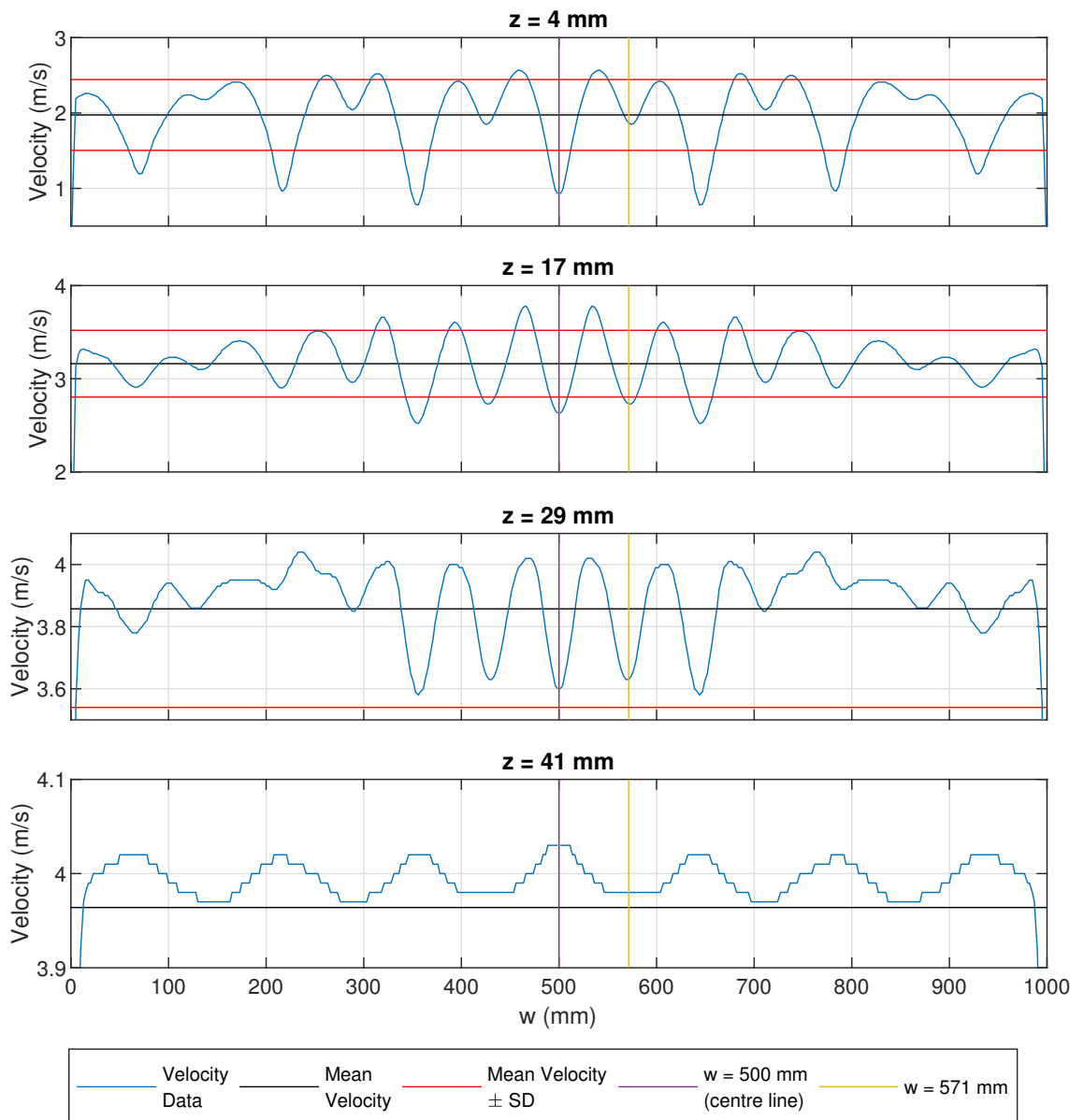


Figure C.3: Velocity profiles across the channel width of step 15, at different values of z , for the 3D simulation of the upstream section of the LNEC spillway using wall boundary conditions. The mean velocity and standard deviation are also shown and the locations of $w = 500$ mm and $w = 571$ mm are indicated